Physics of the Solid State, Vol. 46, No. 1, 2004, pp. 1–4. Translated from Fizika Tverdogo Tela, Vol. 46, No. 1, 2004, pp. 5–9.

Oleg Vladimirovich Losev: Pioneer of Semiconductor Electronics (*Celebrating One Hundred Years since His Birth*)

M. A. Novikov

On May 10, 2003, we celebrated the centenary of the birth date of Oleg Vladimirovich Losev, an outstanding Russian scientist and inventor in the field of radio- and optoelectronics.

In his work at the Nizhni Novgorod Radio Laboratory and later in Leningrad at the Leningrad Central Radio Laboratory and in the physics department of the First Medical Institute in the twenties and thirties of the last century, Losev made a number of important discoveries and inventions that make him a pioneer in semiconductor electronics. It should be noted, however, that the importance of Losev's outstanding scientific achievements is underestimated both in this country and abroad. In connection with the centenary of Losev's birth, it is worth considering in detail and estimating his most outstanding scientific achievements from the modern point of view in order to do this extraordinary scientist, who was ahead of his time, justice.

Losev was born in Tver into the family of a wagon works office worker, retired staff-captain of the Tzar army, and noble man. After he graduated from a Tver non-classical secondary school in 1920, he started to work at the Nizhni Novgorod Radio Laboratory (NNRL), where V.K. Lebedinskiĭ became his supervisor of studies. After NNRL was closed in 1928, Losev, together with other leading collaborators, moved to Leningrad to work at the Central Radio Laboratory (CRL). From 1929 to 1933, at A.F. Ioffe's invitation, Losev carried out investigations at the Ioffe Physicotechnical Institute. From 1937 to 1942, Losev worked at the physics department of the Leningrad First Medical Institute.

On January 22, 1942, Oleg Vladimirovich Losev died of starvation during the Leningrad blockade. The place of his burial is unknown.

Up to the present time, only his works connected with the development of the crystadin were widely known in this country. Losev's first work was devoted to the crystadin and was published in 1922. In that work, Losev showed that, when an additional dc voltage is applied to a crystal detector, it can operate as an amplifier or a generator of electromagnetic waves. In modern terms, this means that in this case a crystalline detector becomes a two-terminal device with a falling current–voltage characteristic.

It should be noted that a generating detector was first demonstrated in 1910 by the Englishman W.H. Eccles. At that time, however, this interesting physical phenomenon did not attract the attention of specialists in the radio field. Evidently, this is connected with the fact that the author explained the mechanism of negative resistance on the basis of heat effects that occur at the metal–semiconductor interface with allowance for the fact that the semiconductor resistance falls with increasing temperature. At that time, it was already known that this mechanism is the basis of the sounding arc, which is used to generate low-frequency radio waves in practical radio engineering. That was the reason why such devices were practically never used at higher frequencies.

Losev's merit consists in that, using the example of a zincite (ZnO) detector, by carrying out a series of very subtle experiments, he showed that in this case heat effects do not play any role and amplification is due to electronic processes at the interface between a metallic

1063-7834/04/4601-0001$26.00 © 2004 MAIK "Nauka/Interperiodica"

tip and a semiconductor crystal. In particular, he discovered that the zincite crystadin can generate and amplify electromagnetic oscillations up to 10 MHz. At that time, this frequency range was not used even for practical purposes. Losev's merit consists in the fact that he applied this phenomenon in practice. He created a series of crystadin radio receivers which were used in a number of state radio stations. Crystadins were especially popular with radio amateurs, who managed to establish even intercontinental radio contacts with the help of simple crystal receivers and transmitters based on a crystadin and energized from batteries with a voltage of several volts. It was the simplicity and practical value of the crystadin that caused a wide wave of interest in it in the world. Newspapers and respectable scientific journals in Europe and America wrote about it as of a sensational invention in the mid 1920s. Many scientists foresaw that the coming revolution in radios would be connected with Losev's crystadin.

Unfortunately, at that time, Losev's discovery was not properly developed. Notwithstanding his heroic efforts, Losev failed to eliminate the main practical drawback of the crystadin, namely, its unstable operation due to mechanical contact of a metal tip with a crystal. Furthermore, in the mid 1920s, the crystadin could not compete with vacuum radio lamps, because that was the period of their most intensive improvement and all the practical problems regarding their usage in radio engineering at that time were solved. These advances, in fact, were due, to a significant degree, to the studies performed at NNRL, where Losev worked.

Despite the efforts of well-known physicists, including Nobel Prize laureate R.A. Millikan, as well as the investigations of Losev himself, the mechanism of the falling current–voltage curve of the crystadin was not puzzled out at that time. Now, it became clear that an understanding of this mechanism could not be gained without quantum mechanics. However, in the mid 1920s, its physical basis had not yet been created and the band theory of semiconductors was developed only in the early 1930s.

Unfortunately, the mechanism of Losev's zincite crystadin has not been explained so far. The point is that, at the present time, about a dozen physical processes are known that lead to the phenomenon of negative resistance. Many specialists link Losev's crystadin effect with Esaki junction, but so far no experiments confirming this hypothesis have been performed. It would be interesting to repeat Losev's experiments with zincite now using modern methods of investigation. This would be especially interesting now as great interest is being shown in this crystal by optoelectronics engineers.

We should reject the opinion of science historians that the interest in Losev's crystadin had completely disappeared by the end of the 1920s. Attempts to use the crystadin were made later as well, but the main point is that Losev's crystadin phenomenon proved that it was possible to create semiconductor devices that can completely substitute for traditional radio lamps. It was in the end of the 1920s that the idea of creating a solid-state analog of a vacuum triode appeared.

As it has been learned recently that this idea was not foreign to Losev. In 1929–1931, while working on the experimental base of the Leningrad Physicotechnical Institute, he continued his studies (following the suggestion of A.F. Ioffe) of the new physical effects in semiconductors that he discovered when working at NNRL. In particular, he investigated a semiconductor device identical to the structure of a point transistor. The operation of this device is known to be based on the control of current flowing between two electrodes with the help of an auxiliary electrode. Losev actually observed this effect, but, unfortunately, the total gain factor was insufficient to amplify a signal. However, for this purpose, he used only a silicized carbon crystal (SiC) and did not use a zincite crystal (ZnO), which has significantly better characteristics in a crystadin amplifier.

Until recently, it was considered that, after being forced to resign from the Physicotechnical Institute, Losev did not return to the idea of semiconductor amplifiers. However, the existence of a very interesting document, written by Losev himself, has recently become known. This document is dated July 12, 1939, and is currently stored at the Polytechnic Museum. The document, titled *Oleg Vladimirovich Losev's Biography*, contains interesting facts from his life and a list of his scientific achievements. The following lines are of special interest: "It has been established that a three-electrode system analogous to a triode and showing negative resistance, like a triode, can be built on the basis of semiconductors. At the present time, I am preparing these findings for publication."

Unfortunately, the fate of these findings has not been established so far; they could have completely changed the notion of transistor invention history, one of the most revolutionary inventions of the twentieth century

Other important scientific merits of Losev are connected with his investigations in the field of electroluminescence and light-emitting diodes (LEDs). Losev's investigations in the field of electroluminescence have been well known since the 1920s, and those studies are referred even now. In the 1920s, the phenomenon of electroluminescence was even called Losev light (Lossew Licht) in the West for some time. For this reason, Losev is justly considered abroad to be a pioneer in the field of electroluminescence. However, it is not known whether Losev was the inventor of LED. He was the first to see huge perspectives in such light sources and point out their high brightness and high response speed. He is also the owner of the first patent for the invention of a device with an electroluminescent light source (light relay).

At the end of the 1970s, when electroluminescent light sources began to be widely used in the West, H.F. Ives came across a small article by H.J. Round

"A Note on Carborundum" in *Electrical World*, **49**, 308 (1907), in which the author (research worker at the Marconi laboratory) reported that he had observed luminescence from a silicized carbon (SiC) detector contact under the influence of an external electric field. There was no other information about the luminescence and about the physics of this phenomenon in the article. At that time, nobody paid any attention to it, and this article did not influence subsequent investigations in the field of electroluminescence. However, some specialists, including Russian ones, consider this author to be the discoverer of the electroluminescence phenomenon. As for Losev, he not only discovered this phenomenon independently, but also carried out a detailed investigation of it on the example of a silicized carbon (SiC) crystal. For example, he discovered that in this case there are two different physical phenomena observed at different contact voltage polarities. Losev discovered not only injection electroluminescence (luminescence II in his terms), which at present time forms the basis of light-emitting diodes and semiconductor lasers, but also the electroluminescence that is emitted before the onset of breakdown (luminescence I), which is also widely used in creating new electroluminescent displays. Later on, luminescence I was also discovered by French scientist G. Destriau, and now it is called the Destriau effect, though Destriau himself attributed the discovery to Losev. Furthermore, Losev managed to advance very far in understanding the physics of these phenomena even when the band theory of semiconductors had not been discovered yet. Thus, modern supporters of attributing the discovery to Round hardly have the right to dispute the outstanding contribution of our fellow countryman to this field of physics and especially to the invention of LED. For example, Popov and Marconi are justly considered to be the inventors of the radio, though it is well known that Hertz was the first to observe radio waves. There are many analogous examples in the history of science.

In evaluating Losev's research activities, it should be noted that, above all, he was an outstanding physicist and experimentalist. Although he worked under exceptionally difficult conditions in the early 1920s, he achieved remarkable scientific results. E.E. Loebner, a well-known American scientist in the field of electroluminescence, wrote the following about Losev in his article "Subhistory of the Light-Emitting Diode," the most part of which was devoted to an analysis of Losev's contribution to the study of electroluminescence and LEDs: "By his pioneering investigations in the field of Light-Emitting Diodes and photodetectors, he contributed to the future progress of light communication. His investigations are so accurate and his publications are so clear that it is easy to imagine now what was happening in his laboratory at that time. His intuitive choice and the art of experiment are astonishing" (see list of publications dedicated to Losev).

It should be added that Losev worked at a time when the physics of semiconductors was basically nonexistent, because quantum solid-state theory had not been created yet (it appeared only ten years later). Now it is clear that progress in semiconductor electronics is impossible without quantum theory of the semiconductor structure. Furthermore, at that time, there was practically no technical basis for experimental investigations in the field of the physics of semiconductors. Even greater amazement comes from Losev's intuition, his art and experimental talent, which allowed him to achieve remarkable results.

In particular, from the very beginning, he saw the common physical nature of the crystadin and injection luminescence, thereby being far ahead of his time. The point is that, after Losev, investigations of semiconductor detectors of electroluminescence were conducted separately and independently by different groups of scientists. Some of them studied only the phenomena connected with rectification in semiconductor structures, which led to the invention of transistors in 1947 and tunnel diodes.

Independently, investigations of electroluminescent light sources were performed. An analysis of their results shows that, for over twenty years after Losev's studies, no progress was achieved toward an understanding of the physics of this phenomenon. The majority of the studies carried out over this period were devoted to devices based on pre-breakdown electroluminescence with the aim of creating different kinds of optic displays. Only in 1951 (almost thirty years after Losev) did K. Lehovec with collaborators show that rectification and electroluminescence have a common nature linked with the behavior of charge carriers in *p*–*n* junctions and that electroluminescence is connected with the recombination of electrons and holes in these junctions. It should be noted that, in his work, Lehovec refers first of all to all Losev's works devoted to electroluminescence.

It was this point of view that allowed Losev to significantly advance the understanding of the physics of semiconductor contacts. By combining the optical and electrophysical methods of investigation of these contacts and using a silicized carbon contact as an example, he was able to develop a layered model of its structure with a detailed description of each layer at the end of the 1920s. It is surprising that this model differs only insignificantly from the modern model.

Highly valuing Losev's achievements, we should note the following fact. Losev stood at the beginning of the probe microscopy of semiconductor structures, which has recently drastically changed both research methods and the technology of semiconductor structures. In 1930–1931, Losev carried out, at a very high experimental level, a series of experiments with angle laps, which expand the zone under investigation, and with a system of electrodes, which were included into a compensation-measuring circuit in order to measure the potentials at different points of a cross section of the layered structure. By moving a thin metal tip across a

lap, he showed, to an accuracy of 1 μm, that the surface layer of a crystal has a complex structure. He revealed that there is a 10-μm-thick active layer in which injection electroluminescence occurs. Based on his investigations, Losev assumed that the reason for unipolar conductivity is the difference between the conditions under which electrons move on either side of the active layer (in modern terms, different types of conductivity). By experimenting with three or more probe electrodes located in these regions, he confirmed this assumption.

From the modern point of view, these investigations are undoubtedly Losev's greatest achievement as a physicist. His invention of LEDs (according to Losev's terminology, electronic generators of light) is difficult to overestimate. LEDs are the undoubted basis of modern optoelectronics. Undoubtedly, the significance of the discovery of LEDs can be compared to that of the transistor or laser in its influence on scientific and technical progress.

It should also be noted that Losev made other important discoveries less known even to specialists. He made a considerable contribution to semiconductor materials technology as well. Losev discovered and experimentally realized the method of arc remelting of semiconductor materials on the example of zincite, which made it possible to considerably improve the characteristics of the zincite crystadin. In the 1930s, Losev carried out a series of studies on the photoeffect in semiconductor structures. In these pioneering studies, it was shown that it is possible to obtain maximally high quantum efficiency in such photodetectors. It was these findings that determined modern progress in developing semiconductor photodetectors. Losev continued to conduct these investigations during the Leningrad blockade until his death.

He discovered the photoeffect in an illuminated silicized carbon detector in 1924 while working at NNRL. Using his method of laps and probe microscopy, he convincingly proved that the effect observed in silicized carbon is indeed due to a photovoltage and the photovoltage appears in a 1- to 3-μm-thick part of the active layer. By investigating powder samples, he discovered a very interesting photo-dielectric effect consisting in the fact that when the SiC contact is illuminated its capacity also changes. Already in the 1930s, I.V. Kurchatov pointed out the value of this series of Losev's studies.

Another of Losev's merits is his pioneering investigations of the photoelectric properties of silicon. In order to choose a material for the production of photocells and photoresistors, Losev examined more than 90 substances. In particular, the photosensitivity of silicon was found to be significant. At the end of the 1930s, he intuited that this material is very perspective.

In the beginning of 1941, Losev started to work on a new theme, "The method of electrolytic photoresistors: Photosensitivity of certain silicon alloys." As usual, his intuition did not fail him this time. Losev felt that the silicon crystal had considerable promise.

The attack of Nazi Germany put scientific investigation into the background, but Losev wanted to finish the work he had begun and he refused to leave the city. Apparently, he managed to finish the work and send it to the *Journal of Technical Physics* in Leningrad. By that time, however, the editorial office had already been evacuated. Unfortunately, after the war ended, no traces of the article were found, and now we can only speculate about its contents.

Among other discoveries, which were also not appreciated by Losev's contemporaries, we should note the effect of transgeneration observed by him in multiloop radio circuits with nonlinear elements. These discoveries were a significant contribution to the development of nonlinear radio engineering, but, unfortunately, they have not yet been properly evaluated and developed.

The above analysis of the scientific achievements and discoveries of Losev shows that he was an extremely talented scientist in the field of semiconductor science and engineering. We can definitely say that each scientific and technical undertaking in the field of physics of semiconductors made by Losev in the 1920s and 1930s was developed later on into an independent perspective branch. This is the reason why Losev is considered a pioneer in modern radio and optoelectronics.

Unfortunately, after the war, the investigations started by Losev were not continued and were gradually forgotten. This was connected with the fact that Losev had no pupils who could carry on his investigations. Another reason was the difficult post-war situation. Apparently, due to Losev's studies, this country had a real chance to become the leader in the field of semiconductor electronics in pre-war years. The fact that Losev's investigations were not developed further in their time accounts for our lagging behind in the field of radios and optoelectronics.

In connection with the scientist's centenary, the staff of the NNRL museum is preparing a collection of articles devoted to O.V. Losev's life and scientific activity for publication. In particular, this collection will contain the article by B.A. Ostroumov "O.V. Losev as the inventor of crystadin," which was written in the beginning of the 1950s but was never published.

PUBLICATIONS DEDICATED TO LOSEV

1. O. V. Losev, *At the Origin of Semiconductor Engineering*, Ed. by G. A. Ostroumov (Nauka, Leningrad, 1972).
2. A. G. Ostroumov and A. A. Rogachev, in *Physics: Problems, History, People*, Ed. by V. M. Tuchkevich (Nauka, Leningrad, 1986).
3. E. E. Loebner, IEEE Trans. Electron Devices **23** (7), 675 (1976).

Translated by A. Titov

Physics of the Solid State, Vol. 46, No. 1, 2004, pp. 10–12. Translated from Fizika Tverdogo Tela, Vol. 46, No. 1, 2004, pp. 15–17.

PROCEEDINGS OF THE CONFERENCE DEDICATED TO O. V. LOSEV (1903–1942)

(Nizhni Novgorod, Russia, March 17–20, 2003)

Structural and Photoluminescence Properties of Heteroepitaxial Silicon-on-Sapphire Layers

S. P. Svetlov*, V. Yu. Chalkov*, V. G. Shengurov*, Yu. N. Drozdov, Z. F. Krasil'nik**, L. V. Krasil'nikova**, M. V. Stepikhova**, D. A. Pavlov***, T. V. Pavlova***, P. A. Shilyaev***, and A. F. Khokhlov***†**

**Physicotechnical Research Institute, Nizhni Novgorod State University, Nizhni Novgorod, 603950 Russia*
e-mail: svetlov@phys.unn.ru

***Institute for Physics of Microstructures, Russian Academy of Sciences, Nizhni Novgorod, 603950 Russia*

****Nizhni Novgorod State University, pr. Gagarina 23, Nizhni Novgorod, 603950 Russia*

Abstract—The growth of erbium-doped silicon layers on sapphire substrates through sublimation molecular-beam epitaxy is studied for the first time. Structural analysis data are given, and the luminescence properties of layers are discussed. Heteroepitaxial silicon-on-sapphire layers grown at a temperature T_s = 600–700°C are found to be fairly perfect in structure. Photoluminescence spectra show a peak at a wavelength of 1.54 μm associated with intracenter transitions in the rare earth Er^{3+} ion. © *2004 MAIK "Nauka/Interperiodica".*

1. INTRODUCTION

One of the promising fields in modern micro- and nanoelectronics is the fabrication of devices and "silicon-on-insulator" structures including heteroepitaxial silicon-on-sapphire (SOS) films. One of the advantages of such structures is their high resistance to radiation and thermal damage and the low power consumption of integral microcircuits based on them [1]. The realization of multifunctional microprocessor circuits on sapphire substrates and the improvement of their integration level require further development of optoelectronic circuits. In this connection, Si-based structures with various rare earth dopants are of particular interest [2].

The basic technique of preparing SOS structures is crystallization from the vapor phase with the involvement of chemical reactions [3]. However, the high deposition temperature (~1000°C) results in the formation of compressive stresses in Si layers because of fairly large differences in the values of the coefficients of linear thermal expansion of silicon and sapphire. In order to increase the crystal perfection, the SOS structures are grown by using molecular-beam epitaxy (MBE) [4]. At low growth temperatures, the effect of a difference in the thermal expansion coefficients between these materials becomes minimal and the density of defects in epitaxial layers decreases.

Our aim was to study the possible growth of Er-doped Si epitaxial layers on sapphire by using the sublimation MBE method. Luminescence of these layers occurs at a wavelength of 1.54 μm.

† Deceased.

2. EXPERIMENTAL

Sapphire plates with the $(1\bar{1}02)$ orientation were used as substrates. Prior to the deposition of Si layers, the plates were annealed at temperatures of 1200–1400°C for 30–90 min directly inside the growth chamber. To form Si and Er atomic beams, a sublimation source (cut from an Er-doped silicon ingot) was heated to a temperature of ~1330°C by passing an electric current through it [5]. In a number of experiments, undoped Si layers were grown on sapphire using KDB-15-grade silicon heated to ~1380°C. The deposition rate was 0.08–0.1 nm/s. The substrate temperature was varied from 500 to 800°C. The residual pressure during the growth of the layers did not exceed 1×10^{-7} Torr. The thicknesses of the grown Si layers were 0.25 to 0.75 μm.

The structure of the deposited layers was analyzed using electron and x-ray diffraction. An ÉMR-102 electron diffractometer was used in the reflection mode at a glancing incident angle and an acceleration voltage of 100 kV. X-ray diffraction spectra were recorded with the aid of a DRON-4 diffracrometer using a Ge(400) monochromator and Cu$K\alpha_1$ radiation. The morphology of the layer surface was analyzed using an Accurex TMX-2100 atomic-force microscope. Photoluminescence was measured using a modernized KSVU-23 device with an MDR-23 base monochromator. Photoluminescence (PL) was excited by an argon laser (514.5-nm line) with a pumping power of ~100 mW. A cooled, highly sensitive EO-817A Ge detector and a standard "lock-in" detection technique were used to record photoluminescence spectra. The spectra were

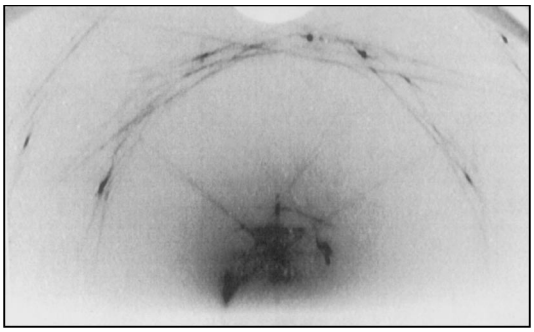

Fig. 1. Electron reflection diffraction pattern of a Si-on-sapphire structure.

measured at temperatures of 77 and 300 K with a resolution of ~6 nm.

3. RESULTS AND DISCUSSION

3.1. Structure of the Grown Layers

We studied the influence of the predepositional annealing temperature of a substrate and the growth temperature on the structure of the grown Si layers. Silicon was evaporated from an undoped source. After annealing of a substrate at a high temperature (~1400°C) for 30 min, Kikuchi lines and stripes were observed in the electron diffraction patterns (Fig. 1), which is indicative of high structural perfection of the surface region of the Si layer. As the growth temperature was increased, the contrast of Kikuchi patterns became higher; i.e., the structure of an epitaxial layer was improved. At the same time, Kikuchi patterns were barely visible in the initial sapphire substrate. This was probably due to the sapphire substrate surface layer being damaged by mechanical polishing.

Silicon layers grown on substrates annealed at 1400°C have a rather smooth surface (Fig. 2a), while the surface of epitaxial layers deposited on substrates annealed at 1200°C looks more rough (Fig. 2b). It seems likely that in the latter case the temperature did not prove high enough to remove carbon and oxygen contaminations from the sapphire surface.

On the substrates annealed at 1400°C, silicon was deposited in layers. X-ray diffraction patterns show that at low growth temperatures (500–550°C) Si layers are preferably oriented along the (110) plane, while at growth temperatures above 600°C, along the (100) plane. The most intense x-ray diffraction peak for such orientation was observed in the layers grown at 700°C. A typical rocking curve obtained for a Si(100) layer is shown in Fig. 3.

After studying the epitaxy of undoped Si layers on sapphire, we grew Er-doped layers. The growth temperature of these layers was 600°C. This temperature was specially chosen somewhat lower than the optimal temperature for obtaining structurally perfect layers

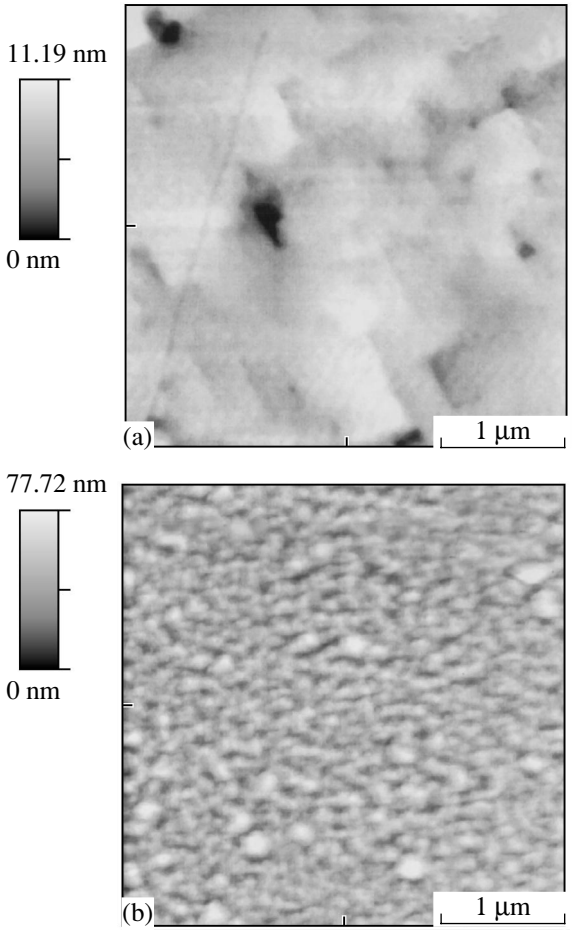

Fig. 2. Atomic-force images of the silicon layer surfaces grown on sapphire substrates preannealed at (a) 1400 and (b) 1200°C.

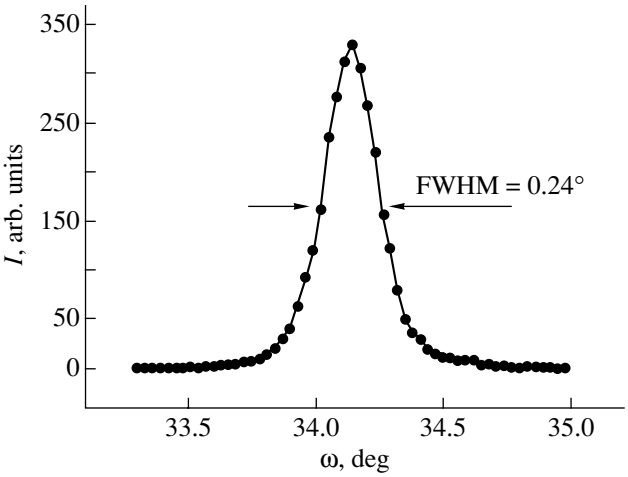

Fig. 3. X-ray diffraction rocking curve [Si(400) reflection] of a Si epitaxial layer grown at T_s = 700°C.

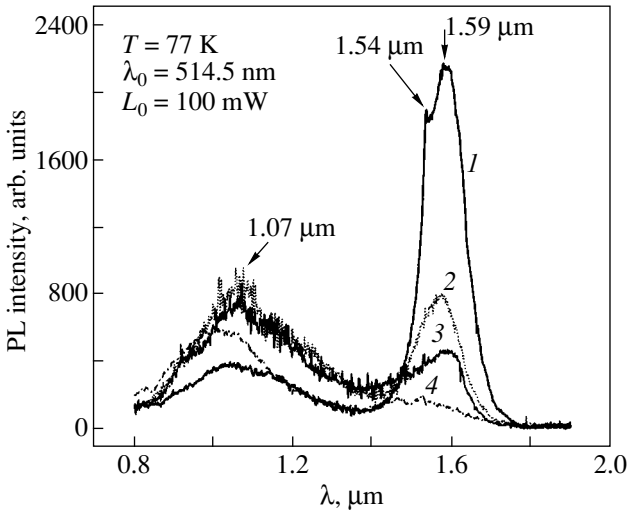

Fig. 4. Photoluminescence spectra of SOS structures. (*1*) Er-doped Si layer; (*2*, *3*) undoped Si layers of various defect structure grown on substrates after prior annealing at 1200 and 1400°C respectively; and (*4*) sapphire substrate.

(700°C) in order to avoid the formation of silicide compounds in Si layers. The Er concentration in the layers was about 5×10^{18} cm^{-3}.

3.2. Photoluminescence Features of SOS Structures

The results of photoluminescence studies of undoped and Er-doped SOS structures are shown in Fig. 4. At a temperature of 77 K, the PL spectrum of an Er-doped SOS structure in the wavelength range 1.5–1.7 μm contains a fairly intense signal with two peaks, at 1.54 and 1.59 μm (Fig. 4). The PL peak at 1.54 μm, considering its position and narrowness, can be assigned to the transition from an excited to the ground state in the rare earth Er^{3+} ion 4*f* shell (transition $^4I_{13/2} \longrightarrow {}^4I_{15/2}$). The other, more intense, line at 1.59 μm is considerably broadened and, judging by its position and relative intensity with respect to the first line, is obviously not related to transitions in the rare earth impurity center. Its shape and width suggest that this PL line comes most probably from defect complexes in the stressed silicon layer or from impurity-center complexes, such as the known defect complexes consisting of carbon and oxygen atoms (*C* and *P* luminescence lines [6]), whose content can be large in epitaxial silicon layers. Indeed, the peak at 1.59 μm was also observed in PL spectra of the SOS structures not doped with the rare earth impurity (not containing the line at 1.54 μm) and the intensity of this peak increased with degradation of the crystalline layer structure. For comparison, Fig. 4 shows the PL spectra of Si epitaxial layers grown on sapphire substrates preliminary annealed at 1200 and 1400°C. The x-ray diffraction data for these samples give rocking-curve half-widths equal to 0.4° and 0.36° and relative Si(400) reflection peak intensities equal to 400 and 3400, respectively. It can be seen that the parameters of the PL line at 1.59 μm correlate closely with the defect structure parameters of the layers. The photoluminescence of the sapphire substrate in SOS structures reveals itself only as a weak signal in the range 0.9–1.2 μm (curve *4* in Fig. 4), which is also present in the spectra of epitaxial layers. It should be noted that, for the structures studied, the PL spectra virtually do not contain the characteristic dislocation-induced (*D*1–*D*4 [7]) lines observed, as a rule, in silicon with a high density of dislocations and structural defects. The PL of SOS structures in the range 1.5–1.7 μm considerably decreases in intensity with increasing temperature and becomes virtually unobservable at 300 K.

4. CONCLUSIONS

Thus, we have shown that sublimation MBE provides a means of growing perfect thin (~0.5-μm-thick) Si layers on sapphire, including Er-doped layers luminescent at a wavelength of 1.54 μm.

ACKNOWLEDGMENTS

This study was supported in part by the Russian Foundation for Basic Research (project nos. 01-02-16439, 02-02-16773) and the Analytical Coordination Center of Innovation, Science, and Engineering Programs ("Fundamental Spectroscopy," project no. 08.02.043).

REFERENCES

1. D. Mead and J. Hine, Rep. Prog. Phys. **8** (3), 327 (1987).
2. N. A. Sobolev, Fiz. Tekh. Poluprovodn. (St. Petersburg) **29**, 1153 (1995) [Semiconductors **29**, 595 (1995)].
3. V. S. Pankov and M. B. Tsybul'nikov, *Epitaxial Silicon Layers on Dielectric Substrates and Devices on Their Basis* (Énergiya, Moscow, 1979).
4. E. D. Richmond, J. G. Pelligrino, M. E. Twigg, *et al.*, Thin Solid Films **192**, 287 (1990).
5. S. P. Svetlov, V. Yu. Chalkov, and V. G. Shengurov, Prib. Tekh. Éksp., No. 4, 141 (2000).
6. W. Kuerner, R. Sauer, A. Doerner, and K. Thonke, Phys. Rev. B **39** (18), 13327 (1989).
7. R. Sauer, J. Weber, and J. Stolz, Appl. Phys. A **36**, 1 (1985).

Translated by A. Zalesskiĭ

Physics of the Solid State, Vol. 46, No. 1, 2004, pp. 101–103. Translated from Fizika Tverdogo Tela, Vol. 46, No. 1, 2004, pp. 102–104.

PROCEEDINGS OF THE CONFERENCE DEDICATED TO O. V. LOSEV (1903–1942)

(Nizhni Novgorod, Russia, March 17–20, 2003)

Effect of Growth Conditions on Photoluminescence of Erbium-Doped Silicon Layers Grown Using Sublimation Molecular-Beam Epitaxy

V. G. Shengurov*, S. P. Svetlov*, V. Yu. Chalkov*, B. A. Andreev, Z. F. Krasil'nik**, and D. I. Kryzhkov****

** Physicotechnical Research Institute, Nizhni Novgorod State University, Nizhni Novgorod, 603950 Russia*
e-mail: svetlov@phys.unn.ru

*** Institute of the Physics of Microstructures, Russian Academy of Sciences, Nizhni Novgorod, 603950 Russia*

Abstract—Erbium-doped epitaxial silicon layers were grown using two different growth techniques, namely, commonly used molecular-beam epitaxy (MBE) and solid-phase epitaxy (SPE). It is shown that an erbium-doped silicon epitaxial layer deposited through SPE on a cold substrate and subsequently annealed displays a more intense photoluminescence at a wavelength of 1.54 μm than do MBE-grown layers. © *2004 MAIK "Nauka/Interperiodica".*

1. INTRODUCTION

There has been an increasing number of publications devoted to the study of Er-doped silicon because of the application potential of this material in Si-based optoelectronic devices working at a wavelength of 1.54 μm [1]. One of the features required of this material intended for use in such silicon-based devices is a high content of optically active erbium centers. For Er doping of Si through ion implantation, high-energy ions (0.5–5 MeV) are used. In this case, defects are formed that survive in part even after a long-term annealing and cause the rare-earth impurity to precipitate [2]. In the course of ion implantation, as well as in other doping techniques, the interaction of Er and Si atoms results in the formation of optically inactive silicide compounds. It has been established that, in order to suppress the formation of such Er and erbium silicide precipitates, Er doping should be performed at low temperatures and be accompanied by co-doping with oxygen to form optically active Er^{3+}-containing centers [3].

Molecular-beam epitaxy (MBE) with co-evaporation of Si and Er makes it possible to grow layers with a total Er concentration up to 10^{22} cm^{-3} [4]. However, the photoluminescence (PL) intensity in layers with an Er concentration above 10^{18} cm^{-3} decreases, probably due to the formation of structural defects [4, 5].

Another method allowing one to grow heavily doped Si layers is solid-phase epitaxy (SPE), which consists of two stages, namely, precipitation of a layer at low temperatures (where the impurity segregation is kinetically suppressed) and subsequent annealing of the amorphous Si film [6]

Our aim was to obtain SPE-grown heavily Er-doped Si layers exhibiting photoluminescence at a wavelength of 1.54 μm.

2. EXPERIMENTAL

Er-doped epitaxial layers were grown in an ultrahigh-vacuum MBE chamber with the aid of the device shown in Fig. 1 [7]. Si was evaporated from a sublimation source in the form of a rectangular bar heated by passing an electric current, and Er was also evaporated

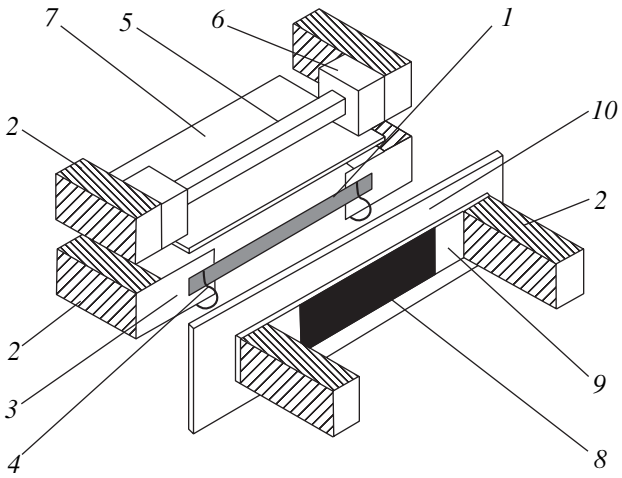

Fig. 1. Device for Si : Er layer growth (schematic). (*1*) Erbium plate, (*2*) current carriers, (*3*) molybdenum springs, (*4*) molybdenum fasteners, (*5*) silicon bar, (*6*) silicon spacer, (*7*) stationary screen, (*8*) substrate, (*9*) molybdenum clamps, and (*10*) movable screen.

1063-7834/04/4601-0101$26.00 © 2004 MAIK "Nauka/Interperiodica"

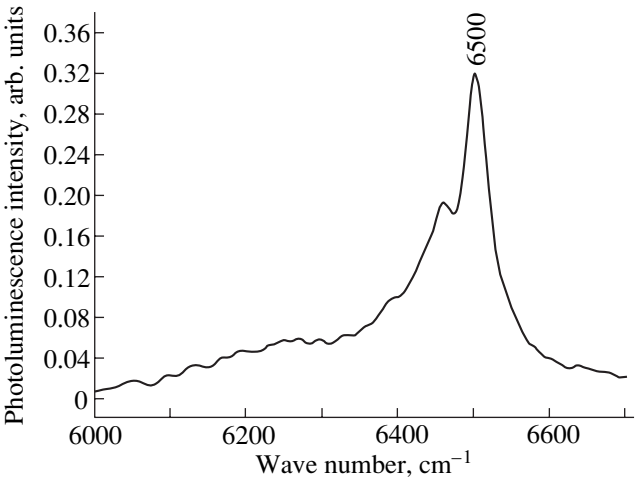

Fig. 2. PL spectrum of an MBE-grown structure recorded at $T = 77$ K for pumping Ar laser power $P = 80$ mW.

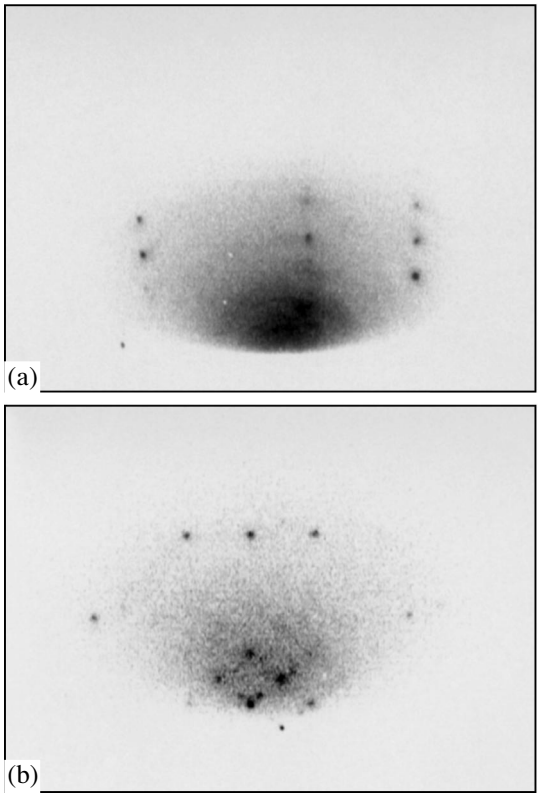

Fig. 3. Electron diffraction patterns taken from the layer surfaces grown on (a) (111)- and (b) (100)-oriented substrates.

from a sublimation source cut from a metal foil. A rectangular Si plate cut along the (100) or (111) plane from a Si KDB-12-grade Si single crystal served as a substrate. A substrate and the sources were heated by passing an electric current. After annealing of a substrate at $T = 1250$°C for 10 min, Si layers were grown through MBE at 500°C or through SPE on a heated substrate with a subsequent *in situ* annealing.

PL spectra were measured at 77 K with the aid of a Fourier BOMEM DA3 spectrometer with a resolution of 1 cm^{-1} under pumping Ar^+ laser radiation (wavelength $\lambda = 514.5$ nm, power 80 mW), illuminating the epitaxial-layer surface. The layer structure was examined using electron diffraction.

3. RESULTS AND DISCUSSION

3.1. Molecular-Beam Epitaxy

After annealing of a substrate, a buffer undoped Si layer ~0.1 μm thick was grown at 1050°C. Then, the temperature was reduced to $T_s = 550$°C, the chamber was filled with oxygen to a pressure of 9.5×10^{-8} Torr, and an Er-doped layer ~0.5 μm thick was grown. The electron concentration in the layer was measured with a *C–V* profilometer to be about 10^{17} cm^{-1}. Figure 2 shows the PL spectrum for this structure measured at liquid-nitrogen temperature. A broad band with a peak at 6500 cm^{-1} is typical of Er^{3+}-ion PL spectra of Si : Er/Si structures grown through sublimation MBE with a metallic Er source and having a higher concentration of oxygen and carbon in comparison to that of Er.

3.2. Solid-Phase Epitaxy

An amorphous Er-doped Si layer was grown at $T_s \approx 150$°C. The layer growth was periodically interrupted to fill the chamber with oxygen to a pressure of 5×10^{-5} Torr. After the layer thickness reached ~50 nm, the substrate temperature was increased up to 800°C and the system was annealed for 30 min. Figure 3 shows electron diffraction patterns of the layer surfaces grown on (111)- and (100)-oriented substrates. It can be seen that the layers formed on a (100) substrate have more perfect structure.

The erbium PL spectrum for an SPE-grown Si epitaxial layer is shown in Fig. 4. This PL spectrum contains a series of strong narrow lines associated with the $^4I_{13/2} \longrightarrow {}^4I_{15/2}$ transition in the $4f$ shell of the Er^{3+} ion forming a known single radiative cubic center [8]. Such a spectrum is usually characteristic of Er in a silicon single crystal with a low oxygen concentration in comparison with that of Er. However, the integrated Er^{3+}-ion PL intensity in the SPE-grown structure is twice that in the MBE-grown structure.

According to the existing models of the growth of an amorphous silicon layer through SPE on a single-crystal substrate in vacuum, the epitaxial-crystallization front moves from the interface between the single crystal and the amorphous layer towards the layer surface during annealing [9]. At an annealing temperature of

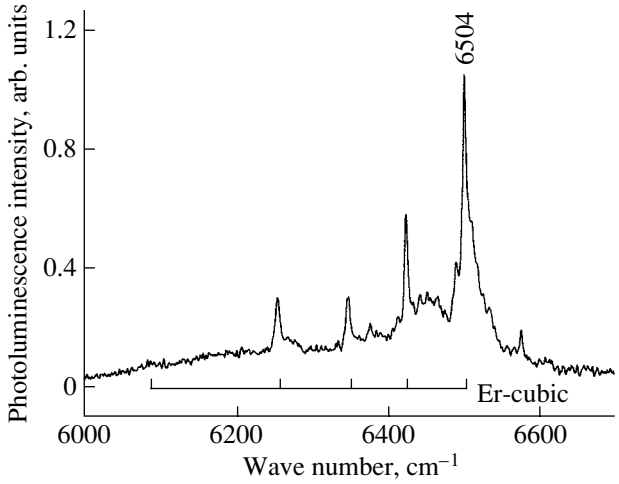

Fig. 4. PL spectrum of an SPE-grown structure. The spectrum was taken under the same conditions as for the spectrum shown in Fig. 2.

600°C, the amorphous Si crystallizes on the single-crystal substrate due to epitaxial ordering of atoms of amorphous silicon near the interface, whereas at a temperature of 800°C additional nucleation and growth of randomly oriented crystallites occurs in the bulk of the amorphous Si. The epitaxial crystallization rate at 800°C is 2.2–10 nm/min. Due to such a high crystallization rate, part of the layer surface becomes occupied by the single-crystal phase and the remainder by the polycrystalline phase upon completion of the annealing. The effect of oxygen on the reduction of crystallization rate was reported in [10]. However, in our experiments, when crystallization was interrupted and oxygen was let in, it is likely that a thin layer of adsorbed gas was formed and captured by the growing layer only partly. As a result, the total amount of oxygen introduced into the layer was very small. This may be the cause of the changes in the Er^{3+}-ion PL spectra observed in SPE-grown Si layers.

4. CONCLUSIONS

Thus, the solid-phase epitaxy method can be used to form a heavily Er-doped layer in an Si film deposited in ultrahigh vacuum. The photoluminescence observed from such a layer is more intense than that from an MBE-grown layer.

ACKNOWLEDGMENTS

This study was supported in part by the Russian Foundation for Basic Research (project nos. 01-02-16439, 02-02-16773) and the Ministry of Industry, Science, and Technology of the Russian Federation (State Contract nos. 40.020.1.1.1161, 40.020.1.1.1159).

REFERENCES

1. N. A. Sobolev, Fiz. Tekh. Poluprovodn. (St. Petersburg) **29**, 1153 (1995) [Semiconductors **29**, 595 (1995)].
2. A. Polman, J. Appl. Phys. **82**, 1 (1997).
3. Y. Ho Xie, E. A. Fitzgerald, and Y. J. Mii, J. Appl. Phys. **70**, 3223 (1991).
4. H. Efeoglu, J. H. Evans, T. E. Jackmann, *et al.*, Semicond. Sci. Technol. **8**, 236 (1993).
5. R. Serna, M. Lohmeier, P. M. Zagwijn, *et al.*, Appl. Phys. Lett. **66**, 1385 (1995).
6. V. G. Zavodiskii and A. V. Zotov, Phys. Status Solidi A **72**, 391 (1982).
7. S. P. Svetlov, V. Yu. Chalkov, and V. G. Shengurov, Prib. Tekh. Éksp., No. 4, 141 (2000).
8. H. Przybylinska, W. Jantsch, Yu. Stepikhova, *et al.*, Phys. Rev. B **54**, 2532 (1996).
9. I. G. Kaverina, V. V. Korobtsov, and V. G. Lifshits, Thin Solid Films **177**, 101 (1984).
10. C. W. Nogee, J. C. Bean, C. Foti, and J. M. Poate, Thin Solid Films **81**, 1 (1981).

Translated by A. Zalesskiĭ

Physics of the Solid State, Vol. 46, No. 1, 2004, pp. 104–108. Translated from Fizika Tverdogo Tela, Vol. 46, No. 1, 2004, pp. 105–109.

PROCEEDINGS OF THE CONFERENCE DEDICATED TO O. V. LOSEV (1903–1942)

(Nizhni Novgorod, Russia, March 17–20, 2003)

High-Efficiency Erbium Ion Luminescence in Silicon Nanocrystal Systems

P. K. Kashkarov*, B. V. Kamenev*, M. G. Lisachenko*, O. A. Shalygina*, V. Yu. Timoshenko*, M. Schmidt, J. Heitmann**, and M. Zacharias****

**Faculty of Physics, Moscow State University, Vorob'evy gory, Moscow, 119992 Russia*

***Max-Planck-Institut für Mikrostrukturphysik, Weinberg 2, Halle, 06120 Germany*

Abstract—The photoluminescence spectra and kinetics of both erbium-doped and undoped multilayer structures of quasi-ordered silicon nanocrystals in a silicon dioxide matrix were studied. It was shown that the optical excitation energy of silicon nanocrystals 2–3 nm in size can be practically completely transferred to Er^{3+} ions in the oxide surrounding the nanocrystals, with its subsequent radiation at 1.5 μm. Possible reasons for the high excitation efficiency of the Er^{3+} ions are discussed, and the conclusion is drawn that the Förster mechanism is dominant in the energy transfer processes occurring in these structures. © *2004 MAIK "Nauka/Interperiodica".*

1. INTRODUCTION

Considerable attention has been focused in recent years on Er^{3+} ion luminescence in crystalline and amorphous silicon (see, e.g., [1, 2]). This interest stems from the need to develop silicon devices capable of emitting efficiently at a wavelength of 1.54 μm (the $^4I_{13/2} \longrightarrow {}^4I_{15/2}$ transitions in the inner 4*f* shell of the Er^{3+} ion), which corresponds to the maximum transparency of fiber communication lines. The development of such optoelectronics devices is hindered, however, by a number of still unsolved problems. For instance, if crystalline silicon (*c*-Si) is used as a matrix for Er^{3+}, strong thermal quenching of the erbium luminescence is observed, which is caused by the nonradiative Er^{3+} ion deexcitation originating from the energy transfer back to the matrix [3]. As a result, the room-temperature luminescence quantum efficiency of *c*-Si : Er samples turns out to be very low. The 1.5-μm photoluminescence (PL) and electroluminescence of erbium-doped amorphous hydrogenated silicon (*a*-Si : H : Er) features a fairly weak temperature dependence [4]. Furthermore, analysis of the PL kinetics in *a*-Si : H : Er suggests that the energy of the electron–hole pairs is transferred to Er^{3+} ions in fairly short (submicrosecond-scale) times, which accounts for the high efficiency of their excitation [5–7]. Because, however, of the existence of various nonradiative energy-loss channels, the erbium luminescence intensity in *a*-Si : H : Er is still not high enough to make this material promising for application in light-emitting devices.

A promising approach to combating these difficulties could be the use of erbium-doped silicon nanocrystals (nc-Si) embedded in an insulating matrix [8–11]. It should be pointed out that, although the wavelength of the erbium luminescence is practically independent of the nature of the matrix because of the "operating" Er^{3+} 4*f* shell being screened by the outer electronic shells, the ion excitation efficiency can be controlled by properly varying the properties of the matrix, for instance, the width of its band gap, and/or the density of electronic states of the defects and impurities contained in the matrix [1, 3]. This can be readily reached in nc-Si structures, because the band gap of nanocrystals can be varied within broad limits by properly varying their dimensions [12, 13]. Furthermore, in Si nanocrystals one can simultaneously attain both a good carrier localization in small space regions near the Er atoms and fairly long (hundreds of microseconds) lifetimes of the electronic excitation [12, 13]. In this case, the energy released in recombination of a photoexcited electron–hole pair can be efficiently transferred to the Er^{3+} ion. Indeed, samples of erbium-doped nc-Si in a SiO_2 matrix exhibit an intense and stable Er^{3+} ion PL even at room temperature [9, 10]. Note that the efficiency of the PL and its lifetime depend strongly on the technique by which the nc-Si/SiO_2 structures were prepared, as well as on the size of the Si nanocrystals [9]. This suggests that layers of quasi-ordered silicon nanocrystals in nc-Si/SiO_2 superlattices, which permit easy tailoring of the nanocrystals to desired sizes, could have application potential [11].

This report deals with a comparative study of the PL spectra and kinetics of multilayered nc-Si/SiO_2 structures, both erbium-doped and not containing this impurity, which makes it possible to judge the efficiency of electronic excitation energy transfer from silicon nanocrystals to the Er^{3+} ions in such structures.

1063-7834/04/4601-0104$26.00 © 2004 MAIK "Nauka/Interperiodica"

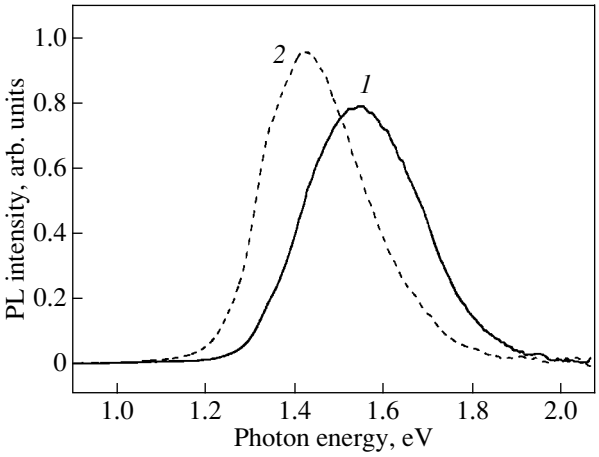

Fig. 1. PL spectra of samples (*1*) A and (*2*) B measured at $T = 300$ K.

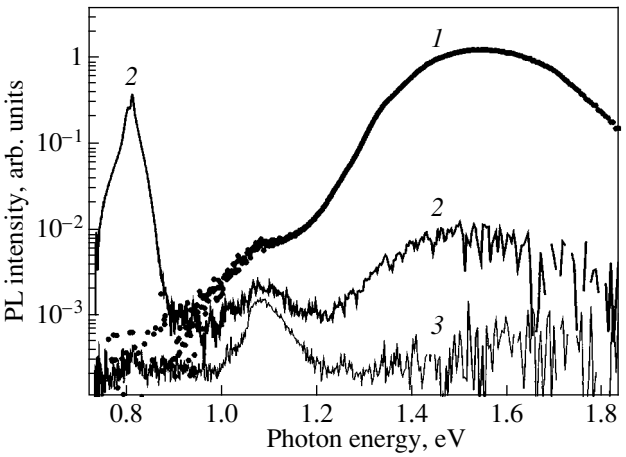

Fig. 2. PL spectra of samples (*1*) A, (*2*) AE, and (*3*) CE obtained at $T = 300$ K.

2. SAMPLES AND EXPERIMENTAL TECHNIQUES

The nc-Si/SiO_2 structures studied here were prepared by successive deposition of SiO and SiO_2 layers on a *c*-Si substrate by reactive sputtering [10, 11]. The SiO layers were 2 and 3 nm thick in samples A and B, respectively. The structures consisted of 40–50 pairs of layers for a total thickness of 200–300 nm. The samples were thermally annealed at a temperature of 1100°C in a nitrogen environment for 60 min to produce layers of closely packed Si nanocrystals separated by SiO_2 layers [11]. As follows from electron microscopy and x-ray diffraction measurements, the nanocrystal size was 2 ± 0.5 and 3.5 ± 0.5 nm in samples A and B, respectively. After the annealing, 300-keV Er^{3+} ions were implanted in part of the structures to a dose of 5×10^{14} cm^{-2}. After the implantation, the samples were thermally annealed at 950°C for 5 min.

Two lots of samples containing Si nanocrystals were prepared in this way: the starting nc-Si/SiO_2 structures (samples A and B) and Er-doped nc-Si/SiO_2 : Er structures (samples AE and BE). According to our estimates, the concentration of Er atoms in the AE and BE samples was approximately equal to that of Si nanocrystals, which, from TEM observations, was ~10^{19} cm^{-3} [11]. Besides the above structures, we also studied samples formed by implanting Er^{3+} ions of the above-mentioned energy and to the same dose into a uniform amorphous SiO_2 film 250 nm thick, with its subsequent fast thermal annealing to remove implantation defects (CE samples).

A pulsed N_2 laser (photon energy 3.68 eV, pulse duration 10 ns, pulse energy density 10 μJ/cm^2, pulse repetition frequency 100 Hz) was employed to excite the PL. The PL spectra were recorded using a computerized spectrometer equipped with an InGaAs photodiode. The measured spectra were corrected for the spectral response of the system. The PL kinetics in the visible region of the spectrum was measured with a PM tube with a time constant of ~30 ns complemented by an InGaAs photodiode with a time constant of ~1 μs to cover the IR region. Because the sensitivity of the latter diode was not high enough, it was used in studies of the initial part of the kinetics only to measure the integrated PL intensity in the range 1.1–1.6 μm. The slow PL relaxation components were recorded using an InGaAs photodiode with a time constant of 0.5 ms. The spectral resolution in the measurement of the erbium PL kinetics was 4 nm.

Most of the studies of the PL spectra and kinetics were conducted in air at a temperature of 300 K. Several PL spectra were also measured in vacuum in the temperature range 10–450 K with the use of a DE-204N closed-cycle cryostat (Advanced Research Systems).

3. RESULTS AND DISCUSSION

Figure 1 shows PL spectra of samples A and B. The A structures containing Si nanocrystals with smaller average dimensions are seen to exhibit a blue-shifted PL spectrum. This shift is known [11, 12] to be usually associated with an increase in the band gap of nc-Si caused by the quantum-confinement effect. The PL spectra have a fairly large band width, with a FWHM of 0.35 eV for samples A and 0.3 eV for samples B.

Our measurements revealed a weak increase (by a factor 1.5–2) in the PL intensity of samples A and B with the temperature decreasing from 300 to 6 K. Such an increase indicates a good passivation of nonradiative recombination centers in the structures under study. Note that the PL external quantum efficiency of samples A at $T = 10$ K was found to be ~1%. Considering the partial transparency of the structures to the pump radiation (see below), this value appears fairly high.

As is evident from Fig. 2, erbium implantation results in a considerable suppression (by more than two

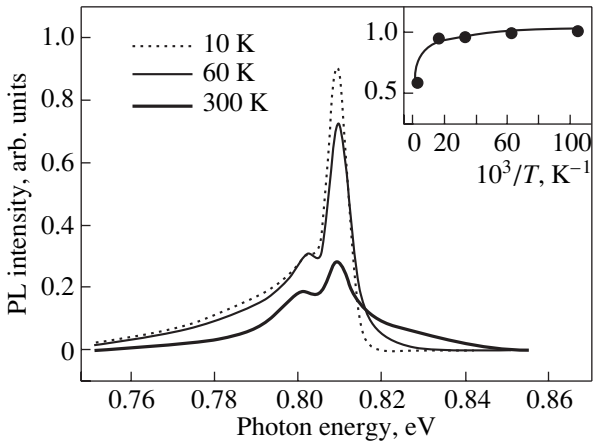

Fig. 3. PL spectra of sample BE measured in the Er^{3+} luminescence band at different temperatures. The inset shows the dependence of integrated erbium PL band intensity on reciprocal temperature.

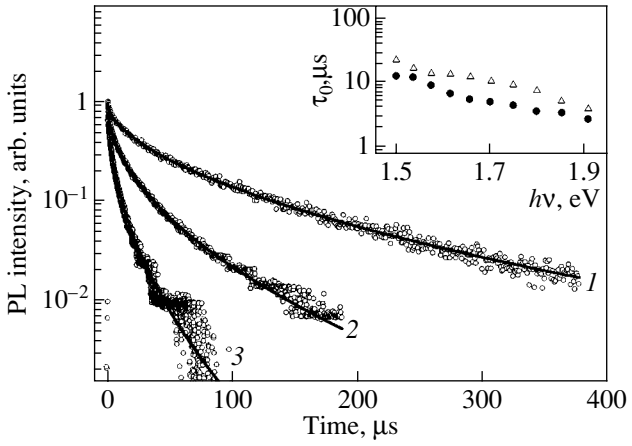

Fig. 4. PL kinetics of samples A obtained at various photon energies: (*1*) 1.5, (*2*) 1.7, and (*3*) 1.9 eV. Symbols are experimental data and solid lines represent fitting by an extended exponential. The inset shows the spectral response of the PL relaxation times obtained by approximation for samples A (triangles) and AE (circles).

orders of magnitude) of the PL characteristic of the undoped nc-Si samples and in the appearance of a strong band near 0.81 eV (λ = 1.535 μm). This band, due to the intracenter $^4I_{13/2} \longrightarrow {}^4I_{15/2}$ transitions, is always observed in Er^{3+} ions embedded in a solid matrix [1, 2]. Quenching of the nc-Si PL and formation of the erbium band were also observed to occur in BE structures with slightly larger nanocrystals. At the same time, the CE samples representing uniform *a*-SiO_2 : Er^{3+} layers exhibited an extremely low PL intensity in the vicinity of 0.8 eV. These samples primarily produced a weak band at 1.1 eV, which originates from interband radiative recombination in the *c*-Si substrate. The band at 1.1 eV in the CE samples and the shoulder observed in the same spectral region in the A and AE samples are apparently due to the penetration of the pump radiation into the single-crystal silicon substrate as a result of the layers under study being partially transparent.

The data displayed in Fig. 2 indicate that Er^{3+} ions in the nc-Si/SiO_2 : Er structures under study are excited through the transfer of electron excitation energy from the Si nanocrystals. Recalling the relative magnitude of the PL intensities in samples A and AE, we can reasonably assume that the energy absorbed by the nanocrystals is largely transferred to the optically active Er^{3+} ions. The actual mechanism of energy transfer will be discussed in more detail below. We note, however, that a certain contribution to the residual nc-Si PL in samples AE and BE comes apparently from the nanocrystals that are so distant from Er^{3+} as to make their interaction with these ions inefficient. As is evident from a comparison of curves *1* and *2*, the nc-Si PL band undergoes a change in its spectral shape after the implantation of Er^{3+} ions in the nc-Si/SiO_2 structures. One clearly sees an enhancement of PL quenching by a few times with the photon energy increasing from 1.3 to 1.7 eV. This can be interpreted, in terms of the mechanism of inhomogeneous broadening of the nc-Si PL band, as indicating a more efficient energy transfer from smaller nanocrystals (i.e., nanocrystals with a larger band gap) [9]. In view of a possible contribution from homogeneous broadening associated with the electron–phonon coupling and polariton effects, this increase in PL quenching with increasing photon energy implies more efficient energy transfer from nonthermalized excitons (i.e., excitons residing in nonstationary or excited states).

Experiments showed that the erbium PL intensity in nc-Si/SiO_2 : Er structures increases noticeably with the temperature decreasing from 300 to 10 K (Fig. 3). At the same time, the band intensity integrated over the spectrum in the range 0.75–0.85 eV increases only by a factor of 1.5 (see inset to Fig. 3). Such an increase indicates a low efficiency of the competing nonradiative recombination channels, for instance, of the energy transfer from Er^{3+} back to the solid matrix or of the recombination at point defects, such as silicon dangling bonds.

Let us turn now to an analysis of the PL kinetics of silicon nanocrystals. As seen from Fig. 4, relaxation of the PL intensity $I_{PL}(t)$ in undoped nc-Si/SiO_2 structures following a laser pulse cannot be fitted by an exponential. Our analysis showed that the PL kinetics can be well approximated by an extended exponential,

$$I_{PL}(t) = I_0 \exp\{-(t/\tau_0)^\beta\}, \qquad (1)$$

where τ_0 is the average time and β is a parameter describing the deviation from exponential behavior.

The PL with the kinetics described by Eq. (1) is usually observed in disordered solid-state systems characterized by a dispersion in the recombination times, for instance, in *a*-Si : H [5, 6] and porous silicon [13]. The value of τ_0 was established to increase from 4 to 25 μs with the photon energy decreasing from 2 to 1.5 eV (see inset to Fig. 4). Note that the parameter β remains practically unchanged and is close to 0.5. This behavior of τ_0 and β was observed in both A and B samples. Moreover, both samples revealed the same (within the experimental error and fitting accuracy) spectral response of the quantities τ_0 and β at the same PL photon energy. At the same time, erbium-doped structures exhibit a decrease in τ_0 by a factor of about 2–2.5, whereas the value of β practically does not change. This effect was observed in samples with nanocrystals of both sizes.

The observation that Er^{3+} implantation brings about quenching of the nc-Si PL intensity by two orders of magnitude (Fig. 2) while the relaxation times of the Er^{3+} PL kinetics decrease only by one half compared to the times recorded for the undoped structures (Fig. 4) suggests the following explanation. It appears that the majority of Si nanocrystals in erbium-doped structures practically do not contribute to the luminescence in the range 1.2–1.9 eV. This may be due to the fact that such nanocrystals have completely transferred the energy to the Er^{3+} ions, followed by luminescence at 0.81 eV. At the same time, the remaining nanocrystals (less than 1%) have shorter PL times because of the interaction with the Er^{3+} ions. The times can also decrease, in principle, as a result of nonradiative recombination on the defects produced by the Er^{3+} implantation. The absence of a noticeable thermal quenching of the PL in the samples under study suggests, however, that the concentration of such defects is low.

Figure 5 displays the PL relaxation kinetics of Er^{3+} ions measured for two luminescence photon energies, 0.81 eV (i.e., at the band maximum) and 0.84 eV (at the short-wavelength side of the band). We readily see that the erbium PL is characterized by a practically exponential kinetics nearly independent of the photon energy. Approximation of the kinetics by Eq. (1) yields the average lifetime $\tau_0 \approx 3$ ms. Such large values of the relaxation time are typical of the intrinsic radiative lifetime of Er^{3+} ions; for instance, in the case of *c*-Si : Er, they are observed only at liquid-helium temperature, where the deexcitation processes are suppressed [1, 2]. The initial part of the erbium PL kinetics measured with a microsecond-scale resolution is presented in the inset to Fig. 5. We readily see that the PL rise times of the Er^{3+} ions do not exceed 1–2 μs, which is shorter than the nc-Si PL band relaxation times. This supports the above assumption of a high efficiency of energy transfer from nanocrystals to the Er^{3+} ions.

Consider a possible mechanism of erbium PL excitation in nc-Si/SiO_2 : Er structures in more detail. In our opinion, the most probable process in the samples

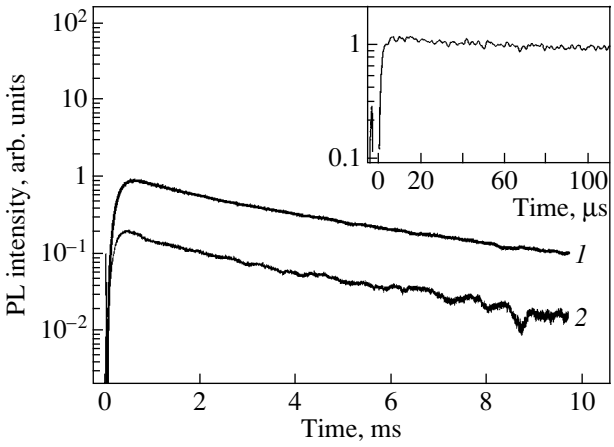

Fig. 5. Er^{3+} PL kinetics for samples AE and BE (time resolution 0.5 ms) obtained for photon energies of (*1*) 0.81 and (*2*) 0.84 eV. The inset shows the initial part of the kinetics measured with a time resolution of 1 μs.

under study is direct energy transfer from excitons in a Si nanocrystal to Er^{3+} ions, for instance, through the Förster mechanism [14]. The states excited in this process are the high-lying Er^{3+} levels, which can be broadened substantially through electric-field fluctuations in the given solid matrix [1, 2]. Because the density of nanocrystals in the oxide matrix of the above structures is quite high (~10^{19} cm^{-3}) and, hence, the nanocrystals are separated by barriers only 1- to -3-nm thick, this mechanism of energy transfer from nanocrystals to the ions present in the matrix appears reasonable. This process becomes still more probable in the cases where the Er^{3+} ion is localized directly at the nanocrystal surface.

The increase in the energy transfer efficiency for nanocrystals of smaller size observed in our experiments may be accounted for by a larger relative penetration of the exciton wave function into the oxide barrier, which has a finite height. The experimental data can be readily interpreted if we assume that the time required for the energy to be transferred from an exciton to Er^{3+} is shorter than the exciton thermalization time. Estimation of the energy transfer time from the exciton to the ion made from the measured PL kinetics yields a value not in excess of a few microseconds. On the other hand, it is known that the thermalization time of nonequilibrium carriers in semiconductor single crystals, which is determined by the electron–phonon interaction processes, is on the order of 10^{-12}–10^{-11} s [15]. Thermalization in a silicon nanocrystal can apparently be slowed down because of a decrease in the number of phonons, which is known to be proportional to $3(N - 1)$, where N is the number of atoms. Note that a decrease in the spin–lattice relaxation times by three to four orders of magnitude was observed to occur in porous silicon with small nanocrystals [16]. The assumption of the exciton thermalization being slowed down in silicon nanocrystals of a small size fits very

well with the increase in the energy transfer efficiency to the Er^{3+} ions observed to occur with decreasing nanocrystal size.

4. CONCLUSIONS

To sum up, we have studied the luminescent properties of nc-Si/SiO_2 multilayer structures containing Er^{3+} ions. It was shown that the energy absorbed in Si nanocrystals can be transferred with a high efficiency to Er^{3+} ions, with its subsequent emission in the 1.5-μm region. We believe that the high efficiency of the erbium PL excitation can be potentially applied in the development of optical amplifiers and light-emitting devices in the 1.5-μm range. Further steps in optimizing the technology for preparing nc-Si/SiO_2 : Er structures, for instance, by increasing the number of layers and the Er^{3+} ion concentration, should apparently favor an increase in the erbium PL efficiency.

ACKNOWLEDGMENTS

This study was supported by the CRDF (project no. RE2-2369), the Russian Foundation for Basic Research (project no. 02-02-17259), and programs of the Ministry of Industry, Science, and Technology of the Russian Federation.

REFERENCES

1. G. S. Pomrenke, P. B. Klein, and D. W. Langer, *Rare Earth Doped Semiconductors* (Pittsburgh, 1993), Mater. Res. Soc. Symp. Proc. MRS, Vol. 301.
2. K. Iga and S. Kinoshita, *Progress in Technology for Semiconductors Lasers* (Springer, Berlin, 1996), Springer Ser. Mater. Sci., Vol. 30.
3. F. Priolo, G. Franzo, S. Coffa, *et al.*, J. Appl. Phys. **78**, 3874 (1995).
4. W. Fuhs, I. Ulber, G. Weiser, *et al.*, Phys. Rev. B **56**, 9545 (1997).
5. E. A. Konstantinova, B. V. Kamenev, P. K. Kashkarov, *et al.*, J. Non-Cryst. Solids **282** (2–3), 321 (2001).
6. B. V. Kamenev, V. Yu. Timoshenko, E. A. Konstantinova, *et al.*, J. Non-Cryst. Solids **299**, 668 (2002).
7. B. V. Kamenev, V. I. Emel'yanov, E. A. Konstantinova, *et al.*, Appl. Phys. B **74** (2), 151 (2002).
8. A. J. Kenyon, C. E. Chryssou, C. W. Pitt, *et al.*, J. Appl. Phys. **91**, 367 (2002).
9. K. Watanabe, M. Fujii, and S. Hayashi, J. Appl. Phys. **90**, 4761 (2001).
10. M. Schmidt, M. Zacharias, S. Richter, *et al.*, Thin Solid Films **397**, 211 (2001).
11. M. Zacharias, J. Heitmann, R. Shcholz, *et al.*, Appl. Phys. Lett. **80**, 661 (2002).
12. D. J. Lokwood, Z. H. Liu, and J. M. Baribeau, Phys. Rev. Lett. **76**, 539 (1996).
13. A. G. Gullis, L. T. Canham, and P. D. J. Calcott, J. Appl. Phys. **82**, 909 (1997).
14. V. M. Agranovich and M. D. Galanin, *Electronic Excitation Energy Transfer in Condensed Matter* (Nauka, Moscow, 1978; North-Holland, Amsterdam, 1982).
15. S. A. Akhmanov, V. I. Emel'yanov, N. I. Koroteev, and V. I. Seminogov, Usp. Fiz. Nauk **147**, 675 (1985) [Sov. Phys. Usp. **28**, 1084 (1985)].
16. E. A. Konstantinova, V. Yu. Timoshenko, and P. K. Kashkarov, Poverkhnost, No. 2, 32 (1996).

Translated by G. Skrebtsov

Physics of the Solid State, Vol. 46, No. 1, 2004, pp. 109–112. Translated from Fizika Tverdogo Tela, Vol. 46, No. 1, 2004, pp. 110–113.

PROCEEDINGS OF THE CONFERENCE DEDICATED TO O. V. LOSEV (1903–1942)

(Nizhni Novgorod, Russia, March 17–20, 2003)

Effect of the *p–n* Junction Breakdown Mechanism on the Er^{3+} Ion Electroluminescence Intensity and Excitation Efficiency in Si : Er Epitaxial Layers Grown through Sublimation Molecular Beam Epitaxy

V. B. Shmagin, D. Yu. Remizov, Z. F. Krasil'nik, V. P. Kuznetsov, V. N. Shabanov, L. V. Krasil'nikova, D. I. Kryzhkov, and M. N. Drozdov

Institute of the Physics of Microstructures, Russian Academy of Sciences, Nizhni Novgorod, 603950 Russia

e-mail: shm@ipm.sci-nnov.ru

Abstract—A series of Si : Er/Si light-emitting diode structures with a smoothly varying *p–n* junction breakdown mechanism, grown through sublimation molecular-beam epitaxy, is used to investigate the effect of the breakdown mechanism on the electroluminescence of the structures. The maximal intensity and excitation efficiency of room-temperature Er^{3+} ion electroluminescence are shown to be attained in diode structures with a mixed breakdown mechanism. © *2004 MAIK "Nauka/Interperiodica".*

1. INTRODUCTION

Photoluminescence (PL) and electroluminescence (EL) from Er^{3+} ions introduced into a single-crystal silicon matrix ($^4I_{13/2} \longrightarrow {}^4I_{15/2}$ transition in the 4*f* shell of the Er^{3+} ion) were first observed twenty years ago [1, 2]. Since then, noticeable advances have been made in the technology for producing light-emitting Si : Er-based structures and in the study of the luminescence excitation and quenching mechanisms operating in these structures. In particular, it has been established that, in diode structures operating in the *p–n*-junction breakdown mode at room temperature, impact EL excitation of Er^{3+} ions is the most efficient mechanism [3]. Electroluminescent *p–n* diodes have been developed that operate in the tunneling- [4] and avalanche breakdown modes [5], and the Er^{3+} ion excitation cross sections have been determined to be 6×10^{-17} [6] and 2.3×10^{-16} cm^2 [7] for diodes operating in the tunneling- and avalanche breakdown modes, respectively.

However, in our opinion, the effect of the *p–n*-junction breakdown mechanism (BM) on the character and excitation efficiency of the EL from Si : Er-based diode structures is still not clearly understood. In particular, it has not been determined in what cases the tunneling- and avalanche breakdown modes offer advantages over each other and electroluminescent diodes in which a mixed *p–n* junction breakdown mechanism is operative have not been studied.

In this work, using a series of light-emitting Si : Er/Si diode structures with a smoothly varying BM as an example, we investigate the dependence of the radiative properties of a structure on the *p–n* junction breakdown mode. These structures were grown through sublimation molecular-beam epitaxy (SMBE) [8].

2. EXPERIMENTAL TECHNIQUE

The electroluminescent pp^+nn^+ diode structures studied in this work were grown through SMBE on *p*-Si : B substrates with (100) orientation and a resistivity of 15 Ω cm. The *n*-Si : Er layer was about 1 μm thick, the carrier concentration was varied from 3×10^{16} to 1×10^{18} cm^{-3}, the growth temperature was ~520°C, and the Er concentration was ~1×10^{18} cm^{-3}. The light-emitting diodes were fabricated using the mesa technology. The mesa area was 2.5 mm^2, with 70% of this area being transparent to the generated light.

The EL spectra were recorded in the range 1.0–1.6 μm with a resolution of 6 nm by using an MDR-23 grating monochromator and an infrared InGaAs photodetector cooled to liquid-nitrogen temperature. In order to excite and detect the EL spectra, we used pulsed drive current modulation (pulse duration 4 ms, repetition frequency ~40 Hz, amplitude up to 500 mA) and the conventional lock-in technique. The current–voltage (*I–U*) characteristics of the diodes were measured in the pulsed mode. The breakdown voltage U_b was determined by extrapolating the linear portion of the *I–U* curve at large reverse bias to its intersection with the voltage axis.

3. EXPERIMENTAL RESULTS AND DISCUSSION

The values of the breakdown voltage U_b for the diode structures studied are listed in the table. By com-

Diode breakdown voltages

Sample	U_b, V	
	T = 300 K	T = 77 K
4A1	2.7	5.1
4A2	3.0	5.4
4A3	3.5	5.6
4A4	3.9	6.0
3A0	5.0	6.6
3A1	6.8	7.1
3A2	8.4	7.8
3A3	11.1	9.6

paring the values of U_b measured at T = 300 and 77 K, it can be seen that a smooth transition takes place from the tunneling (sample 4A1) to the avalanche BM (sample 3A3) in the series of diodes under study. We note that all diode structures were grown in the same growth experiment. The technique used to grow epitaxial structures (including light-emitting Si : Er/Si structures) in which the epitaxial-layer thickness and the carrier concentration vary smoothly along the length of a structure is described in [9].

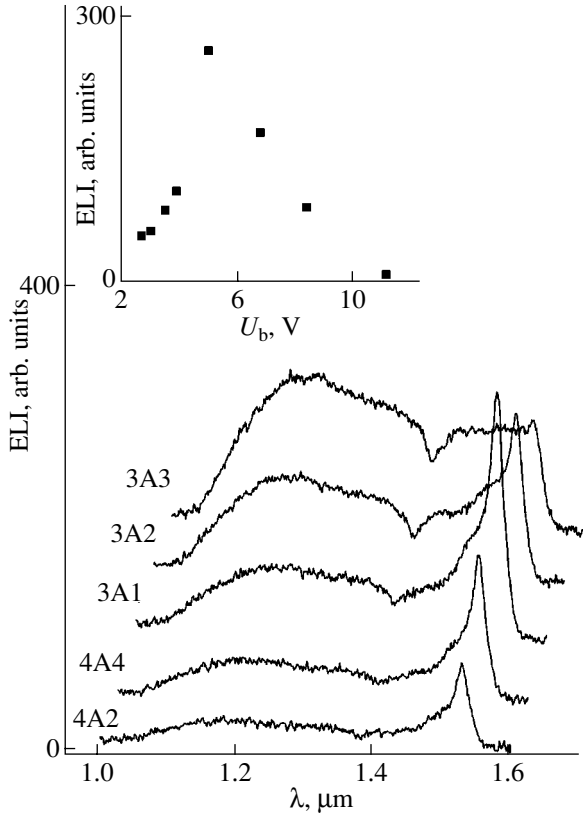

Fig. 1. Electroluminescence spectra of Si : Er/Si diode structures at T = 300 K for a drive current density of 8 A/cm^2. For the sake of convenience, the spectra are shifted along the abscissa and ordinate axes. The inset shows the dependence of the Er^{3+} ion EL intensity on diode breakdown voltage for fixed current density.

Figure 1 shows the evolution of the EL spectra as one goes from tunneling to avalanche diodes. In the series of diodes in which the tunneling BM is dominant (samples 4A1–3A0), the EL spectrum intensity as a whole increases, while the intensity ratio of the erbium EL (the peak at wavelength 1.54 μm) and the hot EL (wide band with a maximum at wavelength 1.2 μm) remains unchanged as the breakdown voltage U_b increases (U_b is assumed to have been measured at room temperature unless otherwise specified). As U_b increases further (samples 3A1–3A3, in which the avalanche BM is dominant), the spectral radiation power density is redistributed: the erbium EL intensity decreases, while the hot EL intensity increases. On the whole, the dependence of the erbium EL intensity on the diode breakdown voltage is described by an asymmetric bell-shaped curve (inset to Fig. 1), with the maximum EL intensity reached in structures with $U_b \sim 5$ V, which corresponds to a mixed *p*–*n*-junction breakdown mechanism [10]. Now, we discuss the possible reasons for the decrease in the erbium EL intensity observed in the diode structures for which the breakdown voltage is higher or lower than the value indicated above.

3.1. Structures in Which the Tunneling Breakdown Mechanism Is Dominant ($U_b \le 5$ V)

It is well known that, in the case where the drive current density is distributed uniformly over the *p*–*n* junction area, the drive current-density dependence of the Er^{3+} ion EL intensity is given by [3]

$$\mathrm{ELI} \propto \frac{\sigma\tau\dfrac{j - j_{th}}{q}}{1 + \sigma\tau\dfrac{j - j_{th}}{q}}, \qquad (1)$$

where ELI is the EL intensity, j is the drive current density, j_{th} is the threshold drive current density, q is the elementary charge, σ is the excitation cross section, and τ is the lifetime of the optically active Er^{3+} ion in the excited state $^4I_{13/2}$. The product $\sigma\tau$ is the characteristic rate at which the EL intensity tends to saturation with increasing drive current density; therefore, this product characterizes the efficiency of the EL excitation.

For all diodes in which the tunneling BM is dominant (samples 4A1–3A0), the theoretical ELI(j) dependence agrees well with the experimental data (Fig. 2a); therefore, Eq. (1) adequately describes the Er^{3+} ion excitation and relaxation in tunneling diodes. As the breakdown voltage increases, the quantity $\sigma\tau$ increases smoothly (inset to Fig. 2a) from 1.4×10^{-20} cm^2 s for U_b = 2.7 V to 9.4×10^{-20} cm^2 s for U_b = 5.0 V; this increase is likely due to the fact that the electron gas is

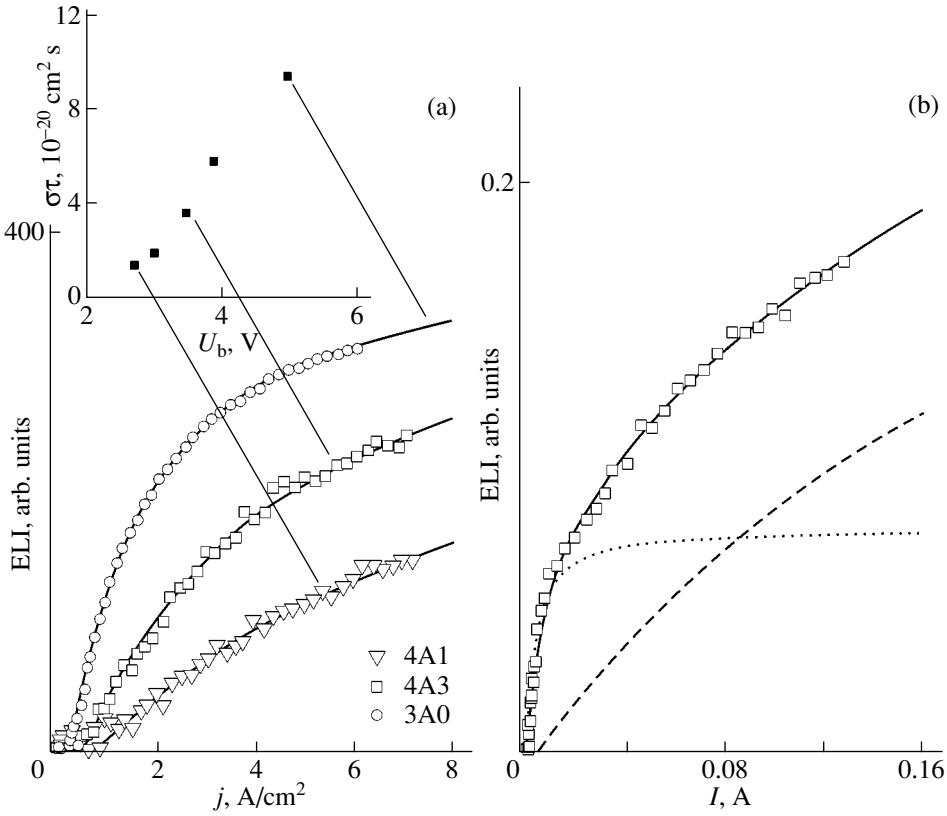

Fig. 2. Dependence of the erbium EL intensity (a) on drive current density and (b) on drive current for diode structures in which (a) the tunneling- or (b) avalanche breakdown mechanism is dominant. The inset shows the dependence of the quantity $\sigma\tau$ on breakdown voltage for tunneling diodes. (b) Dashed and dotted lines represent the contributions from the two terms in Eq. (2) to the experimental ELI(I) dependence.

heated with increasing breakdown voltage of an electroluminescent diode.

Analysis of the data presented in Fig. 2a shows that, at a fixed value of the drive current density, the EL intensity is lower in samples with lower EL excitation efficiency (with smaller values of $\sigma\tau$) and that the decrease in the Er^{3+} ion EL intensity in tunneling diodes with low values of the breakdown voltage (left-hand branch of the ELI(U_b) curve in the inset to Fig. 1) is due to a decrease in the EL excitation efficiency.

3.2. Structures in Which the Avalanche Breakdown Mechanism Is Dominant ($U_b \geq 7$ V)

We correlated the changes in the EL spectra of diode structures with $U_b \geq 7$ V (Fig. 1) with the changes in light emission of the diodes in the visible part of the spectrum; this emission was observed under diode breakdown conditions with the help of an MBS-10 microscope (Fig. 3). In samples 4A1–3A0 ($U_b \leq 5$ V), the light emission is uniform over the portion of the *p–n* junction area not covered with a metal (Fig. 3a) and its intensity increases with the breakdown voltage. Isolated bright spots (microplasmas [11]) are observed on the surface of sample 3A1 ($U_b \approx 6.8$ V; Fig. 3b). In diodes 3A2 and 3A3 ($U_b \geq 8.4$ V), the *p–n* junction breakdown is highly nonuniform; a large number of microplasma spots (about one hundred) are observed on the radiating surface of the *p–n* junction in the breakdown regime (Fig. 3c). In the microplasma breakdown regime, the drive current flows primarily through microplasma filaments; therefore, in the greater part of the space-charge region where there are no microplasmas, the Er^{3+} ion excitation efficiency drops, which causes the integrated erbium EL intensity to decrease. In our opinion, the significant decrease in the Er^{3+} EL intensity observed in samples 3A2 and 3A3, in which the avalanche BM is dominant (the right-hand branch of the ELI(U_b) curve in the inset to Fig. 1), is due to the *p–n* junction breakdown being nonuniform in these samples and, accordingly, to the nonuniform drive current density distribution over the *p–n* junction area. We note that the formation of microplasmas is characteristic of avalanche *p–n* junction breakdown in silicon [11].

The nonuniform drive current density distribution over the *p–n* junction area in diode structures with developed microplasma breakdown manifests itself in the ELI(I) dependence, where I is the drive current (Fig. 2b). The ELI(I) dependence for samples 3A2 and 3A3 can be described adequately under the assumption that

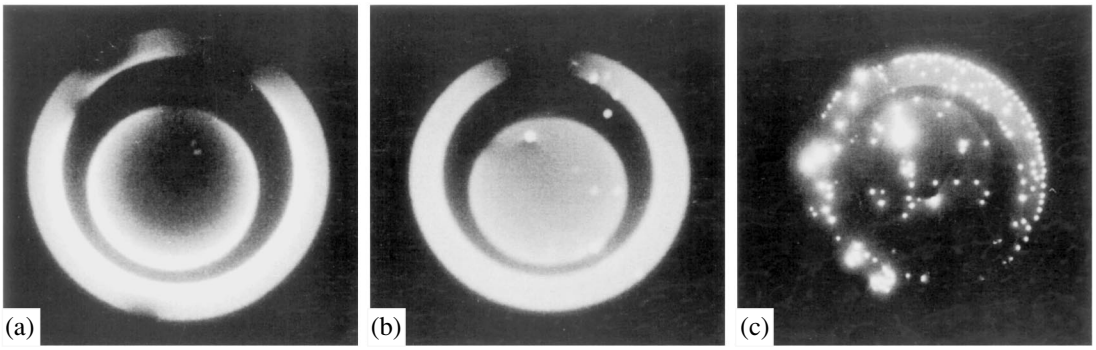

Fig. 3. Photographs of the emission from Si : Er/Si diode structures in the visible part of the spectrum under *p–n* junction breakdown conditions: samples (a) 4A4, (b) 3A1, and (c) 3A3.

the drive current density distribution over the *p–n* junction area is nonuniform in these samples.

Indeed, let us assume that the *p–n* junction area consists of two regions within each of which the drive current density distribution is uniform. Each of these regions is characterized by conductance G_i, area A_i, and threshold drive current density j_i^{th}. In this case, the dependence of the Er^{3+} ion EL intensity on the total drive current I is given by

$$\text{ELI} \propto A_1 \frac{\frac{\sigma\tau}{q}\left(\frac{G_1}{G_1+G_2}\frac{I}{A_1} - j_1^{\text{th}}\right)}{1+\frac{\sigma\tau}{q}\left(\frac{G_1}{G_1+G_2}\frac{I}{A_1} - j_1^{\text{th}}\right)} + A_2 \frac{\frac{\sigma\tau}{q}\left(\frac{G_2}{G_1+G_2}\frac{I}{A_2} - j_2^{\text{th}}\right)}{1+\frac{\sigma\tau}{q}\left(\frac{G_2}{G_1+G_2}\frac{I}{A_2} - j_2^{\text{th}}\right)}. \quad (2)$$

It can be seen from Fig. 2b that the ELI(*I*) dependence for sample 3A2 (avalanche diode) is described adequately by Eq. (2), which confirms our assumption that the erbium ion excitation is nonuniform in structures in which the avalanche BM is dominant.

4. CONCLUSIONS

Thus, we have investigated the electroluminescence from Si : Er/Si diode structures emitted under *p–n* junction breakdown conditions. For diodes in which the avalanche BM is dominant or nearly dominant, the Er^{3+} ion excitation efficiency has been shown to be an order of magnitude higher than that for tunneling diodes. However, as the avalanche breakdown becomes more pronounced, the drive current density distribution over the *p–n* junction area becomes highly nonuniform (microplasma breakdown), with the consequence that the Er^{3+} ion EL intensity decreases noticeably. In our opinion, the electroluminescent diodes operating under mixed-breakdown conditions are preferable, because a compromise is reached in them between, on the one hand, the high Er^{3+} ion EL intensity and excitation efficiency and, on the other, the uniform character of the *p–n* junction breakdown.

ACKNOWLEDGMENTS

This study was supported by the Russian Foundation for Basic Research (project no. 02-02-16773) and the Ministry of Industry, Science, and Technology (State contract no. 40.020.1.1.1159).

REFERENCES

1. H. Ennen, J. Schneider, G. Pomrenke, and A. Axmann, Appl. Phys. Lett. **43**, 943 (1983).
2. H. Ennen, G. Pomrenke, A. Axmann, *et al.*, Appl. Phys. Lett. **46**, 381 (1985).
3. G. Franzo, S. Coffa, F. Priolo, and C. Spinella, J. Appl. Phys. **81**, 2784 (1997).
4. G. Franzo, F. Priolo, S. Coffa, *et al.*, Appl. Phys. Lett. **64**, 2235 (1994).
5. N. A. Sobolev, A. M. Emel'yanov, and K. F. Shtel'makh, Appl. Phys. Lett. **71**, 1930 (1997).
6. S. Coffa, G. Franzo, and F. Priolo, Appl. Phys. Lett. **69**, 2077 (1996).
7. N. A. Sobolev, Yu. A. Nikolaev, A. M. Emel'yanov, *et al.*, J. Lumin. **80**, 315 (1999).
8. V. P. Kuznetsov and R. A. Rubtsova, Fiz. Tekh. Poluprovodn. (St. Petersburg) **34**, 519 (2000) [Semiconductors **34**, 502 (2000)].
9. E. N. Morozova, V. B. Shmagin, Z. F. Krasil'nik, *et al.*, Izv. Ross. Akad. Nauk, Ser. Fiz. **67**, 283 (2003).
10. S. Sze, *Physics of Semiconductor Devices*, 2nd ed. (Wiley, New York, 1981; Mir, Moscow, 1984), Chap. 1.
11. I. V. Grekhov and Yu. N. Serezhkin, *Avalanche Breakdown of p–n Junctions in Semiconductors* (Énergiya, Leningrad, 1980).

Translated by Yu. Epifanov

Physics of the Solid State, Vol. 46, No. 1, 2004, pp. 113–117. From Fizika Tverdogo Tela, Vol. 46, No. 1, 2004, pp. 114–118.

PROCEEDINGS OF THE CONFERENCE DEDICATED TO O. V. LOSEV (1903–1942)

(Nizhni Novgorod, Russia, March 17–20, 2003)

The Role of Microstructure in Luminescent Properties of Er-doped Nanocrystalline Si Thin Films*

M. V. Stepikhova[1], M. F. Cerqueira[2], M. Losurdo[3], M. M. Giangregorio[3], E. Alves[4], T. Monteiro[5], and M. J. Soares[5]

[1] *Institute for Physics of Microstructures, Russian Academy of Sciences, Nizhni Novgorod, 603950 Russia*

[2] *Departamento de Física, Universidade do Minho, Campus de Gualtar, Braga, 4710-057 Portugal*

[3] *Institute of Inorganic Methodologies and Plasmas, IMIP-CNR, via Orabona, Bari, 4-70126 Italy*

[4] *Instituto Técnico Nuclear ITN, EN 10, Sacavém, 2686-953 Portugal*

[5] *Departamento de Física, Universidade de Aveiro, Campus de Santiago, Aveiro, 3700 Portugal*

Abstract—In this contribution, we present a structural and photoluminescence (PL) analysis of Er-doped nanocrystalline silicon thin films produced by rf magnetron sputtering method. We show the strong influence of the presence of nanocrystalline fraction in films on their luminescence efficiency at 1.54 μm studied on a series of specially prepared samples with different crystallinity, i.e., percentage and sizes of Si nanocrystals. A strong increase, by about two orders of magnitude, of Er-related PL intensity in these samples with lowering of the Si nanocrystal sizes from 7.9 to about 1.5 nm is observed. The results are discussed in terms of the sensitization effect of Si nanocrystals on Er ions. © *2004 MAIK "Nauka/Interperiodica".*

1. INTRODUCTION

Recently, Er-doped Si materials were widely studied in context with the interest in temperature-stable light emitters for optical communication systems. The intra-4*f*-shell transitions between the two lowest spin-orbit levels of Er^{3+} ions, namely, the transitions ${}^4I_{13/2} \longrightarrow {}^4I_{15/2}$, occur at 1.54 μm, a wavelength close to that with minimum loss in silica-based optical fibers. The realization of electroluminescence devices on the basis of Si : Er has been reported [1–3]. Nevertheless, the main drawback to using a bulk Si crystal as a host for Er^{3+} is the strong temperature quenching of 1.54 μm luminescence. It appears that this situation may be considerably improved by the incorporation of Er ions in nanocrystal-containing materials. The idea is based on the band-gap widening of nanometer-size Si, which consequently has to result in reducing the thermal quenching for Er luminescence. Moreover, Si nanocrystals that are well known to emit in the visible range (due to the recombination of confined excitons within the nanostructures) may act as efficient sensitizers for rare earth ions [4, 5].

In this contribution, we discuss the luminescent properties of Er-doped nanocrystalline silicon thin films (nc-Si : Er) produced by the rf reactive magnetron sputtering method. The advantages of these films, when compared with the intensively studied nanocrystal-containing SiO_2 structures and *a*-Si : H,O,Er films, is their relatively high conductivity, which makes the material attractive for device applications. One can show that the presence of a crystalline fraction in thin films results in an increase in film conductivity of several orders of magnitude [6]. Er-doped nc-Si : H films with well-defined crystallinity and nanocrystal sizes (varied from 1–3 to 8 nm) were deposited and studied in both the near-IR (1.54 μm) and visible luminescence ranges. The results are discussed in terms of the role of Si nanocrystallites in the luminescent properties of films.

2. EXPERIMENTAL

Erbium-doped nanocrystalline silicon thin films were grown by rf magnetron sputtering in an Ar/H_2 atmosphere on ordinary glass substrates. The procedure applied was similar to that used for the preparation of undoped μc-Si : H films in [7], only modified by the introduction of small pieces of metallic erbium to the c-Si target for Er doping. The target used was c-Si of high purity (99.99%). The erbium was placed in a low erosion area on the silicon target in order to keep a moderate rate of Er impurity. The substrate–target distance was fixed at 55 mm.

Samples with different structural parameters, i.e., different crystalline fraction and grain sizes, were obtained by varying the experimental parameters (RF power, temperature, Er content, and gas-mixture composition). In particular, amorphous films (see Er28) were obtained at low hydrogen dilution, i.e., a low R_H value (see Table 1). Nanocrystalline samples were grown in a H_2-rich atmosphere, where the role of atomic hydrogen is to etch preferentially the amor-

* This article was submitted by the authors in English.

1063-7834/04/4601-0113$26.00 © 2004 MAIK "Nauka/Interperiodica"

Table 1. Growth conditions for erbium-doped nanocrystalline silicon thin films

Sample	Temperature, °C	RF power, W	R_H
Er22	400	80	0.63
Er19	200	80	0.63
Er24	50	80	0.63
Er28	200	150	0.37
Er33	25	80	0.63

Note: $R_H = pH_2/(pH_2 + pAr)$ is the hydrogen fraction.

phous phase and promote the amorphous-to-crystalline transition. The growth conditions of the films are listed in Table 1.

The chemical composition of the films was determined using Rutherford backscattering spectroscopy and elastic recoil detection techniques. The structural characterization was performed using standard micro-Raman spectroscopy under excitation with the 514.5-nm Ar^+ laser line and by x-ray diffractometry in the grazing incidence geometry. For more detailed analysis of the microstructure and film "anatomy," high-resolution transmission electron microscopy (HRTEM) and spectroscopic ellipsometry (SE) were applied. SE spectra of the pseudodielectric function, $\langle\varepsilon\rangle = \langle\varepsilon_1\rangle + i\langle\varepsilon_2\rangle$, were acquired in the 1.5- to 5.5-eV energy range by using a phase-modulated spectroscopic ellipsometer (UVISEL-Jobin Yvon) at an incident angle of 70.5°. SE spectra were analyzed in terms of optical models based on the Bruggeman effective medium approximation (for more details, see [8]). The thickness of the films was evaluated from analysis of the interference pattern in transmission spectra making use of the Swanepoel method [9] and from the spectroscopic ellipsometry data. Photoluminescence (PL) measurements in the near-IR range were performed with a Bruker 66V Fourier-transform spectrometer. The signal was detected with a North-Coast EO-817 liquid nitrogen–cooled germanium detector. The 514.5-nm line of an Ar laser was used for the excitation. PL studies in the visible spectral range were carried out under excitation with a 325-nm line of a cw He–Cd laser with a Spex 1704 monochromator and a cooled Hamamatsu R928 photomultiplier in the detection chain.

3. RESULTS AND DISCUSSION

Figure 1 shows the XRD and Raman spectra for the nc-Si : Er samples studied. The broad band related to the silicon amorphous matrix is present in the spectra for all samples. The Er28 sample grown at higher RF power but in an Ar-rich atmosphere does not show any crystalline peak in either the XRD or Raman spectra (the same behavior was also observed for the Er33 sample). In contrast, the (111), (220), and (311) diffraction peaks of c-Si are visible for all other samples. The peaks are well evident for the Er22 sample grown at high H_2 dilution and a high temperature of 400°C, both parameters promoting the amorphous-to-crystalline transition. The diffraction peaks have a lower intensity for the Er19 and Er24 samples, indicating a decrease in the crystallinity and/or the crystallite grain size, which is also confirmed by the intensity ratio of the Stokes peaks at 480 cm^{-1} (a-Si related) and at 520 cm^{-1} (transverse optical (TO) mode of c-Si) in the Raman spectra (Fig. 1b). The diffraction peak analysis, by fitting a pseudo-Voigt function to the (111) c-Si diffraction peak [7], gives the average crystal size for the Si nanocrystals presented in Table 2. In the same table, the data of Raman spectroscopy are also presented. To analyze the Raman spectra, the TO replica of amorphous structure has been approximated by a Gaussian profile and the

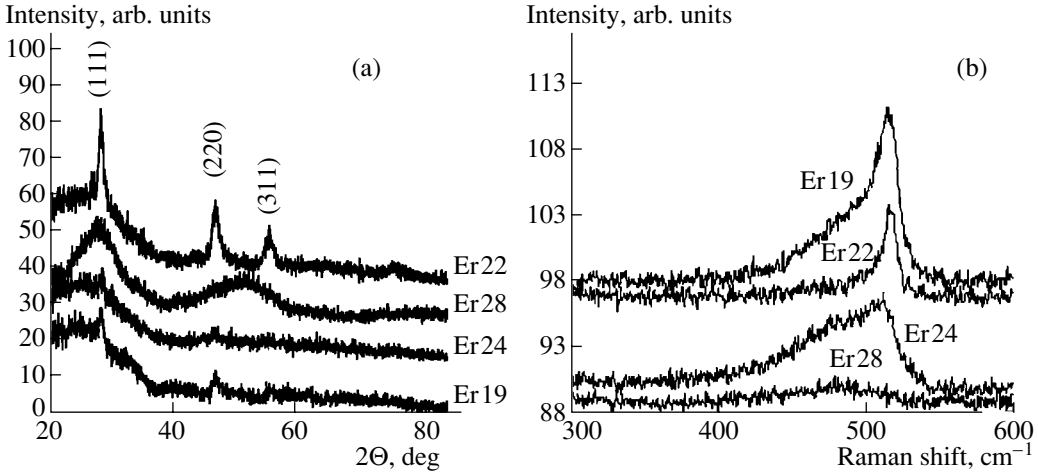

Fig. 1. (a) XRD and (b) Raman spectra of nc-Si : Er thin films.

Table 2. Content of elements, thickness, and structural parameters of nc-Si : Er samples

Sample	Er, %	Si, %	O, %	H, %	d, nm	D_X, nm	D_R, nm	C_R, %	SE data
Er22	0.10	71.7	8.8	17.6	2089	7.0	7.9	65	87% μc-Si
Er19	0.12	62	34	23	483	5.7	6.5	43	31% μc-Si
Er24	0.17	56.5	17.6	25.4	538	3.9	5.5	23	25% μc-Si
Er28	0.11	60.9	2.9	34.3	1295	–	–	0	10% nc-Si
Er33	0.02	73.4	<1	25.8	1499	–	–	0	38% nc-Si

Note: D — average crystal size, R — Raman spectroscopy, X — XRD analysis, C_R — crystalline volume fraction determined by Raman spectroscopy, d — film thickness.

crystalline response analysis was performed on the basis of the strong phonon confinement model [10].

Near-IR photoluminescence spectra measured at 77 K in nc-Si : Er samples are shown in Fig. 2. Let us consider the highly crystalline samples according to XRD and Raman data (samples Er24, Er19, and Er22 with nanocrystal sizes of 5.5–7.9 nm and crystallinity C_R = 23–65%). The spectra of these samples show a luminescence peak at 1.54 μm related to the intraatomic ($^4I_{13/2} \longrightarrow {}^4I_{15/2}$) transitions of Er^{3+} ions. Being relatively broad in a low crystalline sample (sample Er24) with a maximum at 6500 cm^{-1} and a characteristic shoulder at around 6457 cm^{-1}, like for Er in glasslike and amorphous materials [11], the Er-related spectrum transforms in highly crystalline films (sample Er22) in the spectrum with a fine line structure (see inset *A* in Fig. 2), giving evidence for the incorporation of Er ions in regular crystalline surroundings. At the same time, in the spectra of highly crystalline samples, the lines at 7500 and 9435 cm^{-1} appear and increase with the crystallinity and could be assigned following from their energetic position as the defectlike and excitonic transitions in Si crystallites. However, one can see that the

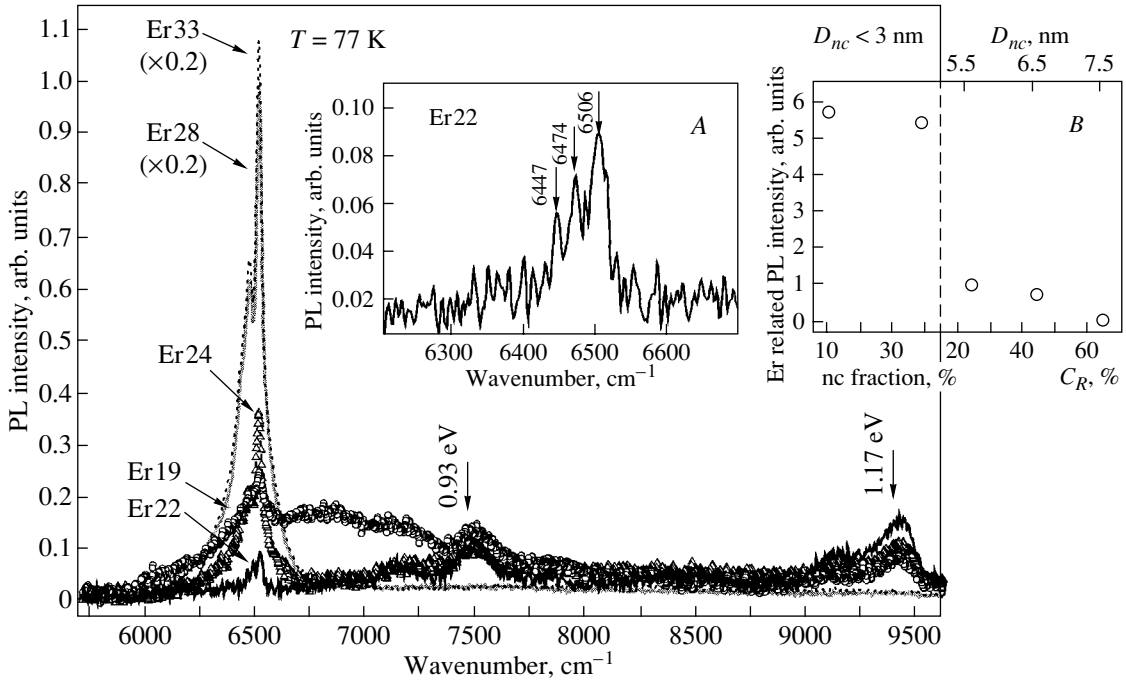

Fig. 2. PL spectra of nc-Si : Er samples with different contents of the crystalline fraction. Insets show (*A*) the enlarged Er-related region in the PL spectrum for sample Er22 and (*B*) the correlation between the PL intensity (Er-related peak) and the presence of a crystalline fraction in nc-Si : Er samples. The right part of inset *B* shows the situation for highly crystalline samples according to XRD and Raman analysis (the C_R and D_R values on the bottom and top axes correspond to the Raman data). On the left part of inset *B*, PL intensities for the samples with a nanocrystallite fraction with 1–3 nm crystallite grain sizes are presented, where the values for the nc fraction are taken from SE data. The luminescence intensities at 1.54 μm in this inset are normalized to the thickness of the films.

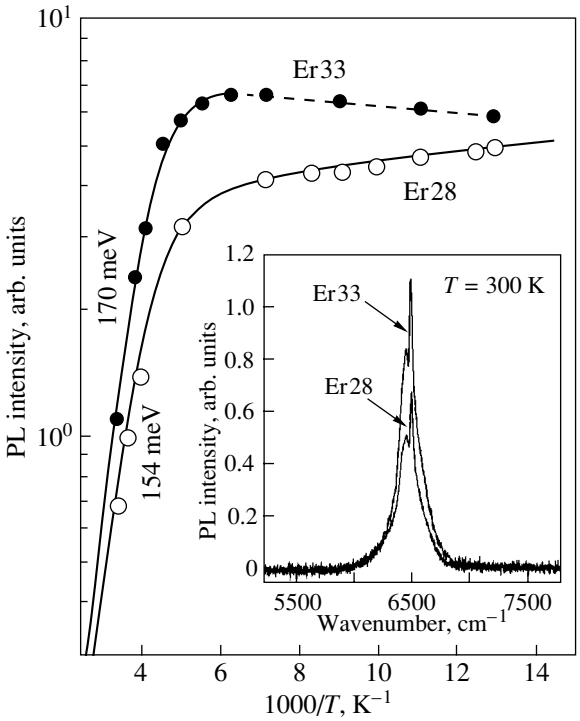

Fig. 3. Temperature dependences of Er-related PL intensity obtained in nc-Si : Er thin films (samples Er28 and Er33). The solid lines are exponential fits of experimental data with deactivation energies of 170 and 154 meV for samples Er33 and Er28, respectively. The inset shows PL spectra of the samples at room temperature.

increase of crystallinity in these samples results in a strong quenching of Er-related photoluminescence. Though the samples have a similar Er atomic percentage (0.1–0.17%, as estimated by RBS), the PL intensity in them reduces by more than an order of magnitude with an increase in the crystalline fraction from 23 to 65% (and crystallite size from 5.5 to 7.9 nm; see inset *B* in Fig. 2).

The most intense Er-related PL was observed in low crystalline samples determined as "amorphous" according to the Raman and XRD analysis (samples Er28 and Er33 in Table 2). In particular, the PL intensity of the Er33 sample exceeds that for highly crystalline sample Er22 by about two orders of magnitude (see inset to Fig. 2) despite the lower Er content. These samples show strong luminescence at room temperature (Fig. 3). The PL intensity decreases only fivefold when going from 77 to 300 K with deactivation energies of 154 and 170 meV.

It seems that it would be difficult to explain this dramatic increase in luminescent efficiency arising upon the transition from crystalline to amorphous film structure even because of the strong difference in the excitation cross sections for Er ions in these two matrices. It is known that the excitation cross section for the direct excitation of Er ions in amorphous matrices is about five orders of magnitude less than that for Er in crystalline Si (8×10^{-21} and 3×10^{-15} cm^2, respectively [12, 13]). Of course, one cannot exclude the role of nonradiative recombination channels in these composite structures. So, we can image that the enlargement of the crystalline fraction will enhance the nanocrystalline interactions in films and, therefore, the probability of excitons propagating in the crystalline network and recombining nonradiatively. However, in fact, we did not observe any direct evidence of a strong influence of nonradiative processes on the luminescent efficiency of the films. There is no strong correlation between the amount of hydrogen in the films and their luminescent

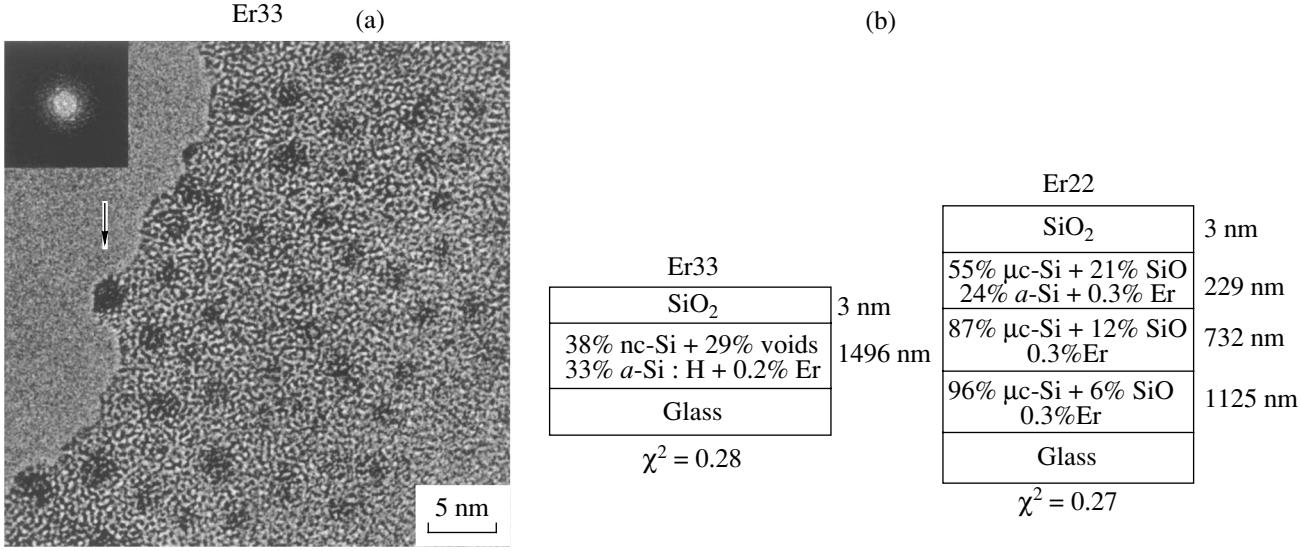

Fig. 4. (a) HRTEM image obtained for sample Er33 and (b) structural models of samples Er33 and Er22 derived from SE analysis.

properties (as a rule, hydrogen passivates the dangling bonds in amorphous/crystalline tissue, thus intensifying PL).We observed even the opposite, an increase in the film PL intensity after annealing at 500°C for 5 h; this procedure depletes the material with hydrogen. Moreover, the presence of oxygen in films, an element known as an "activator" for Er ions, also does not influence noticeably the film luminescence (see Table 2).

One can assume that the luminescence of Er ions in "amorphous" samples is activated by the nanocrystals with very small grain sizes (<3 nm). The first indication of the presence of these nanocrystals in films was obtained in spectroscopic ellipsometry studies. SE data predict the presence of small nanocrystals in samples Er28 and Er33 in an amount of 10 and 38%, respectively (SE analysis of the nc-Si thin films with small nanocrystal grain sizes were discussed in detail in [14]; see also the models in Fig. 4b). Indeed, this prediction can be confirmed by HRTEM measurements. A cross-sectional HRTEM image obtained for the Er33 sample is presented in Fig. 4a. The micrograph shows that the matrix of the a-Si : H films contains a high density of small clusters, which were identified on the basis of electron diffraction analysis as silicon nanocrystals. The lattice fringes corresponding to the (111) planes of silicon are visible in the figure. Statistical analysis of the nanocrystallite size distribution gives a nanocrystal mean radius of about 1.5 nm for this sample. Note a PL response in the visible range at around 700–720 nm was also detected in these samples. We believe that, in our case, the situation is similar to that observed by Fujii *et al.* [15], who studied the correlation between the Er-related PL intensity and the nc-Si grain sizes in nc-Si-containing SiO_2 films doped with Er. These authors obtained a strong, by about two orders of magnitude, increase in the Er PL intensity with lowering the nc-Si grain size from 3.8 to 2.7 nm. Actually, starting with these sizes, one can speak about a remarkable band-gap widening and the role of quantum size effects in Si [16]. Therefore, one can conclude that the seemingly strange increase in PL intensity in our "amorphous samples" can also be understood as a result of the sensitizing effect of Si nanocrystals on Er ions related to the enhancement of the excitation probability for the last ones due to the recombination of electron–hole pairs confined in nanocrystals.

4. SUMMARY

In this contribution, we have demonstrated the possibility of producing, by the reactive magnetron sputtering method, effectively emitting nc-Si : H thin films doped with Er and have discussed their luminescent and structural properties. The nc-Si : Er films with well-defined crystallinity and nanocrystal sizes (varied from 1–3 to 8 nm) were deposited and studied in both the near-IR and visible luminescence ranges. A strong influence of Si nanocrystals on the luminescent properties of the films at 1.54 μm has been observed, where the most intense Er photoluminescence obtained relates to the low crystalline films with nanocrystal grain sizes less than 3 nm. These films demonstrated intense 1.54-μm luminescence at room temperature with a temperature-quenching coefficient (in the range 77–300 K) of only about 5. The results have been explained in terms of the sensitization effect of Si nanocrystals on Er rare-earth ions.

ACKNOWLEDGMENTS

This work was partially supported by the FCT foundation (Portugal) and the Russian Foundation for Basic Research (project no. 01-02-16439).

REFERENCES

1. *Silicon-Based Optoelectronics*, Ed. by S. Coffa and L. Tsybeskov, MRS Bull., No. 23, 16 (1998).
2. J. Stimmer, A. Reittinger, J. F. Nützel, *et al.*, Appl. Phys. Lett. **68**, 3290 (1996).
3. B. Andreev, V. Chalkov, O. Gusev, *et al.*, Nanotechnology **13**, 97 (2002).
4. P. G. Kik and A. Polman, Mater. Sci. Eng. B **81** (1–3), 3 (2001).
5. F. Priolo, G. Franzo, F. Iacona, *et al.*, Mater. Sci. Eng. B **81** (1–3), 9 (2001).
6. M. F. Cerqueira, J. A. Ferreira, and G. J. Adriaenssens, Thin Solid Films **370**, 128 (2000).
7. M. F. Cerqueira, M. Andritschky, L. Rebouta, *et al.*, Vacuum **46**, 1385 (1995).
8. M. Losurdo, M. F. Cerqueira, E. Alves, *et al.*, Physica E (Amsterdam) **16**, 414 (2003).
9. R. Swanepoel, J. Phys. E **16**, 1214 (1998).
10. I. H. Campbell and P. M. Fauchet, Solid State Commun. **58**, 739 (1986).
11. M. Stepikhova, W. Jantsch, G. Kocher, *et al.*, Appl. Phys. Lett. **71**, 2975 (1997).
12. G. N. van Hoven, J. H. Shin, A. Polman, *et al.*, J. Appl. Phys. **78**, 2642 (1995).
13. G. Franzo, V. Vinciguerra, and F. Priolo, Appl. Phys. A **69**, 3 (1999).
14. M. Losurdo, M. M. Giangregorio, P. Capezzuto, *et al.*, Appl. Phys. Lett. (2003) (in press).
15. M. Fujii, M. Yoshida, S. Hayashi, and K. Yamamoto, J. Appl. Phys. **84**, 4525 (1998).
16. T. Takagahara and K. Takeda, Phys. Rev. B **46** (23), 15578 (1992).

Physics of the Solid State, Vol. 46, No. 1, 2004, pp. 118–121. Translated from Fizika Tverdogo Tela, Vol. 46, No. 1, 2004, pp. 119–122.

PROCEEDINGS OF THE CONFERENCE DEDICATED TO O. V. LOSEV (1903–1942)

(Nizhni Novgorod, Russia, March 17–20, 2003)

Intraband Absorption and Emission of Light in Quantum Wells and Quantum Dots

L. E. Vorob'ev*, V. Yu. Panevin*, N. K. Fedosov*, D. A. Firsov*, V. A. Shalygin*, S. Hanna, A. Seilmeier**, Kh. Moumanis***, F. Julien***, A. E. Zhukov****, and V. M. Ustinov******

**St. Petersburg State Technical University, Politekhnicheskaya ul. 29, St. Petersburg, 195251 Russia*

e-mail: LVor@rphf.spbstu.ru

***Physikalisches Institut, Universität Bayreuth, Bayreuth, 95440 Germany*

****Institut d'Electronique Fondamentale, Université Paris-Sud, Orsay, 91405 France*

*****Ioffe Physicotechnical Institute, Russian Academy of Sciences, Politekhnicheskaya ul. 26, St. Petersburg, 194021 Russia*

Abstract—High-resolution spectroscopy in the mid-infrared spectral range is used to study electronic transitions between size-quantization subbands in stepped quantum wells under picosecond interband excitation. The contributions from intersubband and intrasubband absorption of light are separated by using the difference in time profiles of the absorption coefficient for these cases. For stepped quantum wells, spontaneous interband luminescence and superluminescence are studied for different excitation levels. For structures with quantum dots, the intraband absorption spectra for *n*- and *p*-type structures and the spectra of photoinduced intraband absorption and emission (for polarized radiation) for undoped structures are studied. © *2004 MAIK "Nauka/Interperiodica".*

For semiconductor nanostructures with quantum dots (QDs) and stepped quantum wells (QWs), the population inversion between size-quantization levels or subbands is possible when electrons and holes are injected. We propose a scheme of a laser in the mid-IR region based on intraband electron transitions in three-level, stepped QWs or in QDs [1]. A metastable level, which is necessary for the population inversion, is formed in QWs due to a specially chosen potential profile ensuring weak overlap of the wave functions of interacting levels and weakening of scattering by optical phonons; in QDs, a metastable level results from the phonon bottleneck effect. To construct such a laser, studies of the charge carrier energy distributions and of the electron lifetimes and relaxation mechanisms in QDs and QWs are needed.

In this work, we studied different optical phenomena observed under optical interband excitation of nonequilibrium *e–h* pairs in stepped InGaAs/AlGaAs QWs and in InAs/GaAs QDs. In particular, we studied interband photoluminescence (PL) at high excitation levels, including time-resolved PL in the picosecond range, superluminescence, and intraband absorption and intraband spontaneous emission of radiation in the mid-IR range.

1. INTRABAND LIGHT ABSORPTION IN QUANTUM WELLS: HIGH-RESOLUTION STUDIES

We studied structures consisting of 35 layers of undoped GaAs/$Al_xGa_{1-x}As$ quantum wells separated by 20-nm-thick barriers. The potential profile of a single QW is shown in the inset to Fig. 1a. Nonequilibrium electrons are excited in a structure by using a high-power pumping Nd : YLF laser (λ = 523.5 nm, Δt = 4 ps). Probe mid-IR radiation pulses (λ = 4–18 μm), synchronized with pump pulses, are formed by a nonlinear element. The measurements are performed at T = 300 K.

In Fig. 1 we show the measured changes in intraband absorption for different frequencies of pump radiation and different time shifts of the probing pulse with respect to the pump pulse. The observed light-induced absorption contains contributions both from intersubband transitions and from intrasubband absorption by free electrons. The position of the absorption band observed at $\hbar\omega$ = 99 meV is close to the theoretical value of 111.6 meV for the $e2$–$e3$ transition. This difference can be attributed to the deviation of the actual parameters of the structure from the calculated values and to the effect of many-particle interactions on the

1063-7834/04/4601-0118$26.00 © 2004 MAIK "Nauka/Interperiodica"

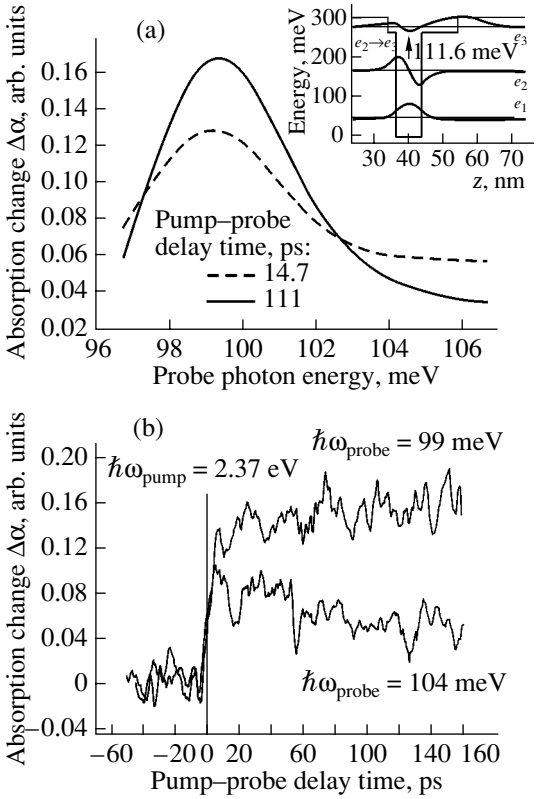

Fig. 1. (a) Spectra of absorption change for QWs for different delay times and (b) the dynamics of the absorption for different frequencies of pump radiation. Transitions are schematically shown in the inset.

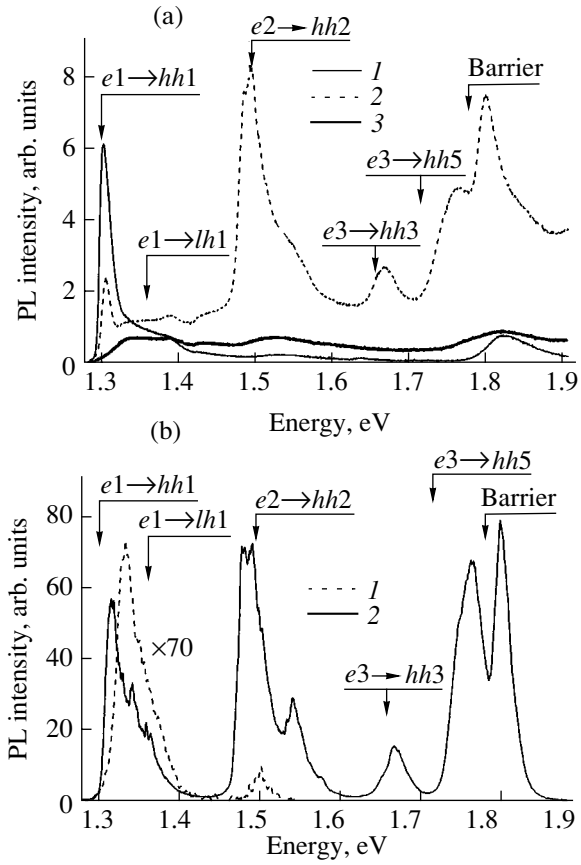

Fig. 2. (a) Surface PL spectra. The distance between the lens (the focal distance 100 mm) and the sample surface is (*1*) 125, (*2*) 105, and (*3*) 100 mm. The arrows indicate the calculated values of the interband transition energies. (b) PL spectra for radiation from the end side of the structure. The pump-pulse energies are (*1*) 0.062 and (*2*) 4.5 μJ. Excitation area is 0.075 × 3 mm. The arrows indicate the calculated values of the interband-transition energies.

energy spectrum; this effect was neglected in our calculations.

The pumping level corresponded to the surface densities of nonequilibrium electrons exceeding 5×10^{12} cm^{-2} per QW. For such a high excitation level, not only the lowest subband $e1$ but also the excited states $e2$ and $e3$ are filled; therefore, one can observe intersubband absorption corresponding to the $e2$–$e3$ transitions.

Intersubband absorption at the center of the band ($\hbar\omega_{probe}$ = 99 meV) and outside the band ($\hbar\omega_{probe}$ = 104 meV) has different time profiles. Absorption at the center of the band increases in time after the end of a pump pulse, whereas the absorption outside the band, on the contrary, decreases. These effects can be explained by strong heating of the electron gas during a pump pulse. A high pumping level and the high photon energy of pump radiation result in strong heating of the electron gas and in the generation of nonequilibrium LO phonons, which slow down the processes of electron cooling. Estimates yield a value of about 5000 K for the electron temperature just after the termination of a pump pulse. Thus, the electrons are distributed between the upper subbands. Due to the electron gas cooling, the electron concentration decreases in subband $e3$ and increases in subband $e2$, thereby increasing the absorption coefficient for transitions $e2$–$e3$. Intrasubband absorption due to free electrons outside the band of $e2$–$e3$ transitions involves electron scattering by equilibrium and nonequilibrium LO phonons. After the end of the pump pulse, the absorption is rather large, but then it decreases due to a decrease in electron temperature and in the number of nonequilibrium phonons.

By analyzing the data obtained, we can find the electron cooling time; when this time is long, it is determined by the lifetime of nonequilibrium LO phonons; if the cooling time is short, it is dictated by the phonon emission time.

2. PHOTOLUMINESCENCE IN QUANTUM WELLS FOR HIGH-INTENSITY PICOSECOND EXCITATION

We studied three-period structures with stepped QWs. The width of the narrow $In_{0.2}Ga_{0.8}As/Al_{0.2}Ga_{0.8}As$ QW is 6 nm, the width of the

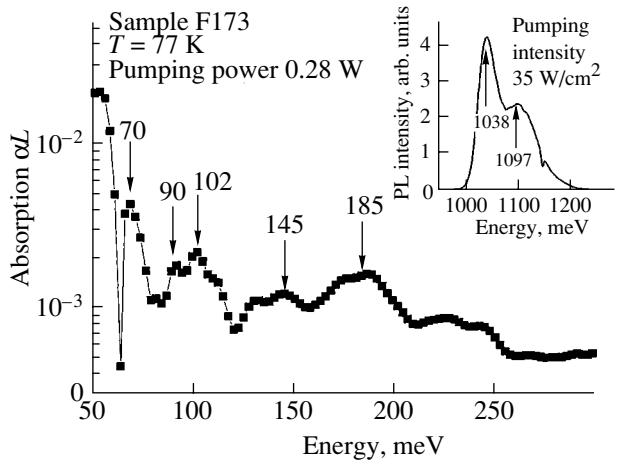

Fig. 3. Photoinduced absorption spectra for undoped QDs. PL spectrum is shown in the inset.

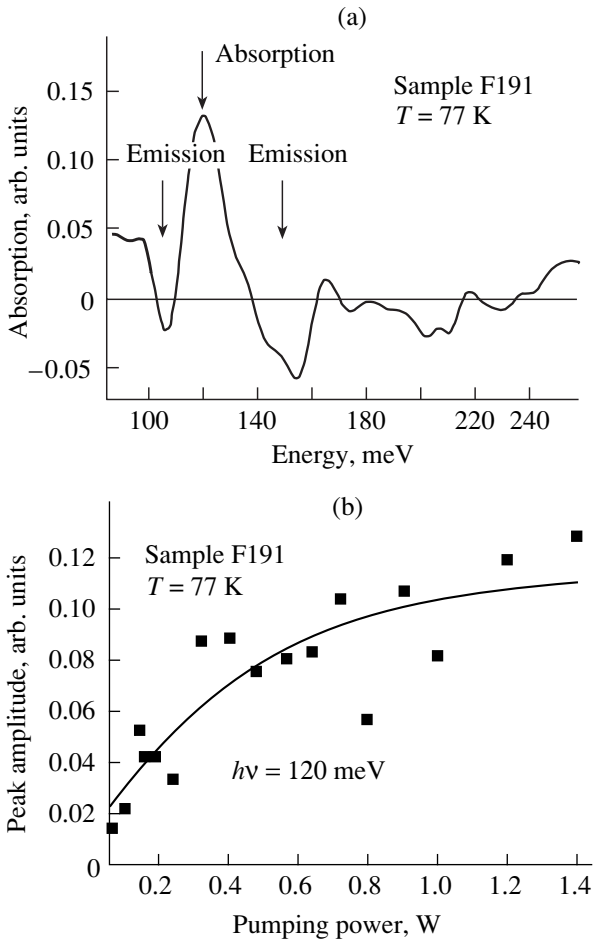

Fig. 4. (a) Absorption spectrum for background radiation related to electron transitions between QD levels in undoped QDs and (b) peak absorption as a function of the pumping power.

wide $Al_{0.2}Ga_{0.8}As/Al_{0.28}Ga_{0.72}As$ QW is 21.2 nm, and the layers with QWs are separated by $Al_{0.28}Ga_{0.72}As$ barriers 20 nm wide. The layers are placed at the center of a waveguide formed by AlGaAs layers with variable composition and built into the *i* layer of the *p–i–n* structure. The samples were optically excited by the second harmonic of the pulsed Nd : YLF laser (λ = 523.5 nm, pulse energy is 4.5 μJ, Δt = 3.2 ps).

Due to the high level of PL excitation by picosecond laser pulses, an appreciable population of upper size-quantization subbands is achieved. Observation of interband electronic transitions from the upper levels is also simplified due to superluminescence.

The results of the study of surface PL are shown in Fig. 2. Under certain conditions, the PL spectrum exhibited clearly defined peaks, which may be related to superluminescence. This phenomenon can be observed for high excitation levels because of the amplification of stimulated radiation in the waveguide, even in the absence of a resonator [2]. For radiation to be amplified, a sufficiently large free path of the light wave is needed. Therefore, when the excitation region is small, the superluminescence disappears and only wide bands of spontaneous PL are observed. There is satisfactory agreement between the spectral positions of PL lines and the calculated energies of interband transitions in QWs and barriers.

For high excitation levels, the number of nonequilibrium LO phonons becomes very large during energy relaxation of hot electrons and the electron energy relaxation rate drops by one or two orders of magnitude. On the other hand, under these conditions, the lifetime of nonequilibrium electron–hole pairs (of the order of 100 ps) is small compared to the interband recombination time. The electron energy relaxation time and the electron lifetime become similar; for this reason, the amplitudes of the peaks related to upper excited states become comparable to the amplitude of the fundamental peak. The dependence of the integrated PL intensity on the pump intensity *I* is sublinear for $I > 10^9$ W/cm^2; in this case, the Auger processes begin to play an important role in interband recombination.

The PL intensity measured from the end face of the structure in the direction of propagation of the waveguide mode is two orders of magnitude higher. This allows one to study superluminescence in more detail. For unpolarized light, the measured PL spectra are shown in Fig. 3. At sufficiently high pumping levels, bright superluminescence lines are observed simultaneously for all spectral intervals corresponding to interband transitions.

3. INTRABAND ABSORPTION AND EMISSION OF LIGHT IN QUANTUM DOTS

Both doped and undoped structures with 15 InAs QD layers covered by $In_{0.12}Ga_{0.88}As$ layers in the GaAs

matrix were studied. The surface density of dots in one layer was 3×10^{10} cm^{-2}. Since we plan to use the undoped structure for further studies under the conditions of generation of stimulated interband radiation, the QDs in this structure were placed in a waveguide formed by AlGaAs layers of variable composition. Samples intended for measurements of absorption were fabricated in multipass geometry. Nonequilibrium carriers were generated under interband optical pumping by Ar laser radiation.

Figure 3 shows the spectrum of photoinduced intraband light absorption for an undoped sample. The features of the spectrum are in good agreement with the calculated energy positions of intraband optical transitions between QD levels and the values of the corresponding matrix elements.

For interband illumination, the background radiation in the mid-IR range passing through the sample is modulated due to variations in the absorption and reflection coefficients, which are affected both by nonequilibrium free carriers and by carriers trapped in QDs. Subtracting the contribution of free electrons from the obtained spectra, we can determine the contribution from electron transitions between QD levels to photoinduced absorption (Fig. 4a). In Fig. 4a, the negative peaks may be related to spontaneous transitions between QD levels and the positive peaks, to absorption, which saturates for high pumping levels (Fig. 4b).

When investigating intraband light absorption in doped samples in the absence of interband illumination, the *p*-polarized light absorption due to electrons and the *s*- and *p*-polarized light absorption due to holes were observed. The absorption intensities for electrons and holes are similar. This result poorly agrees with theoretical calculations predicting a smaller probability for hole transitions. Note that there is no contribution from holes to the photoinduced absorption spectra. This can be due to the concentrations of photoexcited holes in undoped samples being low.

ACKNOWLEDGMENTS

The study was supported by INTAS, the Russian Foundation for Basic Research, the Ministry of Industry, Science, and Technology of the Russian Federation, and the Ministry of Education of the Russian Federation.

REFERENCES

1. A. Kastalsky, L. E. Vorobjev, D. A. Firsov, *et al.*, IEEE J. Quantum Electron. **37** (10), 1356 (2001).
2. V. Ya. Aleshkin, S. A. Akhlestina, B. N. Zvonkov, *et al.*, Fiz. Tekh. Poluprovodn. (St. Petersburg) **29** (4), 590 (1995) [Semiconductors **29**, 307 (1995)].

Translated by I. Zvyagin

Physics of the Solid State, Vol. 46, No. 1, 2004, pp. 122–124. Translated from Fizika Tverdogo Tela, Vol. 46, No. 1, 2004, pp. 123–125.

PROCEEDINGS OF THE CONFERENCE DEDICATED TO O. V. LOSEV (1903–1942)

(Nizhni Novgorod, Russia, March 17–20, 2003)

Photoconductivity of Lead Telluride-Based Doped Alloys in the Submillimeter Wavelength Range

K. G. Kristovskiĭ*, A. E. Kozhanov*, D. E. Dolzhenko*, I. I. Ivanchik*, D. Watson, and D. R. Khokhlov***

**Faculty of Physics, Moscow State University, Vorob'evy gory, Moscow, 119899 Russia*

e-mail: khokhlov@mig.phys.msu.ru

***Department of Physics and Astronomy, University of Rochester, New York, USA*

Abstract—Persistent photoconductivity in a $Pb_{0.75}Sn_{0.25}Te(In)$ alloy initiated by monochromatic submillimeter-range radiation at wavelengths of 176 and 241 μm was observed at helium temperatures. This photoconductivity is shown to be associated with optical excitation of metastable impurity states. © *2004 MAIK "Nauka/Interperiodica".*

Most of the presently used high-sensitivity nonthermal detectors intended for use in the far infrared range are based on doped silicon and germanium. The longest wavelength corresponding to the photoelectric threshold in such radiation detectors that has been reached in uniaxially strained Ge : Ga was $\lambda_r = 220$ μm [1].

A viable alternative to the silicon- and germanium-based radiation detectors is offered by lead telluride–based narrow-gap semiconductors. Doping lead telluride and its solid solutions by Group III elements gives rise to effects not characteristic of the starting material, such as Fermi level stabilization and persistent photoconductivity [2]. In particular, the Fermi level in $Pb_{1-x}Sn_xTe(In)$ alloys with a tin content of $0.22 < x < 0.28$ stabilizes within the band gap to produce semiinsulating states of the semiconductor at low temperatures. Because the effect of Fermi level stabilization brings about homogenization of the electrophysical parameters of the material and because the characteristic energy parameters of the alloy, such as the band gap width and the impurity-state activation energy, are of the order of a few tens of millielectronvolts, the possibility of employing these semiconductors as radiation detectors in the far IR range appears extremely attractive. This possibility was realized [3], and it was found that the sensitivity parameters of a $Pb_{0.75}Sn_{0.25}Te(In)$-based IR radiometer substantially exceed those of their counterparts based on doped silicon and germanium.

However, the key question of the spectral response of the $Pb_{1-x}Sn_xTe(In)$-based radiation detector, in particular, of the red cutoff of the photoeffect in this material, has remained unexplored. The phenomenon of persistent photoconductivity observed in $Pb_{1-x}Sn_xTe(In)$ at low temperatures results in a buildup of nonequilibrium carriers in the allowed band under background radiation present in each standard spectrometer, thus making standard spectral measurements impossible. An instrument that has no background illumination at all but provides the possibility of illuminating a sample with radiation of a fixed wavelength and calibrated intensity is required.

Such an instrument was built and described in [4] (Fig. 1). A sample was fixed to the bottom of a helium bath in evacuated space. The background radiation was eliminated by means of screens cooled to liquid-helium and liquid-nitrogen temperatures. Blackbody radiation with a temperature of 77 or 300 K impinged on the

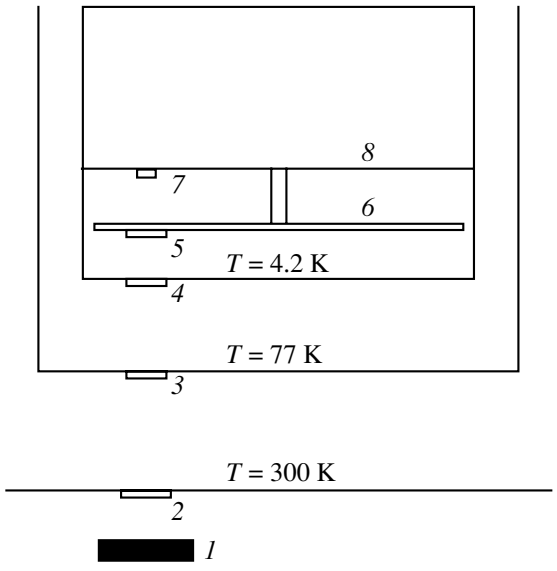

Fig. 1. Setup for measuring photoconductivity spectra of $Pb_{1-x}Sn_xTe(In)$ [4]: (*1*) blackbody, (*2*) entrance window, (*3*) "nitrogen" filter, (*4*) "helium" filter, (*5*) interference filter, (*6*) rotating disk with filters, (*7*) sample, and (*8*) helium bath.

1063-7834/04/4601-0122$26.00 © 2004 MAIK "Nauka/Interperiodica"

sample through the entrance window and a series of cooled filters. Special filters, which were maintained at the liquid-nitrogen or liquid-helium temperature, transmitted only the part of the radiation corresponding to the spectral interval under study. The diaphragm in the "helium" screen made it possible to calibrate the radiation flux striking the sample. Finally, a narrow radiation line was isolated by means of an interference filter mounted on a rotating disk within the helium screen.

However, the interpretation of the results mentioned above has remained open to question. Indeed, the thermal activation energy E_a was calculated from an analysis of the temperature dependence of the resistivity by using the relation $\rho \sim \exp(E_a/2kT)$ rather than $\rho \sim \exp(E_a/kT)$, as is usually accepted when of dealing with impurity states. The calculations made by using the first of the above relations were based on a study of the character of the pressure-induced motion of the impurity level [5]. However, this substantiation is of an indirect nature. If the activation energy of an impurity level is calculated using the second relation, the value of E_a will be one-half of that obtained from the first relation; i.e., it will correspond to a wavelength of 140 μm. Therefore, the conclusion that the metastable impurity states provide a major contribution to the photoresponse at wavelengths of 90 and 116 μm will be invalid.

In this paper, we report on the detection of a photoresponse in a $Pb_{0.75}Sn_{0.25}Te(In)$ film at wavelengths of 176 and 241 μm. $Pb_{0.75}Sn_{0.25}Te(In)$ films were grown through molecular-beam epitaxy on a BaF_2 substrate. The thermal activation energy of the impurity ground state calculated from the relation $\rho \sim \exp(E_a/2kT)$ was 20 meV. The experiment was carried out in the setup shown schematically in Fig. 1. The temperature of the helium screen after filling the helium bath with a cooling agent reached a stationary level in ~30 min. The disk with the filters was initially set in the position where the blackbody radiation impinged on the metal shutter. Since it was fixed to the bottom of the helium bath, the sample was cooled faster than the screen and the disk. Therefore, the sample was initially illuminated by the background radiation of the screen and the disk that had not yet cooled down. This background illumination gave rise to the generation of long-lived nonequilibrium carriers in the sample. To transfer the sample to the unperturbed state, it was warmed with a heater, located close to the sample, after the screen cooling. The increase in the sample temperature to 30 K and subsequent cooling to liquid-helium temperature transferred the electronic system of the sample to a close-to-ground state, with practically all the carriers localized. After this, the disk was rotated such that the radiation with the wavelength determined by the disk filter was directed onto the sample. This rotation usually lasted 3 to 4 s. We studied the kinetics of the current increase through the sample for various voltages across the sample and various blackbody temperatures. Figure 2

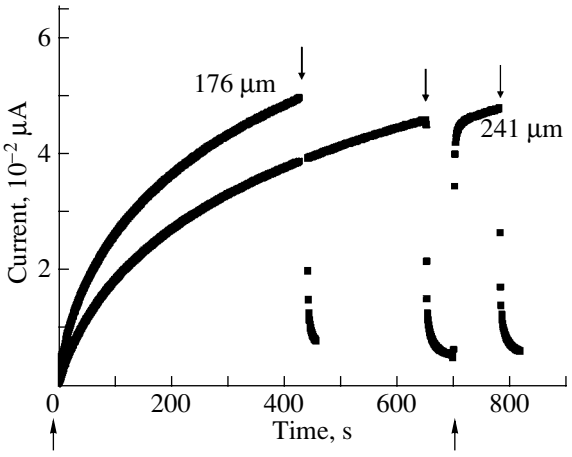

Fig. 2. Kinetics of the rise and fall of the photocurrent plotted for a voltage of 10 mV across the sample and different pump wavelengths. The arrows indicate the times the IR illumination is turned on and off.

plots the experimental data obtained for a sample voltage of 10 mV and a blackbody temperature of 300 K.

A noticeable photoresponse was detected at both wavelengths of the radiation striking the sample. Because our sensitive measuring equipment made it possible to record currents of up to 0.25 μA, we could reliably measure the kinetics of the increase in the photocurrent only at low voltages across the sample, $U <$ 40 mV. At higher voltages, the photocurrent grew so fast that the amplifier became overloaded in a time comparable to the time required to rotate the filter disk, i.e., within a few seconds. The following features in the photoconductivity may be of interest here. First of all, the current rise observed after switching on the illumination follows a strongly nonlinear kinetics. Switching off the illumination triggers a fast decay of the photocurrent, with subsequent slow relaxation to the dark level. If, however, the illumination is switched on again a short time after its removal, the photocurrent rises very fast (in a time comparable to the "fast" relaxation time) to the value recorded just before the illumination removal, after which the previous, relatively slow dynamics of the increase in the photocurrent sets in again. The fast and the slow processes are apparently of essentially different natures.

Another feature may also be noteworthy. The energies of photons corresponding to radiation wavelengths of 176 and 241 μm are substantially less than the thermal activation energy of the impurity ground state, even if this energy is calculated using the relation $\rho \sim \exp(E_a/kT)$. Thus, the results obtained in this study provide direct evidence for the persistent photoconductivity in $Pb_{1-x}Sn_xTe(In)$ originating from photoexcitation of metastable impurity states. The threshold energy for optical excitation of these states is very low. The wavelength of the corresponding photon is longer than at least 241 μm, which, as far as we know, is the largest

value of λ_r for nonthermal radiation detectors. The photoconductivity cutoff of the materials studied here apparently lies at substantially longer wavelengths. One cannot rule out the possibility that the operating range of $Pb_{1-x}Sn_xTe(In)$-based photodetectors extends over the whole submillimeter range.

ACKNOWLEDGMENTS

This study was supported in part by the Russian Foundation for Basic Research (project nos. 01-02-16356, 02-02-17057, 02-02-08083), INTAS (project no. 2001-0184), and a NATO Collaborative Linkage Grant.

REFERENCES

1. E. E. Haller, M. R. Hueschen, and P. L. Richards, Appl. Phys. Lett. **34**, 495 (1979).
2. B. A. Volkov, L. I. Ryabova, and D. R. Khokhlov, Usp. Fiz. Nauk **172**, 875 (2002) [Phys. Usp. **45**, 819 (2002)].
3. S. N. Chesnokov, D. E. Dolzhenko, I. I. Ivanchik, and D. R. Khokhlov, Infrared Phys. **35**, 23 (1994).
4. D. R. Khokhlov, I. I. Ivanchik, S. N. Raines, *et al.*, Appl. Phys. Lett. **76**, 2835 (2000).
5. B. A. Akimov, V. P. Zlomanov, L. I. Ryabova, *et al.*, Fiz. Tekh. Poluprovodn. (Leningrad) **13**, 1293 (1979) [Sov. Phys. Semicond. **13**, 759 (1979)].

Translated by G. Skrebtsov

Physics of the Solid State, Vol. 46, No. 1, 2004, pp. 125–129. Translated from Fizika Tverdogo Tela, Vol. 46, No. 1, 2004, pp. 126–130.

PROCEEDINGS OF THE CONFERENCE DEDICATED TO O. V. LOSEV (1903–1942)

(Nizhni Novgorod, Russia, March 17–20, 2003)

Shallow-Impurity-Assisted Transitions in the Course of Submillimeter Magnetoabsorption of Strained Ge/GeSi(111) Quantum-Well Heterostructures

V. Ya. Aleshkin*, D. B. Veksler*, V. I. Gavrilenko*, I. V. Erofeeva*, A. V. Ikonnikov*, D. V. Kozlov*, and O. A. Kuznetsov**

** Institute of Microstructure Physics, Russian Academy of Sciences, Nizhni Novgorod, 603950 Russia*
e-mail: gavr@ipm.sci-nnov.ru

*** Physicotechnical Research Institute, Nizhni Novgorod State University, pr. Gagarina 23/5, Nizhni Novgorod, 603950 Russia*

Abstract—The submillimeter (f = 130–1250 GHz) magnetoabsorption spectra of strained Ge/GeSi(111) multilayer heterostructures with quantum wells are investigated at T = 4.2 K upon band-gap optical excitation. It is found that the magnetoabsorption spectra contain lines associated with the excitation of residual shallow acceptors. The resonance absorption observed can be initiated by optical transitions between the impurity states belonging to two pairs of Landau levels of holes in germanium quantum-well layers. © *2004 MAIK "Nauka/Interperiodica".*

1. INTRODUCTION

Shallow-level impurities in quantum-well heterostructures have often been studied using far-IR impurity photoconductivity spectroscopy. In recent years, this method has been successfully applied to acceptors in strained Ge/GeSi heterostructures with quantum wells [1–7]. It has been demonstrated that the valence band splitting caused by both elastic strains of layers and quantum-confinement effects leads to a substantial decrease in the effective mass of holes in the quantum-well plane and, as a consequence, to a lower binding energy of acceptors as compared to those characteristic of bulk germanium. In our earlier works [1, 5, 7], important information on the energy spectrum of impurity centers was obtained by measuring the photoconductivity spectra in strong magnetic fields. It was revealed that these spectra contain lines associated with the transitions $1s \longrightarrow 2p_+$ and $1s \longrightarrow 2p_-$ for acceptors located at the centers of germanium quantum wells and at the centers of GeSi barrier layers. However, in strong magnetic fields, the resistance of samples increases significantly, which results in a substantial decrease in the signal-to-noise ratio.

The purpose of this work was to investigate the magnetoabsorption in Ge/GeSi quantum-well heterostructures with residual shallow acceptors upon band-gap optical excitation. It was shown that this method is an efficient tool for investigating shallow-impurity-assisted optical transitions in quantum wells.

2. SAMPLES AND EXPERIMENTAL TECHNIQUE

The $Ge/Ge_{1-x}Si_x$ heterostructures were grown through vapor-phase epitaxy on lightly doped Ge(111) substrates. The total thickness of all the structures grown exceeded the critical value, which led to relaxation of elastic stresses at the heterostructure–substrate interface. As a result, the GeSi layers in the heterostructure turned out to be biaxially extended, whereas the Ge layers were biaxially compressed. The materials were

Table 1. Parameters of the $Ge/Ge_{1-x}Si_x$ heterostructures

Sample no.	x	d_{Ge}, Å	d_{GeSi}, Å	Number of periods	Strain in Ge layers ε_{xx}	Substrate
262b	0.14	120	300	216	3.8×10^{-3}	GÉS-45
307a	0.09	300	230	162	8.7×10^{-4}	GÉS-45
308a	0.09	350	160	162	4.4×10^{-4}	GÉS-45
308b	0.09	330	150	162	4.4×10^{-4}	GDG-40
309a	0.07	850	200	83	4.6×10^{-4}	GÉS-45
309b	0.07	800	200	83	3.3×10^{-4}	GDG-40

1063-7834/04/4601-0125$26.00 © 2004 MAIK "Nauka/Interperiodica"

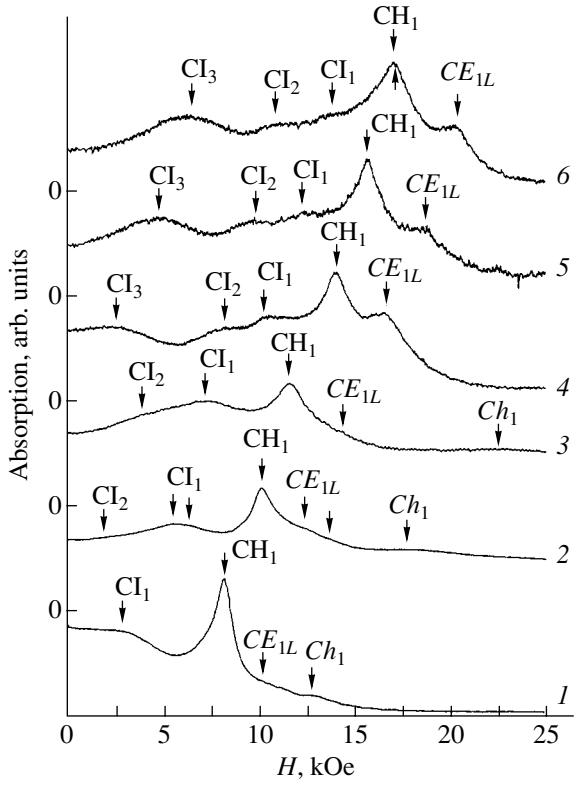

Fig. 1. Magnetoabsorption spectra of sample **308b**. $\hbar\omega$ = (*1*) 1.39, (*2*) 1.67, (*3*) 1.96, (*4*) 2.40, (*5*) 2.65, and (*6*) 2.95 meV.

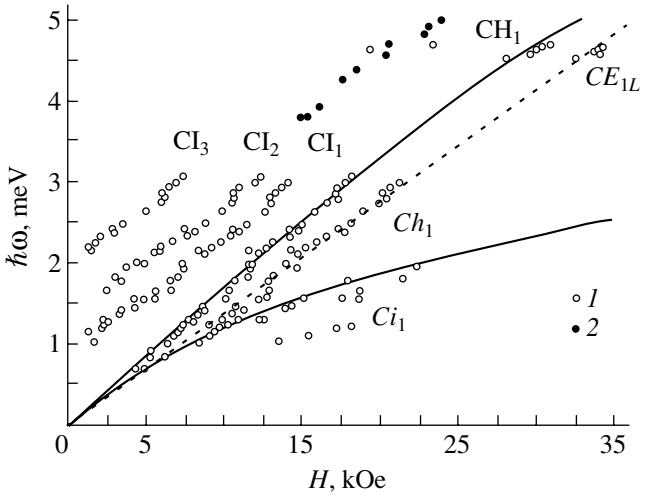

Fig. 2. Energy positions of the resonance lines in (*1*) the magnetoabsorption spectra and (*2*) photoconductivity spectra of sample **308b**. Solid lines indicate the calculated energies of the transitions $0s_1 \longrightarrow 1s_1$ (the CH_1 absorption line) and $3a_1 \longrightarrow 4a_1$ (the Ch_1 absorption line) between the Landau levels (the computational procedure and the notation of the Landau levels are described in [7–10]). The dashed line represents the energy positions of the cyclotron resonance line of electrons in the 1*L* valley ($m_c = 0.083m_0$).

not specially doped, and the concentration of residual acceptor impurities in the samples was of the order of 10^{14} cm^{-3} [1]. The parameters of the studied samples of the $Ge/Ge_{1-x}Si_x$ heterostructures are presented in Table 1. The samples were placed in a light-pipe helium cryostat at the center of a superconducting solenoid. Backward-wave tubes (BWT) were used as submillimeter radiation sources. The magnetoabsorption spectra were recorded at a constant frequency of BWT radiation and magnetic-field sweeping in the Faraday configuration $\mathbf{E}_\omega \perp \mathbf{H}$ at $T = 4.2$ K. The magnetic field was directed along the heterostructure axis. The experiments were performed with both linearly and elliptically polarized microwave radiation. The elliptic polarization was used to determine the sign of charge carriers and was achieved with a reflection-type grid polarizer, which ensured a controlled phase shift between two plane waves linearly polarized in mutually perpendicular directions. The sample was subjected to band-gap optical excitation (modulated with a frequency of 1 kHz) with the use of a gallium arsenide light-emitting diode ($\lambda \approx 0.9$ μm) located near the sample in liquid helium. The radiation passed through the sample was detected using an *n*-InSb crystal according to a standard scheme of lock-in amplification. The signal from the output of the amplifier was entered on a personal computer as a function of the magnetic field with the use of an analog-to-digital converter. The possibility of observing the lines of impurity-assisted transitions in magnetoabsorption spectra upon band-gap photoexcitation stems from the fact that generated free electrons and holes can be captured both by ionized impurities (always contained in the samples due to impurity compensation) and by neutral impurities, which leads to modulation of the impurity absorption. Moreover, strip ohmic contacts were deposited on the sample surface, which made it possible to apply a lateral electric field to the sample. For a number of samples, we measured the submillimeter photoconductivity spectra. In this case, a bias voltage of approximately 1 V was applied to the sample and the submillimeter radiation was modulated with a frequency of 200 Hz [5].

3. RESULTS AND DISCUSSION

Figure 1 shows typical magnetoabsorption spectra of sample **308b**. Figure 2 presents the calculated and experimental data on the energy positions of the resonance lines in the magnetoabsorption spectra and the results of measurements of the photoconductivity spectra. By analogy with the results of investigations into the magnetoabsorption upon band-gap photoexcitation of free carriers in quantizing magnetic fields $\hbar\omega_c \gg k_B T$ (where ω_c is the cyclotron frequency of charge carriers) for other samples of Ge/GeSi heterostructures [8–12], it is reasonable to assign the fundamental absorption line CH_1 to cyclotron resonance of holes. The case in point is the transition from the $0s_1$ lower lying Landau level

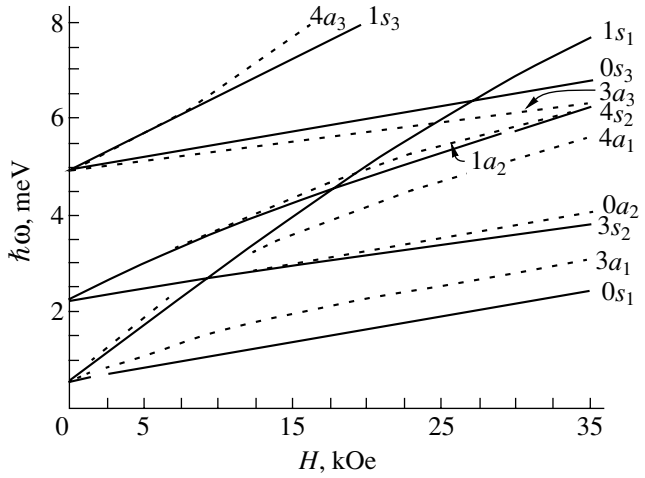

Fig. 3. Calculated energies of the Landau levels of holes in the first three quantum-well subbands for sample **308a** (the computational procedure is described in [7–10]). Designations: the first numeral corresponds to the level number; the letters "s" and "a" denote the symmetric and antisymmetric states, respectively; and the subscript indicates the number of the quantum-well subband.

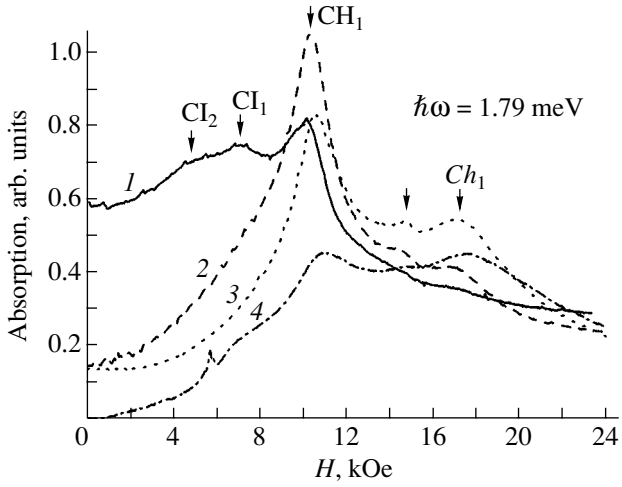

Fig. 4. Magnetoabsorption spectra of sample **308a** in a dc electric field. The intensity of the CI_1 and CI_2 magnetoabsorption lines associated with the impurities gradually decreases with an increase in the applied electric field, whereas the CH_1 and Ch_1 cyclotron lines remains unchanged. E = (*1*) 0, (*2*) 12.5, (*3*) 22.5, and (*4*) 35 V/cm.

to the $1s_1$ level (both levels correspond to heavy holes with an angular momentum $J = -3/2$) (Fig. 3). The Ch_1 line can be associated with the $3a_1 \longrightarrow 4a_1$ transition between the two lower levels belonging to another ladder of the Landau levels of heavy holes with an angular momentum $J = +3/2$. It can be seen from Fig. 2 that the experimental energy positions of these lines are in good agreement with the results of calculations. The CE_{1L} line is attributed to the cyclotron resonance of electrons in the 1*L* valley,[1] which forms the conduction band bottom in GeSi layers, i.e., quantum wells for electrons in the studied structures with thick Ge layers (samples **307**–**309**) [11, 12]. In these samples (unlike the previously studied samples **259** [13], **306** [8–10], and **262**, in which the conduction band bottom is formed by states of the 3*L* valleys in Ge layers [14]), the mean silicon content x and, hence, the elastic strain ε_{xx} in the Ge layers are small in magnitude (Table 1).

In our opinion, the remaining lines, CI_1–CI_3 and Ci_1, can be assigned not to cyclotron resonance of free charge carriers but to shallow-impurity-assisted transitions. This inference was made for the following reasons.

(1) In magnetic fields whose strength exceeds 10 kOe, the energy separation between the lower Landau levels ($0s_1$, $3a_4$) and the higher lying Landau levels exceeds 1 meV (Fig. 3), which is substantially greater than k_BT (0.36 meV at 4.2 K). Consequently, the population of higher lying Landau levels is small and the transitions from these levels should not manifest themselves in the magnetoabsorption spectra.

(2) In quantizing magnetic fields $\hbar\omega_c \gg k_BT$, the cyclotron resonance spectra can involve not only the CH_1 and Ch_1 cyclotron lines associated with the transitions from two lower Landau levels of holes but also the lines of the intersubband cyclotron transitions ($0s_1 \longrightarrow 1s_3$, $0s_1 \longrightarrow 1s_5$) observed for sample **309** with wide Ge quantum wells (d_{Ge} = 800–850 Å) [11, 12]. Among the samples studied in the present work, sample **308** is characterized by the widest Ge quantum wells (d_{Ge} = 330–350 Å). However, even for these quantum wells, the energy separation between the first and third interacting quantum-well subbands is equal to 4.4 meV (Fig. 3), whereas the CI_1–CI_3 impurity lines are clearly observed at considerably lower photon energies (Figs. 1, 2). Therefore, the aforementioned lines cannot be attributed to the intersubband cyclotron resonance.

(3) The extrapolation of the energy positions of the CI_1–CI_3 lines gives a finite (nonzero) energy at $H \longrightarrow 0$ (see also [8–10]).

(4) In a dc electric field (with a voltage up to 35 V/cm), the CH_1 and Ch_1 lines associated with the cyclotron resonance are retained in the magnetoabsorption spectrum (Fig. 4), whereas the intensity of the impurity lines gradually decreases, most likely, as a result of impact ionization of impurities.

(5) As can be seen from Fig. 2, the slope of the curves corresponding to the energy positions of the CI_1–CI_3 lines is identical to that of the CH_1 line. Moreover, the curve describing the energy position of the Ci_1 line is parallel to that of the Ch_1 line. A similar behavior of the impurity lines was observed for samples **309** with very wide quantum wells (d_{Ge} = 850 Å) [11, 12] and for samples with narrower quantum wells, namely, **307a**

[1] This can also be judged from the results of polarization measurements similar to those described in [11, 12].

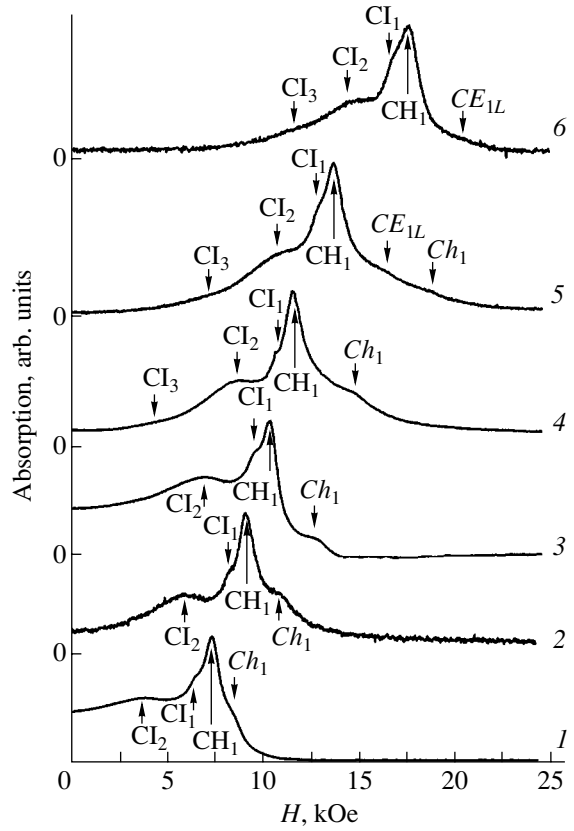

Fig. 5. Magnetoabsorption spectra of sample **307a**. $\hbar\omega$ = (*1*) 1.21, (*2*) 1.48, (*3*) 1.70, (*4*) 1.87, (*5*) 2.22, and (*6*) 2.83 meV.

(d_{Ge} = 300 Å) (Figs. 5, 6), **306a** (d_{Ge} = 200 Å) [8–10], and **262b** (d_{Ge} = 120 Å) (Fig. 7). On this basis, it is reasonable to assume that the CI_1–CI_3 lines can be assigned to the transitions between the impurity states associated with the $0s_1$ and $1s_1$ Landau levels, whereas the Ci_1 line corresponds to the transitions between the states associated with the $3a_1$ and $4a_1$ levels.

Upon band-gap photoexcitation at a low temperature, generated free electrons and holes can be captured both by ionized impurities, i.e., acceptors and donors (always contained in the sample due to impurity compensation), and by neutral impurities (in our case, acceptors). It is unlikely that the observed resonances can be due to transitions involving donor impurities, because, first, the structures under investigation possess *p*-type conductivity (i.e., donors are compensating impurities) and, second, the polarization measurements did not reveal resonance lines with electron polarization among the impurity lines. Undoubtedly, the complete interpretation of the impurity lines observed calls for further experimental and theoretical investigations. However, we can list all the possible acceptor-assisted optical transitions. First, this is the $1s \longrightarrow 2p_+$ transition for acceptors located in the vicinity of the barrier centers. The binding energy reaches a maximum and a minimum at the centers of the quantum well and the barrier, respectively (Table 2). Therefore, in the case of residual impurities (uniformly distributed throughout the structure), it is reasonable to expect that the transitions with energies corresponding to exactly these positions of the impurities will manifest themselves in the spectra (see, for example, [3, 4]). The binding energies typical of acceptors located at the centers of the quantum wells and barriers in Ge/GeSi heterostructures are equal to 7–8 and 2 meV, respectively (Table 2). Hence, it follows that the energies of the transitions involving acceptors located in quantum wells fall outside the energy range covered. Second, the magnetoabsorption

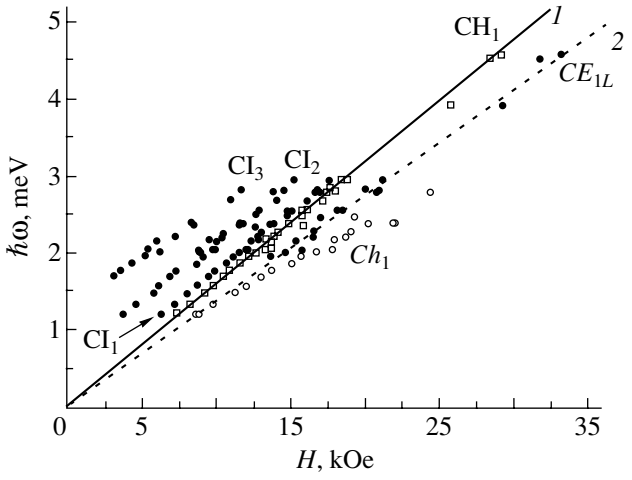

Fig. 6. Energy positions of the resonance lines in the magnetoabsorption spectra of sample **307a** (circles): (*1*) energies of the $0s_1 \longrightarrow 1s_1$ transition (the CH_1 absorption line) calculated according to the procedure described in [7–10] and (*2*) the cyclotron resonance line of electrons in the 1*L* valley.

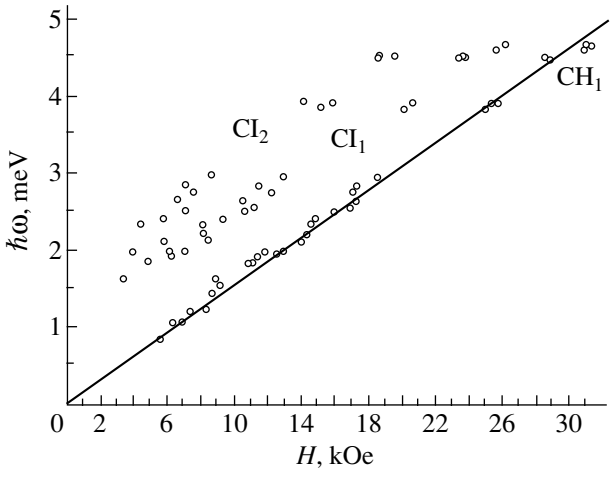

Fig. 7. Energy positions of the resonance lines in the magnetoabsorption spectra of sample **262b** (circles). The solid line represents the energies of the $0s_1 \longrightarrow 1s_1$ transition (the CH_1 absorption line) calculated according to the procedure described in [7–10].

Table 2. Binding energies of shallow acceptor levels in the $Ge/Ge_{1-x}Si_x$ heterostructures (meV)

Sample no.	1*s*	$2p_0$	2*s*	$2p_\pm$
262b (well center)	7.9	Resonant	1.3	1.4
262b (barrier center)	2.1	Resonant	0.6	0.93
307a (well center)	6.9	2.8	1.2	1.5
307a (barrier center)	1.8	0.6	0.4	0.9
308a (well center)	7.5	3.1	1.7	2.0
308a (barrier center)	2.0	0.8	0.5	0.88
309b (well center)	8.4	3.1	2.5	1.8
309b (barrier center)	1.9	0.9	0.4	–

spectra obtained in this work can exhibit transitions between excited acceptors states belonging to different Landau levels. These transitions can occur under band-gap photoexcitation, provided the lifetime of charge carriers is comparable to the relaxation time scale for hot carriers in the excited states [15]. Finally, the band-gap photoexcitation can lead to the formation of A^+ centers due to the capture of an excess hole by a neutral acceptor. According to our estimates [16], the binding energy of A^+ centers in a quantum well is approximately equal to 2 meV; therefore, these centers, as well as the acceptors located in the barriers, can manifest themselves in the spectra.

ACKNOWLEDGMENTS

We would like to thank M.D. Moldavskaya for long-term cooperation laying the groundwork for the present study, E.A. Uskova for preparing the samples use in our measurements, V.L. Vaks and A.N. Panin for their assistance in performing the experiments with backward-wave tubes, and Yu.N. Drozdov for x-ray diffraction investigations of the samples.

This work was supported by the Russian Foundation for Basic Research (project no. 03-02-16808); the Ministry of Industry, Science, and Technology of the Russian Federation; and the Russian Federal program "Integration" (project no. B0039/2102).

REFERENCES

1. V. I. Gavrilenko, I. V. Erofeeva, A. L. Korotkov, *et al.*, Pis'ma Zh. Éksp. Teor. Fiz. **65** (2), 194 (1997) [JETP Lett. **65**, 209 (1997)].
2. V. Ya. Aleshkin, V. I. Gavrilenko, I. V. Erofeeva, *et al.*, Fiz. Tekh. Poluprovodn. (St. Petersburg) **32** (10), 1240 (1998) [Semiconductors **32**, 1106 (1998)].
3. V. Ya. Aleshkin, V. I. Gavrilenko, I. V. Erofeeva, *et al.*, Phys. Status Solidi B **210** (2), 649 (1998).
4. V. Ya. Aleshkin, B. A. Andreev, V. I. Gavrilenko, *et al.*, Fiz. Tekh. Poluprovodn. (St. Petersburg) **34** (5), 582 (2000) [Semiconductors **34**, 563 (2000)].
5. V. Ya. Aleshkin, B. A. Andreev, V. I. Gavrilenko, *et al.*, Physica E (Amsterdam) **7** (3–4), 608 (2000).
6. V. Ya. Aleshkin, B. A. Andreev, V. I. Gavrilenko, *et al.*, Nanotechnology **11** (4), 348 (2000).
7. V. Ya. Aleshkin, V. I. Gavrilenko, D. B. Veksler, and L. Reggiani, Phys. Rev. B **66**, 155336 (2002).
8. V. Ya. Aleshkin, V. I. Gavrilenko, I. V. Erofeeva, *et al.*, in *Proceedings of the Workshop on Nanophotonics* (IFM Ross. Akad. Nauk, Nizhni Novgorod, 1999), p. 114.
9. V. Ya. Aleshkin, V. I. Gavrilenko, I. V. Erofeeva, *et al.*, in *Proceedings of the 6th International Symposium "Nanostructures: Physics and Technology," St. Petersburg, Russia* (1999), p. 356.
10. V. Ya. Aleshkin, V. L. Vaks, D. B. Veksler, *et al.*, Izv. Akad. Nauk, Ser. Fiz. **64** (2), 308 (2000).
11. V. Ya. Aleshkin, D. B. Veksler, V. I. Gavrilenko, *et al.*, in *Proceedings of the Workshop on Nanophotonics* (IFM Ross. Akad. Nauk, Nizhni Novgorod, 2003), p. 11.
12. V. Ya. Aleshkin, D. B. Veksler, V. I. Gavrilenko, *et al.*, Fiz. Tverd. Tela (St. Petersburg) **46** (1), 131 (2004) [Phys. Solid State **46**, 130 (2004)].
13. V. I. Gavrilenko, I. N. Kozlov, O. A. Kuznetsov, *et al.*, Pis'ma Zh. Éksp. Teor. Fiz. **59** (5), 327 (1994) [JETP Lett. **59**, 348 (1994)].
14. V. Ya. Aleshkin and N. A. Bekin, Fiz. Tekh. Poluprovodn. (St. Petersburg) **31**, 171 (1997) [Semiconductors **31**, 132 (1997)].
15. S. V. Meshkov and É. I. Rashba, Zh. Éksp. Teor. Fiz. **76** (6), 2206 (1979) [Sov. Phys. JETP **49**, 1115 (1979)].
16. V. Ya. Aleshkin, V. I. Gavrilenko, and D. V. Kozlov, in *Proceedings of the Workshop on Nanophotonics* (IFM Ross. Akad. Nauk, Nizhni Novgorod, 2003), p. 318.

Translated by O. Borovik-Romanova

Physics of the Solid State, Vol. 46, No. 1, 2004, pp. 13–16. Translated from Fizika Tverdogo Tela, Vol. 46, No. 1, 2004, pp. 18–20.

PROCEEDINGS OF THE CONFERENCE DEDICATED TO O. V. LOSEV (1903–1942)

(Nizhni Novgorod, Russia, March 17–20, 2003)

Edge Electroluminescence of Silicon: An Amorphous-Silicon–Crystalline-Silicon Heterostructure

M. S. Bresler*, O. B. Gusev*, E. I. Terukov*, A. Froitzheim, and W. Fuhs****

**Ioffe Physicotechnical Institute, Russian Academy of Sciences, Politekhnicheskaya ul. 26, St. Petersburg, 194021 Russia*

***Hahn-Meitner-Institut, Abt. Silizium-Photovoltaik, Kekule-Str. 5, Berlin, D-12489 Germany*

Abstract—Silicon edge electroluminescence (EL) was observed on an amorphous-silicon–crystalline-silicon heterostructure (*a*-Si : H(*n*)/*c*-Si(*p*)) in the temperature range from 77 to 300 K. The room-temperature EL internal quantum efficiency of the heterostructure under study was found to be about 0.1%. A theoretical analysis of the emissive properties of the *a*-Si : H(*n*)/*c*-Si(*p*) heterostructure was made in terms of the model of an abrupt planar *p–n* junction and showed that, for optimal doping, the internal quantum efficiency of the EL may be as high as a few percent at a modulation frequency of about 50 kHz. *© 2004 MAIK "Nauka/Interperiodica".*

1. INTRODUCTION

The demand for high-efficiency photonic materials capable of being integrated into standard optical fiber communications lines stimulated interest in the light-emitting properties of silicon. Among the various approaches for silicon-based optoelectronics, the most straightforward path lies in increasing the efficiency of the intrinsic edge electroluminescence (EL) of silicon. An internal quantum efficiency of the EL of about 1% was recently claimed to have been reached in a *p–n* crystalline-silicon homojunction [1, 2]. This value, which is fairly high for silicon, was explained in terms of the EL model based on an abrupt planar silicon *p–n* junction [3].

In this communication, we show that the amorphous *n*-silicon–crystalline *p*-silicon electroluminescent heterostructure, *a*-Si : H(*n*)/*c*-Si(*p*), operates similar to a *p–n* homojunction based on crystalline silicon; namely, the passing of a current through a forward-biased *a*-Si : H(*n*)/*c*-Si(*p*) heterostructure generates silicon edge EL due to exciton recombination in crystalline silicon. Similar to the case of a *p–n* junction based on crystalline silicon, the internal quantum efficiency of an *a*-Si : H(*n*)/*c*-Si(*p*) heterostructure is governed by the radiative recombination coefficient and by the lifetime of the electrons injected into the *c*-Si(*p*) conduction band. The electroluminescent *a*-Si : H(*n*)/*c*-Si(*p*) heterostructure can have a higher external EL quantum efficiency than a *p–n* homojunction based on crystalline silicon.

2. EXPERIMENTAL RESULTS

The amorphous *n*-silicon–crystalline *p*-silicon electroluminescent heterostructure *a*-Si : H(*n*)/*c*-Si(*p*) was prepared through deposition of hydrogenated amorphous silicon, *a*-Si : H, on a *c*-Si(*p*) (crystalline *p*-silicon) substrate. In the course of deposition, the amorphous silicon was doped by phosphorus to a concentration of 10^{19} cm^{-3}. The *a*-Si : H(*n*) film thus obtained was 30 nm thick. An 80-nm-thick transparent conducting electrode for coupling the light out of the *a*-Si : H(*n*) layer was applied by sputtering ZnO(Al). A ring contact was produced on the ZnO(Al) surface through the deposition of aluminum.

The current–voltage curves of the *a*-Si : H(*p*)/*c*-Si(*n*) electroluminescent heterostructure measured at 77 and 300 K are displayed in Fig. 1. Electroluminescence was observed by passing square current pulses through the forward-biased structure and was analyzed by a grating monochromator with a focal length of

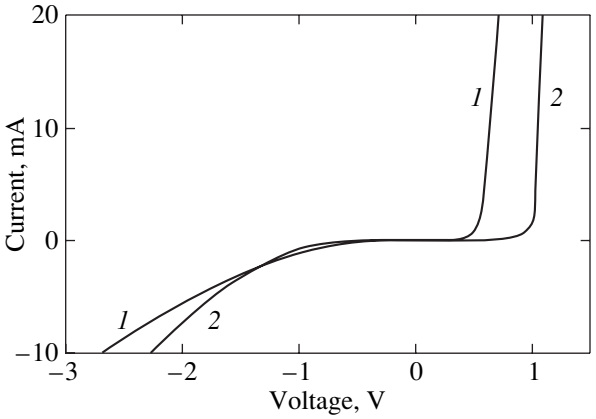

Fig. 1. *I–V* characteristics of an amorphous-silicon-crystalline-silicon heterostructure measured at (*1*) 300 and (*2*) 77 K.

1063-7834/04/4601-0013$26.00 © 2004 MAIK "Nauka/Interperiodica"

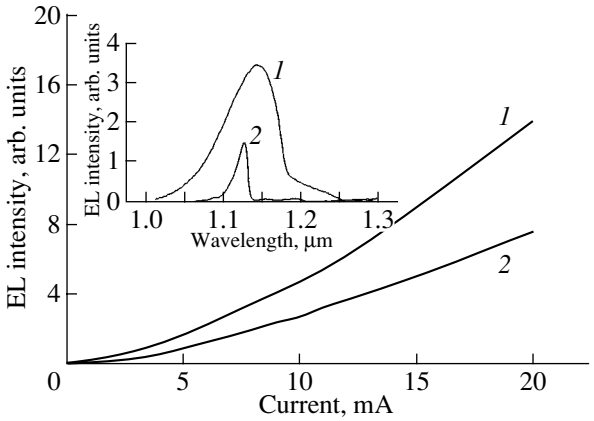

Fig. 2. Silicon edge EL intensity vs. current density measured at (*1*) 300 and (*2*) 77 K at the maximum of the corresponding spectral line. Inset shows EL spectra obtained at the same temperatures.

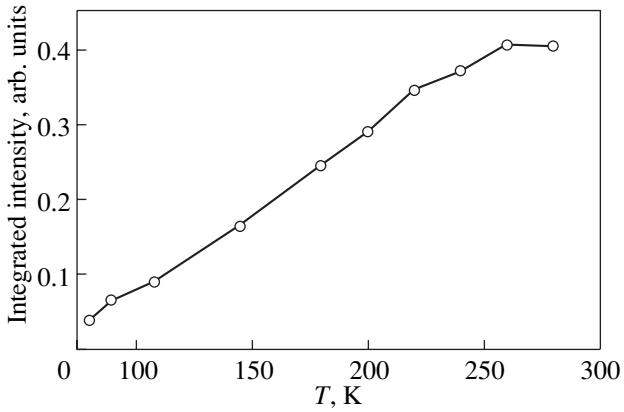

Fig. 3. Temperature dependence of the integrated intensity of silicon edge EL.

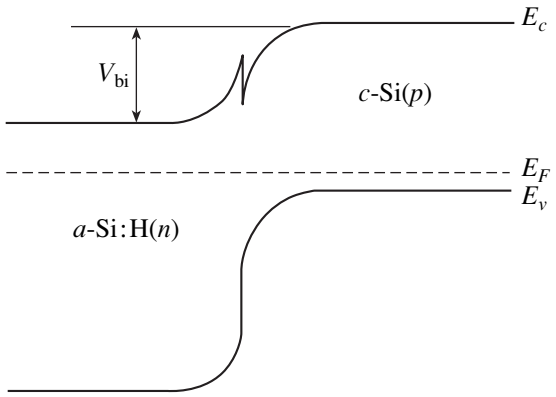

Fig. 4. Energy band diagram for *a*-Si : H/*c*-Si.

822 mm equipped with a cooled germanium photodetector. The EL decay after the current was turned off was recorded using a digital oscillograph. The total time resolution of the measuring system was 3 μs.

Figure 2 presents the current dependence of the EL intensity of the *a*-Si : H(*n*)/*c*-Si(*p*) heterostructure taken at temperatures of 77 and 300 K. The inset shows the EL spectra obtained at these temperatures. The spectra are due to conventional edge luminescence of crystalline silicon. At low temperature, practically all of the intrinsic silicon EL originates from the recombination of free electrons with the involvement of optical phonons. At room temperature, the recombination contributions from free excitons and free carriers are approximately equal; for this reason, the top of the room-temperature spectrum is slightly deformed. As is evident from Fig. 2, the room-temperature EL intensity is considerably higher than that measured at liquid-nitrogen temperature. The edge luminescence decay time measured after the current pulse was turned off at room temperature was 25 μs against less than 3 μs at liquid-nitrogen temperature. Figure 3 shows the temperature behavior of the integrated intensity of the intrinsic EL. We readily see that the intrinsic EL intensity increases with temperature and reaches a maximum at room temperature. Note that similar results on the temperature course of the intensity and decay time of the edge EL have been observed in a crystalline-silicon *p–n* homojunction [1–3].

3. RESULTS AND DISCUSSION

Figure 4 presents an energy diagram of the *a*-Si : H(*n*)/*c*-Si(*p*) heterojunction based on data from [4]. The gap widths of *a*-Si : H and *c*-Si are 1.9 and 1.12 eV, respectively. The band offset in the conduction band is approximately 0.2–0.3 eV. The Fermi level for the *a*-Si : H layer doped by phosphorus to 10^{19} cm^{-3} lies 0.25 eV below the conduction-band bottom [4]. In this case, the electron concentration in the conduction band corresponding to the given Fermi level position (6×10^{16} cm^{-3}) is fairly low for the emitter. At the interface pocket, however, the concentration may reach 5×10^{18} cm^{-3}, a level high enough to attain efficient electron injection.

The analysis of the electroluminescence efficiency of a crystalline-silicon *p–n* junction carried out in [3] showed that a high doping level in the *n* region of a homogeneous *p–n* junction favors the achievement of a good electroluminescence efficiency. In this case, the edge silicon EL would be governed primarily by the *p* region and the internal edge EL quantum efficiency can be written as

$$\eta \approx r_r p_p \tau_n \frac{E_g}{qV_{bi}} \approx \frac{\tau_n}{\tau_\tau}, \qquad (1)$$

where r_r is the radiative recombination coefficient, p_p is the concentration of majority carriers (holes) in the *p* region of the *p–n* junction, τ_n is the total electron lifetime in the *p* region, E_g is the band-gap width of *c*-Si,

q is the electronic charge, and V_{bi} is the potential barrier in the conduction band. Thus, the internal quantum efficiency is determined, as follows from Eq. (1), by the ratio of the total minority-carrier to radiative lifetime. Because the lifetimes depend on the concentrations of majority carriers in the n and p regions, these regions can be doped to an optimum level. Using the data on the dependence of the minority-carrier lifetime on the majority-carrier concentration [5], one can readily calculate the optimum doping level needed to attain the maximum possible internal quantum efficiency of intrinsic EL. The results of the calculation are plotted in Fig. 5. We readily see that the maximum quantum efficiency of the edge EL may be as high as 3% at a p-region carrier concentration of 10^{17} cm^{-3}. At higher concentrations, the quantum efficiency degrades because of the decrease in τ_n brought about by Auger processes, while at low concentrations the radiative recombination probability is low.

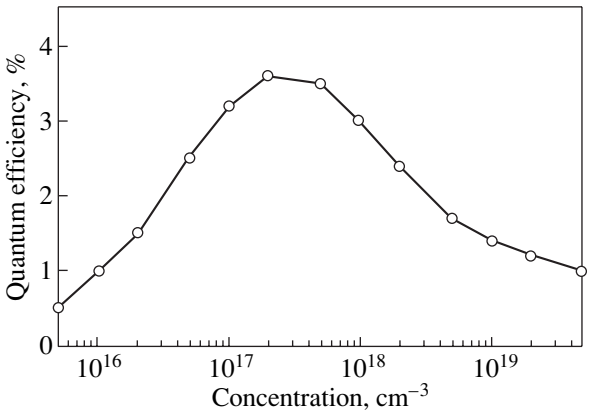

Fig. 5. Calculated dependence of the edge EL quantum efficiency on the doping level of the p region in the p–n junction. T = 300 K. Carrier concentration in the n region 5×10^{18} cm^{-3}.

Using $r_r \sim 10^{-14}$ cm^{-3} s^{-1} for the room-temperature radiative recombination coefficient [6] and $\tau_n \sim 10^{-4}$ s for the minority carrier lifetime in c-Si(p) for an equilibrium charge concentration of 1×10^{16} cm^{-3} [5], we estimated the internal quantum efficiency as 10^{-2}. This value of the internal quantum efficiency is noticeably higher than the experimental value (0.1×10^{-2}).

We believe that this discrepancy may be due to the low quality of our p–n junction. This conjecture is supported by the temperature dependence of the integrated EL intensity displayed in Fig. 3. Because the radiative recombination coefficient r_r should decrease with increasing temperature [6], the growth of the integrated intensity of intrinsic EL with temperature should be assigned, as in the case of the crystalline-silicon p–n homojunction, to the fact that the probability of trapping of the electrons injected into the p region by deep impurities (defects) decreases with increasing temperature. Thus, we believe that the n region of our p–n junction contains a certain concentration of deep attracting recombination centers. The formation of such centers is apparently connected with the penetration of defects into the n region in the course of deposition of the amorphous p-silicon layer.

The first excited metastable level of a deep charged impurity is known to be close, in order of magnitude, to the energy of a shallow acceptor (donor) in silicon; i.e., this level is ~50 meV relative to the edge of the valence or conduction band. At room temperature, the rate of electron trapping to the metastable level mediating the multiphonon electron capture to the ground state can be lower than the rate of reverse carrier ejection from this level into the band. Thus, the probability of nonradiative trapping of injected electrons by deep centers in silicon decreases with increasing temperature. This is what accounts for the increase in the EL intensity and for the observed enhancement of the EL signal decay time after the termination of the current pulse. Note that surface states at the amorphous silicon–crystalline silicon interface may give rise to the same effect.

It is appropriate to compare here the emissive properties of a p–n homojunction based on crystalline silicon and of the a-Si : H/c-Si heterostructure. The external quantum efficiency of the a-Si : H/c-Si electroluminescent structure will be somewhat higher, because the edge radiation of silicon is coupled out through the a-Si : H wide-gap material, which reduces the edge EL absorption. Since the technique used to prepare the a-Si : H(n)/c-Si(p) heterostructures is simpler and considering the compatibility of these structures with the optical devices employed in silicon-based optoelectronics, we believe that these structures may find application in this area.

4. CONCLUSIONS

Thus, we have observed silicon EL in the amorphous silicon–crystalline silicon heterojunction in the region extending from nitrogen temperature to room temperature. The temporal characteristics of the edge EL and the temperature behavior of its intensity in such a structure are very close to those observed with a homogeneous p–n junction based on crystalline silicon. However, the lower energy barrier between the a-Si : H(n) and c-Si(p) conduction bands and the larger band-gap width of amorphous silicon may provide favorable conditions for attaining higher internal and external quantum efficiencies of edge EL in the a-Si : H(n)/c-Si(p) structure.

ACKNOWLEDGMENTS

This study was supported by the Russian Foundation for Basic Research, the Netherlands scientific research foundation (NWO), the Ministry of Industry, Science, and Technology of the Russian Federation,

and the RAS Physical Sciences Division program "New Materials and Structures."

REFERENCES

1. M. A. Green, J. Zhao, A. Wang, *et al.*, Nature **412**, 805 (2001).
2. W. L. Ng, M. A. Lourenço, R. M. Gwilliam, *et al.*, Nature **410**, 192 (2001).
3. O. B. Gusev, M. S. Bresler, I. N. Yassievich, and B. P. Zakharchenya, in *NATO Workshop on Optical Amplification and Stimulation in Silicon, OASIS, Trento* (2002).
4. A. Froitzheim, K. Brendel, L. Elstner, *et al.*, J. Non-Cryst. Solids **299–302**, 663 (2002).
5. V. N. Abakumov, V. I. Perel', and I. N. Yassievich, *Nonradiative Recombination in Semiconductors* (S.-Peterb. Inst. Yad. Fiz. Ross. Akad. Nauk, St. Petersburg, 1997).
6. H. Schlangenotto, H. Maeder, and W. Gerlach, Phys. Status Solidi A **21** (2), 357 (1974).

Translated by G. Skrebtsov

Physics of the Solid State, Vol. 46, No. 1, 2004, pp. 130–137. Translated from Fizika Tverdogo Tela, Vol. 46, No. 1, 2004, pp. 131–137.

PROCEEDINGS OF THE CONFERENCE DEDICATED TO O. V. LOSEV (1903–1942)

(Nizhni Novgorod, Russia, March 17–20, 2003)

Intersubband Cyclotron Resonance of Holes in Strained Ge/GeSi(111) Heterostructures with Germanium Wide Quantum Wells and Cyclotron Resonance of 1*L* Electrons in GeSi Layers

V. Ya. Aleshkin*, D. B. Veksler*, V. I. Gavrilenko*, I. V. Erofeeva*, A. V. Ikonnikov*, D. V. Kozlov*, and O. A. Kuznetsov**

** Institute of Microstructure Physics, Russian Academy of Sciences, Nizhni Novgorod, 603950 Russia*
e-mail: gavr@ipm.sci-nnov.ru

*** Physicotechnical Research Institute, Nizhni Novgorod State University, pr. Gagarina 23, Nizhni Novgorod, 603950 Russia*

Abstract—The submillimeter ($\hbar\omega$ = 0.5–5 meV) magnetoabsorption spectra of strained Ge/$Ge_{1-x}Si_x$(111) multilayer heterostructures with thick Ge layers (d_{Ge} = 300–850 Å, $d_{GeSi} \approx$ 200 Å, $x \approx 0.1$) are investigated at T = 4.2 K upon band-gap optical excitation. It is revealed that the absorption spectra contain cyclotron resonance lines of 1*L* electrons localized in GeSi solid solution layers (unlike the previously studied structures with thin Ge layers as quantum wells for 3*L* electrons). The absorption spectra of the samples with thick Ge layers (d_{Ge} = 800–850 Å) exhibit cyclotron resonance lines of holes due to transitions from the lower Landau levels in the first quantum-well subband to the Landau levels belonging to the third and fifth higher subbands. © *2004 MAIK "Nauka/Interperiodica".*

1. INTRODUCTION

Ge/GeSi heterostructures with quantum wells are convenient model objects for studying the transformation of the energy spectra of charge carriers upon changeover from a bulk semiconductor to strained quantum-well layers. Investigation of these structures makes it possible to elucidate the combined effects of elastic strain and quantum confinement (which can be independently controlled by varying the composition and thickness of the grown layers) on the energy spectra of charge carriers. Up to now, much attention has been focused on the study of the valence band, in which it was assumed that the effective mass of charge carriers substantially decreases as a result of the splitting of light- and heavy-hole subbands.[1] This inference was drawn in a number of works concerned with the charge transfer (see, for example, [1]) and cyclotron resonance observed in both undoped materials (upon band-gap photoexcitation of carriers) [2] and selectively doped samples [3]. Earlier [4], cyclotron resonance was examined using samples with relatively thin Ge layers whose thickness ($d_{Ge} \le$ 200 Å) was of the order of the thickness of $Ge_{1-x}Si_x$ solid solution layers ($x \approx 0.1$). In these objects, the quantum wells for electrons and holes reside in strained Ge layers and the conduction band bottom is formed by states of 3*L* valleys [4]. The cyclotron resonance spectra of holes in these heterostructures contain lines attributed to transitions between the Landau levels in the first quantum-well subband of carriers. However, cyclotron resonance lines of electrons have not been observed.

In this work, we investigated the magnetoabsorption spectra of Ge/GeSi(111) heterostructures with thick Ge layers ($d_{Ge} \ge$ 300 Å) upon band-gap photoexcitation of charge carriers. It was revealed that the absorption spectra of all the samples studied exhibit cyclotron resonance lines of electrons in 1*L* valleys, which form the conduction band bottom in GeSi solid solution layers. In heterostructures with the thickest Ge layers (800–850 Å), the energy separation between the quantum-well subbands of holes and the energies of cyclotron transitions were found to be of the same order of magnitude (up to 5 meV). This made it possible for the first time to observe the transitions to the Landau levels belonging to the highest quantum-well subbands.

2. SAMPLES AND EXPERIMENTAL TECHNIQUE

The Ge/$Ge_{1-x}Si_x$ heterostructures were grown through vapor-phase epitaxy on lightly doped Ge(111) substrates. The table presents the structural parameters and strains for samples **307**–**309** and sample **306a** (studied in our previous works), which were determined using x-ray diffraction analysis. The total thickness of all the structures grown exceeded the critical

[1] In Ge/GeSi heterostructures, quantum wells for holes always reside in the Ge layers [4].

Parameters of the $Ge/Ge_{1-x}Si_x$ heterostructures

Sample no.	x	d_{Ge}, Å	d_{GeSi}, Å	Number of periods	Strain in Ge layers, $\varepsilon_{xx} \times 10^4$	Substrate
306a	0.12	200	260	162	22	GÉS-45
307a	0.09	300	230	162	8.7	GÉS-45
308a	0.09	350	160	162	4.4	GÉS-45
308b	0.09	330	150	162	4.4	GDG-40
309a	0.07	850	200	83	4.6	GÉS-45
309b	0.07	800	200	83	3.3	GDG-40

value, which led to elastic relaxation at the heterostructure–substrate interface. As a result, the Ge layers turned out to be biaxially compressed in the heterostructure, whereas the GeSi layers were biaxially extended. The materials were not specially doped, and the concentration of residual acceptor impurities was of the order of 10^{14} cm^{-3} [5]. The samples were placed at the center of a superconducting solenoid in liquid helium. The magnetic field was directed along the heterostructure axis. Backward-wave tubes were used as radiation sources in the frequency range f = 130–1250 GHz. The measurements were performed in the Faraday configuration $\mathbf{E}_\omega \perp \mathbf{H}$ at a constant frequency of microwave radiation and magnetic-field sweeping at T = 4.2 K. Free charge carriers in the sample were generated under band-gap photoexcitation with the use of a gallium arsenide light-emitting diode ($\lambda \approx 0.9$ μm) located near the sample in liquid helium. The radiation passed through the sample was detected using an n-InSb crystal according to a standard scheme of lock-in amplification. The signal from the output of the amplifier was entered on a personal computer as a function of the magnetic field with the use of an analog-to-digital converter. In order to reduce interference effects in the sample, the substrate surface was ground and tapered with a wedge angle of 2°. The experiments were carried out with linearly and elliptically polarized radiation. The elliptic polarization was used to determine the sign of charge carriers and was achieved with a reflection-type grid polarizer, which ensured a controlled phase shift between two plane waves linearly polarized in mutually perpendicular directions. Moreover, two strip ohmic contacts (3 to 4 mm apart) were deposited on the sample surface, which made it possible to apply a lateral electric field to the sample for heating of charge carriers.

3. CYCLOTRON RESONANCE OF 1*L* ELECTRONS

Figure 1 shows typical cyclotron resonance spectra for sample **309a**. Figure 2 presents the calculated and experimental data on the energy positions of the resonance lines in the magnetoabsorption spectra. These spectra exhibit a large number of lines, which, most likely, can be attributed to the cyclotron resonance of holes, cyclotron resonance of electrons, and different impurity-assisted transitions. It should be noted that, in our earlier works [2, 6–8], we did not observe cyclotron resonance lines of electrons in the magnetoabsorption

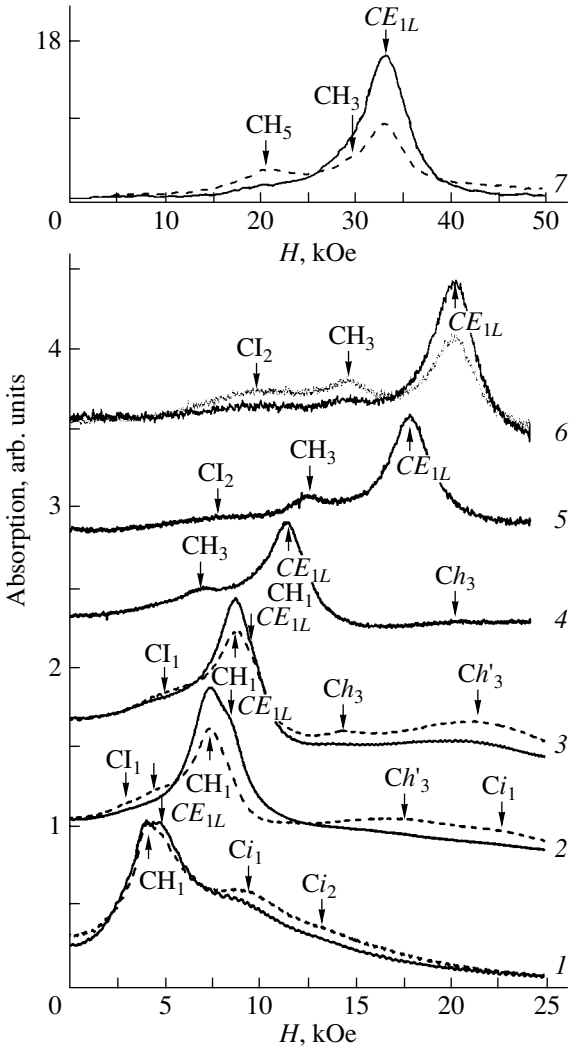

Fig. 1. Magnetoabsorption spectra of sample **309a** for elliptic polarization of BWT radiation. $\hbar\omega$ = (*1*) 0.65, (*2*) 1.16, (*3*) 1.34, (*4*) 1.72, (*5*) 2.51, (*6*) 2.81, and (*7*) 4.73 meV. Solid and dashed lines correspond to different directions of the magnetic field.

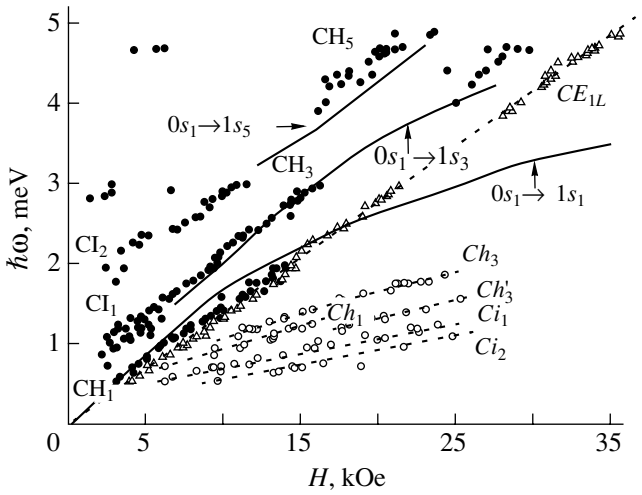

Fig. 2. Energy positions of the resonance lines in the magnetoabsorption spectra of sample **309a** (points). Solid lines indicate the calculated magnetic-field dependences of the energies of the transitions between different Landau levels of holes in the spectral regions where these transitions occur with a sufficiently high intensity. The notation of the Landau levels is given in the caption to Fig. 3. The calculations are performed according to the procedure described in [6–9] with the following parameters of the hole Hamiltonian for Ge quantum wells: $A = 0.99\gamma_1$, $B = 1.98\gamma_2$, and $D = 2.06(3)^{1/2}\gamma_3$, where γ_1, γ_2, and γ_3 are the parameters of the Luttinger Hamiltonian for holes in bulk Ge [10]. Dashed lines represent the energy positions of the cyclotron resonance line of electrons in the 1*L* valley ($m_c = 0.083m_0$).

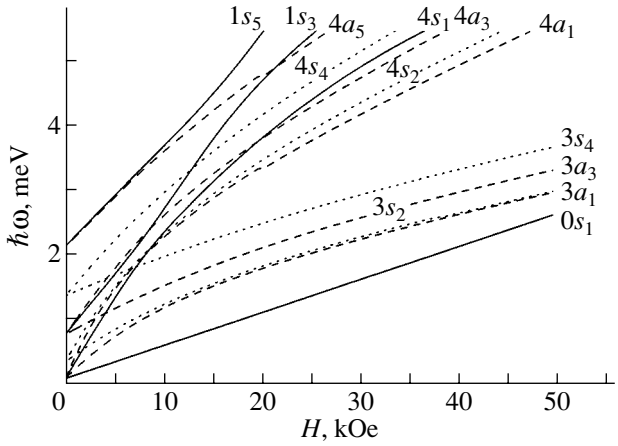

Fig. 3. Energies of the hole Landau levels in the first five quantum-well subbands for sample **309a** according to the calculations using the procedure described in [6–9] with the following parameters of the Luttinger Hamiltonian for holes in bulk Ge: $A = 13.38 = \gamma_1$, $B = 8.48 = 2\gamma_2$, and $D = 19.34 = 2(3)^{1/2}\gamma_3$ [10]. Designations: the first numeral corresponds to the level number; the letters "s" and "a" denote the symmetric and antisymmetric states, respectively; and the subscript indicates the number of the quantum-well subband.

spectra of the Ge/GeSi heterostructures ($d_{Ge} \approx 200$ Å). Figure 3 depicts the calculated (according to the procedure described in [6–9]) "fan-shaped" patterns of the Landau levels of holes in sample **309a** for the first five quantum-well subbands. By analogy with the results of analyzing the cyclotron resonance spectra of samples with narrower quantum wells [6–8], it is reasonable to assume that the fundamental cyclotron resonance line in strong magnetic fields is associated with the $0s_1 \longrightarrow 1s_1$ transition from the lower Landau level of holes. It can be seen from Fig. 3 that, in the energy range 0.5–5 meV, the Landau levels of holes in several quantum-well subbands interact with each other. In particular, the $1s_1$ level (the final state of the basic cyclotron transition $0s_1 \longrightarrow 1s_1$) anticrosses the $1s_3$ level in the third quantum-well subband, which, in turn, anticrosses the $1s_5$ level in the fifth subband. This should result in anticrossing of the cyclotron resonance lines in the $(H, \hbar\omega)$ plane. However, as can be seen from Figs. 1 and 2, the principal line CE_{1L} in the spectra is characterized by a nearly linear frequency dependence of the resonance magnetic field with a slope corresponding to the cyclotron mass $m_c \approx 0.083m_0$. The key to understanding the nature of the CE_{1L} line lies in the results of the polarization measurements, which are presented in Fig. 1 (spectra *7*). From analyzing these spectra, it follows that the observed spectral lines CH_5 and CE_{1L} correspond to different circular polarizations of radiation. Taken together, these facts suggest that the CE_{1L} line can be attributed to the cyclotron resonance of electrons in the 1*L* valley forming the conduction band bottom in the GeSi layers (in the strained Ge layers, the 3*L* valleys of electrons are the lowest valleys).[2] The cyclotron resonance lines of 1*L* electrons are also observed in the spectra of samples **307a** and **308b** (Fig. 4). Thus, the experimental results indicate that, in samples **307a**, **308a**, **308b**, **309a**, and **309b** of the $Ge/Ge_{1-x}Si_x$ heterostructures with thick Ge layers, the quantum wells for electrons reside in the GeSi solid solution layers. It can be seen from the table that the elastic strain ε of germanium layers in these samples is severalfold smaller than that in the previously studied sample **306a**. This difference may stem from the fact that the aforementioned samples are characterized by a larger thickness of the Ge layers, a smaller value of *x*, and, hence, a lower mean silicon content in the heterostructure as compared to these values for sample **306a**. In [4], it was theoretically analyzed how the layer parameters affect the structure of the conduction band bottom in a pseudomorphically grown layer of $Ge/Ge_{1-x}Si_x$. It is seen

[2] The biaxial tension of the GeSi layers in the structure plane is equivalent to a combination of uniform extension (which does not affect the crystal symmetry and the structure of the conduction band bottom) and uniaxial compression along the [111] axis. As a result, the 1*L* valley of electrons shifts toward the low-energy range, whereas the 3*L* valleys shift toward the high-energy range [11]. By contrast, the states of the 3*L* valleys in biaxially compressed Ge layers are the lower states.

from Fig. 5 that, in the ($a_{\|}$, x) plane, the parameters of samples **308a**, **308b**, **309a**, and **309b** fall in region *3*, for which the lowest energy states in the conduction band correspond to the 1*L* valley in the $Ge_{1-x}Si_x$ solid solution. This is in contrast to previously studied sample **306a**, whose parameters lie in region *2*, for which the conduction band bottom is formed by the states of the 3*L* valleys in the Ge layer.[3] It is evident from Fig. 4 that the relative intensity of the CE_{1L} cyclotron resonance line of electrons in sample **307a** is substantially less than those in samples **308b** and **309a**. In Fig. 5, the parameters of sample **307a** lie at the boundary between regions *2* and *3*. This means that, according to the calculations performed in [4], the conduction band in sample **307a** has no discontinuity at the heteroboundary. However, it should be kept in mind that, as was noted in [4], the data presented in Fig. 5 provide only a qualitative assessment, because many of the parameters used in the calculations were previously determined with an insufficient accuracy. Nonetheless, it is seen from a comparison of Figs. 1 and 4 that, unlike the cyclotron resonance spectra of samples **308a** and **309a**, in which the CE_{1L} cyclotron resonance line of electrons is comparable in intensity to the cyclotron resonance lines of holes, in the spectrum of sample **307a**, the CE_{1L} line is hardly distinguishable. This is indirect evidence that the GeSi layers in sample **307a** are not good (i.e., deep on the k_BT scale) quantum wells for electrons.

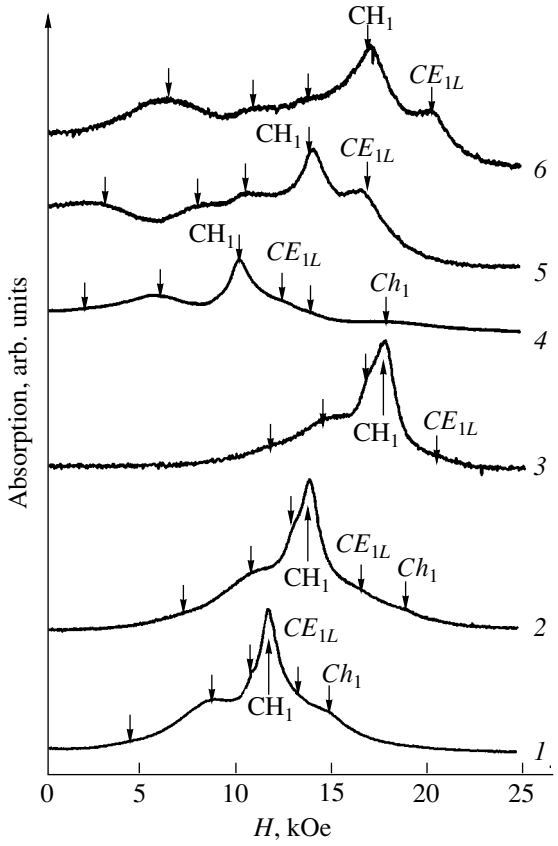

Fig. 4. Cyclotron resonance spectra of (*1–3*) sample **307a** and (*4–6*) sample **308a**. $\hbar\omega$ = (*1*) 1.87, (*2*) 2.22, (*3*) 2.83, (*4*) 1.67, (*5*) 2.40, and (*6*) 2.95 meV.

4. INTERSUBBAND CYCLOTRON RESONANCE OF HOLES

As was noted above, the energies of quantum confinement and magnetic quantization are of the same order of magnitude for sample **309a** with wide quantum wells for electrons. For a nonparabolic law of hole dispersion, the Landau levels of the holes in different quantum-well subbands interact with each other in a very complex manner (Fig. 3). However, it should be remembered that, at 4.2 K, only the lower Landau levels of holes in the first quantum-well subband and, possibly, in the closely spaced second and third subbands can be occupied to a large extent. The selection rules [6–9] allow cyclotron transitions (in the Faraday configuration) between Landau levels of the same parity

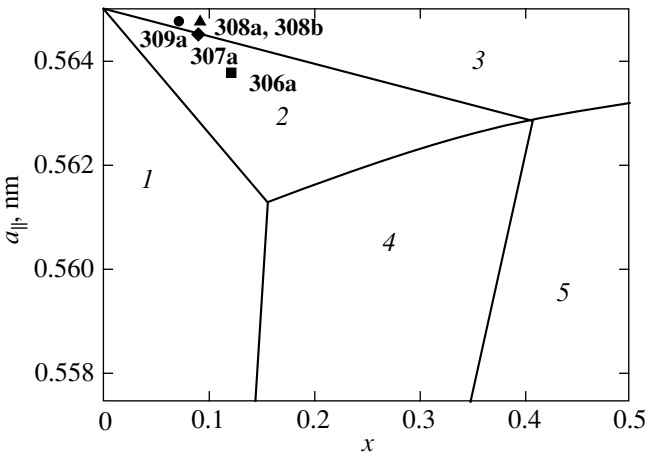

Fig. 5. Boundaries of the regions in the ($a_{\|}$, x) plane for which the lower valleys of the conduction band in pseudomorphic layers of Ge and $Ge_{1-x}Si_x$ solid solution (with equal lattice constants $a_{\|}$ in the layer plane) are arranged identically with respect to each other (without regard for the quantum confinement) [4]. In regions *2* and *3*, the conduction band bottoms are formed by states of the 3*L* valleys in the Ge layer and the 1*L* valleys in the $Ge_{1-x}Si_x$ layer, respectively. Symbols indicate the positions of the parameters for samples **306a**, **307a**, **308a**, **308b**, and **309a**.

[3] In [2, 6–8], the magnetoabsorption under band-gap photoexcitation of charge carriers was investigated in samples **259a** and **306a** ($d_{Ge} \approx 200$ Å), whose parameters correspond to region *2* in Fig. 5, and no cyclotron resonance line of 3*L* electrons was revealed. This can be explained by the fact that, in the range of magnetic fields studied, the magnetic length (200 Å at H = 15 kOe) and the quantum well width are of the same order of magnitude. Therefore, a variation in the magnetic field leads to a change in the electronic spectrum of the Landau levels of 3*L* electrons from a strictly two-dimensional shape (an infinitely narrow quantum well), which is characterized by a cyclotron mass of $0.34m_0$ [12], to a three-dimensional spectrum of the Landau levels with a cyclotron mass of $0.21m_0$. As a consequence, the resonance absorption line can be smeared over a wide range of magnetic fields.

(*s* or *a*), whose numbers (the first numeral in the level notation) differ by unity ($\Delta n = \pm 1$). Specifically, in the absence of mixing of states, the matrix elements should be maximum for transitions between Landau levels belonging to the same quantum-well subband and be approximately equal to zero for intersubband transitions. Consequently, the cyclotron resonance spectra of holes should contain a limited number of absorption lines.

Let us first analyze the possible transitions from the lower Landau level $0s_1$ of holes. It is evident that the CH_1 line observed at low frequencies can be assigned to the $0s_1 \longrightarrow 1s_1$ transition (see also [6–8]). As the energy (magnetic field) increases, the $1s_1$ level interacts with the $1s_3$ level in the third quantum-well subband and then anticrosses it; in turn, the $1s_3$ level anticrosses the $1s_5$ level in the fifth subband (Fig. 3). Upon anticrossing, the $1s_1$, $1s_3$, and $1s_5$ levels "exchange" the wave functions and intensities of the cyclotron transition from the $0s_1$ level. With an increase in the photon energy (magnetic field), this exchange should lead to a decrease in the intensity of the $0s_1 \longrightarrow 1s_1$ transition and an increase in the intensity of the $0s_1 \longrightarrow 1s_3$ transition and then to a decrease in the intensity of the $0s_1 \longrightarrow 1s_3$ transition and an increase in the intensity of the $0s_1 \longrightarrow 1s_5$ transition. This situation is illustrated in Fig. 2, which shows the calculated energy positions of the aforementioned three transitions in the spectral regions where they occur with a sufficiently high intensity. Comparison of the experimental and calculated data presented in Fig. 2 allows us to assign the observed lines CH_3 and CH_5 to the $0s_1 \longrightarrow 1s_3$ and $0s_1 \longrightarrow 1s_5$ transitions, respectively.

Now, we consider the resonances observed in the absorption spectra in stronger magnetic fields than those for the main cyclotron resonance line CH_1 of holes and the cyclotron resonance line CE_{1L} of electrons (Figs. 1, 2). In this range of magnetic fields, the magnetoabsorption spectra of sample **306a** with relatively narrow quantum wells (d_{Ge} = 200 Å) and, correspondingly, with a considerable energy separation between the hole subbands contain the cyclotron resonance line of holes with an effective mass of $0.1m_0$ due to the $3a_1 \longrightarrow 4a_1$ transition from the lower energy state belonging to the second (*a*) ladder of the Landau levels [6–8]. It can be seen from Fig. 3 that, for sample **309a** with wide Ge quantum wells, the $3a_1$ level in magnetic fields up to 25 kOe strongly interacts with the $3a_3$ level, anticrosses it, and exhibits a sublinear dependence of the energy of state on the magnetic field. Similarly, the $4a_1$ level anticrosses the $4a_3$ level, which, in turn, anticrosses the $4a_5$ level. This indicates a strong mixing of the $3a_1$ and $3a_3$ states and also the $4a_1$ and $4a_3$ states in magnetic fields beginning with approximately 10 kOe.

It can be seen from Fig. 2 that the magnetoabsorption spectra of sample **309a** contain five resonance lines (Ch_1, Ch_3, Ch_3', Ci_1, Ci_2) in the magnetic field range to the right of the main cyclotron resonance line CH_1 of holes. A detailed analysis of the absorption spectra (only certain lines observed in this range are shown in Fig. 1) demonstrates that three resonance lines (Ch_1, Ch_3, Ch_3') can be attributed to the cyclotron resonance of holes. In particular, the Ch_1 line, which is observed in magnetic fields of 6 kOe and more (when the interaction between the levels plays an insignificant role), can be assigned to the $3a_1 \longrightarrow 4a_1$ transition. This assignment is confirmed by the fact that the intensity of the Ch_1 line increases with respect to the intensity of the CH_1 line in a weak dc electric field (of the order of several V/cm) that leads to heating of charge carriers and, correspondingly, to an increase in the population of the higher lying Landau level $3a_1$ as compared to that of the $0s_1$ level (see [6–8]). In the case when the photon energy increases above 1 meV, the magnetoabsorption spectra of sample **309a** in magnetic fields of 10–16 kOe contain the higher frequency line Ch_3 in addition to the Ch_1 line (Fig. 2). Note that the greater the magnetic field strength, the lower the intensity of the former line and the higher the intensity of the latter line. As is seen from Fig. 3, it is in this range of magnetic fields that the $4a_1$ level anticrosses the $4a_3$ level; as a result, the matrix element of the transition from the $3a_1$ level to the $4a_1$ level is transformed into the matrix element of the transition from the $3a_1$ level to the $4a_3$ level. Therefore, the Ch_3 line can be attributed to the $3a_1 \longrightarrow 4a_3$ transition. Moreover, in these magnetic fields, there appears a new lower frequency line, namely, Ch_3'. Making allowance for the aforesaid, it is reasonable to assign the Ch_3' line to the $3a_3 \longrightarrow 4a_1$ transition, because the $4a_1$ level after anticrossing the $4a_3$ level is characterized primarily by the wave functions corresponding to the third quantum-well subband of holes.

The measurement of the intersubband cyclotron resonance opens the way to a more precise determination of the parameters of the Luttinger Hamiltonian for holes in Ge/GeSi quantum-well heterostructures. In [6–8], it was noted that, in quantizing magnetic fields, the positions of the cyclotron resonance lines of holes observed in the spectra of samples with narrow Ge quantum wells correspond to effective masses that are 10–15% larger than the calculated values for the bulk parameters of the Luttinger Hamiltonian [10]. This suggests that there is a considerable change in the parameters *A* and *D*, because the cyclotron mass of holes in strained Ge layers is proportional to $(A + D/3^{1/2})^{-1}$ [11]. The observation of the intersubband cyclotron resonance makes it possible to determine the parameters *A* and *D* independently. The point is that the quantum-confinement energy, to a first approximation, is proportional to another of their combinations, namely, (*A* –

$D/3^{1/2}$), i.e., the reciprocal of the classical hole mass in the direction perpendicular to the quantum-well plane. The first calculations (Fig. 2) demonstrated that the energy positions of the intersubband cyclotron resonance lines are highly sensitive to the parameters of the Luttinger Hamiltonian for holes.

5. IMPURITY MAGNETOABSORPTION

As can be seen from Fig. 2, the magnetoabsorption spectra of sample **309a** contain a large number of lines that cannot be assigned to the cyclotron resonance of holes. In particular, these are the CI_1 and CI_2 resonance lines, whose positions correspond to extensions of the CH_3 and CH_5 resonance lines (depicted by the solid curves in Fig. 2), and the resonance lines observed in the frequency range below the frequency of the Ch_1–Ch_3' resonances. In our opinion, the majority of these resonances can be attributed to shallow-impurity-assisted transitions. A detailed analysis of the impurity magnetoabsorption spectra is beyond the scope of this paper (the submillimeter impurity magnetoabsorption spectra of samples with narrower quantum wells $d_{Ge} \leq 350$ Å were considered in [13, 14]). In our recent work [9], we proposed a method for calculating the energy spectrum of the impurity states in quantizing magnetic fields, which is based on expanding the wave function of an impurity center in terms of wave functions of the Landau levels of holes in a quantum well. However, this method proved to be inadequate for describing acceptor energy states in sample **309** with wide quantum wells. For this sample, it is expedient to analyze the experimentally observed features in the behavior of different lines as a function of the frequency, the applied electric field, and the photoexcitation intensity, which would allow us to judge their impurity origin. A simple technique that, in a number of cases, provides a means for separating the cyclotron resonance lines of free carriers and the impurity absorption lines is the heating of charge carriers in a dc electric field (see, for example, [6–8]). Figure 6a shows the magnetoabsorption spectra of sample **309a** at a photon energy of 1.21 meV in different dc electric fields. It can be seen from this figure that, as the heating electric fields increases, the intensity of the CI_1 resonance line decreases to the point of disappearance at $E = 14$ V/cm, whereas the intensity of the main cyclotron resonance line CH_1 of holes changes to a considerably lesser extent. Hence, there are grounds to believe that the CI_1 resonance line is associated with the transitions between impurity states, the lower of which is depleted in response to a dc electric field, for example, due to impact ionization. However, quite a different situation is observed in the magnetoabsorption spectra measured at a photon energy of 1.95 meV (Fig. 6b). In this case, the CH_3 resonance line, which, according to the data presented in Fig. 2, should gradually transform into the CI_1 line, is retained in the spectra over the entire range of heating electric fields; furthermore, the intensity of the CH_3 line initially even increases with an increase in the electric field. This fact not only counts in favor of the assumption that the CI_1 and CH_3 resonance lines have different origins but also confirms our assignment of the CH_3

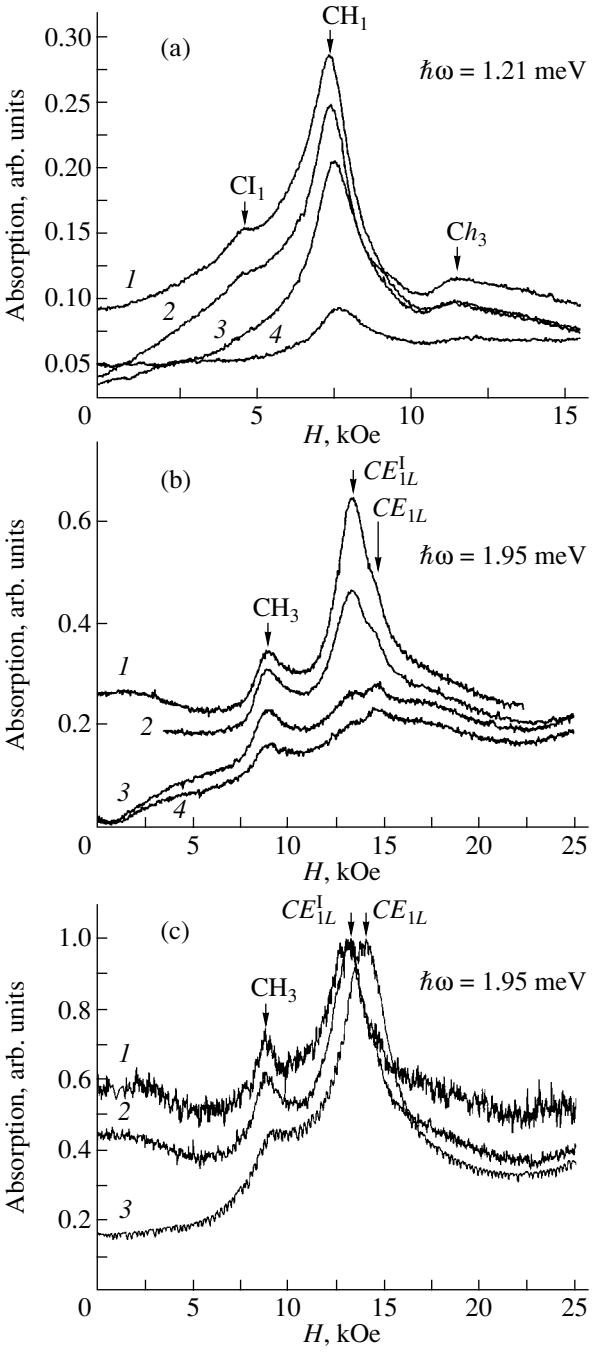

Fig. 6. Magnetoabsorption spectra of sample **309a** in different dc electric fields E and at different intensities of band-gap photoexcitation. (a) E = (*1*) 0, (*2*) 6.8, (*3*) 14, and (*4*) 26 V/cm; photoexcitation with a low intensity. (b) E = (*1*) 0, (*2*) 6.8, (*3*) 14, and (*4*) 16 V/cm; photoexcitation with a low intensity. (c) E = 0, the photoexcitation intensity increases in order of increasing curve number.

line to the intersubband cyclotron resonance of holes due to the $0s_1 \longrightarrow 1s_3$ transition. Indeed, our calculations demonstrate (Figs. 2, 3) that, at a photon energy of the order of 2 meV, the cyclotron transitions from the $0s_1$ level to the $1s_1$ level and, then, to the $1s_3$ level occur to the states lying above the point of their anticrossing. Therefore, the maximum oscillator strength corresponds to the transition to the third subband and the CH_1 resonance line associated with the weaker transition becomes difficult to distinguish from the background of the CE_{1L} cyclotron resonance line of electrons.

Although the CE^{I}_{1L} resonance line is dominant in the magnetoabsorption spectra depicted in Fig. 6b, the data on its energy positions are not presented in Fig. 2. We succeeded in revealing this line in the study of the magnetoabsorption at different intensities of band-gap photoexcitation in combination with dc heating of charge carriers (Figs. 6b, 6c). The CE^{I}_{1L} line is observed against the background of the cyclotron resonance line of 1*L* electrons only at a low intensity of band-gap photoexcitation. An increase in the electric field leads to a drastic decrease in the intensity of the CE^{I}_{1L} line as compared to the intensity of the CE_{1L} cyclotron resonance line of electrons. According to the results of polarization measurements, the CE^{I}_{1L} line corresponds to the electron circular polarization of radiation. Therefore, the new line can be attributed to the transitions between shallow excited states ($\Delta E \approx$ 0.17 meV) of residual donors. In an applied electric field, these states are depleted and the intensity of the CE^{I}_{1L} impurity line decreases, as is the case with acceptors. The influence of the band-gap photoexcitation intensity on the relative population of the donor levels and Landau levels of 1*L* electrons is illustrated in Fig. 6c. At low excitation intensities, the charge carriers are predominantly captured by ionized impurity centers and the fraction of free electrons is small. In this case, the CE^{I}_{1L} line is dominant in the magnetoabsorption spectrum (Figs. 6b, 6c). An increase in the intensity of the band-gap photoexcitation is accompanied by an increase in the intensity of the CE_{1L} cyclotron resonance line of electrons, which, in turn, leads to a considerable shift of the total absorption line (Fig. 6c).

As was already noted, the Ch_1, Ch_3, and Ch_3' cyclotron resonance lines are attributed to the transitions between the Landau levels $3a_1 \longrightarrow 4a_1$, $3a_1 \longrightarrow 4a_3$, and $3a_3 \longrightarrow 4a_1$, respectively. These lines are observed in the frequency range below the frequency corresponding to the main cyclotron resonance line CH_1 of holes. It can be seen from Figs. 2 and 3 that, in this range, there are several more low-frequency absorption lines, the most intense of which is the Ci_1 line observed over a wide range of magnetic fields from 6 to 24 kOe at photon energies ranging from 0.5 to 1.3 meV. This line cannot be assigned to the cyclotron resonance of holes, because no allowed transitions (satisfying the condition $\Delta n = \pm 1$) from the lower (occupied) Landau levels occur in the range 6–24 kOe at such low energies (see Fig. 3). As can also be seen from Fig. 2, the slope of the magnetic-field dependence of the resonance frequency for the Ci_1 line is almost identical to that for the Ch_1, Ch_3, and Ch_3' lines and is severalfold smaller than the slopes for the CH_1, CH_3, CH_5, CI_1, and CI_2 lines. Therefore, we can assume that the Ci_1 line is associated with the transition between two shallow acceptor states belonging to 3*a* and 4*a* Landau levels.[4] Since the Ch_1 line in Fig. 2 is located below the Ci_1, Ch_3, and Ch_3' cyclotron resonance lines, it is quite possible that the given transition occurs from a shallow impurity state at the 3*a* Landau level to a deeper lying impurity state at the 4*a* Landau level. In the case of hydrogen-like donors in GaAs/AlGaAs heterostructures, the $2p_- \longrightarrow 2s$ transition is an analog of the aforementioned transition. In a strong magnetic field, the $2p_-$ level corresponds to an excited state of the Coulomb center at the Landau level $n = 0$, whereas the 2*s* state is the ground (and, hence, deeper) state at the Landau level $n = 1$ (see, for example, [15]).

ACKNOWLEDGMENTS

We would like to thank M.D. Moldavskaya for long-term cooperation laying the groundwork for the present study, E.A. Uskova for preparing the samples use in our measurements, V.L. Vaks and A.N. Panin for their assistance in performing the experiments with backward-wave tubes, and Yu.N. Drozdov for x-ray diffraction investigations of the samples.

This work was supported by the Russian Foundation for Basic Research (project no. 03-02-16808) and the Russian Federal program "Integration" (project no. B0039/2102).

REFERENCES

1. L. K. Orlov, O. A. Kuznetsov, R. A. Rubtsova, *et al.*, Solid State Phenom. **32–33**, 469 (1993).
2. V. I. Gavrilenko, I. N. Kozlov, O. A. Kuznetsov, *et al.*, Pis'ma Zh. Éksp. Teor. Fiz. **59** (5), 327 (1994) [JETP Lett. **59**, 348 (1994)].
3. C. M. Engelhardt, D. Tobben, M. Ashauer, *et al.*, Solid-State Electron. **37**, 949 (1994).
4. V. Ya. Aleshkin and N. A. Bekin, Fiz. Tekh. Poluprovodn. (St. Petersburg) **31** (2), 171 (1997) [Semiconductors **31**, 132 (1997)].

[4] We deliberately do not specify the indices characterizing the number of the quantum-well subband, because, in this range of magnetic fields, the 3*a* and 4*a* states in the first and third subbands undergo strong hybridization (Fig. 3).

5. V. I. Gavrilenko, I. V. Erofeeva, A. L. Korotkov, *et al.*, Pis'ma Zh. Éksp. Teor. Fiz. **65** (2), 194 (1997) [JETP Lett. **65**, 209 (1997)].
6. V. Ya. Aleshkin, V. I. Gavrilenko, I. V. Erofeeva, *et al.*, in *Proceedings of the Workshop on Nanophotonics* (IFM Ross. Akad. Nauk, Nizhni Novgorod, 1999), p. 114.
7. V. Ya. Aleshkin, V. I. Gavrilenko, I. V. Erofeeva, *et al.*, in *Proceedings of the 6th International Symposium "Nanostructures: Physics and Technology," St. Petersburg, Russia* (1999), p. 356.
8. V. Ya. Aleshkin, V. L. Vaks, D. B. Veksler, *et al.*, Izv. Akad. Nauk, Ser. Fiz. **64**, 308 (2000).
9. V. Ya. Aleshkin, V. I. Gavrilenko, D. B. Veksler, and L. Reggiani, Phys. Rev. B **66**, 155336 (2002).
10. J. C. Hensel and K. Suzuki, Phys. Rev. B **9** (10), 4219 (1974).
11. G. L. Bir and G. E. Pikus, *Symmetry and Stain-Induced Effects in Semiconductors* (Nauka, Moscow, 1972; Wiley, New York, 1975).
12. F. Stern and W. E. Howard, Phys. Rev. **163** (3), 816 (1967).
13. V. Ya. Aleshkin, A. V. Antonov, D. B. Veksler, *et al.*, in *Proceedings of the Workshop on Nanophotonics* (IFM Ross. Akad. Nauk, Nizhni Novgorod, 2003), p. 248.
14. V. Ya. Aleshkin, D. B. Veksler, V. I. Gavrilenko, *et al.*, Fiz. Tverd. Tela (St. Petersburg) **46** (1), 126 (2004) [Phys. Solid State **46**, 125 (2004)].
15. S. R. Ryu, Z. X. Jiang, W. J. Li, *et al.*, Phys. Rev. B **54** (16), R11086 (1996).

Translated by O. Borovik-Romanova

Physics of the Solid State, Vol. 46, No. 1, 2004, pp. 138–145. From Fizika Tverdogo Tela, Vol. 46, No. 1, 2004, pp. 138–145.

PROCEEDINGS OF THE CONFERENCE DEDICATED TO O. V. LOSEV (1903–1942)

(Nizhni Novgorod, Russia, March 17–20, 2003)

Magnetotransport Characterization of THz Detectors Based on Plasma Oscillations in Submicron Field-Effect Transistors*

J. Lusakowski[1, 2], W. Knap[1, 3], N. Dyakonova[1], E. Kaminska[4], A. Piotrowska[4], K. Golaszewska[4], M. S. Shur[3], D. Smirnov[5], V. Gavrilenko[6], A. Antonov[6], and S. Morozov[6]

[1] *GES–UMR, CNRS–Université Montpellier 2, Montpellier, 34950 France*

[2] *Institute of Experimental Physics, University of Warsaw, Warsaw, 00-681 Poland*

[3] *Rensselaer Polytechnic Institute, Troy, New York, 121180-3590 USA*

[4] *Institute of Electron Technology, Warsaw, 02-668 Poland*

[5] *Ioffe Institute, Russian Academy of Sciences, St. Petersburg, 194021 Russia*

[6] *Institute for Physics of Microstructures, Russian Academy of Sciences, Nizhni Novgorod, 603950 Russia*

e-mail: gavr@ipm.sci-nnov.ru

Abstract—Magnetotransport characterization of field-effect transistors in view of their application as resonant detectors of THz radiation is presented. Three groups of different transistors based on GaAs/GaAlAs or GaInAs/AlGaAs heterostructures are investigated at liquid–helium temperatures and for magnetic fields of up to 14 T. The magnetic-field dependence of the transistor resistance is used for evaluation of the electron density and mobility in the transistor channel. The electron mobility and concentration determined from magnetotransport measurements are used for the interpretation of recently observed resonant detection of terahertz radiation in 0.15 μm gate length GaAs transistors and for the determination of the parameters of other field-effect transistors processed for resonant and voltage tunable detection of THz radiation. © *2004 MAIK "Nauka/Interperiodica".*

1. INTRODUCTION

The terahertz part of the electromagnetic spectrum lies at the border between wavelengths generated by solid-state electronics and optics. Many excitations observed in condensed matter, liquids, gases, and biological substances correspond to the THz range of frequencies, i.e., to photon energies of ~0.3–30 meV. Spectral analysis in the THz region can be used for studies of these excitations, such as phonons, cyclotron or spin resonance, as well as for investigations of molecular (rotational and vibrational) excitations in liquids, gases, and biological substances. The growing interest in the analysis of signals carried by THz radiation is also related to possible applications of THz spectroscopy for nondestructive sensing and imaging in medicine, the food industry, and defense [1, 2].

Terahertz broadband detectors include bolometers [3–5], pyroelectric detectors, Schottky diodes [6, 7], and photoconductive detectors [8]. An advantage of selective and tunable detectors is that they require no gratings of moving mirrors to perform a spectral analysis. Tunability was demonstrated for photoconductive detectors (GaAs [9], InP [10], InSb) placed in a magnetic field which tuned the energy of optical transitions between the levels of shallow donors or cyclotron and impurity-shifted cyclotron resonance. Such detectors, however, require liquid-helium temperatures and magnetic fields of a few tesla.

For many applications, tuning the response of a detector using an applied voltage is much easier than using a magnetic field. A resonant, voltage-tunable detection based on excitation of plasmon resonance in a two-dimensional electron gas (2DEG) confined in a field-effect transistor (FET) was proposed in the early 1990s [11, 12] and reported only recently [13–15]. A FET, biased by a gate-to-source voltage U_{gs} and subject to electromagnetic radiation, can develop a constant drain-to-source voltage U_{ds}, which has a resonant dependence on the frequency of radiation with maxima at plasma oscillation frequencies [12], $f_N = \omega_N/2\pi$. Resonant plasma frequencies are discrete and given by $\omega_N = \omega_0(1 + 2N)$, where $\omega_0 = \pi s/2L$ and $N = 0, 1, 2, \ldots$. The plasma wave velocity s depends on the carrier density in the transistor channel n and the gate-to-channel capacitance ($C = \varepsilon\varepsilon_0/d$) per unit area: $s = (e^2n/mC)^{1/2}$, where e and m are the electron charge and the effective mass, respectively; ε is the dielectric constant; and d is the gate-to-channel distance. In the gradual channel

* This article was submitted by the authors in English.

approximation, the carrier density in the channel is related to the gate-to-source voltage by the relation $n = CU_0/e$, where U_0 is the gate-to-channel voltage swing, $U_0 = U_{gs} - U_{th}$, and U_{th} is the threshold voltage. The fundamental plasma frequency can be expressed by an approximate relation,

$$f_0 = \frac{1}{4L}\sqrt{\frac{e|U_0|}{m}}. \quad (1)$$

This has two important consequences: (i) a sufficiently short (submicron) FET can operate as a THz detector and (ii) the response frequency of such a detector can be tuned using a gate-to-source voltage.

The width of a resonant curve is determined by the quality factor $\omega_0\tau$, where τ is the electron-momentum relaxation time. Resonant detection becomes possible if the quality factor reaches and exceeds a value of 1. If $\omega_0\tau \ll 1$, plasma oscillations are overdamped and the FET response is a smooth function of ω, as well as of gate-to-source voltage (nonresonant broadband detection [16]).

Resonant and nonresonant detection of THz radiation was recently demonstrated in two field-effect devices: a commercial FET [13, 14, 16] and a double quantum well FET with a periodic grating [16]. In both cases, the frequency of a standing 2D plasmon wave was tuned to a THz frequency by varying the gate-to-source voltage. In Fig. 1, we show an example of the resonant detection of THz radiation performed using a GaAs/GaAlAs FET.

The temperature evolution of spectra shown in Fig. 1 is mainly related to a change in the electron scattering time. A resonant feature (marked by an arrow) starts to become visible below about 30 K because only then does the electron scattering time increase sufficiently for the condition $\omega_0\tau \gg 1$ to be fulfilled. Illumination of the transistor with visible light leads to an additional increase in the electron mobility (μ) and, as a result, to an increase in the quality factor $\omega_0\tau$. This allowed for better resolution of the main resonance (0.6 THz) and observation of the resonant detection of higher harmonics (0.8 and 1.2 THz) of a frequency-multiplied 0.2 THz Gunn diode source, as shown in the inset to Fig. 1.

The most important parameters related to the resonant detection are the electron scattering time and the electron concentration. The former, related to the electron mobility, enters into the quality factor $\omega_0\tau$, which, for a given value of τ, gives a low bound of frequency for which FET can operate as a resonant detector. The electron concentration determines the transistor threshold voltage (which affects the maximum swing voltage directly related to the frequency of plasmon resonance, as shown in Eq. (1)). Therefore, determination of the electron density and mobility in a transistor is a key point in view of its applications as a resonant plasma

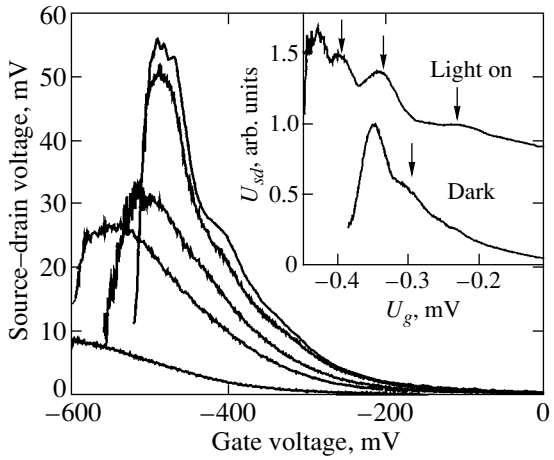

Fig. 1. Photoinduced drain-to-source voltage of GaAs/GaAlAs FET (from group *A*) as a function of gate-to-source voltage and temperature from 8, 20, 60, and 100 K to 200 K (from top to bottom). Inset shows the resonant detection of the 0.6, 0.8, and 1.2 THz radiation from multiplied Gunn diode source (for details, see [13, 16]). Higher Gunn diode harmonics are visible after illumination of FET [14]. The arrows mark positions of 2D plasmon resonances and correspond to detection of 0.6, 0.8, and 1.2 THz from left to right correspondingly (for details, see [13, 14]).

device. The magnetotransport determination of these parameters is addressed in the present work.

The standard equations for the current density (j) in the 2DEG in the presence of a magnetic field (perpendicular to the 2DEG plane) are

$$j_x = \sigma_{xx}E_x + \sigma_{xy}E_y,$$

$$j_y = -\sigma_{xy}E_x + \sigma_{xx}E_y.$$

Here, E_x and E_y are the components of the electric field in the (xy) plane and σ_{xx} and σ_{xy} are components of the conductivity tensor. In the Drude–Boltzmann theory, these components depend on the magnetic field:

$$\sigma_{xx} = \sigma_0/(1 + \mu^2B^2),$$

$$\sigma_{xy} = \sigma_0\mu B/(1 + \mu^2B^2).$$

The boundary conditions for these equations depend on the sample geometry. Two important limiting cases considered in this work are the Hall bar geometry and "transistor geometry" (with the device width D being much larger than the device length L). For a long Hall bar, $L \gg D$. In this case, there is no current in the "y" direction, $j_y = 0$, and the measured $E_x = j_x/\sigma_0$. This means that conductivity (and resistivity) does not depend on the magnetic field. In other words, there is no magnetoresistance. This is a general feature of a degenerate two-dimensional gas. On the other hand, in the case of a very short but wide device ($L \ll D$), the Hall voltage is short-circuited by long current-supplying contacts. Then, $E_y = 0$ and $j_x = \sigma_{xx}E_x$. This geometry is equivalent to that of the Corbino disk. In this case, the

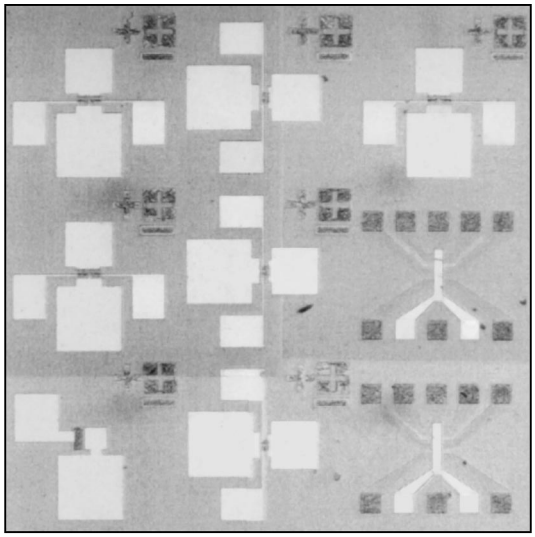

Fig. 2. Photograph of a dice of the group *B* and *C* devices with six lithographically defined transistors, two Hall bars, and a Schottky diode.

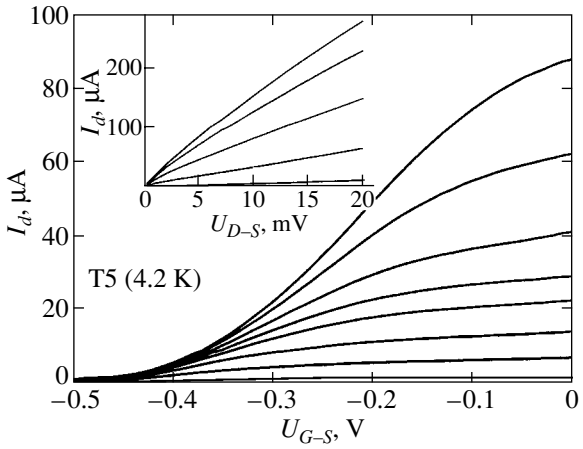

Fig. 3. Example of the characteristics of transistor T5 (from group *B*). Transient characteristics at $T = 4.2$ K as a function of the magnetic field B equal to (from top to bottom) 0, 0.030, 0.051, 0.068, 0.090, 0.140, 0.260, and 1 T. The inset shows output characteristics for gate-source voltage equal to (from top to bottom) 0, –0.1, –0.2, –0.3, and –0.4 V.

measured $E_x = j_x(1 + \mu^2B^2)/\sigma_0$ and one expects a parabolic increase in the sample resistance and a Lorentzian $(1/(1 + \mu^2B^2))$ decrease in the conductance. The coefficient of the parabolic magnetoresistance (or half-width or Lorentzian magnetoconductivity) is equal to the mobility. In quantizing magnetic fields ($\mu B \gg 1$), the conductivity exhibits Shubnikov–de Haas oscillations. These oscillations are periodic as a function of inverse magnetic field ($1/B$), the period depending only on the carrier density.

In this work, different GaAs and GaInAs FETs and Hall-bar test structures were investigated using magnetotransport measurements in high magnetic fields (up to 14 T). We show how magnetoconductivity data make it possible to evaluate the electron mobility and concentration in a transistor channel even for a nonideal geometry. The results are then used to interpret the recently observed resonant detection and to estimate the parameters relevant to the THz detection in these field-effect transistors. The maximum frequency and the quality factor that limit the THz detection in different field-effect structures are discussed.

2. EXPERIMENT AND RESULTS

Three groups of devices, named *A*, *B*, and *C*, were investigated. Group *A* included commercially available Fujitsu FX20 FETs with a gate length (L) of 0.15 μm, gate width (D) of 50 μm, and gate-to-channel separation (d) of ~25 nm. Their threshold voltage varied between –0.2 and –0.5 V, and the electron mobility was estimated to be 0.1–0.2 m^2/Vs at 300 K and 0.5–1.0 m^2/Vs at 4 K.

Transistors and Hall bars of groups *B* and *C* were processed out of MBE-grown high-electron-mobility GaAs/GaAlAs and GaInAs/GaAlAs heterostructures, respectively. The group *B* transistors had a threshold voltage of –0.2 to –0.5 V and an electron mobility of 5–20 m^2/Vs at 4.2 K, while the corresponding values for the group *C* transistors were –1 to –2 V and 1–2 m^2/Vs, respectively. The gate-to-channel distance was $d \sim 160$ and 40 nm for group *B* and *C* transistors, respectively. The same mask was used in the case of *B* and *C* (Fig. 2), which defined transistors with a gate length equal to 0.8, 1.5, and 2.5 μm. The source-to-drain distance was 10 μm for all transistors, and the gate was placed close to the source contact to ensure asymmetry of the transistor (necessary for the detection). Two gated Hall bars and a Schottky diode were fabricated next to each group of the six transistors. Hall structures were used for independent measurements of the electron density and mobility.

Measurements were carried out at liquid-helium temperatures (4.2 or 8 K) after cooling the sample in the dark. A typical set of measurements carried out on transistors involved the following: (i) output characteristics (drain current I_d vs drain-to-source voltage U_{ds}) as a function of U_{gs} voltage and magnetic field B; (ii) transient characteristics (drain current vs gate-to-source voltage U_{gs}) as a function of B; and (iii) magnetoconductivity (drain current vs B) as a function of gate-to-source voltage. (Let us note that, in the following, the gate-to-source voltage is always negative and its increase means an increase in its absolute value.) An example of the experimental data for one of the group *B* transistors is shown in Fig. 3.

In some cases, additional data were taken after illumination of a sample with a red light–emitting diode. Output characteristics were used to determine the range U_{ds} and U_{gs} which the drain current changed linearly

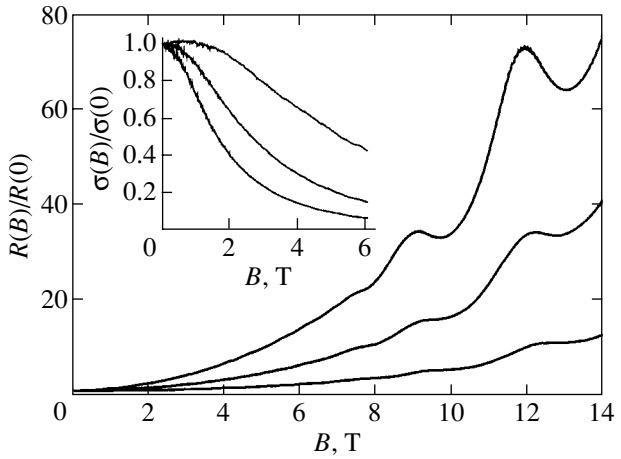

Fig. 4. The resistance of a group *A* transistor, normalized at zero magnetic field, for U_{gs} = 0, 0.2, and 0.3 V (from top to bottom). The inset shows normalized Lorentzian magnetoconductivity $\sigma(B)$ curves characterized by decreasing μ for increasing U_{gs}.

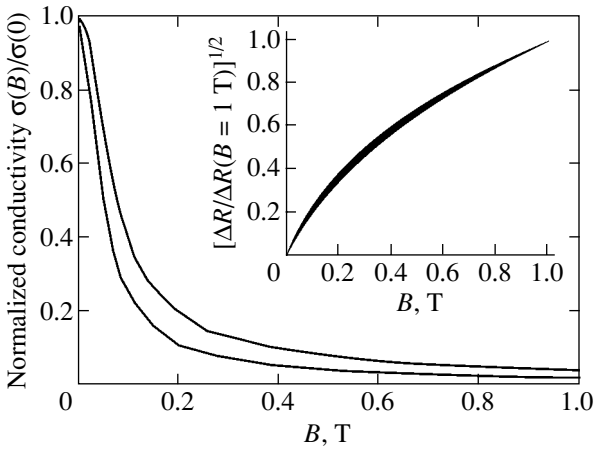

Fig. 5. Influence of the magnetic field on conductivity for transistor T3 (upper line) and T5 (lower line); both transistors are from group *B*. The inset shows a square root of magnetoresistance $R = R(B) - R(0)$ of transistors T3 and T5 normalized to its value at 1 T. The curves correspond to a gate-to-source voltage equal (in volts) of 0, –0.1, –0.2, –0.3, and –0.4 for T5 and 0, –0.1, –0.2, and –0.3 for T3.

with drain-to-source voltage. Transient characteristics allowed determination of the threshold voltage, the values of which are cited in the preceding paragraph.

The analysis of the magnetoconductivity of transistors presented below uses the following scheme. At low magnetic fields, one observes a strong decrease in conductivity with an increase in the magnetic field, which leads to a Lorentz-like shape of the magnetoconductivity curve. This curve is used to estimate the electron mobility in the transistor channel. At large magnetic fields, Shubnikov–de Haas oscillations are observed and used to determine the electron concentration. Measurements were performed for different values of the gate-to-source voltage. Results of measurements carried out on transistors are compared with magnetotransport results obtained for gated Hall bars.

Figure 4 shows an example of a normalized drain-to-source resistance of a group *A* transistor versus the magnetic field for a few values of the gate-to-source voltage. A background of these curves was fitted up to 4 T with a very high accuracy by a parabolic dependence, $1 + \mu^3 B^2$, with the mobility μ as a single fit parameter. We obtained μ equal to 0.60, 0.38, and 0.17 m^2/Vs for U_{gs} equal to 0, –0.2, and –0.3 V, respectively. This decrease in μ corresponds to the broadening of Lorentzian curves shown in the inset to Fig. 4, which present the magnetoconductivity $\sigma(B)$ normalized to its value at B = 0 T. The half-width of each Lorentzian, $B_{1/2}$, is given, of course, by an appropriate value of μ^{-1}. A simple inspection of the Shubnikov–de Haas oscillations in Fig. 4 shows that the number and position of maxima do not change with the applied gate-to-source voltage, which means that, in this transistor, they are mainly due to the ungated part of the source-drain channel. The carrier density obtained from these oscillations (equal to 1.9×10^{12} cm^{-2}) is expected to correlate with the carrier density in the transistor channel at zero gate voltage. (It might be somewhat different depending on the values of the surface potential and of the gate contact built-in voltage.)

Let us concentrate now on measurements carried out on two transistors (T3 and T5 from group *B*). The transistors differed in the length of the gate and the lateral dimension, which were equal to 2.5 and 55 μm for T3 and 1.5 and 25 μm for T5, respectively.

Figure 5 shows the normalized magnetoconductivity for transistors T3 and T5 for zero gate-to-source voltage. Lorentz-like curves show a strong decrease in the drain-to-source conductivity σ with an increase in the magnetic field. Curves of a similar shape were obtained for all gate-to-source voltages; they differ only in their half-width. The shape of the magnetoconductivity curves is not strictly Lorentzian, in contrast to the curves shown in the inset to Fig. 4. This is illustrated in the inset to Fig. 5, which shows the square root of a transistor magnetoresistance $[R(B) - R(0)]^{1/2}$ normalized to its value at 1 T. If the magnetoconductivity were to be described by a Lorentzian $(1 + (B/B_{1/2})^2)^{-1}$, then this figure would show a straight line. We found that the magnetoresistance for all gate-to-source voltages and for both transistors can be described by a Lorentzian-like dependence but with the exponent equal to 1.3 rather than 2. The inverse of the half-width of these Lorentzian-like magnetoconductivity curves, $B_{1/2}^{-1}$, is plotted as a function of the gate-to-source voltage in Fig. 6. This parameter, $B_{1/2}^{-1}$, of a dimension of mobility decreases with increasing gate-to-source volt-

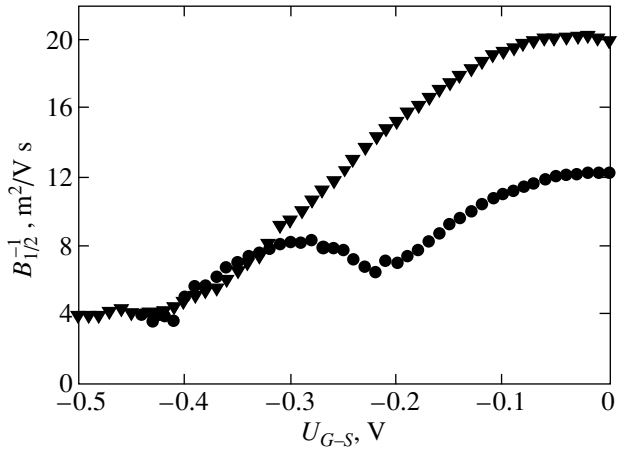

Fig. 6. Inverse of the half-width of magnetoconductivity curves $B_{1/2}^{-1}$ for transistors T5 (L = 1.5 μm, down triangles) and T3 (L = 2.5 μm, solid circles) as a function of gate-to-source voltage U_{gs}.

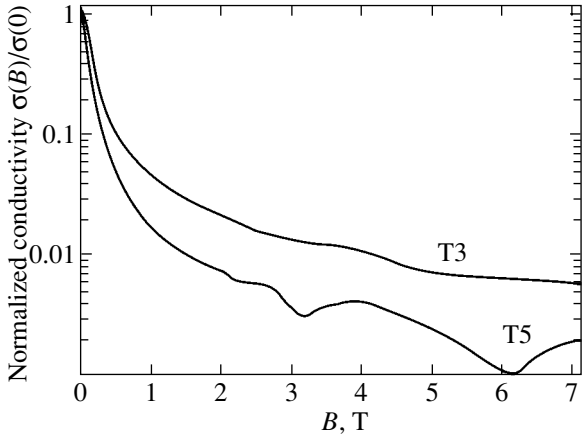

Fig. 7. Magnetoconductance of transistors T3 (upper curve) and T5 (lower curve).

age for transistor T5 (expect for a very small increase at the lowest U_{gs}) and shows a minimum for transistor T5. The curves shown in Fig. 6 coincide for $U_{gs} < -0.3$, which, for both transistors, corresponds to a drain current of about 20% of its value at the zero gate-to-source voltage.

Figure 7 compares the conductivity of transistors T3 and T5 (measured at U_{gs} = 0 V) as function of the magnetic field up to 7 T. After Lorentz-like behavior at low fields, oscillations in the conductivity were observed. Taking into account the positions of minima of the magnetoconductance data, one can evaluate a concentration of the 2DEG, which appears to be 3.0×10^{11} and 3.2×10^{11} cm^{-2} for transistors T3 and T5, respectively. One can note that the oscillations on the magnetoconductance curves are different from the usual traces observed in quantum Hall experiments. This is related to a difference in the sample geometry, which is Corbino-like for the case of the transistors. Gated Hall-bar structures placed close to the transistors were used to perform a precise analysis of the influence of the gate-to-source voltage on the electron mobility and concentration in heterostructures used for transistor fabrication. In Fig. 8, we show examples of results obtained on one of the Hall bars placed together with the group (*C*, GaAs/GaInAs heterostructure). Figure 8 shows the resistance values measured between the Hall-bar probes as a function of the magnetic field. The curves were normalized to their value at B = 0 T, and monotonic background magnetoresistance was subtracted for better visualization. Typical Shubnikov–de Haas oscillations were observed. The period (in B^{-1}) of the oscillations changes with decreasing the gate-to-source voltage swing, which corresponds to a decrease in the electron concentration. It is important to note, however, that not only the carrier density but also the mobility changes with increasing gate voltage; the amplitude of oscillation decreases, and, close to the threshold, they are practically smeared out.

Figure 9 summarizes the mobility and carrier density measurement results. As expected, the carrier density decreases linearly with the application of a negative gate voltage. The linear extrapolation of the density versus gate voltage dependence to zero sheet density yields a threshold voltage equal to U_{th} = –1.6 V. The threshold voltage obtained in this way is different from the "transistor threshold" voltage; this point will be discussed later. The mobility first increases slightly and then rapidly decreases with the gate voltage swing. Typically, we observed a mobility decrease by a factor of 2 to 3 at a gate voltage equal to half of the threshold voltage.

3. DISCUSSION

The following discussion is divided into two parts. First, we consider the possibility of evaluating the electron concentration and mobility in the transistor channel based on magnetoconductivity measurements. In view of this, we discuss the influence of the geometry of the investigated structures on the result of such a procedure. Also, the influence of the gate potential on the carrier density and mobility in transistors and Hall bars is discussed. Second, the electron mobility and concentration determined from magnetotransport measurements are used for the interpretation of recently observed resonant detection and determination of the parameters of new field-effect transistors processed for resonant detection of THz radiation.

The magnetoresistance measured between the source and the drain of the transistor is an integral phenomenon because of two effects: (i) it comprises contributions from both the gated and ungated part of a transistor channel and (ii) the channel geometry is often intermediate between Corbino- and Hall-bar-like.

The gated part of the channel (gate length) was 0.15 μm for the group *A* devices and 0.8–2.5 μm for others. The total channel length was around 1 μm for group *A* devices and 10 μm for groups *B* and *C*. Clear evidence of the importance of the ungated part of the channel can be seen in Fig. 4, which shows Shubnikov–de Haas oscillations of the group *A* transistor. One can see that the positions of maxima/minima do not depend on the gate-to-source voltage but the resistance of the transistor quickly grows with U_{gs}. This is because the oscillations come mainly from the 2D electron gas confined in the ungated part of the transistor. The background changes, however, because the total resistance increases due to the modulation of the transistor channel by the gate voltage.

The mobility μ, determined as a coefficient of the parabolic dependence of resistance, corresponds to an "average" mobility in the entire region between the source and the drain. For the zero gate voltage, the carrier densities in the gated and ungated regions of the channel are nearly the same. However, as is clearly demonstrated by measurements on the gated Hall bars (where the whole conducting region is gated), a gate potential decreases both the mobility and the concentration of electrons (Fig. 9). We also expect that the mobilities in the gated and ungated sections of the device are close at zero gate bias, even though the scattering in the device channel might be affected by the effects related to the metal gate [17]. Once the gate voltage is applied, the mobility under the gate is different from the measured averaged mobility, since mobility is a strong function of electron sheet density. With decreasing gate voltage swing, the resistance of the gated region starts to dominate the total transistor resistance. In this case, the measured (average) mobility approaches the value of mobility under the gate. Therefore, the measurements of the magnetoresistance of the channel allow relatively accurate determination of the mobility in the gated region for small gate voltage swings. In the intermediate region, one obtains the approximate "average" mobility. Comparison of Fig. 6 with Fig. 9 shows, however, that the overall functional dependences of the mobility versus gate voltage in the transistor channel and in the gated Hall bar are similar. The mobility decreases by a factor of 2–3 at half the threshold voltage.

Another point to be discussed is the conducting channel geometry. As mentioned in the Section 1, the interpretation of the transistor magnetoresistance is simple if the conducting channel geometry approaches the limiting case of the Corbino geometry. This condition is fulfilled for a "very wide channel," with the source-to-drain separation length I_c being much smaller than the channel width *D*. In this case, the magnetoresistance is parabolic (or the magnetoconductance is Lorentzian). Such a parabolic ($R \sim 1 + \mu^2 B^2$) behavior was observed for group *A* transistors (gate of 0.15 μm)

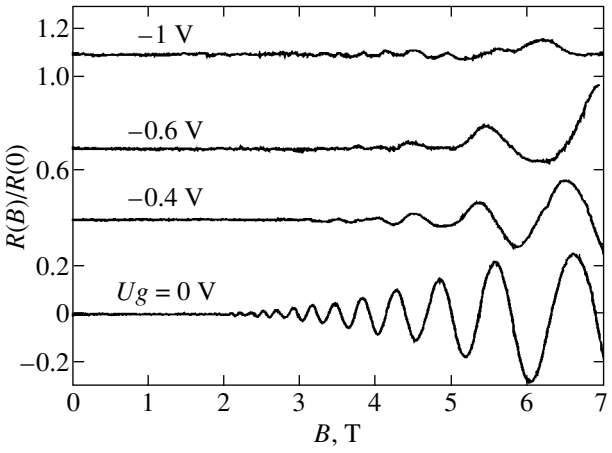

Fig. 8. Shubnikov–de Haas oscillations of magnetoresistance of a Hall bar processed out of a GaInAs/GaAlAs heterostructure (group *C* devices) as a function of the magnetic field for a gate potential equal to 0, 0.4, 0.6, and 1 V (from bottom to top). The curves are normalized at $B = 0$ T and shifted vertically for better visualization.

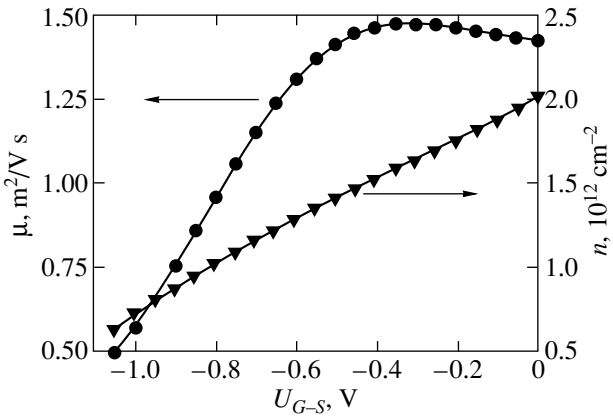

Fig. 9. The electron mobility (squares) and concentration (down triangles) determined from measurements of the Hall effect on a gated Hall bar of a GaInAs/GaAlAs heterostructure from group *C*.

that have a very short ($L_c \sim 1$ μm) and wide ($d \sim 50$ μm) channel.

For transistors T3 and T5, the D/L_c ratio is 5.5 and 2.5, respectively, and the geometry is neither Corbino nor a Hall-bar type. We speculate that the observed exponent of 1.3 is related to the fact that the geometry of the current flow is far from the ideal cases presented above. In particular, an essential part of the current may flow outside of the transistor due to violation of the condition $j_y = 0$. Nevertheless, and in spite of above-mentioned difficulties in the interpretation, one can consider the parameter $B_{1/2}^{-1}$ as an estimate of the electron mobility. This interpretation is consistent with the behavior of the two curves shown in Fig. 6, which coin-

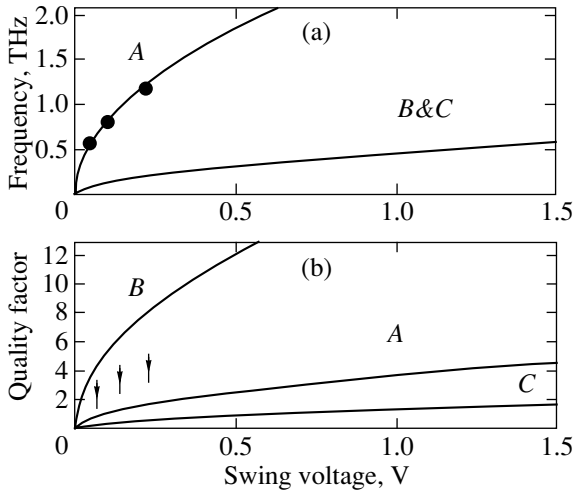

Fig. 10. (a) Frequency of the resonant detection of the group *A*, *B*, and *C* transistors as a function of the swing voltage; (b) quality factor corresponding to a frequency of the resonant detection plotted in (a) for the group *A*, *B*, and *C* transistors.

cide for higher gate-to-source voltage, close to the threshold value (U_{gs} < –0.3 V), when the transistor resistance is determined by the gated section. The fact that we find the same exponent (equal to 1.3) for both transistors confirms that, although determination of the electron mobility as $B_{1/2}^{-1}$ is an approximation, it can be used to compare the electron mobility in different transistors.

It is important to note that both the mobility obtained on gated Hall bars (shown in Fig. 9) and the mobility extracted using $B_{1/2}^{-1}$ values for the transistors (shown in Fig. 6) decrease as the gate-to-source voltage swing decreases. This might be linked to the screening effects, which diminish at smaller electron sheet densities. This decrease reduces the effectiveness of screening of ionized centers and results in a decrease in mobility. The application of the gate voltage also changes the shape of the quantum well at the heterointerface. The quantum well is wider at smaller sheet densities. Hence, the peak of the 2D electron wave function is further away from the heterointerface, which decreases scattering by the interface roughness. This effect can lead to an increase in mobility. It is possible that the nonmonotonic behavior of $B_{1/2}^{-1}$ observed for both transistors (close to zero gate-to-source voltage for T5 and at about –0.2 V for T3) and for the Hall bar at around –0.4 V can be attributed to the interplay of these two mechanisms.

Measurements of the carrier density and mobility made on the gated Hall bars also show that the threshold voltage for the carrier density and for the channel conductivity can be fairly different. From the linear approximation of the carrier density versus gate dependence shown in Fig. 9, we obtained a threshold voltage (voltage for which the carrier density is zero) equal to U_{th} = –1.6 V. If we use the same procedure for conductivity, a threshold voltage of U_{th} = –1.4 V is obtained. This is because both the carrier density and mobility enter into the conductivity and both decrease with an increase in the gate voltage. It is important to note that the threshold in estimations of the plasma wave frequency is the carrier density threshold.

Using the value of the mobility and the threshold voltage determined for different FETs, we can estimate their parameters for possible applications in resonant detectors of terahertz radiation. In Fig. 10, we show the frequency of the resonant detection and the quality factor as a function of the swing voltage. The maximum frequency for a detector is determined by the maximum gate voltage swing and the gate length. As discussed before, the maximum gate voltage swing is determined by "the carrier density threshold voltage;" it is usually slightly more negative than the transistor threshold voltage. The maximum gate voltage swing is about 0.5 V for the group *A* and *B* transistors and 1.5 V for the group *C* transistors. We took a gate length L = 0.15 μm for group *A* and L = 0.8 μm (shortest gates on a dice) for groups *B* and *C*. The mobility was assumed to be 6, 14, and 1 m^2/Vs for groups *A*, *B*, and *C*, respectively.

As can be seen from the figure, the maximum frequency of the group *A* devices is approximately 1.5 THz. The points shown in Fig. 10 represent the results of recent experiments [13, 14]. The plasma resonance observed in the experiments was relatively weak (Fig. 1). This can be understood by looking at the figure presenting the quality factor. One can see that the maximum quality factor that can be obtained for these devices is around 1.5. The reason for this is the relatively low mobility. For group *C*, the maximum frequency is 0.6 THz. The maximum quality factor for this frequency is relatively small, equal to about 2. This means that these devices cannot be used for resonant tunable detection. The best quality factors were obtained for group *B* transistors. At the maximum operation frequency of 0.35 THz (corresponding to the maximal swing voltage of 0.5 V), the quality factor for these devices is larger than 10. These are the most promising devices for high-quality resonant plasma detectors.

In principle, the simplest way to increase the maximum frequency (and the quality factor) is to decrease the gate length (L) (see Eq. (1)). The shortest gate length (L_{min}) for a given type of device can be defined by an approximate relation $L_{min} \sim 5d$, where d is the gate-to-channel distance (in order to preserve the gate control). Looking at the dimensions of the three groups of devices, one can see that the devices of groups *A* ($d \sim 0.025$ μm, $L \sim 0.15$ μm) and *B* ($d \sim 0.16$ μm, $L \sim 0.8$ μm) are close to the limit. Only the heterostructures used for group *C* devices ($d \sim 0.04$ μm, $L \sim 0.8$ μm) can be used for fabricating shorter gate length transistors.

The minimum gate length for these transistors is approximately 0.2 μm. One can expect then to reach a maximum detection frequency of about 2.4 THz with a maximal quality factor of about 6.

In conclusion, transistors processed from GaAs/GaAlAs and GaInAs/GaAlAs heterostructures were investigated by magnetotransport measurements in order to characterize their applicability as resonant tunable detectors of THz radiation. We showed how the electron mobility in the transistor can be evaluated from a magnetic-field dependence of the transistor resistance. High-mobility GaAs/GaAlAs transistors with a quality factor approaching 10 were fabricated. These devices are the most promising (among those investigated) devices for application as resonant detectors.

ACKNOWLEDGMENTS

We thank M. Dyakonov and S. Rumyantsev for helpful discussions.

Financial support from NATO linkage grant no. CLG977520 “Semiconductor Sources for Terahertz Generation” is highly acknowledged. The work at RPI was supported by the National Science Foundation (Program Monitor Dr. James Mink).

REFERENCES

1. A. C. Samuels, D. L. Woolard, T. Globus, *et al.*, in *WOFE-02 Proceedings, Yoon Soo Park*, Ed. by M. S. Shur and William Tang (2002).
2. B. Ferguson and X.-C. Zhang, Nature Mater. **1**, 26 (2002).
3. M. Kroug, S. Cherednichenko, H. Merkel, *et al.*, IEEE Trans. Appl. Supercond. **11**, 962 (2001).
4. P. J. Burke, R. J. Schoelkopf, D. E. Prober, *et al.*, J. Appl. Phys. **85**, 1644 (1999).
5. B. S. Karasik, W. R. McGrath, M. E. Gershenson, and A. V. Sergeev, J. Appl. Phys. **87**, 7586 (2000).
6. T. W. Crow, R. J. Mattauch, R. M. Weikle, and U. V. Bhapkar, in *Compound Semiconductor Electronics*, Ed. by M. Shur (World Sci., Singapore, 1996), p. 209.
7. S. M. Marazita, W. L. Bishop, J. L. Hesler, *et al.*, IEEE Trans. Electron Devices **47**, 1152 (2000).
8. E. E. Haller and J. W. Beeman, in *Proceedings of Far-IR, Submm and mm Detector Technology Workshop, Monterey, CA* (2002) (in press).
9. G. E. Stillman, C. M. Wolfe, and J. O. Dimmock, Solid State Commun. **7**, 5 (1969).
10. W. Knap, J. Lusakowski, K. Karpierz, *et al.*, J. Appl. Phys. **72**, 680 (1992).
11. For review see M. Dyakonov and M. S. Shur, in *Terahertz Sources and Systems*, Ed. by R. E. Miles, P. Harrison, and D. Lippens (Kluwer Academic, Dordrecht, 2001), p. 187.
12. M. Dyakonov and M. S. Shur, Phys. Rev. Lett. **71**, 2465 (1993); IEEE Trans. Electron Devices **43**, 380 (1996); in *Proceedings of 22nd International Symposium on GaAs and Related Compounds* (1996), Inst. Conf. Ser., No. 145, Chap. 5, p. 785.
13. W. Knap, Y. Deng, S. Rumyantsev, *et al.*, Appl. Phys. Lett. **80**, 3433 (2002).
14. W. Knap, Y. Deng, S. Rumyantsev, and M. S. Shur, Appl. Phys. Lett. **81**, 4637 (2002).
15. X. G. Peralta, S. J. Allen, M. C. Wanke, *et al.*, Appl. Phys. Lett. **81**, 1627 (2002).
16. W. Knap, V. Kachorovskii, Y. Deng, *et al.*, J. Appl. Phys. **91**, 9346 (2002).
17. A. A. Grinberg and M. S. Shur, J. Appl. Phys. **58**, 382 (1985).

Physics of the Solid State, Vol. 46, No. 1, 2004, pp. 146–149. Translated from Fizika Tverdogo Tela, Vol. 46, No. 1, 2004, pp. 146–149.

PROCEEDINGS OF THE CONFERENCE DEDICATED TO O. V. LOSEV (1903–1942)

(Nizhni Novgorod, Russia, March 17–20, 2003)

Electron Transport and Terahertz Radiation Detection in Submicrometer-Sized GaAs/AlGaAs Field-Effect Transistors with Two-Dimensional Electron Gas

A. V. Antonov[1], V. I. Gavrilenko[1], E. V. Demidov[1], S. V. Morozov[1], A. A. Dubinov[1], J. Lusakowski[2, 3], W. Knap[2, 5], N. Dyakonova[2], E. Kaminska[4], A. Piotrowska[4], K. Golaszewska[4], and M. S. Shur[5]

[1] *Institute for Physics of Microstructures, Russian Academy of Sciences, Nizhni Novgorod, 603950 Russia*
e-mail: more@ipm.sci-nnov.ru
[2] *GES–UMR, CNRS–Université Montpellier 2, Montpellier, 34950 France*
[3] *Institute of Experimental Physics, University of Warsaw, Warsaw, 00-681 Poland*
[4] *Institute of Electron Technology, Warsaw, 02-668 Poland*
[5] *Rensselaer Polytechnic Institute, Troy, N.Y., 121180-3590 USA*

Abstract—The electronic transport and response in the terahertz range are studied in field-effect GaAs/AlGaAs transistors with a two-dimensional high-mobility electron gas. The special interest expressed in such transistors stems from the possibility of developing terahertz-range radiation detectors and generators on the basis of these devices. Measurements of the value and the magnetic-field dependence of the drain–source resistance are used to estimate the electron density and mobility in the transistor channel. Results of magnetotransport measurements are employed to interpret the nonresonant detection observed in transistors with a gate width from 0.8 to 2.5 μm. © *2004 MAIK "Nauka/Interperiodica".*

1. INTRODUCTION

Recently, great interest has been shown in terahertz-range radiation detection by means of semiconductor devices based on plasma effects. Resonant and nonresonant detection in field-effect transistors with a two-dimensional (2D) electron gas was observed in [1–4]. Those studies were aimed at the development of fast voltage-controlled terahertz-radiation detectors. The terahertz range (0.3–10 THz) corresponds to frequencies of many excitations in condensed media, such as phonons, transitions with the participation of shallow impurities, cyclotron and paramagnetic resonances, and rotational and vibrational excitations in liquids, gases, and biological objects. Main interest is in the use of terahertz radiation in nondestructive testing, visualization, medicine, environmental monitoring, the food industry, and the struggle against terrorism [5, 6]. Currently, broad-band detectors are mainly employed to detect terahertz radiation. The application of selective and tunable detectors to spectral analysis makes it possible to discard diffraction gratings or mechanically tunable interferometers. The sensitivity band can be tuned in semiconductor photoresistors (GaAs [7], InP [8], InSb [9], GaAs/AlGaAs [10, 11]) placed in a magnetic field. However, such detectors always require cooling to liquid-helium temperature and magnetic fields of several teslas. In many cases, it is preferable to operate with a voltage-tunable terahertz-radiation detector. A field-effect transistor with a 2D electron gas in the channel can be used as such a detector. Under ordinary operating conditions, the upper limiting frequency of the field-effect transistor is dictated by the inverse electron transit time through the region under the gate. The use of plasma effects makes it possible to increase the operating frequency of submicrometer field-effect transistors up to the terahertz frequency range [12], since the characteristic velocities of plasma waves can be as high as 10^8 cm s^{-1}, which is significantly higher than the electron drift velocity in the transistor channel. Resonant detection of terahertz radiation has already been demonstrated for two types of field-effect transistors, namely, for a commercial field-effect GaAs/AlGaAs transistor [1,2] and a field-effect transistor with a double quantum well and a grating gate [3].

The resonant frequency of plasma oscillations in the 2D electron gas under the gate is determined by the gate length L and the electron density n, which can be approximately described by a simple formula for a plane capacitor, $n = CU_0/e$, where C is the gate–channel capacitance per unit surface area, $U_0 = U_{GS} - U_{th}$ is the gate-to-channel voltage swing (U_{GS} is the voltage applied to the gate, U_{th} is the pinch-off voltage of the transistor), and e is the elementary charge. In the case

1063-7834/04/4601-0146$26.00 © 2004 MAIK "Nauka/Interperiodica"

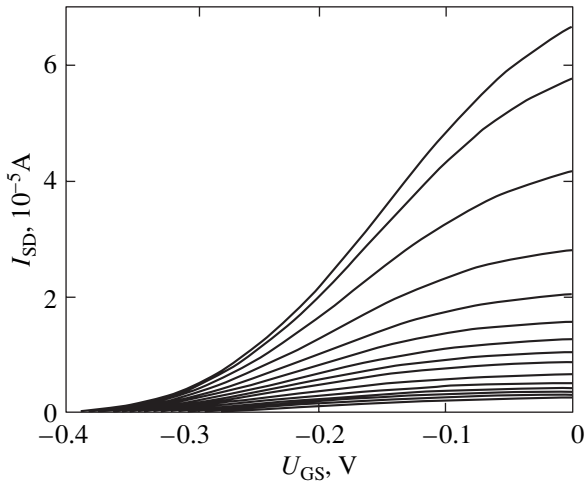

Fig. 1. Transfer characteristics of transistor *T*3* measured at magnetic fields varied from 0 (upper curve) to 0.4 T with a step of 0.05 T and from 0.4 to 1 T with a step of 0.1 T. The source–drain voltage is 20 mV.

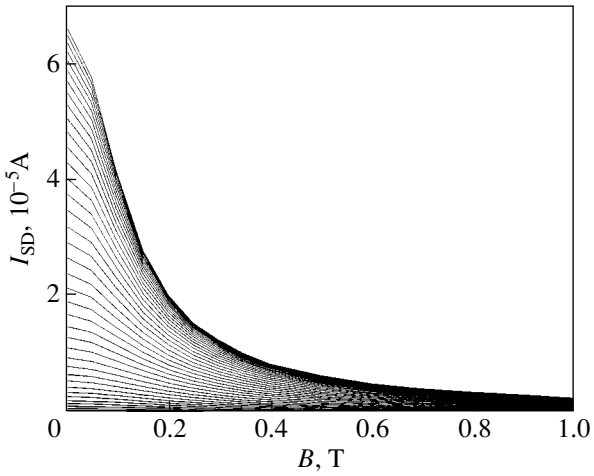

Fig. 2. Magnetic-field dependences of the source–drain current of transistor *T*3* for gate voltage U_{GS} varied from 0 (upper curve) to –0.4 V (with a step of 0.01 V) constructed on the basis of the curves in Fig. 1.

of large values of U_0, the resonant frequency is given by the simple expression

$$f_0 = \frac{1}{4L}\sqrt{\frac{e|U_0|}{m}}. \quad (1)$$

The resonant frequency is highest for a zero gate voltage and vanishes as U_{GS} approaches the pinch-off voltage.

2. EXPERIMENTAL

The transistors under study were produced from a GaAs/AlGaAs heterostructure with a 2D high-mobility electron gas, grown through molecular-beam epitaxy. The distance from the surface to the conducting channel was approximately 160 nm and the drain–source distance was 10 μm for all the transistors. In this paper, we present the measurement results for two transistors with a gate length of 0.8 μm (*T*2) and 2.5 μm (*T*3, *T*3*) and a channel width of 50 μm (*T*2, *T*3*) and 100 μm (*T*3). The gate was positioned in the immediate vicinity of the source. The crystal with the transistors was mounted on a holder for integrated circuits, which then was placed into a countermodule positioned in a light-guide insert in an STG-40 transport helium Dewar. All measurements were carried out at $T = 4.2$ K. Bonding pads of the transistors were connected with holder pins by gold wires. The same pads, together with lead-in metal strips, played the role of a receiving antenna for terahertz radiation. As radiation sources in the range $f =$ 50–700 GHz, we used backward-wave tubes (BWTs) OV-74, OV-32, and OV-30, as well as BWT-based G4-161 and G4-142 signal generators. Radiation was introduced into the transport helium Dewar via a light guide (polished stainless-steel tube) and was focused with the use of a polished brass cone onto the crystal with transistors. Measurements were carried out at a fixed radiation frequency and amplitude modulation at a frequency of 200–1000 Hz. The photovoltage in the source–drain circuit was measured at a negative dc voltage U_{GS} applied to the gate with respect to the source. A conventional lock-in amplifier circuit was used. The signal from the lock-in amplifier output and the gate voltage were stored on a computer by using an analog-to-digital converter. To determine the transistor parameters, the channel dc conductance was measured as a function of the gate voltage and the normal magnetic field.

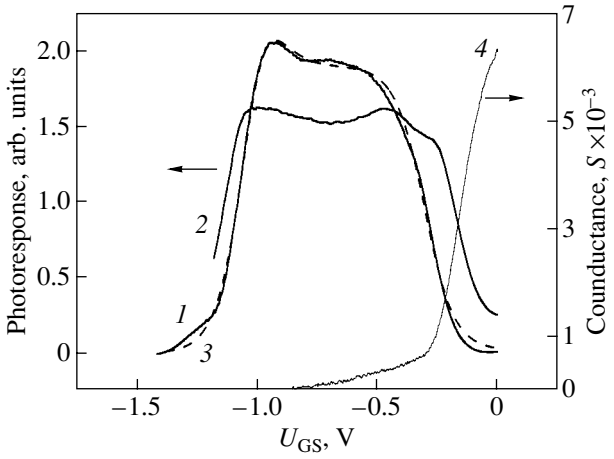

Fig. 3. Gate-voltage dependences of the transistor *T*2 photoresponse (*1*, *2*) measured by us and (*3*) calculated using formula (22) from [4] and (*4*) the measured transfer characteristic of the transistor for different values of *f*: (*1*, *3*) 329 and (*2*) 228 GHz.

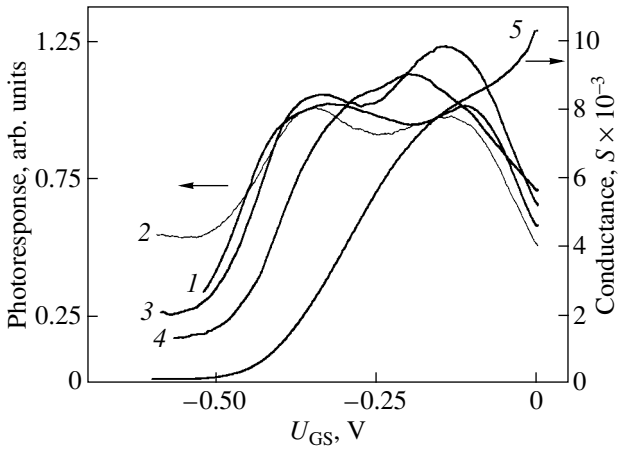

Fig. 4. (*1–4*) Gate-voltage dependences of the transistor *T*3 photoresponse and (*5*) the transfer characteristic of the transistor for different values of *f*: (*1*) 597, (*2*) 629, (*3*) 655, and (*4*) 682 GHz.

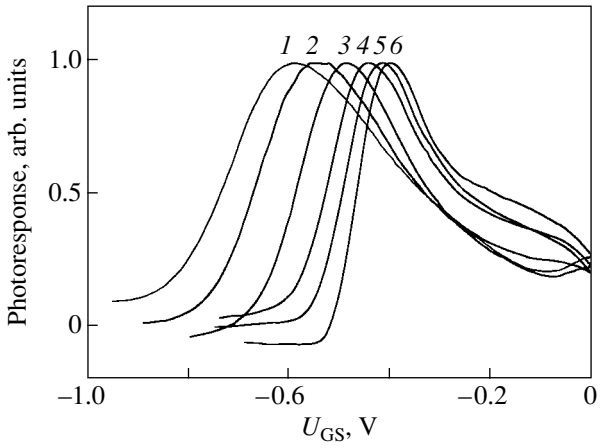

Fig. 5. Gate-voltage dependences of the transistor *T*3 photoresponse (*1*) for the highest radiation power and (*2–6*) for a sequential decrease in the power by half. All the curves are normalized to the strongest response; $f = 78$ GHz.

3. RESULTS AND DISCUSSION

Figure 1 shows the typical gate-voltage dependences of the transistor source–drain current I_{SD} at various magnetic fields. In Fig. 2, these data are reconstructed as magnetic-field dependences at a fixed gate voltage. It can be seen that the transistor is off at the pinch-off voltage $U_{th} = -(0.35–0.40)$ V. By using the dependence of the current on the magnetic field, we can estimate the carrier mobility in the channel from the formula $\mu B_{1/2} = 1$, where $B_{1/2}$ is the magnetic field at which the current decreases by half. For the data shown in Fig. 2, this estimation yields $\mu \approx 7.5 \times 10^4$ cm^2/V s at $U_{GS} = 0$. With this estimate, the lower frequency limit for the observation of a resonant response can be found from the condition $\omega\tau = 1$ to be 50 GHz.

Figure 3 shows the typical gate-voltage dependences of the transistor photoresponse, as well as the measured transfer characteristic. The observed pinch-off voltage $U_{th} = -0.3$ V at a zero gate voltage corresponds, according to Eq. (1), to the resonance frequency $f(0) = 270$ GHz, which should vanish as U_{GS} increases from zero to –0.3 V. Thus, the frequency of 329 GHz (curve *1* in Fig. 3) exceeds the highest resonant frequency. On the contrary, the frequency of 228 GHz (curve *2*) is lower than $f(0)$ and, according to Eq. (1), becomes equal to the plasma frequency of the electron gas under the gate at $U_{GS} \approx -0.1$ V. However, it can be seen that, in this range of the gate voltages, curve *2* in Fig. 3 exhibits no features that could be associated with the resonant response.[1] The observed photoresponse is nonresonant in nature. Rough estimation of the detector sensitivity yields 10^3 V/W. We can see from Fig. 3 that the dependence of the signal on the gate voltage conforms well to that calculated within the nonresonant-response model [4]. Qualitatively, the signal falloff in the range of high gate voltages can be explained by total depletion of the channel. The falloff observed as U_{GS} decreases can be associated with the increase in the channel conductance and with the worse device–antenna matching.

Figure 4 shows the gate-voltage dependences of the photoresponse for transistor *T*3 with an atypical transfer characteristic (curve *5*). This transistor had a channel split into two equal regions each 50 μm wide. We can readily see that the transfer characteristic has two portions corresponding to two values of the pinch-off voltage (approximately –0.2 and –0.4 V). Each of these pinch-off voltage values is associated with a feature observed in the nonresonant response as a function of the gate voltage.

Figure 5 illustrates the operation of the transistor as a microwave detector in the nonlinear mode. It is easily seen that the gate-voltage dependence of the photoresponse is "pulled" into the region of higher negative U_{GS} as the radiation power increases, which seems to be caused by a commensurate increase in the amplitude of the high-frequency gate voltage.

[1] It is the authors' opinion that the absence of a resonant response (in contrast to the data from [1, 2]) can be caused by an insufficiently strong connection of the "plasma resonator" with other elements of the equivalent electric circuit of the transistor. As a result, the resonant response (which should be observed as U_{GS} increases from zero to the pinch-off voltage) can be concealed by the increasing nonresonant response.

REFERENCES

1. W. Knap, Y. Deng, S. Rumyantsev, *et al.*, Appl. Phys. Lett. **80** (18), 3433 (2002).
2. W. Knap, Y. Deng, S. Rumyantsev, and M. S. Shur, Appl. Phys. Lett. **81** (24), 4637 (2002).
3. X. G. Peralta, S. J. Allen, M. C. Wanker, *et al.*, Appl. Phys. Lett. **81** (9), 1627 (2002).

4. W. Knap, V. Kachorovskii, Y. Deng, *et al.*, J. Appl. Phys. **91** (11), 9346 (2002).
5. A. C. Samuels, D. L. Woolard, T. Globus, *et al.*, in *Environmental Sensing of Chemical and Biological Warfare Agents in the THz Region, WOFE-0.2 Proceedings, Yoon Soo Park*, Ed. by Michael S. Shur and William Tang (2002).
6. B. Ferguson and X.-C. Zhang, Nature Mater. **1** (1), 26 (2002).
7. G. E. Stillman, C. M. Wolfe, and J. O. Dimmock, Solid State Commun. **7**, 7 (1969).
8. W. Knap, J. Lusakowskii, K. Karpierz, *et al.*, J. Appl. Phys. **72** (2), 680 (1992).
9. G. Strasser, K. Bochter, M. Witzany, and E. Gornik, Infrared Phys. **32**, 439 (1991).
10. Y. Kawano, Y. Hisanaga, H. Takenouchi, and S. Komiyama, J. Appl. Phys. **89** (7), 4037 (2001).
11. B. A. Andreev, I. V. Erofeeva, V. I. Gavrilenko, *et al.*, Semicond. Sci. Technol. **16** (5), 300 (2001).
12. M. Dyakonov and M. S. Shur, Phys. Rev. Lett. **71** (15), 2465 (1993).

Translated by A. Kazantsev

Physics of the Solid State, Vol. 46, No. 1, 2004, pp. 150–152. Translated from Fizika Tverdogo Tela, Vol. 46, No. 1, 2004, pp. 150–151.

PROCEEDINGS OF THE CONFERENCE DEDICATED TO O. V. LOSEV (1903–1942)

(Nizhni Novgorod, Russia, March 17–20, 2003)

Cyclotron Resonance of Holes in Silicon in Quantizing Magnetic Fields

D. B. Veksler, V. I. Gavrilenko, and K. E. Spirin

Institute of Microstructure Physics, Russian Academy of Sciences, Nizhni Novgorod, 603950 Russia

Abstract—The cyclotron resonance spectra of holes in bulk silicon in quantizing magnetic fields are investigated in the low-temperature range. The data obtained agree well with the results of the numerical calculation performed earlier by Owner-Petersen and Samuelsen for effective cyclotron masses m^*/m_0 and matrix elements M upon transitions between different Landau levels of holes in silicon with a magnetic-field orientation **H** ‖ [001]. © *2004 MAIK "Nauka/Interperiodica".*

1. INTRODUCTION

It is well known that lower Landau levels of holes in diamond-like semiconductors of germanium and silicon are not equally spaced [1, 2]. This is a consequence of the degeneracy of the valence band at the point $\mathbf{k} = 0$ and leads to the fact that, in strong magnetic fields ($\hbar\omega_c \geq k_B T$), the cyclotron resonance spectra exhibit a large number of resonance lines associated with optical transitions between different pairs of energy levels rather than two absorption lines attributed to light and heavy holes. The cyclotron resonance of holes in quantizing magnetic fields has been thoroughly studied in germanium (see, for example, [3]). Surprising as it may seem, only a few papers have been concerned with similar investigations of the cyclotron resonance in silicon [4, 5]. The most comprehensive data on the cyclotron resonance spectra of holes in silicon in the limit of strong magnetic fields are presented in the paper by Owner-Petersen and Samuelsen [5], who compared the results of measurements performed for different orientations of the magnetic field with theoretical data. This comparison allowed those authors to refine considerably the parameters of the dispersion law of holes in silicon [5]. The above investigations were carried out using samples of high-resistance *p*-Si ($\rho_{300\,K} = 3.9$ kΩ cm) in the millimeter-wave band ($j = 45$ GHz) at temperatures ranging from 1.2 to 5 K.

In this work, we carried out similar investigations using a purer sample of *n*-Si ($\rho_{300\,K} \approx 10$ kΩ cm) in the short-wavelength part of the millimeter-wave band at $T = 4.2$ K. A comparison of our results with the theoretical data obtained earlier in [5] showed that the parameters of the dispersion law of holes in silicon call for further refinement.

2. SAMPLES AND EXPERIMENTAL TECHNIQUE

The cyclotron resonance spectra were measured in the automatic magnetic-field scan mode at a constant frequency and $T = 4.2$ K. Samples of bulk silicon prepared in the form of plates $5 \times 5 \times 0.3$ mm in size were placed in a fiber-optic waveguide insert into an STG-40

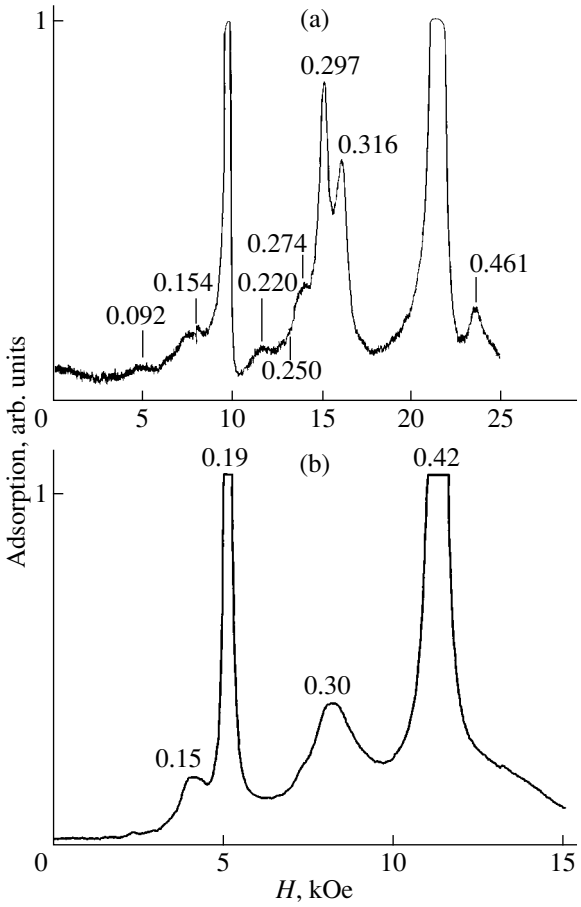

Fig. 1. Cyclotron resonance spectra of photocarriers in silicon at a temperature of 4.2 K and frequencies of (a) 142.8 and (b) 75 GHz. Numbers at the peaks of the curves are the cyclotron masses (expressed in units of m_0).

1063-7834/04/4601-0150$26.00 © 2004 MAIK "Nauka/Interperiodica"

helium storage dewar situated at the center of a superconducting solenoid in such a manner that the magnetic field was directed perpendicular to the plane of the sample: **H** ∥ [001]. Generators based on G4-161 and G4-142 backward-wave tubes were used as radiation sources in the two- and four-millimeter-wave bands, respectively. Free carriers in samples were created under exposure to band-to-band radiation modulated at a frequency of 1 kHz with the use of a gallium arsenide light-emitting diode ($\lambda \approx 0.9$ μm) located near the sample. The microwave radiation passed through the sample was detected using an *n*-InSb crystal. The synchronous detection of signals was accomplished by a standard method, after which the signals were digitized and entered on a personal computer with the use of an analog-to-digital converter.

3. RESULTS AND DISCUSSION

The experimental cyclotron resonance spectra are shown in Fig. 1. In addition to the lines attributed to cyclotron resonances of electrons (m^*/m_0 = 0.19 and 0.42), the spectra exhibit a large number of resonances due to transitions between different Landau levels of holes that are not equally spaced. The transitions characterized by cyclotron masses of approximately $0.15m_0$ and $0.5m_0$ correspond to cyclotron resonances of the classical light and heavy holes, respectively, i.e., cyclotron resonances of the holes occupying Landau levels with large indices. At the same time, the hole lines located between the lines associated with cyclotron resonances of electrons are attributed to transitions between lower Landau levels that are not equally spaced. It is evident that, in strong (quantizing) magnetic fields [i.e., in the case when the ratios $\hbar\omega/k_BT$ are sufficiently large (Fig. 1a)], the relative intensities of "quantum" cyclotron resonance lines (corresponding to effective cyclotron masses of approximately $0.3m_0$) are considerably higher than those in Fig. 1b. The resolution of the lines associated with the quantum cyclotron resonance of holes in the spectrum recorded in this work (Fig. 1a) is substantially higher than that in the spectrum obtained in [5], even though, in the latter case, the ratio $\hbar\omega/k_BT$ is somewhat greater. The better resolution of the cyclotron resonance lines of holes in our spectrum can be explained by the higher purity of the sample.

Figure 2 presents the energy diagram of the lower Landau levels of holes according to the calculations performed in [5]. The table lists the effective cyclotron masses and matrix elements for the energy-level transitions. Transitions *3–13* each occur within their own ladder of Landau levels and have comparable values of the matrix elements. In strong magnetic fields ($\hbar\omega/k_BT \geq 1$), the cyclotron resonance spectra should predominantly contain lines attributed to transitions from the lower Landau levels of holes. Three of the four transitions (transitions *3*, *6*, *9*) are presented in the table.

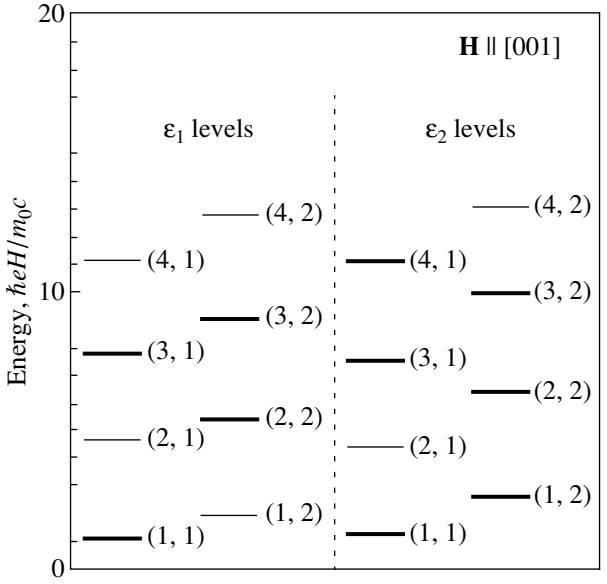

Fig. 2. Calculated energy diagram of lower Landau levels of holes in silicon for the following set of band parameters: $\gamma_1 = 4.25$, $\gamma_2 = 0.35$, $\gamma_3 = 1.39$, and $\kappa = -0.46$ [5].

Transition *9* is characterized by an effective cyclotron mass of $0.292m_0$. As a rough approximation, this transition corresponds to the cyclotron resonance line observed at an effective cyclotron mass of $0.297m_0$ in the spectrum shown in Fig. 1a. Another pronounced line of the quantum cyclotron resonance of holes, which is observed at an effective cyclotron mass of

Calculated values of the effective cyclotron masses m^*/m_0 and matrix elements *M* for transitions between different Landau levels of holes in silicon with magnetic-field orientation **H** ∥ [001] [5]

No.	m^*/m_0	*M*	Transition
1	0.224	0.495	$\varepsilon_1(2, 1) \longrightarrow (3, 2)$
2	0.232	0.432	$\varepsilon_1(1, 1) \longrightarrow (2, 2)$
3	0.264	1.061	$\varepsilon_2(1, 2) \longrightarrow (2, 2)$
4	0.270	1.80	$\varepsilon_1(3, 2) \longrightarrow (4, 2)$
5	0.273	1.46	$\varepsilon_1(2, 2) \longrightarrow (3, 2)$
6	0.285	1.07	$\varepsilon_1(1, 1) \longrightarrow (2, 1)$
7	0.286	1.56	$\varepsilon_2(2, 2) \longrightarrow (3, 2)$
8	0.287	1.70	$\varepsilon_2(3, 1) \longrightarrow (4, 1)$
9	0.292	1.04	$\varepsilon_1(1, 2) \longrightarrow (2, 2)$
10	0.305	1.52	$\varepsilon_1(2, 1) \longrightarrow (3, 1)$
11	0.314	1.45	$\varepsilon_2(2, 1) \longrightarrow (3, 1)$
12	0.314	1.85	$\varepsilon_1(3, 1) \longrightarrow (4, 1)$
13	0.319	1.99	$\varepsilon_2(3, 2) \longrightarrow (4, 2)$

$0.316m_0$ in the spectrum depicted in Fig. 1a, can be assigned to transitions *11–13* (see table). However, all these transitions occur not from the lower but from the higher Landau levels; consequently, their intensities should not be very high. The last (fourth) transition from one of the four lower Landau levels, namely, $\varepsilon_2(1, 1) \longrightarrow (2, 1)$ (not included in the table), is characterized by an effective cyclotron mass of $0.32m_0$. Therefore, it is reasonable to assume that this transition corresponds to the cyclotron resonance line observed at an effective mass of $0.316m_0$ in our spectrum (Fig. 1a). In order to obtain the ultimate answer to this problem, it is necessary to measure the cyclotron resonance in stronger magnetic fields (at the same temperature). As was noted in [5], it is at this orientation of the magnetic field **H** ∥ [001] that the energy location of the transitions from the four lower Landau levels is most sensitive to the parameter γ_2 of the dispersion law of holes, which can thus be refined.

ACKNOWLEDGMENTS

This work was supported by the Russian Foundation for Basic Research (project no. 03-02-16808) and the Ministry of Industry, Science, and Technology of the Russian Federation (State Contract no. 40.072.1.1.1173).

REFERENCES

1. J. M. Luttiger and W. Kohn, Phys. Rev. **97** (4), 869 (1955).
2. J. M. Luttiger, Phys. Rev. **102** (4), 1030 (1956).
3. J. C. Hensel and K. Suzuki, Phys. Rev. B **9** (10), 4184 (1974); Phys. Rev. B **9** (10), 4219 (1974).
4. J. J. Stickler, H. J. Zeiger, and G. H. Heller, Phys. Rev. **127** (4), 1077 (1962).
5. M. Owner-Petersen and M. R. Samuelsen, Phys. Status Solidi **28**, 211 (1968).

Translated by O. Moskalev

Physics of the Solid State, Vol. 46, No. 1, 2004, pp. 153–156. From Fizika Tverdogo Tela, Vol. 46, No. 1, 2004, pp. 152–155.

PROCEEDINGS OF THE CONFERENCE DEDICATED TO O. V. LOSEV (1903–1942)

(Nizhni Novgorod, Russia, March 17–20, 2003)

Plasmon-Induced Terahertz Absorption and Photoconductivity in a Grid-Gated Double-Quantum-Well Structure*

V. V. Popov[1], T. V. Teperik[1], O. V. Polischuk[1], X. G. Peralta[2], S. J. Allen[2], N. J. M. Horing[3], and M. C. Wanke[4]

[1] *Institute of Radio Engineering and Electronics, Saratov Division, Russian Academy of Sciences, Saratov, 410019 Russia*

[2] *Center for Terahertz Science and Technology, University of California, Santa Barbara, California, 93106 USA*

[3] *Department of Physics and Engineering Physics, Stevens Institute of Technology, Hoboken, New Jersey, 07030 USA*

[4] *Sandia National Laboratories, Albuquerque, New Mexico, 87185 USA*

Abstract—The terahertz absorption spectra of plasmon modes in a grid-gated double-quantum-well field-effect transistor structure is analyzed theoretically and numerically using the scattering matrix approach and is shown to faithfully reproduce strong resonant features of recent experimental observations of terahertz photoconductivity in such a structure. © *2004 MAIK "Nauka/Interperiodica".*

Recently, the terahertz (THz) photoconductivity of a double-quantum-well (DQW) field-effect transistor (FET) with a periodic metal-grid gate was observed [1]. It appears that the presence of a DQW is important to produce a strong photoresponse. The position and the strength of the peaks in the photoresponse and photoconductance (the change of channel conductance) are controlled by both the voltage V_g applied to the gate and the period of the grating gate, which strongly suggests that the sharp resonant features are related to plasma oscillations in this composite device. The strongest THz photoresponse occurs when the upper QW is fully depleted under metallic portions of the grating gate, while the lower one remains connected but with laterally modulated electron density. The response is fast (less than 1 μs) and depends on the presence of the DQW channel. Remarkably, the sharpest and strongest resonance response does not occur at the lowest temperatures but rather between 25 and 40 K. The sign of the photoconductance is not unique and depends on the grating period. The physical mechanism responsible for the THz photoconductivity is not evident at this time. Particularly, the temperature dependence, as well as the reversal of sign of the photoconductance, is not understood.

A simple "transmission" model discussed in [1] describing plasma oscillations in the grid-gated DQW FET provided a rough qualitative guide suggesting that the series of frequency-dependent resonances observed in the THz photoconductance corresponds to the excitation of plasma waves in the structure. However, this simple model fails to explain the measured separation in V_g between resonances at different frequencies and the variation of the line shape with frequency.

Far infrared absorption in density-modulated two-dimensional electron systems has been studied theoretically in a series of papers [2–9], including studies of density-modulated bilayers [2, 4, 6] and structures with metal gratings [3, 5].

In this paper, we develop a detailed, realistic model of plasmon electrodynamics in the grid-gated DQW FET structure studied experimentally in [1]. We present the results of our electrodynamic simulation of the THz absorption spectrum taking into account all essential features of the actual composite structure studied in [1], which faithfully reproduce strong resonant features of experimental observations of THz photoconductivity in such a structure.

1. THEORETICAL MODEL

We analyze the THz absorption spectrum in the DQW multilayered laterally periodic structure from [1] (see inset to Fig. 1a) using a scattering matrix approach [10–12]. The scattering matrix approach employed involves the following steps. Within each layer of the structure, the Maxwell equations are rewritten in an in-plane momentum matrix representation starting with decomposition of the magnetic field into a sum of plane waves:

$$\mathbf{H}(x, z, t) = \sum_m \mathbf{H}_m \exp(-i\beta_m x)\exp(ik_z z)\exp(-i\omega t), \quad (1)$$

where $m = 0, \pm1, \pm2, \ldots, \pm M$; $\beta_m = k_x + 2\pi m/L$; L is the period of the structure; and k_x is the reduced in-plane wave vector. In the case under consideration, when THz radiation is incident normally onto the multilayered

* This article was submitted by the authors in English.

1063-7834/04/4601-0153$26.00 © 2004 MAIK "Nauka/Interperiodica"

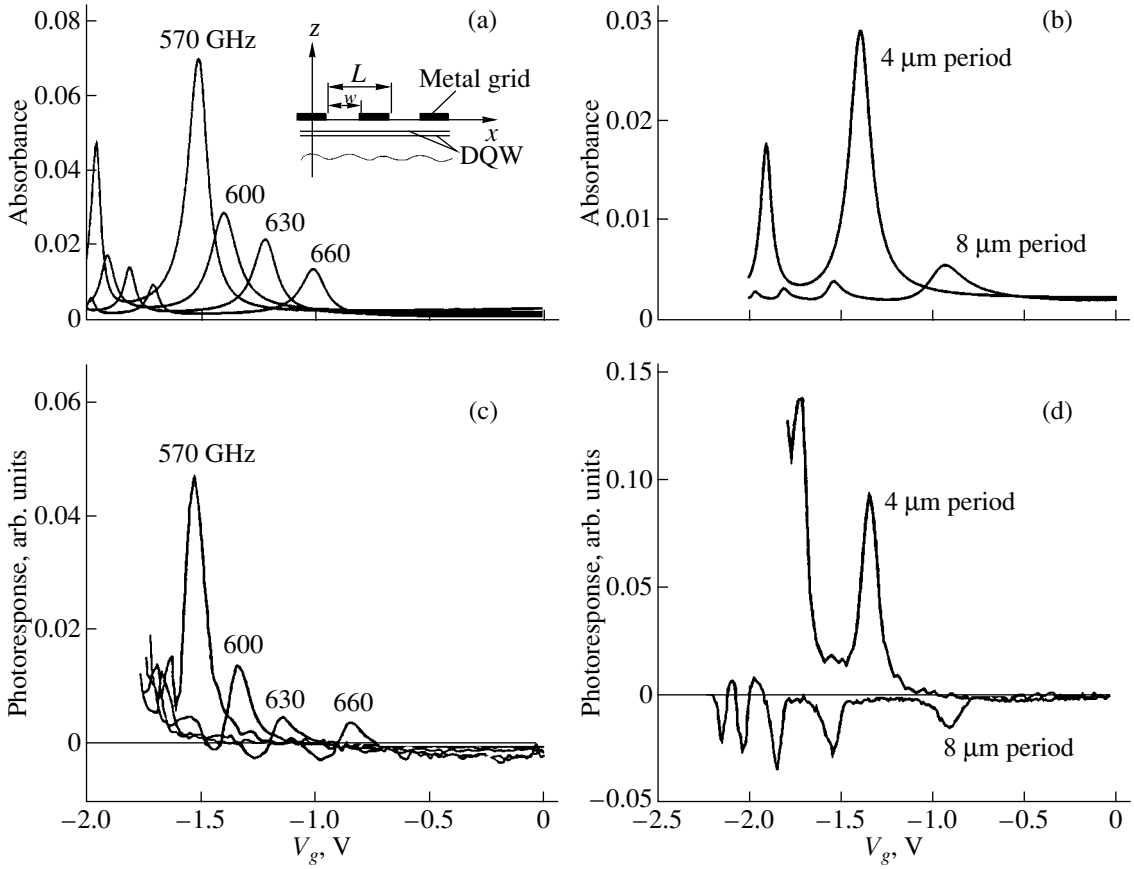

Fig. 1. Calculated absorption spectra: (a) at several different THz frequencies for L = 4 μm and $w = L/2$ and (b) at a frequency of 600 GHz for two different periods of the structure with $w = L/2$; V_{th} = –2.6 V is a fitted value. Other parameters of the structure are given in the text. Terahertz photoresponse measured as a function of gate voltage: (c) for four different frequencies for L = 4 μm and $w = L/2$ and (d) at a frequency of 600 GHz for different periods of the metal gate with $w = L/2$ at T = 25 K, as reported in [1].

structure, $k_x = 0$ and there are only E_{x0} and H_{y0} nonzero components of the electric and magnetic field in the incident wave. Assuming the square profile of the lateral periodicity of the structure, the dielectric function $\varepsilon(x)$ in each layer transforms into matrix $\hat{\varepsilon}$ with elements

$$\varepsilon_{mm'} = \int_{-L/2}^{L/2} \varepsilon(x) \exp\left[-\frac{2\pi(m-m')}{L}\right] dx. \qquad (2)$$

Obviously, for homogeneous layers, we have $\hat{\varepsilon} = \varepsilon\hat{I}$, where ε is constant and $\hat{I}$ is the unit matrix.

As a result, in each layer, we arrive at the matrix eigenproblem

$$\left[\hat{\varepsilon}\left(\frac{\omega^2}{c^2} - \hat{\beta}\hat{\varepsilon}^{-1}\hat{\beta}\right)\right]\mathbf{A} = k_z^2\mathbf{A}, \qquad (3)$$

where $\hat{\beta}$ is the diagonal matrix with elements $\beta_{mm'} = \delta_{mm'}\beta_m$. The $(2M + 1)$-dimensional eigenvectors $\mathbf{A}^{(n)}$, where $n = 1, 2, \ldots, 2M + 1$, have normalized amplitudes of the magnetic field H_{ym} as their components. Eigenvectors $\mathbf{A}^{(n)}$ and $\mathbf{A}^{(n')}$ corresponding to eigenvalues $(k_z^{(n)})^2$ and $(k_z^{(n')})^2$ satisfy the orthogonality relationship $\mathbf{A}^{(n)}\mathbf{A}^{(n')} = \delta_{nn'}$. In particular, for homogeneous layers, the eigenvalue problem (3) yields the eigenvectors $\mathbf{A}^{(n)}$ with components δ_{nm} corresponding to eigenvalues

$$(k_z^{(n)})^2 = \varepsilon\frac{\omega^2}{c^2} - \delta_{nm}\beta_m.$$

Eigenproblem (3) is degenerate with respect to the reversal of sign of the transverse wave vector k_z. Thus, the total field in each layer is a superposition of eigenmodes of form (1) with $k_z = \pm|k_z^{(n)}|$, where $n = 1, 2, \ldots, 2M + 1$, propagating along and counter to z axis. Applying boundary conditions of continuity of E_x and H_y components of the total field at interfaces of the layers, we can relate the amplitudes of waves outgoing from

the whole structure to those of incoming waves in the matrix form:

$$\begin{pmatrix} \mathbf{A}_{\text{out}}^{+} \\ \mathbf{A}_{\text{out}}^{-} \end{pmatrix} = \mathbb{S} \begin{pmatrix} \mathbf{A}_{\text{in}}^{+} \\ \mathbf{A}_{\text{in}}^{-} \end{pmatrix}.$$

Here, superscripts + and – refer to the waves propagating along and counter to the z axis, respectively, and $\mathbb{S}$ is the scattering matrix of the whole structure, which can be written in the 2×2 block matrix form:

$$\mathbb{S} = \begin{pmatrix} \hat{S}_{11} & \hat{S}_{12} \\ \hat{S}_{21} & \hat{S}_{22} \end{pmatrix}.$$

In our particular problem under consideration, we have only one incoming plane wave incident onto the metal-grid gate (i.e., $\mathbf{A}_{\text{in}}^{+} = 0$) and there is only the $m = 0$ nonzero component in the vector $\mathbf{A}_{\text{in}}^{-}$. Thus, we can calculate the amplitudes of reflected and transmitted waves as

$$\mathbf{A}_{\text{out}}^{+} = \hat{S}_{12}\mathbf{A}_{\text{in}}^{-}, \quad \mathbf{A}_{\text{out}}^{-} = \hat{S}_{22}\mathbf{A}_{\text{in}}^{-}.$$

Since the period of the structure under consideration ($L \simeq 4$ μm) is roughly two orders of magnitude shorter than the THz radiation wavelength, only $m = 0$ plane-wave components in the reflected and transmitted waves survive at distances much longer than L away from the structure, while all $m \neq 0$ plane-wave components are evanescent. Ultimately, we can readily calculate reflectivity R, transmittivity T, and absorbance $A = 1 - R - T$. For more detailed description of the scattering matrix formalism for multilayered laterally periodic structures, see, for example, [12].

In carrying out our calculations, we assume that the effective thickness d of the upper and lower QWs in the DQW structure is 10 nm each, the separation between the center planes of the QWs $\Delta = 27$ nm, and the distance between the upper (near to the metal-grid gate) QW and grating gate $h = 385$ nm. We assume that the upper QW is fully depleted under the metallic portions of the grating gate of period L, forming an array of disconnected electron strips of width w with surface electron density $N_U = 1.7 \times 10^{11}$ cm^{-2}. The lower QW is density modulated with $N_L = 2.57 \times 10^{11}$ cm^{-2}, which remains essentially unchanged under the electron strips of the upper QW (i.e., under the open parts of the grating gate). The response of electron gas in QWs to the terahertz electric field $E\exp(-i\omega t)$ is described by a local bulk conductivity in the Drude form,

$$\sigma_{U(L)}(x) = \frac{e^2 N_{U(L)}(x)}{m^* d} \frac{\tau}{1 - i\omega\tau},$$

where e and m^* are the electron charge and effective mass and τ is the phenomenological electron relaxation time.

The electron density in the lower QW under metallic portions of the grating gate as a function of the gate voltage $N_L(V_g)$ was obtained from the parallel plate capacitor model with the gate voltage depletion threshold value V_{th} and zero-gate-voltage electron density in both QWs combined chosen as fitting parameters to the experimental data of [1]. The parallel plate capacitor model assumed in this paper is fairly well justified for characteristic parameters of the structure studied in [1]: $L \gg h > d, \Delta$. This electrostatics problem is solved separately, and the obtained value $N_L(V_g)$ is used as an input parameter in electrodynamic modeling. The metal grating strips are composed of a 20-nm Ti layer covered by a 50-nm Au layer. We took the bulk conductivities as $\sigma_0 = 2.3 \times 10^4$ S/cm for Ti and $\sigma_0 = 4.85 \times 10^5$ S/cm for Au.

Dielectric function $\varepsilon(x)$ entering expression (2) in QW layers is taken as

$$\varepsilon_{U(L)}(x) = \varepsilon_b + i\frac{4\pi\sigma_{U(L)}(x)}{\omega},$$

where $\varepsilon_b = 12.24$ in the background dielectric constant. Inside the metal-grid layer, we assume $\varepsilon(x) = i4\pi\sigma_0/\omega$ at the metal strips and $\varepsilon(x) \equiv 0$ at the grid openings.

2. RESULTS AND DISCUSSION

Figure 1a shows the resonant absorption of incident THz electromagnetic radiation at several frequencies versus gate voltage. It is seen in Figs. 1a and 1c that the variation in the line shape of plasma resonances with frequency is very close to that observed in photoconductivity resonances. In our calculations, we used a fitting parameter $\tau = 10^{-11}$ s. This is roughly an order of magnitude less than the value extracted from the DC mobility [1]. Although the THz measurement temperatures are substantially above that used to measure the DC mobility, it is not likely that the DV mobility has dropped by an order of magnitude. On the other hand, one may consider an inhomogeneous broadening of the plasma resonance: the mean free time for a carrier to traverse a period of the modulation is $\sim L/v_F$, where v_F is the Fermi velocity of electrons in the QWs, yielding $\sim 10^{-11}$ s for characteristic parameters of the structure under consideration, which is the same order of magnitude as the scattering used to fit the data.

The calculated THz absorption spectra and measured THz photoresponse for two different periods of the DQW FET structure are shown in Figs. 1b and 1d. It is evident, for both periods, that the positions of the resonances in photoresponse relate to those of the corresponding plasma resonances, although the signs of the photoresponse measurements are opposite for the different periods involved.

It can be seen in Fig. 1 that the separation between the resonances of THz photoresponse exceeds the calculated separation by about 15%. This may be due to

the fact that the parallel plate capacitor model we use to calculate the equilibrium electron density in the lower QW suffers from a neglect of fringing field effects.

While the resonant positions and strengths are well reproduced by our electrodynamic model, it has not dealt with the physical mechanism whereby excitation of the plasmon resonances induces changes in the DC transport. The sign change shown in Fig. 1d underscores the fact that this mechanism is not at all understood.

More sophisticated modeling taking into account the interwell electron transfer in grid-gated DQW FET structures is now in progress. We believe that this will provide an even better correspondence between theoretical and experimental results, as well as advance understanding of the physical mechanism that gives rise to the change in conductance at resonance.

ACKNOWLEDGMENTS

At the Institute of Radio Engineering and Electronics (Saratov Division), this work was supported by the Russian Foundation for Basic Research (grant no. 03-02-17219). The work of X.G.P. and S.J.A. was supported by the ONR MFEL program, the DARPA/ONR THz Technology, Sensing and Satellite Communications Program, the ARO through Science and Technology of Nano/Molecular Electronics: Theory, Simulation, and Experimental Characterization, and the Sandia National Laboratory. Sandia is a multiprogram laboratory operated by Sandia Corporation, a Lockheed Martin Company, for the United States Department of Energy's National Nuclear Security Administration under contract no. DE-AC04-94AL85000. N.J.M.H. gratefully acknowledges support from the US Department of Defense, DAAD 19-01-1-0592. T.V.T. thanks INTAS for its support (grant no. YSF 2002-153).

REFERENCES

1. X. G. Peralta, S. J. Allen, M. C. Wanke, *et al.*, Appl. Phys. Lett. **81**, 1627 (2002).
2. S. Katayama, J. Phys. Soc. Jpn. **60**, 1123 (1991).
3. R. J. Wilkinson, C. D. Ager, T. Duffield, *et al.*, J. Appl. Phys. **71**, 6049 (1992).
4. S. Katayama, Surf. Sci. **263**, 359 (1992).
5. L. Schaich, P. W. Park, and A. H. MacDonald, Phys. Rev. B **46**, 12643 (1992).
6. C. Steinebach, D. Heitmann, and V. Gudmundsson, Phys. Rev. B **56**, 6742 (1997).
7. B. P. Van Zyl and E. Zaremba, Phys. Rev. B **59**, 2079 (1999).
8. O. R. Matov, O. F. Meshkov, and V. V. Popov, Zh. Éksp. Teor. Fiz. **113**, 988 (1998) [JETP **86**, 538 (1998)].
9. O. R. Matov, O. V. Polischuk, and V. V. Popov, Zh. Éksp. Teor. Fiz. **122**, 586 (2002) [JETP **95**, 505 (2002)].
10. C. D. Ager and H. P. Hughes, Phys. Rev. B **44**, 13452 (1991).
11. D. M. Whittaker and I. S. Culshaw, Phys. Rev. B **60**, 2610 (1999).
12. S. G. Tikhodeev, A. L. Yablonskii, E. A. Muljarov, *et al.*, Phys. Rev. B **66**, 045102 (2002).

Physics of the Solid State, Vol. 46, No. 1, 2004, pp. 157–163. Translated from Fizika Tverdogo Tela, Vol. 46, No. 1, 2004, pp. 156–161.

PROCEEDINGS OF THE CONFERENCE DEDICATED TO O. V. LOSEV (1903–1942)

(Nizhni Novgorod, Russia, March 17–20, 2003)

Destruction and Stabilization of the Electromagnetic Transparency of a Semiconductor Superlattice

Yu. A. Romanov and Yu. Yu. Romanova

Institute for Physics of Microstructures, Russian Academy of Sciences, Nizhni Novgorod, 603950 Russia

e-mail: Jul@ipm.sci-nnov.ru

Abstract—Three types of transparency of a semiconductor superlattice, namely, self-induced, induced, and selective transparency, were studied. The conditions of their existence and the causes of their destruction were revealed. It was shown that the state of self-induced transparency, which is unstable in a harmonic field, can be stable in a biharmonic field. © *2004 MAIK "Nauka/Interperiodica".*

1. INTRODUCTION

Semiconductor superlattices (SLs) become strongly nonlinear and unstable media even in relatively weak electric fields (10^2–10^4 V/cm) [1–4]. The nonlinearity of high-frequency conductance manifests itself clearly as electromagnetic-transparency effects, such as self-induced transparency (SIT) [2, 3], induced transparency (IT) [4], and selective transparency (ST) [1].[1] The ST and SIT effects were predicted long ago, in the 1970s, and were observed experimentally in [5]. The mechanisms of their appearance were studied in [6, 7].

Electrons in SLs are known to exhibit Bloch oscillations (BOs) in a high-frequency field. Contrary to Bloch oscillations of an electron in a static electric field, BOs in the general case are nonlinear and aperiodic [6]. Under the action of a harmonic field $E_1\cos(\omega_1 t)$, the dynamic localization (DL) of an electron occurs in SLs [8]; namely, the constant component of its velocity becomes zero at discrete values of the dimensionless field amplitude $g_1 = eE_1d/\hbar\omega_1$ corresponding to the zeros of the zero-order Bessel function, $J_0(g_1) = 0$. In terms of quasi-energy, this effect corresponds to the collapse of electron quasi-energy minibands [9]. In the simplest case of constant relaxation time τ, SIT appears in the same fields [2, 3]. DL is accompanied by the resonant excitation of electrons caused by the harmonic field, and, hence, the absorption of the field becomes maximal [6]. The absorbed field energy can be transferred by electrons not only to the lattice but also to other fields to amplify them. This behavior can destroy both DL and SIT. Indeed, we showed in [7] that SIT is unstable to both static and harmonic disturbances and can be observed only in an SL with a low electron concentration (the small parameter is $(\omega_0/\omega_1)^2$, where ω_0 is the plasma frequency characterizing the linear oscillations of the SL plasma) and only in transient processes or during a pulsed action on the SL.

In this work, we studied the mechanisms of destruction and stabilization of the SL electromagnetic transparency in a harmonic or biharmonic field, i.e., in a field of the type

$$E(t) = E_C + E_1\cos(\omega_1 t + \delta_1) + E_2\cos(\omega_2 t + \delta_2). \quad (1)$$

2. BASIC RELATIONS

As is usually done, we use the sinusoidal electron dispersion law

$$\varepsilon(\mathbf{k}) = \frac{\Delta}{2}(1 - \cos(k_3 d)) + \frac{\hbar^2 k_\perp^2}{2m^*} \quad (2)$$

and the kinetic Boltzmann equation in the τ approximation

$$\frac{\partial f(\mathbf{k}, t)}{\partial t} + \frac{eE(t)}{\hbar}\frac{\partial f(\mathbf{k}, t)}{\partial k_3} = -\frac{f(\mathbf{k}, t) - f_0(\mathbf{k})}{\tau}, \quad (3)$$
$$f(\mathbf{k}, 0) = f_0(\mathbf{k}),$$

where $\hbar k_3$ and $\hbar k_\perp$ are the longitudinal and transverse (with respect to the SL axis) components of the electron momentum $\hbar\mathbf{k}$, respectively; m^* is the transverse effective electron mass; and $f(\mathbf{k}, t)$ and $f_0(\mathbf{k})$ are the field-excited and equilibrium electron distribution functions, respectively. The electric field E is assumed to be uniform and directed along the SL axis.

[1] Note that, unlike optics, the electromagnetic transparency of an SL is thought to be the disappearance of the reactive component of a current [2, 3] rather than saturation of its dissipative component.

1063-7834/04/4601-0157$26.00 © 2004 MAIK "Nauka/Interperiodica"

Using the periodicity of the electron distribution function in the **k** space, we represent this function in the form of a Fourier series,

$$f(\mathbf{k}, t) = \sum_{\nu=-\infty}^{\infty} F_\nu(k_\perp)\exp(i\nu k_3 d)\Phi_\nu(t), \qquad \Phi_\nu = \Phi_{-\nu}^*, \tag{4}$$

where

$$F_\nu(k_\perp) = \frac{d}{2\pi}\int_{-\pi/d}^{\pi/d} f_0(k)\exp(-i\nu k_3 d)dk_3, \qquad F_\nu = F_{-\nu}^*. \tag{5}$$

According to Eqs. (3)–(5), the multicomponent function Φ_ν satisfies the kinetic equation

$$\tau\frac{d\Phi_\nu(t)}{dt} + [1 + i\nu\tau\Omega(t)]\Phi_\nu(t) = 1, \qquad \Omega(t) = \frac{edE(t)}{\hbar} \tag{6}$$

with the initial conditions $\Phi_\nu(0) = 1$. The electric current density is connected with $\Phi_1(t)$ by the relation $j(t) = -j_0\mathrm{Im}(\Phi_1(t))$, $j_0 = \frac{end}{\hbar}(\Delta/2 - \langle\varepsilon_3\rangle_0)$, where $\langle\varepsilon_3\rangle_0$ is the mean equilibrium value of the longitudinal electron energy, d is the SL period, and n is the equilibrium electron concentration in the SL. For an arbitrary time dependence of the field $E(t)$ and for any electron dispersion law, it is convenient to separate BOs by writing $\Phi_\nu(t)$ in the form

$$\Phi_\nu(t) = a_\nu(t)\psi_\nu(t), \tag{7}$$

where $\psi_\nu(t) = [\psi_1(t)]^\nu = \exp(-i\nu\int_0^t \Omega(t_1)dt_1)$ is the BO eigenfunction, which is the solution to kinetic equation (6) without the collision integral and describes the dynamic (collisionless) field-induced modulation of the electron distribution function. The dissipative function $a_\nu(t)$ describes collision-induced changes in the electron distribution function and satisfies the equation

$$\dot{a}_\nu(t) + \tau^{-1}a_\nu(t) = \tau^{-1}\psi_\nu^*(t). \tag{8}$$

High-frequency BOs (whose spectrum contains only the frequencies $\omega = 0$ and $\omega \gg \tau^{-1}$) are slightly suppressed by collisions. Averaging Eq. (8) over the time interval $\omega^{-1} \ll \Delta t \ll \tau$, we obtain

$$a_\nu(t) = \Phi_\nu(0)\exp\left(-\frac{t}{\tau}\right) + \left[1 - \exp\left(-\frac{t}{\tau}\right)\right]\overline{\psi_\nu^*}(t) + O\left(\frac{1}{\omega\tau}\right), \tag{9}$$

where the overscribed bar means time averaging.

3. SUPERLATTICE IN A BIHARMONIC FIELD

To study the interaction between fields in an SL, we consider the behavior of the SL in biharmonic field (1) with $E_C = 0$, $\omega_1\tau \gg 1$, $g_2 \ll 1$, and arbitrary values of g_1 and ω_2 (here, $g_{1,2} = \Omega_{1,2}/\omega_{1,2}$, $\Omega_{1,2} = eE_{1,2}d/\hbar$). The spectrum of BO velocity $V(k_0, t_0, t)$ in this field consists of three sets: the main spectrum [7], containing frequency ω_1 and its harmonics

$$V(k_0, t_0, t) = V_m\sin[k_0 d + g(\sin(\omega t) - \sin(\omega t_0))] = V_m[c_S(k_0 t_0)\psi_S(t) + c_a(k_0, t_0)\psi_a(t)] \tag{10}$$

[where k_0 is the wave vector of an electron at the instant t_0,

$$\psi_S(t) = \cos(g\sin(\omega t)) = J_0(g) + 2\sum_{n=1}^{\infty} J_{2n}(g)\cos(2n\omega t),$$

$$\psi_a(t) = \sin(g\sin(\omega t)) = 2\sum_{n=1}^{\infty} J_{2n-1}(g)\sin((2n-1)\omega t),$$

$$c_S(k_0, t_0) = \sin[k_0 d - g\sin(\omega t_0)],$$

$$c_a(k_0, t_0) = \cos[k_0 d - g\sin(\omega t_0)],$$

and $V_m = \Delta d/2\hbar$ is the maximum longitudinal electron velocity in the SL] and two spectra shifted by $\pm\omega_2$:

$$\Delta V(k_0, t_0, t) = V_m\sum_{n=-\infty}^{\infty} J_n(g_1)\cos[k_0 d - g_1\sin(\omega_1 t + \delta_1) + n(\omega_1 t + \delta_1)]g_2\sin(\omega_2 t + \delta_2). \tag{11}$$

At $\omega_2 \neq n\omega_1$ (n is an integer), BOs are aperiodic and DL [i.e., $\overline{V}(k_0, t_0) = 0$] occurs at the same values of the field as in a purely harmonic field [i.e., at $J_0(g_1) = 0$] but only for the averaging time $t \longrightarrow \infty$.

In this case, according to Eqs. (7) and (8), the steady-state current at combination frequencies, which is linear in the field E_2, is

$$\Delta j(t) = \frac{1}{2}j_0 g_2\sum_{n=-\infty}^{\infty}(1 + (-1)^{n+n_0}) \times\left\{\left[J_0(g_1)J_{n-n_0}(g_1)\frac{J_{n_0}(g_1)J_n(g_1)}{1 + (\gamma\tau)^2}\right]\right.$$

$$\times \sin[n\omega_1 + \gamma)t + \delta_n] + \frac{J_{n_0}(g_1)J_n(g_1)}{1 + (\gamma\tau)^2}\gamma\tau$$

$$\times\left[\cos((n\omega_1 + \gamma)t + \delta) - \frac{E_2}{E_1}\delta_{nn_0}(1 - \delta_{n_0 0})\right. \qquad (12)$$

$$\left.\times \cos(\omega_1 t + \delta_1)\right]\Bigg\} - \frac{j_0 g_2}{\omega_1\tau}(1 + (-1)^{n_0})$$

$$\times\left[\frac{A_{n_0}(g_1)}{n_0}(1 - \delta_{n_0 0}) + \frac{\omega_2}{\omega_1}B(g_1)\delta_{n_0 0}\right]$$

$$\times \cos(\gamma t + \delta_0) + O\left(\frac{1}{\omega_1\tau}\right),$$

where $\gamma = \omega_2 - n_0\omega_1$; $|\gamma| < \omega_1$; $\gamma\tau$ is arbitrary; $n_0 = 1, 2, \ldots$ is the number of the strong-field harmonic whose frequency is nearest to ω_2; $\delta_n = (n - n_0)\delta_1 + \delta_2$; $\delta_{\nu 0}$ is the Kronecker delta; $B(g) = \sum_{n=1}^{\infty} n^{-2} J_n^2(g)$; and

$$A_\nu(x) = \sum_{n=-\infty}^{\infty} n^{-1} J_n(x) J_{n+\nu}(x)$$

$$= \frac{2}{x}[\delta_{\nu 0} - J_0(x)J_{\nu-1}(x)] + \frac{2\nu - 1}{x}A_{\nu-1}(x) - A_{\nu-2}(x),$$

with $A_0 = 0$ and $A_1(x) = x^{-1}[1 - J_0^2(x)]$ ($\nu = 1, 2, \ldots$). As for the terms of the order $(\omega_1\tau)^{-1}$, we retained only the low-frequency term dominating over the other low-frequency terms in the ranges $J_0(g_1) \cong 0$ and $J_{n_0}(g_1) \cong 0$. We also retained one term quadratic in E_2, which is necessary to understand the mechanism of resonance interaction between the fields. These terms and the terms in which the amplitudes contain parameter γ should be taken into account only at $|\gamma| \ll \omega_1$. Otherwise, they should be dropped and, for convenience, we put $n_0 = 0$ in the rest of the sum.

A comparison of Eqs. (11) and (12) reveals the following features of BOs in the macroscopic current.

(1) As in the case of a static field [6], the shift of the BO spectrum by $\pm\omega_2$ can be considered as an amplitude modulation of the main spectrum (10) with frequency ω_2 or γ. However, now this modulation does not have a random phase and, hence, is not suppressed by collisions and the current spectrum contains all three sets of BO frequencies. (In the case of a static or harmonic field, the spectra for a steady-state current and BOs differ [6].)

(2) If $\gamma\tau \gg 1$, then all harmonics of BOs are high-frequency and the BO eigenfunction averaged over high-frequency oscillations is $\overline{\psi_\nu}(t) \cong J_0(\nu g) = \text{const}$. Therefore [see Eqs. (7), (9)], just as in the case of one harmonic field, the macroscopic current differs from BOs (10) and (11) by only a modulating factor. At $J_0(g_1) = 0$, the SL becomes transparent for both the field E_1 (SIT) and the field E_2 (IT) in time $\sim\tau$. ST appears immediately after the application of the field and is determined by the condition of the absence of the corresponding harmonics in BOs (10) and (11). Therefore, in the case of DL [$J_0(g_1) = 0$], only frequency ω_2 is absent in the non-steady-state current at $t < \tau$, while the harmonics with combination frequencies $n\omega_1 \pm \omega_2$ remain large. Note that, beyond the $\tau = \text{const}$ approximation, the fields of the disappearance of the total current and of only the harmonic with frequency ω_2 are different. This important circumstance facilitates the separation of DL and collapse from IT in experimental studies.

(3) At $0 < |\gamma| \ll \omega_1$, it is convenient to represent the BO spectra as consisting of triplets $n\omega_1$, $n\omega_1 \pm |\gamma|$ and a doublet with $\omega = 0$ and $\omega = |\gamma|$. However, because of the system symmetry (odd-parity nonlinearity), a steady-state current contains only doublets and single lines at even n_0 and only triplets at odd n_0. If $|\gamma| \le \tau^{-1}$, the low-frequency harmonic of BOs is heavily suppressed by collisions and the triplets are diffuse. This leads to substantial changes in the amplitudes of all harmonics with combination frequencies in the steady-state current. In this case, the averaged BO eigenfunction

$$\overline{\psi_\nu}(t) = J_0(\nu g_1) - \nu/2 g_2 J_{n_0}(\nu g_1)[(1 - (-1)^{n_0})$$

$$\times \cos(\gamma t + \delta_0) + i(1 + (-1)^{n_0})\sin(\gamma t + \delta_0)]$$

is not a constant (apart from the particular case when $J_{n_0}(\nu g_1) = 0$) and differs from zero at any value of g_1 and $n_0 \neq 0$. Therefore, IT does not appear and the spectra and character of ST of the current and BOs are different.

(4) In addition to the absence of IT near the resonance frequencies $\omega_2 = n_0\omega_1$, an increase in magnitude of the negative dissipative SL conductivity $\sigma(\omega_2, g_1, \omega_1)$ at the frequency of a weak signal is observed [4, 7]. These narrow resonance regions of weak-signal amplification are parts of rather broad regions of the negative conductivity $\sigma(\omega_2, g_1, \omega_1)$. Figure 1 shows the regions of negative dc conductivity and high-frequency conductivity at the frequency ω_1 of the strong field for $\omega\tau = 10$. The boundaries of regions *2* (heavy lines) correspond to the states with a zero steady-state current (heavy solid segments correspond to the stable states, and dashed and thin solid segments along the abscissa axis correspond to the unstable states), and the boundaries of regions *1* (thin lines) correspond to the states with a zero alternating current. Dot-and-dash curves (ovals) correspond to zero differential dc conductivity of the SL (this conductivity is negative inside the ovals). Due to the high negative values of conductivity $\sigma(\omega_2, g_1, \omega_1)$ near the resonance frequencies (at $|n\omega_1 - \omega_2| \lesssim \tau^{-1}$), effective parametric amplification of coupled Stokes and anti-Stokes oscillations occurs at fre-

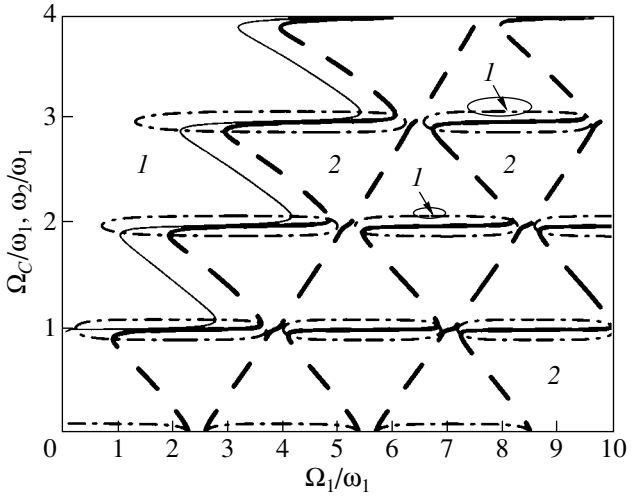

Fig. 1. Regions of negative conductivity for fields E_1 (regions *1*) and E_C ($E_2 = 0$) or E_2 ($E_C = 0$) (regions *2*). $\omega_1\tau = 10$.

quencies $\omega_{2,3} \approx n_{1,2}\omega_1 \pm \tau^{-1}$ ($n_{1,2} = 1, 2, \ldots$), which is one of the main channels of SIT suppression.

(5) In the case of exact resonance ($\gamma = 0$), the current at the frequency $\omega_2 = n_0\omega_1 \gg \tau^{-1}$ is equal to

$$\begin{aligned} j_{\omega_2} &= j_0 g_2 \{ [J_0^2(g_1) - J_{n_0}^2(g_1)] \sin(\omega_2 t + \delta_2) \\ &\quad - [J_0(g_1) J_{2n_0}(g_1) - (-1)^{n_0} J_{n_0}^2(g_1)] \\ &\quad \times \sin(\omega_2 t + \delta_2 - 2\delta_0) \} + j_0 (1 - (-1)^{n_0}) \\ &\quad \times \left[J_0(g_1) J_{n_0}(g_1) \sin(\omega_2 t + n_0\delta_1) \right. \\ &\quad \left. + \frac{1}{\omega_1\tau} A_{n_0}(g_1) \cos(\omega_2 t + n_0\delta_1) \right], \end{aligned} \tag{13}$$

that is, it contains additional terms caused by the parametric resonance of the order $2n_0$ (the second term) and by the generation of the nth harmonic of the strong field (the last term). Since the conductivity $\sigma(\omega_2, g_1, \omega_1)$ is almost purely imaginary in this case, the amplification of the weak signal is mainly determined by parametric resonance. At an odd value of n_0, the parametric generation of a harmonic of the strong field occurs [10]. This process has a hybrid character and includes the ordinary generation of the harmonic and its subsequent continuous parametric amplification. Because of collisions, this generation also exists at $J_0(g_1) = 0$, i.e., under the conditions of DL. In the presence of a static field, which appears, e.g., when SIT is suppressed, the parametric generation of harmonics exists at all integer values of n_0 and the parametric amplification, at half-integer values of n_0 as well. The corresponding conductivities are given in [4, 7]. Since, for exact resonance $\overline{\psi_v}(t) \approx$ const (and is complex), the SL remains transparent and the weak signal is not amplified, collapse of the quasi-energy minibands [for even n_0 and $\delta_0 = n\pi$ or for odd n_0 and $\delta_0 = (n + 1/2)\pi$] takes place. At arbitrary values of δ_0, IT is absent in the SL. The parametric amplification and the generation of harmonics of the strong field are a second substantial channel of SIT suppression in the SL.

(6) The case of $\omega_1 \gg \omega_2 \leq \tau^{-1}(n_0 = 0)$ is specific, since the field frequency coincides with that of a low-frequency harmonic of BOs, which is heavily suppressed by collisions. Therefore, the degree of BO coherence and the collision-induced change in modulation of the BO spectrum are proportional to the same function $J_0(g_1)$. At $J_0(g_1) = 0$, both processes are absent and IT appears (see Eq. (12) at $n_0 = 0$). It should be noted that, beyond the $\tau =$ const approximation, IT also does not appear in this case.

(7) In the case of the resonance $\omega_2 = n_0\omega_1$, an additional velocity component caused by electron motion inside the quasi-energy minibands appears in Eqs. (10) and (11) for BOs. For even values of n_0 at $t < \tau$, this induces a significant rectified current

$$j_C = \frac{ne}{\hbar} \left\langle \frac{\partial \tilde{\varepsilon}(k_3)}{\partial k_3} \right\rangle_0 = j_0 J_{n_0}(g_1) g_2 \sin\delta_0. \tag{14}$$

However, in time τ, collisions suppress this current to a small value $\sim(\omega_1\tau)^{-1} A_{n_0}(g_1)\cos\delta_0$ [see Eq. (12)], which is totally specified by transitions between the quasi-energy minibands. Similarly to absorption in a harmonic field, this rectified current is relatively high in the region $J_0(g_1) = 0$ and $\delta_0 = \pm n\pi$ but appears after the time $\sim\tau$, since the rectified current in BOs [see Eq. (14)] is absent in this case.

(8) At $J_0(g) \approx 0$, the SL has an absolute negative conductivity (ANC) (Fig. 1, region *2*) in a broad band of static fields $0 < \Omega_C \leq \omega_1$. This effect was predicted in [2–4] and observed experimentally in [11]. ANC is another cause of suppression of the SL transparency and manifests itself as the generation of divergent plasma oscillations [7, 12], which result in the spontaneous appearance of a significant static electromotive force in the SL [3, 4, 7].

4. POSSIBLE STABILIZATION OF TRANSPARENCY STATES

Thus, the SIT state in the SL in a harmonic field is unstable to the generation of both static and additional harmonic fields. A static field is usually generated, since the corresponding increment increases rapidly with the field value (Fig. 2) [7]. We will show that an SL transparency state can be stabilized by a second harmonic field with a frequency close to that of the first field. To estimate the required field amplitudes and frequencies, we consider the case of $0 < |\gamma| \ll \omega_1$ (see case (3)

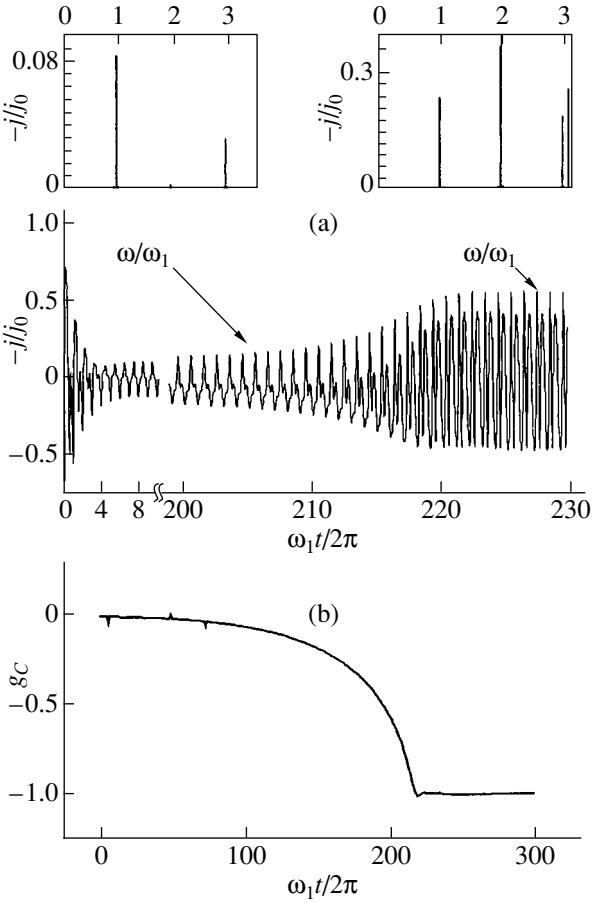

Fig. 2. Setting-in of a stationary static field in an SL with a low electron concentration exposed to a harmonic field. (a) Time evolution and spectra of the current (in the insets) and (b) the time evolution of the mean field. $\omega\tau = 10$ and $(\omega_0/\omega_1)^2 = 0.05$.

of the manifestation of BOs in a macroscopic current) under the assumption that the field E_2 is small but finite ($g_2 < 1$) and that $n_0 = 1$. Owing to parametric mixing and decay of the type $\omega_3 = 2\mu_0\omega_1 \pm \omega_2 = (2\mu_0 + 1)\omega_1 \pm \gamma$, the current spectrum in the SL will contain the frequencies ω_2 and ω_1, odd harmonics $n\omega_1$, and their satellites with even values of n. The current at the combination frequencies is given by

$$\Delta j \approx j_0 \sum_{n=-\infty}^{\infty} (1-(-1)^n) J_0(g_2) J_1(g_2) \times \left\{ \left[J_0(g_1) J_{n-1}(g_1) - \frac{J_1(g_1) J_n(g_1)}{1+(\gamma\tau)^2} \right] \times \sin((n\omega_1 + \gamma)t - \delta_n) + \left[J_1(g_1) J_n(g_1) \frac{\gamma\tau}{1+(\gamma\tau)^2} \right] \cos((n\omega_1 + \gamma)t - \delta_n) \right\}. \quad (15)$$

This current vanishes at the zeros of $J_0(g_2)$ and $J_1(g_2)$. In Eq. (15), unlike in Eq. (12), we kept the Bessel functions that involve the amplitude of the "weak" field E_2; however, for the sake of simplicity, only its fundamental harmonic is retained. The SL dc conductivity in a biharmonic field is

$$\sigma_C(\Omega_C, \Omega_1, \Omega_2, \omega_1) = \sum_{\mu_{1,2}=-\infty}^{\infty} J_{\mu_1}(g_1) J_{\mu_2}(g_2) \times \frac{\Omega_C + \mu_1\omega_1 + \mu_2\omega_2}{1 + (\Omega_C + \mu_1\omega_1 + \mu_2\omega_2)^2 \tau^2}. \quad (16)$$

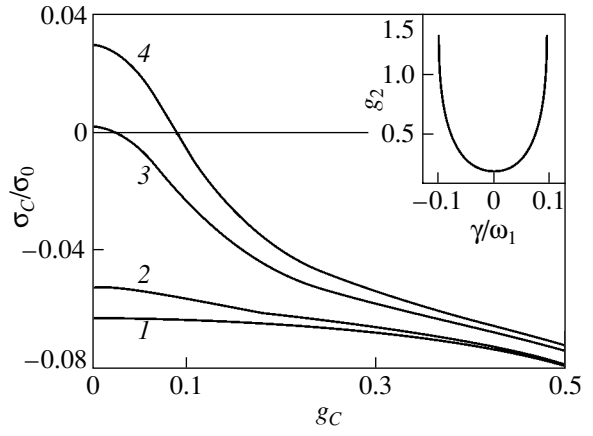

Fig. 3. Static conductivity of the SL in a biharmonic field near the SIT state of the first field at (*1*) $g_2 = 0$, (*2*) 0.1, (*3*) 0.25, and (*4*) 0.3. $\gamma = 0.03\omega$. The inset shows the region $\sigma_C > 0$ on the plane of the weak field parameters (γ, g_2). $g_1 = 2.405$.

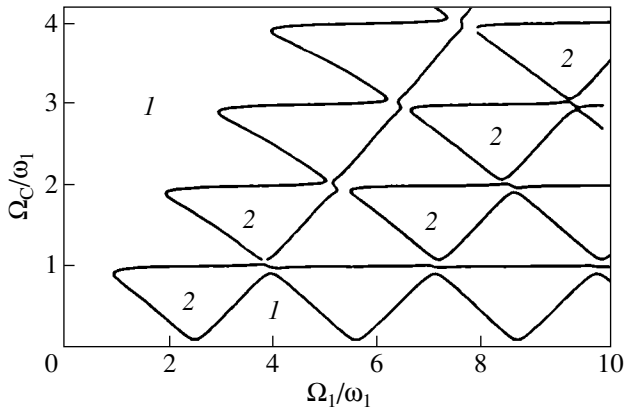

Fig. 4. Instability regions *2* of the static field in the presence of a biharmonic field for $g_2 = 0.3$, $\gamma = 0.025\omega_1$, and $\omega_1\tau = 10$. In regions *1*, the static field is stable.

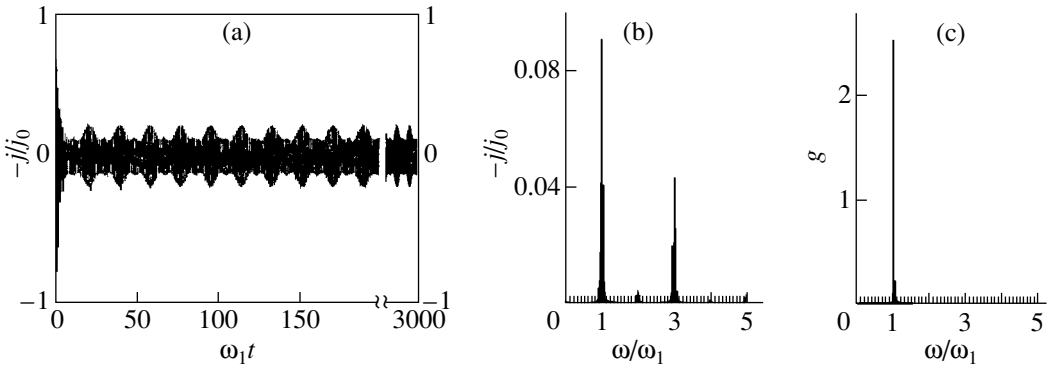

Fig. 5. Stable SIT state in a biharmonic field with $\tilde{V}_0 = 2.526$, $\omega_2 = 1.05\omega_1$, $\omega\tau = 10$, and $(\omega_0/\omega_1)^2 = 0.05$. (a) Current oscillogram, (b) current spectrum, and (c) voltage spectrum. $\tilde{V}_0 = \dfrac{eV_0}{N\hbar\omega_1(1 + C_S/C_1)}$, where C_S is the linear SL capacitance.

Formula (16) is valid for a biharmonic field with arbitrary amplitudes but incommensurable frequencies ($n_1\omega_1 \neq n_2\omega_2$). The conductivity (16) is shown in Fig. 3. As shown above, in a purely harmonic field ($E_2 = 0$), the dc conductivity at small E_C is negative in the SIT "windows" (i.e., ANC appears). However, as an additional harmonic field $E_2(t)$ (with the corresponding frequency) appears, the energy of the first field is transferred not only to the static but also to the second field. The transferred energy increases with E_2. As a result, beginning from a certain value of the field amplitude E_2, the conductivity $\sigma_C(\Omega_C, \Omega_1, \Omega_2, \omega_1)$ becomes positive (only the severe mode of exciting a static emf is retained). Figure 3 (inset) shows the region of positive values of $\sigma_C(\Omega_C \longrightarrow 0)$ in the (γ, g_2) plane. Note that this region of parameters is not completely equivalent to the region of a stable transparency state, since at $\gamma \longrightarrow 0$ the SIT also disappears (the characteristic frequencies are the values of ω_2 corresponding to the step $\omega_2/\omega_1 \approx 1$). Figure 4 shows how the static-field instability regions displayed in Fig. 1 vary when the SL is additionally exposed to a second relatively weak harmonic field ($g_2 = 0.3$). It is seen that ANC disappears at $E_C = 0$ and shifts toward high static fields.

It is easy to show that the instability regions of a static field in the presence of a biharmonic field with incommensurable frequencies are also regions of linear instability of a third harmonic field with a frequency ω_3 that is not a multiple of ω_1 and ω_2 (with Ω_C/ω_1 replaced by ω_3/ω_1). Thus, the regions of $J_0(g_1) \approx 0$ can become stable to weak ($g_C < 0.1$ in the given example) fluctuations of the static field and to low-frequency perturbations in the presence of a biharmonic field with certain parameters. As an example, Fig. 5 shows numerically calculated internal voltage and current in an SL which is connected to a dc open circuit and to which an external biharmonic voltage $V(t) = V_0[\sin(\omega_1(t) + 0.1\sin(\omega_2 t)]$ is applied with $\omega_2 = 1.05\omega_1$ and $\tilde{V}_0 = 2.526$.[2] As can be seen from Fig. 5, an SL transparency state (small currents of ~0.08 at the fundamental harmonic, of ~0.04 at the third harmonic, and of even smaller values at the combination harmonics $2\omega_1 \pm \gamma$) appears after time $\sim\tau$ and then persists. In a purely harmonic field with the same parameters (Fig. 2), the transparency state is broken within ~200 field-oscillation periods and then a significant static field with $g_C \sim 1$ and currents of ~0.3 at the first-, second-, and third-harmonic frequencies appear. As shown by numerical calculation, similar stabilization of a transparency state in the SL takes place in a multifrequency field whose spectrum lies in a narrow frequency band near ω_1 ($\Delta\omega \approx \tau^{-1}$).

5. CONCLUSIONS

(1) The IT effect can appear in a weakly dissipative SL placed in a high-frequency harmonic field ($\omega\tau \gg 1$) only in cases where (a) the fields applied to the SL have high frequencies ($\omega_{1,2}$, $|n\omega_1 - \omega_2| \gg \tau^{-1}$, $n = \pm 1, 2, \ldots$) or (b) $\omega_1 \gg \omega_2 \leq \tau^{-1}$.

(2) The causes of the breaking of transparency states in the SL are (a) an increase in magnitude of the negative dissipative conductivity near resonance frequencies ($|n\omega_1 - \omega_2| \leq \tau^{-1}$), which results in effective parametric amplification of coupled Stokes and anti-Stokes oscillations (with frequencies $\omega_{2,3} \approx n_{1,2}\omega_1 \pm \tau^{-1}$, i.e., with frequencies that are close but not equal to multiples of the external-field frequency); (b) the parametric amplification and generation of harmonics of the external field; and (c) absolute negative conductivity, which leads to the spontaneous generation of significant static fields.

[2] The equivalent circuit and the corresponding equation can be found in [7]. This circuit contains an N-period SL, an exterior capacity C_1, and a voltage source.

(3) Transparency states that occur in an SL exposed to a biharmonic field with arbitrary amplitudes are also unstable. In a biharmonic field with frequencies close to each other (if the amplitude of one of the field components is relatively low), the SL can be in a transparency state stable to low-frequency fluctuations.

ACKNOWLEDGMENTS

This work was supported by the Russian Foundation for Basic Research (project no. 01-02-16446), the Ministry of Industry and Science of the Russian Federation, and the Russian Academy of Sciences program "Low-Dimensional Quantum Structures."

REFERENCES

1. Yu. A. Romanov, Fiz. Tekh. Poluprovodn. (Leningrad) **5**, 1434 (1971) [Sov. Phys. Semicond. **5**, 1256 (1971)]; Opt. Spektrosk. **33**, 917 (1972).
2. A. A. Ignatov and Yu. A. Romanov, Fiz. Tverd. Tela (Leningrad) **17** (11), 3388 (1975) [Sov. Phys. Solid State **17**, 2216 (1975)].
3. A. A. Ignatov and Y. A. Romanov, Phys. Status Solidi **73**, 327 (1976).
4. L. K. Orlov and Yu. A. Romanov, Fiz. Tverd. Tela (Leningrad) **19** (3), 726 (1977) [Sov. Phys. Solid State **19**, 421 (1977)]; Yu. A. Romanov, V. P. Bovin, and L. K. Orlov, Fiz. Tekh. Poluprovodn. (Leningrad) **12**, 1665 (1978) [Sov. Phys. Semicond. **12**, 987 (1978)].
5. M. C. Wanke, A. G. Markelz, K. Unterrainer, *et al.*, in *Physics of Semiconductors*, Ed. by N. Scheffter and R. Zimmerman (World Sci., Singapore, 1996), p. 1791.
6. Yu. A. Romanov and Yu. Yu. Romanova, Fiz. Tverd. Tela (St. Petersburg) **43** (3), 520 (2001) [Phys. Solid State **43**, 539 (2001)].
7. Yu. A. Romanov and Yu. Yu. Romanova, Zh. Éksp. Teor. Fiz. **118** (5), 1193 (2000) [JETP **91**, 1033 (2000)].
8. O. N. Dunlap and V. M. Kenkre, Phys. Rev. B **34**, 3625 (1986); Phys. Lett. A **127**, 438 (1988).
9. M. Holthaus, Z. Phys. B **89**, 251 (1992); M. Holthaus and D. Hone, Phys. Rev. B **47**, 6499 (1993).
10. Yu. A. Romanov, Izv. Vyssh. Uchebn. Zaved., Radiofiz. **23**, 617 (1980).
11. B. J. Keay, S. Zenner, S. J. Allen, *et al.*, Phys. Rev. Lett. **75**, 4102 (1995).
12. Yu. A. Romanov, Fiz. Tverd. Tela (Leningrad) **21** (3), 877 (1979) [Sov. Phys. Solid State **21**, 513 (1979)].

Translated by K. Shakhlevich

Physics of the Solid State, Vol. 46, No. 1, 2004, pp. 164–169. Translated from Fizika Tverdogo Tela, Vol. 46, No. 1, 2004, pp. 162–167.

PROCEEDINGS OF THE CONFERENCE DEDICATED TO O. V. LOSEV (1903–1942)

(Nizhni Novgorod, Russia, March 17–20, 2003)

On a Superlattice Bloch Oscillator

Yu. A. Romanov and Yu. Yu. Romanova

Institute for Physics of Microstructures, Russian Academy of Sciences, Nizhni Novgorod, 603950 Russia
e-mail: romanov@ipm.sci-nnov.ru

Abstract—The differential dc and hf conductivities of semiconductor superlattices with various electron miniband dispersion relations are studied. It is shown that, due to the anharmonicity of Bloch oscillations, the hf conductivity can be negative at frequencies equal to integral multiples of the Bloch frequency. This effect can arise even in the regions where the differential dc conductivity is positive. The results of the study suggest that superlattices with a miniband dispersion law in which the effective electron mass is positive in a sizable part of the miniband and decreases as the electron energy increases can be used to generate and amplify terahertz-range (microwave) fields. *© 2004 MAIK "Nauka/Interperiodica".*

In semiconductor superlattices (SLs), the quasimomentum Brillouin zones and the allowed electron energy bands of the original homogeneous materials break up into relatively narrow (10^5–10^7 cm^{-1}) Brillouin minizones and narrow (10^{-3}–10^{-1} eV) allowed and forbidden energy minibands. Because of the smallness of these minibands, electron Bloch oscillations (BOs) occur and Wannier–Stark energy levels arise in an SL even in relatively weak static electric fields (10^2–10^4 V/cm). The BOs are characterized by the Bloch (Wannier–Stark) frequency $\Omega_C = eE_Cd/\hbar$ and the quasiclassical amplitude of spatial oscillations $Z_C = \Delta/2eE_C$, where E_C is the strength of a static electric field applied along the axis of the SL with a spatial period d and energy miniband width Δ, e is the electronic charge, and $\hbar$ is the Planck constant. In the case of $d = 100$ Å and $E_C = 4$ kV/cm, the BO frequency is $f_C \equiv \Omega_C/2\pi \approx 1$ THz. It is important that the Bloch frequency Ω_C is independent of the miniband dispersion law and is determined only by the SL period and the electric field strength in the SL. The miniband dispersion relation manifests itself in the anharmonicity of spatial oscillations of electrons. In the case of the conventionally assumed sine dispersion law, these oscillations are harmonic. The existence of BOs in SLs has been convincingly confirmed in a number of experiments, and their anharmonicity has also been observed experimentally. These facts suggest that semiconductor SLs can be used to develop a terahertz Bloch oscillator whose frequency can be continuously tuned by a static electric field [1].

Another important feature of the SL is the presence of regions with a negative effective electronic mass in the SL Brillouin zone. These regions may be of considerable size. For example, in the case of a sine dispersion law, the effective electron mass is negative in one half of the SL Brillouin zone. In minibands of two- and three-dimensional SLs, there are regions with negative longitudinal and transverse effective masses. Due to the existence of such regions (whose size and position in the SL Brillouin zone can be controlled), the SLs offer promise as NEMAG-like radiation sources [2].

Bragg reflections and negative effective electron masses are the reason for the occurrence of negative dc and hf (dynamic) differential conductivities (NDCs) in SLs. In an SL with sine minibands, these conductivities become negative simultaneously and in the same range of strong electric fields for which $\Omega_C\tau > 1$ (τ is the electron velocity relaxation time). Therefore, terahertz-range oscillations in such SLs are suppressed because of the development of relatively low-frequency domain instability. These oscillations can occur in a semiconductor SL whose current–voltage (*I–U*) characteristics have a range over which the dc differential conductivity is positive and the hf differential conductivity is negative. Such a situation can be realized in several different ways: (i) by displacing the range of negative values of the dc differential conductivity toward high fields ($\Omega_C\tau > 1$) while preserving the negative hf differential conductivity in lower fields; (ii) by displacing the range of negative hf differential conductivity toward low static fields ($\Omega_C\tau < 1$) while leaving the static *I–U* characteristic unchanged or, in general, by separating the electric-field ranges of negative dc and hf differential conductivities; or, finally, (iii) by "opening" an additional channel for the direct current to flow in a narrow range of static electric fields where the hf differential conductivity is negative (i.e., at the "operating point").

To attain these ends, we can vary the dispersion relations in the electron energy minibands [3], turn on or off (weaken) certain electron scattering mechanisms (especially those involving optical phonons), or make use of electron tunneling between minibands [4]. This work is dedicated to the issues outlined above.

In order to elucidate the mechanisms of the occurrence of NDC in an SL and the possibility of control-

1063-7834/04/4601-0164$26.00 © 2004 MAIK "Nauka/Interperiodica"

ling it, we consider the simple case of one miniband with an additive electron dispersion law:

$$\varepsilon(k) = \varepsilon_3(k_3) + \varepsilon_\perp(k_\perp), \quad \varepsilon_\perp(k_\perp) = \frac{\hbar^2 k_\perp^2}{2m}, \qquad (1)$$

where $\varepsilon(k)$ and k are the energy and quasi-wave vector of an electron, respectively; $\varepsilon_3(k_3)$, k_3 and $\varepsilon_\perp(k_\perp)$, $k_\perp$ are their longitudinal and transverse components (with respect to the SL axis), respectively; and m is the effective transverse electron mass. We consider the following two qualitatively different dispersion laws for the longitudinal energy $\varepsilon_3(k_3)$: (i) a sine law

$$\varepsilon_3(k_3) = \frac{\Delta}{2}[1 - \cos(k_3 d)] \qquad (2)$$

in which case, as mentioned above, the effective electron mass is negative in one half of the SL Brillouin zone, and (ii) a "superparabolic" (idealized) law

$$\varepsilon(k_3) = \frac{\hbar^2}{2}\begin{cases} k_2^2/m_1, & 0 < |k_3| < k_i \\ k_3^2/m_2 - 2k_i(1/m_2 - 1/m_1)(|k_3| - k_i/2) & \\ k_i < |k_3| < \pi/d, & \end{cases} \qquad (3)$$

which consists of two parabolas matched at the points $k_3 = \pm k_i$, where $0 < k_i < \pi/d$. If $m_2 = m_1$ or $k_i = 0$ (π/d), Eq. (3) reduces to a parabolic dispersion relation, while in the case of $m_2 = -m_1 < 0$ and $k_i = \pi/2d$ Eq. (3) becomes a reasonable approximation to the sine dispersion law given by Eq. (2). It is very significant that, in a miniband with dispersion law (3) with $m_{1,2} > 0$, regions with a negative effective mass are absent and there are only Bragg reflection points $k_3 = \pm\pi/d$ at the boundaries of the SL Brillouin zone. We are particularly interested in dispersion relation (3) with $m_1 \gg m_2 > 0$, i.e., in minibands in which the effective electron mass decreases with increasing electron energy. Such a dispersion law takes place in hole quantum layers [5].

We use the following physical model to consider the dynamics of an electron in the SL and its scattering by optical phonons in the presence of a static electric field. It is assumed that the SL miniband width Δ is approximately equal to the energy of an optical phonon $\hbar\omega_0$ and that the phonon emission time τ_0 by an electron is much shorter than the other relaxation times, in particular, $\tau_0 \ll \tau$. If in the so-called passive quasi-momentum range [where $\varepsilon(k) < \hbar\omega_0$] there is no electron scattering ($\Omega_C\tau \longrightarrow \infty$) and $\hbar\omega_0 = \Delta$, then an electron with energy $\varepsilon_\perp(k_\perp) < \hbar\omega_0$ moves in quasi-momentum space at a constant velocity until its energy becomes equal to $\varepsilon(k) = \hbar\omega_0$ and its longitudinal quasi-wave vector is equal to the corresponding value $k_3^{(0)}(k_\perp) \le \pi/d$. Thereafter, the following alternatives are possible. (1) Either the electron transfers to the so-called active region of quasi-momentum space [$\varepsilon(k) > \hbar\omega_0$, $k_3^{(0)}(k_\perp) < |k_3| \le \pi/d$] and, reaching the SL Brillouin boundary ($k_3 = \pi/d$), undergoes specular reflection from it (thereby hopping to the point $k_3 = -\pi/d$) and, continuing in motion against the field, reenters the passive region without emitting an optical phonon or (2) the electron, moving in the active region, emits an optical phonon with a probability $\alpha(k_\perp, E_C)$ and transfers to the region of energies $\varepsilon(k) \approx 0$. According to the energy conservation law, the transverse momentum of the electron decreases (the electron momentum can remain unchanged only when a phonon is emitted exactly at the miniband edge $k_3 = \pi/d$. Then, all the processes described above repeat again and again. As a result, the transverse electron momentum $k_\perp \longrightarrow 0$ and its steady-state distribution becomes a needle-shaped distribution described by a superposition of two Baraff functions [6],

$$f_C(k) = 8\pi^2 n d\delta^2(k_\perp) \times \frac{\alpha(0, E_C)\theta(k_3 - \pi/d) + [1 - \alpha(0, E_C)]\theta(\pi/d - k_3)}{2 - \alpha(0, E_C)}, \qquad (4)$$

where $\theta(x)$ is a theta function, $\alpha(0, E_C)$ is the effective optical-phonon emission probability for an electron with transverse quasi-wave vector $k_\perp \approx 0$, and n is the electron concentration. The time required for this distribution to set in increases with decreasing scattering probability $\alpha(k_\perp, E_C)$.

The formation of an anisotropic free-carrier momentum distribution that is highly extended along the electric field direction in a semiconductor is referred to as streaming [7]. For $\alpha(0, E_C) = 1$ (the absolutely rigid phonon "roof"), expression (4) reduces to a usual needle-shaped Baraff function [6] describing the hot-electron distribution in homogeneous semiconductors in the case of ideal streaming ($\tau_0 = 0$, $\tau \longrightarrow \infty$). Clearly, BOs do not arise in this case and, hence, no effects characteristic of SLs are observed (except a possible specific electron dispersion law with, in particular, regions of negative effective masses). For $\tau_0 \neq 0$, the electron momentum distribution in homogeneous semiconductors expands in both the longitudinal and transverse directions (with respect to the applied electric field) because of the penetration of electrons into the active region [8].

The streaming in SLs has specific fundamental features:

(1) The depth of penetration of an electron into the active region is mainly determined by the position of the miniband top rather than by the optical-phonon emission probability. Therefore, the streaming in an SL is narrower than that in the corresponding bulk materials.

(2) If the optical-phonon emission probability $\alpha(0, E_C) < 1$, then two-sided streaming occurs in an SL; that is, the momentum distribution function is needle-shaped and is nonzero not only for positive but also for negative values of the electron quasi-momentum.

(3) The quasi-momentum dependence of the electron velocity is nonlinear, which significantly affects the character of the SL conductivity.

In the case of one-sided streaming [$\alpha(0, E_C) = 1$], the electron motion is a combination of periodic motion at frequency $2\Omega_C$ and translation (in coordinate space) with velocity $\langle V \rangle = (d/\pi\hbar)\int_0^{\pi/d} \frac{\partial \varepsilon(k_3)}{\partial k_3} dk_3$. Under the conditions of two-sided streaming [$\alpha(0, E_C) < 1$], the electron motion is characterized by two frequencies (Ω_C, $2\Omega_C$) and by the average translation velocity, which is $\alpha(0, E_C)$ times lower than that for one-sided streaming.

The case of $\hbar\omega_0 \gtrsim \Delta$ is of importance. In this case, the electrons that are scattered into a cylindrical domain of radius $\delta_k \approx \sqrt{2m(\hbar\omega_0 - \Delta)}$ in quasi-momentum space are trapped and reside in this domain for an infinitely long time, because they are not scattered by optical phonons. Therefore, such electrons are accumulated with time after the electric field is switched off. However, as the electric field is increased, optical-phonon emission by electrons with smaller values of $\hbar k_\perp$ also becomes possible (due to the tunneling effect); the domain where electrons are trapped narrows (to a certain size) and its boundary becomes diffuse (but to a smaller extent than in homogeneous semiconductors). In this domain, electrons are mixed but do not leave it when they emit optical phonons.

Now, let us discuss the part played by quasi-elastic electron scattering in the passive region. In general, this scattering can be taken into account only by using numerical methods (e.g., the Monte Carlo method). Since our aim is to investigate the hf conductivity of an SL in a qualitative way, we make several simplifying assumptions in order to solve the problem analytically.

(1) We assume that the phonon roof is rigid, i.e., that the penetration depth of electrons with $k_\perp > \delta_k$ into the active region is infinitely small. (In this case, the probability $\alpha(0, E_C)$ can be much less than unity.) Under these conditions, due to quasi-elastic scattering, a trapped electron will leave the "trap" and be accelerated by the electric field; having reached the boundary of the active region, the electron will emit an optical phonon and revert rapidly to the state with energy $\varepsilon(k) \approx 0$. With allowance for the conservation of the number of particles, these processes can be described approximately by the collision integral

$$\frac{f(k, t) - (2\pi)^3 n(t)\delta^3(k)}{\tau_C}, \tag{5}$$

where $f(k, t)$ and $n(t)$ are the distribution function and concentration of trapped electrons, respectively, and τ_C is the lifetime of an electron in the trap. The time τ_C is close to the electron velocity relaxation time τ introduced above (not including optical phonon scattering). We will assume these times to be equal and will designate each of them as τ. Since the phase volume is relatively small, the probability of electron scattering without leaving the trap is small and such scattering can be approximately taken into account in collision integral (5) by slightly decreasing the time τ.

(2) Since collisions in the passive region are assumed to occur rarely ($\Omega_C\tau > 1$), the number of untrapped electrons is small ($\Omega_C\tau$ times smaller than that of trapped electrons). The untrapped electrons make a small, nonresonant contribution to the hf current. For simplicity, we neglect this contribution and put $n(t) = n = \text{const}$ in Eq. (5).

(3) Since the cylindrical region in which electrons are trapped is narrow, we will assume that the trapped electrons emit optical phonons with the same effective probability α (independent of $k_\perp$) when they are located exactly at the miniband edge (at the point $k_3 = \pi/d$). To simplify the analysis of the results, we assume that this probability is also independent of the applied electric field.

Under these assumptions, the electron distribution function $f(k_3, t)$ integrated over $k_\perp$ is determined in the range $-\pi/d < k_3 < \pi/d$ using the one-dimensional Boltzmann equation

$$\frac{\partial f(k_3, t)}{\partial t} + \frac{eE(t)}{\hbar}\frac{\partial f(k_3, t)}{\partial k_3} = -\frac{f(k_3, t) - 2\pi n\delta(k_3)}{\tau} + \alpha\frac{eE(t)}{\hbar} f(\pi/d, t)\delta(k_3) \tag{6}$$

with the boundary condition

$$f(-\pi/d, t) = (1 - \alpha) f(\pi/d, t). \tag{7}$$

In Eq. (6), the terms involving delta functions can be treated as point sources of electrons and describe optical-phonon scattering of electrons. In solving this (homogeneous) equation separately in the ranges $(-\pi/d, 0)$ and $(0, \pi/d)$, these terms can be conveniently replaced by the condition of conservation of the number of particles

$$\int_{-\pi/d}^{\pi/d} f(k_3, t)\frac{dk_3}{2\pi} = n \tag{8}$$

or by the corresponding boundary condition at the point $k_3 = 0$, which is obtained by integrating Eq. (6) over a vicinity of the point $k_3 = 0$.

Equation (6) corresponds to the commonly used Drude model, which assumes that, in any collision (in the passive region), an electron transfers to the state of zero energy and that the collisions are characterized by the relaxation time τ. When using this model, we need not take into account the assumptions made above. Therefore, we will also use Eq. (6) in the case of $\Omega_C\tau < 1$ and include all particles, rather than only trapped ones, in the distribution function $f(k_3, t)$. We realize that this

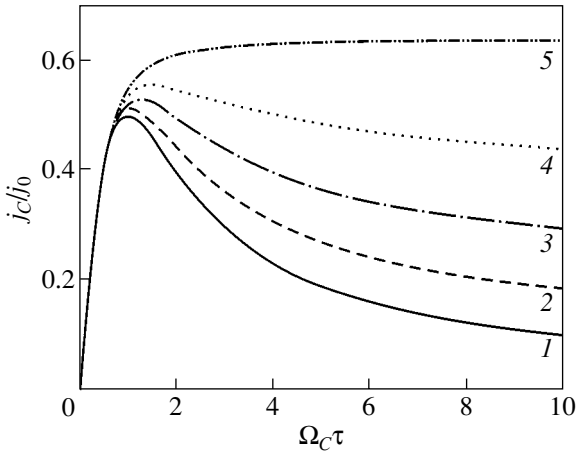

Fig. 1. *I–U* curves of an SL with a sine miniband dispersion law for various values of the probability α of optical-phonon emission by electrons at the miniband edge: (*1*) 0, (*2*) 0.25, (*3*) 0.5, (*4*) 0.75, and (*5*) 1.

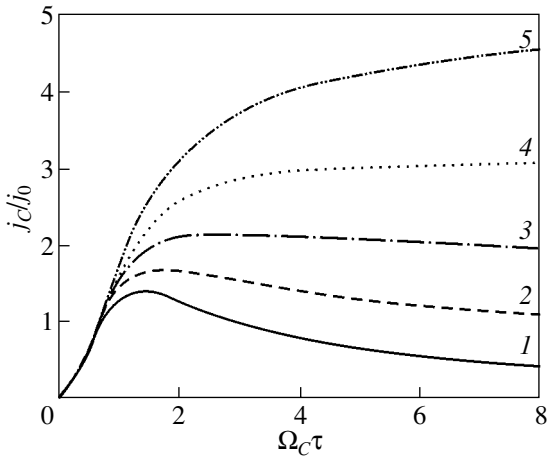

Fig. 2. *I–U* curves of SLs with a superparabolic miniband dispersion law for $\eta \equiv m_1/m_2 = 10$ and $\beta \equiv k_i d/\pi = 0.5$. Labeling conventions are the same as those in Fig. 1.

approximation is fairly crude and can give only a qualitative description of the results.

Within the model described above, we find the electron distribution function and the conductivity of an SL in the field

$$E(t) = E_C + E_1\cos(\omega t), \tag{9}$$

where the static-field strength can have an arbitrary value, while the amplitude of the harmonic field satisfies the condition $E_1 \ll \hbar|\omega + i\tau^{-1}|/ed$; therefore, we consider an approximation linear in E_1. For the sake of convenience, we introduce an additional argument, the inverse relaxation time τ^{-1}, in the distribution function and conductivity. In this notation, the solution to Eq. (6) with conditions (7) and (8) has the form

$$f(k_3, t, \tau^{-1}) = f_C(k_3, \tau^{-1}) + f_1(k_3, t, \tau^{-1}), \tag{10}$$

where

$$f_C(k_3, \tau^{-1}) = \frac{2\pi nd}{\Omega_C\tau} \times \frac{\exp\left(-\dfrac{k_3 d}{\Omega_C\tau}\right)}{\left[1 - \exp\left(-\dfrac{\pi}{\Omega_C\tau}\right)\right]\left[1 + (1-\alpha)\exp\left(-\dfrac{\pi}{\Omega_C\tau}\right)\right]} \tag{11}$$

$$\times \begin{cases} 1, & 0 < k_3 < \pi/d \\ (1-\alpha)\exp\left(-\dfrac{2\pi}{\Omega_C\tau}\right), & -\pi/d < k_3 < 0, \end{cases}$$

$f_C(k_3, \tau^{-1})$ is the electron distribution function in a static field, and

$$f_1(k_3, t, \tau^{-1}) = f_1(k_3, \tau^{-1})\exp(-i\omega t),$$
$$f_1(k_3, \tau^{-1}) = (i/\omega\tau)(E_1/E_C) \tag{12}$$
$$\times [f_C(k_3, \tau^{-1}) - f_C(k_3, \tau^{-1} - i\omega)]$$

is the variation of this function caused by a weak harmonic field. Therefore, the dynamic differential conductivity $\sigma(\omega, \tau^{-1})$ is related (in the approximation at hand) to the total dc conductivity $\sigma_C(\tau^{-1})$ by the relation

$$\sigma(\omega, \tau^{-1}) = (i/\omega\tau)[\sigma_C(\tau^{-1}) - \sigma_C(\tau^{-1} - i\omega)]. \tag{13}$$

The conductivities introduced above are defined by the conventional relations between the current density $j(t)$ and the field $E(t)$

$$j(t) = \frac{e}{\hbar}\int_{-\pi/d}^{\pi/d}\frac{\partial\varepsilon(k_3)}{\partial k_3}f(k_3, t)\frac{dk_3}{2\pi} = j_C + j_1(\omega)\exp(-i\omega t),$$
$$j_C = \sigma_C E_C, \quad j_1(\omega) = \sigma(\omega)E(\omega). \tag{14}$$

We note that distribution functions (11) and (12) found by us are independent of the miniband dispersion law. This feature significantly alleviates the problem of elucidating the part played by the dispersion law in the occurrence of the NDC in an SL. This circumstance justifies using the crude approximation described above. It can be shown that Eqs. (12) and (13) are also valid under less restrictive assumptions.

Now, we present the *I–U* curves and dynamic conductivities of SLs calculated numerically using dispersion relations (2) and (3) and Eqs. (11)–(14).

Figures 1 and 2 show the *I–U* curves of SLs with sine and superparabolic miniband dispersion laws cal-

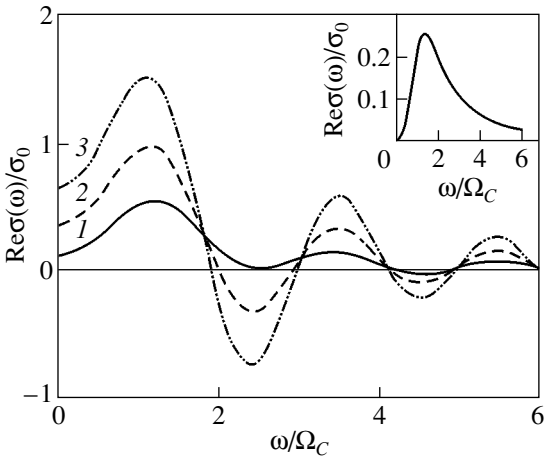

Fig. 3. Dynamic SL conductivities for a sine (inset) and a superparabolic miniband dispersion law with $\beta = 0.5$ and different values of η: (*1*) 1, (*2*) 5, and (*3*) 10; $\alpha = 0$ and $\Omega_C\tau = 1$.

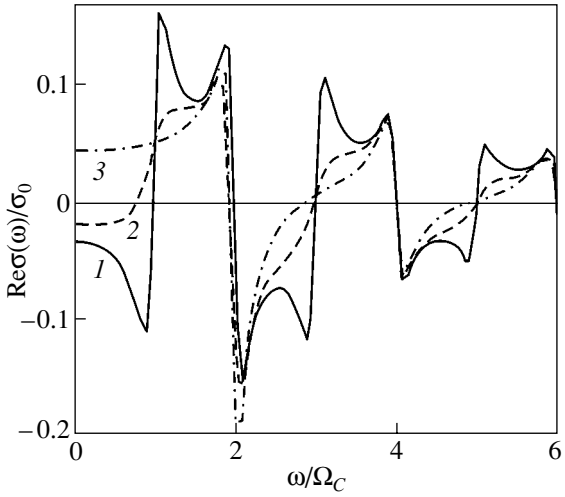

Fig. 4. Dynamic SL conductivities in the case of a superparabolic dispersion law for various values of α: (*1*) 0, (*2*) 0.5, and (*3*) 1; $\Omega_C\tau = 10$, $\beta = 0.5$, and $\eta = 10$.

culated for different values of the probability α of optical-phonon emission by an electron at the miniband edge (more detailed results can be found in [3]). It can be seen from Figs. 1 and 2 that the existence of regions with negative values of the effective electron mass in the miniband is not a necessary condition for the dc differential conductivity to be negative. This conductivity can be negative even in SLs with parabolic and superparabolic miniband dispersion laws (for which the effective electron mass is positive everywhere), and its sign in these cases is dictated by Bragg reflections of electrons (Bragg reflections are more important, because they change the electron velocity direction, whereas a change in sign of the effective mass affects only the magnitude of the electron velocity). When Bragg reflections of electrons are suppressed by optical phonons, the negative dc conductivity may disappear altogether. Such conductivity will persist only if the effective electron mass is negative in a sizable portion (usually, larger than one half) of the SL Brillouin zone volume [3]. The desirable shift of the range of negative values of the dc conductivity toward high static fields takes place when the effective electron mass decreases with increasing electron energy. For example, in the absence of optical-phonon scattering ($\alpha = 0$), the dc conductivity becomes negative at $\Omega_C\tau = 1$ in SLs with a sine miniband dispersion law, at $\Omega_C\tau \approx 1.17$ in SLs with a parabolic miniband, and at $\Omega_C\tau \approx 1.4$ in SLs with the dispersion law given by Eq. (3) with $\beta = k_i d/\pi = 0.5$ and $\eta = m_1/m_2 = 10$. When the optical-phonon scattering of electrons is strong, this shift is much larger than the values presented above.

The dynamic SL conductivities for these electron dispersion laws are shown in Figs. 3–5. It can be seen that, due to the anharmonicity of BOs (associated with the electron dispersion differing from a sine law), the hf differential conductivity becomes negative at frequencies equal to integral multiples of the Bloch frequency even in fields for which the dc differential conductivity of the SL is positive. At $\alpha = 0$ (Fig. 3), a necessary condition for this effect to occur is $\omega \sim n\Omega_C > \tau^{-1}$ ($n = 2, 3, \ldots$); that is, the spread of the nth BO harmonic must be small, whereas the spread of the fundamental harmonic can be strong, $\Omega_C\tau < 1$. As the value of η is increased, the dynamic NDC increases in magnitude. In SLs with a sine dispersion law, higher BO harmonics are absent; therefore, the dynamic differential conductivity cannot be negative in such fields.

If the miniband width in an SL is of the order of the optical-phonon energy and the optical-phonon emission probability is large ($\alpha \approx 1$) at the transit frequency (which is twice the Bloch frequency in the case in question) and at its integral multiples (i.e., at the frequencies of even BO harmonics), then the dynamic NDC arises because of one-sided streaming and self-modulation of the electron quasi-momentum distribution. The dc NDC may be absent in this case for any value of the applied static field. This mechanism of the dynamic NDC is not related directly to BOs of electrons and is operative even in the absence of BOs. The existence of the dynamic NDC due to streaming and to electron distribution self-modulation in bulk semiconductors was predicted in [8] and observed experimentally in [9]. In the case of two-sided streaming, the dynamic NDC can occur at frequencies of both even and odd BO harmonics. As the optical-phonon emission probability α increases, the NDC decreases in magnitude at frequencies of odd BO harmonics and increases at frequencies of even BO harmonics (Fig. 4), because BOs disappear as $\alpha \longrightarrow 1$. It is important that the resonance values of NDC arise on the left and on the right of the frequencies of odd and even BO harmonics, respectively. This feature is due to inversion of the partial electron distribu-

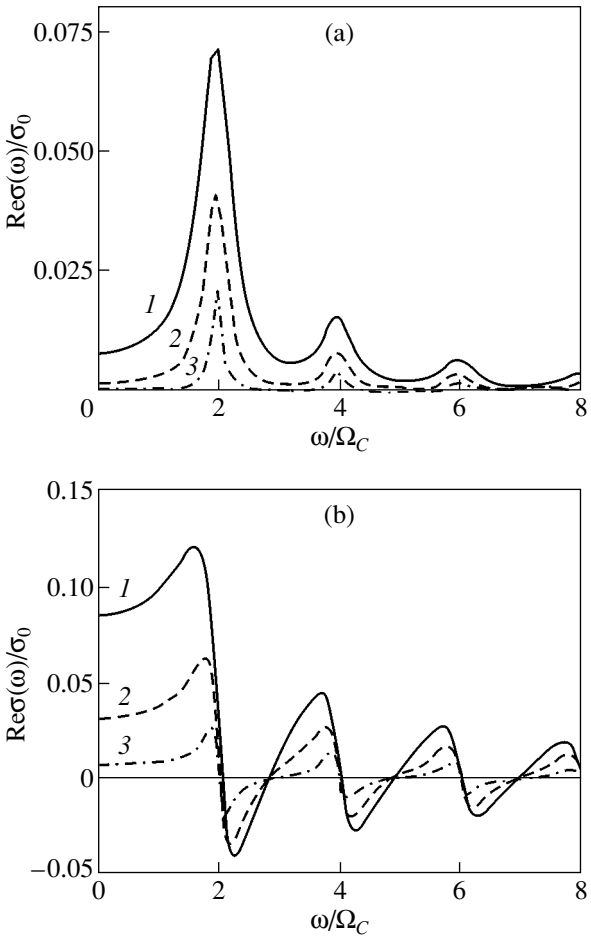

Fig. 5. Dynamic SL conductivities in the case of one-sided streaming ($\alpha = 1$) for different values of $\Omega_C\tau$: (*1*) 3, (*2*) 5, and (*3*) 10 for (a) sinusoidal and (b) parabolic minibands.

tions over Fourier components of the dispersion relation in SLs with miniband dispersion relations differing from a sine law. It is worth noting that, in SLs with a sine-law miniband, optical phonons suppress both the dc and dynamic NDCs over the entire frequency range (Fig. 5). Generally, it can be shown that the existence of ranges of negative values of the effective electron mass in the miniband has an adverse effect on the high-frequency NDC caused by one-sided streaming and by self-modulation of the electron quasi-momentum distribution. From Figs. 1–4, it also follows that, as α and η increase, the range of dc NDC shifts toward high static fields, whereas the range of dynamic NDC shifts toward weak fields (becoming finite at $\Omega_C\tau = 1$) and increases in magnitude.

Thus, SLs in which the minibands are not sinusoidal can be used to generate and amplify terahertz-range (microwave) fields with frequencies equal to integral multiples of the Bloch frequency in the regime where low-frequency domain instability is suppressed. Systems in which the effective electron mass decreases with increasing electron energy are suitable for this purpose. Such dispersion laws can be realized in SLs and two-dimensional hole-conduction layers. SLs with two closely spaced minibands are also appropriate if the upper miniband is significantly wider than the lower one and optical phonons are emitted by electrons at the top of the upper miniband.

ACKNOWLEDGMENTS

This study was supported by the Russian Foundation for Basic Research (project nos. 01-02-16446, 02-02-17495), the Russian Academy of Sciences program “Low-Temperature Quantum Structures,” and the Ministry of Industry, Science, and Technology of the Russian Federation.

REFERENCES

1. L. Esaki and R. Tsu, IBM J. Res. Dev. **14**, 61 (1970).
2. H. Kroemer, Phys. Rev. **109**, 1856 (1958).
3. Yu. A. Romanov, Fiz. Tverd. Tela (St. Petersburg) **45** (3), 529 (2003) [Phys. Solid State **45**, 559 (2003)].
4. L. K. Orlov and Yu. A. Romanov, Fiz. Tekh. Poluprovodn. (Leningrad) **19**, 1877 (1985) [Sov. Phys. Semicond. **19**, 1157 (1985)]; Izv. Vyssh. Uchebn. Zaved., Radiofiz. **32**, 282 (1989).
5. Y. C. Chang and R. B. James, Phys. Rev. B **39**, 12672 (1989).
6. G. A. Baraff, Phys. Rev. **133**, A26 (1964).
7. W. E. Pinson and A. Bray, Phys. Rev. **136**, A1449 (1964).
8. A. A. Andronov and V. A. Kozlov, Pis’ma Zh. Éksp. Teor. Fiz. **17**, 124 (1973) [JETP Lett. **17**, 87 (1973)].
9. L. E. Vorob’ev, S. N. Danilov, V. N. Tulupenko, and D. A. Firsov, Pis’ma Zh. Éksp. Teor. Fiz. **73**, 253 (2001) [JETP Lett. **73**, 219 (2001)].

Translated by Yu. Epifanov

Physics of the Solid State, Vol. 46, No. 1, 2004, pp. 17–21. Translated from Fizika Tverdogo Tela, Vol. 46, No. 1, 2004, pp. 21–25.

PROCEEDINGS OF THE CONFERENCE DEDICATED TO O. V. LOSEV (1903–1942)

(Nizhni Novgorod, Russia, March 17–20, 2003)

The Influence of P^+, B^+, and N^+ Ion Implantation on the Luminescence Properties of the SiO_2:nc-Si System

D. I. Tetelbaum*, O. N. Gorshkov*, V. A. Burdov*, S. A. Trushin*, A. N. Mikhaylov*, D. M. Gaponova, S. V. Morozov**, and A. I. Kovalev*****

** Physicotechnical Research Institute, Nizhni Novgorod State University, pr. Gagarina 23/3, Nizhni Novgorod, 603950 Russia*
e-mail: Tetelbaum@phys.unn.ru

*** Institute of Microstructure Physics, Russian Academy of Sciences, Nizhni Novgorod, 603950 Russia*

**** Bardin Central Research Institute of Ferrous Metallurgy, Vtoraya Baumanskaya ul. 9/23, Moscow, 107005 Russia*

Abstract—The possible mechanisms of the influence of implanted impurities of Group III and V elements on the luminescence properties of a system consisting of silicon nanocrystals in SiO_2 are considered and generalized. The effect of boron and nitrogen ion implantation on the photoluminescence intensity is investigated experimentally. The experimental results and previously reported data on the ion-implantation doping with phosphorus are discussed in terms of the mechanisms under consideration. The state of implanted phosphorus is determined using x-ray photoelectron spectroscopy. It is shown that the enhancement and degradation of the photoluminescence depend on the type of implanted impurities and the conditions of postimplantation heat treatment. © *2004 MAIK "Nauka/Interperiodica".*

1. INTRODUCTION

In recent years, systems consisting of nanocrystalline silicon inclusions in silicon dioxide (SiO_2:nc-Si) have attracted considerable attention of many researchers due to the manifestation of quantum-size effects responsible for their unique combination of properties, such as luminescence in the visible and near-IR spectral regions, resonant tunneling, etc. The doping of SiO_2:nc-Si has opened up new possibilities for modifying the electrical and optical properties of the system. However, there are only a few works concerned with investigating the influence of impurity atoms (in particular, shallow donors and acceptors) on the properties of the SiO_2:nc-Si system; moreover, the results obtained in those works are contradictory [1–7].

Ion implantation is a very convenient method for introducing impurity atoms into a system. First, ion implantation is one of the most universally employed processes of SiO_2:nc-Si production; the synthesis and doping of the material can be performed both in combination and, if necessary, individually under specified temperature conditions of postimplantation annealing. Second, ion implantation imposes little or no restrictions on the type and concentration of implanted impurities.

Earlier [5–7], we experimentally investigated how the ion-implantation doping of the SiO_2:nc-Si system with phosphorus affects the photoluminescence (PL) properties and compared the experimental data with the results of theoretical calculations. In the present work, we attempted to generalize several models describing the influence of shallow-level impurities on the photoluminescence and presented new experimental evidence in support of these particular models.

2. MAIN FEATURES OF THE INFLUENCE OF SHALLOW-LEVEL IMPURITIES ON THE PHOTOLUMINESCENCE

The main photoluminescence band, which is associated with silicon nanocrystals in the SiO_2:nc-Si system, is observed in the wavelength range 750–900 nm [8–11]. At present, there exist two points of view regarding the origin of the photoluminescence band in this range. According to the first approach [8–10], the photoluminescence is caused by the interband transition of an excited electron from the lower energy level of the conduction band (hereafter, it will be referred to as the c level) of a silicon quantum dot to the upper level of the valence band (the v level). Within the second approach [11, 12], it is assumed that an excited electron from an energy level of the conduction band first is nonradiatively captured in an interfacial level (located at the interface between the silicon nanocrystal and the SiO_2 matrix) and then emits a photon upon the transition to either the v level or another interfacial level that has captured an excited hole from the v level. In both approaches, the photoluminescence intensity is controlled by a competing process, namely, nonradiative recombination. Dangling bonds at the nc-Si/SiO_2 interface can serve as nonradiative-recombination centers. The currently available models of the influence of impurity atoms on the photoluminescence can be separated into three groups. According to models of the first group, the mechanism of this influence is associated

1063-7834/04/4601-0017$26.00

with the possibility of generating and annihilating nonradiative-recombination centers. Models of the second group allow for the transformation of the state of the electronic system of nanocrystals as quantum dots, i.e., the direct effect of impurities on the probability (rate) of radiative transitions. Models of the third group describe the influence of dopants on the formation, structural state, and morphology of silicon nanoinclusions upon ion implantation and subsequent annealing. Let us analyze these models in greater detail.

(**i**) The photoluminescence intensity should increase in the case where the introduction of impurity atoms leads to a decrease in the concentration of dangling bonds (nonradiative-recombination centers) at the nc-Si/SiO_2 interface. This decrease in the concentration of nonradiative-recombination centers can result from a decrease in mechanical stresses (arising upon heat treatment) because of the close values of the thermal expansion coefficients of the silicon inclusions and the SiO_2 matrix [2]. However, the influence of implanted impurities of Group V elements on the photoluminescence intensity can be associated with another mechanism of passivation [6] (by analogy with hydrogen) due to the termination of dangling bonds with impurity atoms.

(**ii**) In our previous works [5, 6], we proposed an electronic mechanism of photoluminescence enhancement upon dissolution of donor atoms in silicon nanocrystals. In essence, this mechanism is as follows. In the absence of donors, the excitation of photoluminescence requires excitation of an electron from the v level to the conduction band, which leads to the creation of an exciton. Upon dissolution of a donor atom in a silicon nanocrystal, this atom loses an excess electron to the conduction band. In turn, this electron recombines with a hole created upon the transfer of an electron from the v level, which provides an additional photoluminescence channel.

(**iii**) Another electronic mechanism of doping effect is also proposed for quantum dots. Since bulk silicon is an indirect-band-gap semiconductor, the transition from the c level to the v level with photon emission, generally speaking, is a forbidden transition due to the momentum nonconservation in this process. However, in a quantum dot, the electron state is characterized by a momentum distribution with finite dispersion, which provides a means for conserving the total momentum upon the transition. The probability of radiative hole–electron recombination occurring without the participation of phonons appears to be proportional to the ratio $(a/r)^8$ [7] (where a is the lattice parameter and r is the size of the nanocrystal) and remains very small (10^2–10^4 s^{-1}) for typical sizes of quantum dots (3–5 nm). In this case, according to our estimates, the introduction of donor atoms does not lead to an appreciable increase in the recombination probability. The analysis showed that the phonon-assisted transitions occur with a substantially higher probability. In the situation where the transition is attended by emission or absorption of one phonon, the reciprocal of the radiative recombination time is characterized by a considerably smoother dependence on the quantum dot size [i.e., $(a/r)^3$] and is approximately equal to 10^6 s^{-1} at $2r$ = 3–5 nm. We calculated the probability of photon emission occurring with the participation of phonons when one hydrogen-like donor atom is located at the center of the silicon quantum dot. According to these calculations, a slight increase in the recombination probability (by 10–15%) is associated primarily with the fact that the perturbing potential of the impurity atom admixes higher energy states to the ground states of electrons and holes, which, in turn, leads to an increase in the overlap of the electron and hole wavefunctions in the **k** space. The contribution of these states with a high energy for a single impurity atom is rather small. This explains the relatively small increase in the recombination probability. However, an increase in the donor concentration most likely results in a considerably greater increase in the probability of the interband radiative transition and, hence, in the photoluminescence intensity.

(**iv**) Fujii *et al.* [1–3] made the assumption that the incorporation of shallow-level impurities into silicon nanocrystals should lead to quenching of the photoluminescence due to the Auger process. Earlier, this process was theoretically analyzed by Lannoo *et al.* [13], who considered the situation where more than one exciton can appear in the quantum dot upon excitation. However, the theory developed by those authors cannot be directly extended to our case, because an excess charge carrier introduced by an impurity atom resides in the Coulomb field of the core of a donor or acceptor impurity center, which was ignored in [13]. Indeed, the experiments performed in [14] demonstrated that no complete quenching of the photoluminescence occurs even through a large number of phosphorus atoms are incorporated into each nanocrystal.

(**v**) Kachurin *et al.* [14] proposed a mechanism of photoluminescence enhancement upon ion-implantation doping with phosphorus, which is based on the high-dose effect [15]. Within this approach, allowance is made for the fact that, at high concentrations, implanted phosphorus impurities favor crystallization of amorphous silicon. As a result, upon annealing, implanted phosphorus should bring about the transformation of silicon nanoinclusions [which, without doping, would remain in the amorphous (nonluminescent) state] into the crystalline (luminescent) state.

(**vi**) Impurity atoms can also affect the formation of silicon nanocrystals in a different way [4]. In particular, the precipitates formed by impurity atoms during annealing can serve as centers of heterogeneous nucleation of silicon nanoinclusions. In the process, the number of silicon nanocrystals should increase and, hence, their mean size should decrease. This should result in an enhancement of the photoluminescence, provided the silicon nanocrystals are not too small in size. How-

ever, if the excess of silicon in the matrix is insufficient, part of the silicon nanocrystals will be so small in size that they cannot be involved in an ensemble of silicon inclusions as luminescence centers in this spectral range and, consequently, the photoluminescence will be weakened.

3. SAMPLES AND EXPERIMENTAL TECHNIQUE

For ion implantation, we used 0.3- to 0.6-μm-thick SiO_2 films thermally grown on a silicon substrate. The implantation of Si^+ ions was performed at an ion energy E = 140 keV. The dose of implanted ions Φ_{Si} was equal to 1×10^{17} cm^{-2}. After the ion implantation, the samples were annealed in a dried nitrogen stream at temperatures of 1000 and 1100°C for 2 h. The films with silicon nanocrystals thus prepared and the films not subjected to annealing after the silicon ion implantation were doped through implantation with phosphorus, boron, and nitrogen ions under the following conditions: E = 150 keV and $\Phi_P = 1 \times 10^{16}$ cm^{-2} for P^+ ions, E = 60 keV and $\Phi_B = (0.1–10) \times 10^{16}$ cm^{-2} for B^+ ions, and E = 70 keV and $\Phi_N = (0.1–100) \times 10^{15}$ cm^{-2} for N^+ ions. The ion energies were chosen in such a way as to provide penetration of the ions throughout the thickness of the film. The density of the ionic current in the course of implantation was no higher than 3 μA/cm^2; therefore, the increase in sample temperature did not exceed several tens of degrees. After the ion implantation, the samples were annealed at a temperature of 1000 or 1100°C for 2 h. The photoluminescence spectra were measured in the wavelength range 700–1100 nm upon excitation with an Ar laser (λ = 488 nm). The state of the chemical elements was investigated using x-ray photoelectron spectroscopy on an ESCALAB MKZ (VG) spectrometer (monochromated AlK_α radiation). The Ag $3d_{5/2}$ peak was recorded with a spectrometer resolution of 1.0 eV. Prior to recording the x-ray photoelectron spectra, the samples were etched with an Ar^+ ion beam (8 keV) until the C 1s line associated with accidental carbon contaminations of the surface disappeared.

4. RESULTS AND DISCUSSION

In our earlier works [5, 6], we demonstrated that the phosphorus ion doping of the SiO_2:nc-Si system prepared through ion implantation followed by annealing at 1000°C leads to a considerable enhancement of the photoluminescence. As an illustration, Fig. 1 shows the dependence of the photoluminescence intensity on the dose of implanted phosphorus ions [6]. It is assumed that the photoluminescence enhancement can occur through a combination of mechanisms **i**, **ii**, and, possibly, **iii**. However, as was shown in [7, 16], the phosphorus ion doping of the system prepared under other annealing conditions can result in quenching of the

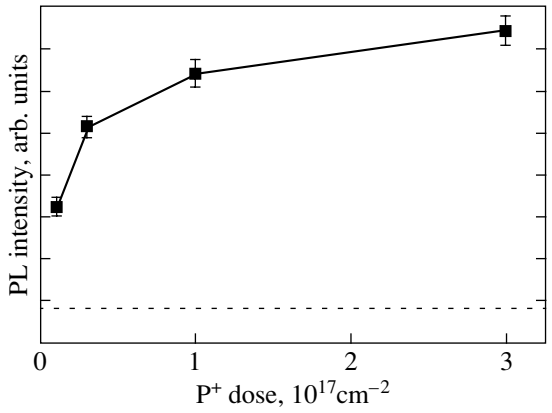

Fig. 1. Dependence of the PL intensity on the dose of implanted phosphorus ions for the SiO_2:nc-Si system prepared at 1000°C. The dashed line indicates the initial PL intensity.

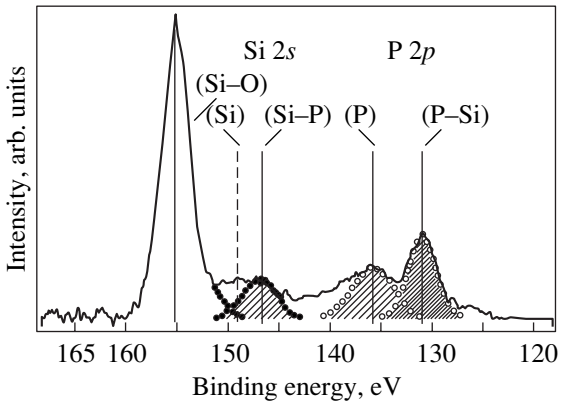

Fig. 2. X-ray photoelectron spectrum of the SiO_2:nc-Si system prepared at 1100°C, doped with phosphorus, and then annealed at 1100°C.

photoluminescence. In [7, 16], the SiO_2:nc-Si system prepared at 1100°C was doped with phosphorus ions followed by successive isochronal annealings at progressively higher temperatures. It seems likely that, in this case, the preparation conditions are favorable for precipitating phosphorus from a supersaturated solid solution. The precipitation brings about an increase in the mechanical stresses and, as a consequence, the breaking of bonds, i.e., the formation of nonradiative-recombination centers. The x-ray photoelectron spectra also indicate that phosphorus is incorporated into silicon nanocrystals and can precipitate in them at high temperatures (Fig. 2). As is clearly seen from Fig. 2, the x-ray photoelectron spectrum exhibits peaks attributed to free phosphorus and peaks associated with the phosphorus atoms bonded to the silicon atoms. Since phosphorus readily dissolves in SiO_2 and forms bonds with oxygen atoms (phosphorosilicate glass) [2, 17], it is

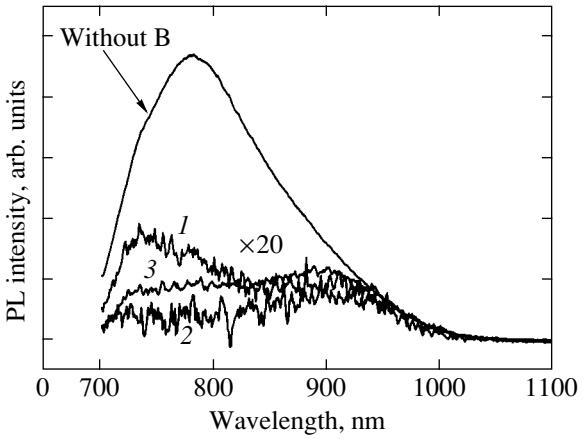

Fig. 3. Photoluminescence spectra of the SiO_2:nc-Si system prepared at 1000°C, doped with boron, and then annealed at 1000°C. Dose of B^+ ions: (*1*) 10^{15}, (*2*) 10^{16}, and (*3*) 10^{17} cm^{-2}.

highly improbable that the phosphorus precipitates are located in the SiO_2 matrix rather than in the silicon nanocrystals or at their interfaces.

The ion-implantation doping with boron (performed under the same conditions for which phosphorus ion implantation provides an enhancement of photoluminescence) leads to photoluminescence quenching (Fig. 3). In our opinion, this phenomenon can be explained in terms of the trivalent state of boron and the large difference between the covalent radii of boron and silicon. Let us consider a pentavalent (phosphorus) atom substituting for a silicon atom located at the nc-Si/SiO_2 interface in the vicinity of the dangling bond. In this case, the pentavalent phosphorus atom donates four electrons for the formation of "normal" bonds with the nearest neighbor atoms, whereas the fifth electron terminates the dangling bond. Within this interpretation, the doping with Group III elements (boron) can bring about the formation of new dangling bonds. The mechanical stresses arising in the SiO_2:nc-Si system upon dissolution of an impurity atom in the lattice of silicon nanocrystals depend on the difference between the covalent radii. The larger the difference, the stronger the stresses. The ion-implantation doping with a small B^+ dose leads not only to the quenching of photoluminescence but also to a shift in the maximum of the photoluminescence band toward the short-wavelength range. This can be explained as follows. The photoluminescence spectrum is a superposition of peaks corresponding to nanocrystals of different sizes. The larger the crystal size, the greater the shift in the maximum of the photoluminescence band toward the long-wavelength range [13]. At low concentrations, the mean distance between the boron atoms is of the order of the nanocrystal size. It is evident that the probability of boron being incorporated into large-sized nanocrystals is higher than that into small-sized nanocrystals. Consequently, the photoluminescence of large-sized nanocrystals is quenched to a greater extent as compared to that of small-sized nanocrystals. As a result, the maximum of the photoluminescence band is shifted toward the blue spectral range.

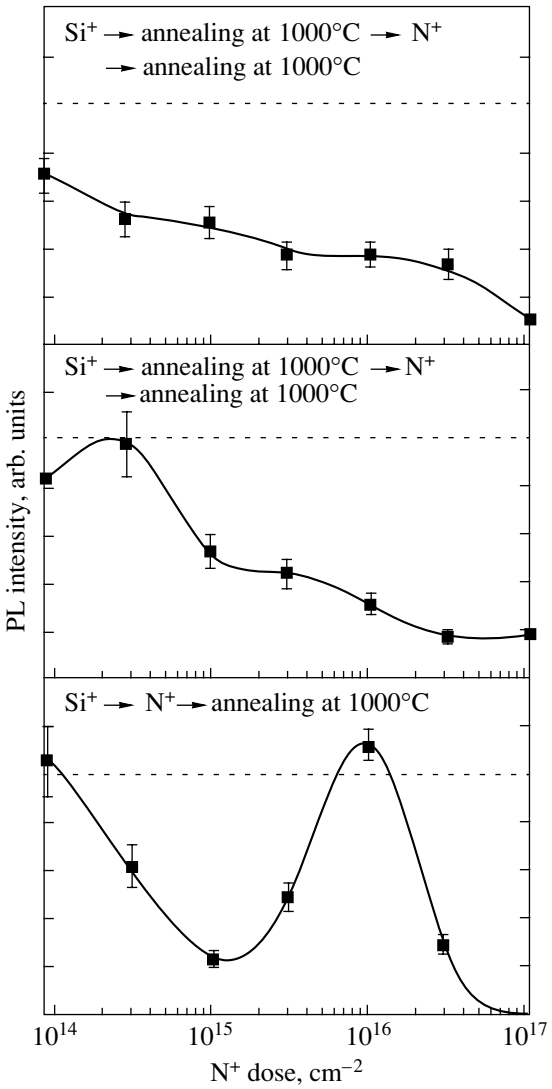

Fig. 4. Effect of ion-implantation doping with nitrogen on the PL intensity for the SiO_2:nc-Si system prepared and doped under different conditions. The dashed line indicates the initial PL intensity.

Unlike phosphorus and boron, nitrogen poorly dissolves in silicon and can form Si_xN_y precipitates. Actually, the ion-implantation doping with nitrogen leads to photoluminescence quenching (Fig. 4). It should be noted that, when nitrogen is introduced immediately after the silicon ion implantation, the dependence of the photoluminescence intensity on the dose of implanted nitrogen ions exhibits nonmonotonic behavior. According to Kachurin *et al.* [4], the nonmonotonic dose dependence of the photoluminescence intensity can be associated with the influence of nitrogen ions on the

formation of nanocrystals. At certain concentration ratios of nitrogen and silicon, the Si_xN_y precipitates serve as nucleation centers of new silicon nanocrystals and, thus, bring about the enhancement of the photoluminescence. With a further increase in the nitrogen dose (the number of silicon nanocrystals), the deficit of the silicon dissolved in the SiO_2 matrix and the decrease in the sizes of the nanocrystals formed begin to manifest themselves (see mechanism **vi**).

5. CONCLUSIONS

Thus, the effect of ion-implantation doping on the luminescence properties of the SiO_2:nc-Si system is governed by a number of structural and electronic factors. The role played by each factor depends on the type of implanted impurity, the impurity concentration, and the heat treatment conditions. As a result, the doping can lead to either enhancement or degradation of the photoluminescence. In this respect, the ion-implantation doping opens up fresh opportunities for investigating the physicochemical mechanisms of impurity effects and, in particular, for experimental verification of theoretical models.

ACKNOWLEDGMENTS

We would like to thank V.K. Vasil'ev and D.L. Vaĭnshteĭn for their assistance in performing the experiments and G.A. Kachurin for his participation in discussions of the results and helpful remarks.

This work was supported by the International Association of Assistance for the promotion of cooperation with scientists from the New Independent States of the former Soviet Union (project INTAS no. 00-0064) and the program of the Ministry of Education of the Russian Federation "Higher School Research in Priority Directions of Science and Engineering" (subprogram no. 205).

REFERENCES

1. M. Fujii, S. Hayashi, and K. Yamamoto, J. Appl. Phys. **83**, 7953 (1998).
2. M. Fujii, A. Mimura, S. Hayashi, and K. Yamamoto, Appl. Phys. Lett. **75** (2), 184 (1999).
3. A. Mimura, M. Fujii, S. Hayashi, *et al.*, Phys. Rev. B **62** (19), 12625 (2000).
4. G. A. Kachurin, S. G. Yanovskaya, K. S. Zhuravlev, and M.-O. Ruault, Fiz. Tekh. Poluprovodn. (St. Petersburg) **35** (10), 1235 (2001) [Semiconductors **35**, 1182 (2001)].
5. D. I. Tetelbaum, O. N. Gorshkov, S. A. Trushin, *et al.*, Nanotechnology **11**, 295 (2000).
6. D. I. Tetelbaum, S. A. Trushin, V. A. Burdov, *et al.*, Nucl. Instrum. Methods Phys. Res. B **174**, 123 (2001).
7. V. A. Burdov, O. N. Gorshkov, A. N. Mikhaylov, *et al.*, Izv. Akad. Nauk, Ser. Fiz. **67** (2), 186 (2003).
8. G. A. Kachurin, I. E. Tischenko, K. S. Zhuravlev, *et al.*, Nucl. Instrum. Methods Phys. Res. B **122**, 571 (1997).
9. K. S. Min, K. V. Scheglov, C. M. Yang, *et al.*, Appl. Phys. Lett. **69**, 2033 (1996).
10. B. Garrido Fernandez, M. Lopez, C. Garcia, *et al.*, J. Appl. Phys. **91** (2), 798 (2002).
11. T. Shimizu-Iwayama, K. Fujita, S. Nakao, *et al.*, J. Appl. Phys. **75**, 7779 (1994).
12. Y. Kanemitsu and S. Okamato, Phys. Rev. B **58**, 9652 (1998).
13. M. Lannoo, C. Delerue, and G. Allan, J. Lumin. **70**, 170 (1996).
14. G. A. Kachurin, S. G. Yanovskaya, D. I. Tetel'baum, and A. N. Mikhaylov, Fiz. Tekh. Poluprovodn. (St. Petersburg) **37** (6), 738 (2003) [Semiconductors **37**, 713 (2003)].
15. *Problems in Radiation Technology of Semiconductors*, Ed. by L. S. Smirnov (Nauka, Novosibirsk, 1980).
16. D. I. Tetelbaum, S. A. Trushin, A. N. Mikhaylov, *et al.*, Physica E: Low-Dimens. Syst. Nanostruct. **16** (3–4), 410 (2003).
17. J. B. Beales and C. R. Day, Phys. Chem. Glasses **21** (1), 5 (1980).

Translated by O. Borovik-Romanova

Physics of the Solid State, Vol. 46, No. 1, 2004, pp. 170–172. Translated from Fizika Tverdogo Tela, Vol. 46, No. 1, 2004, pp. 168–170.

PROCEEDINGS OF THE CONFERENCE DEDICATED TO O. V. LOSEV (1903–1942)
(Nizhni Novgorod, Russia, March 17–20, 2003)

Bose Condensation of Interwell Excitons in Lateral Traps: A Phase Diagram

A. A. Dremin, A. V. Larionov, and V. B. Timofeev

Institute of Solid State Physics, Russian Academy of Sciences, Chernogolovka, Moscow oblast, 142432 Russia

e-mail: timofeev@issp.ac.ru

Abstract—The luminescence of interwell excitons in GaAs/AlGaAs double quantum wells (*n–i–n* heterostructures) containing large-scale random-potential fluctuations was studied. The study dealt with the properties of an exciton whose photoexcited electron and hole are spatially divided between the neighboring quantum wells under density variation and at temperatures of down to 0.5 K. We investigated domains ~1 μm in size, which act as macroscopic exciton traps. Once the resonance laser pump power reaches a certain threshold, a very narrow delocalized exciton line appears (with a width less than 0.3 meV), which grows strongly in intensity with increasing pump power and shifts toward lower energies (by approximately 0.5 meV) in accordance with the exciton buildup in the lowest state in the domain. As the temperature increases, this spectral line disappears in a nonactivated manner. This phenomenon is assigned to Bose condensation occurring in the quasi-two-dimensional system of interwell excitons. The critical exciton density and temperature were determined within the temperature interval studied (0.5 to 3.6 K), and a phase diagram specifying the exciton condensate region was constructed. © *2004 MAIK "Nauka/Interperiodica".*

An intense search has been under way in recent years [1–16] to establish the existence of Bose–Einstein exciton condensation in two-dimensional (2D) semiconductor heterostructure systems. In quasi-two-dimensional quantum confined systems, Bose condensation can take place at finite temperatures. Spatial confinement in the quantum-well plane may originate from large-scale random-potential fluctuations associated with variation in the quantum-well width at heterointerfaces. Excitons are easier to accumulate in systems with lateral confinement, and the density of excitons in such regions may greatly exceed their average density [13]. Therefore, the critical conditions conducive to Bose condensation of interwell excitons are easier to realize in lateral domains. With this purpose in mind, we studied the properties of interwell excitons under variation of their density and temperature in GaAs/AlGaAs double quantum wells with large-scale random-potential fluctuations produced by the MBE growth interruption technique at quantum-well walls [17].

A metal mask (an aluminum film) 100 nm thick was deposited on the surface of an *n–i–n* structure with the architecture described in [9]. Circular holes with a minimum size of down to 0.5 μm were etched in this film by using electron beam lithography. The luminescence signals were excited and detected through holes prepared in this manner. Results indicating exciton condensation were obtained with a sample pumped optically through windows less than 1 μm in diameter. The heavy-hole interwell excitons (1*s* HH excitons) were excited resonantly using tunable Ti sapphire laser pumping.

When the pumping is increased (to ≥50 μW), a narrow line appears abruptly at the violet edge of the wide band associated with localized excitons (Fig. 1). The intensity of this line increases superlinearly with pumping (see inset to Fig. 1), and the line narrows and shifts by about 0.5 meV toward lower energies. The minimum width of this line is 350 μeV for a spectrometer spectral slit width of about 200 meV. As the pumping is increased still further (above 0.5 mW), the narrow interwell exciton line starts to broaden monotonically and shift toward higher energies.

The line intensity I decreases with increasing temperature with only a small variation of the linewidth, until at $T = 3.6$ K this line disappears against the structureless background of the localized-exciton spectrum, which retains its shape (Fig. 2). It is essential that the decrease in the line intensity I with increasing temperature does not have an activated character. By measuring the temperature dependence of the line intensity I at different pumping levels, we established the following temperature behavior: $I_T \propto [1 - (T/T_C)^\alpha]$, where I_T is the line intensity at temperature T, T_C is the critical temperature at which this line disappears in the spectrum at a given fixed excitation, and $\alpha \leq 1.5$.

The observed phenomenon exhibits all features typical of a phase transition associated with the Bose condensation of excitons; namely, a new, collective exciton phase forms as a critical density and a critical tempera-

1063-7834/04/4601-0170$26.00 © 2004 MAIK "Nauka/Interperiodica"

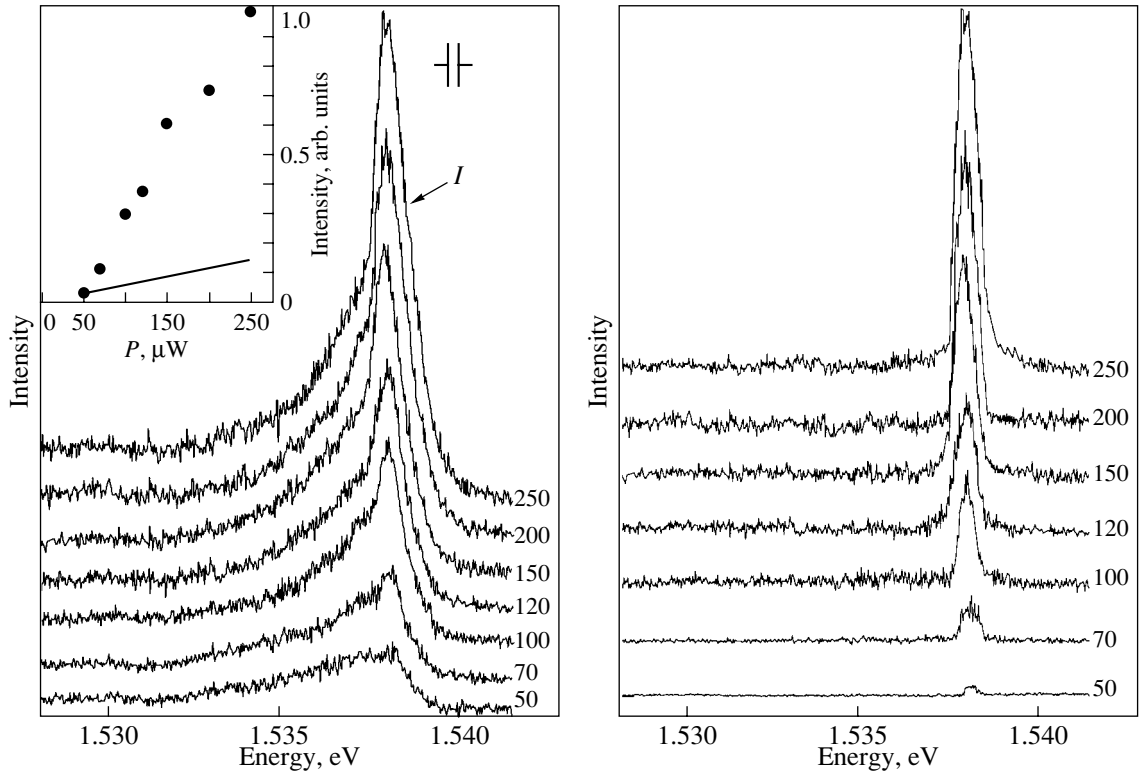

Fig. 1. Photoluminescence spectra of interwell excitons, I_{ex}, measured at different direct-exciton resonant excitation power levels. The numbers next to the spectra identify the pump power in μW. The spectra shown on the right were obtained by subtracting the structureless continuum under the line. $T = 1.51$ K.

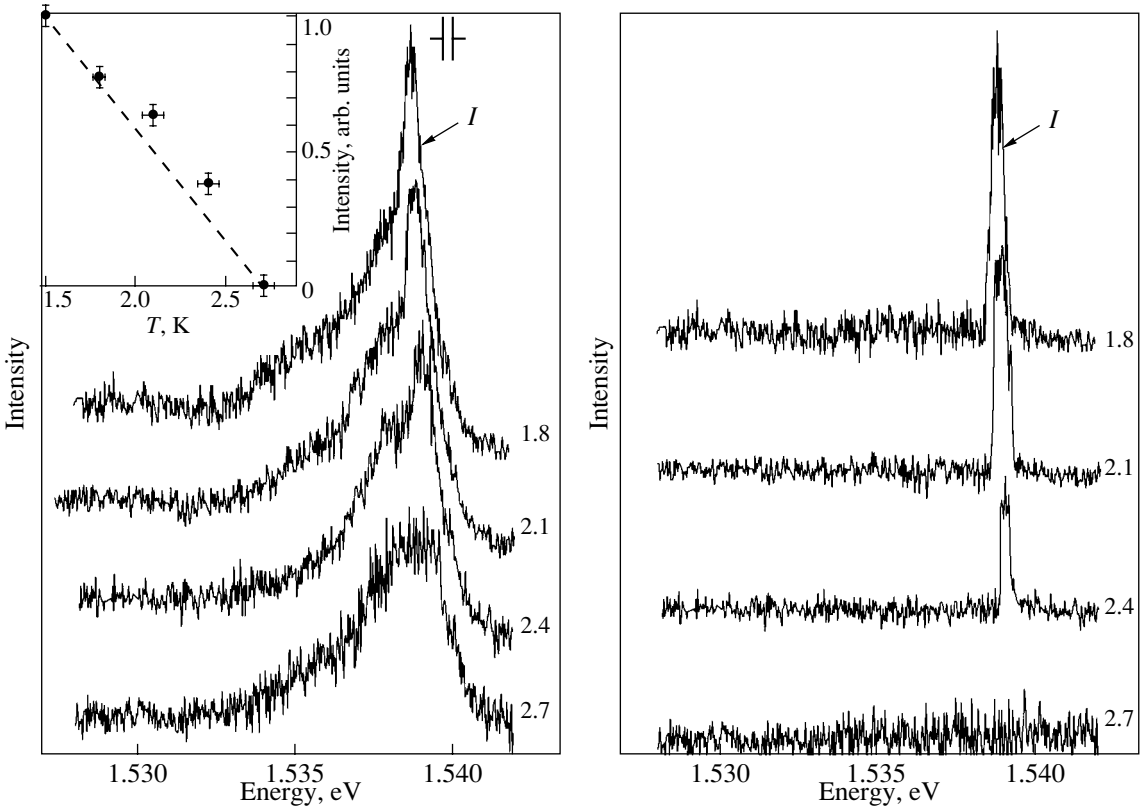

Fig. 2. Temperature dependence of the intensity of the narrow photoluminescence line obtained at a pump power of 150 μW. The numbers next to the spectra are temperatures measured in kelvins. The spectra shown on the right were obtained by subtracting the structureless continuum under the line.

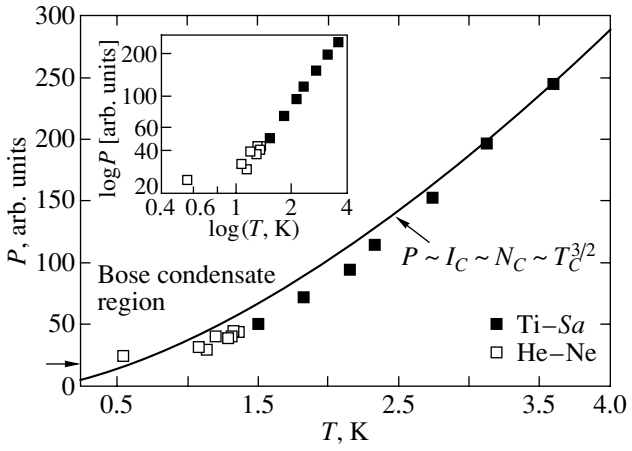

Fig. 3. Phase diagram of the Bose condensate of interwell excitons obtained in the temperature interval 0.5–3.6 K.

ture are reached. We attempted to establish a phase diagram including the region of the Bose condensate of interwell excitons. To do this, we studied the dependence of the photoluminescence spectra on pump power at fixed values of temperature in the interval 0.5–3.6 K and determined the threshold power P_C at which the narrow line appears (or disappears) in the spectrum. The phase diagram was constructed in the P_C–T coordinates in the region within which the intensity of the narrow line depends linearly on the pump power. The phase diagram thus obtained is presented in Fig. 3 in both a linear and a log–log scale.

The Bose condensation is observed to occur within a limited interval of exciton concentrations, $N_{\text{loc}} < N_{\text{ex}} < N_{\text{I–M}}$. The lower limit is due to the strong exciton localization at defects. We estimated the density of localized states in our structures as $N_{\text{loc}} \leq 3 \times 10^9$ cm^{-2}. It is the localized states that account for the unusual shape of the phase diagram at low temperatures. The upper bound is related to the excitons breaking down at the insulator–metal transition, $N_{\text{I–M}} \leq 10^{11}$ cm^{-2}. This density corresponds to a dimensionless parameter $r_S = 1/\sqrt{\pi N_{\text{I–M}}}a_{\text{B}} \leq 2$.

ACKNOWLEDGMENTS

This study was supported by the Russian Foundation for Basic Research and the State research and development program on nanostructures.

REFERENCES

1. Yu. E. Lozovik and V. I. Yudson, Pis'ma Zh. Éksp. Teor. Fiz. **22**, 556 (1975) [JETP Lett. **22**, 274 (1975)].
2. T. Fukuzawa, E. E. Mendez, and J. M. Hong, Phys. Rev. Lett. **64**, 3066 (1990).
3. L. V. Butov, A. Zrenner, G. A. Abstreiter, *et al.*, Phys. Rev. Lett. **73**, 304 (1994); L. V. Butov, in *Proceedings of the 23rd International Conference on Physics of Semiconductors, Berlin* (1996).
4. V. B. Timofeev, A. V. Larionov, A. S. Ioselevich, *et al.*, Pis'ma Zh. Éksp. Teor. Fiz. **67**, 580 (1998) [JETP Lett. **67**, 613 (1998)].
5. V. V. Krivolapchuk, E. S. Moskalenko, A. L. Zhmodikov, *et al.*, Solid State Commun. **111**, 49 (1999).
6. L. V. Butov, A. Imamoglu, A. V. Mintsev, *et al.*, Phys. Rev. B **59**, 1625 (1999).
7. A. V. Larionov, V. B. Timofeev, J. M. Hvam, *et al.*, JETP **90**, 1093 (2000).
8. L. V. Butov, A. V. Mintsev, Yu. E. Lozovik, *et al.*, Phys. Rev. B **62**, 1548 (2000).
9. A. V. Larionov, V. B. Timofeev, J. M. Hvam, *et al.*, Pis'ma Zh. Éksp. Teor. Fiz. **75**, 233 (2002) [JETP Lett. **75**, 200 (2002)].
10. L. V. Butov, C. W. Lai, A. L. Ivanov, *et al.*, Nature **417**, 47 (2002).
11. L. V. Butov, A. C. Gossard, and D. S. Chemla, Nature **418**, 751 (2002).
12. D. Yoshioka and A. H. MacDonald, J. Phys. Soc. Jpn. **59**, 4211 (1990); X. M. Chen and J. J. Quinn, Phys. Rev. Lett. **67**, 895 (1991).
13. Xuejun Zhu, P. L. Littlewood, M. S. Hybersten, and T. Rice, Phys. Rev. Lett. **74**, 1633 (1995).
14. J. Fernandez-Rossier and C. Tejedor, Phys. Rev. Lett. **78**, 4809 (1997).
15. Yu. E. Lozovik and O. L. Berman, Zh. Éksp. Teor. Fiz. **111**, 1879 (1997) [JETP **84**, 1027 (1997)].
16. Yu. E. Lozovik and I. V. Ovchinnikov, Pis'ma Zh. Éksp. Teor. Fiz. **74**, 318 (2001) [JETP Lett. **74**, 288 (2001)].
17. S. W. Brown, T. A. Kennedy, D. Gammon, *et al.*, Phys. Rev. B **54**, R17339 (1996).

Translated by G. Skrebtsov

Physics of the Solid State, Vol. 46, No. 1, 2004, pp. 173–175. Translated from Fizika Tverdogo Tela, Vol. 46, No. 1, 2004, pp. 171–173.

PROCEEDINGS OF THE CONFERENCE DEDICATED TO O. V. LOSEV (1903–1942)

(Nizhni Novgorod, Russia, March 17–20, 2003)

Electronic States and Vibration Spectra of CdTe/ZnTe Quantum Dot Superlattices

V. S. Bagaev*, L. K. Vodop'yanov*, V. S. Vinogradov*, V. V. Zaĭtsev*, S. P. Kozyrev*, N. N. Mel'nik*, E. E. Onishchenko*, and G. Karczewski**

**Lebedev Physical Institute, Russian Academy of Sciences, Leninskiĭ pr. 53, Moscow, 119991 Russia*
e-mail: evgeny@lebedev.ru
***Institute of Physics, Polish Academy of Sciences, Warsaw, 02-668 Poland*

Abstract—Electronic and vibrational states in CdTe/ZnTe quantum dot superlattices are studied using optical spectroscopy techniques (photoluminescence in a wide temperature range, IR reflection, and Raman scattering). The effect of the ZnTe barrier layer thickness on the luminescence spectra of the structures is discussed. The luminescence from electronically coupled islands is assumed to be due to spatially indirect excitons because of the specific features of the CdTe/ZnTe heterostructure band structure. A combination of quantum-dot vibrational modes, which has not been observed earlier, is detected in the Raman spectra. Analysis of the lattice IR reflection spectra shows that, in the case of large barrier thicknesses between the quantum-dot planes, elastic stresses are concentrated in the $Zn_{1-x}Cd_xTe$ layers, whereas in structures with lower barrier thicknesses the elastic-strain distribution exhibits a more complicated pattern. *© 2004 MAIK "Nauka/Interperiodica".*

1. Structures with multiple quantum-dot (QD) planes, which are sometimes called quantum dot superlattices (QDSLs), were grown by molecular-beam epitaxy on GaAs (100) substrates. First, a CdTe buffer layer 4.5 μm thick was deposited on a substrate and then a QDSL consisting of 200 CdTe layers 2.5 monolayers (MLs) thick each was grown on it, with the layers separated from each other by ZnTe barriers with a thickness varying from 12 to 75 MLs. The grown structures were examined with a JEOL 2000EX transmission electron microscope with a resolution of 0.27 nm. Analysis of the lattice parameters, which varied along the growth direction, showed that each of the QDs was a layer of the $Zn_{1-x}Cd_xTe$ solid solution in which there were regions (islands) 2 nm thick and 6–10 nm in diameter (QDs) enriched in cadmium. It was found that, in the case of ZnTe barrier layers less than 25 MLs thick, the QDs in adjacent layers were correlated in position [1].

Photoluminescence spectra were excited by an He–Cd laser (wavelength 4416 Å) and recorded in the temperature range 5–150 K. A DFS-24 double-pass monochromator with a limiting resolution better than 0.1 Å was used to analyze the spectra. The lattice IR reflection spectra at 300 K were recorded on a Bruker IFS-55 Fourier spectrometer with a spectral resolution higher than 1 cm^{-1}. Raman spectra were excited with different Ar^{2+}-laser lines and measured with an U-1000 spectrometer in the back scattering geometry (spectral resolution 1 cm^{-1}). The scattered light was analyzed along the direction of structure growth (z axis) for the sample orientation $x \parallel [100]$, $y \parallel [010]$, and $z \parallel [001]$. According to the selection rules, Raman scattering only by optical phonons is allowed in this configuration.

2. Figure 1 shows luminescence spectra of QDSLs with ZnTe barrier layers 12, 25, and 75 MLs thick (samples B12, B25, B75, respectively) recorded at 5 K. The luminescence spectrum of sample B75 is virtually identical to those from structures with single CdTe/ZnTe QD planes and with a comparable nominal CdTe layer thickness (see, e.g., [2]). However, the situation becomes radically different as the CdTe barrier layer thickness is decreased. For a barrier layer thickness equal to 25 MLs, the luminescence line is considerably (more than two times) narrower than in the case

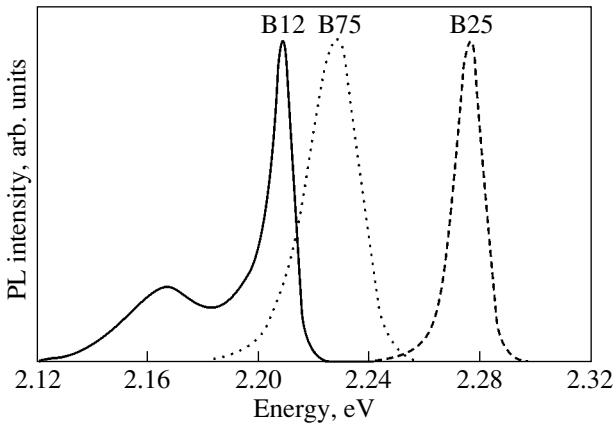

Fig. 1. Photoluminescence spectra taken from QD superlattices with ZnTe barrier layers 12, 25, and 75 MLs thick.

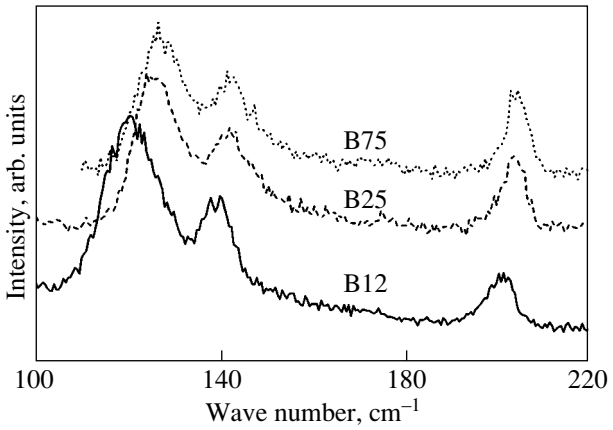

Fig. 2. Raman spectra of samples B12, B25, and B75. For the sake of pictorial convenience, the spectra are shifted along the ordinate axis.

of isolated layers. This effect is likely due to a decreased spread in the QD sizes formed during the growth of structures with a large number of QD layers and was first observed for SiGe/Si QD superlattices [3]. As the barrier thickness is decreased to 12 MLs, an additional band appears in the luminescence spectrum. This band is due to excitons localized on correlated islands in adjacent QD planes.

The activation energy for luminescence quenching was determined from the temperature dependence of the integrated QDSL luminescence intensity. As the ZnTe barrier layer thickness is decreased, this energy decreases from more than 60 meV for sample B75 to less than 30 meV for sample B12. The temperature dependences of the QDSL luminescence exhibit a very interesting property: as the temperature is increased, the luminescence is quenched more rapidly in the case of electronically coupled islands. In sample B12, as the temperature is increased to 80 K, only the line from isolated $Zn_{1-x}Cd_xTe$ islands survives in the luminescence spectrum. This property is surprising at first glance (because the energy level for coupled islands is deeper than that for isolated ones) and is likely due to specific features of the $Zn_{1-x}Cd_xTe$/ZnTe heterostructure band structure. For this heterostructure, the valence band offset is almost entirely caused by the strains due to the difference in lattice parameters between the two materials. In structures with small distances between QD layers, spatially indirect excitons can form because of the strains in the ZnTe barrier layer (see Section 3). We believe that such a situation occurs in the case of electronically coupled islands, because it is in the region between two CdTe QDs that the strains in the ZnTe barrier layer are maximal and can cause a potential well for a light hole to arise in this region. A situation similar in certain respects was observed in GaAs/AlAs superlattices [4], where local changes in the thickness of GaAs and AlAs layers caused a change in the structure type; namely, in regions with thicker GaAs layers, light emission was due to direct excitons, whereas on the whole the light emission from the structure was associated with indirect excitons.

A potential well that is produced for a hole by elastic strains and Coulomb interaction with an electron (for which a fairly deep potential well arises in a $Zn_{1-x}Cd_xTe$ layer for the $Zn_{1-x}Cd_xTe$/ZnTe structures) is rather shallow, and the characteristic radiative recombination time of an indirect exciton significantly exceeds that of a direct exciton. Due to both these factors, the luminescence from electronically coupled islands will be quenched fairly rapidly with increasing temperature. The temperature dependences of CdTe/ZnTe QD superlattice luminescence will be analyzed in detail in a future publication.

3. Due to the formation of QDs, both the electronic and phonon spectra are rearranged, which manifests itself in the Raman scattering spectra. Figure 2 shows Raman spectra of samples B12, B25, and B75 excited by the 4880-Å line. As an example, let us discuss the spectrum of the QDSL with a barrier thickness of 25 MLs. There are three bands in this Raman spectrum. The high-frequency band at 201 cm^{-1} corresponds to the ZnTe LO phonon mode, whose frequency is 2 cm^{-1} lower than that in the bulk ZnTe. The other two bands lie in the range of vibrational CdTe excitations. The band corresponding to the CdTe LO phonon mode at 171 cm^{-1} is missing from the Raman spectrum. The mode observed at 139 cm^{-1} is close to the CdTe TO phonon mode (140 cm^{-1}) but is Raman-active. The strong low-frequency band at 126 cm^{-1} is not typical of II–VI compounds. We note that the observed Raman spectrum is resonant in character. Indeed, the Raman spectrum obtained from the same 25-MLs sample under excitation with the 5145-Å line exhibits the main features of the spectrum excited with the 4880-Å line but has a much lower intensity. By comparing the Raman spectra of different samples, it can be seen that all observed bands shift toward lower energies with increasing ZnTe barrier layer thickness. This effect is due to a decrease in the lattice parameter averaged over the sample volume.

The experimental data obtained are analyzed in detail in [5]; here, we will dwell only on the main conclusions. The vibrational modes with frequencies near 140 and 120 cm^{-1} may be identified with the symmetric Coulomb (interface) QD mode and with the symmetric phonon mode confined in a QD, respectively. This mode combination has not been observed earlier in QD structures.

The presence of a thick CdTe buffer layer hampers the observation of vibrational excitations in QDs in IR reflection spectra. However, these spectra can provide information on elastic strains in the structures under study. Figure 3 shows the reflection spectra of samples B12 and B25. The reflection band near 270 cm^{-1} is the reststrahlen band of the GaAs substrate, and the fea-

tures observed in the spectra near 140 and 170 cm^{-1} correspond to CdTe and ZnTe vibrational modes in the buffer layers and QDSL.

The mathematical treatment of the experimental spectra was performed using an analysis of the variance in terms of a model structure consisting of a thin film (a QDSL and a buffer layer) deposited on a semi-infinite substrate. The calculated GaAs lattice mode frequency for a substrate with a CdTe buffer layer 4.5 μm thick deposited on it is 267 cm^{-1}, which is 3 cm^{-1} less than the lattice mode frequency of the bulk GaAs crystal, and the decay constant γ for this mode is calculated to be 8 cm^{-1}.

The following very interesting effect was detected in studying the dependence of the ZnTe vibrational mode on the barrier layer thickness. On the basis of analyzing the variance, it was established that in sample B12, in which the barrier layer is the thinnest (12 MLs), ZnTe vibrations are represented by a single strong mode at $\omega_{t1} = 172$ cm^{-1}. In sample B25, the frequency of the strong mode increases to $\omega_{t1} = 173.5$ cm^{-1} and an additional mode appears at $\omega_{t2} = 169$ cm^{-1}. In sample B75 (not represented in Fig. 3), in which the ZnTe barrier layers separating $Zn_{1-x}Cd_xTe$ layers are 75 MLs thick, ZnTe vibrations are represented by two modes, at $\omega_{t1} = 176$ cm^{-1} and $\omega_{t2} = 165$ cm^{-1}, and their oscillator strengths are comparable in magnitude.

As the barrier layer thickness is varied, the strong-mode frequency ω_{t1} varies from 172 to 176 cm^{-1} and, within the limits of experimental error, reaches the transverse-mode frequency $\omega_t = 177$ cm^{-1} of pure ZnTe. Therefore, in sample B12, the thin ZnTe barrier layers are highly stretched by the adjacent $Zn_{1-x}Cd_xTe$ layers and by the thick CdTe buffer layer. In sample B75, the barrier layers are sufficiently thick for the elastic stresses to relax in them.

4. Thus, we have investigated the temperature dependences of the luminescence spectra of CdTe/ZnTe QD superlattices. The light emission from electronically coupled CdTe islands was proposed to be due to spatially indirect excitons. It has been established that, in structures with thick ZnTe barrier layers separating QD planes, elastic strains are concentrated in $Zn_{1-x}Cd_xTe$ layers, whereas in structures with thinner barrier layers the elastic-strain distribution exhibits a more complicated pattern. In Raman spectra, we detected a combination of QD vibrational modes that has not been observed earlier.

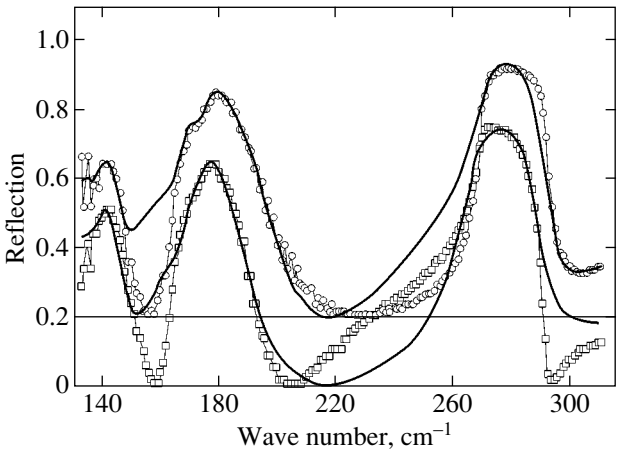

Fig. 3. Lattice IR reflection spectra for samples B12 and B25. The experimental data are represented by squares for B12 and by circles for B25. Solid lines are the calculated spectra. For pictorial convenience, the spectrum taken from sample B25 is shifted by 0.2 along the ordinate axis.

ACKNOWLEDGMENTS

This study was supported by the Russian Foundation for Basic Research (project nos. 03-02-16854, 03-02-17110) and the Russian Academy of Sciences Committee for support of young scientists.

REFERENCES

1. S. Mackowski, G. Karczewski, T. Wojtowicz, *et al.*, Appl. Phys. Lett. **78**, 3884 (2001).
2. V. V. Zaĭtsev, V. S. Bagaev, and E. E. Onishchenko, Fiz. Tverd. Tela (St. Petersburg) **41**, 717 (1999) [Phys. Solid State **41**, 647 (1999)].
3. J. Tersoff, C. Teichert, and M. G. Lagally, Phys. Rev. Lett. **76**, 1675 (1996).
4. D. Luerssen, A. Oehler, R. Bleher, and H. Kalt, Phys. Rev. B **59**, 15862 (1999).
5. L. K. Vodop'yanov, V. S. Vinogradov, N. N. Mel'nik, and G. Karczewski, Pis'ma Zh. Éksp. Teor. Fiz. **77**, 171 (2003) [JETP Lett. **77**, 143 (2003)].

Translated by Yu. Epifanov

Physics of the Solid State, Vol. 46, No. 1, 2004, pp. 176–178. Translated from Fizika Tverdogo Tela, Vol. 46, No. 1, 2004, pp. 174–176.

PROCEEDINGS OF THE CONFERENCE DEDICATED TO O. V. LOSEV (1903–1942)

(Nizhni Novgorod, Russia, March 17–20, 2003)

Resonant Stokes and Anti-Stokes Raman Scattering of Light in CdSe/ZnSe Nanostructures

M. Ya. Valakh*, V. V. Strelchuk*, G. N. Semenova*, and Yu. G. Sadofyev**

** Institute of Semiconductor Physics, National Academy of Sciences of Ukraine, pr. Nauki 45, Kyiv, 03028 Ukraine*

*** Lebedev Physical Institute, Russian Academy of Sciences, Leninskiĭ pr. 53, Moscow, 117927 Russia*

e-mail: valakh@isp.kiev.ua

Abstract—Raman scattering spectra of CdSe/ZnSe multilayer nanostructures with a CdSe insert of a nominal thickness of 2.1 monolayers were studied. A heavy dependence of the intensity and of the frequency position of the multiphonon Stokes and anti-Stokes LO bands on the exciting photon energy was detected. The results obtained are interpreted as a resonance with various exciton transitions in the CdSe insert and barrier ZnSe layers. A difference between the Stokes and anti-Stokes frequencies of LO bands observed as the resonance conditions are varied confirms the inhomogeneous nature of the photoluminescence band of CdSe quantum dots.

1. INTRODUCTION

Semiconductor quantum dots (QDs) based on wide-band-gap II–VI compounds are a promising material for the development of efficient light-emitting optoelectronic devices. The driving force of the QD self-assembling process is the elastic stress fields arising due to the difference between the substrate and heterolayer lattice constants. The formation of three-dimensional (3D) coherently strained QDs causes a decrease in the elastic energy of the system. Nanometer-sized (10–100 nm) CdSe QDs were grown by molecular-beam epitaxy (MBE). In contrast, e.g., to the case of InAs/GaAs heterostructures, CdSe layer deposition is accompanied by active interdiffusion and segregation of Cd atoms at CdSe/ZnSe heterointerfaces. These processes are caused by a high nonequilibrium density of cation vacancies forming during the epitaxial growth. As a result, a 10-MLs-thick two-dimensional (2D) layer of mixed $Zn_{1-x}Cd_xSe$ composition is formed in the ZnSe host during deposition of a CdSe epitaxial layer with a nominal thickness of 0.5–3.0 monolayers (MLs). This layer contains nanoislands enriched with Cd. An increase in the thickness of the deposited CdSe layer causes an increase in the Cd concentration in the 2D layer and islands [1].

This study is devoted to Stokes and anti-Stokes Raman scattering (RS) of light and photoluminescence (PL) excited nonresonantly in both ZnSe layers and CdSe QDs.

2. EXPERIMENTAL

CdSe/ZnSe structures were grown by MBE on semi-insulating GaAs(100). The samples contained either a single CdSe insert with a nominal thickness of 3.5 MLs or twelve CdSe layers 2.1 MLs thick separated by ZnSe barrier layers. The thickness of a barrier layer was 18 nm, and the thicknesses of the buffer and cap ZnSe layers were 200 and 100 nm, respectively. The buffer ZnSe and barrier ZnSe layers were grown at 280 and 230°C, respectively. The CdSe layers were deposited at 230°C. To initiate the formation of 3D CdSe islands, heating to 340°C was used, followed by cooling to 230°C in selenium vapor. The transition from the 2D deposited CdSe layer to the formation of 3D structures was monitored *in situ* by using a high-energy electron diffractometer.

The RS and PL spectra were measured in the reflection geometry by using a DFS-24 double spectrometer. The spectra were excited by discrete emission lines of an Ar^+ laser. The RS spectral resolution was 1–2 cm^{-1}. The frequency position of a spectral line was determined with an accuracy better than 0.2 cm^{-1} due to simultaneous measurement of laser plasma lines in the spectrum.

3. RESULTS AND DISCUSSION

Figure 1 shows the PL spectra of a multilayer CdSe/ZnSe structure with a nominal thickness of the CdSe insert of 2.1 MLs observed under resonant excitation in the region of intrinsic absorption of ZnSe layers (Fig. 1a) and in the region of the emission band of CdSe QDs (Fig. 1b). The spectra contain an intense asymmetric band of the CdSe QD emission at 2.559 eV (Fig. 1a) and 2.554 eV (Fig. 1b). The band has a structure on its high-energy slope at room temperature and on its low-energy slope at a low temperature. The band asymmetry is interpreted as being due to the simultaneous contribution to PL coming from the 2D wetting $Zn_{1-x}Cd_xSe$ layer (regions with a lowered Cd content contributing to the high-energy wing) and from CdSe

1063-7834/04/4601-0176$26.00 © 2004 MAIK "Nauka/Interperiodica"

QDs (the low-energy wing) [2]. At an excitation energy E = 2.71 eV, the resonant first- and second-order RS lines are observed against the background of band-to-band PL of the ZnSe layers. At E = 2.54 eV, the resonant RS spectrum is observed in both the Stokes and anti-Stokes regions.

We can see from Fig. 1 that the anti-Stokes PL band (Fig. 1b) is insignificantly shifted to low energies in comparison with the Stokes band (Fig. 1a) and is narrower (by 4–6 meV in half-width). The excitation mechanism of the CdSe QD anti-Stokes PL at low temperatures is interpreted as two-step absorption through the levels of vacancy-type defects localized at the QD interface [3]. Under resonant excitation, two-step absorption through the QD energy levels also significantly contributes to anti-Stokes PL excitation in the QD absorption region [4]. At elevated temperatures, thermal excitation of carriers from low- into high-energy ground states of various QDs also becomes appreciable.

A number of features of the spectrum in Fig. 1 are worth noting. First, this spectrum virtually continuously extends in energy from the ZnSe layer absorption edge to the peak of the CdSe QD emission band, which may be indicative of significant fluctuations in the $Zn_{1-x}Cd_xSe$ solid-solution composition of the 2D insert layer and in the sizes of small CdSe QDs. Second, the ZnSe layer PL is observed for both Stokes and anti-Stokes PL excitation modes. The anti-Stokes PL is induced by a significant number of hot photoexcited carriers generated due to two-step absorption through the QD and defect levels. Due to intrasubband relaxation of photoexcited electron–hole pairs, nonequilibrium LO phonons can be generated.

Figure 2 shows the Stokes and anti-Stokes RS spectra of the CdSe/ZnSe multilayer structure observed under resonant excitation in the ZnSe layer absorption band (Fig. 2a) and in the transparent region of all the heterostructure layers (Fig. 2b). Low excitation energy densities (less than 10 W/cm^2) were used in both regions. Analysis of the RS spectra excited in the ZnSe absorption region is complicated by the fact that in this region the resonant RS cross section and the absorption coefficient, which defines the light penetration depth into the sample, vary rapidly with frequency. The situation is also complicated by the difference in the resonance properties of the Stokes and anti-Stokes RS components. The anti-Stokes RS intensity is highest when the exciton transition frequency (i.e., the position of the PL peak in our case) coincides with the exciting light frequency (input resonance) and is low under the conditions of resonance with scattered light (output resonance) [5]. On the contrary, for the Stokes RS component, the LO-phonon RS intensity is higher in the case of the output resonance. Thus, for anti-Stokes RS, in contrast to the resonant Stokes RS, the resonance with exciting light dominates. Hence, the intensities of the "Stokes" and "anti-Stokes" signals should be compared taking this fact into account. In the case under consid-

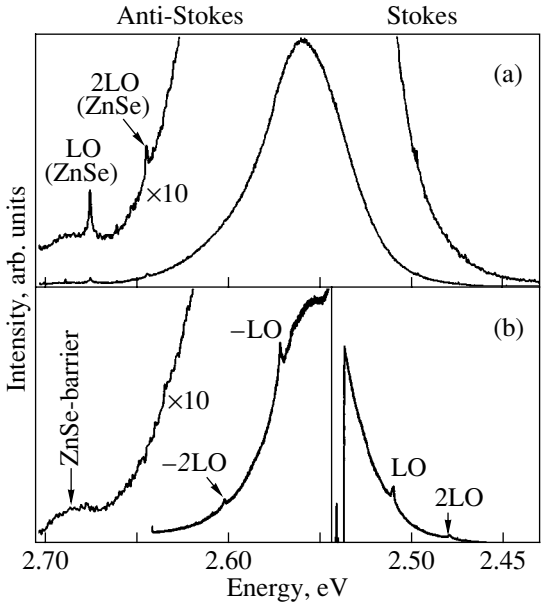

Fig. 1. PL spectra of the CdSe/ZnSe nanostructure with twelve CdSe inserts of a nominal thickness of 2.1 MLs for E_{exc} equal to (a) 2.71 and (b) 2.54 eV; T = 300 K.

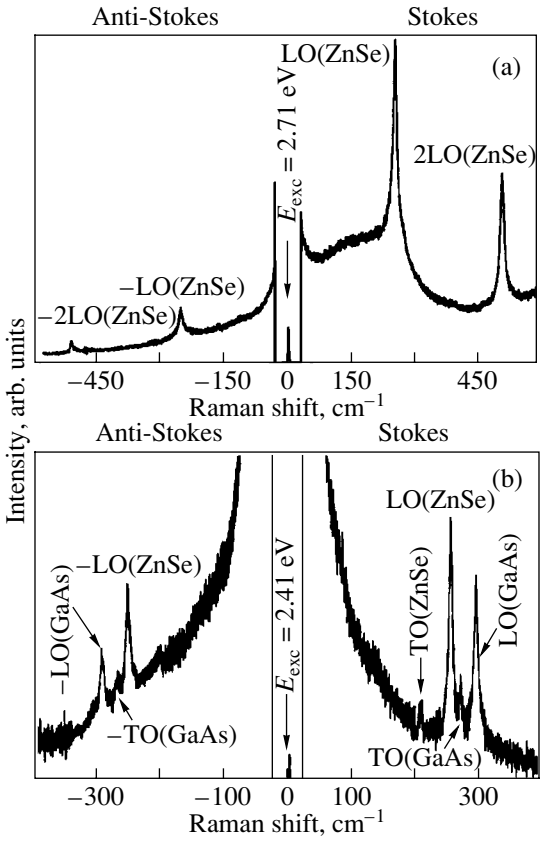

Fig. 2. RS spectrum of the multilayer CdSe/ZnSe nanostructure with a CdSe insert of a nominal thickness of 2.1 MLs for E_{exc} equal to (a) 2.71 and (b) 2.41 eV; T = 300 K.

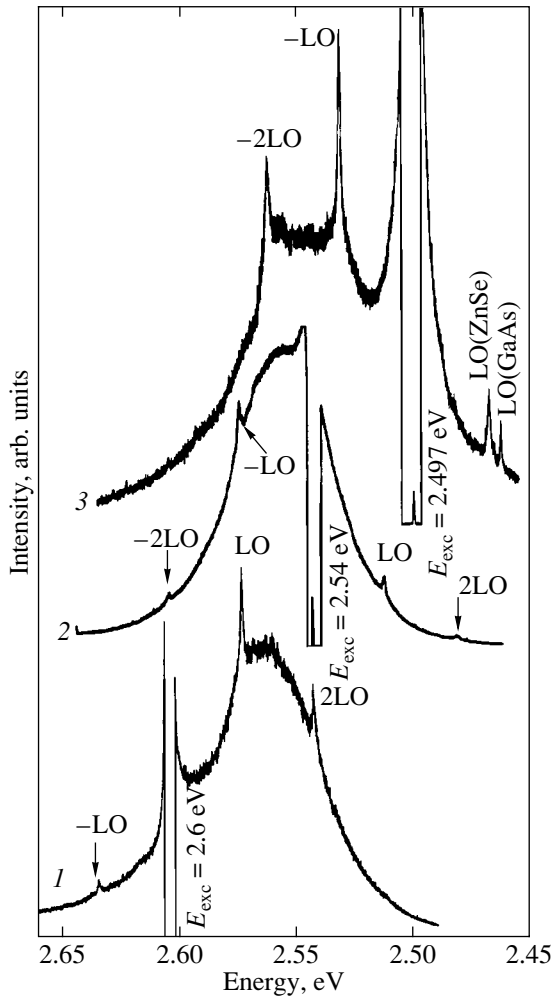

Fig. 3. Resonant RS spectra of the multilayer CdSe/ZnSe structure at various excitation photon energies. T = 300 K.

eration (Fig. 2a), the Stokes RS conditions are closer to the output resonance with ZnSe PL. Hence, the Stokes LO(ZnSe) and 2LO(ZnSe) RS line intensities are much higher than the intensities of the corresponding anti-Stokes LO-phonon RS lines, whose strengthening is associated with the input resonance conditions. It is interesting to note that, although the Stokes and anti-Stokes LO phonon RS lines are characterized by almost identical half-widths, their appreciable broadening (Γ = 10–11 cm^{-1}) seems to be indicative of the presence of structural defects and of a nonuniform strain distribution in probed ZnSe layers.

Figure 2b shows the Stokes and anti-Stokes RS spectrum of this structure under nonresonant excitation by photons with an energy of 2.41 eV, which is smaller than the energy gap E_g of ZnSe layers (2.69 eV) and less than the energy corresponding to the QD exciton emission band peak (2.554 eV). It can be seen that, in addition to the LO- and TO-phonon RS lines ($\nu \approx$ 206.4 cm^{-1}) of the barrier ZnSe layers, the Stokes RS spectrum contains the strong LO-phonon line ($\nu \approx$ 292.4 cm^{-1}) and the weak TO phonon line ($\nu \approx$ 269 cm^{-1}) of the GaAs substrate. The corresponding phonon lines of ZnSe and GaAs are also observed in the anti-Stokes region, but they have a lower intensity.

The difference between the resonance dependences of the Stokes (I_S) and anti-Stokes (I_{AS}) RS components can be seen from Fig. 3. As the excitation photon energy is varied within the QD emission band from the high- to the low-energy wing (curves *1*–*3*), the intensity ratio I_S/I_{AS} decreases. Moreover, an appreciable shift of the PL band peak to lower energies is observed when the low-energy band wing is excited (curve *3*).

We compared the frequencies of the Stokes and anti-Stokes LO-and 2LO-phonon RS bands for various excitation conditions with respect to the PL band peak. The difference between these frequencies, which is particularly noticeable for 2LO and –2LO bands, indicates resonant RS with various radiative electron transitions, which are responsible for the inhomogeneous broadening of the QD emission band associated with fluctuations in the QD sizes and, particularly, in the Cd content.

4. CONCLUSIONS

Thus, we have studied the resonance dependence of the Stokes and anti-Stokes RS spectra excited near the CdSe QD exciton transitions. It was shown that the anti-Stokes LO-phonon RS intensity increases due to the input resonance with QD electron transitions and to nonequilibrium LO phonons generated in intrasubband relaxation of photoexcited electron–hole pairs. The fact that the 2LO- and –2LO-band frequencies vary with the resonance conditions confirms the inhomogeneous nature of the PL band.

ACKNOWLEDGMENTS

This study was supported by the joint Russian–Ukrainian program “Nanophysics.”

REFERENCES

1. N. Peranio, A. Rosenauer, D. Gerthsen, *et al.*, Phys. Rev. B **61**, 16015 (2000); D. Litvinov, A. Rosenauer, D. Gerthsen, and N. N. Ledentsov, Phys. Rev. B **61**, 16819 (2000).
2. C. S. Kim, M. Kim, S. Lee, *et al.*, J. Cryst. Growth **214–215**, 761 (2000).
3. M. Ya. Valakh, Yu. G. Sadofyev, N. O. Korsunska, *et al.*, Semicond. Phys. Quantum Electron. Optoelectron. **5** (3), 254 (2002).
4. M. Ya. Valakh, N. O. Korsunska, Yu. G. Sadofyev, *et al.*, Mater. Sci. Eng. B (2003) (in press).
5. A. A. Klochikhin, A. G. Plyukhin, L. G. Suslina, and E. B. Shadrin, Fiz. Tverd. Tela (Leningrad) **18** (7), 1909 (1976) [Sov. Phys. Solid State **18**, 1112 (1976)].

Translated by A. Kazantsev

Physics of the Solid State, Vol. 46, No. 1, 2004, pp. 179–187. Translated from Fizika Tverdogo Tela, Vol. 46, No. 1, 2004, pp. 177–184.

SEMICONDUCTORS AND DIELECTRICS

The Influence of Hydrostatic Pressure on the Static and Dynamic Properties of an InSe Crystal: A First-Principles Study

K. Z. Rushchanskiĭ

Institute of Solid-State Physics and Chemistry, Uzhgorod National University, ul. Podgornaya 46, Uzhgorod, 88000 Ukraine

e-mail: kr@iss.univ.uzhgorod.ua

Received December 18, 2002; in final form, March 27, 2003

Abstract—The pressure dependences of the crystallographic parameters of the γ-InSe structure in the range up to 15 GPa are theoretically investigated using the density-functional method. It is established that, in the range from 7 to 11 GPa, the pressure dependences of the lattice parameters exhibit an anomalous behavior: the rigidity of the lattice increases in the direction of the weak bond and decreases in the plane of the layers. The layer thickness is characterized by a nonmonotonic pressure dependence. The numerical values of the lattice parameters of the crystal structure under compression are determined, and the pressure dependences of the vibrational frequencies at the center of the Brillouin zone are calculated theoretically. The results of the theoretical calculations are in good agreement with the available experimental data. © *2004 MAIK "Nauka/Interperiodica".*

1. INTRODUCTION

Indium chalcogenide compounds have attracted considerable research attention over the latter half of the 20th century due to their interesting physical properties and specific chemical structure. An increase in the indium content in chalcogenides $In_2X_3 \longrightarrow InX \longrightarrow In_4X_3$ (X = Se, Te) leads to a lowering of the symmetry and complication of the chemical bonding, which manifests itself, first, in the transformation of indium cations from the trivalent state (in In_2X_3) into a mixed-valence state and, second, in an increase in the strength of In–In bonds [1]. Among the indium chalcogenides, the InSe compound has been studied most extensively. Increased interest in these materials has been associated with their potential use in nonlinear optics [2, 3], solar-energy converters [4], highly sensitive optical sensors operating in the infrared range [5], solid-state electric current sources [6, 7], and highly sensitive strain gauges [8]. Since indium chalcogenide compounds possess strong anisotropy of chemical bonding, it is possible to modify their physical properties through intercalation [9]. From the applied standpoint, these compounds are of special interest owing to the possibility of forming high-quality heterojunctions with the use of both van der Waals epitaxy [10–12] and a less laborious mechanical procedure, namely, by bringing them into direct optical contact [13–17].

Moreover, these objects are especially attractive from fundamental standpoint. In the last decade, there have appeared many works concerned with experimental and theoretical investigations of the influence of external pressure on their physical properties. The main objective of these experiments is to gain a deeper insight into the electronic properties of layered semiconductors, because the use of external pressure opens up new possibilities for controlling the anisotropy of chemical bonding. A great body of data available in the literature on the pressure dependences of the optical and kinetic properties of indium chalcogenides is due to the fact that these properties are governed primarily by the electronic subsystem of the material. Since the electronic structure of the studied objects is characterized by a van der Waals gap, the intralayer and interlayer interactions manifest themselves under pressure in radically different ways. After reaching a certain pressure, these differences become less pronounced (the so-called trimerization of the properties of a layered crystal [18]).

Recent investigations have provided comprehensive information on the influence of external pressure on the optical properties and band structure [19], the dielectric properties of GaS, GaSe, and InSe crystals [20], the x-ray absorption spectra of InSe [21], and the vibrational spectra [22]. However, to the best of my knowledge, first-principles studies of the effect of pressure on the dynamic properties and structure of InSe crystals have not been performed before. The lack of detailed x-ray diffraction data on the structural transformation under pressure is partially compensated for with experimental information obtained by Pellicer-Porres *et al.* [21]. Unfortunately, the data reported in [21] are far from complete, although they have made it possible to calculate theoretically the effect of pressure on the energy spectrum of charge carriers in the InSe compounds [19].

A detailed knowledge of changes in the interatomic interactions occurring in indium chalcogenides under

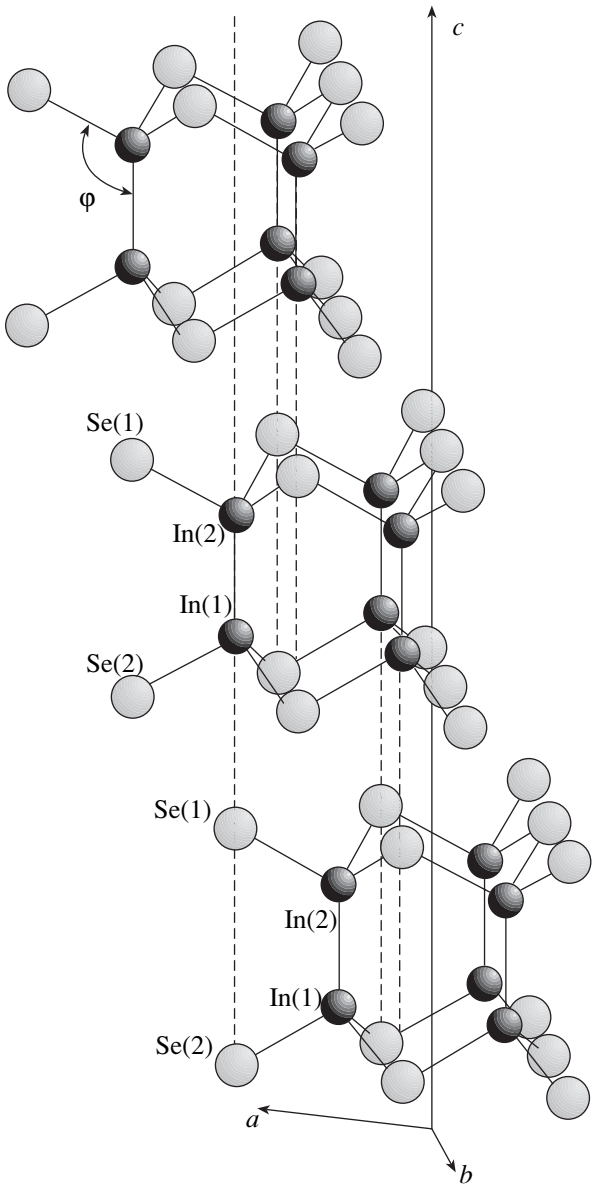

Fig. 1. Crystal structure of γ-InSe. The rhombohedral unit cell contains two indium and two selenium atoms forming the structure of one layer. Solid lines represent the axes of an extended hexagonal cell with three layers of γ-InSe.

deformations of different types is of more than theoretical interest, because it becomes possible to thoroughly investigate a great variety of problems concerning the intercalation, the formation of solid solutions, the mechanisms of hopping conduction, the elastic properties, the properties governed by deformation effects, the growth of single crystals, and the preparation of thin films of the studied compounds. In this respect, the purpose of the present work was to carry out a first-principles theoretical investigation of the structural transformations and changes in the vibrational properties of an InSe crystal under external hydrostatic pressure.

2. CRYSTAL STRUCTURE OF InSe AND THE PRESSURE DEPENDENCE OF THE LATTICE PARAMETERS

The crystal structure of InSe was determined using x-ray diffraction in [23, 24]. The known polytypes of this crystal are the hexagonal β (D_{6h}^4, $P6_3/mmc$), hexagonal ε (D_{3h}^1, $P\bar{6}m2$), and trigonal γ (C_{3v}^5, $R3m$) modifications. The γ polytype has been studied most thoroughly. This is explained by the fact that the compounds grown by the Bridgman method crystallize in the γ modification [23]. The rhombohedral unit cell of γ-InSe contains two formula units, which form the structure of one layer (Fig. 1). This structure is formed according to the scheme Se–In–In–Se, in which the In–Se interaction has an ionic–covalent character and the In–Se sublayers are linked together by the In–In covalent bonds perpendicular to the layer plane. According to the x-ray diffraction investigations performed by Rigoult *et al.* [24], each sublayer has an asymmetric (slightly distorted) structure. The displacement of layers with respect to each other in the γ modification is described by the vector $\mathbf{t} = (\mathbf{a} + \mathbf{b})/3$, where **a** and **b** are the basis vectors of the hexagonal unit cell. The lattice parameters and fractional atomic coordinates in the hexagonal setting are listed in Table 1.

As was shown by Schwarz *et al.* [25], the γ modification under external pressure is retained up to 10.5 GPa (at room temperature) and then undergoes a first-order phase transition to a rock-salt-type structure. The NaCl modification possesses metallic properties (whereas the γ-InSe modification under normal conditions is a semiconductor with band gap E_g = 1.35 eV [26]). The compressibility of the γ phase is strongly anisotropic in character: the compressibility is small and exhibits a nearly linear behavior along the *a* axis, on the one hand, and is significant and has a nonlinear behavior along the *c* axis, on the other. At pressures close to 7 GPa, the structure undergoes progressive irreversible transformations, which manifest themselves in the optical absorption spectra and the vibrational properties.

The most recent data on the pressure dependences of the local environment of selenium atoms in InSe crystals were obtained by Pellicer-Porres *et al.* [21] from an analysis of the x-ray absorption spectra. In my opinion, the most important inferences drawn in [21] that can be compared with the theoretical results obtained in the present work can be summarized as follows.

The pressure dependence of the interatomic distances is adequately described by the first-order equation of state [27]:

$$d = d_0\left(1 + \frac{B_0'}{B_0}P\right)^{-1/3B_0'}, \qquad (1)$$

Table 1. Calculated and experimental [24] crystallographic parameters of the γ-InSe structure

Atom		Experiment	Theory	Deviation
Fractional coordinates (x, y, z)	In(1)	0, 0, 0.00000	0, 0, 0.00043	
	In(2)	0, 0, 0.11102	0, 0, 0.11096	–0.05%
	Se(1)	0, 0, 0.82834	0, 0, 0.82864	–0.04%
	Se(2)	0, 0, 0.61666	0, 0, 0.61599	–0.11%
a, Å		4.002	3.953	–1.2%
c, Å		24.946	24.138	–3.2%
Distances and angles		Experiment	Theory	Deviation
$d_{\text{In(1)–Se(2)}}$, Å		2.6258	2.5944	–1.2%
$d_{\text{In(1)–In(2)}}$, Å		2.7695	2.6678	–3.7%
$d_{\text{In(2)–Se(1)}}$, Å		2.6335	2.5935	–1.5%
∠In(1)–In(2)–Se(1)		118.673°	118.344°	–0.27%
∠In(2)–In(1)–Se(2)		118.364°	118.388°	0.02%

Note: The unit cell parameters and fractional atomic coordinates are given in the hexagonal setting.

where d_0 is the interatomic distance under normal conditions, B_0 is the bulk modulus, and B_0' is the derivative of this modulus with respect to pressure.

The pressure dependence of the In–Se distance (at pressures of less than or equal to 7.1 GPa) is described by the following parameters: $d_0 = 2.634$ Å and $B_0 = 116 \pm 20$ GPa for $B_0' = 5$. At pressures above 7.1 GPa, the In–Se distance jumpwise increases and becomes equal to approximately 2.7 Å at 10 GPa. The parameter a of the hexagonal lattice is characterized by a stronger dependence on the pressure ($B_0 = 44$ GPa for $B_0' = 5$). The In–In–Se angle calculated at 10 GPa is equal to 121.4° (under normal conditions, this angle is 118.7°).

3. DESCRIPTION OF THE METHOD

The ground state and vibrational properties were investigated in the plane-wave approximation of the density-functional theory [28]. The calculations were carried out with nonlocal norm-conserving *ab initio* pseudopotentials in the form proposed by Hartwigsen *et al.* [29]. The $5s^25p^1$ and $4s^24p^4$ electron configurations were used for valence electrons of indium and selenium atoms, respectively. The exchange–correlation interaction was included in the local-density approximation in the parametric form [30], which reproduces the exact results of the quantum-mechanical calculations for a homogeneous electron gas [31]. The nonlocality of the pseudopotentials was taken into account by components for the s, p, and d channels. The s channel of the corresponding potential was used as a local component. The nonlinear character of the exchange–correlation interaction of the valence electrons with electrons of the atomic core and the relativistic effects for core electrons were allowed for in the pseudopotential. The spin–orbit interaction was not considered in the treatment performed in this work.

The calculations were carried out with the ABINIT code [32] involving the pseudopotential and plane-wave basis sets and based on an efficient fast Fourier transform algorithm [33] (for transforming wave functions between the real and reciprocal spaces), the conjugate-gradient band method [34], the potential-based conjugate-gradient algorithm, which made it possible to determine the self-consistent potential [35], and the perturbation-theory algorithms. Details of the computation of the responses to atomic displacements and homogeneous electric fields are given in [36]. Subsequent calculations of the dynamic matrices, Born effective charges, permittivity tensors, and interatomic force constants are described in [37].

Integration over the Brillouin zone was performed by the special-point method [38] with the use of six points in the irreducible region of the Brillouin zone. The basis set of plane waves was limited by a maximum kinetic energy of 20 Ry. The chosen basis set was analyzed for sufficiency. It was demonstrated that, upon the inclusion of 19 special points of integration and the choice of the maximum kinetic energy equal to 30 Ry, a change in the calculated frequency of vibrational modes was no more than 0.5 cm^{-1}. Therefore, the calculations were carried out in the region of convergence.

4. RESULTS AND DISCUSSION

4.1. Static Properties

The total energy of the InSe system was calculated as a function of the unit cell volume in the range from an experimental unit cell volume of 115.29 Å^3 to 60% of this value. The results of these calculations are presented in Fig. 2.

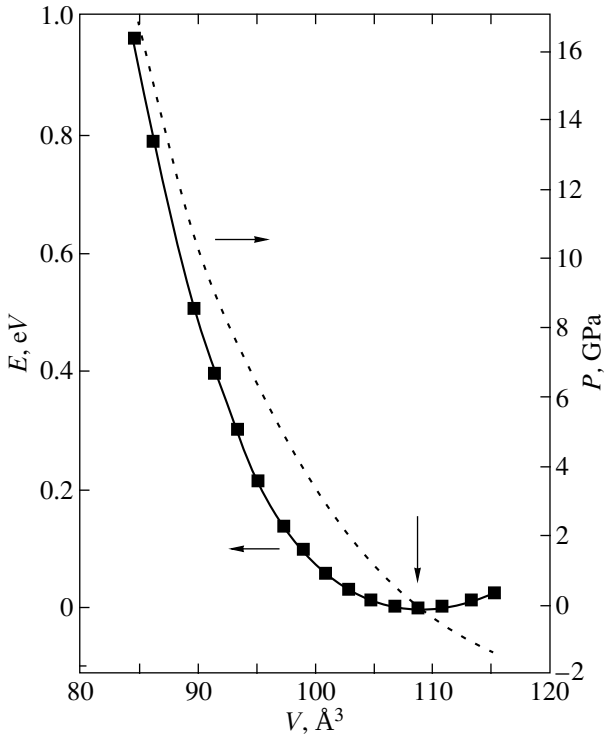

Fig. 2. Dependences $E(V)$ and $P(V)$. The vertical arrow indicates the position of the theoretically calculated equilibrium configuration. Symbols are the calculated values of $E(V)$. The solid line represents the dependence $E(V)$ approximated by the first-order equation of state (2). The dashed line corresponds to the dependence $P(V)$.

The dependence $E(V)$ is adequately described by the first-order equation of state [27]:

$$E = E_0 + \frac{B_0 V}{B_0'}\left[\frac{(V_0/V)^{B_0'}}{B_0' - 1} + 1\right] - \frac{B_0 V_0}{B_0' - 1}, \quad \text{“}\partial\text{Ù} \quad 4\text{F3}$$

where V_0 = 108.9 Å^3 is the equilibrium volume, B_0 = 29 GPa, and B_0' = 6.2. Setting B_0' = 5, we obtain V_0 = 108.47 Å^3 and B_0 = 34 GPa.

The calculated equilibrium volume differs from the experimental value (at 300 K [24]) by 5.5%. This discrepancy is characteristic of calculations performed in the local-density approximation for exchange–correlation interactions. The crystallographic parameters for the calculated equilibrium configuration and the relevant experimental data are compared in Table 1. As can be seen from this table, the fractional coordinates are reproduced with a reasonable accuracy. The decrease in the calculated interatomic distances as compared to the experimental values is associated with the decrease in the unit cell parameters due to the use of the local-density approximation alone in our calculations. The inclusion of this approximation especially affects the length of the In–In covalent bond, which is characterized by a nonuniform distribution of the valence electron density [39].

Let us now consider the pressure dependences of the crystallographic parameters (Fig. 3). It can be seen from Fig. 3a that the pressure dependences of the interatomic distances $d_{\text{In–In}}$ and $d_{\text{In–Se}}$ exhibit a monotonic behavior and are well approximated by the first-order equation of state (1) with parameters $B_{0\text{In–Se}}$ = 82 GPa and $B_{0\text{In–In}}$ = 57 GPa (in both cases, the parameter B_0' is equal to five for adequate comparison with the available experimental data). Although the calculated parameter $B_{\text{In–Se}}$ differs from the experimental value (116 ± 20 GPa [21]), this disagreement can be explained by the nonmonotonic experimental dependence $d_{\text{In–Se}}(P)$ in the range of pressures close to 4 GPa (Fig. 3a, curve *3*). The parameter $B_{0\text{In–Se}}$ = 116 GPa was obtained by averaging the experimental values up to 7 GPa, whereas this dependence in the pressure range up to 4 GPa is steeper than the averaged dependence. Therefore, the dependence at low pressures should be described by a smaller value of $B_{0\text{In–Se}}$. As can be seen from Fig. 3a, the slope of the calculated pressure dependence of the In–Se bond length agrees with the slope of the experimental curve up to a pressure of 3 GPa despite the small error in the determination of the bond length.

The pressure dependence of the In–In interatomic distance is characterized by the parameter $B_{0\text{In–In}}$. This parameter is smaller than the corresponding parameter for the In–Se bond, which indicates a low rigidity of the In–In bond. This fact is in complete agreement with the data on the lattice dynamics in InSe crystals [40], according to which the force constant of the In–Se bond is larger than that of the In–In bond.

The dependence of the parameter a of the hexagonal lattice on the pressure exhibits a smooth behavior up to 7 GPa corresponds to the bulk modulus B_0 = 44 GPa (Fig. 3b). This is in complete agreement with the experimental data. However, in the pressure range from 7 to 11 GPa, the calculated pressure dependence becomes steeper. The dependence of the angle α of the rhombohedral unit cell on the pressure (Fig. 3c) is also characterized by a specific feature (a decrease in the angle α) in the pressure range 7–11 GPa.

The distance between the selenium atoms of different layers monotonically decreases over the entire pressure range and is adequately described by expression (1) with parameters B_0 = 9 GPa and B_0' = 3.8 (or B_0 = 7.3 GPa at B_0' = 5, but with a considerably larger error).

As could be expected, the bulk modulus for the pressure dependence of parameter c of the hexagonal unit cell is substantially smaller than that of parameter a. In the range from 7 to 11 GPa, the pressure dependence of parameter c is nonmonotonic and the parameter itself remains almost unchanged. Therefore, the decrease in the unit cell volume at these pressures is primarily due to the decrease in parameter a. However, at pressures above 11 GPa, the pressure dependence regains its initial behavior and parameter c decreases monotonically.

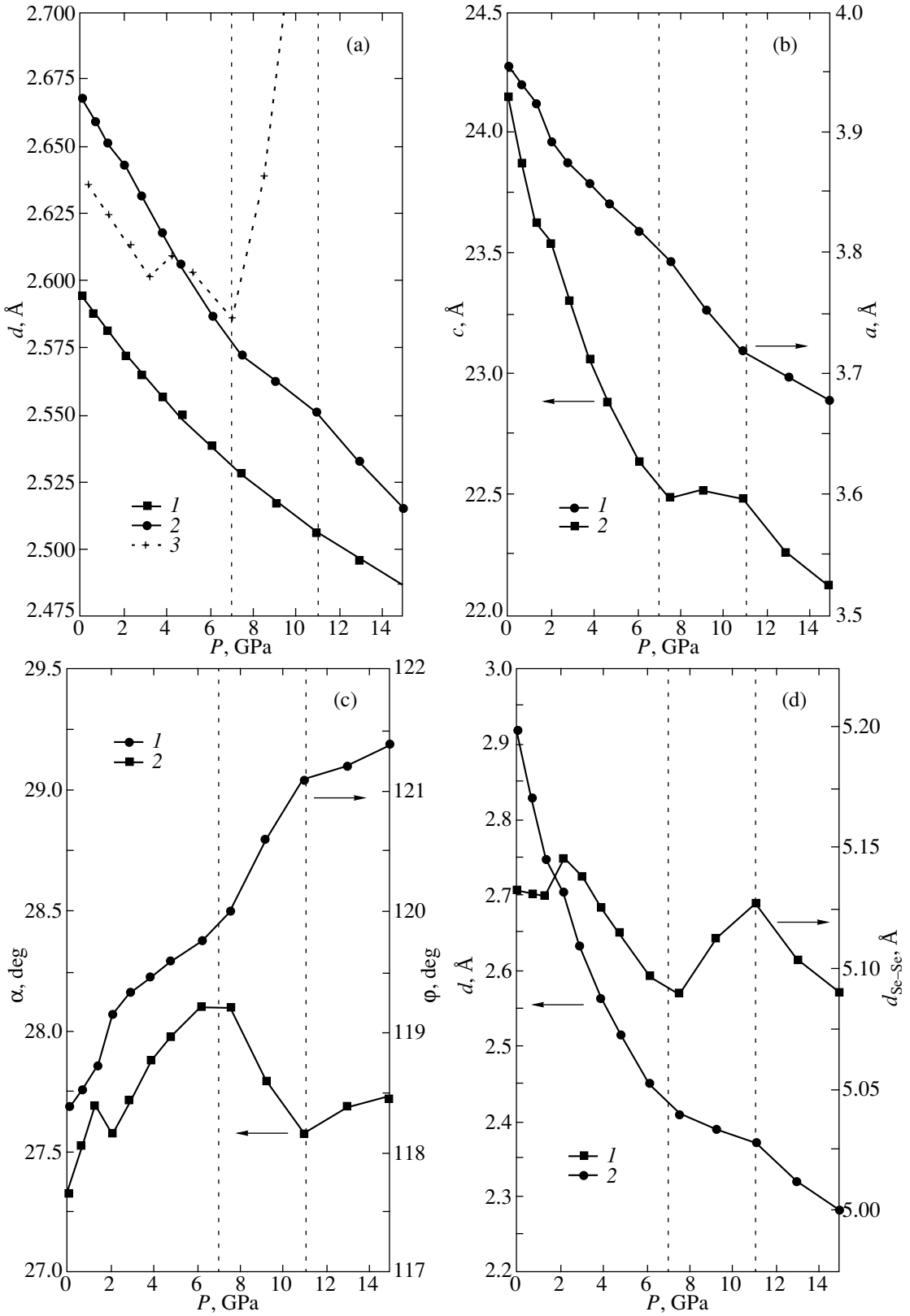

Fig. 3. Pressure dependences of the crystallographic parameters of the γ-InSe structure. (a) (*1*, *2*) Calculated and (*3*) experimental [21] pressure dependences of the interatomic distances (*1*, *3*) $d_{In–Se}$ and (*2*) $d_{In–In}$. (b) Pressure dependences of the unit cell parameters (*1*) *a* and (*2*) *c* in the hexagonal setting. (c) Pressure dependences of (*1*) the angle φ and (*2*) the angle α between the basis vectors of the unit cell in the rhombohedral setting. (d) Pressure dependences of (*1*) the layer thickness $d_{Se–Se}$ and (*2*) the distance between adjacent layers. Dashed lines indicate the pressure range from 7 to 11 GPa in which the pressure dependences exhibit specific features associated with the structural transformations.

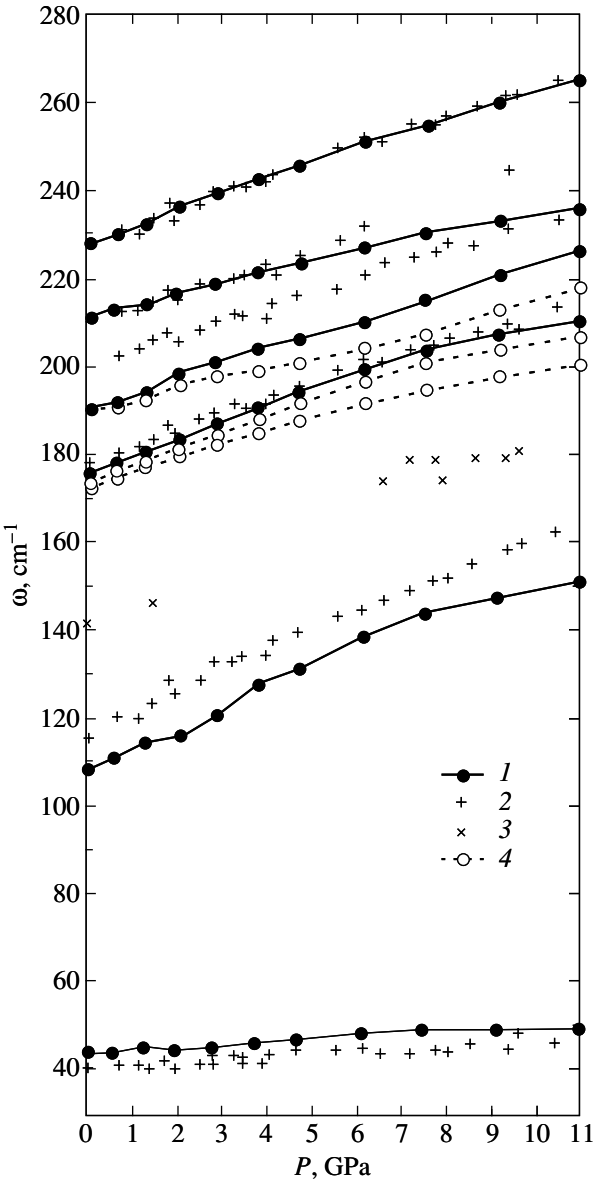

Fig. 4. Theoretical and experimental [22] dependences of the vibrational frequencies on the external hydrostatic pressure for the γ-InSe crystal: (*1*) calculated frequencies of the experimentally observed vibrational modes, (*2*) experimental frequencies of the observed vibrational modes, (*3*) experimental frequencies of the additional mode induced at a pressure of 7 GPa and retained after decompression, and (*4*) calculated frequencies of the experimentally unobservable modes.

The calculated pressure dependence of the layer thickness (or, what is the same, the distance between the selenium atoms of the same layer) exhibits nonlinear behavior (Fig. 3d). As the pressure increases, the layer thickness remains nearly constant at pressures below 1.5 GPa, drastically increases at ~2 GPa, and then monotonically decreases in the pressure range up to ~7 GPa. Above this pressure, the layer thickness increases to an equilibrium value (at ~11 GPa) and then again decreases. Specific features at these pressures can also be observed in the pressure dependence of the angle φ between the In–In and In–Se bonds (Fig. 1). It can be seen from Fig. 3c that the pressure dependence of the angle φ, even though monotonic, is far from linear, as was assumed in [19]. The calculated angle φ at a pressure of 10 GPa is equal to 121.1° (the experimental estimate of φ is 121.4° [24]). Under equilibrium conditions, this angle is calculated to be φ = 118.4° (the experimental value of φ at 300 K is 118.7°). A comparison of the dependences $d_{Se–Se}(P)$ and φ(*P*) shows that the layer thickness increases in the ranges of pressures at which the angle φ increases significantly, i.e., at approximately 2 GPa and from 7 to 11 GPa. It is these considerable changes in the angle φ (against the background of a monotonic decrease in the In–Se and In–In interatomic distances) that are responsible for the increase in the layer thickness.

Therefore, in the range of the experimentally observed phase transformation (7–11 GPa), the calculated dependences of the parameters *a* and *c* exhibit an anomalous behavior. This manifests itself in the fact that the rigidity of the lattice decreases along the direction of the strong bond and increases along the direction perpendicular to the layers.

The possible mechanism of the pressure-induced phase transition in InSe was considered by Pellicer-Porres *et al.* [21], who proposed the following evolution of the structure in the course of the phase transformation into the NaCl modification. As follows from the experimental data (see [21] and references therein), under a pressure of approximately 7 GPa at room temperature, there arise local vibrations and the number of free charge carriers increases. These irreversible processes are associated with the breaking of In–In bonds, i.e., with the formation of defect states. An increase in the pressure leads to an increase in the concentration of free charge carriers, which is explained by the increase in the number of broken In–In bonds. According to the estimates, at a pressure of 10 GPa, there are ten unit cells for each defect state. At pressures above 10 GPa, the material undergoes a transformation throughout the bulk with the formation of a NaCl-type structure. An important role in this transformation is played by atomic vibrations. In particular, annealing at a temperature of 250°C and a pressure of only 4 GPa results in a structural transformation [22]. Since the properties of the ground state were determined in terms of the density-functional theory at absolute zero temperature, our calculations did not reveal structural transformation. However, the anomalies observed in the pressure dependences of the crystallographic parameters are most likely caused by the formation of defects due to atomic vibrations at nonzero temperatures.

It should be noted that, at a pressure of 10 GPa, the volume decreases by 16% with respect to the equilibrium volume. This also agrees well with the experimen-

Table 2. Calculated and experimental vibrational frequencies for the γ-InSe crystal

Reference	E	A	E	E_{TO}	E_{LO}	A_{TO}	A_{LO}	A
This work, ω (cm^{-1})	43.68	108.10	172.46	175.18	210.63	189.47	190.0	227.21
[42]				178	212	190	199	
[43]				173	205	191	199	
[44]				178	210	189	198	
[45]				178	214	202	203	
[22]	40.3	115.8		177	208.2		199.7	226.3
	Rigid modes			Intralayer vibrations				
$\partial\omega/\partial P$ (cm^{-1}/GPa) [22]	0.68 ± 0.24	5.41 ± 0.28		4.27 ± 0.24	3.60 ± 0.15		3.32 ± 0.22	4.33 ± 0.20
$\partial\omega/\partial P$ (cm^{-1}/GPa) (this work)	0.84	5.45		4.45	2.97		3.99	4.23
$\partial^2\omega/\partial P^2$ (cm^{-1}/GPa^2) [22]	-0.01 ± 0.02	-0.10 ± 0.03		-0.9 ± 0.02	–		-0.01 ± 0.02	-0.06 ± 0.02
$\partial^2\omega/\partial P^2$ (cm^{-1}/GPa^2) (this work)	−0.02	−0.11		−0.10	−0.06		−0.07	−0.07

tally determined decrease in the volume (14.8%) upon the phase transition [25].

4.2. Dynamic Properties

The occurrence of structural transformations in the InSe compound under hydrostatic pressure was independently confirmed by the experimental data on the influence of pressure on the Raman spectra obtained by Ulrich *et al.* [22]. As was noted above, apart from the vibrational modes observed in the γ-InSe crystal under normal conditions, the Raman spectra exhibit vibrations at a frequency of approximately 165 cm^{-1}, which arise at pressures above 7 GPa and persist after decompression (with the corresponding decrease in the frequency; see Fig. 4). This mode was assigned to local vibrations associated with structural defects that encourage phase transformation at a pressure of ~10 GPa [25].

The influence of pressure on the vibrational spectrum was not analyzed theoretically in [22]. With the aim of determining the mode symmetry and identifying two-photon processes, the phonon dispersion was calculated in [22] in the framework of the rigid-ion model [41]. Panella *et al.* [11] examined the interface modes in an InSe/Si(111)-(1 × 1)–H heterojunction and carried out first-principles calculations of the phonon spectrum of the InSe crystal. However, to the best of my knowledge, first-principles investigations of the pressure dependences of the vibrational modes have never been performed. In the present work, I carried out these calculations using available experimental data in order to confirm the reliability of the calculated static characteristics.

The results of these calculations are presented in Table 2 and Fig. 4. The equilibrium configuration corresponding to a minimum in the dependence $E(V)$ was used as the initial configuration. A comparison of the results obtained (Table 2) shows that the calculated vibrational frequencies and their pressure dependences are in good agreement with the experimental data.

Although the low-frequency rigid mode E attributed to slip displacements of the layers with respect to each other is well reproduced, the frequency of the mode A that corresponds to opposite displacements of the layers as a whole along the direction of the weak bond is slightly underestimated. This discrepancy can be explained by the use of the local-density approximation, which does not include the van der Waals interaction. Most likely, additional allowance made for the van der Waals attraction involved in the interlayer interaction should result in a somewhat larger value of the interlayer force constant and in complete agreement between the calculated and experimental data. Another reason for this discrepancy is that the calculated frequencies were determined at absolute zero temperature, whereas the experimental data were obtained at room temperature. Since the mode under consideration is characterized by a strong anharmonicity (as follows from the dependences depicted in Fig. 4 and the values of $\partial\omega/\partial P$ in Table 2), the above circumstance can also explain the underestimated frequency of the A mode.

It is worth noting that the frequency of the longitudinal mode A associated with the opposite displacements of the In–Se sublayers with respect to each other along the direction of the weak bond is underestimated by 8–10 cm^{-1}, even though all the other experimental data are well reproduced. The calculated value of the LO–TO splitting is of the order of 1 cm^{-1}. According to the majority of experimental works, the splitting is approximately equal to 9 cm^{-1}. On the other hand, Jandl *et al.* [45] experimentally obtained a splitting of approximately 1 cm^{-1} (but, in this case, the frequency of the TO mode was 202 cm^{-1}).

The calculated pressure dependences of the vibrational frequencies and the available experimental data

are in good agreement. The sole exception is provided by the aforementioned two modes. However, the pressure dependences of these modes also agree well with the experimental data, except for systematic deviation of the calculated frequencies from the experimental frequencies toward the low-energy range.

The pressure dependences of the frequency of the experimentally unobservable modes are also plotted in Fig. 4. Under equilibrium conditions, no LO–TO splitting occurs in the *E* mode. However, this mode is split with an increase in the pressure and, at 11 GPa, the splitting is approximately equal to 9 cm^{-1}. It can be seen from Fig. 4 that, in the pressure range from 3 to 7 GPa, the frequency of the A_{TO} mode increases more slowly than the frequencies of the other vibrations. Since the frequency of this mode is predominantly determined by the In–In interatomic interaction between two In–Se sublayers, the above finding is indirect evidence in favor of the hypothesis that the formation of defect states is associated with the breaking of In–In bonds.

It should be noted that all frequencies of the lattice vibrations exhibit a smooth monotonic dependence on the pressure. The calculations performed within simple models of the lattice dynamics of the studied crystal (for example, in terms of the simplest chain model [40, 41]) demonstrate that good agreement between the experimental and theoretical vibrational frequencies can be achieved even in the model of axially symmetric force constants, which disregard the elasticity of flexure of the valence bond and are determined primarily by the rigidity of the In–In and In–Se bonds and the van der Waals interaction between selenium atoms of different layers. Since the aforementioned interatomic distances monotonically change under pressure (Fig. 3a, curves *1*, *2*; Fig. 3d, curve *2*), the frequencies of lattice vibrations are also characterized by a smooth dependence.

In general, the above results are indirect evidence in support of the reliability of the data obtained in the preceding section on the structural transformations under hydrostatic pressure.

5. CONCLUSIONS

Thus, the structural transformations of the γ-InSe crystal under hydrostatic pressure were investigated theoretically. It was demonstrated that the dependence $E(V)$ is adequately described by the first-order equation of state. The calculated bulk modulus of the γ-InSe crystal is equal to 29 GPa at $B_0' = 6.2$. The pressure dependences of the lattice parameters of the γ-InSe crystal exhibit a nonmonotonic behavior in the range 7–11 GPa. The layer thickness is also characterized by a nonmonotonic pressure dependence with specific features at a pressure of 2 GPa and in the range 7–11 GPa.

The vibrational properties of the crystal and the frequencies of lattice vibrations at the center of the Brillouin zone were investigated as a function of external hydrostatic pressure. The results of the calculations are in good agreement with the available experimental data.

The results obtained in this work can be used both as initial data for detailed theoretical investigations and in the interpretation of experimental data on the pressure dependences of the crystallographic parameters, the electronic and vibrational properties of γ-InSe, the deformation potentials, etc.

REFERENCES

1. L. I. Man, R. K. Karakhanyan, and R. M. Imamov, Kristallografiya **6**, 1166 (1974).
2. R. S. Putnam and D. G. Lancaster, Appl. Opt. **38**, 1513 (1999).
3. R. A. Kaindl, F. Eickemeyer, M. Woerner, and T. Elsaesser, Appl. Phys. Lett. **75**, 1060 (1999).
4. J. P. Martinez, A. Segura, J. L. Waldes, and A. Chevy, J. Appl. Phys. **62**, 1477 (1987).
5. V. N. Katerinchuk, M. É. Kovalyuk, and A. D. Ogorodnik, Neorg. Mater. **32**, 937 (1996).
6. C. Julien, M. Jouanne, P. A. Burre, and M. Balkanski, Solid State Ionics **28–30**, 1167 (1988).
7. M. Balkanskii, P. Gomes da Costa, and R. F. Wallis, Phys. Status Solidi B **194**, 175 (1996).
8. V. V. Dragomeretskiĭ, Z. D. Kovalyuk, V. K. Kiva, and A. I. Seredyuk, USSR Inventor's Certificate No. 178,511.
9. P. Gomes da Costa, M. Balkanski, and R. F. Wallis, Phys. Rev. B **43**, 7066 (1991).
10. M. O. D. Camara, A. Mauger, and I. Devos, Phys. Rev. B **65**, 205308 (2002).
11. V. Panella, A. L. Glebov, J. P. Toennis, *et al.*, Phys. Rev. B **59**, 15772 (1999).
12. E. Wisotzki, A. Klein, and W. Jaegermann, Thin Solid Films **380**, 263 (2000).
13. E. P. Zaretskaya, V. F. Gremenok, Y. V. Rud, *et al.*, Diffus. Defect Data, Part B: Solid State Phenom. **80–81**, 293 (2001).
14. V. N. Katerinchuk, Z. D. Kovalyuk, T. V. Betsa, *et al.*, Pis'ma Zh. Tekh. Fiz. **27** (4), 62 (2001) [Tech. Phys. Lett. **27**, 424 (2001)].
15. Yu. A. Nikolaev, V. Yu. Rud, and E. I. Terukov, Semiconductors **34**, 677 (2000).
16. V. N. Katerinchuk, Z. D. Kovalyuk, V. V. Netyaga, and T. V. Betsa, Pis'ma Zh. Tekh. Fiz. **26** (17), 6 (2000) [Tech. Phys. Lett. **26**, 754 (2000)].
17. V. N. Katerinchuk, Z. D. Kovalyuk, and A. L. Ogorodnik, Fiz. Tekh. Poluprovodn. (St. Petersburg) **28**, 2096 (1994) [Semiconductors **28**, 1157 (1994)].
18. Yu. M. Orishchin and I. M. Stakhira, Fiz. Tekh. Poluprovodn. (Leningrad) **10**, 2111 (1976) [Sov. Phys. Semicond. **10**, 1256 (1976)].
19. F. J. Manjón, D. Errandonea, A. Segura, *et al.*, Phys. Rev. B **63**, 125330 (2001).
20. D. Errandonea, A. Segura, V. Munoz, and A. Chevy, Phys. Rev. B **60**, 15866 (1999).
21. J. Pellicer-Porres, A. Segura, V. Munoz, and A. San Miguel, Phys. Rev. B **60**, 3757 (1999).

22. C. Ulrich, M. A. Mroginski, A. R. Goni, *et al.*, Phys. Status Solidi B **198**, 121 (1996).
23. L. I. Man, R. M. Imamov, and S. A. Semiletov, Kristallografiya **21**, 628 (1976) [Sov. Phys. Crystallogr. **21**, 355 (1976)].
24. J. Rigoult, A. Rimsky, and A. Kuhn, Acta Crystallogr. B **36**, 916 (1980).
25. U. Schwarz, A. R. Goni, K. Syassen, *et al.*, High Press. Res. **8**, 396 (1991).
26. M. Balkanskii, C. Julien, and M. Jouanne, J. Power Sources **20**, 213 (1987).
27. F. D. Murnaghan, Proc. Natl. Acad. Sci. USA **30**, 244 (1944).
28. W. Kohn and L. J. Sham, Phys. Rev. **140**, A1133 (1965).
29. C. Hartwigsen, S. Goedecker, and J. Hutter, Phys. Rev. B **58**, 3641 (1998).
30. J. P. Perdew and Y. Wang, Phys. Rev. B **33**, 8800 (1986).
31. D. M. Ceperley and B. J. Alder, Phys. Rev. Lett. **45**, 566 (1980).
32. The ABINIT Code is a Common Project of the Universite Catholique de Louvain, Corning Incorporated, and Other Contributors, URL http://www.pcpm.ucl.ac.be/abinit.
33. S. Goedecker, SIAM J. Sci. Comput. (USA) **18**, 1605 (1997).
34. M. C. Payne, M. P. Teter, D. C. Allan, *et al.*, Rev. Mod. Phys. **64**, 1045 (1992).
35. X. Gonze, Phys. Rev. B **54**, 4383 (1996).
36. X. Gonze, Phys. Rev. B **55**, 10337 (1997).
37. X. Gonze and C. Lee, Phys. Rev. B **55**, 10355 (1997).
38. H. J. Monkhorst and J. D. Pack, Phys. Rev. B **13**, 5188 (1976).
39. P. Gomes da Costa, R. G. Dandrea, R. F. Wallis, and M. Balkanski, Phys. Rev. B **48**, 14135 (1993).
40. T. Ikari, S. Shigetomi, and K. Hashimoto, Phys. Status Solidi B **111**, 477 (1982).
41. P. Brüesch, *Phonons: Theory and Experiments*, Vol. 1: *Lattice Dynamics and Models of Interatomic Forces* (Springer-Verlag, Berlin, 1982).
42. C. Julien, M. Eddrief, M. Balkanski, and A. Chevy, Phys. Rev. B **46**, 2435 (1992).
43. N. M. Gasanly, B. M. Yvadov, V. I. Taganov, and E. A. Vinogradov, Phys. Status Solidi B **89**, K43 (1978).
44. K. R. Allakhverdiev, S. S. Babaev, E. Y. Salaev, and M. M. Tagyev, Phys. Status Solidi B **96**, 177 (1979).
45. S. Jandl, M. Banville, and J. Deslandes, Can. J. Phys. **59**, 198 (1981).

Translated by O. Borovik-Romanova

Physics of the Solid State, Vol. 46, No. 1, 2004, pp. 188–191. Translated from Fizika Tverdogo Tela, Vol. 46, No. 1, 2004, pp. 185–188.

MAGNETISM AND FERROELECTRICITY

Temperature Dependences of the Dielectric Properties of Lithium–Titanium Ferrite Ceramics

A. V. Malyshev, V. V. Peshev, and A. M. Pritulov

Tomsk Polytechnical University, pr. Lenina 30, Tomsk, 634034 Russia

e-mail: peshev@tpu.ru

Received December 10, 2002; in final form, May 13, 2003

Abstract—Temperature dependences of the real ε' and imaginary ε" parts of the complex permittivity of lithium–titanium ferrite ceramics are measured in the frequency range 10^2–10^6 Hz at different test-signal amplitudes and dc bias voltages. It is found that the dielectric characteristics of the ceramic samples drastically change in narrow temperature ranges. The assumption is made that relaxators whose reorientation is due to tunneling transitions of electrons inside "bivalent iron ion–trivalent metal ion" pairs are involved in polarization processes. Under certain conditions, the reorientation of relaxators can have collective character. *© 2004 MAIK "Nauka/Interperiodica".*

1. INTRODUCTION

It is known that the conductivity σ and complex permittivity ε* substantially affect the propagation of electromagnetic waves in ferrite materials and, hence, can be responsible for the functional properties of ferrite-based devices. At present, there are many works concerned with the electrical properties of ferrites [1–10]. As a rule, dependences of the conductivity σ and complex permittivity ε* on the frequency *f* and temperature *T* for polycrystalline ferrites are interpreted within either the model of interlayer polarization [1] or the model of interlayer polarization involving surface states of grain boundaries [2]. Since interlayer polarization is caused primarily by charge transfer, the charge transfer mechanism affects the characteristics of the interlayer polarization. It is believed that charge transfer proceeds either through migration of charge carriers over the impurity band [3, 4] or through hoppings of carriers over localized energy levels due to electron–phonon interactions [5]. The hopping mechanism of charge transfer in ferrites is associated with the presence of bivalent iron ions and electron transitions between variable-valence ions, for example, $Fe^{2+} + Me^{3+} \longrightarrow Fe^{3+} + Me^{2+}$ [6]. It has been established that the higher the Fe^{2+} concentration, the higher the conductivity and the larger the real part ε' of the permittivity. On this basis, it has been assumed that these transitions are responsible for charge transfer and polarization [7–9]. In this case, there is no need to invoke the Koops model, because the recharging of ion pairs $Fe^{2+} + Me^{3+} \longrightarrow Fe^{3+} + Me^{2+}$ can be considered as the reorientation of dipoles in an ac electric field. Since the components of ion pairs are crystal-forming ions, the large value of ε' can be explained by the high concentration of ion pairs. When electron transitions in these pairs occur through phonon-assisted tunneling, it can be expected that the characteristic time of polarization will depend not only on the temperature but also on the time of action of the polarizing field (or, in the case of an ac electric field, on the frequency) and its strength.

It is known that electric dipoles at high concentrations bring about the spontaneous formation of electric domains. Since the Fe^{2+} content varies over a wide range, the concentrations of dipoles can also change significantly. It can be assumed that the high permittivity ε for ferrites is caused not only by the interlayer polarization but also by the polarization due to either individual recharging of ion pairs, recharging of pairs involved in spontaneously formed electric domains, or recharging of pairs contained in domains induced by the electric field.

The aim of this work was to elucidate the possible mechanism of relaxation polarization in lithium–titanium ferrite ceramics. For this purpose, we investigated the temperature dependences of the real ε' and imaginary ε" parts of the complex permittivity at different frequencies and amplitudes of the test signal in the presence and absence of a dc bias voltage.

2. SAMPLES AND EXPERIMENTAL TECHNIQUE

In our experiments, we used ferrites of composition $Li_{0.649}Fe_{1.598}Ti_{0.5}Zn_{0.2}Mn_{0.051}O_4$ doped with 0.22 wt % Bi_2O_3. Samples were synthesized under working conditions according to the ceramic technique and were then sintered in air at $T = 1280$ K for 120 min. After sintering, the samples were ground on both sides from the initial thickness $d = 1$ mm to a thickness of 0.22 mm. As a result, the samples had the form of pellets 13 mm in diameter. Then, silver contacts were applied to the sample surface through thermal evaporation under vacuum. The diameter of the measuring contact was equal

to 5 mm. The pellets with contacts were subjected to normalizing annealing at $T = 570$ K for $t = 1$ h. The magnetic Curie temperature T_C for the ferrite ceramics thus prepared was equal to 575 K. We measured the capacitance C and conductance G, i.e., the conductivity governed by both conduction current and the polarization current component coinciding in phase with the electric field. The measurements were carried out in the temperature range 300–600 K. In the course of measurements, the samples were heated and cooled at a rate of 2 K/min. The experiments were performed at test-signal frequencies $f = 100$, 10^3, 10^4 (an E7-14 bridge), and 10^6 Hz (an E7-12 bridge). The real ε' and imaginary ε'' parts of the permittivity were calculated from the standard formulas: $\varepsilon' = Cd/(S\varepsilon_0)$, $\tan\delta = G/(\omega C)$, and $\varepsilon'' = \varepsilon'\tan\delta$, where ε_0 is the permittivity of free space, ω is the circular frequency of the polarizing field, and $\tan\delta$ is the dielectric loss tangent.

3. RESULTS AND DISCUSSION

The temperature dependences of the real ε' and imaginary ε'' parts of the complex permittivity measured at a test-signal amplitude $U_{test} = 56$ mV are depicted in Fig. 1. It can be seen from Fig. 1a that the polarization involves no less than two stages and the permittivity $\varepsilon' = F(T)$ at saturation (ε'_{sf}) for the low-temperature stage depends on the frequency and decreases with an increase in the frequency. Below, we will consider only the most pronounced low-temperature stage. The absence of relaxation peaks in the dependences $\varepsilon'' = F(T)$ (Fig. 1b) suggests that the conduction current substantially exceeds the active component of the relaxation current. The temperature dependences of the conductance $G(T)$ used for calculating the values of ε'' are virtually independent of the frequency. The measurements were performed during heating and cooling of the samples. The curves $\varepsilon'' = F(T)$ measured in the course of heating and cooling coincide with each other. The dependences $\varepsilon' = F(T)$ are characterized by an insignificant hysteresis at a frequency of 100 Hz, which decreases with an increase in the frequency.

Note that the temperature dependences of the permittivity ε' can be well approximated within the model of interlayer polarization. In this case, the conduction current is dominant; therefore, the activation energy of relaxation E_a should be equal to the activation energy of charge transfer $E_{a\sigma}$. The activation energy E_a, which is determined from the dependences $\varepsilon'(T)$ in the framework of this model, is equal to 0.36–0.38 eV. However, the dependences $\varepsilon''(T)$ can be described only at activation energies $E = (0.7–0.74)$ eV $> E_a$. Since $E_a \neq E_{a\sigma}$ and the temperature dependences of the conductance $G(T)$ for the studied samples are almost identical at different frequencies, the experimental temperature dependences of the real ε' and imaginary ε'' parts of the permittivity and also the large values of ε' have defied explanation in terms of interlayer polarization.

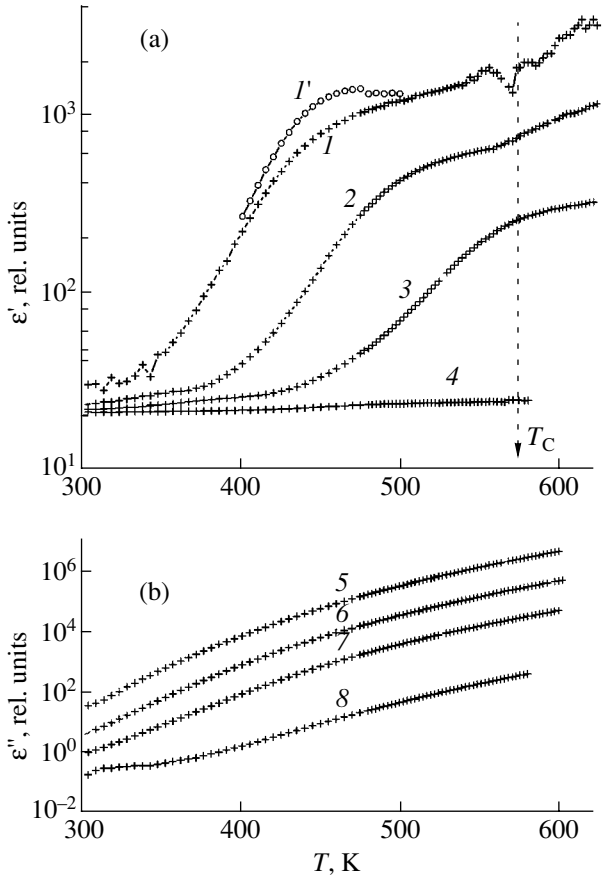

Fig. 1. Temperature dependences of (a) real ε' and (b) imaginary ε'' parts of the complex permittivity measured at the test-signal amplitude $U_{test} = 56$ mV in the course of (*1–8*) heating and (*1'*) cooling. Frequency: (*1*, *1'*, *5*) 10^2, (*2*, *6*) 10^3, (*3*, *7*) 10^4, and (*4*, *8*) 10^6 Hz.

The data presented in Fig. 1a cannot be explained in the framework of the Debye model, because the value of ε'_{sf} depends on the frequency. Recall that, within the Debye model, the relaxation time $\tau(T)$ does not depend on the duration of the polarizing voltage pulse and, hence, on the test-signal frequency. Consequently, the value of ε'_{sf} is equal to the static permittivity ε_s and does not depend on the frequency f, even though there are distributions of the activation energy E_a and preexponential factor τ_0. Therefore, for $\tau(T) = \text{const}(f)$, at any test-signal frequency, there always (theoretically) exists a temperature range in which virtually all relaxators are involved in the reorientation and the permittivity ε' reaches the same value ε_s.

In the case when the polarization is caused by either the reorientation of electric domains in ferroelectrics [11] or the reorientation of relaxators due to tunneling of charge carriers [5] between centers of localization, the number of dipoles involved in this process is limited by the duration of polarizing-field action. Under these

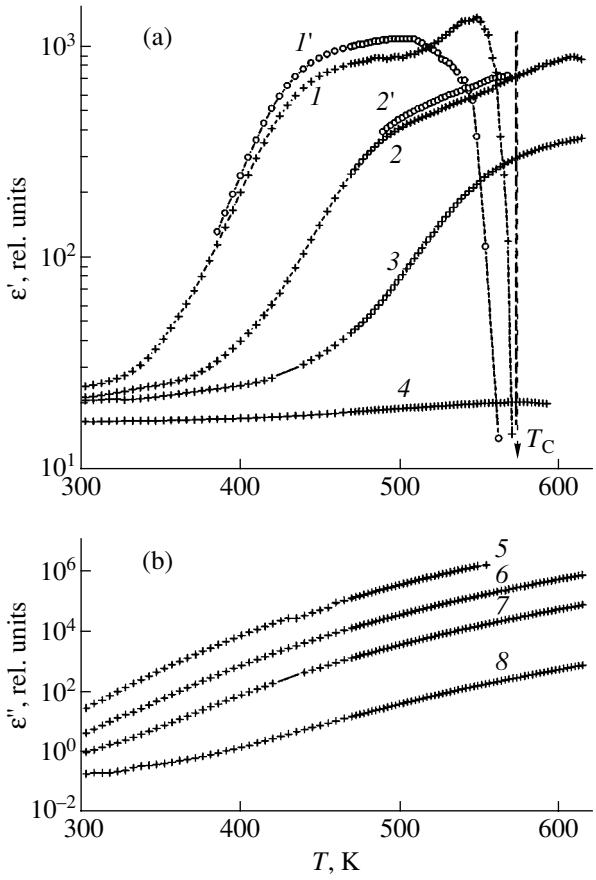

Fig. 2. Temperature dependences of (a) real ε' and (b) imaginary ε" parts of the complex permittivity measured at the test-signal amplitude U_{test} = 2800 mV in the course of (*1*–*8*) heating and (*1*', *2*') cooling. Frequency: (*1*, *1*', *5*) 10^2, (*2*, *2*', *6*) 10^3, (*3*, *7*) 10^4, and (*4*, *8*) 10^6 Hz.

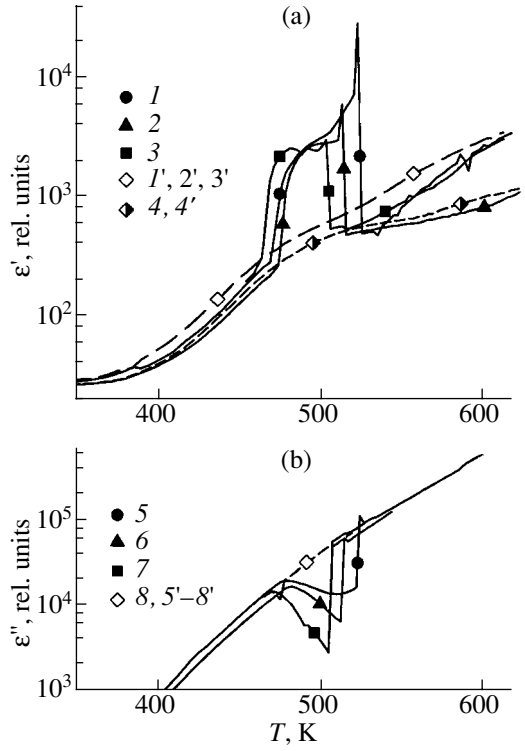

Fig. 3. Temperature dependences of (a) real ε' and (b) imaginary ε" parts of the complex permittivity measured at the test-signal amplitude U_{test} = 56 mV and frequency f = 10^3 Hz in the course of (*1*–*8*) heating and (*1*'–*8*') cooling at dc polarizing voltages U_p: (*1*, *1*', *5*, *5*') 0.2, (*2*, *2*', *6*, *6*') 0.25, (*3*, *3*', *7*, *7*') 0.3, and (*4*, *4*', *8*, *8*') 0 V.

conditions, the real part of the permittivity at saturation ε'_{sf} is a decreasing function of the frequency (see Fig. 1a).

In order to elucidate the influence of the polarizing-field strength of the permittivity, we measured the temperature dependences of ε' and ε" at the same frequencies and the test-signal amplitude U_{test} = 2800 mV (Fig. 2). As can be seen from Fig. 2a, the dependences ε' = $F(T)$ have a considerable hysteresis at a frequency of 100 Hz, which decreases with an increase in the frequency. These dependences exhibit an anomalous behavior, which manifests itself in a drastic decrease in the values of ε' with an increase in the temperature beginning with T = 550 K (Fig. 2a, curves *1*, *1*').

The hysteresis observed in the dependence ε' = $F(T)$ and a sharp decrease in the values of ε' (Fig. 2a, curves *1*, *1*') indicate that the ferrite possibly possess ferroelectric-like properties. However, these features are observed only at a high test-signal amplitude U_{test} = 2.8 V and a long duration of polarizing-field action (f = 100 Hz). When an ac electric field with a high strength and a low frequency is applied to the sample, the concentration of dipoles oriented along the same direction can reach large values in certain time intervals. The interaction between dipoles within these intervals can lead to specific features in the behavior of polarization (due to the collective reorientation of the dipoles) and, possibly, to the formation of electric domains. Thus, we believe that the features revealed in the temperature dependences of the permittivity ε' are associated with the collective character of the dipole reorientation during part of the half-cycle of the ac electric field. To put it differently, the electric field at regular intervals induces a ferroelectric-like state in the dipole system.

In this respect, it is of interest to investigate the temperature dependences of the dielectric properties under conditions where the dc polarizing voltage U_p and the ac test-signal voltage U_{test} = 56 mV < U_p are applied to the sample. In this case, the test signal does not change the state of the dipole system and serves only for testing, whereas the concentration of dipoles oriented by the dc electric field does not depend on the test-signal frequency. It can be expected that, at a dc polarizing voltage U_p, the specific features in the temperature dependences of the dielectric characteristics should be observed at frequencies f > 100 Hz (unlike the depen-

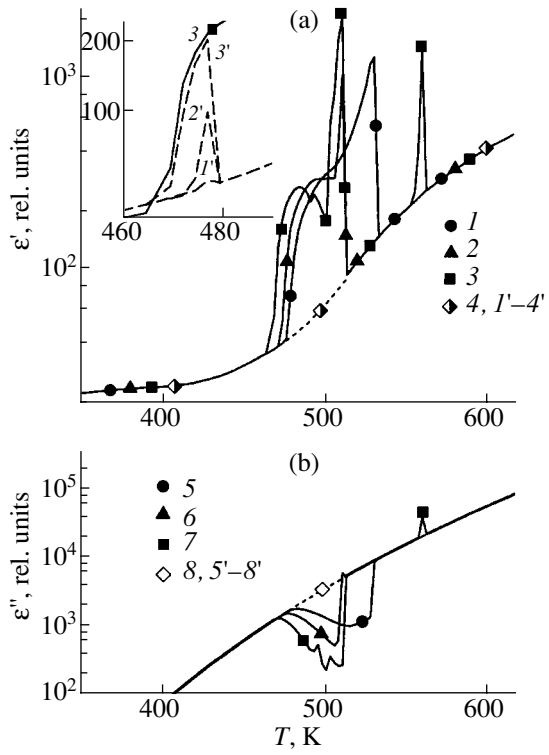

Fig. 4. Temperature dependences of (a) real ε' and (b) imaginary ε'' parts of the complex permittivity measured at the test-signal amplitude U_{test} = 56 mV and frequency f = 10^4 Hz in the course of (*1*–*8*) heating and (*1*'–*8*') cooling at dc polarizing voltages U_p: (*1*, *1*', *5*, *5*') 0.2, (*2*, 2', *6*, *6*') 0.25, (*3*, *3*', *7*, *7*') 0.3, and (*4*, *4*', *8*, *8*') 0 V. The inset shows the specific features in the dependences ε'(*T*) measured during (*1*'–*3*') cooling. Curve *3* in the inset is depicted for comparison.

dences shown in Fig. 1, for which U_{test} is also equal to 56 mV).

Figure 3 shows the dependences ε'(*T*) and ε''(*T*) measured at a low test-signal voltage U_{test} and dc polarizing voltage U_p = 0–0.3 V in the course of heating and cooling. The measurements were performed with a temperature step of 2 K. Actually, these dependences at $U_p \neq 0$ exhibit a pronounced temperature hysteresis. Analysis of the dependences ε'(*T*) and ε''(*T*) measured during heating at $U_p \neq 0$ shows that the values of ε' jumpwise increase and the values of ε'' jumpwise decrease in the same temperature range 460–530 K. The drastic changes observed in the dielectric characteristics start and end at temperatures T_{start} and T_{end}, respectively. Note that the temperature T_{end} monotonically decreases with an increase in the dc polarizing voltage U_p. Similar features are observed in the temperature dependences of the dielectric characteristics measured at a frequency of 10 kHz (Fig. 4). As was expected, the temperatures T_{start} and T_{end} at f = 10 kHz are equal to those at f = 1 kHz; i.e., these temperatures depend on the dc polarizing voltage U_p and are independent of the frequency f at low test-signal voltages U_{test}. The inset shows the specific features in the dependences ε'(*T*) measured during cooling.

4. CONCLUSIONS

Thus, it was established that the activation energy of relaxation polarization differs from the activation energy of charge transfer and that the conductivity does not depend on the frequency. This means that the interlayer polarization makes an insignificant contribution to the high permittivity ε' in the frequency and temperature ranges covered. It is found that the dielectric characteristics of the ceramic samples drastically change in narrow temperature ranges. The features observed in the temperature dependences of the dielectric characteristics can be associated with the collective reorientation of dipoles; in turn, the collective polarization is most likely induced by the electric field.

REFERENCES

1. G. G. Koops, Phys. Rev. **83** (1), 121 (1951).
2. V. P. Miroshkin, Ya. I. Panova, and V. V. Pasynkov, Phys. Status Solidi A **66**, 779 (1981).
3. E. P. Svirina, Izv. Akad. Nauk SSSR, Ser. Fiz. **34** (6), 1162 (1970).
4. Sh. Sh. Bashkirov, A. D. Liberman, V. V. Parfenov, and V. I. Sinyavskiĭ, Izv. Akad. Nauk SSSR, Neorg. Mater. **15** (3), 516 (1979).
5. F. K. Lotgering, J. Phys. Chem. Solids **25** (1), 95 (1964).
6. V. P. Miroshkin, Ya. I. Panova, and T. V. Stakhieva, Phys. Status Solidi A **66**, 503 (1981).
7. A. V. Ramana Reddy, G. Ranga Mohan, D. Ravinder, and B. S. Boyanov, J. Mater. Sci. **34**, 3169 (1999).
8. G. Ranga Mohan, D. Ravinder, A. V. Ramana Reddy, and B. S. Boyanov, Mater. Lett. **40**, 39 (1999).
9. Radha and D. Ravinder, Indian J. Pure Appl. Phys. **33**, 74 (1995).
10. M. A. El Hiti, J. Magn. Magn. Mater. **192**, 305 (1999).
11. M. E. Lines and A. M. Glass, *Principles and Applications of Ferroelectrics and Related Materials* (Oxford Univ. Press, Oxford, 1977; Mir, Moscow, 1981).

Translated by O. Borovik-Romanova

Physics of the Solid State, Vol. 46, No. 1, 2004, p. 192.

ERRATA

Erratum: "Phase Separation of the Spin System in the $La_{0.93}Sr_{0.07}MnO_3$ Crystal" [Phys. Solid State 45 (12), 2297 (2003)]

S. F. Dubunin, V. E. Arkhipov, S. G. Teploukhov, V. D. Parkhomenko, N. N. Loshkareva, and N. I. Solin

In the article of S. F. Dubunin, V. E. Arkhipov, S. G. Teploukhov, V. D. Parkhomenko, N. N. Loshkareva, and N. I. Solin, the name of the first author should read S. F. Dubinin.

1063-7834/04/4601-0192$26.00 © 2004 MAIK "Nauka/Interperiodica"

Physics of the Solid State, Vol. 46, No. 1, 2004, pp. 22–26. Translated from Fizika Tverdogo Tela, Vol. 46, No. 1, 2004, pp. 26–30.

PROCEEDINGS OF THE CONFERENCE DEDICATED TO O. V. LOSEV (1903–1942)

(Nizhni Novgorod, Russia, March 17–20, 2003)

Photoluminescence and Structural Defects in Silicon Layers Implanted by Iron Ions

É. A. Shteĭnman*, V. I. Vdovin, A. N. Izotov*, Yu. N. Parkhomenko***, and A. F. Borun*****

** Institute of Solid-State Physics, Russian Academy of Sciences, Chernogolovka, Moscow oblast, 142432 Russia*

*** Institute for Chemical Problems of Microelectronics, B. Tolmachevskiĭ per. 5, Moscow, 109017 Russia*

**** Moscow State Institute of Steel and Alloys, Leninskiĭ pr. 4, Moscow, 117936 Russia*

Abstract—The photoluminescence spectra of silicon samples implanted by $^{56}Fe^{+}$ ions [energy, 170 keV; dose, 1×10^{16}, $(2–4) \times 10^{17}$ cm^{-2}] and annealed at temperatures of 800, 900, and 1000°C are measured. The structure of the samples at each stage of treatment is investigated using transmission electron microscopy (TEM). It is found that the phase formation and morphology of crystalline iron disilicide precipitates depend on the dose of iron ions and the annealing temperature. A comparison of the dependences of the intensity and spectral distribution of the photoluminescence on the measurement temperature, annealing temperature, and morphology of the $FeSi_2$ phase revealed the dislocation nature of photoluminescence. © *2004 MAIK "Nauka/Interperiodica".*

1. INTRODUCTION

The semiconductor phase β-$FeSi_2$ is a promising material, because it can easily be integrated with silicon technology and emits in the range of 0.8 eV owing to the direct-gap electronic structure with a band gap of approximately 0.85 eV at room temperature [1]. However, practical application of this material presents considerable difficulties for a number of reasons. In particular, Lange [2] revealed that continuous layers of β-$FeSi_2$ with a high degree of structural perfection do not exhibit luminescence properties. Gumarov *et al.* [3] established that crystalline and strained states of iron disilicide particles and their morphology substantially depend on the conditions of ion-beam synthesis. Moreover, the luminescence properties of these particles appeared to be different. Grimaldi *et al.* [1] and Martinelli *et al.* [4] showed that elastically strained ball-shaped particles involved in a defect-free matrix do not possess luminescence properties, whereas unstrained disk-shaped particles in a matrix with a large number of defects emit with an energy of 0.8 eV. Many authors have noted that the origin of this emission is not clearly understood, because the *D*1 line associated with the dislocation luminescence is observed in the same spectral range. From the aforesaid, it is clear that elucidation of the nature of the emission in this range is an important problem. The purpose of the present work was to reveal the origin of the luminescence in the range of 0.8 eV in silicon samples containing iron disilicide precipitates formed during ion-beam synthesis and characterized by different morphology.

2. EXPERIMENTAL TECHNIQUE

Iron ions $^{56}Fe^{+}$ with an energy of 170 keV and doses of 1×10^{16} and $(2–4) \times 10^{17}$ cm^{-2} were implanted into *n*-Si(100) wafers (KÉF-4, 5) 75 mm in diameter at a temperature of 350°C. Thermal annealing was carried out in an argon atmosphere at temperatures of 800–1000°C for 30 min. The structure of the samples was investigated by transmission electron microscopy (TEM) with the use of a JEM 200CX electron microscope. The TEM observations were performed on longitudinal foils (oriented along the wafer surface) and cross sections. The sizes of rounded particles and grains in the form of polyhedra were characterized by the diameters of the circumscribed circles. The photoluminescence (PL) of the samples placed in an optical helium cryostat was excited by an Ar laser (514.5 nm) and was then recorded on standard phase-sensitive instruments with the use of an MDR-2 wide-aperture monochromator and a cooled germanium photoresistor.

3. RESULTS

It is found that the phase formation and morphology of crystalline iron disilicide precipitates depend on the dose of iron ions and the annealing temperature. In the general case, the surface region of the silicon wafer after ion-beam synthesis contains misoriented (with respect to the silicon matrix) single-crystal grains and small-sized rounded particles of iron disilicide and also dislocations. The single-crystal structure of particles and grains is confirmed by the appearance of numerous extra reflections in the diffraction pattern and the moiré contrast in the electron microscope images.

1063-7834/04/4601-0022$26.00 © 2004 MAIK "Nauka/Interperiodica"

3.1. Implantation with a Dose of 1×10^{16} cm^{-2}

The photoluminescence spectrum of the implanted sample exhibits only exciton luminescence of silicon due to the excitation of the undistorted layer of the substrate. In the photoluminescence spectrum of the sample annealed at 800°C (sample **1**), the broad band with a maximum at 0.807 eV is dominant (Fig. 1a). The position of this maximum exactly coincides with that of the dislocation photoluminescence line *D*1. An increase in the sample temperature to 50 K leads to a decrease in the intensity of the band. Note that the degree of quenching of the long-wavelength wing is considerably smaller than that of the other portion of the band. Such a behavior of the photoluminescence band indicates that the emitting centers responsible for this luminescence have different natures.

The TEM investigations of sample **1** revealed that the surface region of the wafer contains rounded particles and dislocations (Fig. 2). The particle sizes vary from 3 to 30 nm, and the density of particles exceeds 8×10^{10} cm^{-2}. The dislocation density can be approximately estimated at $>10^{10}$ cm^{-2}. The moiré contrast fringes of different particles are considerably misoriented. This suggests that particles are irregularly arranged in the silicon matrix. The diffraction pattern exhibits a relatively small number of extra reflections, which are predominantly located within the fringe passing through the {220} main reflections. These extra reflections precisely correspond to the reflections from the (114), (422), and (313) planes of the β-$FeSi_2$ phase. The other few weak extra reflections coincide with fringes for the (040), (204), and (222) reflections of the β-$FeSi_2$ phase.

In the photoluminescence spectrum of the sample annealed at 900°C (sample **2**), the *D*1 line is also dominant, even though the intensity of this line decreases compared to that for sample **1** and the other lines *D*2–*D*4 of the dislocation luminescence are clearly observed in the spectrum (Fig. 1b). It should be noted that the exciton photoluminescence is characterized by a rather high intensity.

3.2. Implantation with a Dose of 2×10^{17} cm^{-2}

The sample implanted with a dose of 2×10^{17} cm^{-2} (like the sample implanted at a lower dose and annealed at 800°C) involves particles and dislocations. The difference lies in the increase in the density ($\geq 2 \times 10^{11}$ cm^{-2}) and the sizes (20–50 nm) of particles. The diffraction pattern contains a large number of extra reflections, among which there are very intense reflections with a regular arrangement. This indicates that the total volume of iron disilicide particles increases and they are more regularly oriented in the Si matrix. For the most part, the particles are characterized by the reflections from the (114) planes of the β-$FeSi_2$ phase. Moreover, a regular arrangement is observed for the reflections from the (202) and (224) planes of the β-$FeSi_2$ phase.

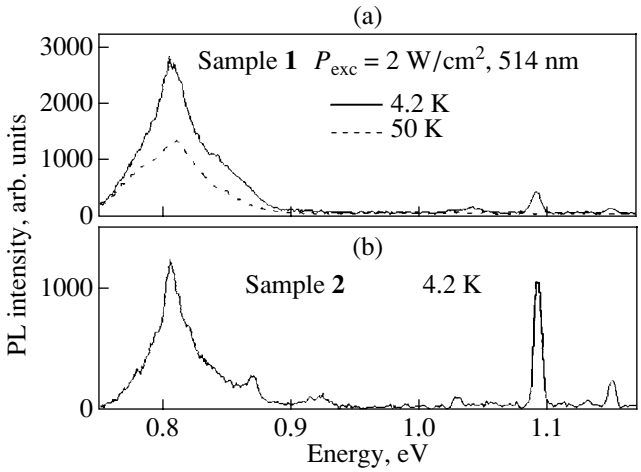

Fig. 1. Photoluminescence spectra of the samples implanted with an iron ion dose of 1×10^{16} cm^{-2} and annealed at temperatures of (a) 800 and (b) 900°C.

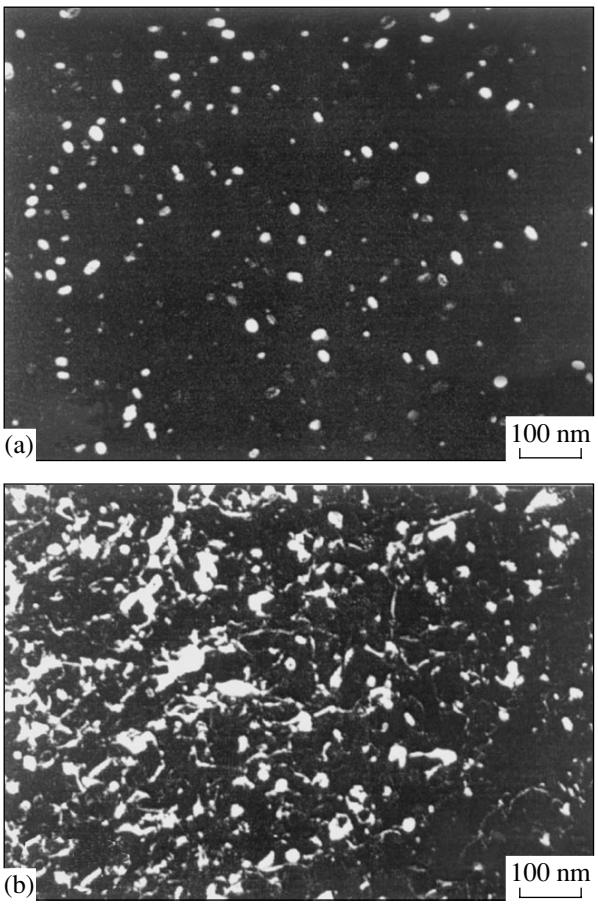

Fig. 2. TEM dark-field images of the sample implanted with an iron ion dose of 1×10^{16} cm^{-2} and annealed at a temperature of 800°C: (a) β-$FeSi_2$ particles (extra reflection) and (b) dislocations (⟨220⟩ main reflection).

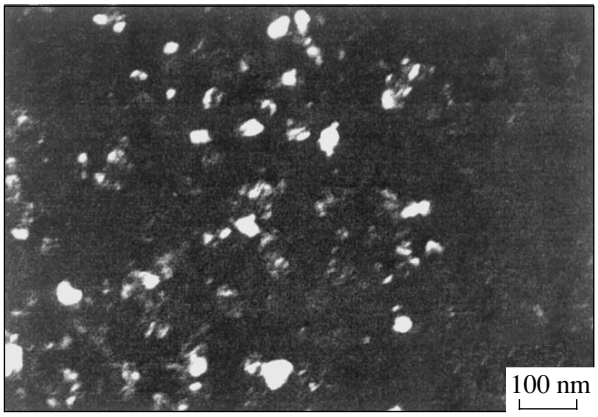

Fig. 3. TEM image of the sample implanted with an iron ion dose of 2×10^{17} cm^{-2} and annealed at a temperature of 900°C (⟨220⟩ main reflection).

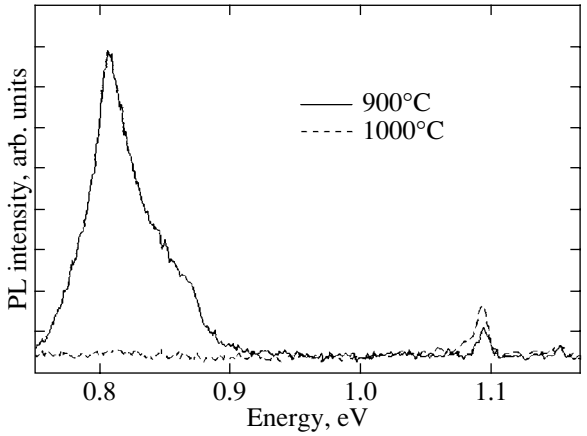

Fig. 4. Photoluminescence spectra of the samples implanted with an iron ion dose of 2×10^{17} cm^{-2} and annealed at temperatures of 900 and 1000°C.

In general, all the extra reflections observed in the diffraction pattern coincide with those typical of the β-$FeSi_2$ phase. The photoluminescence spectrum of this sample does not involve the band at 0.8 eV, even though it contains iron disilicide particles and dislocations.

Annealing of this sample at 900°C (sample **3**) results in the formation of a discontinuous layer composed of strongly misoriented grains with sizes from 0.1 to 0.7 μm (Fig. 3). Rounded particles 10–55 nm in size are observed against the background of grains and open regions. The density of particles is nonuniform and reaches a maximum on open regions (approximately 2×10^{10} cm^{-2}). A homogeneous dense dislocation network extends over the entire surface of the sample. Examination of the cross section of the sample revealed that grains are predominantly planar in shape; however, their thickness varies from 100 to 200 nm. A number of grains emerge on the surface. Other grains are covered with a relatively thick silicon layer containing particles. The three-dimensional dislocation network has a cellular structure and extends from the lower boundary of the iron disilicide layer into silicon to a depth of 400 nm. The diffraction pattern exhibits numerous extra reflections coinciding with those characteristic of the β-$FeSi_2$ phase. Isolated particles and individual grains are simultaneously observed in the dark-field images in extra reflections, which suggests their identical crystal structure. The photoluminescence spectrum of this sample exhibits an intense band at 0.807 eV (Fig. 4).

Annealing of the initial implanted sample at 1000°C leads to the formation of a discontinuous layer that has a similar shape but consists of large-sized single-crystal fragments. The density of rounded particles is substantially lower, and the dislocation structure remains almost unchanged. The diffraction pattern contains regularly arranged extra reflections typical of the α-$FeSi_2$ phase. No photoluminescence peak is observed in the range 0.7–1.1 eV in the spectrum of this sample (Fig. 4).

3.3. Implantation with a Dose of 4×10^{17} cm^{-2}

At an implantation dose of 4×10^{17} cm^{-2}, we also studied samples of three types, including the initial implanted sample and the samples annealed at 900 and 1000°C. The fundamental difference between these materials and those implanted with a dose of 2×10^{17} cm^{-2} resides in the fact that the continuous layer of iron disilicide in the former materials is formed even at the implantation stage. The other structural features of the materials remain approximately the same, including the formation of the β-$FeSi_2$ and α-$FeSi_2$ phases at the corresponding annealing temperatures. These materials (irrespective of the type of iron disilicide phase) are characterized by a complete absence of photoluminescence in the spectral range under study.

4. DISCUSSION

The results obtained demonstrate that the β-$FeSi_2$ phase crystallizes during implantation of iron ions into silicon at a temperature of 350°C. The misorientation of moiré fringes of the particles and the presence of a large number of irregularly arranged extra reflections in the diffraction pattern indicate that particles are randomly distributed over the silicon matrix. A similar distribution of β-$FeSi_2$ particles was observed by Grimaldi *et al.* [1] in the case when the implantation of iron ions was performed into a preliminarily amorphized silicon layer and was accompanied by solid-phase epitaxy at a temperature of 600°C followed by annealing at 800°C for 20 h. A comparison of these data allows us to assume that, in our samples, the implantation is attended by the amorphization of the surface silicon

layer and its recrystallization due to *in situ* annealing. It should be noted that this assumption is not consistent with the data obtained in [1], according to which the heating of the sample to 250–300°C in the course of implantation suppresses amorphization of the material. However, it is obvious that the β-$FeSi_2$ phase crystallizes upon *in situ* annealing at a temperature considerably below 800°C. The phase is formed through successive stages of nucleation of isolated particles and growth of large-sized particles to grains in the form of polyhedra with a pronounced crystallographic faceting. Nucleated particles are distributed throughout the depth of the implanted layer. In turn, grains are predominantly formed from particles in the layer bulk, grow, and emerge on the wafer surface.

The dislocation structure is formed concurrently with the formation of particles in the course of *in situ* annealing upon implantation. The mechanism of prismatic slip of dislocation loops under the action of crystallized particles is ruled out, because the volume per atom in the orthorhombic lattice of the β-$FeSi_2$ phase (12.5 Å) is smaller than that of silicon (20.0 Å). Moreover, it is clearly seen that the dislocation loop arrangement characteristic of this mechanism is absent in the TEM images. Most likely, the dislocation structure in the form of the dense three-dimensional network arises from the crossing of numerous *V*-shaped dislocations generated in a transition region between amorphous and crystalline silicon during the solid-phase epitaxy [5].

An analysis of the experimental data shows that there is a clear correlation between the luminescence of the material in the range of 0.8 eV and the structural features of the silicon layer prepared by ion-beam synthesis. The intense luminescence at 0.8 eV is observed only for samples **1**–**3** with a high density of particles and dislocations. As was noted above, the photoluminescence spectrum of sample **1** ($D_{Fe} = 1 \times 10^{16}$ cm^{-2}, 800°C) exhibits a band with the features characteristic of the photoluminescence line *D*1. The data on the temperature quenching of this band demonstrate that it is a superposition of lines of different natures. The above behavior of the photoluminescence intensity counts in favor of the dislocation origin of this band, because the temperature behavior of the intensity of the photoluminescence in the β-$FeSi_2$ phase does not depend on the wavelength [4]. The long-wavelength wing of the dislocation photoluminescence band is attributed to the recombination at dislocation–impurity complexes. In particular, as was established earlier in [6], dislocation–oxygen complexes make a contribution to this luminescence and the thermal stability of the long-wavelength wing is higher than that of the lines *D*1 and *D*2 owing to the higher ionization energy at the upper level. The short-wavelength wing of the photoluminescence band is also associated with dislocation and arises upon the formation of oxygen precipitates in the samples with dislocations.

For the majority of samples studied, the photoluminescence spectra do not exhibit bands in the energy range 0.75–1.1 eV, which is explained by different factors. First, these bands are absent in the spectra of all the initial implanted samples (*in situ* annealed at a temperature below 800°C) regardless of the dislocation density and the morphology of the β-$FeSi_2$ phase (isolated particles, discontinuous layer, continuous layer). The possible reason for the absence of the luminescence in these samples is the high density of nonradiative-recombination centers due to the generation of point defects in the course of implantation. Furthermore, the photoluminescence bands are not observed in the spectra of all samples containing the continuous layer of iron disilicide irrespective of the type of phase: β-$FeSi_2$ (900°C) or α-$FeSi_2$ (1000°C). It seems likely that the metallic conductivity inherent in the α-$FeSi_2$ phase is responsible for the absence of luminescence in the α-$FeSi_2$ samples with continuous and discontinuous layers. It is known that the presence of metallic precipitates leads to a drastic decrease in the lifetime [7, 8] and, as a consequence, to complete quenching of photoluminescence. In the case of the β-$FeSi_2$ phase, the reason for the absence of the luminescence in the sample with a continuous layer ($D_{Fe} = 4 \times 10^{17}$ cm^{-2}) remains unclear. As regards the dislocation photoluminescence lines in the spectrum of the same sample, we can suggest at least two possible reasons for their absence. The first reason is associated with the radiation-induced defects: the concentration of these defects at large doses can prove too high to ensure their annealing in 30 min. The second reason is the absorption of the main portion of exciting radiation in the layer of iron disilicide whose band gap is narrower than the band gap of silicon. The absence of exciton photoluminescence from the substrate layer below the boundary of penetration of iron ions confirms the profound effect of defects formed in the course of implantation.

The above inferences regarding the dependence of the quantum yield of photoluminescence on structural defects refer primarily to the silicon matrix and radiative-recombination centers in it and, to a considerably lesser extent, to particles of the β-$FeSi_2$ phase. Actually, apart from the excitation transfer from the silicon matrix to iron disilicide particles (whose mechanism still remains unknown), there exists a direct excitation of the β-$FeSi_2$ phase due to absorption of the exciting laser radiation. Therefore, if we assume that the β-$FeSi_2$ phase is at least partially responsible for the photoluminescence, it is hard to explain the absence of luminescence from the continuous layer of the β-$FeSi_2$ phase (see the data for the sample implanted with a dose of 4×10^{17} cm^{-2}). A serious argument in support of the dislocation nature of the observed luminescence is provided by the intensity distribution in the photoluminescence spectra of samples **1** and **2**, which were implanted with the same ion dose but were annealed at different temperatures. The half-width of the dominant lumines-

cence band of the sample annealed at 900°C is approximately 10 meV less than that of the sample annealed at 800°C. This is characteristic of the *D*1 line in the case of rapid cooling of the sample after annealing and is associated with the partial depinning of dislocations from oxygen precipitates. Moreover, the spectrum of sample **2** exhibits other lines of the dislocation photoluminescence, which also confirms the dislocation origin of the entire spectrum. Sample **3** ($D_{Fe} = 2 \times 10^{17}$ cm^{-2}, 900°C) contains similar structural elements and also the β-$FeSi_2$ polycrystalline discontinuous layer, which covers approximately 50% of the sample surface. It is interesting to note that the shape of the dominant band in the spectra of samples **1** and **3** turns out to be virtually identical, whereas the intensity of this band for sample **3** is approximately 40% lower than the intensity of the band for sample **1**. This can be explained by the fact that a considerable part of the dislocation network is shielded by the β-$FeSi_2$ polycrystalline layer. Otherwise (under the assumption that this band is assigned to the β-$FeSi_2$ phase), the band intensity should increase as a result of a substantial increase in the phase volume in sample **3**. Moreover, the same discontinuous layer does not shield β-$FeSi_2$ particles, because, in the silicon matrix, they are located above grains that do not emerge on the surface. These findings indirectly confirm the dislocation nature of the luminescence under investigation.

5. CONCLUSIONS

Thus, we investigated the formation of iron disilicide phases and elucidated the influence of the structural features on the photoluminescence in silicon layers implanted by iron ions. It was found that there is a correlation between the luminescence of the material in the range of 0.8 eV and the structural features of the silicon layer prepared by ion-beam synthesis. This luminescence was not revealed in the photoluminescence spectra of as-implanted samples (*in situ* annealed at a temperature below 800°C) and annealed samples with a continuous layer of iron disilicide. Intense luminescence was observed only in the samples with a high density of β-$FeSi_2$ particles and dislocations. These samples were prepared at iron ion doses of $\leq 2 \times 10^{17}$ cm^{-2} and annealing temperatures of 800–900°C. It was established that, in these materials, dislocations and their complexes with oxygen are primarily responsible for the luminescence in the range of 0.8 eV.

ACKNOWLEDGMENTS

This work was supported in part by the International Association of Assistance for the promotion of cooperation with scientists from the New Independent States of the former Soviet Union, project INTAS no. 2001-0194.

REFERENCES

1. M. G. Grimaldi, C. Bongiorno, C. Spinella, *et al.*, Phys. Rev. B **66**, 085319 (2002).
2. H. Lange, Phys. Status Solidi B **201**, 3 (1997).
3. G. G. Gumarov, V. Yu. Petukhov, V. A. Shustov, and I. B. Khaibullin, Nucl. Instrum. Methods Phys. Res. B **127–128**, 321 (1997).
4. L. Martinelli, E. Grilli, D. B. Migas, *et al.*, Phys. Rev. B **66**, 085320 (2002).
5. V. I. Vdovin, A. K. Gutakovskiĭ, Yu. A. Nikolaev, and M. G. Mil'vidskiĭ, Izv. Akad. Nauk, Ser. Fiz. **65** (2), 281 (2001).
6. E. A. Steinman and H. G. Grimmeiss, Semicond. Sci. Technol. **13**, 124 (1998).
7. A. Cavallini, M. Vandini, F. Corticelli, *et al.*, Inst. Phys. Conf. Ser. **134** (3), 115 (1993).
8. V. Kveder, M. Kittler, and W. Schröter, Phys. Rev. B **63**, 115208 (2001).

Translated by O. Borovik-Romanova

Physics of the Solid State, Vol. 46, No. 1, 2004, pp. 27–31. Translated from Fizika Tverdogo Tela, Vol. 46, No. 1, 2004, pp. 31–34.

PROCEEDINGS OF THE CONFERENCE DEDICATED TO O. V. LOSEV (1903–1942)

(Nizhni Novgorod, Russia, March 17–20, 2003)

Phonon-Assisted Radiative Electron–Hole Recombination in Silicon Quantum Dots

V. A. Belyakov*, V. A. Burdov*, D. M. Gaponova, A. N. Mikhaylov*, D. I. Tetelbaum*, and S. A. Trushin***

** Nizhni Novgorod State University, pr. Gagarina 23, Nizhni Novgorod, 603950 Russia*

*** Institute of the Physics of Microstructures, Russian Academy of Sciences, Nizhni Novgorod, 603950 Russia*

e-mail: burdov@phys.unn.ru

Abstract—The temperature dependence of the photoluminescence (PL) spectrum of silicon quantum dots (QDs) is studied both theoretically and experimentally, and the time of the corresponding electron–hole radiative recombination is calculated. The dependence of the recombination time on the QD size is discussed. The experiment shows that the PL intensity decreases by approximately 60% as the temperature increases from 77 to 293 K. The calculated characteristic recombination time has only a weak temperature dependence; therefore, the decrease in the PL intensity is associated primarily with nonradiative transitions. It is also shown that the phonon-assisted radiation is much more efficient than the zero-phonon emission. Moreover, the zero-phonon recombination time depends on the QD radius R as R^8, whereas the phonon-assisted recombination time depends on this radius as R^3. *© 2004 MAIK "Nauka/Interperiodica".*

In the past decade, considerable attention has been given to the investigation of nanostructures containing silicon quantum dots (QDs). This interest is associated, in particular, with the ability of Si nanocrystals to emit electromagnetic energy efficiently at room temperature. The experimentally obtained photoluminescence (PL) spectra have a peak at energies from 1.4 to 1.8 eV, depending on the QD size. In this case, the photoluminescence itself is associated either with direct electron–hole interband recombination or with interband transitions involving the interface states. Along with the radiative transitions, nonradiative transitions (for example, Auger processes) take place in the quantum dots. For this reason, the PL intensity, proportional to the quantum efficiency of the photon generation, is usually determined by the following formula (see, e.g., [1]):

$$I \propto \frac{\tau_{nr}}{\tau_{nr} + \tau_r}, \qquad (1)$$

where τ_r and τ_{nr} are the characteristic times of the radiative and nonradiative transitions, respectively. Equation (1) determines the photoluminescence as a function of temperature and of the nanocrystal size. Therefore, it is necessary to know both τ_r and τ_{nr}.

The dependence of the photoluminescence on temperature and QD size has been the subject of many experimental studies (see, e.g., [1–7]). Most of these papers reported a negligible temperature dependence of the photoluminescence; namely, the PL intensity observed at room temperature was only 2–3 times smaller than that at 10 K. However, there is some scatter in the experimental results obtained by different authors, which appears to be due to differences in the nanocrystal formation and experimental conditions.

In this paper, we study the PL spectra and the times of the electron–hole recombination for the nc-Si : SiO_2 system produced through implantation of Si ions followed by annealing. SiO_2 layers were thermally grown on a Si substrate in the "dry–wet–dry" cycle. Then, they were irradiated with Si^+ ions (150 keV, 10^{17} cm^{-2}) and annealed in a dry nitrogen flow at 1000°C for two hours. The photoluminescence was excited by an Ar laser (λ = 488 nm). The PL spectra were measured at 293 and 77 K. It can be seen from Fig. 1 that the luminescence peak at ~1.6 eV (usually associated with the Si nanocrystals) observed at 77 K is about 1.6 times higher than that at 293 K.

According to Eq. (1), the PL intensity does not depend on temperature in the case of $\tau_r \ll \tau_{nr}$. Thus, the difference between the experimentally obtained intensities at 77 and 293 K indicates that the condition $\tau_r \ll \tau_{nr}$ is not satisfied in the range 77 K < T < 293 K. Hence, either τ_r and τ_{nr} are of the same order of magnitude or the probability of the nonradiative transitions is much larger than the probability of the radiative transitions.

In order to clarify the question, theoretical analysis is required. For this purpose, we analytically calculated the probability of radiative interband recombination in a quantum dot. It was shown in [8, 9] that, although the probability of the conduction-to-valence band electron transition with single-photon emission is nonzero, it is fairly small (only ~10^3 s^{-1} for a 4-nm quantum dot) in comparison with the probability of nonradiative transi-

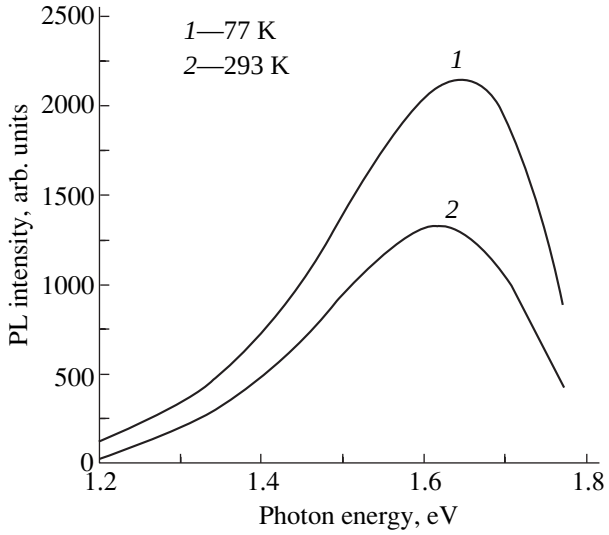

Fig. 1. PL spectrum of SiO_2 layers irradiated with Si^+ ions. Radiation dose 10^{17} cm^{-2}. The samples were annealed at 1000°C for two hours.

tions. In what follows, it is shown that the phonon-assisted radiative transitions (in which single-photon emission is accompanied by the emission or absorption of at least one phonon) are much more probable.

Let us consider a Si nanocrystal (QD) of radius R implanted into an amorphous SiO_2 layer, and let us assume that the QD electron subsystem interacts with the electromagnetic field and vibrations of the crystal lattice. The total phonon-assisted electron–hole recombination rate, equal to the reciprocal of the radiative transition time, is determined in the second-order perturbation theory as

$$\tau_{cv}^{-1} = \frac{2\pi}{\hbar}\sum_{\mathbf{k},\sigma}\sum_{\mathbf{q},\gamma}\left|\sum_{a}\frac{W_{ia}U_{af}+U_{ia}W_{af}}{\varepsilon_a-\varepsilon_i}\right|^2 \times[\delta(E_f+\hbar\omega_\sigma(\mathbf{k})+\hbar\nu_\gamma(\mathbf{q})-E_e) + \delta(E_f+\hbar\omega_\sigma(\mathbf{k})-\hbar\nu_\gamma(\mathbf{q})-E_e)]. \quad (2)$$

Here, the matrix elements of the electron–photon ($\hat{W}$) and electron–phonon ($\hat{U}$) interaction operators are calculated between the initial i (or the final f) and an intermediate state a; E_h and E_e are the energies at the valence band top and the conduction band bottom, respectively (below, these energies are determined by solving the Schrödinger equation); and ε_a and ε_i are the total energies of the intermediate and initial states, respectively, including not only the energies of the electrons but also the energies of the photons and phonons. The photon and phonon frequencies are denoted as $\omega_\sigma(\mathbf{k})$ and $\nu_\gamma(\mathbf{q})$, respectively, and the operators $\hat{W}$ and $\hat{U}$ are given by the relationships

$$\hat{W} = \sum_{\mathbf{k},\sigma}\sqrt{\frac{2\pi\hbar e^2}{m_0^2\omega_\sigma(\mathbf{k})V}}(\hat{c}_{\mathbf{k},\sigma}+\hat{c}^+_{\mathbf{k},\sigma})(\mathbf{e}_{\mathbf{k},\sigma}\hat{\mathbf{p}}), \quad (3)$$

$$\hat{U} = -\sum_{\mathbf{q},\gamma}\sum_{n,m}(S_{nm}(\mathbf{q},\gamma)\hat{a}_n^+\hat{a}_m\hat{b}_{\mathbf{q},\gamma} + S_{nm}(-\mathbf{q},\gamma)\hat{a}_n^+\hat{a}_m\hat{b}^+_{\mathbf{q},\gamma}). \quad (4)$$

Here, $\hat{c}^+_{\mathbf{k},\sigma}$ ($\hat{c}_{\mathbf{k},\sigma}$), $\hat{a}^+_{\mathbf{k},\sigma}$ ($\hat{a}_{\mathbf{k},\sigma}$), and $\hat{b}^+_{\mathbf{k},\sigma}$ ($\hat{b}_{\mathbf{k},\sigma}$) are the creation (annihilation) operators of photons, electrons, and phonons, respectively; $-e$ and m_0 are the charge and mass of a free electron; $\hat{p}$ is the electron momentum operator; and V is the volume of a photon resonator. The quantity $S_{nm}(\mathbf{q},\gamma)$ is determined by

$$S_{nm}(\mathbf{q},\gamma) = \mathbf{e}_{\mathbf{q},\gamma}\sqrt{\frac{\hbar}{2MN\nu_\gamma(\mathbf{q})}}\int d\mathbf{r}\Psi_n^*\Psi_m\exp(i(\mathbf{qr}))\nabla U_0, \quad (5)$$

where M is the mass of a Si atom, N is the number of unit cells in the nanocrystal, Ψ_m is the electron wave function in state m, and U_0 is the lattice potential. The vectors $\mathbf{e}_{\mathbf{k},\sigma}$ and $\mathbf{e}_{\mathbf{q},\gamma}$ define the direction of oscillations of the electric field and the atoms in the crystal lattice, respectively.

The initial state corresponds to an electron–hole pair being in the ground state and an ensemble of photons and phonons, whose distribution over $\mathbf{k}$, σ and $\mathbf{q}$, γ is described by the Bose–Einstein statistics. In the final state, the valence band is completely occupied and the conduction band is empty. The number of photons in the final state always increases by one, whereas the number of phonons is either larger or smaller by one than that in the initial state.

In order to find the electron wave functions in the envelope-function approximation, we must solve the equation

$$\hat{H}_{ij}F_j(\mathbf{r}) = EF_i(\mathbf{r}). \quad (6)$$

Here, $\hat{H}_{ij}$ is a matrix differential operator, $F_j(\mathbf{r})$ is the envelope function, and E is the energy. In the absence of spin–orbit interaction (which is weak in silicon), the operator $\hat{H}_{ij}$ in the valence band is the following 3×3 matrix [10]:

$$\hat{H}_{ij}^{(h)} = \delta_{ij}\left(\hat{H}_{0h}+\frac{\hbar^2}{2m_0}\frac{L-M}{3}(\hat{\mathbf{k}}^2-3\hat{k}_j^2)\right) + (\delta_{ij}-1)\frac{\hbar^2}{2m_0}N\hat{k}_i\hat{k}_j, \quad (7)$$

where L, M, and N are equal to 6.8, 4.43, and 8.61, respectively [11], and $\hat{H}_{0h}$ is the isotropic operator obtained by averaging the Hamiltonian (7) over the angles

$$\hat{H}_{0h} = -\frac{\hbar^2}{2m_h}\hat{\mathbf{k}}^2. \quad (8)$$

Here, $m_h = 3m_0/(L + 2M)$ is the isotropic effective hole mass, equal to $0.19m_0$. The wave vector and the energy are measured from their values at the Γ point.

In the conduction band, the Hamiltonian $\hat{H}_{ij}$ should be written as a 2×2 matrix in the vicinity of one of the three physically nonequivalent X points of the Brillouin zone [12]. In the [001] direction, for example, the matrix elements of the Hamiltonian are given by

$$\hat{H}_{11}^{(e)} = \hat{H}_{22}^{(e)} = \hat{H}_{0e} + \frac{\hbar^2}{6}\left(\frac{1}{m_t} - \frac{1}{m_l}\right)\hat{k}_x\hat{k}_y + \frac{i\hbar^2 k_0}{m_l}\hat{k}_z,$$
$$\hat{H}_{12}^{(e)} = (\hat{H}_{21}^{(e)})^+ = \hbar^2\left(\frac{1}{m_t} - \frac{1}{m_0}\right)\hat{k}_x\hat{k}_y + \frac{i\hbar^2 k_0}{m_l}\hat{k}_z, \quad (9)$$

where the wave vector is measured from the X point; m_t and m_l are the transverse and longitudinal effective masses, respectively; $k_0 \approx 0.144 \times 2\pi/a_0$ is the distance between the X point and the nearest energy minimum in the $\mathbf{k}$ space; and a_0 is the lattice constant. The isotropic averaged Hamiltonian $\hat{H}_{0e}$ is

$$\hat{H}_{0e} = \Delta_{X\Gamma} + \frac{\hbar^2}{2m_e}\hat{\mathbf{k}}^2, \quad (10)$$

where $m_e = 3m_l m_t/(2m_l + m_t)$ is the isotropic effective electron mass and $\Delta_{X\Gamma} = 1.215$ eV [12] is the energy difference between the conduction band at the X point and the valence band at the Γ point.

Equation (6) was solved in [13] in the approximation of infinitely high barriers by using the operators given by Eqs. (7)–(10). This made it possible to find the wave functions and energies of the ground states of the electrons and holes (they are assumed to be known below). The ground-state energy in the valence band is

$$E_h = -\frac{\hbar^2\pi^2}{2m_h R^2}. \quad (11)$$

This level remains triply degenerate (the spin is not taken into account); the corresponding wave functions are

$$\Psi_{h1} = v_x(\mathbf{r})|0\rangle, \quad \Psi_{h2} = v_y(\mathbf{r})|0\rangle, \quad \Psi_{h3} = v_z(\mathbf{r})|0\rangle, \quad (12)$$

where $v_x(\mathbf{r})$, $v_y(\mathbf{r})$, and $v_z(\mathbf{r})$ are the Bloch functions of the bulk crystal at the Γ point and $|0\rangle$ is the s-type envelope function, which is the same for these three states. This function can be found as the solution of the Schrödinger equation with the isotropic Hamiltonian (8) corresponding to its ground state.

Without considering the spin, the lowest level in the conduction band is sixfold degenerate and has the energy

$$E_e = \Delta_{X\Gamma} + \frac{E_0 + E_1 - Q}{2} - \sqrt{\frac{(E_1 - E_0 - Q)^2}{4} + J^2}, \quad (13)$$

where E_0 and E_1 are the energies of the s and p states of the isotropic Hamiltonian (10) and are equal to $\hbar^2\pi^2/2m_eR^2$ and $\hbar^2\mu^2/2m_eR^2$, respectively. Here, μ is the first root of the equation $x\cos x = \sin x$ and the quantities J and Q are

$$J = \frac{\hbar^2 k_0}{\sqrt{3}m_l R}\frac{2\pi\mu}{\mu^2 - \pi^2}, \quad Q = \frac{\hbar^2}{R^2}\frac{2\mu^2}{15}\left(\frac{1}{m_t} - \frac{1}{m_l}\right).$$

The corresponding wave functions can be chosen in the following form (as an example, we cite only two of the six wave functions corresponding to the X point in the [001] direction; the other functions can be built in the same way):

$$\Psi_{e1} = \cos(\lambda)u_{1z}(\mathbf{r})|0\rangle + \sin(\lambda)u_{2z}(\mathbf{r})|z\rangle,$$
$$\Psi_{e2} = \cos(\lambda)u_{2z}(\mathbf{r})|0\rangle - \sin(\lambda)u_{1z}(\mathbf{r})|z\rangle, \quad (14)$$

where $u_{1z}(\mathbf{r})$ and $u_{2z}(\mathbf{r})$ are the Bloch functions of the bulk crystal at the X point and the parameter λ is determined by the relationships

$$\cos 2\lambda = \frac{E_1 - E_0 - Q}{\sqrt{(E_1 - E_0 - Q)^2 + 4J^2}},$$
$$\sin 2\lambda = \frac{2J}{\sqrt{(E_1 - E_0 - Q)^2 + 4J^2}}.$$

It should be noted that an attempt to calculate the probability of the interband phonon-assisted transition has already been made [14]. However, the calculation of the envelope functions and electronic energies in that paper was in error and gave rise to recombination times that were overestimated by more than order of magnitude in comparison with our results.

The reciprocal time of the phonon-assisted electron–hole recombination calculated from Eq. (2) using wave functions (12) and (14) is

$$\tau_{cv}^{-1} = \frac{\Lambda e^2 \varepsilon^{3/2}\hbar k_0^2 \cos^2\lambda}{24\pi^2 m_l^2 Mc^3(E_e - E_h)}\left(\frac{a_0}{R}\right)^3 \frac{\coth(\hbar\nu/2k_B T)}{\nu}, \quad (15)$$

where $a_0 = 0.543$ nm is the silicon lattice constant, k_B is Boltzmann's constant, T is the temperature, $\varepsilon \approx 12$ is the dielectric constant, ν is the frequency of transverse optical (TO) phonons at the Brillouin zone boundary at

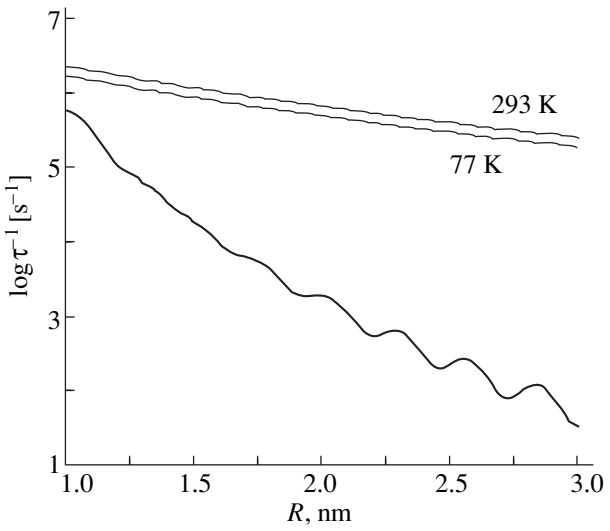

Fig. 2. The probability of electron–hole recombination as a function of the QD radius. The upper curves correspond to phonon-assisted transitions, and the lower curve, to zero-phonon transitions.

the X point ($\hbar\nu \approx 57.5$ meV [15]), and the parameter Λ determines the intensity of the electron–phonon interaction and is equal to

$$\Lambda = \frac{53}{6}\sum_{i=1}^{2}\sum_{j=1}^{3}\sum_{s=x,y}\left|\frac{2\pi}{m_0 a_0}(P_z P_s)_{ij} + \left(\frac{\hbar^2}{2m_0}\left(\frac{2\pi}{a_0}\right)^2 - \Delta_{X\Gamma}\right)\frac{(P_s)_{ij}}{\hbar}\right|^2. \quad (16)$$

The numerical coefficient 53 is a result of integration over phonon wave vectors in Eq. (2), and 1/6 of the double sum over i and j is the average over all the possible degenerate initial and final states. The matrix elements are determined by the formula

$$B_{ij} = \frac{1}{V_0}\int_{V_0} d\mathbf{r}\, u_i^*(\mathbf{r})\hat{B}v_j(\mathbf{r}),$$

where integration is performed over the unit cell volume $V_0 = a_0^3/4$ and the functions $v_j(\mathbf{r})$ are defined by Eq. (12). The functions $u_i(\mathbf{r})$ are the periodical parts of the corresponding Bloch function at the X point and differ from the functions $u_{iz}(\mathbf{r})$ in Eq. (14) by the absence of the exponential factor. In the further numerical estimates, it is assumed that both terms under the absolute-value sign in Eq. (16) are equal to each other and $(P_s)_{ij}^2/2m_0 = (4/3)$ eV for any value of i and j [14].

It should also be noted that not only TO phonons but also longitudinal optical and transverse acoustic phonons are excited in the bulk silicon. However, according to [14, 15], the intensity of their interaction with electrons is one and two orders of magnitude smaller, respectively, than that for TO phonons. Assuming that the QD finite size cannot change the results drastically, we took into account only the TO-phonon contribution in Eq. (15).

For the reciprocal of the zero-phonon radiative electron–hole recombination time, we have

$$\tau_0^{-1} = \frac{e^2\varepsilon^{3/2}P^2(E_e - E_h)}{12\pi^4 m_0^2\hbar^2 c^3}\left(\frac{a_0}{R}\right)^8(\cos^2(\lambda)\cos^2(2\pi R/a) + 3\mu^2/\pi^2\sin^2(\lambda)\sin^2(2\pi R/a)), \quad (17)$$

where the parameter P is determined by the Fourier amplitudes of the Bloch functions; its value is close to $(P_s)_{ij}$. A comparison of Eqs. (15) and (17) reveals two important differences between the phonon-assisted and zero-phonon radiative transitions.

First, the recombination time for phonon-assisted transitions depends on the QD size much more weakly than that for zero-phonon transitions, namely, as R^3 instead of R^8. Thus, we have $\tau_{cv}^{-1} \gg \tau_0^{-1}$ and this inequality becomes much more stronger as the QD size R grows (see Fig. 2). Second, the recombination time corresponding to phonon-assisted transitions depends (though only weakly) on the temperature (Fig. 2); namely, as the temperature increases from 77 to 293 K, the time τ_{cv} decreases by approximately 20–25%.

Since the inequality $\tau_{cv} \ll \tau_0$ is satisfied in a wide range of QD sizes ($R \geq 1$ nm), it is obvious that the phonon-assisted photoluminescence is typical of QDs. Therefore, in Eq. (1), which determines the quantum efficiency and PL intensity, the recombination time τ_r should be replaced by τ_{cv} rather than by τ_0. According to Eq. (1), the observed 1.6 times decrease in the PL intensity can be achieved only if the nonradiative transition time τ_{nr} diminishes even more drastically. This means that the nonradiative transitions make the main contribution to the electron–hole recombination.

ACKNOWLEDGMENTS

This work was supported by the program "Universities of Russia" (project no. UR.01.01.057).

REFERENCES

1. S. Takeoka, M. Fujii, and S. Hayashi, Phys. Rev. B **62** (24), 16820 (2000).
2. Y. Kanemitsu and S. Okamoto, Phys. Rev. B **56** (24), 15561 (1997).
3. Y. Kanemitsu, Phys. Rev. B **53** (20), 13515 (1996).
4. Y. Kanemitsu, N. Shimizu, T. Komoda, *et al.*, Phys. Rev. B **54** (20), 14329 (1996).
5. T. Shimizu-Iwayama, S. Nakao, and K. Saitoh, Appl. Phys. Lett. **65** (14), 1814 (1994).

6. G. A. Kachurin, I. E. Tischenko, K. S. Zhuravlev, *et al.*, Nucl. Instrum. Methods Phys. Res. B **122**, 571 (1997).
7. D. I. Tetelbaum, S. A. Trushin, V. A. Burdov, *et al.*, Nucl. Instrum. Methods Phys. Res. B **174**, 123 (2001).
8. T. Takagahara and K. Takeda, Phys. Rev. B **46** (23), 15578 (1992).
9. D. I. Tetelbaum, V. A. Burdov, S. A. Trushin, and A. N. Mikhaylov, in *Proceedings of 10th International Symposium on Nanostructures: Physics and Technology* (St. Petersburg, 2002), p. 206.
10. A. I. Ansel'm, *Introduction to the Theory of Semiconductors* (Nauka, Moscow, 1978).
11. M. Voos, Ph. Uzan, C. Delalande, *et al.*, Appl. Phys. Lett. **61** (10), 1213 (1992).
12. A. A. Kopylov, Fiz. Tekh. Poluprovodn. (Leningrad) **16** (12), 2141 (1982) [Sov. Phys. Semicond. **16**, 1380 (1982)].
13. V. A. Burdov, Zh. Éksp. Teor. Fiz. **121** (2), 480 (2002) [JETP **94**, 411 (2002)].
14. M. S. Hybertsen, Phys. Rev. Lett. **72** (10), 1514 (1994).
15. O. J. Glembocki and F. H. Pollak, Phys. Rev. B **25** (2), 1193 (1982).

Translated by A. Poushnov

Physics of the Solid State, Vol. 46, No. 1, 2004, pp. 32–34. Translated from Fizika Tverdogo Tela, Vol. 46, No. 1, 2004, pp. 35–38.

PROCEEDINGS OF THE CONFERENCE DEDICATED TO O. V. LOSEV (1903–1942)

(Nizhni Novgorod, Russia, March 17–20, 2003)

Formation of Two-Dimensional Photonic-Crystal Structures in Silicon for Near-Infrared Region Using Fine Focused Ion Beams

A. F. Vyatkin, E. Yu. Gavrilin, Yu. B. Gorbatov, V. V. Starkov, and V. V. Sirotkin

Institute of Microelectronic Technology and Ultra-High-Purity Materials, Russian Academy of Sciences, Chernogolovka, Moscow oblast, 142432 Russia

e-mail: Vyatkin@ipmt-hpm.ac.ru

Abstract—One of the two variants of producing two-dimensional photonic crystals in silicon is the formation of ordered macropore structures in a silicon substrate. The characteristic pore dimensions (the diameter and the wall thickness between pores) determine the wavelength range in which such a pore structure exhibits the properties of a photonic crystal. For the near-infrared region, these dimensions approach 1 μm or fall in a submicron region. An ordered structure of macropores with such dimensions is formed in this work using fine focused ion beams to provide the stimulating effect of implanted ions on pore nucleation in given sites on the silicon substrate surface. Pores are shown to nucleate at sites subjected to ion irradiation even at a low implantation dose (2×10^{13} ion/cm^2). A model describing the orienting effect of ion irradiation on pore nucleation is proposed.

1. INTRODUCTION

As elements for micro- and nanophotonics, photonic crystals are very promising materials, especially in the near-infrared region, used in modern communication equipment. Silicon-based photonic crystals are important in this connection, since the use of silicon and its highly developed microelectronic technology makes it possible to realize integrated solutions for which both microelectronic and optical schemes can be arranged on one chip.

Two-dimensional photonic crystals in silicon are ordered structures of macropores on a silicon substrate. The characteristic pore dimensions (the diameter and the wall thickness between pores) determine the operating wavelength range of such a porous structure. For the near-infrared region, these dimensions approach one micrometer or fall in a submicron region [1]. It is difficult to form ordered macroporous silicon with such pore dimensions by the methods used at present to produce macroporous silicon having pores with a high aspect ratio, namely, plasmochemical etching through masks and electrochemical deep anodic etching. It is also known that, for example, irradiation of the *n*-Si surface with boron ions terminates anodic etching in irradiated sites [2] and this was attributed to the inversion of the conduction type in these zones.

In this work, we try to find a new solution to this complex problem by using fine focused ion beams to favor the stimulating effect of implanted ions on pore nucleation in given sites on the silicon substrate surface. Since ion beams can be focused to nanoscale sizes, we can expect that their application will solve the problem of formation of photonic crystals for the near-infrared region.

2. EXPERIMENTAL

We showed earlier [3] that the anodic etching of silicon is a two-stage process consisting of pore nucleation and growth stages. The pore growth rate is specified by the parameters of anodic etching, such as the current density, voltage, electrolyte composition, and temperature, whereas the density of nucleating pores is determined by processes that are still unclear. In this work, we created an ordered structure of implanted sites on the silicon surface with fine focused ion beams. Then, such an irradiated silicon wafer was subjected to deep anodic etching.

For experiments, we used (100) *p*-Si wafers with a resistivity of 5–8 Ω cm. The energy of singly charged gallium ions was 25 keV. The diameter of an ion beam on the sample surface was 100 nm, and the current density was about 1 A/cm^2. The structures were exposed to an ion beam moving across the sample surface with the PROXY computer program. The exposure dose was determined by the exposure time of the beam at a point and was varied from 2×10^{13} to 6×10^{14} cm^{-2}. The maximum dose was chosen to ensure minimum sputtering of the surface at irradiated sites (the maximum thickness of a sputtered layer at a dose of 6×10^{14} cm^{-2} was calculated to be smaller than 0.5 nm). The minimum dose (2×10^{13} cm^{-2}) was dictated by the device. The minimum exposure time at a point was 10 μs. The size of an exposed site was 100 nm, and the center-to-center

1063-7834/04/4601-0032$26.00

distance of the sites was varied from 1 to 5 μm. The process of deep anodic etching was performed at room temperature in a solution of hydrofluoric acid in dimethylformamide (DMF) (the volume ratio was HF : DMF = 1 : 9) at a current density of 9 mA cm^{-2}. The etching depth, geometrical dimensions of pores, and interpore spacing were determined using optical and electron-microscopic images taken from ordered and disordered regions of longitudinal and transverse polished sections of samples.

3. EXPERIMENTAL RESULTS

The deep anodic etching of the silicon samples preirradiated with gallium ions showed that pores nucleated only in irradiated sites. When studying the samples irradiated to various doses and then etched, we did not find any dependence of pore formation on the irradiation dose over the whole dose range. Figure 1 shows an optical photograph of the sample surface with arranged pores. It is seen that pores are arranged regularly with a period of 2.4 μm in the region preirradiated with a fine focused ion beam (Fig. 1, left-hand side).

Beginning from a certain value of the pore center-to-center distance, an increase in this value lead to the formation of pores not only in the implanted sites but also between them due to deep anodic etching. This effect is called "the proximity effect" and is described in [3]. A decrease in the interpore distance to 1 μm results in a number of implanted sites falling out of the ensemble of growing pores; i.e., part of the pores with a center distance of 1 μm that form in the initial stage of etching cease to grow upon further deep anodic etching. Moreover, the center distance tends to 2.4 μm. It should be noted that a center distance of 2.4 μm is characteristic of spontaneous nonuniform deep anodic etching of a silicon sample having the same resistivity (Fig. 1, right-hand side).

However, the initiating effect of ion irradiation on pore nucleation manifests itself only if the depth of doping silicon with a gallium impurity exceeds a certain critical value. For implantation of 25-keV gallium ions, the entire depth profile of the doping impurity in the silicon substrate lies within ~50 nm. If the ion irradiation is carried out through an oxide layer ~20 nm thick (which means a decrease in the depth of doping), the stimulating effect of the ion irradiation disappears and the process of pore nucleation and growth becomes spontaneous and random.

4. DISCUSSION OF THE RESULTS

The orienting effect of the focused ion beam on the formation of a pore ordered structure can be interpreted in terms of the following scheme of the process of electrochemical etching. It is well established that electrochemical etching of silicon is accompanied by macropore formation under the conditions of a deficiency of charge carriers supplied to the site of electrochemical reaction. Therefore, in the initial stage, etching takes place at "weak" sites in the first atomic layer, e.g., at sites where doping impurities are located. The removal of an atom from the first layer facilitates etching of the neighboring atoms in the first layer. The process proceeds in the first layer until a doping atom of the second layer becomes uncovered. At that instant, etching extends to the second atomic layer. Then, the process repeats itself in the third and the following layers. It is obvious that not all of the pore nucleation centers have the same rate of propagation into the crystal, since the probability of meeting a doping atom in the next layer is different for each nucleating pore. For this reason, only part of the nucleating pores have a chance to extend deep into the crystal.

This scheme of electrochemical etching allows us to develop a computer model for this process. The physical principles forming the basis for this model are the following.

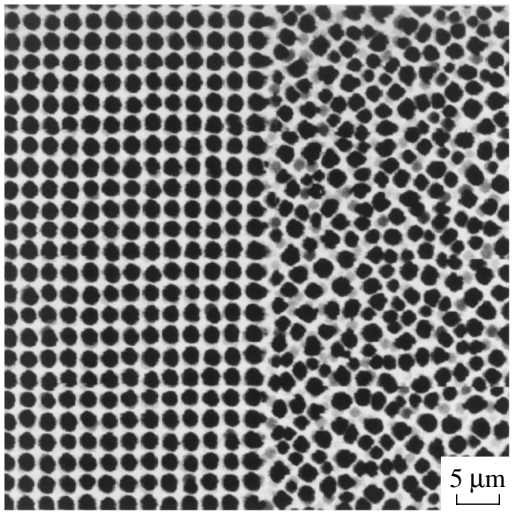

Fig. 1. Optical photograph of the silicon wafer surface subjected to deep anodic etching.

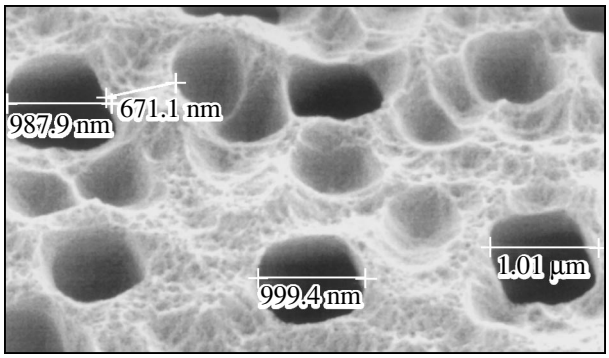

Fig. 2. Scanning electron microscope image of the silicon wafer surface subjected to deep anodic etching under the conditions of spontaneous pore nucleation.

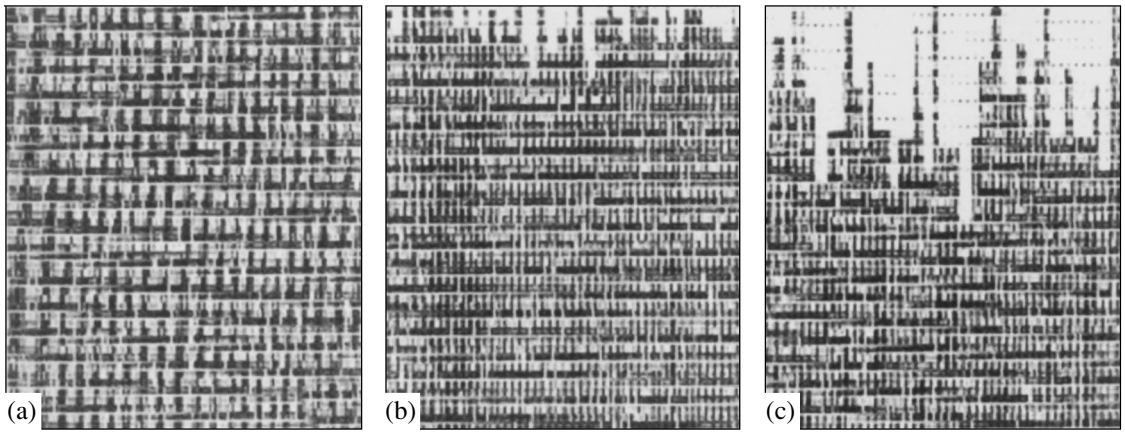

Fig. 3. Two-dimensional representation of three sequential stages of deep anodic etching: (a) initial stage, (b) when the etching front reaches the tenth monolayer of silicon, and (c) when the etching front reaches the 20th monolayer. Open symbols represent impurity atoms, and solid symbols are silicon atoms.

(1) Macropores form in silicon under the conditions of a charge-carrier deficiency at the silicon–electrolyte interface; therefore, the process of etching silicon starts only in preferred sites on the wafer surface.

(2) These sites are assumed to be the sites where impurities located.

(3) The removal of an impurity to the electrolyte solution (etching-out of impurities) opens up possibilities for the lateral extension of silicon etching at a significant rate in the layer from which the impurity was removed.

(4) Once the lateral front of silicon etching reaches a site of an impurity in the second layer, the etching process extends immediately to this layer and proceeds laterally in it. The rate of the lateral motion of the etching front is equal to the rate of lateral etching in the first layer until a two-atom step forms. The rate of lateral etching of a two-atom step is taken to be an order of magnitude smaller than the rate of lateral etching of a one-atom step.

(5) When an impurity becomes uncovered in the third layer, the process of etching extends to the third layer, and so on. The rate of lateral etching of a three-atom step and each next step is taken to be an order of magnitude smaller than that of the previous step.

(6) This scenario is valid only to a certain depth of etching a pore in silicon, i.e., only for the initial stage of etching. Once all charge carriers supplied to the silicon–electrolyte interface are concentrated at the bottom of the pores formed, the process of etching passes into the stage of pore growth and its parameters are specified by other characteristics, such as the current density, bias voltage, electrolyte composition, and the temperature of the silicon–electrolyte system.

The model proposed implies that not all of the impurity centers on the silicon wafer surface will be sources for forming pores. A pore will grow into the bulk of silicon if the doping atom on the wafer surface on which the pore nucleated is such that the probability of meeting another doping atom in each next layer in the direction normal to the surface is higher than a certain critical value, depending on the impurity concentration in the silicon crystal. Therefore, in the case of random spontaneous pore formation on the silicon wafer surface, an ensemble of undeveloped pores (craters) will arise with a small number of pores extended deep into the silicon wafer. This behavior is observed experimentally on real silicon wafers subjected to anodic etching (Fig. 2). The same result is predicted by the model described above (Fig. 3).

5. CONCLUSIONS

(1) We have shown that fine focused ion beams can be used to form ordered macropore structures in silicon.

(2) We have proposed a model that describes the initial stage of macropore formation in silicon. This model implies that implantation from a fine focused ion beam leads to a local increase in the impurity concentration in an irradiated zone and, hence, to an increased probability of meeting a doping atom in each next layer in this zone, which provides pore growth deep into the bulk of silicon at this site (according to the model proposed).

(3) The simulation results agree qualitatively with the experimental data, which lends support to the validity of the fundamental tenets of this model.

REFERENCES

1. T. F. Krauss and R. M. De La Rue, Prog. Quantum Electron. **23**, 51 (1999).
2. E. V. Astrova and T. N. Vasunkina, Fiz. Tekh. Poluprovodn. (St. Petersburg) **36** (5), 593 (2002) [Semiconductors **36**, 564 (2002)].
3. A. Vyatkin, V. Starkov, V. Tzeitlin, *et al.*, J. Electrochem. Soc. **149** (1), G7 (2002).

Translated by K. Shakhlevich

Physics of the Solid State, Vol. 46, No. 1, 2004, pp. 35–39. Translated from Fizika Tverdogo Tela, Vol. 46, No. 1, 2004, pp. 39–43.

PROCEEDINGS OF THE CONFERENCE DEDICATED TO O. V. LOSEV (1903–1942)

(Nizhni Novgorod, Russia, March 17–20, 2003)

Effect of the Postimplantation-Annealing Temperature on the Properties of Silicon Light-Emitting Diodes Fabricated through Boron Ion Implantation into *n*-Si

N. A. Sobolev*, A. M. Emel'yanov*, E. I. Shek*, and V. I. Vdovin**

**Ioffe Physicotechnical Institute, Russian Academy of Sciences, Politekhnicheskaya ul. 26, St. Petersburg, 194021 Russia*
e-mail: nick@sobolev.ioffe.rssi.ru

***Institute for Chemical Problems of Microelectronics, Bol'shoĭ Tolmachevskiĭ per. 5, Moscow, 119017 Russia*

Abstract—The effect of the temperature of postimplantation annealing on the electroluminescence and the electrophysical and structural properties of light-emitting diodes fabricated by the implantation of boron ions into *n*-Si with a resistivity of 0.5 and 500 Ω cm is studied. All spectra contain strong electroluminescence (EL) peaks associated with band-to-band radiative transitions. An increase in the annealing temperature from 700 to 1100°C is accompanied by a monotonic increase in the quantum efficiency for the dominating EL peak and in the effective minority-carrier lifetime in the base of the light-emitting diodes and by the transformation of extended structural defects. Analysis of the experimental data shows that the extended structural defects formed are most likely to affect the EL properties via the formation or gettering of the radiative or nonradiative recombination centers rather than via preventing the removal of charge carriers to nonradiative recombination centers. The maximum internal quantum efficiency is reached after annealing at 1100°C (where extended structural defects are absent) and is estimated to be 0.4% at 300 K. © *2004 MAIK "Nauka/Interperiodica".*

1. INTRODUCTION

Luminescence in single-crystalline silicon (*c*-Si) caused by band-to-band transitions or defects is studied for creating new optoelectronic devices. It was shown in [1] that efficient silicon light-emitting diodes (LEDs) with a band-to-band spectrum could be fabricated by using a relatively simple method of boron ion implantation into *n*-Si followed by annealing at 1000°C. Those authors assumed that high quantum efficiency was related to the formation of dislocation loops with a certain density and size in a thin diode-base layer adjacent to the *p–n* junction. Such loops are assumed to induce local stress fields that modify the band structure of a crystal, thus preventing the removal of charge carriers to nonradiative recombination centers and favoring their intense band-to-band radiative recombination. To confirm or refute these model concepts, it is necessary to study luminescence in *c*-Si having extended defects of various density, size, and physical nature. The spectrum of extended defects that form in *c*-Si as a result of ion implantation and annealing can be controlled by varying the temperature and atmosphere of postimplantation annealing.

In this work, we study 1.0- to 1.6-μm electroluminescence (EL) and structural defects in *p–n* structures formed upon implantation of boron ions into single-crystalline *n*-Si wafers (having significantly different levels of doping with phosphorus) and subsequent annealing.

2. EXPERIMENTAL

The *p–n* structures were formed through the implantation of boron ions (energy $E = 40$ keV, dose $D = 1 \times 10^{15}$ cm^{-2}) into (100) *n*-Si KÉF-0.5 and KÉF-500 wafers 370 and 410 μm thick, respectively. To create ohmic contact, phosphorus ions ($E = 75$ keV, $D = 1 \times 10^{15}$ cm^{-2}) were implanted into the back side of the wafers. Isochronous 20-min postimplantation annealings were performed in an argon atmosphere at a temperature T_{ann}, and then the samples were furnace-cooled to 600°C and removed from the furnace to the air. T_{ann} was varied from 700 to 1100°C. Instead of being annealed in Ar, several structures were annealed at 900 and 1000°C in a chlorine-containing atmosphere created by an oxygen flow with 1 mol % carbon tetrachloride. During implantation and annealing, the Si surface was coated with an 87-nm-thick layer of thermal SiO_2. LEDs with mesalike edge contours were formed using a standard technology by depositing Al onto the front and back sides of the wafers. The working areas of the *p–n* junctions were 1.5 mm^2.

To excite EL, diodes were energized with a pulsed 32-Hz voltage at a pulse duration of 0.5–2.0 ms and a current amplitude of up to 1000 mA. EL spectra were recorded at 80–300 K using an MDR-23 monochromator, InGaAs photodetector, and a selective nanovoltmeter. The resolution of the system was 3 nm. Radiation was collected from the surface of a *p–n* junction not covered with aluminum and was sent into the entrance

1063-7834/04/4601-0035$26.00 © 2004 MAIK "Nauka/Interperiodica"

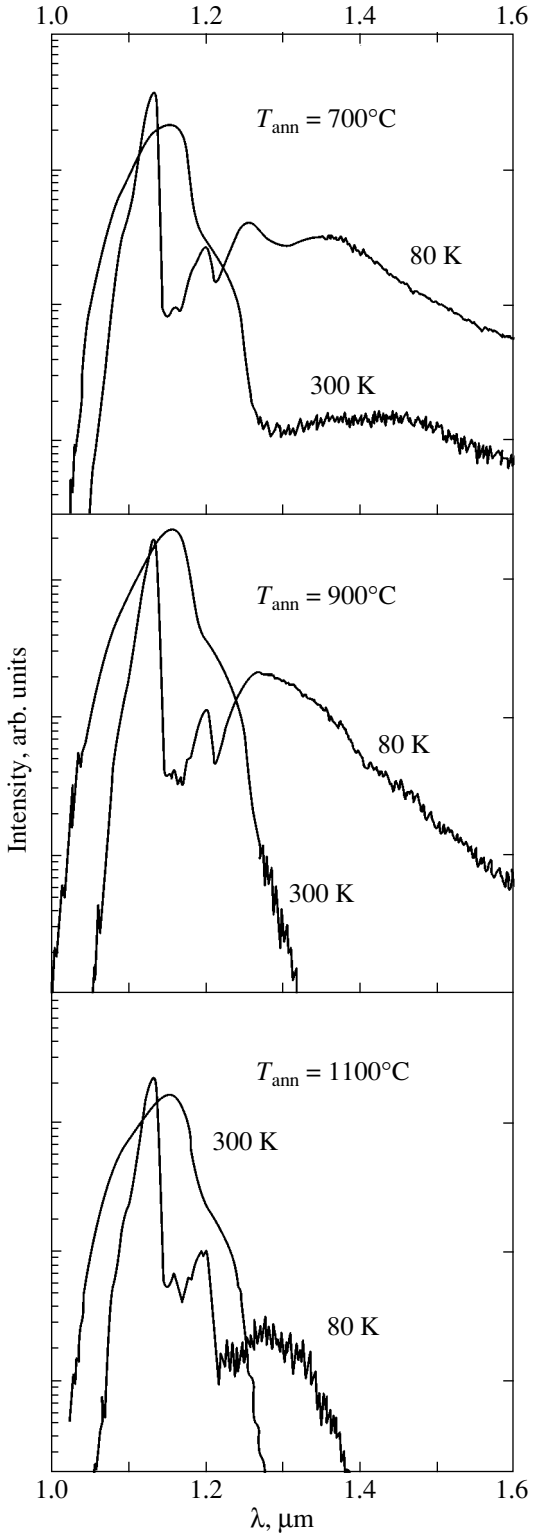

Fig. 1. EL spectra of KÉF-500-based diodes annealed at various temperatures T_{ann}.

slit of the monochromator. To measure the quantum efficiency, we deposited a nickel coating (instead of an Al coating), which transmitted one-sixth of the radiation, onto the back side of the diodes. The radiation from the back side of a diode was collected with a lens system to be directed to the entrance window of an FD-10 AG germanium photodiode. The external quantum efficiency η_{ext} was determined by measuring the photoelectric current of the Ge photodiode with allowance for its current–illumination characteristic, the solid angle over which the radiation was collected, and the losses in the lens system, in the silicon (because of collecting the radiation from the back side of a wafer), and in the Ni coating. The diode radiation distribution over a hemisphere was assumed to be isotropic. Moreover, we assumed that the whole radiation focused on the entrance window of the photodiode, which was made of a minilens mounted into the case, was collected on the photoreceiving area. To calculate the internal quantum efficiency η_{int}, we used the ratio $\eta_{ext}/\eta_{int} = 0.013$ [2], which was obtained theoretically for a planar light-emitting diode and for a semiconductor refractive index of 3.6. The effective minority-carrier lifetime τ_p in the n base of the p^+–n–n^+ structures was determined, by using the Lax method [3], from the lifetime of the phase of a high reverse conductance induced by the application of forward and backward current pulses to a diode. Structural defects were studied by transmission electron microscopy in the two-beam diffraction mode using foils oriented parallel to the wafer surface.

3. RESULTS AND DISCUSSION

Figures 1 and 2 show the EL spectra (measured at 80 and 300 K) of the diodes that were made on the KÉF-500 (Fig. 1) and KÉF-0.5 (Fig. 2) wafers and annealed in an Ar atmosphere at various temperatures T_{ann}. The current was 250 mA. For convenience, the EL intensity is given on the logarithmic scale. The spectra at 80 K contain a strong EL peak with a maximum at a wavelength $\lambda \approx 1.13$ μm and a weaker EL peak at $\lambda \approx 1.2$ μm; the two peaks are mainly caused by exciton radiation with the participation of phonons [4]. Moreover, at 80 K, the EL spectra of the KÉF-500-based diodes annealed at 700 or 900°C and of the KÉF-0.5-based diodes annealed at 700°C exhibit a broad EL band at 1.2–1.6 μm caused by defects. Defect-induced EL also exists in the KÉF-500-based diodes annealed at 1100°C, but it extends to $\lambda \approx 1.4$ μm. The observed specific features of the appearance of centers of the defect-induced EL for the two types of diodes under study are likely due to the difference in the defect structures and impurity compositions of the initial Si wafers.

The spectra measured at 300 K contain a strong EL peak with a maximum at $\lambda \approx 1.15$ μm due to band-to-band radiative transitions in silicon with the participation of phonons [4]. A broad band of defect-induced EL at 1.2–1.6 μm is observed only in the KÉF-500-based diode annealed at 700°C. For comparison, Fig. 3 shows the current dependences of the EL intensities at the maxima of the wavelength distributions (EL_m) mea-

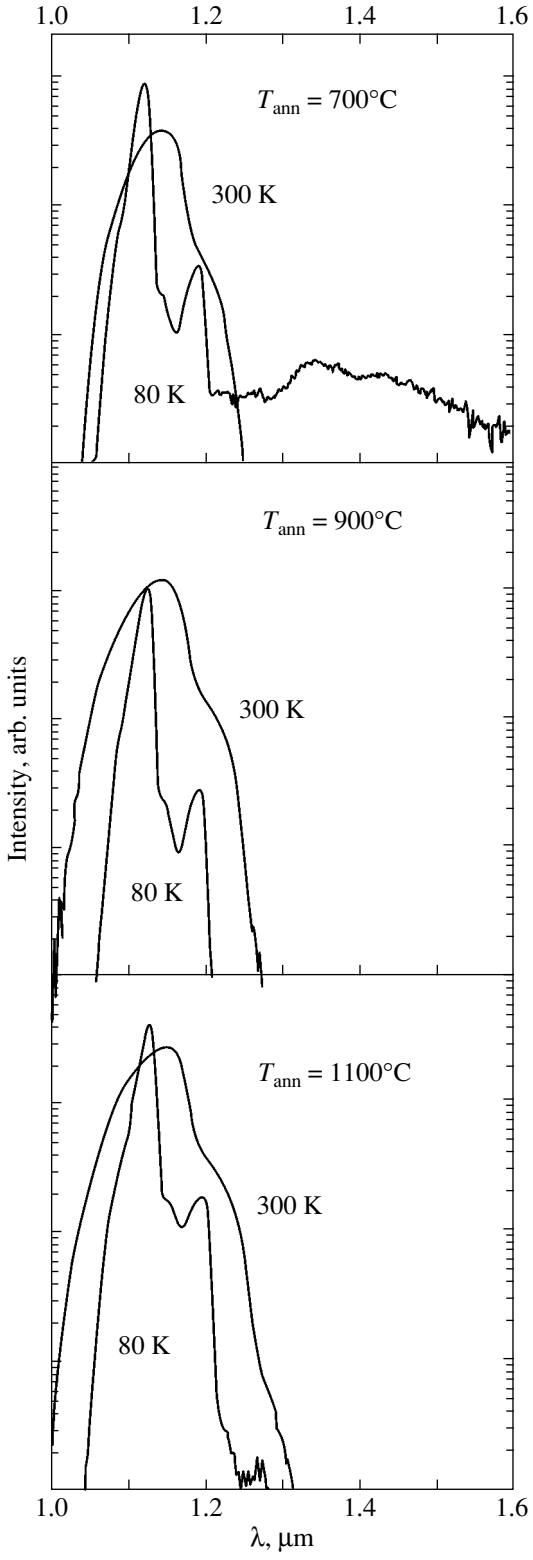

Fig. 2. EL spectra of KÉF-0.5-based diodes annealed at various temperatures T_{ann}.

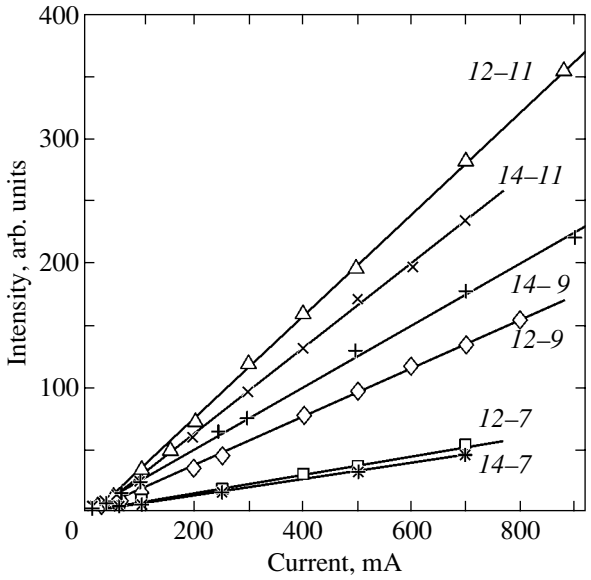

Fig. 3. Current dependences of the EL intensities at λ = 1.15 μm for (*14–7*, *14–9*, *14–11*) the KEF-500-based diodes and (*12–7*, *12–9*, *12–11*) the KÉF-0.5-based diodes. (*14–7*, *12–7*) T_{ann} = 700, (*14–9*, *12–9*) 900, and (*14–11*, *12–11*) 1100°C.

sured at 300 K. For all samples, the current dependences of EL_m are virtually linear after a short initial nonlinear segment. Because of the linear character of the current dependences of EL_m, the internal quantum efficiency η_{int} ceases to depend on the current at sufficiently high currents. Figure 4 shows the current dependences of the internal quantum efficiency measured at 300 K on the KÉF-0.5-based diodes annealed in an Ar atmosphere. It is seen that, as the temperature of postimplantation annealing increases, η_{int} increases monotonically and reaches its maximum (~0.4%) after annealing at 1100°C. This value far exceeds the room-temperature quantum efficiencies of all other types of *c*-Si-based structures that radiate beyond the range of band-to-band transitions. Moreover, apart from structures where radiation is caused by defects or nanoinclusions, the intensity of band-to-band EL is not limited by the concentration of optically active centers.

The experimental dependences of the effective minority-carrier lifetimes on the forward current constructed for the same structures at 300 K are given in Fig. 5. The values of τ_p were found to be independent of the current (at currents ≥100 mA) and to increase monotonically with the annealing temperature from $\tau_p \approx 1$ μs at T_{ann} = 700°C to $\tau_p \approx 6$ μs at T_{ann} = 1100°C. A comparison of the experimental dependences shown in Figs. 4 and 5 indicates that the values of quantum efficiency are approximately proportional to the effective minority-carrier lifetimes. Insignificant variations in EL_m or η_{int} at high current densities were detected in the KÉF-500-based light-emitting diodes annealed under the same conditions.

The use of a chlorine-containing atmosphere instead of Ar for postimplantation annealing does not change

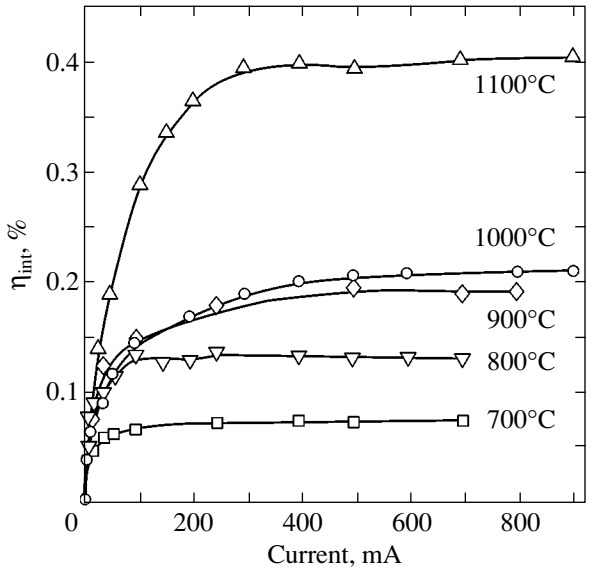

Fig. 4. Current dependences of the internal EL quantum efficiency at 300 K for the KÉF-0.5-based diodes annealed in Ar at various T_{ann}.

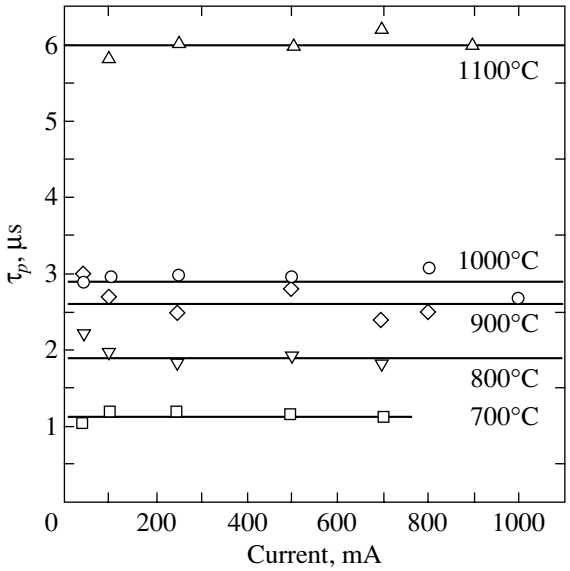

Fig. 5. Current dependences of the minority-carrier lifetime at 300 K for the KÉF-0.5-based diodes annealed in Ar at various T_{ann}.

the character of the current dependences of EL_m and η_{int}. However, the maximum values of internal EL quantum efficiency are increased for the KÉF-500-based diodes annealed at T_{ann} = 900°C by 20% and at T_{ann} = 1000°C by 55% and for the KÉF-0.5-based diodes, by 35 and 75%, respectively. Approximately the same gains are detected for the minority-carrier lifetimes. This effect is caused by a decrease in the concentration and, apparently, by a change in the type of nonradiative recombination centers because of the change in the annealing atmosphere. The value of this effect increases with the annealing temperature.

Figure 6 shows spectra (measured at various temperatures) of the defect-induced EL in a KÉF-500-based sample annealed at 700°C. As is seen, the intensity of the EL peak with a maximum at $\lambda \sim 1.26$ μm (measured at 80 K) decreases faster with increasing temperature than does the intensity of the broad EL band at $\lambda \sim 1.2$–1.6 μm. This can be due to the physical nature of the centers responsible for this peak and for this broad EL band being different. It is known [5] that annealing at 700°C of *c*-Si implanted with boron ions leads to the formation of rodlike defects consisting of point-defect clusters and having various habit planes. Indeed, the results of our electron-microscopic investigation showed that such defects were predominant in the KÉF-500-based structures annealed at T_{ann} = 700°C (Fig. 7a). The projections of the defects are extended mainly along the ⟨100⟩ directions; however, there are also defects oriented along the ⟨110⟩ directions. The defect lengths vary significantly and are 38–55 nm for small defects and 220–270 nm for large ones. Conceivably, the short defects are the defects that are inclined to the surface of a foil and cut during the preparation of the foil. The total density of the rodlike defects is $\sim 5 \times 10^{10}$ cm^{-2}. Apart from the defects indicated above, this sample contains closed prismatic dislocation loops 20–100 nm in size with a density that is about two orders of magnitude smaller. Analysis of the available experimental data on the luminescence of *c*-Si subjected to radiation followed by annealing at 600–1100°C [6–8] indicates that the broad peaks of defect-induced EL in question cannot be explained by the rodlike defects and closed prismatic dislocation loops alone. Therefore,

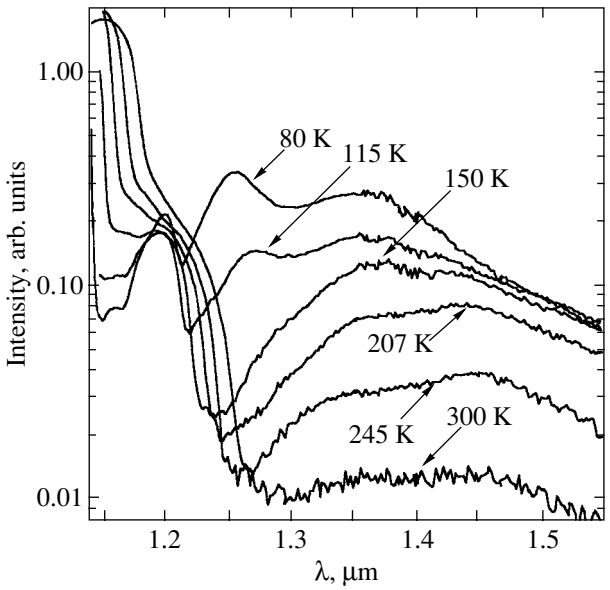

Fig. 6. EL spectra (measured at various temperatures) of a KÉF-500-based diode annealed at 700°C.

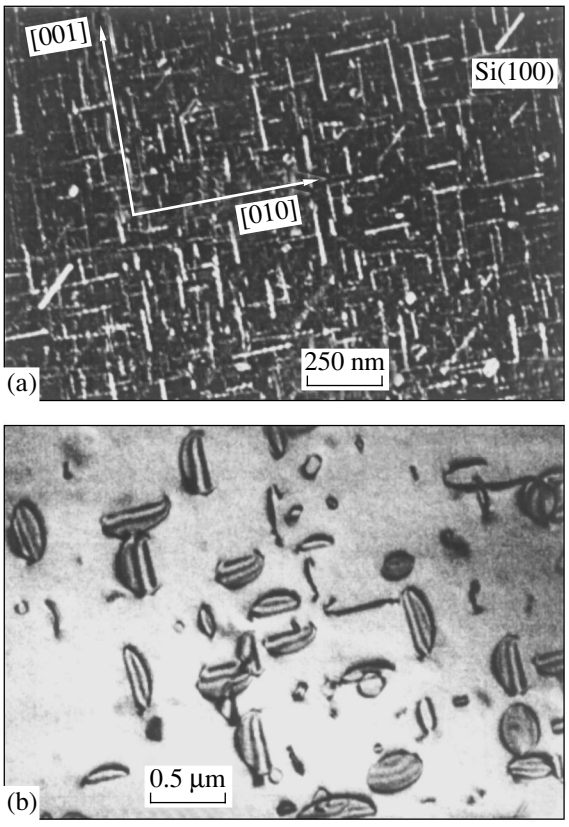

Fig. 7. Electron-microscopic images of a KÉF-500-based diode annealed in Ar at (a) 700°C (dark field, **g** = ⟨220⟩) and (b) 1000°C (bright field, **g** = ⟨400⟩).

further studies are required to establish the physical nature of optically active centers. A KÉF-500-based sample annealed in Ar at T_{ann} = 1000°C (at which light-emitting diodes were fabricated in [1]) contains Frank loops and closed prismatic dislocation loops (Fig. 7b). The Frank loops have two characteristic sizes, 200–230 and 380–515 nm. The total density of the Frank loops is about 4×10^8 cm^{-2}. The closed prismatic dislocation loops are 50–190 nm in size, and their density is about 2.5×10^8 cm^{-2}. In the KÉF-500-based sample annealed at T_{ann} = 1100°C, no extended structural defects were found, and the EL quantum efficiency in the range of band-to-band transitions at 300 K in this sample was higher than in the diodes containing extended defects.

Thus, a high quantum efficiency of band-to-band radiation that is sufficient for practical applications (e.g., in silicon optrons) has been observed in light-emitting diodes containing structural defects of different nature with strongly different densities. Moreover, the EL quantum efficiency was maximum in a diode without extended structural defects. Analysis of the EL and of the electrophysical and structural properties of the diodes indicates that, under the experimental conditions, structural defects affect the EL properties via the formation or gettering of nonradiative recombination centers rather than via preventing the removal of charge carriers to the nonradiative recombination centers. For structures formed on low-doped substrates, the defects forming in *c*-Si as a result of implantation with boron ions and postimplantation annealing at a relatively low temperature (~700°C) can serve as a source of EL in the range 1.2–1.6 μm at various operating temperatures, including room temperature.

ACKNOWLEDGMENTS

This work was supported in part by INTAS (grant no. 2001-0194), the Russian Foundation for Basic Research (project nos. 02-02-16374, 02-02-16692), and the Department of Physical Sciences of the Russian Academy of Sciences within the framework of the scientific program "New Materials and Structures."

REFERENCES

1. Wai Lek Ng, M. A. Lourenco, R. M. Gwilliam, *et al.*, Nature **410**, 192 (2001).
2. A. A. Bergh and P. J. Dean, *Light-Emitting Diodes* (Clarendon, Oxford, 1976; Mir, Moscow, 1979).
3. B. Lax and S. F. Neustadter, J. Appl. Phys. **25** (9), 1148 (1954).
4. R. A. Smith, *Semiconductors*, 2nd ed. (Cambridge Univ. Press, Cambridge, 1978; Mir, Moscow, 1982).
5. A. L. Aseev, L. I. Fedina, V. Hoehl, and H. Barch, *Clustering of Interstitial Atoms in Silicon and Germanium* (Nauka, Novosibirsk, 1991).
6. G. Davies, Phys. Rep. **176** (3–4), 83 (1989).
7. S. Coffa, S. Libertino, and C. Spinella, Appl. Phys. Lett. **76** (3), 321 (2000).
8. N. A. Sobolev, O. B. Gusev, E. I. Shek, *et al.*, Appl. Phys. Lett. **72** (25), 3326 (1998).

Translated by K. Shakhlevich

Physics of the Solid State, Vol. 46, No. 1, 2004, pp. 40–44. Translated from Fizika Tverdogo Tela, Vol. 46, No. 1, 2004, pp. 44–48.

PROCEEDINGS OF THE CONFERENCE DEDICATED TO O. V. LOSEV (1903–1942)

(Nizhni Novgorod, Russia, March 17–20, 2003)

Silicon LEDs Emitting in the Band-to-Band Transition Region: Effect of Temperature and Current Strength

A. M. Emel'yanov, N. A. Sobolev, and E. I. Shek

Ioffe Physicotechnical Institute, Russian Academy of Sciences, Politekhnicheskaya ul. 26, St. Petersburg, 194021 Russia

e-mail: nick@sobolev.ioffe.rssi.ru

Abstract—The parameters of silicon light-emitting diodes (LEDs) prepared through boron implantation into *n*-Si, followed by annealing at 700–1200°C, were studied. The maximum room-temperature internal quantum efficiency of electroluminescence (EL) in the region of band-to-band transitions was estimated as 0.4% and reached at an annealing temperature of 1100°C. This value did not vary more than twofold within the operating temperature range 80–500 K. The EL growth and decay kinetics was studied at various currents. Following an initial current range of nonlinear dependence, the EL intensity scaled linearly with the current. It is shown that interpretation of this result will apparently require a revision of some present-day physical concepts concerning carrier recombination in silicon diodes. © *2004 MAIK "Nauka/Interperiodica".*

1. INTRODUCTION

The luminescence associated with impurities and defects in Si single crystals (*c*-Si) has been attracting considerable interest over the past decade in connection with the development of novel radiation sources for use in optoelectronics. By contrast, the electroluminescence (EL) of *c*-Si in the band-to-band transition region is known to a much lesser extent. Research in this area appears to be important at least from the standpoint of providing a baseline for all other types of *c*-Si-based light-emitting structures. Because of the indirect band-to-band transitions and very scarce relevant studies, *c*-Si was largely considered to hold little promise in the development of high-efficiency light-emitting diodes (LEDs) with a band-to-band emission spectrum. These concepts were convincingly unproved only in recent years, when it was shown [1, 2] that the quantum efficiency of band-to-band emission in *c*-Si at room temperature can be comparable to that of the light-emitting diodes based on direct-band-gap semiconductors. Note that the high quantum efficiency was obtained in [2] using a relatively simple technique compatible with the technique of integrated circuits; In [2], *p–n* structures were prepared through boron implantation into single-crystal *n*-Si, with subsequent annealing at 1000°C. The structures reported here were also produced by ion implantation followed by annealing. The main goals of our study were to (i) determine the post-implantation annealing temperature that would be optimal for reaching the maximum EL efficiency, (ii) to investigate the variation of the EL parameters over an operating temperature range broader than the one covered in [2], (iii) to measure the current dependences of the EL intensity and quantum efficiency, (iv) to study the EL kinetics at different currents, and (v) to compare the results thus obtained with measurements of the minority-carrier effective lifetimes.

2. EXPERIMENTAL TECHNIQUES

We prepared *p–n* junctions by using boron ion implantation at energy $E = 40$ keV to a dose $D = 1 \times 10^{15}$ cm^{-2} into 0.37-mm-thick (100)-oriented KÉF-0.5 *n*-Si plates. To obtain Ohmic contacts, phosphorus ions ($E = 75$ keV, $D = 1 \times 10^{15}$ cm^{-2}) were implanted into the back side of the plates. Post-implantation anneals were performed in an argon environment (at a temperature T_t) for a duration of 20 min, followed by furnace-cooling in Ar down to 600°C and subsequent removal to the air. T_t was varied from 700 to 1200°C in steps of 100°C. All anneals were carried out with an 87-nm-thick thermal SiO_2 film present on the Si surface. The maximum EL quantum efficiency in the band-to-band region at 300 K was reached at $T_t = 1100$°C. Therefore, all the graphs presented below refer to diodes fabricated at $T_t = 1100$°C. Diodes were formed using the standard mesa structure technology after deposition of Al electrodes on the front side of the plate and of Ni contacts on the back side of the plate. The working areas of the *p–n* junctions were 1.5 mm^2. The EL was excited by applying a pulsed 32-Hz voltage to the diodes with pulses 0.1–2.0 ms in duration. The EL spectra were obtained with a monochromator, an InGaAs photodetector, and a selective nanovoltmeter. When measuring the quantum efficiency, the radiation directed onto the entrance window of a Ge photodiode was collected by a lens system from the back side of the plate through a nickel coating, which transmitted 1/6 of the total radiation flux. The external quantum efficiency η_{ext} was determined from measurements of the following quan-

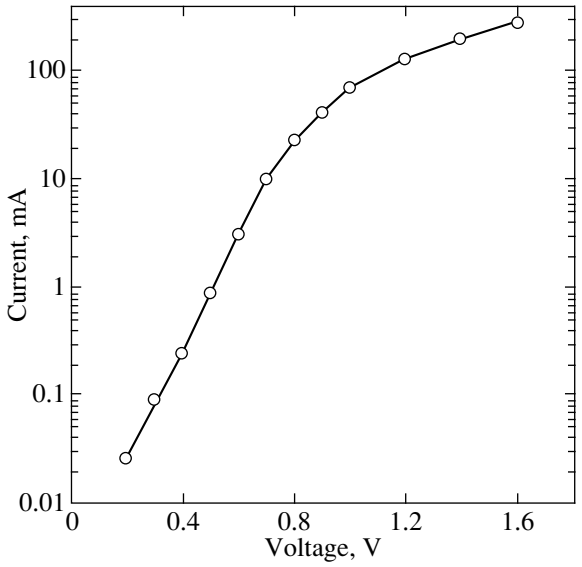

Fig. 1. Forward branch of the *I–V* characteristic at 300 K.

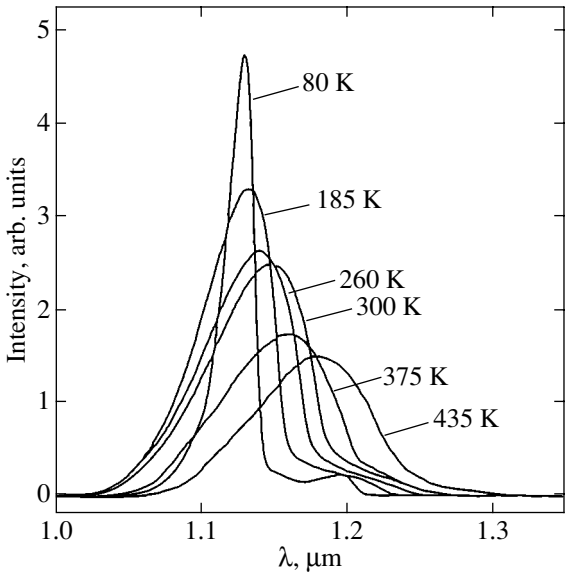

Fig. 2. EL spectra of the diode under study measured at a current of 250 mA and various temperatures. Resolution 3 nm.

tities: the photocurrent of the Ge photodiode, the current–power sensitivity, the solid angle within which the radiation was collected, and the losses in the lens system, in the silicon (because the radiation was coupled out the back side of the plate), and in the Ni coating. The diode radiation was assumed to be isotropic within the hemisphere. It was also assumed that all of the radiation focused onto the entrance window of the FD-10 AG photodiode, which actually represented a minilens built into the casing, was collected onto the photodetector sensitive area. The internal quantum efficiency η_{int} was calculated from the relation $\eta_{ext}/\eta_{int} = 0.013$ [3], which was derived theoretically for a plane junction LED and for a semiconductor refractive index equal to 3.6. The effective minority carrier lifetime τ_p was obtained, following the technique proposed in [4], from measurements of the forward current pulse amplitude, as well as of the amplitude and duration of the part of the reverse current pulse corresponding to the phase of the high inverse conductivity. The EL kinetics was studied with the use of a germanium photodiode operating at room temperature. The response time of the light-detecting device to a square light pulse in this regime of operation was 1 μs.

3. EXPERIMENTAL RESULTS AND DISCUSSION

The forward branch of the diode *I–V* curve measured at 300 K is presented in Fig. 1. Figure 2 shows EL spectra of the diode under study measured at 250 mA and various temperatures in the band-to-band transition region. It is usually assumed (see, e.g., [5]) that the EL in this spectral region is dominated by exciton-mediated radiative recombination at temperatures close to 80 K and by free carrier recombination at temperatures close to 300 K and higher. The long-wavelength shift of the EL spectrum with increasing temperature (Fig. 3) is associated primarily with the decreasing width of the *c*-Si band gap. Figure 4 displays the temperature dependence of the wavelength-integrated EL intensity (ELIs). As is evident from Fig. 4, the light-emitting diodes can operate at least up to ~200°C. Because ELIs is directly proportional to the quantum efficiency at a fixed current, the quantum efficiency is seen to vary by a factor of less than two in the temperature range stud-

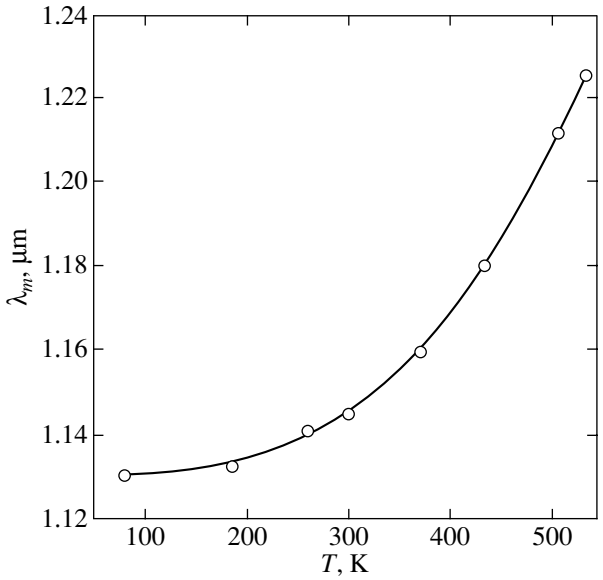

Fig. 3. Temperature dependence of the wavelength λ_m corresponding to the maximum of the EL intensity measured at a current of 250 mA.

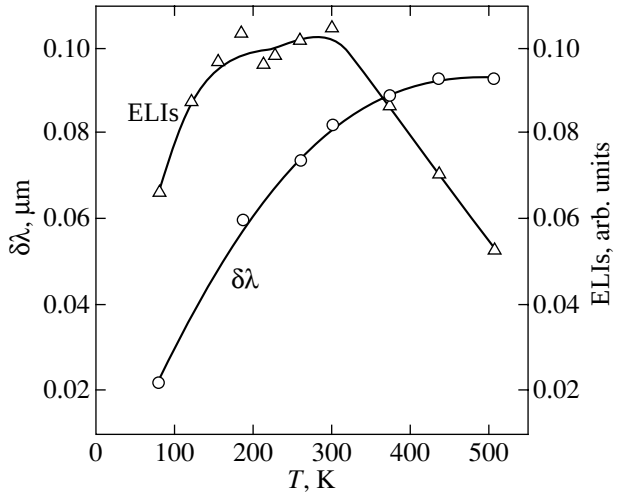

Fig. 4. Temperature dependences of the integrated EL intensity (ELIs) and of the peak half-width δλ measured at a current of 250 mA.

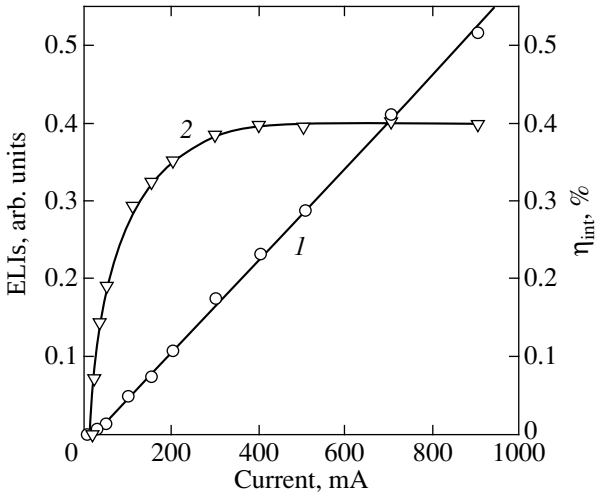

Fig. 5. Current dependences of (*1*) the integrated EL intensity and (*2*) internal quantum efficiency measured at 300 K.

ied. Figure 4 also displays the temperature dependence of the EL peak half-width. Following a small initial range of nonlinear behavior, the dependences of integrated EL intensity on current obtained in the diodes under study at 80, 300, and 500 K are practically linear. As a consequence, the quantum efficiency becomes practically current-independent at high enough currents. The current dependences of ELIs and η_{int} measured at 300 K are displayed in Fig. 5. The current dependences of the EL intensity at the maximum of the wavelength distribution do not differ in character from the dependences of ELIs on current (Fig. 6). This suggests that the current can slightly heat the sample, which may produce EL spectral broadening.

The ranges of the linear EL dependence on current at the maximum of the wavelength distribution of the EL were also observed by us at other *p–n* structure annealing temperatures. A linear variation of the band-to-band EL intensity in *c*-Si and, accordingly, a current-independent η_{ext} (at high enough currents) have also been observed in other studies [1, 6, 7]. However, no explanation of this effect has been offered thus far. Variation of the density of the forward current through a *p–n* junction is accompanied usually by a variation in the concentration *p* of the minority carriers (holes) in the diode base. Let us denote the concentration of electrons in the conduction band of the diode *n* base by *n* and the concentration of the recombination levels filled with electrons by *m*. Then, the number of band-to-band radiative recombination events per unit time per unit volume will be βnp and that of nonradiative recombination events will be γmp (where β and γ are coefficients characterizing the recombination probabilities). Recalling the definition of the internal quantum efficiency (in equilibrium conditions) of a nonsymmetrical *p–n* junction in which the recombination occurs in the diode base, we can write

$$\eta_{int} = \int_0^L \beta npdx/(j/q)$$
$$= \int_0^L \beta npdx/\left[\int_0^L \gamma mpdx + \int_0^L \beta npdx\right] \quad (1)$$
$$= \int_0^L \beta npdx/\int_0^L (p/\tau)dx,$$

where q is the elementary charge, j is the current density, L is the base thickness, $x = 0$ corresponds to the *p–n* junction, and τ is the minority-carrier lifetime. If τ does not depend on p, we have $\eta_{int} \cong$ const for

$$\beta n \cong \text{const}. \quad (2)$$

Condition (2) is satisfied at low injection levels, where p is considerably smaller than n. However, according to our estimates, in the ranges of the linear ELIs current dependences obtained on our diodes, the conditions of low injection level were, on the average, not met. A high injection level was also reported in the study of a *p–i–n* structure described in [6]. Equation (2) is also satisfied for $\beta \sim 1/n$. This conclusion is, however, in conflict with the universally accepted concepts [6, 8, 9].

As follows from Eq. (1), the condition $\eta_{int} = \text{const}$ can also be met if

$$m = \alpha n, \quad (3)$$

where α is a coefficient of proportionality. In this case, we obtain

$$\eta_{int} = \beta/(\alpha\gamma + \beta) \quad (4)$$

and, therefore, τ varies with n (in inverse proportion). This dependence is at odds with the nonradiative-

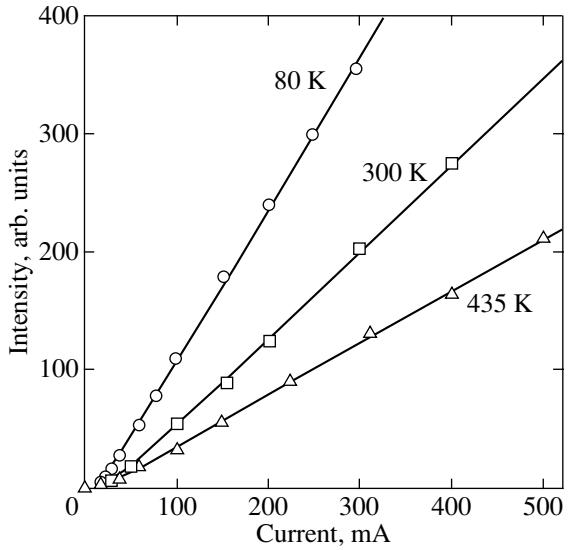

Fig. 6. Current dependences of the EL intensity at the wavelength corresponding to its maximum measured at various temperatures.

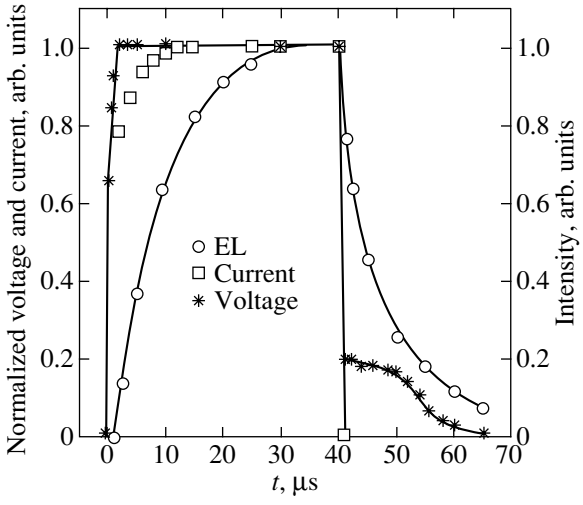

Fig. 7. EL kinetics (EL) and the corresponding evolution of the diode voltage and current normalized against their maximum values measured at 300 K and a current pulse amplitude of 300 mA.

recombination theory of Shockley–Read, according to which τ should be independent of n and p at a high injection level [10]. Note that the experimentally observed τ_p being practically independent of current cannot be considered unambiguous evidence that the dependence of τ on p is absent, at least for the reason that the relation proposed in [4] for determining τ_p was derived for the case of τ being independent of p (see, for instance, [10]). The value of β was calculated theoretically [6, 8, 9], and $\alpha\gamma$ in our case can be obtained from Eq. (4) using η_{int} measurements.

If all carriers injected into the base become bound to form excitons, we have

$$\eta_{int} = \int_0^L (w/\xi)dx / \int_0^L (w/\tau)dx, \quad (5)$$

where w is the exciton density and ξ is the exciton radiative lifetime. If ξ = const, the condition η_{int} = const is satisfied for τ = const.

In the case where τ does not depend on p and condition (2) is upheld, one can derive an expression describing the rise in the band-to-band EL intensity with the time t elapsed since the application of a square current pulse of density j to the structure. As before, we consider a nonsymmetric p–n junction and recombination in the diode base. With the notation $\int_0^L p dx = P$, the rate of variation of the quantity P with time can be written as

$$dP/dt = j/q - P/\tau. \quad (6)$$

The solution to Eq. (6) is

$$P(t) = (j\tau/q)[1 - \exp(-t/\tau)]. \quad (7)$$

For $t = \tau$, we have $P \cong 0.63(j\tau/q) = 0.63P_{max}$ (where P_{max} is the maximum value of P). If condition (2) is met, the quantity P is directly proportional to the EL intensity; therefore, in our case, the EL intensity should reach a value equal to 0.63 of its maximum value in time $t \cong \tau$. The kinetics of the EL rise and decay measured with our diode at a current of 300 mA and temperature of 300 K is presented graphically in Fig. 7. At 300 K, the time needed for the EL intensity to reach 0.63 of the maximum level, $\tau_{0.63}$, was about 9 μs for all currents studied in the range 80–500 mA. The EL decay time constant and τ_p were also practically current-independent within the above range and constituted ~6 μs. With due account of the inertia in the operation of the light-measuring system, as well as of the delay in the current amplitude value becoming steady (Fig. 7) and of the error in the τ_p measurement, the difference found between the measured values of τ_p and $\tau_{0.63}$ cannot be considered to contradict the model used here. Said otherwise, the experimental results obtained here are not at variance with the assumption of τ being independent of p and of condition (2) being valid. The delay in the onset of the current with respect to the voltage (Fig. 7) in the diode under study should be probably assigned to modulation of the base resistance [10]. Note that, other conditions being equal, $\tau_{0.63}$ decreased as a result of the factors causing the decrease in τ_p, for instance, a decrease in T_t or in the diode operating temperature. Other publications [1, 2, 6] dealing with investigation of the parameters of high-efficiency silicon light-emitting diodes did not present the results of direct measurements of τ_p [2, 6] or of the EL kinetics [1]. This makes comparison of our results with the results obtained in the above studies difficult.

Assuming that η_{int} is independent of current due to condition (3) being met, the equation for the variation in quantity P with time needed to describe the EL intensity rise kinetics can be cast in the form

$$dP/dt = j/q - (\alpha\gamma + \beta)\int_0^L npdx. \quad (8)$$

We readily see that this equation does not have a simple solution and requires that additional conditions be formulated, because, unlike Eq. (6), it contains two (P and $\int_0^L npdx$) rather than one (P) unknown which vary with time.

4. CONCLUSIONS

To sum up, by using boron implantation into *n*-Si and subsequent annealing, we have prepared silicon light-emitting diodes with a high internal quantum EL efficiency (according to our estimates, up to ~0.4%) in the band-to-band transition region. This efficiency varied less than twofold within the operating temperature interval from 80 to 500 K. The presence of a range of linear dependence of the EL intensity on current has been demonstrated to be a fairly typical property of high-efficiency silicon band-to-band LEDs prepared by different techniques and operating at various temperatures. It was first shown that interpretation of this effect would apparently require revision of some heretofore accepted concepts, such as the minority carrier lifetime being constant or the radiative-recombination probability of the electrons and holes remaining unchanged under variation of the injected carrier concentration at high injection levels. The kinetics of the EL and of τ_p were measured and compared for the first time. The results of the comparison are not inconsistent with the assumption of the lifetime τ and of the quantity βn being independent of minority-carrier concentration.

ACKNOWLEDGMENTS

This study was supported by INTAS (grant no. 2001-0194), the Russian Foundation for Basic Research (project no. 02-02-16374), and the Russian Academy of Sciences (Physical Sciences Division) program "New Materials and Structures."

REFERENCES

1. M. A. Green, J. Zhao, A. Wang, *et al.*, Nature **412**, 805 (2001).
2. Wai Lek Ng, M. A. Lourenco, R. M. Gwilliam, *et al.*, Nature **410**, 192 (2001).
3. A. A. Bergh and P. J. Dean, *Light-Emitting Diodes* (Clarendon, Oxford, 1976; Mir, Moscow, 1979).
4. B. Lax and S. F. Neustadter, J. Appl. Phys. **25** (9), 1148 (1954).
5. R. A. Smith, *Semiconductors*, 2nd ed. (Cambridge Univ. Press, Cambridge, 1978; Mir, Moscow, 1982).
6. Th. Dittrich, V. Yu. Timoshenko, J. Rappich, and L. Tsybeskov, J. Appl. Phys. **90** (5), 2310 (2001).
7. W. Michaelis and M. H. Pilkuhn, Phys. Status Solidi **36**, 311 (1969).
8. W. van Roosbroeck and W. Shockley, Phys. Rev. **94** (6), 1558 (1954).
9. R. D. Altukhov and E. G. Kuzminov, Solid State Commun. **111**, 379 (1999).
10. Yu. R. Nosov, *Switching in Semiconductor Diodes* (Nauka, Moscow, 1968; Plenum, New York, 1969).

Translated by G. Skrebtsov

Physics of the Solid State, Vol. 46, No. 1, 2004, pp. 45–48. Translated from Fizika Tverdogo Tela, Vol. 46, No. 1, 2004, pp. 49–52.

PROCEEDINGS OF THE CONFERENCE DEDICATED TO O. V. LOSEV (1903–1942)

(Nizhni Novgorod, Russia, March 17–20, 2003)

New Mechanisms of Localization of Charge Carriers in Nanosilicon

I. V. Blonskyy, A. Yu. Vakhnin, V. N. Kadan, and A. K. Kadashchuk

Institute of Physics, National Academy of Sciences of Ukraine, pr. Nauki 46, Kiev, 03028 Ukraine
e-mail: blon@iop.kiev.ua

Abstract—This paper reports on the results of investigations into the spectral dependences of thermally stimulated luminescence and the temperature dependences of tunneling luminescence in highly oxidized porous silicon samples. Two new mechanisms of localization of charge carriers are considered in terms of the specific features revealed in the spectral dependences of the thermally stimulated luminescence and nonmonotonic temperature dependences of the Becquerel index of tunneling luminescence decay. The proposed mechanisms of charge carrier localization are associated with structure heterogeneities inherent in these objects, namely, superficial SiO_x oxide shells ($0 < x \le 2$) enclosing silicon particles and an undulating structure of silicon wires.

1. INTRODUCTION

The localization of charge carriers and excitons in semiconductor media of different dimension is one of the most important electronic phenomena. As is known, there are many mechanisms responsible for the localization of electronic excitations. In this paper, we will not concern ourselves with all these mechanisms but will dwell briefly on only two of them. The localization mechanisms we are interested in are associated with the dimensionality of the medium and clearly manifest themselves in low-temperature photoluminescence (PL). The first mechanism, which is characteristic of three-dimensional media, governs the localization of electronic excitations in semiconductor solid solutions. These objects exhibit partial composition disordering, and, consequently, the crystal potential contains a fluctuation component of the white-noise type. In the case where the energy, geometric, and kinetic criteria are met, the potential wells encourage the localization of excitons and charge carriers, which is accompanied by inhomogeneous broadening of the localized states. Algorithms for determining the parameters of localized states have been developed and their validity has been confirmed for II–VI semiconductor solid solutions on the basis of both the theoretical models proposed for these systems (see, for example, [1]) and the low-temperature PL data obtained by selective excitation techniques (see, for example, [2]).

The mechanism of localization of electronic excitations in two-dimensional structures (for example, superlattices) is similar in many respects to the first mechanism. It is known that, in two-dimensional objects, the fluctuation component of the crystal potential is determined by the variation in the quantum-well width. In general, the features of the manifestation of localized states in low-temperature PL spectra of two-dimensional structures resemble those observed for semiconductor solid solutions. However, there are some differences associated with the two-dimensional nature of the density of states (see, for example, [3]). In quasi-one-dimensional and quasi-zero-dimensional structures, the processes of localization of electronic excitations and their spectral manifestations are less well understood. This can be judged from the ongoing discussion of the nature of the main luminescence band for porous silicon. As is known, highly oxidized porous silicon samples consist of a complex mixture of quasi-zero-dimensional and quasi-one-dimensional silicon particles enclosed in superficial SiO_x oxide shells ($0 < x \le 2$) involving different trapping states. These states are primarily responsible for the luminescence properties of porous silicon materials, even though their role is not completely understood. In our previous works [4, 5], we proposed a model of filling of trapping states upon photoexcitation of the silicon core through an Auger electron process occurring under conditions of spatial confinement of carriers, i.e., in an activation manner. In nanoparticles, the Auger electron process dominates, because the cross section W of this process varies with an increase in the distance R between interacting particles as $W \sim R^{-6}$. For example, at $R \approx 10$ nm, we obtain $W \approx 10^{15}$ cm^{-2}, which almost coincides with the cross section of the unit cell. According to the proposed model of a "two-stroke charge piston," the charge piston acts in turn on the electron and hole components due to the Auger electron process and pushes them into SiO_x shells, followed by localization of the charge carriers [4, 6]. This model offers a satisfactory explanation for a number of features of the main luminescence band in the spectra of porous silicon, namely, the nonmonotonic temperature dependence of the integrated

1063-7834/04/4601-0045$26.00 © 2004 MAIK "Nauka/Interperiodica"

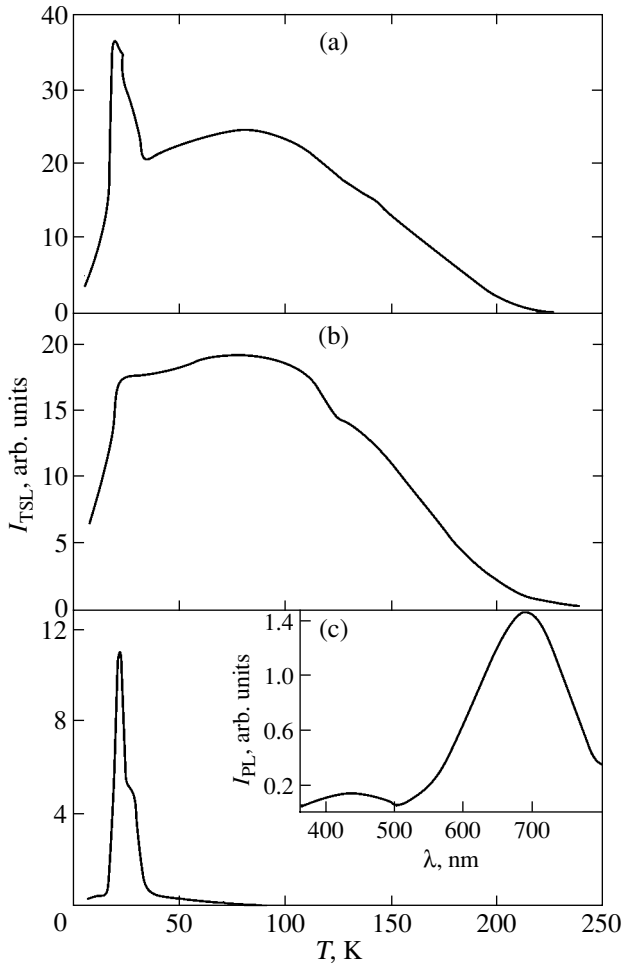

Fig. 1. Spectral dependences of the thermally stimulated luminescence in highly oxidized porous silicon samples: (a) the total PL spectrum, (b) PL in the wavelength range $\lambda > 640$ nm, and (c) PL in the wavelength range $\lambda < 580$ nm. The inset shows a typical PL spectrum of porous silicon.

intensity, nonlinearity of the luminous characteristics, spectral dependence of the "luminescence decay" effect, etc. However, in our opinion, the proposed model calls for further experimental corroboration. In this respect, one of the main objectives of the present work was to verify experimentally the validity of the model of a two-stroke charge piston. Moreover, we revealed the specific features of localized states in one-dimensionally irregular media. For this purpose, we investigated the spectral dependences of thermally stimulated luminescence (TSL) and the temperature dependences of tunneling luminescence in highly oxidized porous silicon samples prepared using a standard procedure.

2. SPECTRAL DEPENDENCES OF THERMALLY STIMULATED LUMINESCENCE

Thermally stimulated luminescence is a universally accepted tool for studying the activation spectrum of trapping states. Investigation into the spectral composition of thermally stimulated luminescence is of particular interest, especially with due regard for the spatial inhomogeneity of silicon nanocrystallites and for the purpose of revealing a correlation between the nanocrystallite structure (silicon core, peripheral SiO_x oxide shells, $x \leq 2$) and the shape of the TSL spectrum. It should be noted that, for highly oxidized porous silicon, the nature of the main reddish orange PL band (λ_{max} = 680 nm) remains rather controversial, whereas the weaker blue band (λ_{max} = 440 nm) is almost universally assigned to defect states of SiO_x shells. Therefore, with knowledge of the correlation between the spectral composition of the photoluminescence (in particular, the blue emission band) and the shape of the TSL spectrum, it is possible to judge occupation of traps of an SiO_x shell upon photoexcitation of the silicon core and to determine their activation energies E_A.

In this work, we will not dwell on the experimental techniques used in our measurements, because they were thoroughly described in our earlier works [3, 6]. Note only that the spectral dependences of the thermally stimulated luminescence were measured either during heating at a rate of 0.15 K/s or upon fractional thermoluminescence. The results of these measurements are presented in Fig. 1. Without going into details (also described in [3, 6]), we draw the main conclusion that there is a one-to-one correspondence between the main PL band (λ_{max} = 680 nm) and the broad TSL component (at ≈90 K), on the one hand, and the blue PL band (λ_{max} = 440 nm) and the narrow TSL doublet (at 25 K), on the other. This suggests that the trapping states of the oxide shells are filled upon photoexcitation of the silicon core. The above inference is supported by the results obtained by Kux *et al.* [7], who studied the temperature dependence of the decay kinetics of the blue PL band. It was revealed in [7] that, upon cooling from room temperature to liquid-helium temperature, the decay kinetics (apart from the main nanosecond component) exhibits a millisecond component beginning from approximately 30 K. These authors brought forward a number of arguments in support of the assignment of the millisecond component to shallow-lying (≈25–30 K) trapping states of the peripheral oxide layers. All these findings count in favor of the model of a two-stroke charge piston [4, 5].

Thermally stimulated luminescence is characterized by a feature that is also specific to the reddish orange PL band. The case in point is the extremely large width of the high-temperature TSL component, which indicates considerable dispersion of the activation energy E_A. The temperature dependence of the activation energy E_A can easily be determined from the experimental data presented in Fig. 1 and the algorithms proposed in [3, 5]. The dependence thus obtained is depicted in Fig. 2. It should be noted that the limiting value $E_A \approx 0.3$ eV is approximately equal to the half-width of the reddish orange PL band. In order to eluci-

date the nature of the broad spectrum of the activation energy of trapping states related to the silicon core, we analyzed several models. In this paper, we will briefly consider the most realistic model associated with one more type of structural heterogeneity of porous silicon, an undulating structure of individual silicon wires. The results of numerous structural investigations of porous silicon indicate that variations in the thickness of an individual silicon wire can be significant and irregular; moreover, these variations are observed for wire segments of different lengths. From analyzing the standard expression relating the energy of electronic excitations to the crystallite sizes along the quantum-confinement axis, we can infer that the above structural features of silicon wires should favor the formation of a one-dimensional fluctuation component of the crystal potential whose wells at certain parameters can be treated as topological traps (see insets to Fig. 2). In this case, the dispersion of the activation energy $E_A = 0.3$ eV could reflect a wide scatter in the thicknesses of different segments of the silicon wire. Although this scatter in the thicknesses is actually observed within both an individual wire and an ensemble of wires, the proposed model should be considered only a hypothesis. With the aim of justifying this model, we investigated the temperature dependences of the tunneling luminescence and analyzed the obtained results in the framework of approaches developed by different authors.

3. TEMPERATURE DEPENDENCES OF TUNNELING LUMINESCENCE

The recombination of charge carriers due to tunneling transitions is accompanied by the emission of light, which is referred to as tunneling luminescence. This luminescence is characterized by a very low intensity and decay of the Becquerel type ($I_{lum} \sim t^{-\beta}$, where $\beta \approx 1$). In our experiments, the kinetics of tunneling luminescence was measured after completion of the photoexcitation of the samples at delay times ranging from 1 to 1000 s and a signal buildup time of ≈1 s. Moreover, we examined how the temperature affects the kinetics of tunneling luminescence in the range from 4.2 to 300 K. The results obtained are thoroughly described in [4, 5]. In the present work, we will discuss new aspects of the problem under investigation. Figure 3 shows the temperature dependence of the Becquerel index $\beta(T)$ calculated from the data reported in [4, 5]. It is worth noting that the dependence $\beta(T)$ exhibits nonmonotonic behavior. We attempted to interpret the nonmonotonic dependence $\beta(T)$ in the framework of different theoretical approaches that account for tunneling charge transfer in an ensemble of localized states. In our opinion, the approaches developed by the group of researchers under the guidance of Goldanskii (see [8]) and Arkhipov *et al.* [9] provide the most correct qualitative explanation of the dependence $\beta(T)$. Following these approaches, all centers of charge carrier localization are divided into two groups. The first group involves centers separated by distances that exclude the possibility of charge transfer occurring between them. These are typical isolated traps playing the role of sinks for charge carriers. The second group consists of centers spaced at distances that allow charge transfer between them. Goldanskii and coworkers referred to these ensembles as diffusion clusters. According to [8, 9], electron transfer can occur through two mechanisms depending on the nature and degree of disordering of the medium: (i) the mechanism of hopping migration (over isolated centers) [8] and (ii) the mechanism of

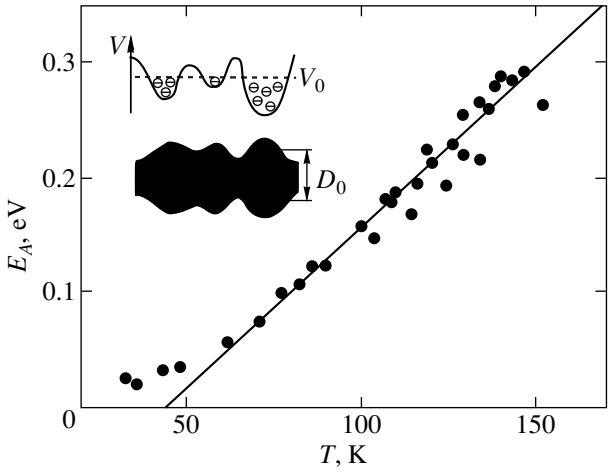

Fig. 2. Temperature dependence of the average activation energy $\langle E_A \rangle$ for trapping states. Insets illustrate the origin of topological traps in silicon wires due to variations in their diameter D_0.

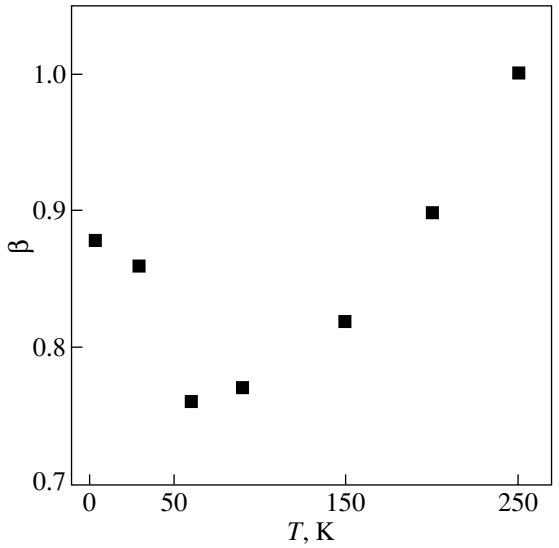

Fig. 3. Temperature dependence of the Becquerel index β of tunneling luminescence decay.

multiple retrapping [9]. The latter mechanism, in essence, is as follows. A charge carrier undergoes transfer through thermally activated hopping from the trapping state to the nearest band state, executes diffusive motion until another trap located at a point of the space is attained, is retrapped at this point, again undergoes thermally activated transfer to a band state, is retrapped at a new point of the space, etc. This process is called dispersive transport or non-Gaussian diffusion. Making allowance for the possible retrapping of charge carriers, Berlin *et al.* [8] derived a relationship for the Becquerel index. On this basis, we can explain the nonmonotonic behavior of $\beta(T)$. By generalizing the above model to porous silicon with an irregular structure of silicon wires (see insets to Fig. 2), we assumed that very short thick segments of silicon wires serve as isolated trapping centers (topological traps), whereas extended segments of silicon wires with a constant thickness play the role of band states. The multiple retrapping of charge carriers between these regions can be responsible for the nonmonotonic dependence $\beta(T)$ (Fig. 3). The proposed hypothesis is in reasonable qualitative agreement with the assumption regarding the influence of topological traps on the shape of the TSL spectrum. However, this hypothesis calls for more rigorous theoretical justification.

4. CONCLUSIONS

Thus, the results obtained in this work lent support to the validity of the proposed model of a two-stroke charge piston that acts in turn on the electron and hole components due to an Auger electron process occurring under conditions of spatial confinement of charge carriers in silicon nanoparticles. This model offers a satisfactory explanation for both the activation nature of the localization of charge carriers in traps of oxide shells and the charge accumulation in these shells.

Moreover, we revealed the specific features of the one-dimensional confinement of charge carriers in topological traps upon thermally stimulated luminescence and tunneling luminescence.

ACKNOWLEDGMENTS

This work was supported by the Intergovernmental Russian–Ukrainian program “Nanophysics and Nanoelectronics” (grant “Electrical and Optical Properties of Nanostructures Based on Silicon and Germanium”) and the program of the National Academy of Sciences of Ukraine “Physical and Astrophysical Basic Research in the Structure and Properties of Matter on the Macroscopic and Microscopic Levels.”

REFERENCES

1. E. Cohen and M. D. Sturqe, Phys. Rev. B **15** (2), 1039 (1977).
2. S. Permodorov, A. Resznitsky, and S. Verbin, Phys. Status Solidi B **113** (2), 589 (1982).
3. I. V. Blonskiĭ, V. N. Karataev, D. D. Kolendritskiĭ, *et al.*, Fiz. Tverd. Tela (St. Petersburg) **34** (10), 3256 (1992) [Sov. Phys. Solid State **34**, 1742 (1992)].
4. I. V. Blonskiĭ, M. S. Brodin, A. Yu. Vakhnin, *et al.*, Fiz. Nizk. Temp. **28** (8/9), 978 (2002) [Low Temp. Phys. **28**, 706 (2002)].
5. I. V. Blonskiĭ, M. S. Brodin, A. Yu. Vakhnin, *et al.*, Mikrosist. Tekh., No. 2 (2003) (in press).
6. I. V. Blonskyy, M. S. Brodyn, A. Yu. Vakhnin, *et al.*, Phys. Lett. A **279**, 391 (2001).
7. A. Kux, D. Kovalev, and F. Koch, Appl. Phys. Lett. **66** (1), 49 (1995).
8. Yu. A. Berlin, N. I. Chekunaev, and V. I. Goldanskii, J. Chem. Phys. **92** (12), 7540 (1990).
9. V. I. Arkhipov, V. R. Nikitenko, and A. I. Rudenko, Fiz. Tekh. Poluprovodn. (Leningrad) **21** (4), 1125 (1987) [Sov. Phys. Semicond. **21**, 685 (1987)].

Translated by O. Borovik-Romanova

Physics of the Solid State, Vol. 46, No. 1, 2004, pp. 49–55. Translated from Fizika Tverdogo Tela, Vol. 46, No. 1, 2004, pp. 53–59.

PROCEEDINGS OF THE CONFERENCE DEDICATED TO O. V. LOSEV (1903–1942)

(Nizhni Novgorod, Russia, March 17–20, 2003)

Si/Ge Nanostructures for Optoelectronics Applications

V. A. Egorov[1, 2, 4], G. É. Cirlin[1, 2, 4], A. A. Tonkikh[1, 2, 4], V. G. Talalaev[3, 4], A. G. Makarov[2], N. N. Ledentsov[2], V. M. Ustinov[2], N. D. Zakharov[4], and P. Werner[4]

[1] *Institute of Analytical Instrumentation, Russian Academy of Sciences, Rizhskiĭ pr. 26, St. Petersburg, 190103 Russia*
e-mail: cirlin@beam.ioffe.rssi.ru; egorov_v@mail.ru

[2] *Ioffe Physicotechnical Institute, Russian Academy of Sciences, Politekhnicheskaya ul. 26, St. Petersburg, 194021 Russia*

[3] *Fock Institute of Physics, St. Petersburg State University, ul. Pervogo Maya 100, Petrodvorets, St. Petersburg, 198504 Russia*

[4] *Max-Planck-Institut für Mikrostrukturphysik, Halle(Saale), D-06120 Germany*

Abstract—The optical and structural properties of multilayer Si/Ge structures with precritical, as well as close-to-critical, germanium inclusions in a silicon matrix, for which the transition from the two-dimensional to island growth occurs, were studied. The possibility of obtaining intense photoluminescence at room temperature in both cases under optimally chosen growth parameters is demonstrated. The proposed approaches to producing an active region appear promising for applications in silicon-based optoelectronics. © *2004 MAIK "Nauka/Interperiodica".*

1. INTRODUCTION

We are presently witnessing a considerable worldwide interest in the search for possible ways to develop silicon-based light-emitting semiconductor devices. Efficient radiative recombination in silicon is complicated by its indirect-band-gap structure; however, if a means of increasing the efficiency is found, this would immediately make it possible to integrate optoelectronics and modern microelectronics devices on the same substrate, with silicon forming the basis. The presently known approaches to solving this problem are the use of porous silicon [1], quantum wells in the Si/Ge system, and Si/Ge and Si/Ge/C quantum dots [2], as well as of InAs/Si [3] and other direct-band-gap III–V materials, and the doping of silicon by rare-earth elements [4]. These approaches have met with partial success and also have certain shortcomings. For instance, preparing high-quality heteroepitaxial layers on a Si surface needed to obtain quantum wells and quantum dots is complicated by the lattice misfit, which accounts for a large number of defects in the growing layer of the material, and by the generation of strains in a III–V semiconductor layer because of a considerable difference between the linear-expansion coefficients of Si and of the III–V material. Doping Si by rare earth elements, for instance, by erbium, gives rise to impurity luminescence, whereas successful device application (in particular, for injection lasers) requires efficient band-to-band luminescence. The possibility of preparing a fast germanium detector integrated on a silicon chip was demonstrated in [5]. However, when using Ge/Si quantum wells (both materials have an indirect band-gap structure) as active elements for light-emitting devices, it is not possible to achieve efficient carrier collection to the recombination region and, thus, to reach a high luminescence intensity at room temperature. The above considerations stimulate the search for new ways to solve the problem of increasing the efficiency of radiative recombination in silicon-based semiconductor structures.

The first part of this report proposes a method of carrier localization in the active region consisting of nanometer-sized Ge islands with lateral dimensions less than the hole Bohr radius obtained through molecular-beam epitaxy (MBE) deposition of submonolayer coatings of germanium on silicon. Such inclusions should give rise to a partial change in the wave-vector selection rules and to the possible formation of a localized exciton (which forms in the interaction of a free electron with a hole bound to a germanium island) that is stable up to room temperatures, thus increasing the radiative recombination efficiency. This situation can be realized in the cases where the Coulomb attraction energy for the electron is stronger than the repulsive potential barrier created by the germanium nanoisland in the conduction band. To increase the radiative recombination efficiency further, we propose performing multiple vertical stacking of layers containing germanium submonolayer inclusions separated by a silicon spacer. The proposed technique for obtaining submonolayer inclusions of germanium in a silicon matrix makes it possible to attain a good localization of holes and, accordingly, of excitons; the islands should be coherent because of their small size, and the accumulated elastic strains in the structure would be small because of the small amounts of germanium used as the active regions, which gives grounds to expect a good

1063-7834/04/4601-0049$26.00 © 2004 MAIK "Nauka/Interperiodica"

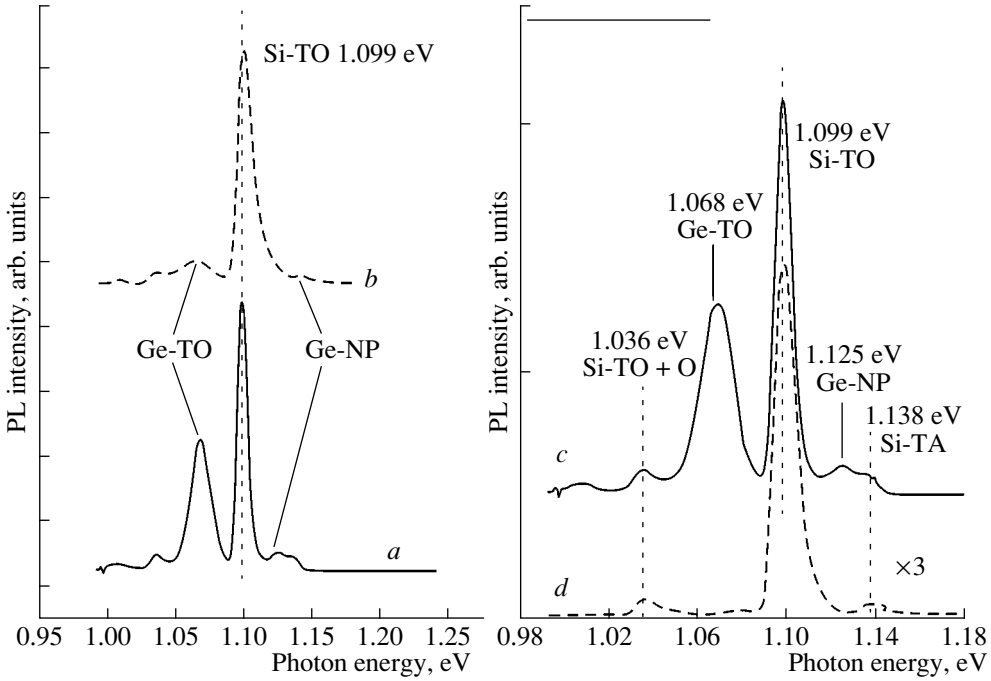

Fig. 1. PL spectra obtained at 15 K on samples with (*a*) 0.5 and (*b*) 1.0 ML of Ge in each unit layer of the structure and on samples prepared (*c*) in the growth-interrupting mode after deposition of each Ge layer and (*d*) without growth interruption.

crystallographic quality and low density of defects representing nonradiative recombination centers.

In the second part of this work, the fabrication of defect-free multilayer Si/Ge structures with quantum dots that radiate in the vicinity of 1.55 μm at room temperature is reported. The integrated intensity of the photoluminescence band originating from the quantum-dot radiation features a superlinear dependence on the optical pumping density. The results of studies of the optical and structural properties of such systems as functions of the growth parameters are presented.

2. EXPERIMENT

The experimental samples were MBE grown on semi-insulating Si(100) substrates in a Riber SIVA45 setup. The substrates were subjected to a pregrowth chemical treatment [6] to ensure removal of the oxide layer under heating to T_s = 840°C. The deviation from uniformity of the temperature distribution field produced by the substrate heater with a rotated sample did not exceed 5%. The samples actually represented a buffer silicon layer 100 nm thick (grown at T_s = 600°C), Ge/Si (20 pairs) superlattices, and a 20-nm-thick silicon cap layer. The thickness of a Ge layer was 0.7–9 Å, and that of a silicon spacer, 40–50 Å. The growth temperature of the active region was 600–750°C. In several samples, the silicon spacer was doped by an *n*-type impurity (Sb). The growth rates for Si and Ge, maintained constant by means of mass spectrometers tuned to atomic masses 28 (Si) and 74 (Ge), were 0.5 and 0.02–3 Å/s, respectively, in this growth process. The pressure in the growth chamber in these experiments was less than 5×10^{-10} Torr. The deposition of the active region was monitored *in situ* by using high-energy electron diffraction in the reflection geometry. The photoluminescence (PL) was excited by an Ar^+ laser (λ = 488 nm). To measure the PL dependence on pump density, the laser beam was focused on a spot 10^3 μm^2 in area on the sample surface. The PL temperature dependence was measured in a helium cryostat. The PL signal was collected by a monochromator interfaced to a Ge photodetector cooled by liquid nitrogen (Edinburgh Instruments, Inc). In constructing the PL dependences on pump power, the spectra were normalized against the photodetector sensitivity. The structural studies were conducted using transmission electron microscopy (TEM) on a JEM 4010 (accelerating voltage 400 kV) and CM 20 (200 kV).

3. RESULTS AND DISCUSSION

3.1. Si/Ge Structures with Submonolayer Inclusions

Our earlier studies of the optical properties of Si/Ge structures with submonolayer germanium inclusions [7] revealed new lines in the PL spectra of these samples; these lines were not observed in the spectrum of the silicon substrate and were assigned to radiation from the Si/Ge superlattice. Interestingly, if an integer number of Ge monolayers was deposited, the integrated intensity of the corresponding PL peak was ~20 times weaker than in the case of deposition of 0.5 ML

(Figs. 1a, 1b). Structural studies showed that a germanium layer obtained by depositing an integer number of monolayers is practically monatomic, whereas in a submonolayer film germanium merges to form nanoislands up to a few monolayers thick [8]. The differences in the structural and optical properties can be accounted for in the following way. The film of a monolayer coverage is singular, while in the case of the surface being incompletely covered local nonuniformities form on it. When the substrate material is deposited on top, the generated elastic stresses can favor the creation of three-dimensional islands under certain conditions. The island size is governed by the balance between the elastic and surface energies. If two-dimensional nuclei are smaller than the critical size, it is energetically preferable for the islands to have a three-dimensional structure, while larger islands retain their planar form. In our case, deposition of 0.5 ML Ge produces first relatively small germanium islands of monatomic height on the silicon surface, because this amount of material is insufficient to cover the whole surface. After that, these plane islands are overgrown by a silicon spacer, which changes the balance between the surface and elastic energies. If these islands are less than the critical size, they transform from planar to three-dimensional; otherwise, they retain their shape.

To substantiate this mechanism, we prepared samples by interrupting the growth immediately after the Ge layer deposition. The growth-interrupting mode stimulates germanium adatom migration over the surface, with the result that plane nanoislands thus obtained are larger in size than those obtained without the interruption. Figures 1c and 1d display PL spectra for samples grown without interruption and with a 120-s interruption. In the spectrum obtained in the second case, the PL peak corresponding to radiation from the Si/Ge superlattice practically cannot be seen. TEM observations likewise do not reveal any three-dimensional nanoislands in the sample prepared in the growth-interrupting mode. These results show that, in this case, the two-dimensional islands were above the critical size, so that overgrowth by the silicon spacer did not stimulate the formation of three-dimensional inclusions and the Ge islands retained their plane shape.

Because the holes in the Ge islands become efficiently localized in the Si/Ge structures under study, while electron localization in the islands is partially suppressed by the repulsive potential of the barrier, we proposed additional doping of the matrix by an *n*-type impurity as a means of increasing the PL intensity. With an optimally chosen doping level, the PL efficiency increases by up to 50 times compared to the undoped structure. Figure 2 shows PL spectra measured at 15 K on a doped Si/Ge sample and an InAs sample with quantum dots in an $In_{0.12}Ga_{0.88}As$ quantum well (thus permitting intense generation at a wavelength of 1.3 μm at room temperature). The internal quantum efficiency of the latter sample was estimated to be close to 100%

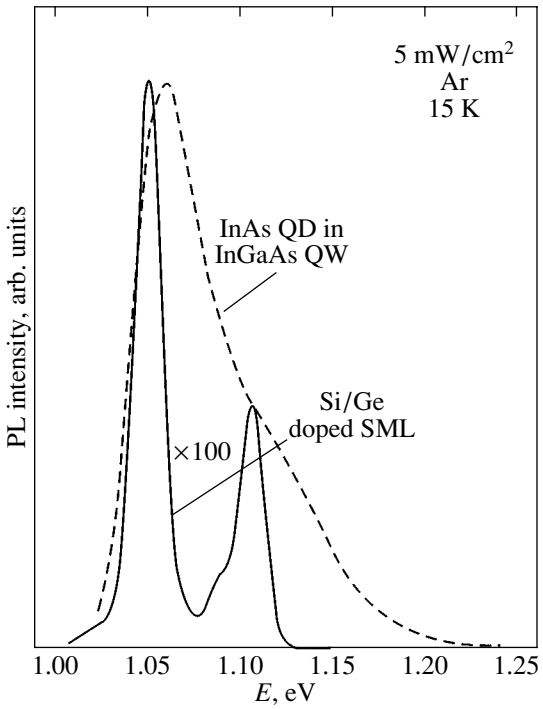

Fig. 2. Comparison of PL spectra of InAs quantum dots in an InGaAs quantum well and of a Sb-doped Si/Ge multilayer quantum-dot structure.

[9]. It should be pointed out that our doped Si/Ge sample with submonolayer inclusions produces a PL intensity only two orders of magnitude lower than that of the sample with direct-gap InAs quantum dots in a GaAs matrix. Furthermore, we have recently demonstrated that the integrated PL intensity exhibits a superlinear dependence on excitation density [10] in Si/Ge structures with submonolayer Ge inclusions, which makes the above method a promising approach for developing silicon-based light-emitting devices.

3.2. Si/Ge Quantum-Dot Structures

We studied structures made up of 20 Ge layers 0.7- to 0.9-nm thick separated by a 5-nm-thick silicon spacer. After deposition of the Ge layer, the surface was maintained in a Sb flux for 20–30 s (delta doping); as a result, the adjoining 2 nm of the spacer were doped by an *n*-type impurity, while the remaining 3 nm of the spacer were left undoped. Figure 3 presents typical TEM images of the cross section (Fig. 3a) and surface plane (Fig. 3b) of the Si/Ge quantum-dot structures under study. Despite the small spacer thickness, the structures do not exhibit any structural defects. We clearly see Ge islands with lateral dimensions of ~80 nm whose height varies from 3 to 5 nm. The highest islands are located in the central part of the structure. The average surface density of the islands as estimated from Fig. 3b is $\sim 1 \times 10^{10}$ cm^{-2} in each layer. The

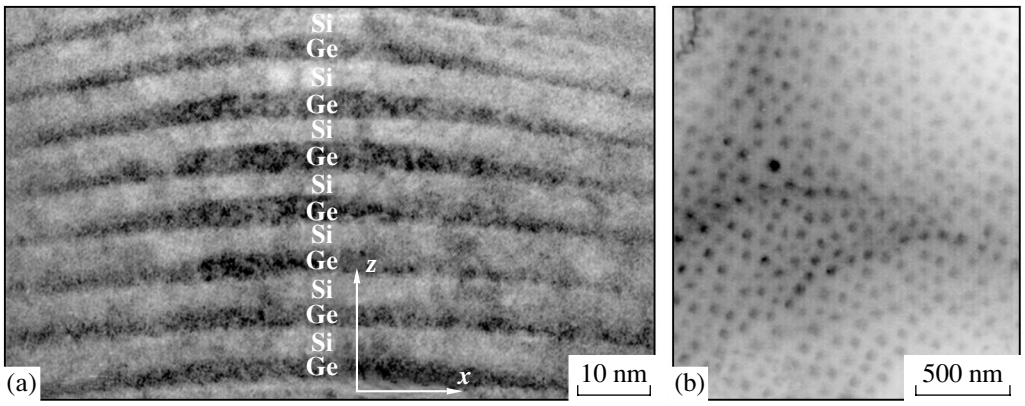

Fig. 3. High resolution TEM images (a) of a cross section and (b) of the surface plane of an optimized Ge/Si sample with quantum dots.

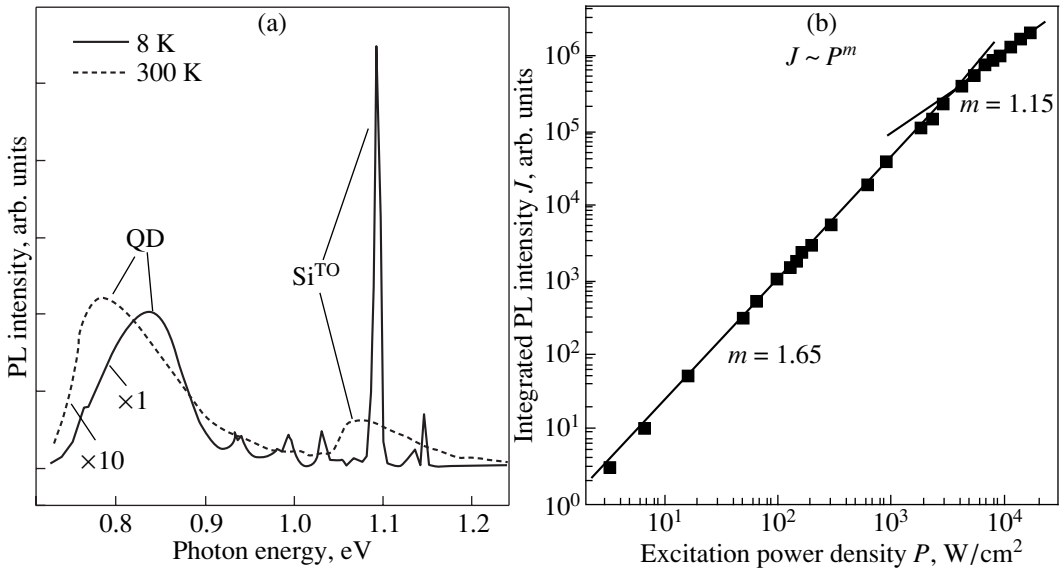

Fig. 4. (a) PL spectra of an optimized Ge/Si quantum-dot sample for an excitation density of 1 W/cm^2 and (b) pump density dependence obtained at room temperature.

islands are highly ordered in both vertical and horizontal directions.

Figure 4a displays PL spectra obtained at room and liquid-helium temperatures for a Ge/Si quantum-dot sample prepared under the optimally chosen growth conditions. The PL radiation emitted from the Ge quantum dots (the corresponding peak is denoted by QD) remains fairly intense even at room temperature, and its intensity is only one tenth of that measured at 4 K. Figure 4b presents the dependence of the integrated PL intensity of the peak due to radiation from the Ge quantum dots on the optical pump density, drawn on a log–log scale. The data fit the relation $J = P^m$, where J is the PL intensity, P is the pump density, and the exponent m is equal to 1.6 over a broad range of excitation densities, from 3 to 6000 W/cm^2. At higher excitation levels, the PL intensity continues to follow a superlinear relation with $m = 1.15$. As far as we know, this type of relation has never been observed in second-order transitions in the Si/Ge system. For instance, the exponent m for the Si/Ge quantum-dot system studied in [11] was estimated as 0.78 for the quantum-dot PL (second-order transition) and as 0.96 for the radiation from the wetting layer (quasi-first-order transition).

We also studied the effect of the germanium deposition rate on the optical properties of such structures. Figure 5a shows PL spectra obtained at 4 K for samples grown at rates V_{Ge} = 0.02 Å/s (sample A) and 0.2 Å/s (sample B). As the growth rate decreases, the PL line shifts considerably to shorter wavelengths. Figure 5b

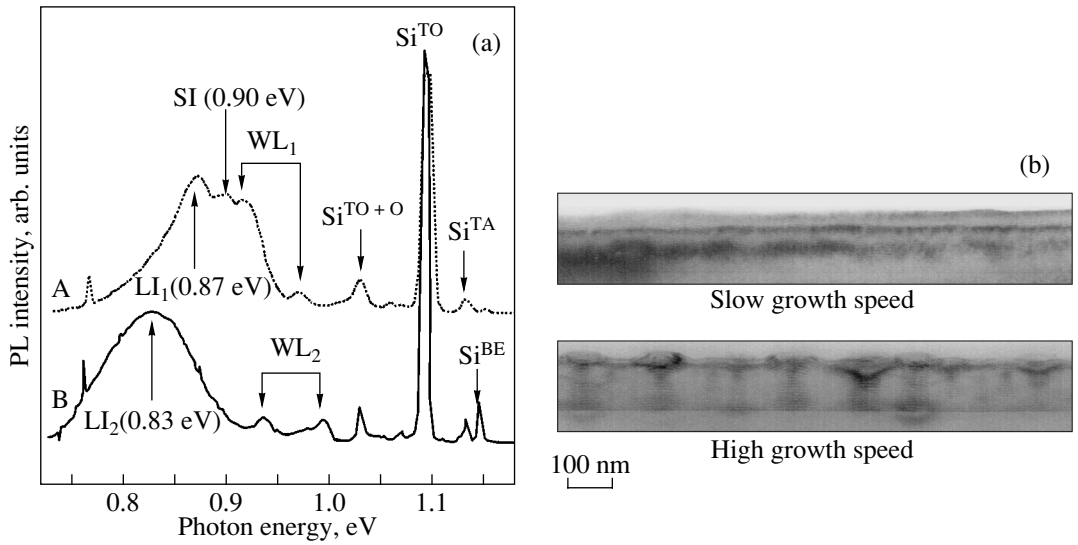

Fig. 5. (a) PL spectra obtained at 4 K for a Ge/Si multilayer structure with a 7-Å-thick Ge layer in each unit layer, which were grown at growth rates V_{Ge} = 0.02 (sample A) and 0.2 Å/s (sample B). The graph shows PL lines responsible for the radiation from the silicon matrix (Si^{TO}, Si^{TA}, Si^{TO+O}), the wetting layer (WL), small islands (SI), and large islands (LI). (b) TEM image of a cross section of the samples grown at different rates.

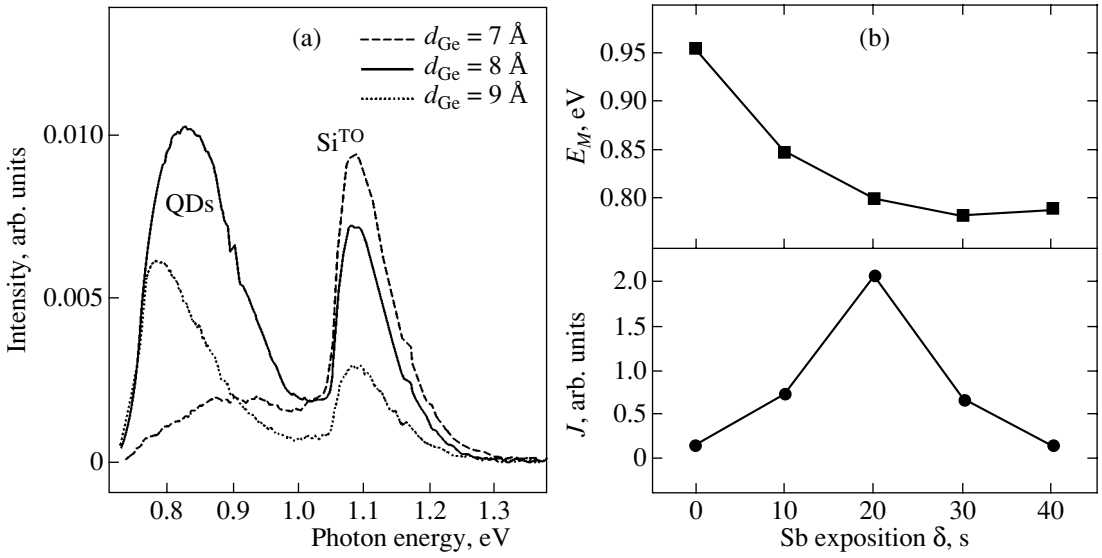

Fig. 6. (a) PL spectra obtained at room temperature for Ge/Si multilayer structures with different Ge layer thicknesses in each unit layer, V_{Ge} = 0.15 Å/s; (b) position of the PL peak (E_M) and radiation intensity J plotted vs surface hold time under the Sb flow.

displays TEM images of a cross section of these samples, which show that the germanium islands obtained at smaller growth rates are lower and that in the initial layers of the structure three-dimensional islands do not form at all. The germanium island thickness as estimated from these photomicrographs is 1–2 nm for the low growth rate and 3–5 nm for the high growth rate. The islands grown at different deposition rates likewise differ in shape; indeed, the low-rate islands are flatter, while those grown at the higher rate are pyramid-shaped. The TEM surface images of the sample grown at a low rate exhibit islands of two groups with different dimensions. These groups provide different contributions to the total PL (denoted in Fig. 5a by SI and LI for the small and large islands, respectively). At room temperature, however, the PL intensity of the islands grown at a low rate drops rapidly. The WL peaks, which are due to the radiation from the wetting layer, also lie at different spectral positions, which is consistent with the assumption that smoothing of the surface is energeti-

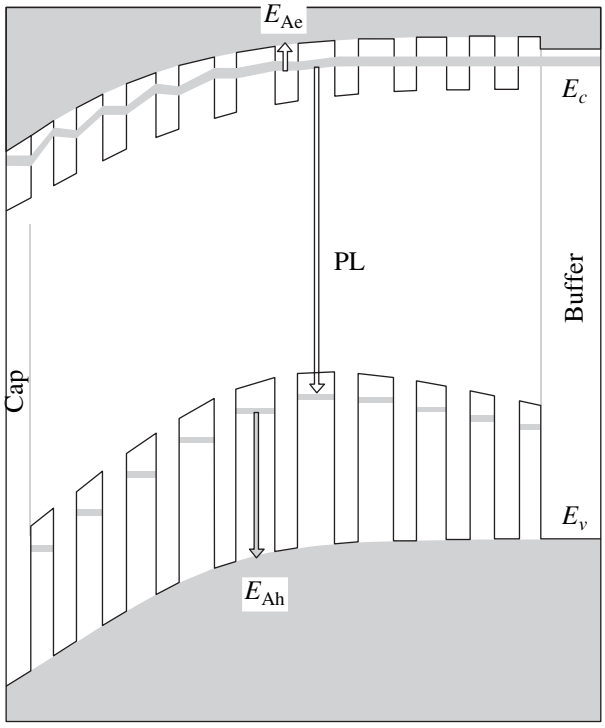

Fig. 7. Band diagram of a multilayer Ge/Si structure (schematic).

cally more favorable at low growth rates, as observed earlier for the InAs/GaAs system [12].

Figure 6a presents room-temperature PL spectra of Si/Ge multilayer structures with different Ge thicknesses in each unit layer of the superlattice. The Ge deposition rate used in these experiments was 0.15 Å/s. The PL intensity is obviously maximum in the case where the Ge thickness was 8 Å in each layer of the structure and then decreases considerably with either an increasing or decreasing amount of deposited Ge. Thus, there is an optimum thickness of the germanium layer needed to attain strong PL which depends on other growth parameters, for instance, the germanium deposition rate.

One of the goals of our growth experiments consisted in studying the effect of antimony doping on the electronic and optical properties of the structure. The PL measurements performed on samples differing in the doping level revealed that the Sb concentration substantially influences the optical properties of the samples. The PL is the strongest at a comparatively low doping, which is estimated from secondary ion mass spectrometry data as $n \sim 10^{17}$ cm^{-3}. Both an increase and a decrease in the doping level bring about a drop in the radiation intensity by a few times. At the highest doping levels [$n \sim (5–7) \times 10^{18}$ cm^{-3}] attainable by MBE at the substrate temperatures used, the PL peak shifts toward higher energies. This effect may be due to a change in the conduction band profile of the Si spacer at the Si/Ge interface, as was the case in [13].

The dependence of the optical properties of the samples consisting of Ge layers of the optimum thickness of 8 Å deposited at V_{Ge} = 0.15 Å/s on the doping level is shown graphically in Fig. 6b. The PL intensity is the strongest for the sample whose surface was maintained under a Sb flux for 20 s after deposition of each Ge layer. The PL peak is red-shifted as the hold time is increased to 20 s; then, after the maximum wavelength of 1.6 μm has been reached, the peak undergoes a blue shift. Note that, in structures with the Ge thickness in each layer differing from the optimum 8 Å, one can achieve efficient PL by properly choosing the other growth parameters, namely, the germanium deposition rate and the doping level.

Summing up the above experimental studies of the effect of the doping level, the amount of deposited germanium in each layer of the structure, and its deposition rate on the optical and structural properties, we propose the following interpretation of the superlinear dependence of integrated PL intensity on excitation density. We believe that this dependence can be readily understood under the assumption that the electron wave functions overlap with the formation of a miniband in the growth direction whereas the holes remain localized in the quantum wells formed by Ge inclusions. The corresponding band diagram is shown schematically in Fig. 7. Note the band bending near the upper layers of the structure, which appears because of the antimony atom segregation. One may conceive here two versions: (a) if the miniband penetrates into the surrounding silicon matrix, partial ejection of carriers into the matrix will make the PL intensity relatively weak, and (b) if the miniband is isolated from the Si matrix (as shown in Fig. 7), the PL intensity will be high and the exponent m will become greater than unity as a result of the formation of a heterojunction of the first type and of the corresponding increase in the exciton oscillator strength. The band edge bending needed for this situation to be realized is provided by the corresponding Sb doping level, which affects the miniband formation and, in the final count, the optical properties of Si/Ge multilayer quantum-well structures in a dominant way.

4. CONCLUSIONS

Thus, we have demonstrated the possibility of obtaining intense luminescence at room temperature near the 1.55-μm wavelength, which is of considerable importance for the development of long-distance fiber communications. The radiation intensity grows superlinearly with increasing pump density with the nonlinearity exponent m = 1.6 within a broad range of pump densities. The proposed approach to the creation of an active region appears promising for the development of silicon-based light emitting diodes.

ACKNOWLEDGMENTS

This study was supported in part by the Ministry of Industry, Science, and Technology of the Russian Federation. One of the authors (G. É. C.) expresses warm gratitude to the Alexander von Humboldt Stiftung.

REFERENCES

1. S. F. Fang, K. Adomi, S. Iyer, *et al.*, J. Appl. Phys. **68**, R31 (1990).
2. N. N. Ledentsov, in *Proceedings of the 23rd International Conference on the Physics of Semiconductors*, Ed. by M. Scheffler and R. Zimmermann (World Sci., Singapore, 1996), Vol. 1, p. 19.
3. N. D. Zakharov, P. Werner, U. Gösele, *et al.*, Appl. Phys. Lett. **76**, 2677 (2000).
4. S. Coffa, G. Franzo, and F. Priolo, Appl. Phys. Lett. **69**, 2077 (1996).
5. L. Colace, G. Masini, G. Asanto, *et al.*, Appl. Phys. Lett. **76**, 1231 (2000).
6. G. É. Cirlin, P. Verner, U. Gösele, *et al.*, Pis'ma Zh. Tekh. Fiz. **27** (1), 31 (2001) [Tech. Phys. Lett. **27**, 14 (2001)].
7. G. E. Cirlin, V. A. Egorov, B. V. Volovik, *et al.*, Nanotechnology **12**, 417 (2001).
8. N. D. Zakharov, P. Werner, U. Gösele, *et al.*, Mater. Sci. Eng. B **87**, 92 (2001).
9. S. S. Mikhrin, A. E. Zhukov, A. R. Kovsh, *et al.*, Semiconductors **34**, 119 (2000).
10. A. G. Makarov, N. N. Ledentsov, A. F. Tsatsul'nikov, *et al.*, Fiz. Tekh. Poluprovodn. (St. Petersburg) **37** (2), 219 (2003) [Semiconductors **37**, 210 (2003)].
11. J. Wang, G. L. Jin, Z. M. Jiang, *et al.*, Appl. Phys. Lett. **78**, 1763 (2001).
12. G. E. Cirlin, V. N. Petrov, A. O. Golubok, *et al.*, Surf. Sci. **377–379**, 895 (1997).
13. A. V. Dvurechenskiĭ and A. I. Yakimov, Fiz. Tekh. Poluprovodn. (St. Petersburg) **35** (9), 1143 (2001) [Semiconductors **35**, 1095 (2001)].

Translated by G. Skrebtsov

Physics of the Solid State, Vol. 46, No. 1, 2004, pp. 5–9. Translated from Fizika Tverdogo Tela, Vol. 46, No. 1, 2004, pp. 10–14.

PROCEEDINGS OF THE CONFERENCE DEDICATED TO O. V. LOSEV (1903–1942)

(Nizhni Novgorod, Russia, March 17–20, 2003)

Electroluminescence Efficiency of Silicon Diodes

M. S. Bresler, O. B. Gusev, B. P. Zakharchenya, and I. N. Yassievich

Ioffe Physicotechnical Institute, Russian Academy of Sciences, Politekhnicheskaya ul. 26, St. Petersburg, 194021 Russia

e-mail: mikhail.bresler@mail.ioffe.ru

Abstract—The intrinsic electroluminescence (EL) of a silicon light-emitting diode with a forward-biased *p–n* junction is studied. The substantial enhancement of the integrated EL intensity observed with the temperature increasing from the liquid-nitrogen to room-temperature level, which is paralleled by an increase in the EL decay time when the current through the diode is terminated, indicates thermal suppression of the nonradiative recombination channel associated with deep traps. A simple model developed by us for the radiative processes occurring in a *p–n* junction offers an interpretation for all the experimental data obtained. It is shown that the internal quantum efficiency of the EL may reach a level of a few percent under optimal doping of the diode *p* and *n* regions. © *2004 MAIK "Nauka/Interperiodica".*

1. INTRODUCTION

Room-temperature electroluminescence (EL) of silicon is a topic of considerable current interest. Silicon is a material with application potential in optoelectronics and is compatible with standard integrated circuit technology, including ultralarge-scale integration (ULSI). Currently, silicon optoelectronics are developing in three directions, namely, (i) the application of silicon-based quantum structures [1–3], (ii) the introduction of rare earth impurities [4, 5], and (iii) the use of new approaches to the investigation of the edge luminescence itself [6, 7]. Despite considerable progress having been reached recently in the first two areas, the problem of developing efficient silicon-based optoelectronic devices remains unsolved. This is probably why researchers have again resumed investigation of the intrinsic luminescence of silicon in an attempt to increase the external quantum efficiency of the luminescent emission of a light-emitting structure [6] or to optimize the *p–n* junction itself with the purpose of attaining the maximum possible intensity of intrinsic silicon emission [7]. It is maintained [7] that the dislocation loops forming in the course of boron implantation favor an increase in the internal EL quantum efficiency at room temperature. Unfortunately, the reported experimental data leave room for doubt in this respect.

The present communication reports the first observation and study of the edge EL of a forward-biased alloyed silicon diode. Our experimental data are close to those quoted in [7], where the *p–n* structure was prepared by implanting boron into an *n*-type substrate. We developed a simple model of the recombination processes occurring in a forward-biased *p–n* junction. This model is capable of accounting for the totality of our experimental data, including the increase in the EL intensity with temperature in the interval extending from liquid-nitrogen temperature to room temperature, which was observed both by us and in [7]. We also determined the optimal parameters of the *p–n* junction necessary to attain the maximum possible internal quantum efficiency of edge EL and the highest modulation frequency.

2. EXPERIMENTAL RESULTS

We used a standard alloyed silicon diode, with part of its metal casing removed to couple out the radiation. The donor concentration in the *n*-type substrate was $\sim 1 \times 10^{15}$ cm^{-3}. The acceptor concentration in the *p* layer was 5×10^{19} cm^{-3}. These parameters are typical of a conventional abrupt *p–n* junction. In the region 77–300 K, all donors and acceptors are ionized; as a result, the concentrations of the electrons and holes are equal to those of the donors and acceptors, respectively. The *I–V* characteristics of our light-emitting diode measured at liquid-nitrogen temperature and room temperature had the usual pattern (Fig. 1). The intrinsic silicon EL was observed in the interval from liquid-nitrogen temperature to room temperature with current pulses through the diode of up to 100 mA. The radiation was collected from the diode side surface and directed into a grating spectrometer equipped with a cooled germanium photodetector. The EL decay time after termination of the diode current was measured using a digital oscillograph. The time resolution of the measuring circuit, limited by the germanium photodetector response, was 5 μs.

Figure 2 shows EL spectra of our light-emitting diode structure for temperatures of 77 and 300 K obtained with a forward-biased *p–n* junction. Practically all of the intrinsic silicon EL radiation formed at liquid-nitrogen temperature is due to free-exciton annihilation, the line at 1.13 μm originating from recombi-

1063-7834/04/4601-0005$26.00 © 2004 MAIK "Nauka/Interperiodica"

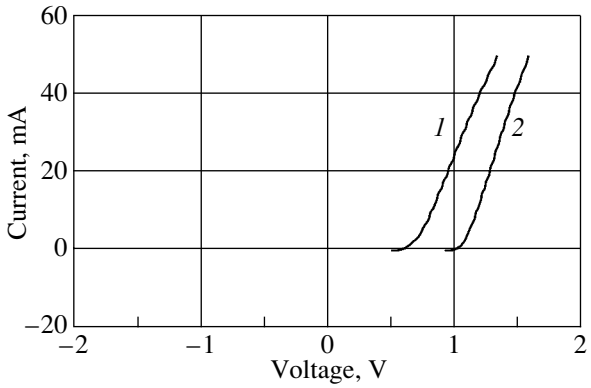

Fig. 1. *I–V* characteristics of the diode at *T* equal to (*1*) 300 and (*2*) 77 K.

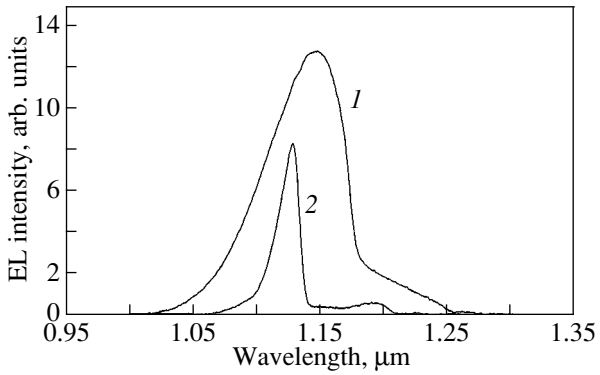

Fig. 2. EL spectra of a silicon diode structure obtained at *T* equal to (*1*) 300 and (*2*) 77 K with a dc current of 20 mA through the diode.

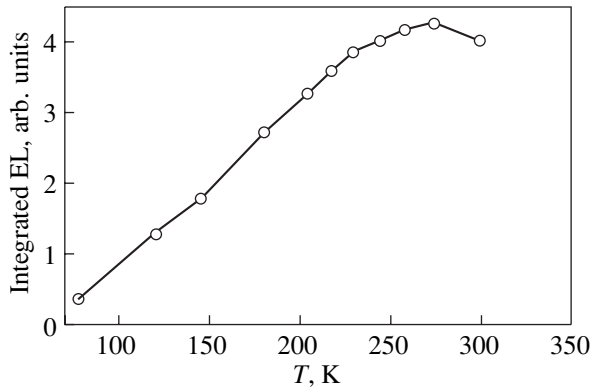

Fig. 3. Integrated edge EL intensity plotted vs temperature. Points are experimental data. The current through the structure is 20 mA.

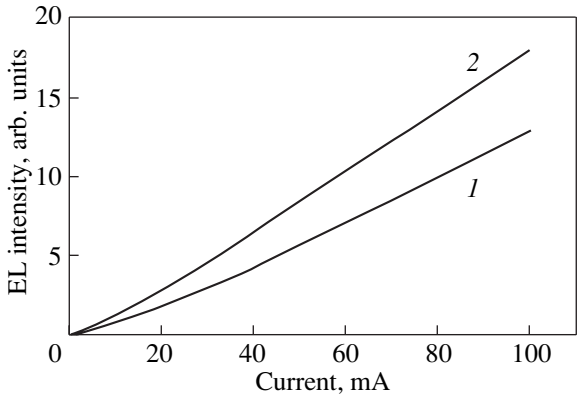

Fig. 4. Edge EL intensity of the diode structure plotted vs. current through the *p–n* junction for *T* equal to (*1*) 100 and (*2*) 300 K.

nation involving the emission of one transverse optical phonon, and the 1.18-μm line originating from that with the emission of two phonons. At room temperature, we observed a slight shift of the EL line maximum relative to its position at liquid-nitrogen temperature. This shift is less than the temperature-induced narrowing of the silicon band gap and is accounted for by the fact that the edge luminescence spectrum at room temperature consists of nearly equal contributions due to the recombination of free carriers with excitons. No other luminescence lines were observed in the wavelength interval from 1.0 to 1.7 μm.

Figure 3 plots the dependence of the integrated intrinsic silicon EL intensity on temperature obtained by passing a dc current through the *p–n* junction. This dependence is seen to have a linear section and a maximum at a temperature close to room temperature, which is in agreement with the data from [7]. The dependence of the integrated intensity of the intrinsic EL on current was practically linear at both liquid-nitrogen temperature and room temperature (Fig. 4). The decay time of the EL intensity following termination of the current pulse was less than 5 μs (the time resolution of the measuring circuit) at 80 K and was 20 μs at room temperature. The external quantum efficiency of our structure reached a level on the order of 10^{-4}.

Interestingly, our experimental data practically coincide with the results reported in [7]. The latter were obtained on a *p–n* junction prepared by implanting boron into an *n*-type phosphorus-doped substrate.

3. RESULTS AND DISCUSSION

To interpret the experimental results obtained, we used the conventional model of a forward-biased abrupt *p–n* junction. If the thickness of the depleted layer is less than the carrier diffusion length, no recombination takes place in the depleted layer. The rate of radiative recombination in the *n* layer of the structure can be written as

$$R_n = r_r n_n \Delta p = r_r n_n p_n \left(e^{\frac{qV}{kT}} - 1 \right) e^{-\frac{x - l_n}{L_p}}, \qquad (1)$$

where r_r is the radiative recombination coefficient, n_n is the concentration of majority carriers (electrons in the n region), Δp is the concentration of the holes injected into the n region, p_n is the concentration of minority carriers (holes) in the n region of the p–n junction at thermodynamic equilibrium, V is the voltage across the p–n junction, L_p is the hole diffusion length in the n region, l_n is the depleted-layer thickness in the n region, and x is the distance from the boundary of the p–n junction.

We performed measurements with dc current passed through the p–n junction. Therefore, it is convenient to substitute the current expressed through the I–V characteristic of the p–n junction into Eq. (1):

$$j = j_0\left(e^{\frac{qV}{kT}} - 1\right) \equiv q\left(\frac{D_n n_p}{L_n} + \frac{D_p p_n}{L_p}\right)\left(e^{\frac{qV}{kT}} - 1\right), \quad (2)$$

where L_n is the electron diffusion length in the p region; D_n and D_p are the diffusion coefficients of electrons and holes, respectively; and n_p is the equilibrium concentration of the minority carriers (electrons) in the p region.

Integration of Eq. (1) over x yields the photon flux density emitted from the n region in the direction perpendicular to the plane of the p–n junction:

$$I_n = r_r n_n p_n L_p \frac{j}{q}\left(\frac{D_p p_n}{L_p} + \frac{D_n n_p}{L_n}\right)^{-1}. \quad (3)$$

In the same way, one can find the photon flux density emitted from the p region:

$$I_p = r_r n_p p_p L_n \frac{j}{q}\left(\frac{D_p p_n}{L_p} + \frac{D_n n_p}{L_n}\right)^{-1}. \quad (4)$$

Because $n_n p_n = p_p n_p$, the ratio of the EL intensities emitted from the two sides of the p–n junction can be written as

$$\frac{I_n}{I_p} = \frac{L_p}{L_n} = \sqrt{\frac{D_p \tau_p}{D_n \tau_n}}, \quad (5)$$

which means that the EL intensity ratio for the n and p regions is determined only by the diffusion length ratio of the minority carriers injected into these regions.

Figure 5 displays the averaged lifetimes of electrons and holes in the p and n regions, respectively, taken from [8]. For our structure, the lifetime of holes in the n region is 2×10^{-5} s (for a donor concentration of 10^{15} cm^{-3}), whereas for electrons in the p region (for an acceptor concentration of 5×10^{19} cm^{-3}) the corresponding time is 10^{-8} s. To estimate the diffusion coefficients, we made use of the data on mobilities from [9]. The diffusion coefficient of holes for the doping levels corresponding to our p–n junction is about four times greater than that of the electrons. Therefore, the diffusion length of holes L_p is a few tens of times larger than that of electrons, L_n. Accordingly, the n region provides the major contribution to the edge EL in the structure under study. Using the above estimates and the majority carrier concentration ratio $p_n/n_p \sim 10^4$, we find from Eq. (3)

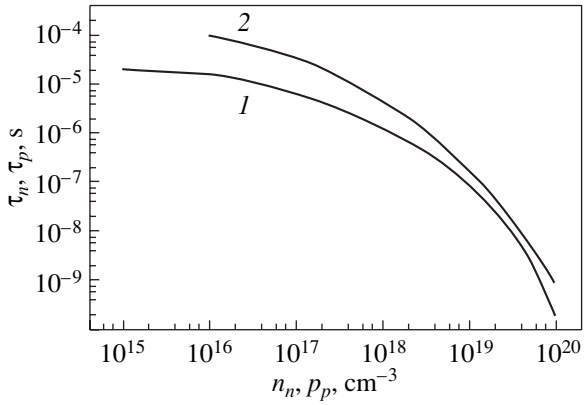

Fig. 5. Minority carrier lifetime vs. majority carrier concentration plots at $T = 300$ K [8]: (*1*) τ_n and (*2*) τ_p.

$$I_n \approx r_r n_n p_n L_p \frac{j}{q}\left(\frac{D_n n_p}{L_n} + \frac{D_p p_n}{L_p}\right)^{-1} = r_r n_n p_n L_p^2 \frac{j}{q D_p p_n} = r_r n_n \tau_p \frac{j}{q}. \quad (6)$$

As seen from Eq. (6), the integrated EL intensity is linear in current density (in accordance with the data in Fig. 4) and its temperature dependence is determined by the temperature behavior of the hole lifetime in the n region and by that of the radiative recombination coefficient r_r.

It was shown in [10] that the radiative recombination coefficient for indirect-gap radiative transitions of excitons and free carriers scales with increasing temperature as

$$r_r \propto \sqrt{\frac{E_x}{kT}}\left[1 + 2\frac{E_x}{kT}\exp\left(\frac{E_x}{kT}\right)\right]\coth\left(\frac{\Theta}{2T}\right), \quad (7)$$

where E_x is the exciton binding energy and Θ is the Debye temperature of the transverse optical phonon. Because of the high Debye temperature, the last factor in Eq. (7) is practically temperature-independent and equal to unity. The first term in the brackets in Eq. (7) describes the band-to-band recombination of free carriers (with due allowance made for the Coulomb interaction between them), whereas the second term corresponds to the free-exciton recombination. Thus, the temperature dependence of the radiative recombination coefficient is governed primarily by the decrease in the free-exciton concentration. It is this temperature-induced decrease in the radiative recombination coefficient that accounts for the usually observed decrease in the photoluminescence intensity with increasing temperature.

However, our experimental data indicate that the EL intensity and its decay time after the current pulse is turned off increase with temperature. To explain these observations, one has to assume that the hole lifetime τ_p increases with temperature faster than the radiative recombination coefficient r_r decreases.

We believe that the *n* region of the diode under study contains a certain concentration of traps acting as recombination centers [this concentration should be less than that of the majority carriers (electrons)]. On the other hand, data obtained on the photoluminescence of *n*-type samples with the same doping level show their luminescence intensity to decrease with temperature, which means that they do not contain such recombination centers as the *n* region of the diode. We assume that the traps in the diode *n* region arise because the defects forming under heavy doping of the *p* region penetrate into the *n* region. Note that the defect penetration depth into the *p* region should in this case be large enough, at least on the order of the diffusion length of the minority carriers $L_p = (D_p\tau_p)^{1/2} \approx (3 \times 10^{-5})^{1/2} \approx 60$ μm.

It is quite possible that the hole lifetime τ_p is governed by the nonradiative trapping of holes by deep attracting centers. In this case, the trapping process can be divided into two stages. In the first stage, the holes are trapped into higher lying Coulomb states, to drop subsequently down through the densely spaced energy spectrum of these states (the cascade mechanism of trapping). However, the dense spectrum of high excited states extends, as a rule, only to a depth of the order of the shallow-center Bohr binding energy, i.e., about 45–50 meV in silicon. This spectrum is separated from the ground state by a large energy gap, and as a result the second trapping stage (transition to the ground state) requires a high energy transfer and can occur in a nonradiative manner only as a multiphonon process, with a considerably lower probability. Therefore, a trapped carrier can reside for a long enough time in the last excited state that one may consider this state metastable and describe the total recombination process by the two-level center model. The recombination process involving a metastable level with a characteristic energy E_t is discussed in [8].

As the temperature increases, the carriers residing in the metastable state are more likely to be ejected back into the band than go to the ground state. In this case, the effective minority carrier lifetime begins to grow exponentially with temperature:

$$\tau_T \propto \exp(-E_t/kT). \tag{8}$$

The carrier lifetime increases up to the point where thermal activation becomes sufficiently strong and the multiphonon-assisted carrier transition from the first excited to the ground state of the recombination center is more likely to occur than the reverse ejection into the band. In this temperature region, the increase in the carrier lifetime slows down, to be subsequently replaced by a decrease in τ_p.

Thus, we associate the observed growth in the EL intensity with temperature with the increasing effective lifetime of the injected holes. As follows from our consideration, this growth in intensity implies the existence of deep nonradiative recombination centers in the sample, i.e., insufficient quality of the diode emitter part.

4. OPTIMAL LIGHT-EMITTING DIODE PARAMETERS FOR THE EDGE ELECTROLUMINESCENCE FROM SILICON

So far, we have studied edge EL in silicon by using standard-type light-emitting structures, i.e., with a lightly doped *n* region and a heavily doped *p*-type region. This technology is appropriate for diodes employed as current rectifiers, because they should have a high reverse breakdown voltage. At the same time, a good backward branch of the *I–V* characteristic is of no use for a light-emitting structure and, therefore, one can vary the doping levels of the *n* and *p* regions so as to reach the maximum efficiency of the edge EL in the light-emitting structure. We carried out a calculation of the optimum diode structure that would provide the maximum possible quantum efficiency of intrinsic EL. The internal quantum efficiency can be written in the form

$$\eta = \frac{h\nu(I_n + I_p)}{jV} \equiv \frac{h\nu(j/q)r_rA_I}{jV}, \tag{9}$$

where the numerator describes the edge EL power and the denominator is the electrical power consumed by the diode. Assuming $V \cong E_g/q$ and recalling that $h\nu \cong E_g$, we can recast the expression for the internal quantum efficiency as

$$\eta = r_rA_I \equiv r_rn_np_p(L_n + L_p)\left(\frac{D_pp_p}{L_p} + \frac{D_nn_n}{L_n}\right)^{-1}. \tag{10}$$

This relation has a very simple physical meaning; namely, if, for instance, the main contribution to the EL comes from the *p* region of the *p–n* junction, the internal quantum efficiency is simply the ratio of the total lifetime of minority carriers (electrons) to the radiative lifetime:

$$\eta = r_rp_p\tau_n \equiv \frac{\tau_n}{\tau_r}. \tag{11}$$

Figure 6 plots the internal quantum efficiency calculated by means of Eq. (10) for various doping levels of the *p–n* junction. The value used for the radiative recombination coefficient, $r_r = 10^{-14}$ cm^3 s^{-1}, was taken from [10]. Interestingly, a decrease in the mobility, which is proposed in [7] as a means to attain a higher internal quantum efficiency, can bring about, as is evident from Eq. (11), a decrease in the EL intensity only.

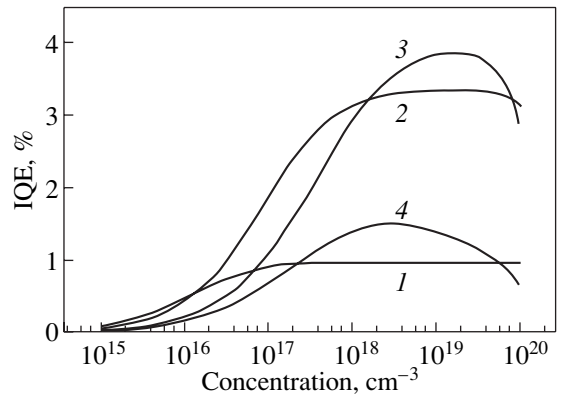

Fig. 6. Internal quantum efficiency (IQE) vs. electron concentration n_n in the *n* region of the *p*–*n* junction plotted for various values of the hole concentration p_p in the *p* region: (*1*) 10^{16}, (*2*) 10^{17}, (*3*) 10^{18}, and (*4*) 10^{19} cm^{-3}.

Our estimates based on literature data suggest that the light-emitting structures used currently to study the intrinsic silicon EL are far from being optimal. A diode with concentrations $n_n = 10^{19}$ cm^{-3} and $p_p = 1.4 \times 10^{16}$ cm^{-3} was reported in [6] to have an internal quantum efficiency of about 1%, which is in agreement with our calculations. By contrast, the structure studied in [7] and characterized by doping levels of 10^{19} and 10^{15} cm^{-3} for the *p* and *n* regions, respectively, could be expected to have a quantum efficiency of the order of 0.01% only. The EL quantum efficiency of our diode is estimated to be exactly of this order of magnitude.

Note that the decay times of edge luminescence at room temperature measured in our study and reported in [7] practically coincide and are equal to 20 μs, which agrees with the data in Fig. 5. At the same time, the internal quantum efficiency obtained in [7] is approximately 0.5%, which is clearly at odds with our result. We believe the reason for this discrepancy could be incorrect measurement of the quantum efficiency in [7].

As seen from Fig. 6, the maximum quantum efficiency of the recombination radiation is attained when the *n* region is doped to 10^{19} cm^{-3} and the *p* region is doped to 10^{18} cm^{-3}. In this case, the major contribution to the luminescence is provided by the *p* region and the comparatively high quantum efficiency is due to the large electron diffusion length. For higher *n*-region dopings, the quantum efficiency drops as a result of the enhanced Auger recombination of the minority carriers, while lower doping levels bring about a decrease in the radiative recombination probability proportional to the product $n_n p_p$. Because high doping levels are usually accompanied by the formation of defects in high concentrations, a carrier concentration in the *p* region of about 10^{17} cm^{-3} would probably be more favorable. As follows from Fig. 6, an optimally designed light-emitting diode with an *n*-region concentration of 10^{17} cm^{-3} and a concentration in the *p* region of 10^{17} cm^{-3} could have an internal quantum efficiency of up to 3% at a modulation frequency of 50 kHz.

ACKNOWLEDGMENTS

This study was supported by the Russian Foundation for Basic Research, the Netherlands scientific research foundation (NWO), the Ministry of Industry, Science, and Technology of the Russian Federation, and the RAS Physical Sciences Division program "New Materials and Structures."

REFERENCES

1. Z. H. Lu, D. J. Lockwood, and J. M. Baribeau, Nature **378**, 258 (1995).
2. K. D. Hirschman, L. Tsybeskov, S. P. Duttagupta, and P. M. Fauchet, Nature **384**, 338 (1996).
3. G. Franzò, A. Irrera, E. C. Moreira, *et al.*, Appl. Phys. A **74** (1), 1 (2002).
4. G. Franzò, F. Priolo, S. Coffa, *et al.*, Appl. Phys. Lett. **64** (17), 2235 (1994).
5. B. Zheng, J. Michel, F. Y. G. Ren, *et al.*, Appl. Phys. Lett. **64** (21), 2842 (1994).
6. M. A. Green, J. Zhao, A. Wang, *et al.*, Nature **412**, 805 (2001).
7. W. L. Ng, M. A. Lourenço, R. M. Gwilliam, *et al.*, Nature **410**, 192 (2001).
8. V. N. Abakumov, V. I. Perel', and I. N. Yassievich, *Nonradiative Recombination in Semiconductors* (S.-Peterb. Inst. Yad. Fiz. Ross. Akad. Nauk, St. Petersburg, 1997).
9. C. Jacoboni, C. Canali, G. Ottaviani, and A. Alberigi Quaranta, Solid-State Electron. **20** (2), 77 (1977).
10. H. Schlangenotto, H. Maeder, and W. Gerlach, Phys. Status Solidi A **21** (2), 357 (1974).

Translated by G. Skrebtsov

Physics of the Solid State, Vol. 46, No. 1, 2004, pp. 56–59. Translated from Fizika Tverdogo Tela, Vol. 46, No. 1, 2004, pp. 60–62.

PROCEEDINGS OF THE CONFERENCE DEDICATED TO O. V. LOSEV (1903–1942)

(Nizhni Novgorod, Russia, March 17–20, 2003)

Ge/Si Quantum Dots in External Electric and Magnetic Fields

A. V. Dvurechenskiĭ, A. I. Yakimov, A. V. Nenashev, and A. F. Zinov'eva

Institute of Semiconductor Physics, Siberian Division, Russian Academy of Sciences, pr. Akademika Lavrent'eva 13, Novosibirsk, 630090 Russia

e-mail: dvurech@isp.nsc.ru

Abstract—Electric field-induced splitting of the lines of exciton optical transitions into two peaks is observed for Ge/Si structures with quantum dots (QDs). With increasing field, one of the peaks is displaced to higher optical transition energies (blue shift), whereas the other peack is shifted to lower energies (red shift). The results are explained in terms of the formation of electron–hole dipoles of two types differing in the direction of the dipole moment; these dipoles arise due to the localization of one electron at the apex of the Ge pyramid and of the other electron under the base of the pyramid. By using the tight-binding method, the principal values of the *g* factor for the hole states in Ge/Si quantum dots are determined. It is shown that the *g* factor is strongly anisotropic, with the anisotropy becoming smaller with decreasing QD size. The physical reason for the dependence of the *g* factor on quantum-dot size is the fact that the contributions from the states with different angular-momentum projections to the total wave function change with the QD size. Calculations show that, with decreasing QD size, the contribution from heavy-hole states with the angular-momentum projections ±3/2 decreases, while the contributions from light-hole states and from states of the spin-split-off band with the angular-momentum projections ±1/2 increase. *© 2004 MAIK "Nauka/Interperiodica".*

1. QUANTUM DOTS IN AN ELECTRIC FIELD

Application of an electric field to a system of quantum dots (QDs) results in energy-level shifts in optical transitions (the Stark effect in quantum-confinement systems; see, e.g., [1, 2]). Most studies of the Stark effect have been performed on type-1 (InAs/GaAs) heterostructures. The red shift of optical transition energies in an electric field was observed in those studies. In type-2 heterostructures, electrons and holes are localized on different sides of the heterointerface and, once their spatial separation is sufficiently large, one may expect a strong manifestation of the Stark effect.

The Ge/Si structures with QDs form type-2 heterojunctions. When an electron–hole pair is photogenerated, the hole is localized in Ge, whereas the electron is located in the potential well formed in Si near the vertex of the Ge pyramid. Such an excitation is called the spatially indirect exciton. If a biexciton is formed, holes still remain localized in Ge; however, for the second electron, localization under the base of the Ge pyramid appears to be energetically more favorable [3]. Such a geometrical configuration results in opposite orientations of the dipoles with respect to the electric field directed along the symmetry axis of the Ge pyramid (along the growth axis; Fig. 1).

Interband optical transitions in Ge/Si systems with QDs in an electric field were studied in [4] using photocurrent spectroscopy. Two conditions have to be satisfied for experimental observation of the Stark effect. First, the size of Ge nanocrystals must be sufficiently small for the spectrum of electronic states to be discrete. The other condition is that the spatial electron–hole separation must be such that the electric dipole moments are sufficiently large. To satisfy these conditions, the method of heteroepitaxy of Ge on Si with the addition of oxygen before Ge deposition was developed in [4]. This method provides the possibility of forming hemispherical Ge islands with a size of the base of the nanocluster of about 6 nm and a height of 3–4 nm.

The electric field ranged up to 100 kV/cm. For low electric fields, a symmetric photocurrent peak is observed at a photon energy of about 1040 meV for the structures studied; this peak is attributed to indirect excitonic transitions between the hole ground state in Ge and the ground state of an electron localized in Si near the Ge/Si heterointerface. An electron–hole pair generated by photoexcitation dissociates into its components due to thermal fluctuations (the measurements are made at room temperature) and contributes to the photocurrent. The width of the photocurrent peak increases with electric field, and, finally, the peak splits into two peaks. As the electric field is increased further, the energy positions of these two peaks are displaced in opposite directions (the red and blue shifts; Fig. 2).

1063-7834/04/4601-0056$26.00 © 2004 MAIK "Nauka/Interperiodica"

These results have a sufficiently simple qualitative explanation in terms of the conception of the two dipoles that are formed on Ge quantum dots and have opposite directions with respect to the applied electric field. For one of the dipoles, the external field increases the overlap of the wave functions of the electron and the hole and, therefore, increases the exciton binding energy and gives rise to a blue shift in the photocurrent spectrum. For the dipole of the opposite direction, the overlap of the wave functions decreases, thereby producing a decrease in the exciton binding energy and a red shift of the photocurrent peak.

Perturbation-theory estimations of the spatial separations between electrons and holes and the experimental data on the electric-field dependence of the photocurrent peaks yield values that agree with the geometrical QD configuration obtained by electron microscopic studies.

2. QUANTUM DOTS IN A MAGNETIC FIELD

A splitting of discrete levels of an atom or a QD (artificial atom) in a magnetic field (Zeeman effect) is determined by the magnetic-moment projection on the field direction. In turn, the magnetic moment is related to the angular momentum by the Lande factor, which actually determines the value of the splitting of discrete levels. The Lande splitting factor for a free electron (≈2) describes the interaction of the electronic ±1/2 spin states with an external magnetic field. In solids, the *g* factor is substantially different from the *g* factor for free electrons due to the interaction with the lattice potential. With lowering the dimensionality of the system from the three-dimensional (3*D*) to the two-dimensional (2*D*) case and further, the quantum-confinement effects also change the carrier *g* factor. For example, for electrons in low-dimensional systems, the quantization results in substantial renormalization of the value of the *g* factor [5] and in its strong anisotropy [6]. The Lande factor contains quantitative information on the change in the semiconductor band structure with decreasing dimensionality and has been studied in numerous experimental and theoretical papers. For electron states, there are papers in which the *g* factor of an electron in a quantum well or a QD was calculated [7]. For hole states, the Zeeman effect has been studied theoretically and experimentally for structures with quantum wells.

In the case of QDs, the existence of confinement potential not only in the growth direction (as in the case of 2*D* structures) but also an equally strong quantization in the lateral direction should produce a significant renormalization of the *g* factor for hole states. In addition, for QDs in strained heterostructures, nonhomogeneity of strains inside quantum dots also strongly affects the *g* factor. Comparison of a quantum dot and a quantum well, both grown in the ⟨100⟩ direction, shows that in the latter structure there are no shear strains ε_{xy}, ε_{xz}, and ε_{yz} (here, **z** is the growth direction and **x** and **y** lie in the base plane of the pyramid), resulting in mixing of the states of light and heavy holes and of the states of the spin-split-off band [8]. Such strains exist in QDs.

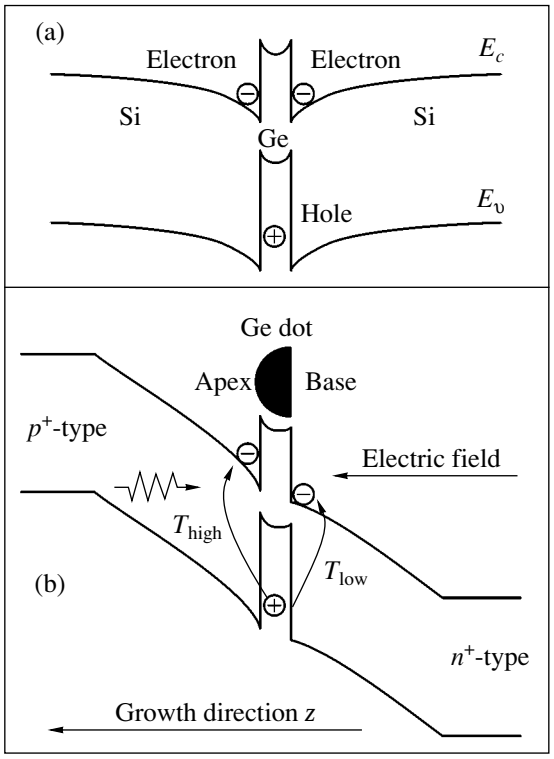

Fig. 1. (a) Band structure of the Ge/Si type-2 heterostructure along the growth direction passing through the center of symmetry of a Ge quantum dot and (b) band structure of the *p–i–n* diode under reverse bias (schematic).

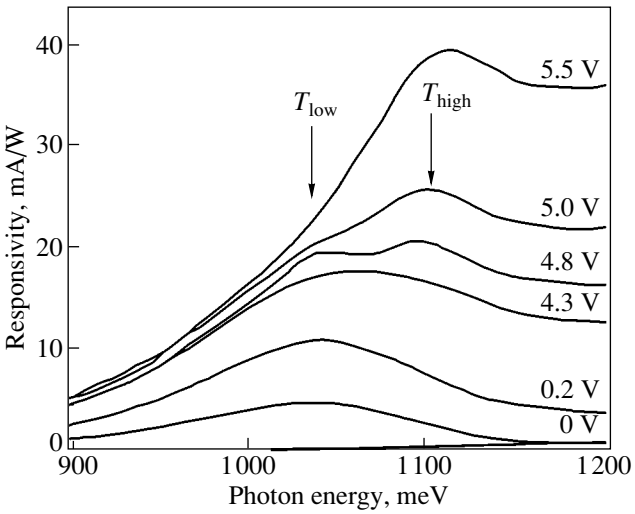

Fig. 2. Dependence of photocurrent spectra on reverse bias.

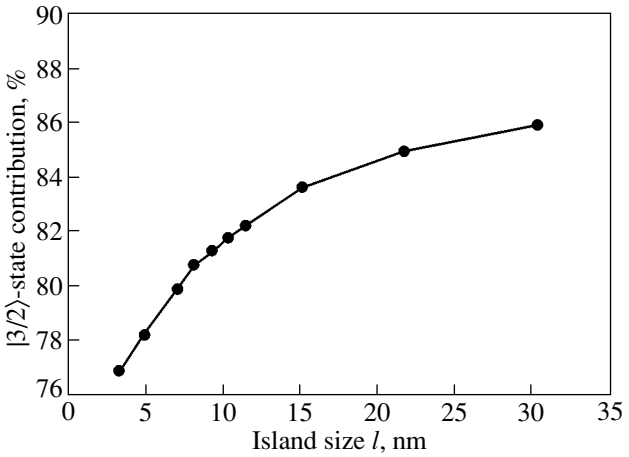

Fig. 3. Contribution from the $J_z = \pm 3/2$ states to the hole ground state as a function of the lateral size of a germanium island 1.5 nm in height.

Thus, for quantum dots, quantization in all three directions and nonhomogeneity of strains should significantly modify the *g* factor of hole states due to the mixing of the energy bands.

In [9], a method is suggested for calculating the *g* factor for hole states in quantum dots by using the tight-binding approach. This method takes into account a specific form of the quantizing potential (not necessarily described by an analytical function) and can be applied to calculate the *g* factor for QDs of any shape and of arbitrarily small size. This method can also be applied to electronic states in QDs.

If the Zeeman splitting of levels is small compared to the size-quantization energy, then the *g* factor depends only on the direction of the magnetic field and can be written in the first-order perturbation theory as

$$|g| = 2\sqrt{\langle\psi|\mathbf{n}\hat{\mathbf{M}}_{QD}|\psi\rangle^2 + |\langle\psi|\mathbf{n}\hat{\mathbf{M}}_{QD}|\psi^*\rangle|^2},$$

where **n** is a unit vector in the magnetic field direction, ψ and ψ^* are the wave functions of the level considered, and $\hat{\mathbf{M}}_{QD}$ is the magnetic-moment operator for a hole.

Calculations for a Ge/Si system with QDs show that the *g* factor of a hole in the ground state is strongly anisotropic, with the longitudinal component g_{zz} of the *g* factor being an order of magnitude larger than the transverse components g_{xx} and g_{yy}. For example, for a typical Ge island with base size $l = 15$ nm and height $h = 1.5$ nm, the values of the *g* factor components are $g_{zz} = 12.28$, $g_{xx} = 0.69$, and $g_{yy} = 1.59$.

From the calculated dependence of the *g* factor on the size of Ge islands, it follows that the *g*-factor anisotropy increases with the island size. Such a behavior of the *g* factor is mainly determined by the increased contribution from the states with the angular-momentum projections $J_z = \pm 3/2$ on the symmetry axis of the Ge island (Fig. 3).

The probability of Zeeman transitions is directly related to the character of the wave function. For the states with $J_z = \pm 3/2$ in the magnetic field $\mathbf{H} \parallel \mathbf{z}$, induced transitions between the Zeeman sublevels with $J_z = +3/2$ and $J_z = -3/2$ are forbidden by the selection rules; for allowed transitions, the condition $\Delta J_z = \pm 1$ must be satisfied. The admixture of the $J_z = \pm 1/2$ states facilitates the transitions between Zeeman sublevels of the ground state in the Ge island; therefore, with decreasing island size, the suppression of Zeeman transitions becomes weaker.

In the case of a dc magnetic field $\mathbf{H} \parallel \mathbf{z}$, the microwave field $\mathbf{H}_\omega$ lies in the plane of the QD layer and the Zeeman transition probability is proportional to the square of the matrix element of the magnetic moment component μ in the direction of the microwave field. In the special case of the microwave field $\mathbf{H}_\omega$ directed along [110], the particle magnetic moment component μ is proportional to the principal value g_{xx} of the **g** tensor and, for $\mathbf{H}_\omega \parallel [\bar{1}10]$, the particle-magnetic-moment component μ is proportional to g_{yy}. Accordingly, the transition probabilities are determined by the squares of these components of the *g* tensor, g_{xx}^2 ($\mathbf{H}_\omega \parallel [110]$) and g_{yy}^2 ($\mathbf{H}_\omega \parallel [\bar{1}10]$).

In the case of a dc magnetic field $\mathbf{H} \perp \mathbf{z}$, the magnetic-moment component μ lies in the plane perpendicular to the base plane and, in the special case of the microwave field $\mathbf{H}_\omega$ directed along [100], it is proportional to the principal value g_{zz} of the *g* tensor. The transition probability in this case is proportional to g_{zz}^2. For the obtained values of the *g* factor, the probabilities of induced transitions for the two directions of the magnetic field ($\mathbf{H} \parallel \mathbf{z}$ and $\mathbf{H} \perp \mathbf{z}$) differ by a factor of approximately 100.

ACKNOWLEDGMENTS

This study was supported by the Russian Foundation for Basic Research (project nos. 02-02-16020, 03-02-16526), the program "Universities of Russia" (project no. UR.01.01.019), and INTAS (grant no. 2001-0615).

REFERENCES

1. J. A. Barker and E. P. O'Reilly, Phys. Rev. B **61**, 13840 (2000).
2. P. W. Fry, I. E. Itskevich, D. J. Mowbray, *et al.*, Phys. Rev. Lett. **84**, 733 (2000).

3. A. I. Yakimov, A. V. Dvurechenskiĭ, and A. I. Nikiforov, Pis'ma Zh. Éksp. Teor. Fiz. **73** (10), 598 (2001) [JETP Lett. **73**, 529 (2001)].

4. A. I. Yakimov, A. V. Dvurechenskii, A. I. Nikiforov, *et al.*, Phys. Rev. B **67** (12), 125318 (2003).

5. M. Bayer, V. B. Timofeev, T. Gutbrod, *et al.*, Phys. Rev. B **52**, R11623 (1995).

6. V. K. Kalevich, B. P. Zakharchenya, and O. M. Fedorova, Fiz. Tverd. Tela (St. Petersburg) **37** (1), 283 (1995) [Phys. Solid State **37**, 154 (1995)].

7. A. A. Kiselev, E. L. Ivchenko, and U. Rössler, Phys. Rev. B **58**, 16353 (1998).

8. G. L. Bir and G. E. Pikus, *Symmetry and Strain-Induced Effects in Semiconductors* (Nauka, Moscow, 1972; Wiley, New York, 1975).

9. A. V. Nenashev, A. V. Dvurechenskiĭ, and A. F. Zinov'eva, Zh. Éksp. Teor. Fiz. **123** (2), 362 (2003) [JETP **96**, 321 (2003)].

Translated by I. Zvyagin

Physics of the Solid State, Vol. 46, No. 1, 2004, pp. 60–63. Translated from Fizika Tverdogo Tela, Vol. 46, No. 1, 2004, pp. 63–66.

PROCEEDINGS OF THE CONFERENCE DEDICATED TO O. V. LOSEV (1903–1942)

(Nizhni Novgorod, Russia, March 17–20, 2003)

Photoluminescence of Self-Assembled GeSi/Si(001) Nanoislands of Different Shapes

N. V. Vostokov, Z. F. Krasil'nik, D. N. Lobanov, A. V. Novikov, M. V. Shaleev, and A. N. Yablonskiĭ

Institute of the Physics of Microstructures, Russian Academy of Sciences, Nizhni Novgorod, 603950 Russia
e-mail: anov@ipm.sci-nnov.ru

Abstract—The dependence of the photoluminescence spectra of structures with self-assembled GeSi/Si(001) islands on Ge deposition temperature was studied. The position of the island photoluminescence peak maximum was found to shift nonmonotonically with decreasing Ge deposition temperature. The blue shift of the island photoluminescence peak with the growth temperature decreasing from 600 to 550°C is assigned to the change in the island shape occurring in this temperature interval accompanied by a strong decrease in the average island height. © *2004 MAIK "Nauka/Interperiodica".*

1. INTRODUCTION

The formation of three-dimensional self-assembled islands caused by the lattice misfit between Ge and Si has been experimentally observed to occur on the Si(001) surface within a broad range of Ge deposition temperatures [1–3]. By properly varying the Ge deposition temperature, one can obtain both large nanoislands, >100 nm in the lateral dimension [1, 2], and extremely small islands (quantum dots) whose maximum size does not exceed 15–20 nm [2, 3]. The growth temperature affects not only the size of the islands but also their shape [1] and composition [4]. The dimensions of the islands and their shape and composition are the parameters that determine the position of the energy bands in nanoisland structures. The dependence of these parameters on growth temperature should give rise to a substantial difference between the band diagrams of structures with nanoislands grown at different temperatures, which, in turn, should influence their optical properties. We report here on a study of the growth and photoluminescence (PL) of structures with self-assembled GeSi/Si(001) islands grown within a broad Ge deposition temperature interval (460–700°C).

2. EXPERIMENTAL TECHNIQUE

The structures under study were grown on Si(001) substrates from solid sources through molecular-beam epitaxy. The structures intended for investigating the surface morphology consisted of a Si buffer layer grown at 700°C and a Ge layer with an equivalent thickness d_{Ge} = 7–8 monolayers (MLs) (1 ML ≈ 0.14 nm) deposited within the temperature interval T_g = 460–700°C. In structures designed for optical studies, a Si cap layer whose growth temperature coincided with the deposition temperature of Ge was grown on the deposited Ge. The surface morphology of the structures was studied with a Solver P4 atomic force microscope (AFM). The PL spectra were measured with a BOMEM DA3.36 Fourier spectrometer equipped with a cooled InSb detector. An Ar^+ laser (514.5 nm line) served for optical pumping.

3. RESULTS AND DISCUSSION

Earlier studies of the growth of GeSi nanoislands performed at Ge deposition temperatures $T_g \geq 600$°C showed [1–4] that, at an effective thickness of deposited Ge d_{Ge} = 7–8 MLs, the formations appearing on the surface are of two types differing in shape and size, namely, pyramidal and dome-shaped islands. It was found in [4] that for $T_g \geq 600$°C the growth of islands is strongly affected by the formation of a GeSi alloy in the islands, which is caused by Si diffusion into the islands accelerated by the elastic strain fields generated by the latter. AFM studies of these structures revealed that for d_{Ge} = 7–8 MLs the dominant species is the dome-shaped islands, which have a larger height and are larger in size in the growth plane as compared to the pyramidal islands (Fig. 1a). As T_g is lowered from 700 to 600°C, the islands decrease monotonically in size (Fig. 1d) and their surface density increases (Fig. 1e). The growth in the island surface density is caused by a slowing down of surface diffusion of atoms setting in as the temperature decreases. The decrease in the island size with decreasing T_g is associated with suppression of the Si diffusion into the islands and an increase in the Ge content in the latter [4].

As the Ge deposition temperature decreases from 600 to 550°C, the growth of self-assembled islands undergoes a qualitative change (Fig. 1). Lowering T_g by as little as 50°C brings about an order-of-magnitude

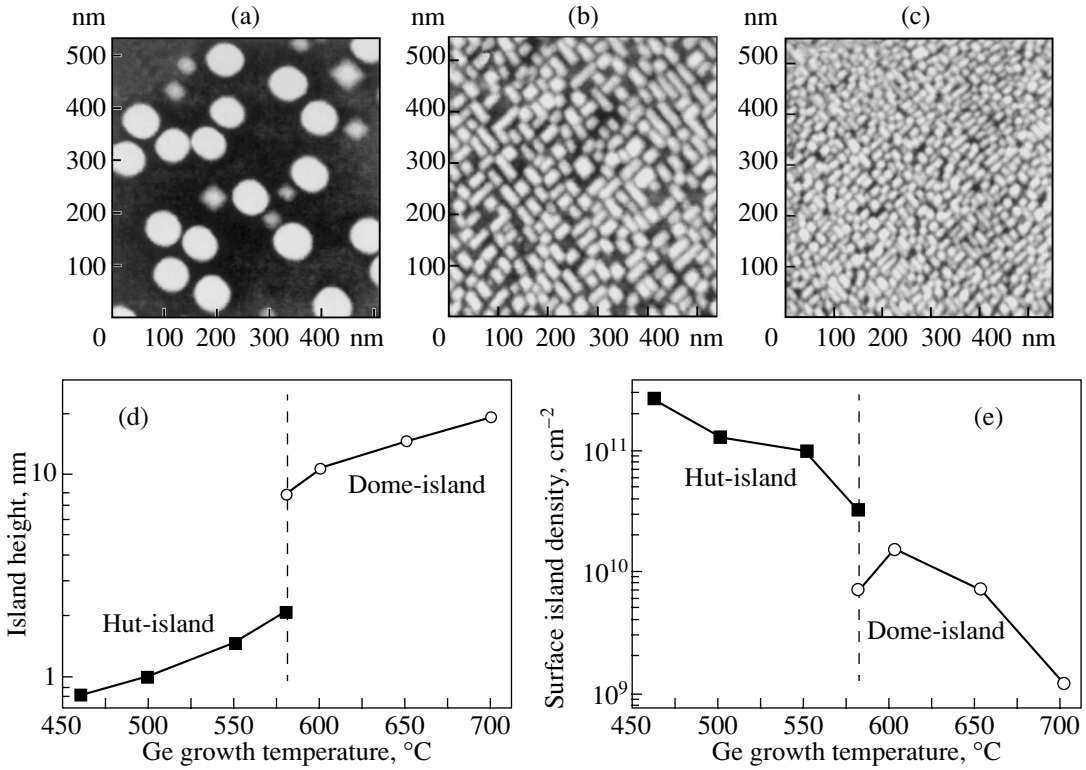

Fig. 1. (a–c) AFM surface photomicrographs of structures grown at 600, 550, and 460°C, respectively (image span 500 × 500 nm), and (d, e) plots of the average height of islands and their surface density vs Ge deposition temperature. The dashed lines in panels c and d separate the regions of existence of the hut- and dome-shaped islands and correspond to T_g = 580°C.

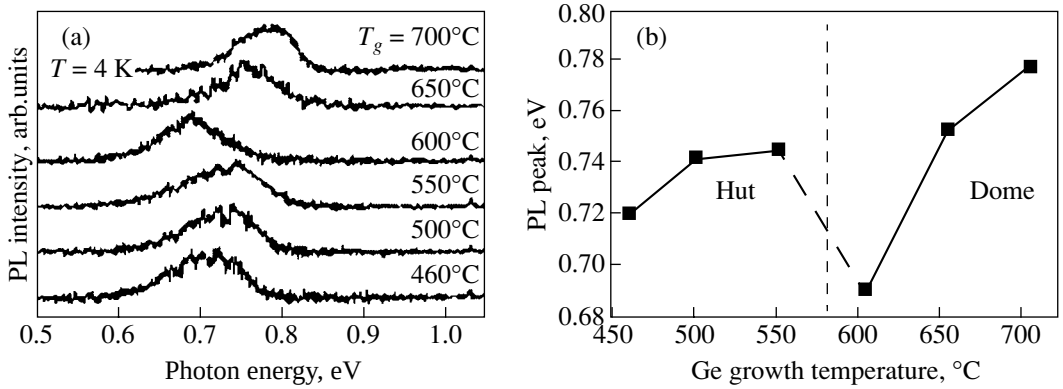

Fig. 2. (a) PL spectra of structures with islands grown at different Ge deposition temperatures and (b) position of the island PL peak maximum plotted vs T_g. The PL spectra were measured at 4 K using an InSb detector.

increase in the surface density of islands (Fig. 1e), with the island height decreasing about fivefold (Fig. 1d). The sharp change in the island parameters is connected with the formation of so-called hut islands [5] (with a rectangular base extended in the ⟨100⟩ or ⟨010⟩ direction) on the surface (Fig. 1b). Islands of this type appear at T_g = 580°C [6] (Fig. 1) and become dominant on the surface of the structures for $T_g \le 550$°C and d_{Ge} = 7–8 MLs (Fig. 1b). As T_g is lowered from 550 to 460°C, the height of the hut islands decreases monotonically and their surface density increases (Fig. 1). At T_g = 460°C, the hut islands are 0.7–1.0 nm high, their size in the growth plane becomes 15–30 nm, and their surface density is $N_s = 2.5 \times 10^{11}$ cm^{-2} (Fig. 1c).

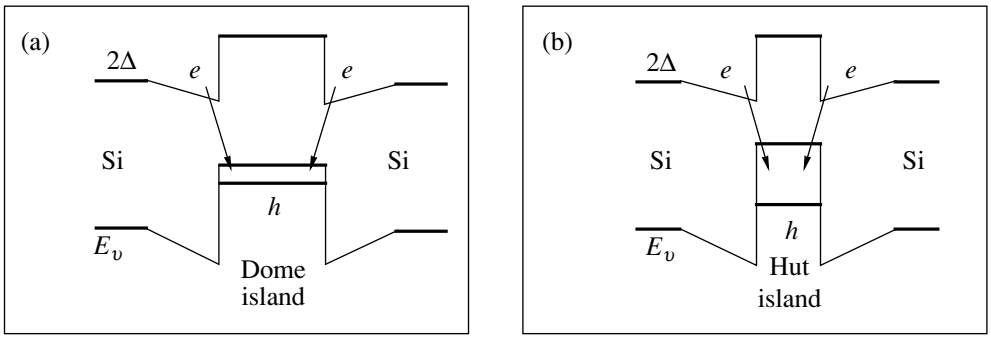

Fig. 3. Model of the indirect optical transition for (a) dome- and (b) hut-shaped islands (schematic). The positions of the valence band top and of 2Δ electron valleys in the islands and their neighborhood are specified. The arrows identify the indirect optical transition.

Studies of PL spectra of all our structures revealed a broad PL peak in the low-energy part of the spectra (Fig. 2a). This PL peak is assigned to the indirect optical transition between the holes in the islands and electrons located in Si at the type-II heterointerface with an island [7]. A substantial part of the PL signal from the islands grown at $T_g \le 650$°C was shown in [8] to lie at energies below the low-energy cutoff of the operating range of a cooled Ge detector. To avoid modification of the island PL signal by the spectral response of the Ge detector, we measured the PL spectra with a less sensitive cooled InSb detector with a cutoff at a longer wavelength.

A comparison of the PL spectra due to structures grown at different Ge deposition temperatures showed the position of the island PL peak maximum (E_{isl}) to depend nonmonotonically on T_g (Fig. 2). As in the case of island growth, the $E_{isl}(T_g)$ relation can be divided into two parts (Fig. 2b).

In the first part, with $T_g \ge 600$°C, E_{isl} decreases monotonically with decreasing growth temperature. As the temperature decreases, the optical transition energy in islands is affected by the following two major factors: a decrease of the islands in size and a change in their composition. For $T_g \ge 600$°C, the first factor affects the optical transition energy in the islands only weakly, because even at $T_g = 600$°C the uncapped dome-shaped islands are higher than 10 nm (Fig. 1d), so the size quantization effects exert only a weak influence on the position of the first size-quantization level of holes in the islands. As a result, the hole energy level in islands is located close to the valence band top (Fig. 3a). The position of the island PL peak is affected primarily by the dependence of the island composition on growth temperature. The red shift of the island PL peak should be assigned to suppression of Si diffusion into the islands occurring with decreasing growth temperature and, accordingly, to an increase in the Ge content in the islands [4], which gives rise to an increase in the valence-band offset at the silicon–island heterointerface and, hence, to a decrease in the indirect optical transition energy [8] (Fig. 3a).

The $E_{isl}(T_g)$ dependence has a feature at $T_g = 550$–600°C; more specifically, the island PL peak becomes blue-shifted by ~50 meV with T_g decreasing from 600 to 550°C (Fig. 2). Studies of island growth revealed that it is in this T_g interval that the island morphology undergoes a substantial change (Fig. 1). As shown above, for $T_g > 580$°C, the surface of the structures is dominated by dome-shaped islands with a height greater than 10 nm and for $T_g < 580$°C, by hut islands with a height of ≤2 nm (Fig. 1d). The sharp decrease in the island height brings about a substantial increase in the influence of size quantization on the hole energy level position in the islands. As a result, despite the increase in the valence-band offset at the Si-island heterointerface associated with the increase in Ge content in the islands that occurs with decreasing T_g, the first size-quantization level of the island holes shifts (is forced) toward the Si valence band top (Fig. 3b); as a result, the optical transition energy in the islands increases and the PL line exhibits the observed shift.

The monotonic decrease in E_{isl} with T_g decreasing from 550 to 460°C is assigned to suppression of variations in the island parameters as the islands become overgrown. It is known that, as the Si cap layer grows, the Si content in the islands increases and their height decreases [9]. As the overgrowth temperature is lowered from 500 to 390°C, these processes were shown to become largely suppressed [10]. Thus, as the growth temperature decreases from 550 to 460°C, the height of the capped islands increases, as does their average Ge content. Both these processes bring about a decrease in the optical transition energy in the islands (Fig. 3b) and, accordingly, a red shift of the island PL peak.

ACKNOWLEDGMENTS

This study was supported by the Russian Foundation for Basic Research (project no. 02-02-16792), INTAS NANO (project no. 01-444), and programs of

the Ministry of Industry, Science, and Technology of the Russian Federation.

REFERENCES

1. T. I. Kamins, E. C. Carr, R. S. Williams, and S. J. Rosner, J. Appl. Phys. **81**, 211 (1997).
2. O. P. Pchelyakov, Yu. B. Bolkhovityanov, A. V. Dvurechenskiĭ, *et al.*, Fiz. Tekh. Poluprovodn. (St. Petersburg) **34**, 1281 (2000) [Semiconductors **34**, 1229 (2000)].
3. M. W. Dashiell, U. Denker, C. Muller, *et al.*, Appl. Phys. Lett. **80**, 1279 (2002).
4. A. V. Novikov, B. A. Andreev, N. V. Vostokov, *et al.*, Mater. Sci. Eng. B **89**, 62 (2002).
5. U.-W. Mo, D. E. Savage, B. S. Swartzentruber, and M. G. Lagally, Phys. Rev. Lett. **65**, 1020 (1990).
6. O. G. Schmidt, C. Lange, and K. Eberl, Phys. Status Solidi B **215**, 319 (1999).
7. V. Ya. Aleshkin, N. A. Bekin, N. G. Kalugin, *et al.*, Pis'ma Zh. Éksp. Teor. Fiz. **67**, 46 (1998) [JETP Lett. **67**, 48 (1998)].
8. N. V. Vostokov, Yu. N. Drozdov, Z. F. Krasil'nik, *et al.*, Pis'ma Zh. Éksp. Teor. Fiz. **76** (6), 425 (2002) [JETP Lett. **76**, 365 (2002)].
9. P. Sutter, E. Mateeva, J. S. Sullivan, and M. G. Lagally, Thin Solid Films **336**, 262 (1998).
10. A. Rastelli, E. Muller, and H. von Kanel, Appl. Phys. Lett. **80**, 1438 (2002).

Translated by G. Skrebtsov

Physics of the Solid State, Vol. 46, No. 1, 2004, pp. 64–66. Translated from Fizika Tverdogo Tela, Vol. 46, No. 1, 2004, pp. 67–69.

PROCEEDINGS OF THE CONFERENCE DEDICATED TO O. V. LOSEV (1903–1942)

(Nizhni Novgorod, Russia, March 17–20, 2003)

Synthesis of Ordered Ge–Si Heterostructures Containing Ultrasmall Germanium Nanoclusters

Yu. B. Bolkhovityanov, S. Ts. Krivoshchapov, A. I. Nikiforov, B. Z. Ol'shanetskiĭ, O. P. Pchelyakov, L. V. Sokolov, and S. A. Teys

Institute of Semiconductor Physics, Siberian Division, Russian Academy of Sciences, pr. Akademika Lavrent'eva 13, Novosibirsk, 630090 Russia

e-mail: pch@isp.nsc.ru

Abstract—Different techniques for the fabrication of structures containing ensembles of ultrasmall germanium nanoclusters distributed with a high density over the substrate surface are discussed. How to control the morphology and ordering of these ensembles is also discussed. *© 2004 MAIK "Nauka/Interperiodica".*

With the advent of quantum nanostructures (especially of the structures containing quantum dots), the traditional, indirect-gap semiconductors Si and Ge are being considered as promising optical materials. This is the main reason behind the continuously increasing interest in studying silicon- and germanium-based quantum structures. In particular, the physical effects that have been observed experimentally in these structures in recent years are used to create an element basis for microwave electronics in the gigahertz and terahertz range, optical electronic devices, and quantum computer engineering. Thus, the development of techniques for fabricating Si-based nanostructures containing ultrasmall (<5 nm) germanium quantum dots is of great importance.

The ordering effect observed in arrays of quantum-size islands in Ge–Si heterostructures makes it possible to produce systems of defect-free quantum dots that are relatively small in size (10–100 nm) with a surface density of 10^{10}–10^{11} cm^{-2}. In this case, the atomic-like characteristics observed in the electronic and optical spectra of these objects become more pronounced. It is no wonder that these heterostructures were used to reveal single-electron effects in an array of islands for the first time [1]. However, the majority of the subsequent studies were devoted to the electronic properties of quantum dots in III–V compounds. This was due to a number of factors: (1) the impressive progress made in the field of heteroepitaxy of III–V compounds; (2) the possibility of producing type-I heterostructures (in which the jumps in the conduction and valence bands are opposite in sign), which is significant for the optical properties of systems; and (3) the small effective masses of charge carriers, which makes it possible to observe size-quantization effects at relatively large island sizes. InAs–GaAs structures were the first III–V compounds used to investigate the properties of quantum dots [2, 3]; presently, the interest in such nanosystems is still growing. To expand the use of Si-based structures containing germanium nanoclusters, it is important to find ways to decrease the size of such nanoclusters and increase their surface density and degree of ordering.

The present concepts on the early stage of self-assembling and ordering of nanoclusters during Ge and Si heteroepitaxy have been analyzed in a number of reviews [4–8]. It has been shown that the formation of nanoclusters at temperatures above 600°C is affected by interdiffusion [9].

The transition from layer-by-layer growth to nucleation of three-dimensional (3*D*) islands has been studied in the Ge-on-Si heterosystem for a long time. At relatively low synthesis temperatures (300–500°C), the interdiffusion between the deposit and substrate can be neglected [10, 11]. As was first shown in [4], there are no misfit dislocations in such islands, even when the island thickness significantly exceeds the critical thickness. It was precisely these publications that launched intensive studies into the formation mechanism of stressed islands and the peculiarities in their ordering: it was found how to produce arrays of defect-free 3*D* nanoobjects, which are of practical significance in nanoelectronics.

Apart from the difference in the internal and surface energies, lattice parameters, and elastic strains between epitaxial films and three-dimensional Ge islands on Si substrates, the main factor affecting the initial stage of heteroepitaxy is the film–substrate interface energy, as well as the structure and composition of the Si-substrate surface, which determine the interface energy. In particular, these factors determine the morphological stability of the continuous pseudomorphic (wetting) Ge layer, on which island self-assembling occurs at the later stages of the growth (Stranski–Krastanow mechanism). These factors also affect the form, size, and spatial distribution of Ge nanoclusters in the first atomic

1063-7834/04/4601-0064$26.00 © 2004 MAIK "Nauka/Interperiodica"

layers, whose coalescence results in the formation of a wetting layer.

The formation of 3*D* islands involves an early stage of island nucleation followed by further development of the island nuclei. The key features of the island nucleation in the epitaxial heterosystem are determined by the energy balance between the deposit and substrate surfaces and by the balance between the layer–substrate interface energy and the internal volume energy of the islands. The free energy of a newly formed nucleus on the substrate surface can be written as a sum of three terms [12]:

$$\Delta G = -V\Delta\mu + \gamma s + E_i(V, h/l).$$

Here, the first term is the work required to produce a new nucleus of volume *V*, $\Delta\mu$ is the thermodynamic driving force of crystallization (supersaturation), the second term is the work required to form the extra surface area *s*, and γ is the surface energy of the nucleus (strictly speaking, this term should take into account the difference between the nucleus surface energy and the substrate–nucleus interface energy). The third term is the additional energy associated with elastic strains of the nucleus. The first two terms in this expression are the classical version of the nucleation theory (see, e.g., [13]), whereas the last term appears only in the case of stressed island films. When the lattice misfits are as large as those in the Ge–Si system, this additional energy depends not only on the volume of the nucleus but also on its shape (*h*/*l* is the ratio of the nucleus height to the its lateral size). Thus, the third term in the above equation is of importance in the transition from the two-dimensional (2*D*) to 3*D* configuration. According to the calculations performed in [12], this term is a rapidly decreasing function of *h*/*l*. The more pronounced the three-dimensional character of a stressed nucleus, the more noticeable the effect of elastic relaxation (decrease in strains in the regions of the nucleus that are most remote from the substrate) and the smaller the additional contribution from the strains to the free energy of the nucleus. The surface energy of the "Ge layer (and the Ge island)–Si substrate" system also depends on the Ge layer thickness and the germanium-island shape [14]. In particular, a decrease in the thickness of the Ge layer results in a more pronounced dependence of the island shape on the interface energy. This statement was confirmed in [15, 16], where it was experimentally shown that dense arrays of ultrasmall quantum dots can be produced by depositing CaF_2 layers and oxygen monolayers. However, the ordering of Ge quantum dots might be expected to be most pronounced in the case of heteroepitaxy on a clean single-crystal Si surface. In spite of the extremely large number of experimental studies and detailed analytical reviews [4–8], no evidence has been reported that an array of ordered nanoclusters can arise in the course of formation of a pseudomorphic wetting layer. Let us consider several aspects of this problem.

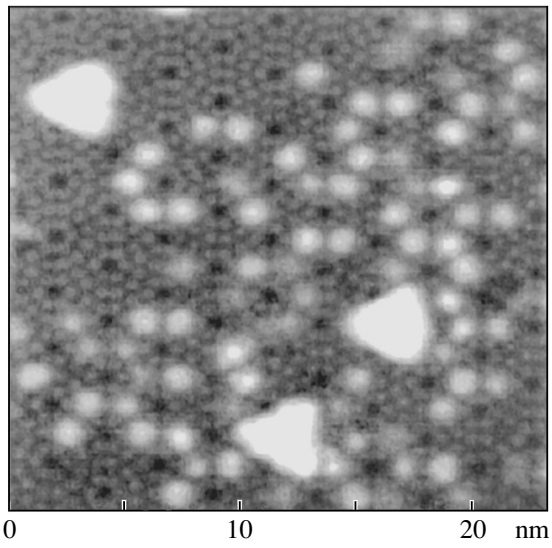

Fig. 1. STM image of Ge nanoclusters on the Si (111) 7×7 surface.

In the case of homoepitaxy, when the stresses in the layer are minimal, 3*D* islands are not nucleated on the sufficiently clean surface of any semiconductor and a film grows either through the step motion (step–layer growth) or through the nucleation and coalescence of 2*D* islands. Similar to homoepitaxy, strains are insignificant at the earliest stages of the heteroepitaxy; the surface condition of the substrate is a more important factor in this case. For this reason, the morphology of the growth of the first monolayer on atomically clean surfaces in the cases of homoepitaxy and heteroepitaxy is the same. Thus, it can be concluded that the self-assembling of ultrasmall nanoislands can be observed at the initial stage of the growth of the pseudomorphic wetting Ge layer through the formation of 2*D* islands. The shape and surface distribution of the islands can be controlled by changing the structural state of the Si-layer surface, which was experimentally confirmed in [16–21]. The influence of 7×7 reconstruction of the Si (111) surface on the formation of metal (In, Mn, Ag) [18] and Ge [17–20] nanoclusters less than 5 nm in size was demonstrated in [18, 19] (Fig. 1). It was shown that metal and Ge nuclei arise primarily inside the half of the 7×7 unit cell in the stacking-fault position. Such clusters are characterized by significant temperature stability. Even after annealing at 350°C over 2 h, fragments of nanoclusters remain on the Si surface between relatively large Ge islands (Fig. 2).

It is likely that nanocluster ordering can be controlled by using impurity superstructures, whose unit cells can have different sizes and structure. In particular, such superstructures can be formed on the Si surface by metal impurities (see, e.g., [22–24]). To date, these conjectures have not been confirmed experimentally and stimulate further detailed studies of the mech-

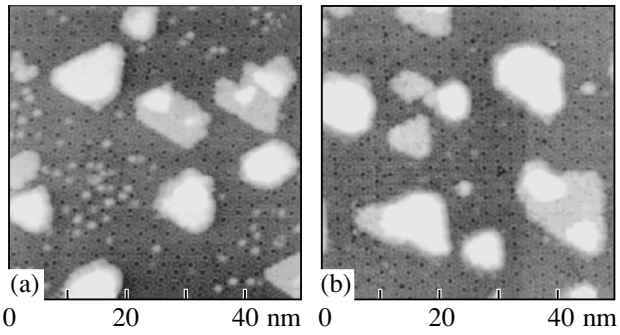

Fig. 2. STM images of the Si (111) 7 × 7 surface with Ge nanoclusters and islands at a 0.4-bilayer coverage (a) before and (b) after 2-h annealing at 350°C.

anisms of semiconductor nanocluster ordering through the modification of surface superstructures.

ACKNOWLEDGMENTS

This work was supported by the Russian Foundation for Basic Research (project no. 03-02-16506-a) and the Ministry of Industry, Science, and Technology of the Russian Federation (state contract no. 37.039.1.1.0041).

REFERENCES

1. A. I. Yakimov, V. A. Markov, A. V. Dvurechenskii, and O. P. Pchelyakov, Philos. Mag. **65**, 701 (1992).
2. D. Leonard, M. Krishnamurthy, C. M. Reaves, *et al.*, Appl. Phys. Lett. **63**, 3203 (1993).
3. J.-M. Marzin, J.-M. Gerard, A. Izrael, and D. Barrier, Phys. Rev. Lett. **73**, 716 (1994).
4. D. J. Eaglesham and M. Cerullo, Phys. Rev. Lett. **64**, 1943 (1990).
5. F. Liu and M. G. Lagally, Surf. Sci. **386**, 169 (1997).
6. P. Moriarty, Rep. Prog. Phys. **64**, 297 (2001).
7. T. I. Kamins, K. Nauka, and R. S. Williams, Appl. Phys. A **73**, 1 (2001).
8. K. Brunner, Rep. Prog. Phys. **65**, 27 (2002).
9. N. V. Vostokov, I. V. Dolgov, Yu. N. Drozdov, *et al.*, J. Cryst. Growth **209**, 302 (2000).
10. T. I. Kamins, G. Medeiros-Ribeiro, D. A. A. Ohlberg, and R. Stanley Williams, J. Appl. Phys. **85**, 1159 (1999).
11. G. Capellini, M. De Seta, and F. Evangelisti, Appl. Phys. Lett. **78** (3), 303 (2001).
12. P. Müller and R. Kern, J. Cryst. Growth **193**, 257 (1998).
13. A. A. Chernov, E. I. Givargizov, and Kh. S. Bagdasarov, *Modern Crystallography*, Ed. by B. K. Vaĭnshteĭn, A. A. Chernov, and L. A. Shuvalov (Nauka, Moscow, 1980), Vol. 3.
14. F. Liu and M. G. Lagally, Phys. Rev. Lett. **76**, 3156 (1996).
15. A. I. Yakimov, A. S. Derjabin, L. V. Sokolov, *et al.*, Appl. Phys. Lett. **81** (3), 499 (2002).
16. A. I. Nikiforov, V. A. Cherepanov, and O. P. Pchelyakov, Mater. Sci. Eng. B **89** (1–3), 180 (2002).
17. U. Kohler, O. Jusuko, G. Pietch, *et al.*, Surf. Sci. **321**, 248 (1991).
18. S. A. Teys and B. Z. Olshanetsky, Phys. Low-Dimens. Semicond. Struct., Nos. 1–2, 37 (2002).
19. O. P. Pchelyakov, Yu. B. Bolkhovityanov, A. I. Nikiforov, *et al.*, NATO Sci. Ser. 2: Math., Phys., Chem. **65**, 371 (2001).
20. J. Li, J. Jia, X. Liang, *et al.*, Phys. Rev. Lett. **88**, 066101 (2002).
21. L. Yan, H. Yang, H. Gao, *et al.*, Surf. Sci. **498**, 83 (2002).
22. O. Hellman, J. Appl. Phys. **76**, 3818 (1994).
23. S. Parikh, M. Lee, and P. Bennett, Surf. Sci. **356**, 53 (1996).
24. X. Lin, H. Mai, I. Chizhov, and R. Willis, J. Vac. Sci. Technol. B **14**, 995 (1996).

Translated by A. Poushnov

Physics of the Solid State, Vol. 46, No. 1, 2004, pp. 67–70. Translated from Fizika Tverdogo Tela, Vol. 46, No. 1, 2004, pp. 70–73.

PROCEEDINGS OF THE CONFERENCE DEDICATED TO O. V. LOSEV (1903–1942)

(Nizhni Novgorod, Russia, March 17–20, 2003)

Correlation between the Energy of SiGe Nanoislands and Their Shape and Size

M. Ya. Valakh*, V. N. Dzhagan*, Z. F. Krasil'nik, P. M. Lytvyn*, D. N. Lobanov**, E. V. Mozdor*, A. V. Novikov**, V. A. Yukhymchuk*, and A. M. Yaremko***

** Institute of Semiconductor Physics, National Academy of Sciences of Ukraine, Kiev, 03028 Ukraine*
e-mail: valakh@isp.kiev.ua

*** Institute of Microstructure Physics, Russian Academy of Sciences, Nizhni Novgorod, 603600 Russia*

Abstract—The total energy of self-assembled SiGe nanoislands on a silicon substrate is investigated theoretically as a function of their geometric and physical parameters. It is demonstrated that the growth temperature and the silicon content in nanoislands affect the minimum of their energy. The results of numerical calculations for nanoislands are compared with experimental data obtained by atomic-force microscopy. © *2004 MAIK "Nauka/Interperiodica".*

1. INTRODUCTION

Self-assembled germanium nanoislands grown through molecular-beam epitaxy of germanium on silicon or $Si_{1-x}Ge_x$ substrates have been intensively studied in recent years. The considerable interest expressed in these objects is associated with both the fundamental aspects of problems in the physics of nanometer-sized solid-state structures and possible practical applications [1].

Despite the large number of papers devoted to the formation of nanoislands, the mechanisms responsible for the formation of nanoislands in the form of pyramids or domes and for the transition from one form to another are not clearly understood. The elucidation of these mechanisms is the main subject of our investigation.

2. SAMPLES AND EXPERIMENTAL TECHNIQUE

The structures studied in this work were prepared by molecular-beam epitaxy on a Si(001) substrate with a 200-nm-thick buffer silicon layer preliminarily grown on it. Two series of samples were used in our experiments. For samples of the first series, the thickness of germanium layers was varied from 5.5 to 11 monolayers (ML) and the growth temperature was constant and equal to 700°C. For samples of the second series, the thickness of germanium layers was constant and equal to 9 ML but the epitaxial growth was carried out at different temperatures (600, 700, 750°C). The size and shape of the nanoislands were controlled using a Nanoscope III-a atomic-force microscope (AFM).

3. EXPERIMENTAL RESULTS

Examination of the AFM images of the structures with nanoislands revealed that the size distribution of nanoislands can be either bimodal or unimodal depending on the growth temperature and the number of deposited germanium monolayers. This is explained by the fact that the nanoislands grown on the surface can have both pyramidal and domal shapes or only one of these shapes. The size and shape of the nanoislands depend on the growth temperature. An increase in the temperature of epitaxial deposition of germanium brings about a change in the chemical potential of the structure and an increase in the coefficient of diffusion of silicon atoms from the silicon substrate to the nanoislands. Analysis of the AFM images demonstrated that, during the growth, the pyramidal nanoislands retain their shape due to a proportional increase in their lateral sizes and height. After the critical volume is reached, the pyramids transform into dome-shaped nanoislands owing to the formation of new lateral facets whose angles with the substrate are greater than those of the pyramids. The changes in the shape of the nanoislands are caused by a more efficient relaxation of stresses in nanoislands with a larger ratio of the height to the lateral size [2].

4. THEORETICAL ANALYSIS AND DISCUSSION

4.1. Energy of the Strained Structure

An analytic expression describing the energy of a dislocation-free germanium island was derived by Tersoff *et al.* [3, 4]. This expression makes it possible to analyze the changes in the shape of the island. When deriving this expression, those authors made the following assumptions: (a) the island in the form of a trun-

cated pyramid of height h has a rectangular base of width s and length t, and (b) the base forms an angle θ with any lateral facet of the island.

The total energy of the island can be represented in the form

$$E = E_s + E_r, \tag{1}$$

where E_s is the total energy of the surface and the interface and E_r is the change in the elastic energy due to relaxation. The expression for E_s has the form

$$\begin{aligned} E_s &= st(\gamma_i + \gamma_t - \gamma_s) + 2(s+t) \\ &\times [h\gamma_e \operatorname{cosec}\theta - h\cot\theta(\gamma_t + \gamma_s - \gamma_i)/2], \end{aligned} \tag{2}$$

where γ_s, γ_e, γ_t, and γ_i are the surface energies (per unit area) of the substrate, the facets and the top of the island, and the island–substrate interface, respectively. In the case where the growth of nanoislands occurs through the Stranski–Krastanov mechanism, expression (2) can be simplified because $\gamma_t = \gamma_s$ and $\gamma_i = 0$ [3].

The relaxation energy in a quasi-two-dimensional approximation ($s \gg h$, $t \gg h$) has the following form:

$$\begin{aligned} E_r &= -2ch^2[s\ln(te^{3/2}/h\cot\theta) \\ &+ t\ln(se^{3/2}/h\cot\theta)]. \end{aligned} \tag{3}$$

Here, $c = \sigma_b^2(1-\nu)/2\pi\mu$, σ_b stands for the components of the stress tensor for bulk germanium; and ν and μ are the Poisson ratio and the shear modulus of the silicon substrate, respectively.

It follows from relationships (1)–(3) that the total energy of an island cannot be expressed as a function of the volume, because it is a composite function of the lateral sizes (s, t), height (h), angle (θ), and volume (c) and surface parameters (γ_s, γ_e) of the island. According to the model proposed by Tersoff and Tromp [3], the height h increases slowly as compared to the parameters s and t; hence, it can be considered to be constant.

In [3, 4], the energy E of a nanoisland was analyzed in two cases.

(A) The total volume was not fixed, and the specific energy E/V was minimized instead of the energy E to give $s = t = a_0$. However, the existence of a minimum of the energy E at these values of s and t does not follow from the mere fact that the specific energy E/V has a minimum at the same parameters. Furthermore, the minimum of the energy E can exist in quite a different region (s, $t \neq a_0$). Therefore, the physical conclusions drawn from the above consideration call for detailed analysis. Evidently, this reasoning was obvious to Tersoff and LeGoues [4], and they considered another case (B).

(B) The energy E was minimized in [4] at a fixed volume of the nanoisland. It was found that the minimum of the energy E corresponds to the parameters $s = t = h\cot\theta$, depends only on the geometric sizes, and does not depend on the physical parameters c, γ_s, γ_e, etc., which is surprising. Moreover, as was shown by Zhang and Bower [5], the shape of the nanoislands should depend not only on the energy but also on the kinetic processes. In this connection, we once again consider the problem formulated in [3, 4] in order to analyze relationships (1)–(3) taking into account all quantities, namely, s, t, h, γ_s, γ_e, and θ. By varying these parameters, we can judge the presence or absence of the global minimum of the energy E and elucidate how the growth temperature, the deposition rate, and the number of germanium monolayers affect the parameters of the nanoislands.

Expressions (1)–(3) can be conveniently written in relative units:

$$\tilde{s} = s/h, \quad \tilde{t} = t/h, \quad \tilde{\gamma}_e = \gamma_e/ch, \quad \tilde{\gamma}_s = \gamma_s/ch. \tag{4}$$

In this case, the expression for the total energy takes the form

$$\begin{aligned} E = 2ch^3\Big\{&(\tilde{s}+\tilde{t})(\tilde{\gamma}_e\operatorname{cosec}\theta - \tilde{\gamma}_s\cot\theta) \\ &-\left(\tilde{s}\ln\left(\frac{\tilde{t}}{\alpha\cot\theta}\right) + \tilde{t}\ln\left(\frac{\tilde{s}}{\alpha\cot\theta}\right)\right)\Big\}, \end{aligned} \tag{5}$$

where $\alpha = e^{-\frac{3}{2}}$. In this model, h is a constant and the product ch^3 has the dimension of energy (all the other quantities in braces are expressed in relative units). This function is too composite to be treated analytically. Therefore, we analyzed this function numerically. The results obtained are presented in Figs. 1–3. This simulation demonstrated that the dependence $E(\theta)$ can have a minimum at angles in the range $0 < \theta < \pi/2$, provided the values of $\tilde{\gamma}_s$ and $\tilde{\gamma}_e$ are close or equal to each other (Fig. 1). It should be noted that, in this case, we analyzed the dependence $E(\theta)$ only mathematically by varying different parameters and not imposing physical limitations. All the physical conclusions should be related to the minimum of the energy E. The numerical analysis demonstrates (Fig. 1) that the minimum of the energy E appears only when the values of $\tilde{\gamma}_s$ and $\tilde{\gamma}_e$ are not very small (in our case, when the values of $\tilde{\gamma}_s$ and $\tilde{\gamma}_e$ are greater than or equal to 5). On the other hand, under the condition $\tilde{\gamma}_s < \tilde{\gamma}_e$ (Fig. 1, curve *7*), the minimum energy $E_{\min}$ corresponds to the angle $\theta = \pi/2$ and the nanoisland should grow in the form of a prism. Note that the minimum energy $E_{\min}$ and the relevant angle θ (Fig. 2) depend on the ratio between $\tilde{\gamma}_s$ and $\tilde{\gamma}_e$ (at constant values of $\tilde{s}$ and $\tilde{t}$), which disagrees with the results obtained in [4]. From analyzing the results presented in Fig. 2, we can conclude that there do not exist such values of $\tilde{s}$ and $\tilde{t}$ for which the energy E has a glo-

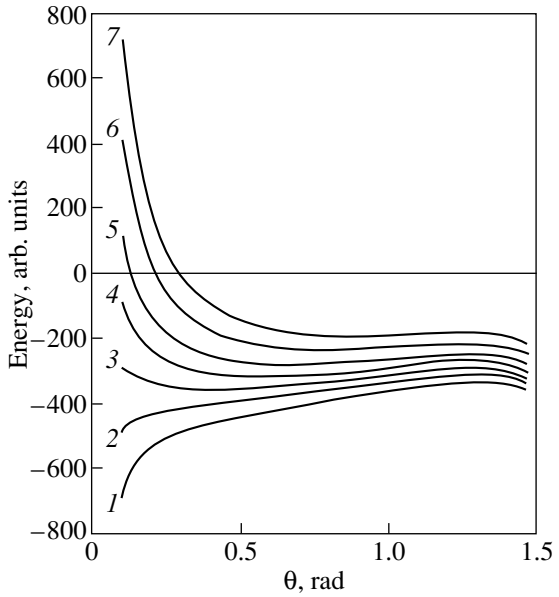

Fig. 1. Dependences of the energy of a nanoisland on the angle θ at constant parameters $\tilde{s} = \tilde{t} = 5$ and $\tilde{\gamma}_s = 5$ and the parameter $\tilde{\gamma}_e$ ranging from (*1*) 4.6 to (*7*) 5.8.

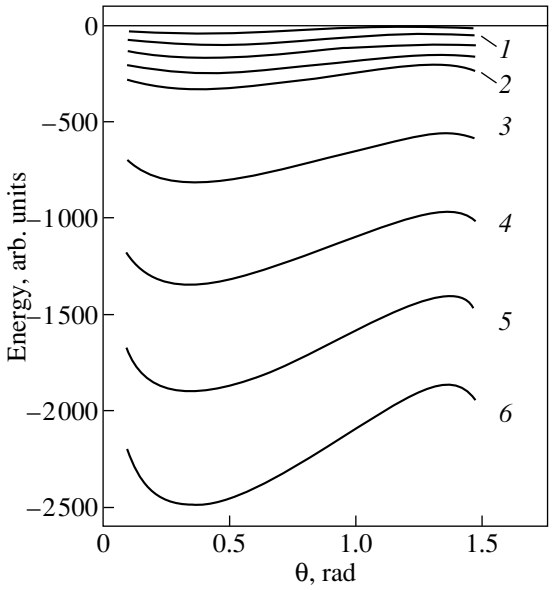

Fig. 2. Dependences of the energy of a nanoisland on the angle θ at constant parameters $\tilde{\gamma}_s = \tilde{\gamma}_e = 6$ and different parameters $\tilde{s}$ and $\tilde{t}$ ($\tilde{s} = \tilde{t}$): (*1*) 10, (*2*) 50, (*3*) 100, (*4*) 150, (*5*) 200, and (*6*) 250.

bal minimum: the larger the values of $\tilde{s}$ and $\tilde{t}$, the lower the energy of the system. Therefore, theoretically, the values of *s* and *t* tend to increase indefinitely.

It can be seen from Fig. 1 that, at given constant parameters $\tilde{s}$, $\tilde{t}$, and $\tilde{\gamma}_s$, the change in $\tilde{\gamma}_e$ leads only to a shift of the curves $E(\theta)$ but does not result in their intersection. However, these curves can intersect other curves (the figure for this is not presented) corresponding to different values of $\tilde{s}$ and $\tilde{t}$ and to equal values of $\tilde{\gamma}_e$.

4.2. The Influence of the Growth Temperature and Silicon Content in Nanoislands on the Total Energy E of Nanoislands

All the above reasoning concerns only nanoislands of pure germanium. The experimental results obtained by many authors, particularly by Krasilnik *et al.* [2], demonstrate that the growth of germanium nanoislands on a silicon substrate is accompanied by the diffusion of silicon atoms. The content of silicon in nanoislands increases with an increase in the growth temperature, which is confirmed by Raman spectroscopy [2]. As the content of silicon in nanoislands increases, the lattice mismatch between the nanoislands and the substrate becomes less pronounced and, consequently, the stresses in the nanoislands decrease. In a linear approximation, we can write the following relationship: $\sigma_b = \sigma_{b0}(1 - \alpha_c x)$, where α_c is an arbitrary factor in the range $0 < \alpha_c < 1$.

There exists one more factor affecting the mechanical stresses due to the difference between the linear thermal expansion coefficients of SiGe nanoislands and the silicon substrate. According to the thermodynamics of a strained system [6], the mechanical stress can be represented in the form $\sigma_b = \sigma_{b0} + K\alpha_T(T - T_0)$, where σ_{b0} is the stress at a temperature T_0, K is the bulk modulus, α_T is the thermal expansion coefficient, and $T - T_0$ is the difference between the temperatures. The mechanical stresses increase in proportion to the difference $\alpha_{Si} - \alpha_{Ge}$ with an increase in the temperature. In the temperature range where this difference is constant, the mechanical stress takes the form

$$\sigma_b = \sigma_{b0}\left[1 + \beta_T\left(\frac{T}{T_0} - 1\right)\right](1 - \alpha_c x),$$
$$\beta_T = \frac{K\Delta\alpha_T T_0}{\sigma_{b0}}. \quad (6)$$

It should be noted that, in a certain temperature range, the thermal expansion coefficient α_T and the silicon content x oppositely affect the mechanical stresses in the nanoisland and the resultant stress σ_b depends on which of these factors predominates.

Figure 3 shows the dependences $E(\theta)$ for three sets of parameters $\tilde{s}$ and $\tilde{t}$ at $x = 0$ and 0.5. It can be seen from this figure that, in the case where silicon is absent in nanoislands ($x = 0$, curves *1*), all the dependences exhibit a minimum and $E_{min} < 0$. As the content of silicon in the nanoislands increases to 0.5, the values of $\tilde{\gamma}_s$ and $\tilde{\gamma}_e$ change in accordance with relationships (4) and the dependence $c \sim (\sigma_b)^2$; this leads to an upward shift

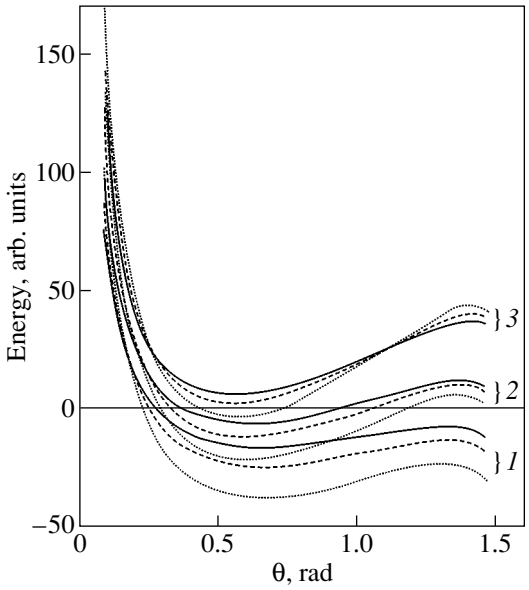

Fig. 3. Dependences of the energy of a nanoisland on the angle θ for three sets of parameters x and β (x is the silicon content in the nanoisland, and β is the thermal expansion coefficient): (*1*) $x = 0$, $\beta = 0$; (*2*) $x = 0.5$, $\beta = 0.3$; and (*3*) $x = 0.5$, $\beta = 0$. In each set, the solid, dashed, and dotted lines correspond to parameters $\tilde{s} = \tilde{t} = 10$, $\tilde{s} = \tilde{t} = 12$, and $\tilde{s} = \tilde{t} = 15$, respectively.

of the dependences $E(\theta)$, two of which exhibit a minimum energy $E_{min} > 0$ (Fig. 3, curves *3*). From the physical standpoint, this means that the nucleated islands will dissociate at these parameters. Taking into account the thermal expansion coefficients ($\beta \neq 0$), we can obtain the dependences represented by the series of curves *2*. In this case, the total energy E changes more slowly than that for $\beta = 0$ and all nanoislands are retained, because, for all curves *2*, we have $E_{min} < 0$, unlike the two upper curves *3*. This result demonstrates that the effects associated with variations in the silicon content x in the nanoislands and those caused by changes in the thermal expansion coefficients β can partially compensate for each other; consequently, the relative sizes (h/t, s) of the nanoislands change insignificantly as the temperature increases. It can also be seen from Fig. 3 that the nanoislands with small parameters $\tilde{t}$, $\tilde{s} = t$, s/h are unstable. This means that, at constant parameters t and s, the nanoislands with the largest heights h will dissociate first.

5. CONCLUSIONS

Thus, the detailed analysis of the growth of strained SiGe nanoislands demonstrated that their size depends on the growth temperature, silicon content in the nanoislands, and number of deposited germanium monolayers. The results of numerical treatment allowed us to conclude that the decrease in the elastic energy of the nanoislands leads to an increase in their lateral size as compared to the height. The increase in the growth temperature affects the ratio between the surface and volume characteristics of the nanoislands in a complicated manner. For given values of temperature, silicon content in the nanoislands, and growth time, there exists a limiting ratio of the height to the lateral size which determines the shape of the nanoislands.

ACKNOWLEDGMENTS

This work was supported by the Ukrainian–Russian program “Nanophysics” and the International Association of Assistance for the promotion of cooperation with scientists from the New Independent States of the former Soviet Union, project no. INTAS 01 0444.

REFERENCES

1. K. Bruner, Rep. Prog. Phys. **65**, 27 (2002).
2. Z. F. Krasilnik, P. M. Lytvyn, D. N. Lobanov, *et al.*, Nanotechnology **13**, 81 (2002).
3. J. Tersoff and R. M. Tromp, Phys. Rev. Lett. **70** (18), 2782 (1993).
4. J. Tersoff and F. K. LeGoues, Phys. Rev. Lett. **72** (22), 3570 (1994).
5. Y. W. Zhang and A. F. Bower, Appl. Phys. Lett. **78** (18), 2706 (2001).
6. L. D. Landau and E. M. Lifshitz, *Course of Theoretical Physics*, Vol. 7: *Theory of Elasticity*, 4th ed. (Pergamon, New York, 1986; Nauka, Moscow, 1987).

Translated by O. Moskalev

Physics of the Solid State, Vol. 46, No. 1, 2004, pp. 71–73. Translated from Fizika Tverdogo Tela, Vol. 46, No. 1, 2004, pp. 74–76.

PROCEEDINGS OF THE CONFERENCE DEDICATED TO O. V. LOSEV (1903–1942)

(Nizhni Novgorod, Russia, March 17–20, 2003)

Photoluminescence of Si/Ge Nanostructures Grown by Molecular-Beam Epitaxy at Low Temperatures

T. M. Burbaev, V. A. Kurbatov, A. O. Pogosov, M. M. Rzaev, N. N. Sibel'din, and V. A. Tsvetkov

Lebedev Physical Institute, Russian Academy of Sciences, Leninskiĭ pr. 53, Moscow, 119991 Russia

e-mail: burbaev@maill.lebedev.ru

Abstract—Multilayer Si/Ge nanostructures grown by molecular-beam epitaxy at low temperatures (250–300°C) of germanium deposition are studied using photoluminescence and atomic-force microscopy (AFM). It is assumed that, upon low-temperature epitaxy, the wetting layer is formed through the intergrowth of two-dimensional (2*D*) and three-dimensional (3*D*) nanoislands. © *2004 MAIK "Nauka/Interperiodica".*

1. INTRODUCTION

It is known that high-temperature (500–700°C) epitaxy of germanium on silicon proceeds according to the Stranski–Krastanov mechanism. A continuous strained (wetting) layer of germanium is formed when the thickness of the germanium layer becomes equal to approximately two monolayers (ML). In the silicon matrix, this layer manifests itself as a quantum well for holes. In the case when the critical thickness exceeds 4 ML, there arise three-dimensional nanoislands, namely, quantum dots, on the strained wetting layer [1–4]. It is also known that, at an epitaxy temperature of 360°C and below, the formation of nanoislands is suppressed because of the low rate of diffusion of adatoms [4]. At first glance, these data disagree with the results obtained in previous investigations into the properties of islands grown by epitaxy in the temperature range 200–300°C [5–7].

In this work, the structural and optical properties of Si/Ge nanostructures grown through molecular-beam epitaxy at low temperatures (250–300°C) were investigated using photoluminescence and atomic-force microscopy (AFM).

2. SAMPLES AND EXPERIMENTAL TECHNIQUE

The nanostructures used in our experiments were grown using a Riber SIVA 45 apparatus at the Institute of Semiconductor Physics, Linz University, Austria. It should be noted that a change in the germanium layer thickness by only 1 ML brings about significant variations in the morphology and optical properties of the nanostructures. For this reason, all the structures under investigation should be grown using the same apparatus. All the structures grown consisted of four or five layers. Each layer was composed of a silicon layer 25.5 nm thick and a germanium layer with a mean technological thickness of 2–12 ML. For AFM observations, the upper germanium layer of samples was not covered with silicon. The growth rate of silicon and germanium layers was equal to 0.005 nm/s.

During the growth of nanostructures, we observed reflection high-energy electron diffraction (RHEED) patterns. At 250°C, the initial reconstruction of the silicon surface was retained in the course of the growth of all nanostructures (the thickest germanium layer was equal to 10 ML). The main reflections were smeared and broadened only slightly. At 300°C, three-dimensional growth was observed only in the case when the technological thickness of the germanium layer was 12 ML. Examination of the growth of nanostructures at these temperatures allowed us to conclude that no three-dimensional growth of nanoislands through the Stranski–Krastanov mechanism occurs at 250°C; however, at 300°C, three-dimensional islands are formed by this mechanism when the thickness of the germanium layer reaches 12 ML.

The surface morphology was analyzed using an AFM SOLVER P47 atomic-force microscope. The photoluminescence spectra were measured at a temperature of 2 K. A semiconductor laser ($\lambda = 0.66$ μm) was used as an excitation source ($h\nu = 1.87$ eV). The highest radiation power was 70 mW, and the radiation power density at the sample usually amounted to 4 W/cm^2. The radiation from the samples was measured using a nitrogen-cooled germanium *p–i–n* photodiode.

3. RESULTS AND DISCUSSION

Figure 1 shows the AFM images of the surfaces of the structures grown at a temperature of 300°C. For a germanium layer thicker than 2 ML, the surface of the structure contains large-sized flat islands ($500 \times 500 \times 0.5$ nm^3), which do not cover extended surface regions. For a layer thickness of 3 ML, the lateral sizes of

1063-7834/04/4601-0071$26.00 © 2004 MAIK "Nauka/Interperiodica"

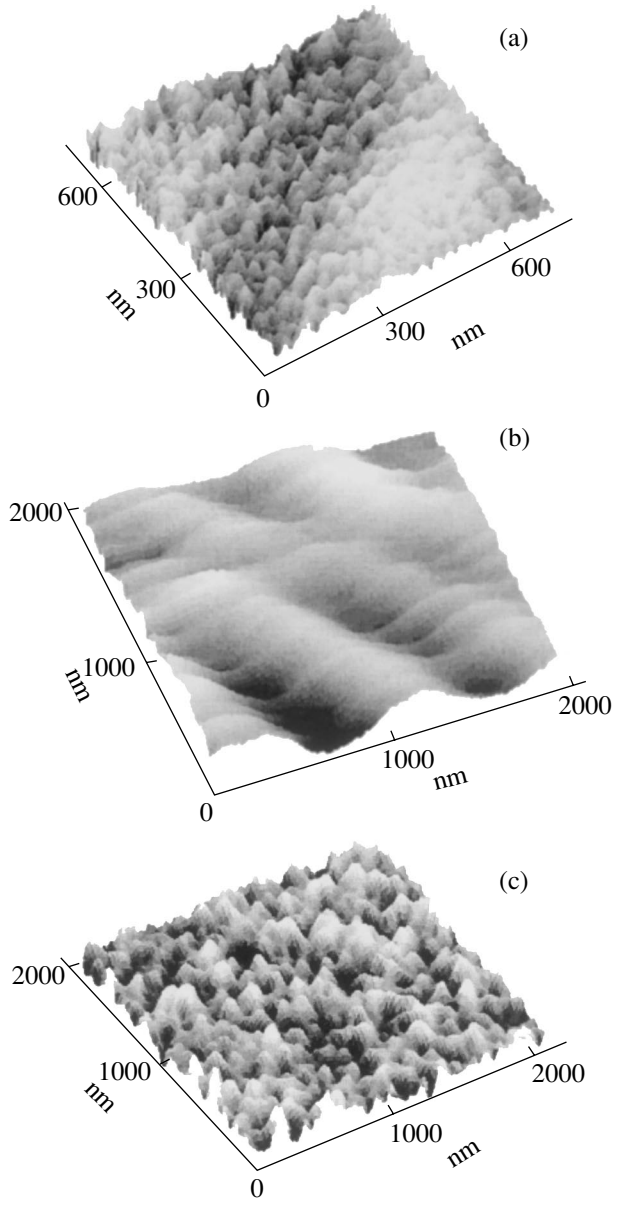

Fig. 1. AFM images of the surfaces of the structures grown at a temperature of 300°C. Mean thickness of germanium layers in the structures: (a) 3, (b) 5, and (c) 12 ML.

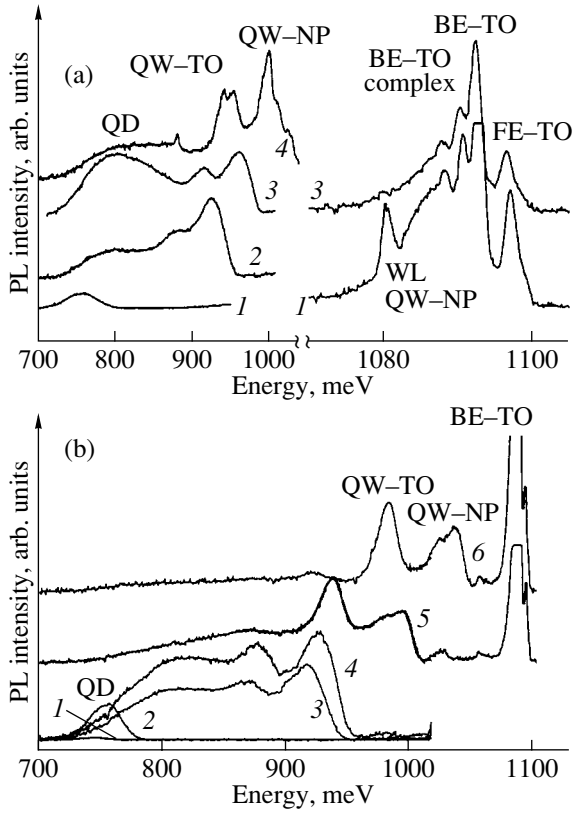

Fig. 2. Photoluminescence spectra of the Si/Ge nanostructures grown at temperatures of (a) 300 and (b) 250°C. For clarity, the spectra are shifted along the ordinate axis. Mean thickness of germanium layers: (a) (*1*) 5, (*2*) 3.5, (*3*) 3, and (*4*) 2.5 and (b) (*1*) 7, (*2*) 5, (*3*) 3.5, (*4*) 3, (*5*) 2.5, and (*6*) 2 ML. Designations: QW–TO and QW–NP are the phonon (silicon) and zero-phonon lines of the quantum-well emission, respectively; QD is the line of the quantum-dot emission; BE–TO complex and BE–TO are the phonon lines of emission of bound-exciton complexes and bound excitons in silicon, respectively; FE–TO is the line of emission of free excitons in silicon; and WL is the wetting layer.

islands decrease to ≈30 nm and they cover extended surface regions (Fig. 1a). However, when the layer thickness increases to 5 ML, the surface becomes smooth and the island relief disappears (Fig. 1b). In the case when the mean thickness of the germanium layer reaches 10–12 ML, the islands with a lateral size ≥50 nm arise again (Fig. 1c).

We assume that, during the growth of nanostructures at 300°C, a wetting layer with a thickness of 3–5 ML is formed through the coalescence of two-dimensional (2*D*) and three-dimensional (3*D*) nanoislands. For a layer thickness of 10–12 ML, the quantum dots are formed on the wetting layer according to the Stranski–Krastanov mechanism.

The above inference is confirmed by the results of analyzing the photoluminescence spectra shown in Fig. 2. Figure 2a illustrates the evolution of the emission spectra of 2*D* and 3*D* nanoislands with an increase in the thickness of the germanium layer. As the layer thickness increases from 2 to 3 ML, the intensity of quantum-well emission decreases, whereas the intensity of quantum-dot emission increases. However, with a further increase in the layer thickness to 5 ML, the emission of 2*D* and 3*D* nanoislands almost ceases and a line appears at an energy of 1080 meV. This line is attributed to the wetting layer. For a germanium layer thicker than 7 ML, the emission of the wetting layer also vanishes and only the emission of the silicon substrate manifests itself in the spectra.

It should be noted that the dependence of the energy location of the zero-phonon line in the photoluminescence spectrum of 2*D* nanoislands on the mean thickness of germanium layers lies substantially below the

theoretical curve for the strained germanium layer on the silicon substrate [8] and corresponds to a partially relaxed layer. The photoluminescence line of the wetting layer is located at an energy of 1080 meV, which is close to the energy predicted from the theoretical curve [8], and corresponds to the strained germanium layer. An analogous conclusion regarding partial relaxation of the germanium layer, which precedes the formation of the wetting layer, was drawn by us from analyzing the Raman spectra of the structures grown using a KATUN'-type apparatus [9]. It should be noted that the quantum dots formed on a similar wetting layer through the Stranski–Krastanov mechanism exhibit weak photoluminescence.

The evolution of the photoluminescence spectra of 2*D* and 3*D* nanoislands with an increase in the thickness of the germanium layer for the nanostructures grown at a temperature of 250°C is illustrated in Fig. 2b. In this case, no continuous wetting layer is formed at any thickness of the germanium layer. An increase in the layer thickness in a narrow range (5–6 ML) leads to a considerable narrowing of the photoluminescence line of 3*D* nanoislands and an abrupt increase in its intensity.

4. CONCLUSIONS

Thus, the results obtained in this study demonstrated that a decrease in the temperature of molecular-beam epitaxy to 250–300°C leads to a radical change in the mechanism of growth of germanium on silicon. At the initial stage of the growth, 2*D* and 3*D* nanoislands arise with no formation of a continuous wetting layer.

ACKNOWLEDGMENTS

We would like to thank Professor F. Scheffler for providing an opportunity to perform our investigations at his laboratory.

This work was supported by the Russian Foundation for Basic Research (project no. 03-02-17191), the "Low-Dimensional Quantum Structures" program of the Presidium of the Russian Academy of Sciences (project no. 7.12), and the State Program of Support for Leading Scientific Schools of the Russian Federation.

REFERENCES

1. O. P. Pchelyakov, Yu. B. Bolkhovitinov, A. V. Dvurechenskiĭ, *et al.*, Fiz. Tekh. Poluprovodn. (St. Petersburg) **34** (11), 1281 (2000) [Semiconductors **34**, 1229 (2000)].
2. G. Abstreiter, P. Schittenhelm, C. Engel, *et al.*, Semicond. Sci. Technol. **11**, 1521 (1996).
3. P. Schittenhelm, C. Engel, F. Findeis, *et al.*, J. Vac. Sci. Technol. B **16** (3), 1575 (1998).
4. O. G. Schmidt, C. Lange, and K. Eberl, Appl. Phys. Lett. **75**, 1905 (1999).
5. A. B. Talochkin, A. V. Efanov, V. A. Markov, and A. I. Nikiforov, Izv. Ross. Akad. Nauk, Ser. Fiz. **63** (2), 290 (1999).
6. V. A. Markov, H. H. Cheng, Chih-ta Chia, *et al.*, Thin Solid Films **369**, 79 (2000).
7. T. M. Burbaev, T. N. Zavaritskaya, V. A. Kurbatov, *et al.*, Fiz. Tekh. Poluprovodn. (St. Petersburg) **35** (8), 979 (2001) [Semiconductors **35**, 941 (2001)].
8. J. Brunner, J. F. Nutzel, M. Gail, *et al.*, J. Vac. Sci. Technol. B **11**, 1097 (1993).
9. T. M. Burbaev, V. A. Kurbatov, T. N. Zavaritskaya, *et al.*, Izv. Ross. Akad. Nauk, Ser. Fiz. **67** (2), 163 (2003).

Translated by N. Korovin

Physics of the Solid State, Vol. 46, No. 1, 2004, pp. 74–76. Translated from Fizika Tverdogo Tela, Vol. 46, No. 1, 2004, pp. 77–79.

PROCEEDINGS OF THE CONFERENCE DEDICATED TO O. V. LOSEV (1903–1942)

(Nizhni Novgorod, Russia, March 17–20, 2003)

Stepwise Dependence of the Photoconductivity of Si/Ge Structures with Quantum Dots on the Interband Illumination Intensity

O. A. Shegaĭ, V. A. Markov, and A. I. Nikiforov

Institute of Semiconductor Physics, Siberian Division, Russian Academy of Sciences, pr. Akademika Lavrent'eva 13, Novosibirsk, 630090 Russia

e-mail: shegai@thermo.isp.nsc.ru

Abstract—It was found that a stepwise increase in the interband light intensity causes an increase in the low-temperature lateral photoconductivity of a Si/Ge structure containing six layers of germanium quantum dots in a silicon host. As was previously observed in structures with a single layer of quantum dots, strengthening of the driving field results in the step positions shifting to lower light intensities. This effect was also found to take place under a dark driving field. The results are discussed in terms of the percolation theory of nonequilibrium electrons localized in the states between quantum dots. © *2004 MAIK "Nauka/Interperiodica".*

1. INTRODUCTION

The study of the lateral photoconductivity (PC) mechanisms in Si/Ge/Si structures containing self-assembling germanium quantum dots (QDs) is of interest because of the application potential of these structures in optoelectronics [1]. Previously, we reported on the detection of a stepwise increase in the lateral PC of structures with a single QD layer caused by an increase in the interband illumination intensity [2, 3]. The observed effect was explained in terms of the theory of percolation [4] of nonequilibrium carriers over localized states arising in the silicon matrix between QDs due to spatial stress relaxation in the vicinity of QDs [5]. In this paper, we report on the detection of a stepwise increase in the PC signal under interband illumination in structures with six germanium QD layers and on the influence of a dark driving field on the step position.

2. EXPERIMENTAL

Strained Si/Ge/Si structures were grown (using molecular-beam epitaxy) through the Stranski–Krastanow mechanism on Si(001) substrates and contained six QD layers with a nominal Ge thickness of N_{Ge} = 8 and 10 monolayers (MLs). The QD layers were separated by silicon layers 25 nm thick. The layers containing QDs were grown on a buffer silicon layer ~100 nm thick and were coated by a cap Si layer ~20 nm thick. A decrease in the Ge layer growth temperature to T_g = 250°C resulted in a high QD density ($N_{QD} \approx 10^{11}$ cm^{-2}) and small QD sizes (the lateral size was ~10 nm).

The PC was measured at T = 4.2 K. The light intensity was swept by increasing the current through a red light–emitting diode placed near the sample with an illuminated area of 1.5 × 0.2 mm. The signals proportional to the sample conductivity and to the illumination intensity of the sample were recorded using a computer.

3. RESULTS AND DISCUSSION

Figure 1 shows the light-intensity dependences of the lateral PC at various values of the driving field for a structure with six QD layers and N_{Ge} = 8 MLs and the dependence of the step position on the driving field (dots indicate experimental data, the curve is a result of exponential fitting). Figure 2 shows analogous dependences for a structure with N_{Ge} = 10 MLs. As in the previous study with a single QD layer [2, 3], a stepwise increase in the PC signal is observed. The step positions are shifted to lower light intensities with increasing driving field. As in the structure with a single QD layer, the dependence of this shift for the structure with N_{GS} = 8 MLs is exponential with a similar characteristic voltage value $U_0 \approx 2$ V [2, 3]; for the structure with N_{Ge} = 10 MLs, this dependence is linear (Fig. 2).

Figure 3 shows the influence of the dark driving field on the PC step position in both QD structures. Initially, the dependence of the lateral PC on the interband light intensity was measured at a certain fixed value of the driving field. Then, a voltage of 100 V was applied to the structure for a few seconds in the dark and the dependence of the PC was measured again at the initial value of the driving field. We can see that the step is shifted to lower light intensities after applying the voltage in the dark for both structures. The shift for the structure with N_{Ge} = 10 MLs exceeds that for the struc-

1063-7834/04/4601-0074$26.00 © 2004 MAIK "Nauka/Interperiodica"

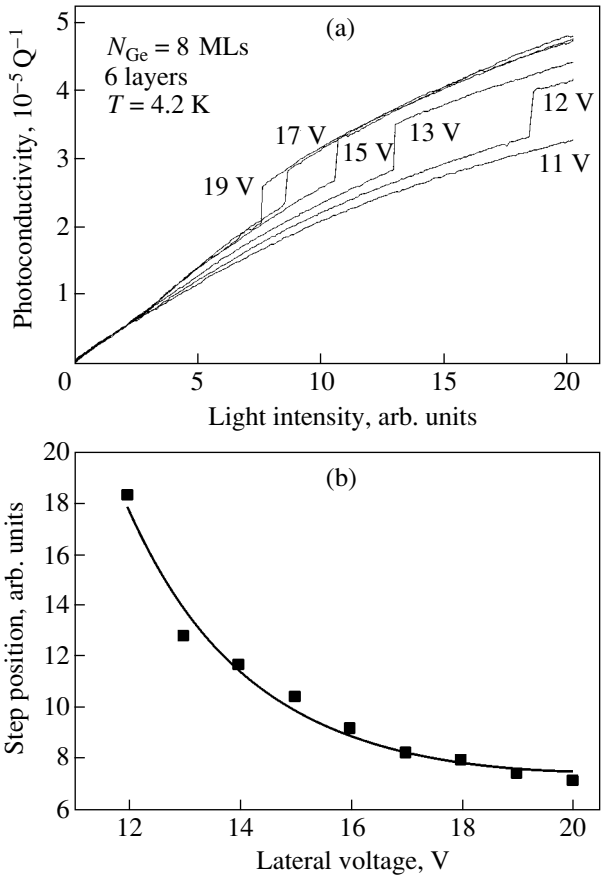

Fig. 1. (a) Dependence of the lateral photoconductivity of a structure with six QD layers (nominal thickness of each layer is 8 MLs) on the interband light intensity at various driving fields and (b) the dependence of the PC step position on the lateral field.

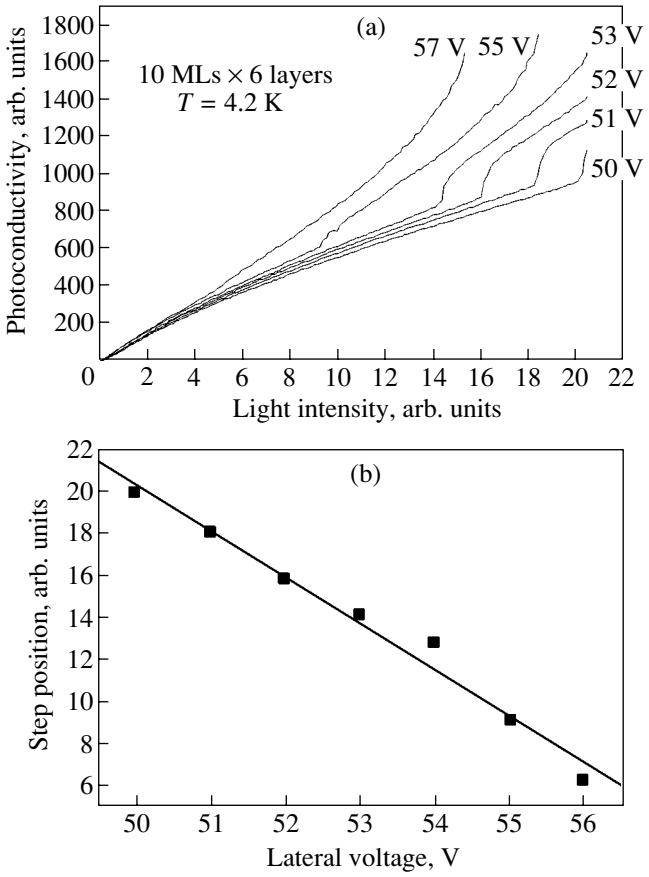

Fig. 2. The same as in Fig. 1 but for a nominal layer thickness of 10 MLs.

ture with N_{Ge} = 8 MLs by approximately four times. It was indicated that the shift depends linearly on the dark field.

We analyzed the results of the study in terms of the model of nonequilibrium carrier percolation over localized states between QDs suggested by us previously. These states arise due to spatial stress relaxation in the vicinity of QDs [5]. The states are in the QD plane, with each of these states being at the same distance from at least three nearest QDs. Fluctuations in the distance between QDs and in their lateral size cause the localization potential to fluctuate.

Interband illumination causes localization of nonequilibrium electrons in the states described above. At low interband light intensities, the concentration of nonequilibrium carriers is lower than that of QDs and holes are mostly localized in QD states. At high intensities, holes are localized between QDs. If the QD Coulomb potential that trapped a hole is higher than the repulsing potential due to the inhomogeneous stresses in the vicinity of the QD, an electron forms a bound state on the QD [5]. Carriers localized in states between QDs form exciton states, whose concentration is controlled by the interband light intensity and which do not affect the structure conductivity. Strengthening of the driving field results in splitting of the excitons into carriers localized in the same place. When the quasi-Fermi level of electrons that are in localized states between QDs reaches the percolation threshold, a stepwise increase in the PC signal is observed. The higher the lateral field, the larger the number of dissociated excitons and the lower the light intensity at which the step arises. The values of the lateral field at which a PC step arises are much higher for the structure with N_{Ge} = 10 MLs than those for the structure with N_{Ge} = 8 MLs. This fact is explained by the larger energy band relief amplitude caused by increased stresses in QDs in the structures with larger QDs.

Apart from lateral relaxation of stresses around QDs, transverse relaxation of stresses in the structure growth direction also takes place. Since the dependences of the PC on the interband light intensity for the structure with N_{Ge} = 8 MLs almost do not differ from those for the structures with a single QD layer, transverse relaxation of stresses in the regions between neighboring QD layers in the former structure is complete. For the structure with large lateral sizes of QDs

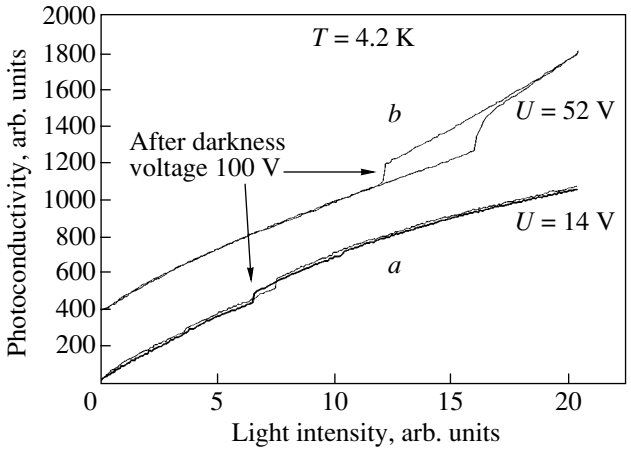

Fig. 3. Influence of the dark voltage (100 V) on the interband light intensity dependence of the lateral photoconductivity for structures containing six QD layers with a Ge layer thickness of (a) 8 MLs and (b) 10 MLs (for convenience, the curves are shifted upward).

(N_{Ge} = 10 MLs) and identical distances between neighboring QD layers, mutual strengthening of the strain fields takes place, which increases the band relief amplitude.

We are of the opinion that the PC step position shift in the QD structures under a dark voltage is caused by carrier injection from the contacts into the structure. After the dark voltage is switched off, a certain fraction of electrons can be in the localized states between QDs for a rather long time due to the band relief. In the structure with a high band relief potential (N_{Ge} = 10 MLs), the number of electrons localized between QDs is larger than that in the structure with N_{Ge} = 8 MLs, which results in the percolation threshold being reached at significantly lower interband light intensities.

4. CONCLUSIONS

Thus, a stepwise increase has been detected in the dependence of the lateral photoconductivity of Si/Ge structures with several QD layers on the interband light intensity. Strengthening of the driving field causes a shift of the step position to lower light intensities. It has been found that the dark driving field affects the step position, whose shift depends essentially on the QD lateral sizes. The results were interpreted in terms of the theory of percolation over localized states arising due to spatial stress relaxation in the vicinity of quantum dots.

ACKNOWLEDGMENTS

This study was supported by the Russian Foundation for Basic Research, projects no. 03-02-16466 and 03-02-16468.

REFERENCES

1. O. P. Pchelyakov, Yu. B. Bolkhovityanov, A. V. Dvurechenskiĭ, *et al.*, Fiz. Tekh. Poluprovodn. (St. Petersburg) **34** (11), 1281 (2000) [Semiconductors **34**, 1229 (2000)].
2. O. A. Shegai, V. A. Markov, A. I. Nikiforov, *et al.*, Phys. Low-Dimens. Semicond. Struct. **1–2**, 261 (2002).
3. O. A. Shegaĭ, K. S. Zhuravlev, V. A. Markov, *et al.*, Izv. Ross. Akad. Nauk, Ser. Fiz. **67** (2), 192 (2003).
4. B. I. Shklovskiĭ and A. L. Éfros, *Electronic Properties of Doped Semiconductors* (Nauka, Moscow, 1979; Springer, New York, 1984).
5. O. A. Shegaĭ, K. S. Zhuravlev, V. A. Markov, *et al.*, Fiz. Tekh. Poluprovodn. (St. Petersburg) **34** (11), 1363 (2000) [Semiconductors **34**, 1311 (2000)].

Translated by A. Kazantsev

Physics of the Solid State, Vol. 46, No. 1, 2004, pp. 77–79. Translated from Fizika Tverdogo Tela, Vol. 46, No. 1, 2004, pp. 80–82.

PROCEEDINGS OF THE CONFERENCE DEDICATED TO O. V. LOSEV (1903–1942)

(Nizhni Novgorod, Russia, March 17–20, 2003)

Growth and Structure of Ge Nanoislands on an Atomically Clean Silicon Oxide Surface

A. I. Nikiforov, V. V. Ul'yanov, O. P. Pchelyakov, S. A. Teys, and A. K. Gutakovskiĭ

Institite of Semiconductor Physics, Siberian Division, Russian Academy of Sciences, pr. Akademika Lavrent'eva 13, Novosibirsk, 630090 Russia

e-mail: nikif@isp.nsc.ru

Abstract—Experimental data on the formation of self-organized Ge islands on an atomically clean oxidized Si(100) surface are presented. On the oxidized silicon surface, the Volmer–Weber growth mechanism is operative rather than the Stranski–Krastanow mechanism, which operates in the case of Ge growth on a clean silicon surface. The Ge growth is accompanied by a significant change (as large as 7%) in the surface unit cell size of the Ge lattice with respect to that for silicon. For Ge films up to five monolayers thick, the nanoisland dimensions at the bottom are smaller than 10 nm and the island density is higher than 2×10^{12} cm^{-2}. © *2004 MAIK "Nauka/Interperiodica".*

1. INTRODUCTION

The study of the self-organization of nanometer-sized islands is of interest in several areas of solid-state physics. For surface physics and the physics of condensed matter, the study of the mechanisms of nanostructure growth and of concomitant atomic processes proceeding on the surface is of interest. Nanoislands have also been a subject of considerable interest in semiconductor physics, because they can be employed as quantum-confinement systems. An example is the heterosystem of germanium grown on the Si surface, in which Ge islands can be treated as quantum dots. On the Si(100) surface, dislocation-free germanium islands 10–100 nm in size were observed to appear after a continuous Ge film was formed [1]. Such islands can be made sufficiently small in size for the quantum-confinement effects to manifest themselves at temperatures up to room temperature [2].

The minimal size of Ge islands that form during film growth on a clean silicon surface is 15 nm. The size of Ge islands can be made smaller and their density higher by growing a germanium film on an atomically clean oxidized surface prepared directly in a molecular-beam epitaxy (MBE) setup. The possibility of producing an oxide layer on a silicon surface under conditions of an ultrahigh-vacuum has been known for a fairly long time. It was first demonstrated in [3] that different conditions of etching and oxide film growth can be created by varying the oxygen pressure and temperature. Quite recently, this technique was developed further when the formation of an ultrathin oxide layer was related to further growth of an epitaxial silicon layer [4]. Prior oxidation of the silicon surface makes it possible to significantly decrease germanium islands in size and increase their density. It was shown in [5, 6] that, when islands grow on an oxidized Si(111) surface, their lateral dimensions are less than 10 nm and their density is higher than 10^{12} cm^{-2}. In [5], it was suggested that in this case silicon oxide is locally deoxidized by germanium (through the disproportionation reaction), which is accompanied by desorption of germanium monoxide. At such sites, germanium nanoislands jointed coherently with the silicon nucleate. However, there are no data on island deformation and its relaxation in germanium–silicon oxide heterojunctions.

The objective of this work is to determine the mechanism of a Ge island film growing on an atomically clean oxidized Si surface and to produce an array of ultrasmall Ge nanoislands of high density.

2. EXPERIMENT

Island films were produced in a Katun'-S MBE chamber. Silicon was evaporated using an electron-beam evaporator (EBE). A germanium flux was formed either by the EBE or by an effusion cell with a boron nitride crucible. Dopants (Sb, B) were evaporated from effusion cells. Analysis was performed using a quadrupole mass spectrometer, a quartz crystal monitor, and a reflection high-energy electron (20 keV) diffractometer. Diffraction patterns were recorded during the island growth with a CCD camera and were stored on computer. The software package made it possible to record diffraction patterns at a rate of 10 frames per second. The Ge growth rate was 10 monolayers (MLs) per minute. The temperature was varied from room temperature to 700°C. Si(100) substrates were employed with a misorientation of less than 0.5°. Oxidation was performed in the MBE chamber at an oxygen pressure of up to 10^{-4} Pa and a substrate temperature of 400–

1063-7834/04/4601-0077$26.00 © 2004 MAIK "Nauka/Interperiodica"

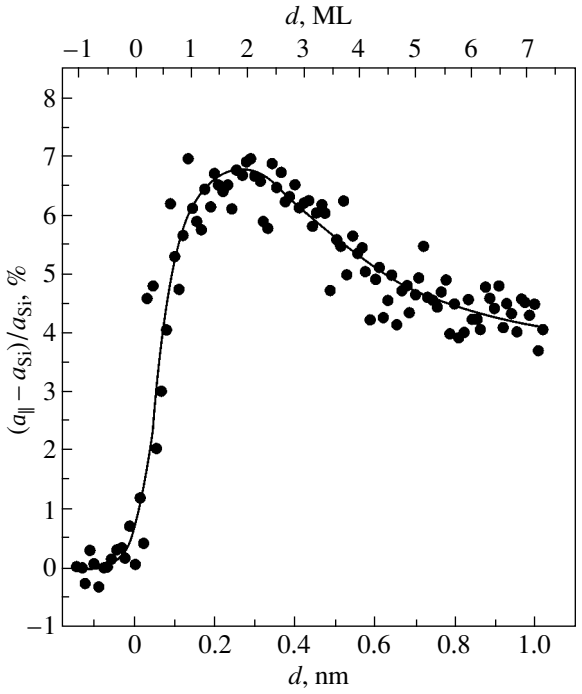

Fig. 1. Variations in the two-dimensional surface unit cell parameter $a_{\|}$ during the Ge film growth on the oxidized Si(100) surface.

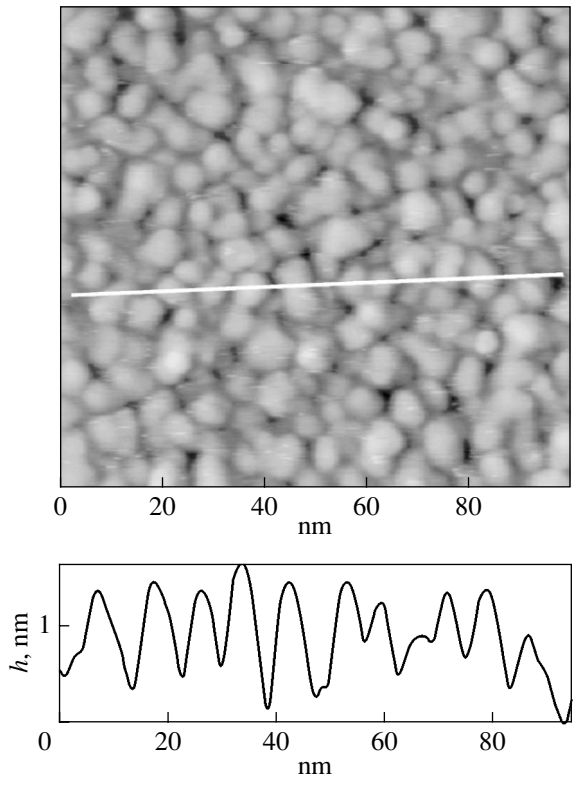

Fig. 2. Scanning tunneling microscopic image of an array of Ge islands on a silicon oxide surface and the morphology change profile along the light line; d_{Ge} = 3 MLs and T_s = 650°C.

500°C. After pumping out the oxygen, germanium was deposited on the oxidized surface.

3. RESULTS AND DISCUSSION

The growth of a Ge film on an oxidized silicon surface was monitored with the use of electron diffraction patterns by recording both the qualitative changes in structure and morphology of a growing film surface and quantitative data on the elastic strain of the surface unit cell [7]. To analyze the initial stage of the Ge film growth on an oxidized silicon surface, we recorded the changes in intensity of the specular reflection and of the three-dimensional electron reflection diffraction (3D reflections). These reflections are very sensitive to changes in the surface roughness; in particular, the appearance of a 3D reflection indicates the presence of three-dimensional objects on the surface under examination. In the case of film growth on a clean surface, oscillations of the specular reflection intensity, its vanishing, and the appearance of a 3D reflection when the Ge film thickness becomes larger than four monolayers indicate layer-by-layer growth of the wetting layer followed by the formation of three-dimensional islands. In the case of Ge film growth on an oxidized surface, the intensity of these reflections changes even after deposition of one monolayer and no oscillation in the specular reflection intensity is observed. These features suggest that the wetting layer does not form on the oxidized surface. Indeed, as the first monolayer is deposited, an adsorbed germanium layer forms on the SiO_2 surface and then transforms into three-dimensional islands when the next monolayers are deposited. Therefore, in the case of a Ge film growing on an oxidized silicon surface, the Volmer–Weber mechanism is operative rather than the Stranski–Krastanow growth mechanism, which operates in the case of a clean silicon surface.

To analyze the Ge lattice strains, we determined the changes in the (two-dimensional) surface unit cell parameter $a_{\|}$. For this purpose, we recorded the variations in the distance between the diffraction pattern spots corresponding to the parameter $a_{\|}$. Figure 1 shows the change in $a_{\|}$ during the Ge film growth with respect to the value of this parameter at the silicon surface. It can be seen from Fig. 1 that, as the film grows, the surface unit cell of the Ge lattice varies significantly with respect to that for Si, which remains constant. The variation reaches 7%, as in the case of a film growing on a clean Si(100) surface [7]. In the beginning, elastically strained islands grow. Then, $a_{\|}$ decreases to the value characteristic of bulk germanium, which is indicative of complete plastic relaxation of the islands. Such a behavior of the parameter $a_{\|}$ is analogous to that in the case of germanium heteroepitaxy on a clean Si(100) surface, but in the former case the relaxation of strained Ge islands comes to a close much earlier and the three-dimensional islands that form after the first monolayer

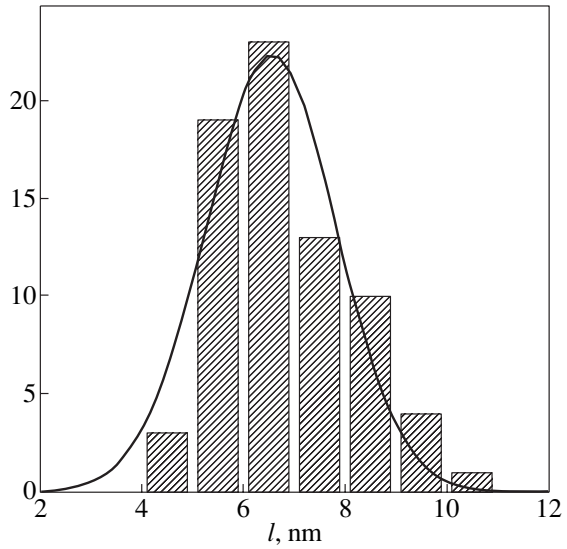

Fig. 3. Distribution of Ge islands in size at the bottom for d_{Ge} = 3 MLs and T_s = 650°C.

is deposited already have the maximal value of the two-dimensional surface unit cell parameter. Therefore, the maximum elastic strain already exists in the nuclei of three-dimensional islands.

Islands differ in size and density depending on the thickness of the deposited germanium. For film thicknesses of up to 5 MLs, the dimensions of islands at the bottom are less than 10 nm and their density is higher than 2×10^{12} cm^{-2}. Figure 2 shows a scanning tunneling microscopic image of an array of Ge islands formed on a silicon oxide surface after three germanium monolayers were deposited at a substrate temperature of 650°C. The distribution of Ge islands in size at their bottom in this case (d_{Ge} = 3 MLs, T_s = 650°C) is shown in Fig. 3. It can be seen that not only small islands but also islands with dimensions that are larger by an order of magnitude and with a significantly lower density are formed as the effective thickness of deposited germanium increases. Therefore, when the thickness of a germanium film deposited on the oxidized Si(100) surface is greater than 1 nm, a bimodal distribution of islands in terms of size and density is observed. This conclusion is also confirmed by electron-microscopic studies.

ACKNOWLEDGMENTS

This study was supported by the Russian Foundation for Basic Research, project nos. 03-02-16468 and 03-02-16506.

REFERENCES

1. D. J. Eaglesham and M. Cerullo, Phys. Rev. Lett. **64**, 1943 (1990).
2. A. I. Yakimov, A. V. Dvurechenskii, Yu. Yu. Proskuryakov, *et al.*, Thin Solid Films **336**, 332 (1998).
3. J. J. Lander and L. Morrison, J. Appl. Phys. **33**, 2098 (1962).
4. Y. Wei, M. Wallace, and A. C. Seabaugh, J. Appl. Phys. **81**, 6415 (1997).
5. A. A. Shklyaev, M. Shibata, and M. Ichikawa, Phys. Rev. B **62**, 1540 (2000).
6. A. Barski, M. Derivaz, J. L. Rouviere, and D. Buttard, Appl. Phys. Lett. **77**, 3541 (2000).
7. A. I. Nikiforov, V. A. Cherepanov, O. P. Pchelyakov, *et al.*, Thin Solid Films **380**, 158 (2000).

Translated by Yu. Epifanov

Physics of the Solid State, Vol. 46, No. 1, 2004, pp. 80–84. Translated from Fizika Tverdogo Tela, Vol. 46, No. 1, 2004, pp. 83–87.

PROCEEDINGS OF THE CONFERENCE DEDICATED TO O. V. LOSEV (1903–1942)

(Nizhni Novgorod, Russia, March 17–20, 2003)

Growth of Germanium Nanoislands and Nanowires on Singular and Vicinal Si(111) Surfaces Prior to the Formation of a Wetting Layer

S. A. Teys, A. B. Talochkin, K. N. Romanyuk, and B. Z. Olshanetsky

Institute of Semiconductor Physics, Siberian Division, Russian Academy of Sciences, pr. Akademika Lavrent'eva 13, Novosibirsk, 630090 Russia

e-mail: teys@isp.nsc.ru

Abstract—The growth of germanium nanoislands and nanowires on singular and vicinal Si(111) surfaces is investigated by scanning tunneling microscopy (STM). It is shown that the formation of a Ge wetting layer on the Si(111) surface at germanium deposition rates of approximately 10^{-3} BL/min and epitaxial temperatures of 350–500°C occurs through the island or multilayer growth mechanism. This makes it possible to prepare arrays of Ge islands with a height of 3 BL and a density of 10^9–10^{12} cm^{-2}. The growth of Ge nanowires with a constant height and a width dependent on the Ge coverage is observed on vicinal Si(111) surfaces. It is found that the surface diffusion coefficients of Ge adatoms on the Ge(5×5) surface are severalfold larger than those on the Si(7×7) surface. The Raman spectra of optical phonons on the Si(111) surface with Ge nanoislands 3 BL in height contain a number of lines associated with the quantization of the phonon spectrum along the [111] growth direction. © *2004 MAIK "Nauka/Interperiodica".*

1. INTRODUCTION

The photosensitive and light-emitting properties of structures with Ge islands on an Si(100) surface have been intensively investigated in recent years [1–4]. The growth of germanium layers on silicon substrates occurs through the Stranski–Krastanov mechanism. In this case, the formation of a strained Ge wetting layer is followed by the three-dimensional growth of Ge islands. According to scanning tunneling microscopy (STM), the homoepitaxial growth of silicon on the Si(111) surface at the initial stages [5] and the formation of a Ge wetting layer on the Si(111) surface [6–9] proceed by the island mechanism. Nanoislands grow in height and form second and third layers, which serves as an example of the growth through the multilayer mechanism [7, 10].

In this work, we performed STM investigations of the growth of germanium nanoislands and nanowires on singular and vicinal Si(111) surfaces at stages of the formation of a wetting layer and the onset of three-dimensional growth of germanium islands at low growth rates.

2. EXPERIMENTAL TECHNIQUE

In our experiments, we used *n*-Si and *p*-Si samples ($12 \times 3 \times 0.4$ mm in size) with a resistivity of 5–10 Ω cm. The preparation of atomically clean surfaces, germanium epitaxy, and STM observations were performed on a RIBER–OMICRON instrument under ultrahigh vacuum. The experimental conditions were described in detail in our earlier work [9]. The growth of germanium layers was carried out at temperatures of 350–500°C and deposition rates of 10^{-2}–10^{-3} BL/min (1 BL = $a_0 = 1.44 \times 10^{15}$ atoms/cm^2 is a bilayer of Ge atoms). The STM images of the surface were obtained at room temperature. Tungsten tips prepared by electrolytic etching in an alkaline solution served as STM probes. The Raman spectra of optical phonons were recorded on a DFS-52 spectrometer upon excitation with an Ar laser at wavelength $\lambda = 488$ nm. In order to avoid oxidation of the growth surface, the structures grown were rapidly transferred in a nitrogen atmosphere from the growth chamber to a liquid-nitrogen cryostat.

3. RESULTS AND DISCUSSION

At the initial stages of heteroepitaxial growth, Ge atoms are deposited in the form of clusters in halves of unit cells of the Si(7×7) surface structure [6, 9, 11]. An increase in the Ge amount on the surface leads to the coalescence of clusters and the formation of triangular islands [6, 9, 12]. When the Ge epitaxial growth occurs at a temperature of 380°C and a rate of 4×10^{-3} BL/min, the density of clusters increases and, at a maximum, exceeds the density of larger sized three-dimensional islands by a factor of approximately 10 (Fig. 1). With a further increase in the Ge coverage to 0.5 BL, the clusters on the surface undergo complete decomposition and give way to islands whose density (2×10^{10} atoms/cm^2) remains constant at coverages of less than 0.8–1.0 BL. At such low growth rates, the height

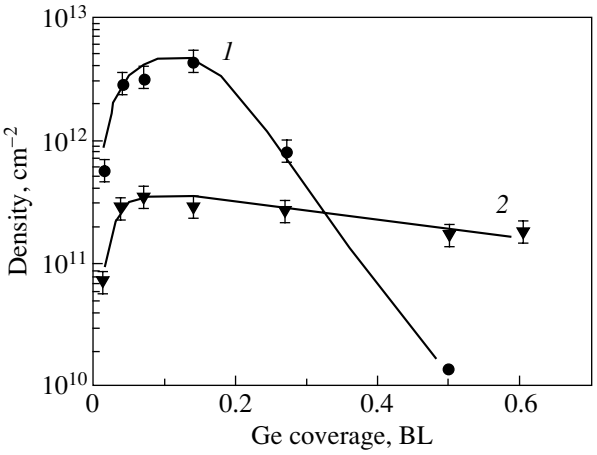

Fig. 1. Density of (*1*) Ge clusters and (*2*) Ge islands on the Si(111) surface as a function of the Ge coverage. The growth temperature is 380°C, and the growth rate is 4×10^{-3} BL/min.

of the majority of islands on Si(111) terraces reaches 3 BL. The subsequent growth of islands proceeds only in the substrate plane until a continuous wetting layer is formed. A distinguishing feature of the self-assembled growth of nanoislands in the Ge/Si(111) system is that the island size is limited by a height of 3 BL. The reason for this limitation still remains unclear. However, with a high probability, this limitation can be associated with the specific features of the mechanisms of diffusion and incorporation of adatoms into the reconstructed surface of a diamond-like crystal lattice, because a similar growth at low deposition rates was observed during homoepitaxial growth of silicon on Si(111) [12].

The linear dependence of the logarithm of the island density on the epitaxial temperature indicates the kinetic limitation of island nucleation. Therefore, arrays of three-layer Ge islands with a density of 10^9–10^{12} cm^{-2} can be grown on the Si(111) surface prior to the formation of a continuous wetting layer.

The growth of islands in height occurs through the migration of Ge atoms from the lower terrace to the upper terrace, because the amount of Ge arriving at the island top is too small to provide the formation of the second and third layers. The migration effect is the second specific feature of the self-assembling of Ge atoms on the Si(111) surface. The third feature responsible for the self-assembling is the formation of the (7×7) surface structure on both the substrate and the surface of growing islands. The lateral sizes of islands are multiples of the size of the (7×7) unit cell. The island edges coincide with the boundaries of the (7×7) cells. The surface structure plays an important role in the mass transfer along the surface. At a coverage of ~0.5 BL, the (7×7) surface structure occupies approximately 70% of the island surface area, whereas the (5×5) structure occupies only 30% of the island surface area. However, when islands merge together into a continuous layer at

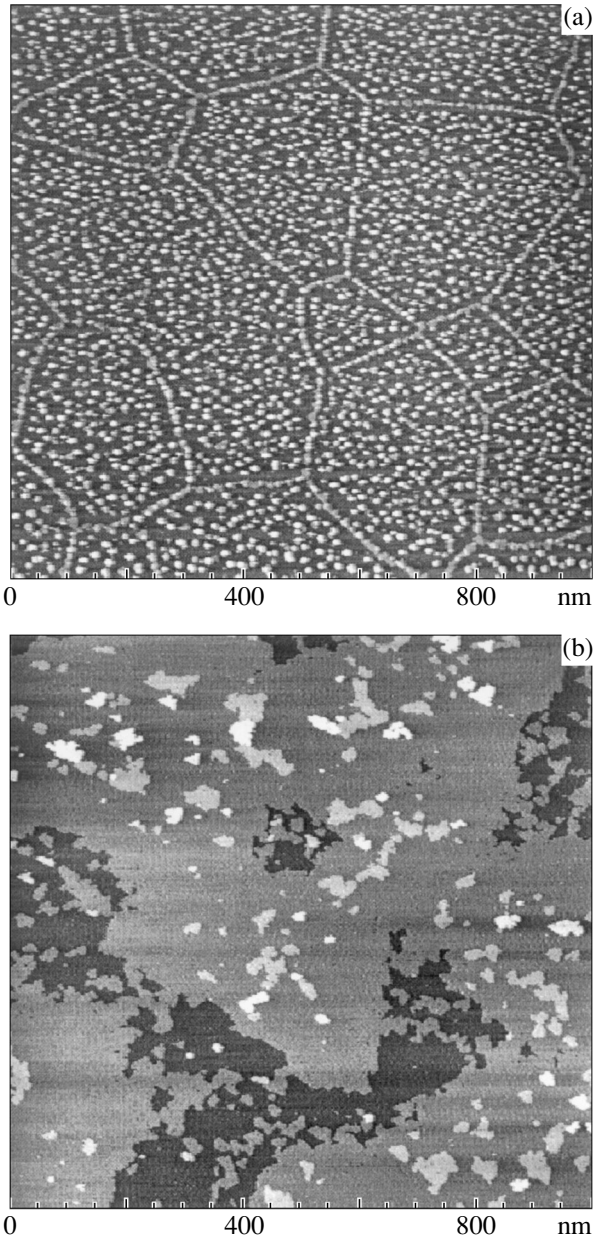

Fig. 2. STM images of the surface after deposition of 0.3-BL-thick Ge layers (temperature, 350°C; deposition rate, 4×10^{-3} BL/min) on different initial surfaces: (a) the Si(111)-(7×7) surface and (b) the Si(111)-(7×7) surface with a Ge(111)-(5×5) layer.

a coverage of approximately 3 BL (or at smaller coverages during growth at higher temperatures), the (5×5) structure is observed over the entire surface. Therefore, the (7×7) structure transforms into the (5×5) structure at the island tops. This transformation into the new surface structure results in a considerable increase in the rate of surface diffusion of adsorbed Ge atoms. This is qualitatively illustrated in Fig. 2, which shows the STM images of two different surfaces after Ge epitaxy at a temperature of 350°C. Figure 2a displays the STM

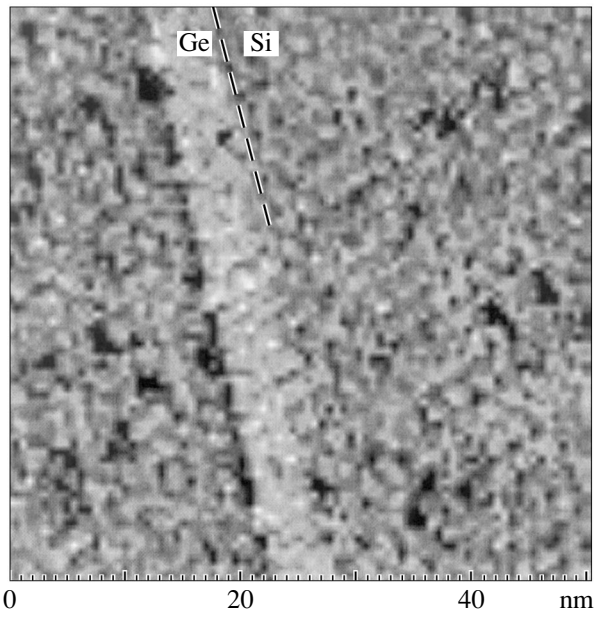

Fig. 3. STM image of the Ge nanowire with a height of 1 BL and a width equal to the size of two (7×7) unit cells (tunneling current, constant voltage, fixed distance to the surface).

image of the surface after germanium deposition directly on the clean Si(111) surface with a (7×7) structure. The STM image of the surface after Ge epitaxy on the Si(111) substrate with a Ge(5×5) continuous layer (preliminarily deposited at 550°C) is reproduced in Fig. 2b. It can be seen from these figures that the densities of islands on the terraces differ by a factor of ~40. In our opinion, a drastic increase in the migration length leads to a qualitative change in the island growth. The density of nuclei of new islands on the wetting layer with a (5×5) structure decreases significantly despite numerous surface defects.

It is revealed that vicinal Si(111) surfaces deviating from the (111) plane by several degrees involve steps with a height equal to the interplanar distance ($1d_{111}$). Upon the deviation in the opposite directions $[11\bar{2}]$ and $[\bar{1}\bar{1}2]$, the step edges contain atoms with one dangling bond (steps of the first type) and atoms with two dangling bonds (steps of the second type), respectively. A smooth decrease in the temperature in the phase transition range on the surface with steps of the second type is attended by the formation of steps 3 BL ($3d_{111}$) in height (in addition to steps of height $1d_{111}$). The fraction of steps $3d_{111}$ in height on the surface increases with an increase in the angle of deviation from the (111) plane [13].

Upon the interaction of Ge with steps of the first type, the initially smooth edge of the step acquires a sawtooth shape; i.e., steps of the first type are gradually replaced by steps of the second type. The incorporation of Ge adatoms into the step edge results in the formation of a depletion region (the region free of islands) along the step. The depletion region on steps of the first type on the side of the upper terrace is larger than that on the lower terrace. This suggests a lower energy barrier to the incorporation of Ge atoms into the step on the side of the upper terrace. After Ge epitaxy on the surface with steps of the second type, the edges of initial steps remain smooth and a chain of merging islands is formed on the side of the upper terrace. We determined the regions of depletion in islands in the vicinity of steps and the width of Ge nanowires formed along the steps with a specially developed program for analyzing STM images. It was found that, for steps of the second type, the depletion region on the side of the lower terrace always exceeds the depletion region on the side of the upper terrace. Moreover, the number of Ge atoms incorporated into the step edge on the side of the lower terrace is less than that on the side of the upper terrace. These findings indicate that Ge atoms migrate from the lower terrace to steps of the second type on the upper terrace.

Thus, the mechanism of growth of perfect triangular islands becomes clear. Germanium atoms migrate through steps of the second type to upper layers. As a result, Ge atoms from the upper and lower terraces are incorporated into steps of the first type. A rapid growth and disappearance of steps of the first type in islands and a continuous migration of Ge atoms to the second layer favor an increase in the island height.

If the epitaxial growth of germanium nanoislands occurs on steps of the second type at high temperatures under conditions where the amount of surface defects decreases and the migration length of Ge atoms becomes comparable to the terrace width, the height of Ge nanowires can reach 1 BL. Figure 3 displays an STM image of the Si step with a Ge nanowire 1 BL in height, which was obtained in a tunneling current mode. The formation of the Ge nanowire with a width equal to the size of two (7×7) unit cells suggests that the surface structure affects the self-assembled growth. It can be seen from Fig. 3 that, compared to the Ge nanoislands, the Ge nanowires are more perfect nanoobjects with constant width and height. The Ge growth along steps of height $3d_{111}$ is also of considerable interest. For these steps, the height of the grown Ge nanowire is limited by 3 BL, as is the case with islands; moreover, the width of the nanowire depends on the coverage and is a multiple of the size of the (7×7) unit cell.

We also studied the Raman spectra of optical phonons on the Si(111) surface containing Ge islands with a height of 3 BL and a density of approximately 2×10^{10} cm^{-2} [14]. It was revealed that the Raman spectra exhibit a series of phonon lines (Fig. 4). The vertical arrow in Fig. 4 indicates the location of the peak assigned to triply degenerate phonons of bulk germanium at $T = 77$ K (305 cm^{-1}). In our case, the degeneracy is removed by mechanical stresses in the

Ge/Si(111) system. The Ge islands are strained as a result of compression in the (*xy*) growth plane and extension along the *z* growth direction. Since the lateral sizes of islands substantially exceed the height, the effect of lateral faces can be ignored and the strain in the (111) plane can be treated as homogeneous. The components of the strain tensor in the (111) growth plane are designated as $\varepsilon_{xx} = \varepsilon_{yy} = \varepsilon$. The component ε_{zz} can be determined from the boundary condition $\sigma_{zz} = 0$, where σ_{zz} is the component of the stress tensor. By transforming the strain tensor in terms of the (100) system and applying the Hooke law, we determine the components of the stress tensor in this system. After the inverse transformation with due regard for the boundary condition, we obtain the strain along the [111] direction:

$$\varepsilon_{zz} = -2\varepsilon_{xx}(C_{11} + 2C_{12} - C_{44})/(C_{11} + 2C_{12} + 2C_{44}) = -0.92\varepsilon,$$

where C_{11}, C_{12}, and C_{44} are the components of the elastic compliance tensor for germanium. The components of the stress tensor in the growth plane can be written in the form

$$\sigma = \sigma_{xx} = \sigma_{yy} = 3C_{44}\varepsilon(C_{11} + 2C_{12})/(C_{11} + 2C_{12} + 2C_{44}).$$

These stresses split the state of the optical phonon with the wave vector $\mathbf{k} = 0$ into the singlet (LO) and triplet (TO) states. The expressions for the dependence of the frequency of these phonons on the biaxial stress in a plane perpendicular to the (111) plane were derived in [15]:

$$\Omega_L = \omega_0 + \Delta\Omega_h - (1/3)\Delta\Omega, \quad (1)$$

$$\Omega_T = \omega_0 + \Delta\Omega_h + (2/3)\Delta\Omega, \quad (2)$$

where ω_0 is the frequency of optical phonons of germanium; $\Delta\Omega_h = 2\sigma(S_{11} + 2S_{12})(p + 2q)/6\omega_0$ is the hydrostatic component of the frequency shift; $\Delta\Omega = \Omega_T - \Omega_L = \sigma S_{44} r/2\omega_0$ is the LO–TO splitting; S_{11}, S_{12}, and S_{44} are the components of the elastic constant tensor; and *p*, *q*, and *r* are the anharmonicity constants of germanium. According to the experimental data obtained in [16], the anharmonicity constants are as follows: $p = -1.47\omega_0^2$, $q = -1.93\omega_0^2$, and $r = -1.08\omega_0^2$. After substituting numerical values of all the parameters into expressions (1) and (2), we have

$$\Delta\Omega_T = \Omega_T - \omega_0 = -1.306\varepsilon\omega_0,$$

$$\Delta\Omega_L = \Omega_L - \omega_0 = -0.322\varepsilon\omega_0.$$

The strain ε is used as a fitting parameter.

The height of Ge islands is limited by $h = 3$ BL $= 3a_0$, which leads to a substantial change in the phonon spectrum. The spectrum of phonons with wave vectors **k** along the [111] direction is quantized according to the

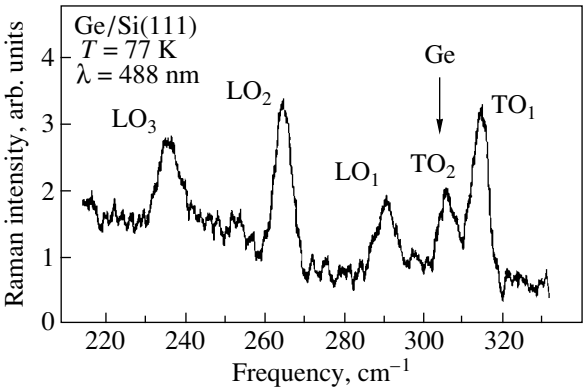

Fig. 4. Raman spectrum of optical phonons on the Si(111) surface with Ge nanoislands at a temperature of 77 K.

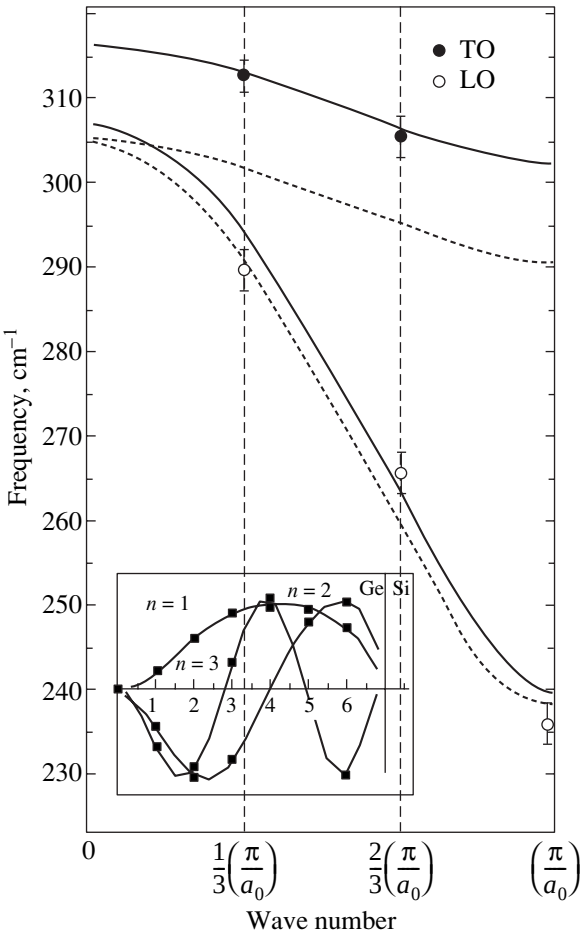

Fig. 5. Dispersion curves for optical phonons in germanium along the [111] direction. Dashed lines correspond to the results of calculations performed in [17]. Solid lines are the dispersion curves obtained with allowance made for the strain of germanium island. Circles indicate the optical-phonon frequencies measured in Ge quantum dots. The inset shows the dependences of the amplitude of atomic vibrations according to calculations within the model of a one-dimensional chain.

condition for the formation of a standing wave: $\mathbf{k}_n = (\pi/h)n$, where n is an integer. Consequently, there exist only three vibrational modes of TO and LO phonons (n = 1, 2, 3) in the Brillouin zone. The inset to Fig. 5 shows the vibration amplitudes of atoms (N) for three longitudinal optical modes (n = 1, 2, 3) calculated in terms of the model of a one-dimensional chain consisting of six atoms. Within this model, it is assumed that the amplitude of atomic vibrations is equal to zero at N = 7 (i.e., at the interface with Si) and that the first atom has a dangling bond (i.e., it is located on a free surface).

The dispersion curves for optical phonons of germanium in the first Brillouin zone in the [111] direction are depicted in Fig. 5. The circles indicate the experimental phonon frequencies that correspond to wave vectors $\mathbf{k}_n$ at n = 1, 2, and 3. The dashed lines are the dispersion curves calculated in [17] for optical phonons of bulk germanium in the [111] direction. The solid lines represent the dispersion curves calculated in [17] and shifted according to expressions (1) and (2). These shifts for TO and LO phonons are determined by the quantities $\Delta\Omega_T$ and $\Delta\Omega_L$. The strain ε was obtained from the best fit to the experimental frequencies. As a result, the strain was estimated as $\varepsilon = -0.029 \pm 0.003$. This value slightly differs from the strain of –0.04, which should correspond to the pseudomorphic growth of germanium on silicon and was observed in Ge quantum dots grown on the Si(100) surface [18].

4. CONCLUSIONS

Thus, the results obtained in this work can be summarized as follows. The wetting layer in the Ge/Si(111) system at germanium deposition rates of approximately 10^{-3} BL/min is formed through the island or multilayer growth mechanism. The Ge epitaxial growth at low rates and temperatures of 350–500°C provides the formation of arrays of Ge islands with a height of 3 BL and a density of 10^9–10^{12} cm^{-2} on the silicon surface until a continuous wetting layer is formed. The self-assembled growth of Ge nanoislands on the Si(111) surface is substantially affected by the following factors: the migration of Ge atoms from the lower terrace to the upper terrace on steps of the second type, the limitation of the Ge nanoisland height to three bilayers, and the ordering effect of the (7×7) surface structure. An increase in the rate of Ge surface diffusion upon formation of the (5×5) structure on the surface of the wetting layer leads to a crossover of the mechanism of Ge island growth at coverages of more than 3 BL. Smooth Ge nanowires whose width is a multiple of the size of the (7×7) unit cell and a height is 1 or 3 BL can be grown along steps of the second type. The Raman spectra of optical phonons on the Si(111) surface with Ge nanoislands contain a series of phonon lines associated with the quantization of the phonon spectrum along the [111] growth direction. The strain of Ge nanoislands is determined.

ACKNOWLEDGMENTS

This work was supported by the Russian Foundation for Basic Research (project nos. 01-02-16844-a, 03-02-16506-a) and the Ministry of Industry, Science, and Technology of the Russian Federation (state contract no. 40.012.1.1.1153).

REFERENCES

1. V. A. Markov, H. H. Cheng, Chih-ta Chia, *et al.*, Thin Solid Films **369**, 79 (2000).
2. O. P. Pchelyakov, Yu. B. Bolkhovityanov, A. V. Dvurechenskii, *et al.*, Thin Solid Films **367**, 75 (2000).
3. O. P. Pchelyakov, Yu. B. Bolkhovityanov, A. V. Dvurechenskiĭ, *et al.*, Fiz. Tekh. Poluprovodn. (St. Petersburg) **34** (11), 1281 (2000) [Semiconductors **34**, 1229 (2000)].
4. K. Brunner, Rep. Prog. Phys. **65**, 27 (2002).
5. U. Koehler, J. E. Demuth, and R. J. Hamers, J. Vac. Sci. Technol. A **7**, 2860 (1989).
6. U. Koehler, O. Jusko, G. Pietsch, *et al.*, Surf. Sci. **248**, 321 (1991).
7. B. Voigtlaender and A. Zinner, Surf. Sci. **351**, L233 (1996).
8. N. Motta, A. Sgarlata, R. Calarco, *et al.*, Surf. Sci. **406**, 254 (1998).
9. S. A. Teys and B. Z. Olshanetsky, Phys. Low-Dimens. Struct., Nos. 1–2, 37 (2002).
10. J. Tersoff, A. W. Denier van der Gon, and R. M. Tromp, Phys. Rev. Lett. **72** (2), 266 (1994).
11. Y. P. Zhang, L. Yan, S. S. Xie, *et al.*, Surf. Sci. **498**, L60 (2002).
12. B. Voigtlaender, Surf. Sci. Rep. **43**, 127 (2001).
13. J. Wei, X. S. Wang, J. L. Goldberg, *et al.*, Phys. Rev. Lett. **68**, 3885 (1992).
14. A. B. Talochkin and S. A. Teys, Pis'ma Zh. Éksp. Teor. Fiz. **75** (6), 314 (2002) [JETP Lett. **75**, 264 (2002)].
15. I. I. Novak, V. V. Baptizmanskiĭ, and L. V. Zhoga, Opt. Spektrosk. **43**, 252 (1977) [Opt. Spectrosc. **43**, 145 (1977)].
16. F. Cerdeira, C. J. Buchenauer, F. H. Pollak, and M. Cardona, Phys. Rev. B **5**, 580 (1972).
17. W. Weber, Phys. Rev. B **15**, 4789 (1977).
18. A. B. Talochkin, V. A. Markov, A. I. Nikiforov, and S. A. Teys, Pis'ma Zh. Éksp. Teor. Fiz. **70**, 279 (1999) [JETP Lett. **70**, 288 (1999)].

Translated by O. Borovik-Romanova

Physics of the Solid State, Vol. 46, No. 1, 2004, pp. 85–88. Translated from Fizika Tverdogo Tela, Vol. 46, No. 1, 2004, pp. 88–90.

PROCEEDINGS OF THE CONFERENCE DEDICATED TO O. V. LOSEV (1903–1942)

(Nizhni Novgorod, Russia, March 17–20, 2003)

Composition and Elastic Stresses in Multilayer Structures with $Si_{1-x}Ge_x$ Nanoislands

M. Ya. Valakh*, V. N. Dzhagan*, P. M. Lytvyn*, V. A. Yukhymchuk*, Z. F. Krasil'nik, A. V. Novikov**, and D. N. Lobanov****

** Institute of Semiconductor Physics, National Academy of Sciences of Ukraine, Kiev, 03028 Ukraine*

*** Institute of Microstructure Physics, Russian Academy of Sciences, Nizhni Novgorod, 603600 Russia*

e-mail: valakh@isp.kiev.ua

Abstract—The composition and mechanical stresses in $Si_{1-x}Ge_x$ nanoislands involved in multilayer and single-layer structures grown under the same conditions are determined using Raman spectroscopy. It is demonstrated that an increase in the content of silicon in the nanoislands contained in a multilayer structure does not enhance their relaxation (as compared to that in a single layer) due to the absence of a free surface. The experimental scattering spectrum of folded acoustic phonons contains bands with sufficiently small half-widths, which indicates high quality of the grown superlattices with nanoislands. © *2004 MAIK "Nauka/Interperiodica".*

1. INTRODUCTION

The majority of heterostructures exhibiting new electronic and optoelectronic properties are based on III–V semiconductors, which are widely used in modern electronics built on well-developed and relatively cheap silicon technology. For purposes of increasing the operating frequency of microcircuits, integrating their elements into technological processes, and improving the emission efficiency, new functional principles have been introduced into silicon electronics, for example, the use of quantum dots with a discrete energy spectrum [1–3]. One way to obtain arrays of quantum dots is the self-assembled growth of germanium nanoislands on a silicon substrate through the Stranski–Krastanov mechanism. The essence of this method is a crossover from the two-dimensional growth to the three-dimensional growth of nanoislands due to a decrease in the elastic energy of the system.

In this work, multilayer structures with $Si_{1-x}Ge_x$ nanoislands were studied by Raman spectroscopy and atomic-force microscopy (AFM) and the results obtained were compared with available data for similar single-layer structures.

2. SAMPLES AND EXPERIMENTAL TECHNIQUE

The structures were prepared by molecular-beam epitaxy of germanium on an Si(001) substrate with a 250-nm-thick buffer silicon layer preliminarily grown on it. A germanium layer with a thickness of 7.5 monolayers (ML) was deposited on the buffer at a temperature of 600°C, after which the islands formed were coated with a 26-nm-thick silicon layer. This procedure was repeated six times. Similar single-layer structures were grown for comparison. In the samples used in AFM measurements, the upper layer of islands was not coated with silicon. The Raman spectra were recorded on a T64000 Jobin Yvon spectrometer equipped with a CCD camera in the frequency range of optical vibrations of the $Si_{1-x}Ge_x$ solid solution, and the phonon spectra were measured on a DFS-24 spectrometer with a photomultiplier and a system of photon counting in the low-frequency range. In the latter case, the sample was under vacuum. An Ar^+ laser with a wavelength of 488 nm was used for excitation. The AFM investigations were performed on a Nanoscope III-a microscope operating in tapping mode.

3. RESULTS AND DISCUSSION

It is known that, in multilayer structures with quantum dots and a sufficiently thin spacer layer, the island growth is characterized by a vertical correlation due to the distribution of mechanical stresses in the spacer layer [3–5]. The content x and the elastic strain ε of nanoislands can be determined from the Raman data, as was shown in [6–8] for single-layer structures with self-assembled Ge/Si nanoislands. The frequency location of the bands in the Raman spectrum is related to the content x and elastic strain ε by the expressions [6]

$$\omega_{Ge-Ge} = 282.5 + 16x - 385\varepsilon, \quad (1)$$

$$\omega_{Ge-Si} = 400.4 + 14.2x - 575\varepsilon, \quad (2)$$

$$\omega_{Si-Si} = 520.5 - 62x - 815\varepsilon. \quad (3)$$

In order to determine the content x and elastic strain ε more correctly, it is necessary to estimate the effect exerted by other factors on the frequency location of the

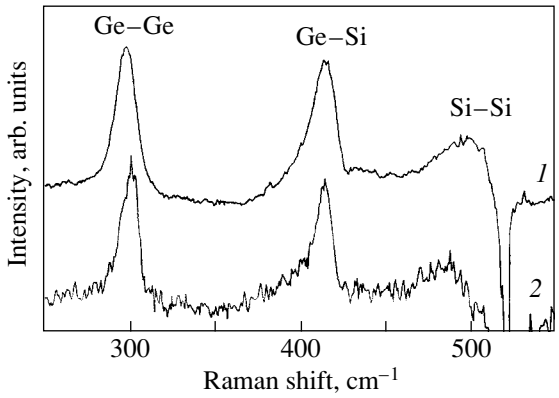

Fig. 1. Raman spectra of (*1*) multilayer and (*2*) single-layer structures with $Si_{1-x}Ge_x$ nanoislands. The contribution from the silicon substrate to the spectrum is subtracted.

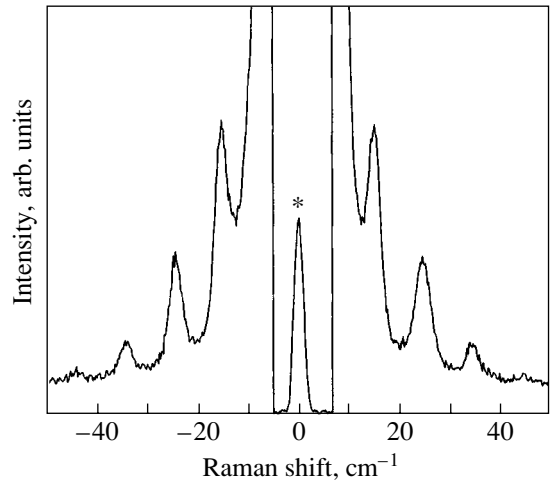

Fig. 2. Stokes and anti-Stokes parts of the Raman spectrum of folded acoustic phonons of a multilayer structure with $Si_{1-x}Ge_x$ nanoislands.

bands in the Raman spectrum. In our case, the effect of the spatial confinement of phonons on their frequencies can be disregarded because of the sufficiently large size of the islands. According to transmission electron microscopy, the height of the islands is equal to 5–6 nm and their lateral sizes are 50–70 nm. The contribution from the silicon substrate to the Raman spectrum of the single-layer structure can be subtracted. For multilayer structures, this problem is complicated, because both the substrate and all silicon spacer layers make a contribution to the Raman spectrum. The occurrence of elastic strains in these layers leads to a low-frequency shift of the ω_{Si-Si} vibration band with respect to its location in the spectrum for an unstrained silicon substrate. However, this shift is small compared to the shift caused by elastic strains in real solid solutions of islands with composition $Si_{1-x}Ge_x$.

As is known [9], the dependence of the frequency location of the Ge–Si vibration band on the content x is linear only in the range $0 \le x \le 0.4$. In this connection, we approximated this dependence for the unstrained SiGe solid solution by the second-degree polynomial in the range $0.4 \le x \le 1$. Taking into account the linear dependence of the frequency of this band on the elastic strain ε, we obtain the following relationship:

$$\omega_{Ge-Si} = 387 + 81x - 78x^2 - 575\varepsilon. \quad (4)$$

After substituting the experimental frequencies of the Ge–Ge, Ge–Si, and Si–Si vibrations (298.8, 416, and 496.5 cm^{-1}, respectively) (Fig. 1, curve *1*) and graphically solving the system of equations (1)–(4), as was done by Groenen *et al.* [6], we found $x = 0.6$ and $\varepsilon = -0.015$. A close value can be obtained from the ratio of the integrated intensities of the bands attributed to the Ge–Ge and Ge–Si vibrations: $I_{Ge-Ge}/I_{Ge-Si} = x/2(1-x)$.

Except for the $Si_{1-x}Ge_x$ nanoislands, the contribution to the Raman spectrum can be made by the Ge–Ge vibrations in a thin wetting germanium layer and the Si–Ge vibrations at the interface between this layer and the silicon spacer layer [10]. However, according to the selection rules [11], scattering by a two-dimensional wetting layer in the scattering geometry $001(100, 100)00\bar{1}$ used in our case is forbidden; moreover, the thin transient SiGe layer formed at a growth temperature of 600°C substantially decreases the probability of exciting interfacial Si–Ge vibration modes.

In order to evaluate how the silicon spacer layer affects the parameters of the nanoislands, we studied a single-layer structure with $Si_{1-x}Ge_x$ nanoislands grown without a Si-cap layer. From analyzing the Raman spectra of this structure (Fig. 1, curve *2*), we obtained $x = 0.75$ and $\varepsilon = -0.013$. The higher content of silicon in nanoislands of the multilayer structure is explained by additional diffusion of silicon atoms from spacer layers. This should result in a more efficient relaxation of elastic stresses. However, the nanoislands involved in multilayer structures are surrounded by silicon on all sides and, consequently, the relaxation is retarded.

The low-frequency Raman spectrum of the multilayer structure under investigation exhibits a series of clearly defined equidistant bands (Fig. 2). For two-dimensional flat superlattices, these bands are associated with scattering by folded acoustic phonons that arise from the artificial periodicity in the growth direction [1, 12, 13]. As far back as 1956, Rytov [14] proposed a theoretical model for describing the phonon spectrum of two-dimensional superlattices. More recently, Milekhin *et al.* [15] used this model to advantage in the case of superlattices with quantum dots. Cazayous *et al.* [16, 17] proposed the mechanism responsible for Raman scattering in superlattices with quantum dots irrespective of the number of layers in the superlattices. According to their model, the low-frequency bands are observed upon interference of acoustic phonons with a set of localized electron states. This

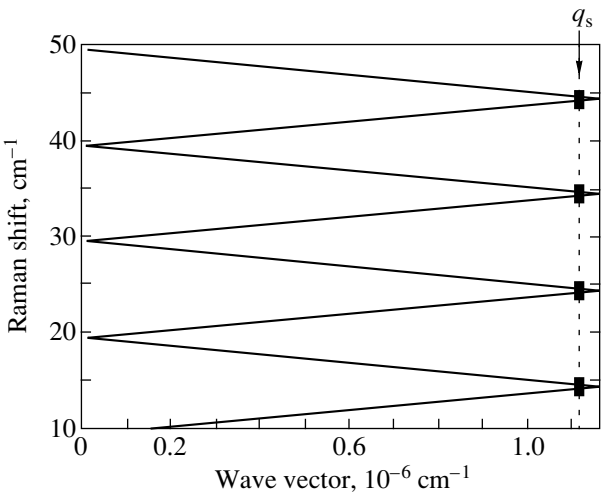

Fig. 3. Theoretical dispersion curve for a multilayer structure with $Si_{1-x}Ge_x$ nanoislands.

interference occurs with the participation of phonons of the whole Brillouin zone due to the breaking of translational symmetry in the layers with nanoislands. The interference model allows one to determine not only the frequency locations of the peaks but also the fine structure of the lines and their intensity. In our calculations, we used the Rytov theory, because, as was demonstrated in [17], the frequency locations of the bands calculated in the framework of the interference model and the Rytov theory coincide for the structures containing no less than five to six layers of quantum dots.

It is known that the resultant dispersion curve for a superlattice can be obtained by folding the initial branch for the bulk material into a minizone with $q_{max} = \pi/d$, where d is the lattice constant. In the case when a periodic structure scatters laser radiation with a wave vector q_s, the Raman spectrum exhibits doublets, whose positions correspond to the points marked on the dispersion curve depicted in Fig. 3. According to the selection rules, this superlattice is characterized only by longitudinal acoustic phonons. The table presents the experimental and calculated frequencies of these phonons for the wave vector $q_s = 4\pi n_\lambda/\lambda = 1.14 \times 10^6$ cm^{-1}, where λ is the wavelength of exciting laser radiation and n_λ is the mean value of the refractive index of this structure ($n_\lambda = 4.33$ for $\lambda = 488$ nm). For our structure, the acoustic impedances of the layers differ insignificantly and, hence, the frequencies of the doublets can be calculated by a simplified formula [13]:

$$\omega = V_{SL}\left(\frac{2\pi}{d}\right)m \pm V_{SL}q_s,$$

$$V_{SL} = d\left(\frac{d_1^2}{V_1^2} + \frac{d_2^2}{V_2^2} + \left(R + \frac{1}{R}\right)\frac{d_1 d_2}{V_1 V_2}\right)^{-1/2},$$

$$R = \frac{V_1\rho_1}{V_2\rho_2},$$

where ρ_1 and ρ_2 are the densities, d_1 and d_2 are the thicknesses of the layers, V_1 and V_2 are the velocities of sound in the layers, and ω is the frequency of the phonon.

The Raman spectra were calculated as a superposition of two groups of phonons propagating in the growth direction through the islands and only wetting layers, respectively. It can be seen from the table that the theoretical frequencies of the acoustic phonons agree well with the experimental results.

Experimental and theoretically calculated frequencies of folded acoustic phonons (in cm^{-1}) in the Raman spectrum

	m							
	+1	–2	+2	–3	+3	–4	+4	–5
Theory	14.7	15.1	24.7	24.9	34.6	35	44.6	45
Experiment	15		24.8		34.6		44.5	

4. CONCLUSIONS

Thus, we investigated the influence of silicon spacer layers on the composition and elastic stresses in $Si_{1-x}Ge_x$ nanoislands during the growth of multilayer island structures. The above analysis of the Raman spectra demonstrated that the silicon content in a multilayer structure with nanoislands increases as compared to that in a single layer of nanoislands, whereas the residual elastic strain remains nearly unchanged. The increase in the content of silicon in the nanoislands is favorable for relaxation of mechanical stresses, but the absence of a free surface in the nanoislands does not permit them to relax entirely. The experimental scattering spectrum of folded acoustic phonons contains bands with sufficiently small half-widths, which indicates that the grown superlattices with nanoislands are of high quality. The theoretically calculated frequencies of these bands agree well with the experimental results.

ACKNOWLEDGMENTS

This work was supported by the Ukrainian–Russian program “Nanophysics” and the International Association of Assistance for the promotion of cooperation with scientists from the New Independent States of the former Soviet Union, project no. INTAS 01-444.

REFERENCES

1. V. V. Mitin, V. A. Kochelap, and M. A. Strocio, *Quantum Heterostructures: Microelectronics and Optoelectronics* (Cambridge Univ. Press, Cambridge, 1999).

2. O. P. Pchelyakov, Yu. B. Bolkhovitnyakov, A. V. Dvurechenskiĭ, *et al.*, Fiz. Tekh. Poluprovodn. (St. Petersburg) **34** (11), 1281 (2000) [Semiconductors **34**, 1229 (2000)].
3. C. Teichert, Phys. Rep. **365**, 335 (2002).
4. D. A. Tenne, V. A. Haisler, A. I. Toropov, *et al.*, Phys. Rev. B **61** (20), 13785 (2000).
5. O. G. Schmidt and K. Eberl, Phys. Rev. B **61** (20), 13721 (2000).
6. J. Groenen, R. Carles, S. Christiansen, *et al.*, Appl. Phys. Lett. **71** (26), 3856 (1997).
7. Z. F. Krasil'nik, P. M. Lytvyn, D. N. Lobanov, *et al.*, Nanotechnology **13**, 81 (2002).
8. A. V. Novikov, B. A. Andreev, N. V. Vostokov, *et al.*, Mater. Sci. Eng. B **89**, 62 (2002).
9. J. C. Tsang, P. M. Mooney, F. Dacol, and J. O. Chu, J. Appl. Phys. **75** (12), 8098 (1994).
10. S. De Gironcoli, E. Molinari, R. Schorer, and R. Abstreiter, Phys. Rev. B **48** (12), 8959 (1993).
11. R. Schorer, G. Abstreiter, S. de Gironcoli, *et al.*, Phys. Rev. B **49** (8), 5406 (1994).
12. C. Colvard, T. A. Gant, M. V. Klein, *et al.*, Phys. Rev. B **31** (4), 2080 (1985).
13. A. B. Talochkin, V. A. Markov, Yu. A. Pusep, *et al.*, Superlattices Microstruct. **10** (2), 179 (1991).
14. S. M. Rytov, Akust. Zh. **2** (1), 71 (1956) [Sov. Phys. Acoust. **2**, 67 (1956)].
15. A. Milekhin, N. P. Stepina, A. I. Yakimov, *et al.*, Eur. Phys. J. B **16**, 355 (2000).
16. M. Cazayous, J. Groenen, J. R. Huntzinger, *et al.*, Phys. Rev. B **64**, 033306 (2001).
17. M. Cazayous, J. Groenen, A. Zwick, *et al.*, Phys. Rev. B **66**, 195320 (2002).

Translated by O. Moskalev

Physics of the Solid State, Vol. 46, No. 1, 2004, pp. 89–91. Translated from Fizika Tverdogo Tela, Vol. 46, No. 1, 2004, pp. 91–93.

PROCEEDINGS OF THE CONFERENCE DEDICATED TO O. V. LOSEV (1903–1942)

(Nizhni Novgorod, Russia, March 17–20, 2003)

Self-Assembling of Ge Quantum Dots in the CaF_2/Ge/CaF_2/Si Heteroepitaxial System and the Development of Tunnel-Resonance Diode on Its Basis

L. V. Sokolov[1, 2], A. S. Deryabin[1], A. I. Yakimov[1], O. P. Pchelyakov[1], and A. V. Dvurechenskiĭ[1]

[1] *Institute of Semiconductor Physics, Siberian Division, Russian Academy of Sciences, pr. Akademika Lavrent'eva 13, Novosibirsk, 630090 Russia*

[2] *Tomsk State University, Tomsk, 634050 Russia*

e-mail: sokolov@isp.nsc.ru

Abstract—A CaF_2/Ge/CaF_2/Si(111) heteroepitaxial structure with Ge quantum dots was grown by molecular-beam epitaxy. A negative differential conductivity and conductivity oscillations caused by resonant hole tunneling were observed at room temperature. The energy spacing between the levels in quantum dots, as determined from the oscillation period, is 40–50 meV depending on the Ge dot size. © *2004 MAIK "Nauka/Interperiodica".*

1. INTRODUCTION

Low-dimensional objects, such as quantum dots (QD), which make it possible to study single-electron and quantum effects, continue to attract the attention of scientists. The smallest sizes, most attractive from the viewpoint of physical effect detection, have been achieved for QDs grown by self-assembling. To this end, Ge/Si and InAs/GaAs semiconductor heterojunctions are most commonly used. Nanometer-sized objects have also been grown in dielectric hosts, e.g., Si–CaF_2 [1] and Si–SiO_2 [2]. In the former case, the nanoobjects were thin silicon strips grown along atomic steps on the CaF_2 film surface, and in the latter, the nanoobjects were produced without using epitaxial technology.

It seems promising to employ the Ge/CaF_2 heterojunction for producing QDs [3]. CaF_2 is characterized by a very wide band gap (~12 eV, which suggests growth of deep quantum wells) and can be rather easily grown by molecular-beam epitaxy (MBE) on the Si(111) surface. This makes it possible to use the CaF_2/Si(111) heterojunction as a substrate. CaF_2 grown on a Si surface has cubic crystal structure and a lattice parameter close to that of silicon. For this reason, it can be assumed that, as in the Ge/Si heterostructure, Ge film epitaxy on the CaF_2/Si heterostructure will be accompanied by self-assembling of Ge nanoislands.

2. EXPERIMENTAL

As substrates of CaF_2/Si heterostructures, p^+-type Si(111) wafers were used. After conventional chemical processing with deposition of a thin buffer oxide layer, the wafers were placed into an ultrahigh-vacuum chamber of an MBE setup, where the substrate surface was finally cleaned and a heterostructure was grown on it. Ge and CaF_2 molecular beams were generated by crucible sources; the CaF_2 beam was formed through sublimation of a bulk calcium fluorite crystal from a graphite crucible. The typical Ge and CaF_2 growth rates were ~0.16 and ~0.25 nm/s, respectively. During substrate preparation and epitaxial growth of the Ge and CaF_2 films, the surface structure was monitored by using high-energy (~40 keV) electron diffraction (HEED) in the reflection geometry. The substrate was heated by radiation from a tantalum strip heater.

After Si surface cleaning, HEED showed a distinct diffraction pattern from the Si(111) 7×7 superstructure. This superstructure was changed by the (1×1) structure immediately after deposition of the first CaF_2 monolayer. The typical surface relief of a 10-nm-thick CaF_2 film is shown in Fig. 1. We can see that flat pyramids consisting of atomically smooth terraces separated by monatomic steps arise on the CaF_2 film surface. It can also be concluded that plastic relaxation of mismatch stresses begins even at this film thickness. This is indicated by the set of straight lines representing traces of glide dislocations. Their density is not high; therefore, the process of mechanical stress relaxation is at its initial stage.

The transverse electric transport in the produced structures can be studied if the layers containing Ge islands are tunnel-transparent for carriers. For this reason, we investigated ~2-nm-thick CaF_2 films. It was

1063-7834/04/4601-0089$26.00 © 2004 MAIK "Nauka/Interperiodica"

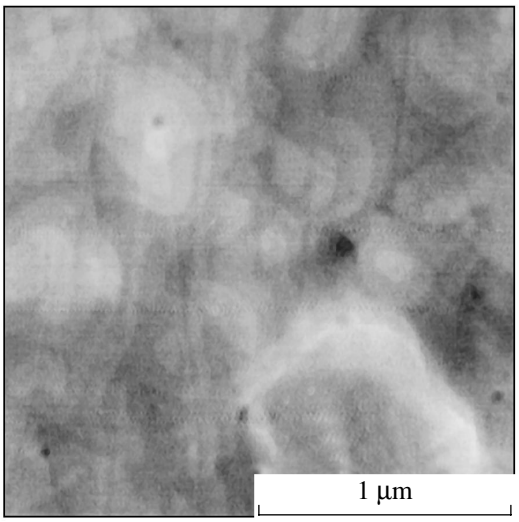

Fig. 1. Atomic-force microscopic pattern of the surface relief of a CaF_2 epitaxial film.

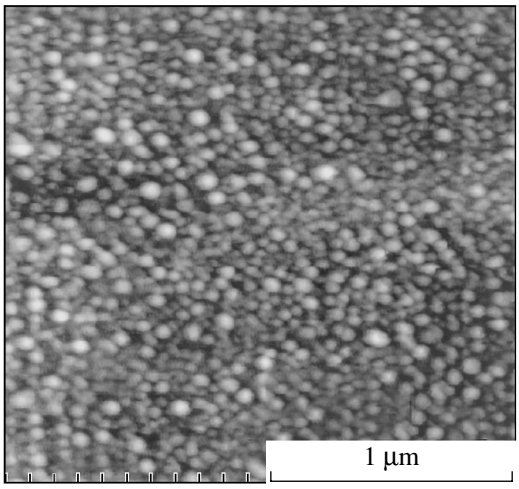

Fig. 2. Atomic-force microscopic pattern of a $Ge/CaF_2/Si$ heterostructure with Ge islands.

ascertained that CaF_2 films had better electric characteristics if they were grown in two stages. Films were grown at a substrate temperature of ~520°C, and then the samples were annealed at 700–750°C for an hour. Due to this procedure, the fluoride film resistivity increased by three orders of magnitude up to $\sim 10^9\ \Omega$ cm.

After a thin fluoride film was grown, an ensemble of Ge islands formed on its surface. The substrate temperature in this process was 430–490°C. The HEED data showed that a Ge film has a smooth surface at the initial growth stage; islands arise at an average thickness of ~3 nm. Their formation causes a sharp change in the HEED pattern. Point reflections characteristic of three-dimensional diffraction from islands appear instead of the extended diffraction strands typical of a smooth film surface. Atomic-force microscopy of the surface of such heterostructures also showed the presence of islands (Fig. 2).

After the Ge island formation, a second, 2-nm-thick, CaF_2 film was grown. Thereafter, the sample was annealed again at 700–750°C. At the final stage, a 20-nm-thick p^+-type Ge layer was grown at the heterostructure surface to provide an ohmic contact for electric measurements.

Electric measurements were carried out on mesas (see Fig. 3) 0.7×0.7 mm in size produced by plasma-chemical etching in the CF_4 etchant. Gold areas deposited onto the sample surface through vacuum evaporation served as a mask for etching and as top contacts.

3. RESULTS OF ELECTRICAL MEASUREMENTS

The differential conductance $G = dI/dV$ of the grown two-barrier structures was measured at room temperature using the conventional two-point probe technique. The applied voltage amplitude was ~1 mV at a frequency of 15 Hz. Figure 4 shows the measured tunneling current versus the voltage for two samples produced under various conditions of Ge island growth. Both curves feature regions of zero conductivity and quasi-periodic oscillations with periods $\Delta V \approx 100$ and 80 mV for samples 131 and 120, respectively. Regions of negative differential conductivity are also clearly seen. The structure of oscillations was fully reproduced in multiple bias-voltage sweeps. At the same time, oscillations were entirely absent for similar samples containing no Ge QDs.

Based on these data, it can be assumed that the conductance oscillations observed are most likely caused by hole tunneling through the energy states in Ge islands, rather than by the single-particle charge effects.

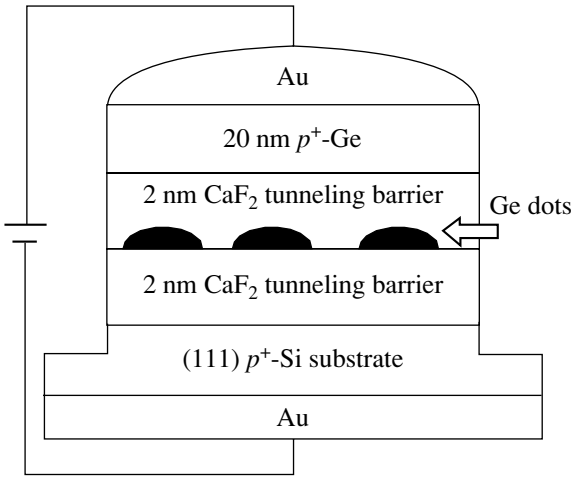

Fig. 3. Structure of a tunnel-resonant diode based on the $CaF_2/Ge/CaF_2/Si$ heterostructure (schematic).

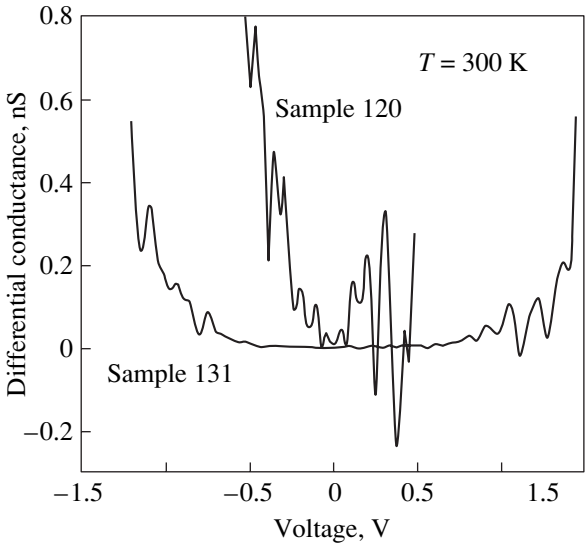

Fig. 4. Bias-voltage dependences of the differential conductance.

Certainly, the charge effects play an important role in tunneling experiments, where a moving charge carrier may be delayed in an island. This effect is possible in highly asymmetric tunneling junctions, in which the transmittance of the second (thicker) barrier is much lower than that of the first (thinner) barrier [4]. Obviously, this is not the case for the two-barrier structures under study, in which both barriers have the same thickness.

In the case of a symmetric structure, the distance between the conductance peaks should be equal to the double energy gap between the levels of QD hole states. This energy gap was 50 and 40 meV in samples 131 and 120, respectively. The difference is caused by the different growth conditions and, hence, different QD sizes. The Ge film in sample 120 was grown at 490°C, while that in sample 131 was grown at 430°C. This decrease in temperature resulted in smaller island sizes and, hence, in an increased energy gap between the quantum levels. By analogy with self-assembling Ge nanoislands on the Si(001) surface [5], it can be assumed that a distance of 40–50 meV between the energy levels corresponds to Ge islands 10–15 nm in size on the CaF_2/Si(111) surface.

In conclusion, it should be noted that the CaF_2/Ge/CaF_2/Si(111) heterostructures with self-assembling Ge QDs may be used as a basis for developing tunnel-resonant diodes operating at room temperature.

ACKNOWLEDGMENTS

This study was supported by the Russian Foundation for Basic Research, project no. 00-02-17900.

REFERENCES

1. V. Ioannou-Sougleridis, V. Tsakiri, A. G. Nassiopoulov, *et al.*, Phys. Status Solidi A **165**, 97 (1998).
2. Y. Inoue and A. Tanaka, J. Appl. Phys. **86**, 3199 (1999).
3. A. I. Yakimov, A. S. Derjabin, L. V. Sokolov, *et al.*, Appl. Phys. Lett. **81** (3), 499 (2002).
4. U. Meirav and E. B. Foxman, Semicond. Sci. Technol. **10**, 255 (1995).
5. A. V. Dvurechenskii, A. V. Nenashev, and A. I. Yakimov, Nanotechnology **13**, 75 (2002).

Translated by A. Kazantsev

Physics of the Solid State, Vol. 46, No. 1, 2004, pp. 92–96. Translated from Fizika Tverdogo Tela, Vol. 46, No. 1, 2004, pp. 94–97.

PROCEEDINGS OF THE CONFERENCE DEDICATED TO O. V. LOSEV (1903–1942)

(Nizhni Novgorod, Russia, March 17–20, 2003)

Resonant Raman Scattering by Strained and Relaxed Germanium Quantum Dots

A. G. Milekhin*, A. I. Nikiforov*, M. Yu. Ladanov*, O. P. Pchelyakov*, S. Schulze, and D. R. T. Zahn****

** Institute of Semiconductor Physics, Siberian Division, Russian Academy of Sciences, pr. Akademika Lavrent'eva 13, Novosibirsk, 630090 Russia*

e-mail: milekhin@thermo.isp.nsc.ru

*** Institut für Physik, Technische Universität Chemnitz, Chemnitz, D-09107 Germany*

Abstract—This paper reports on the results of resonant Raman scattering investigations of the fundamental vibrations in Ge/Si structures with strained and relaxed germanium quantum dots. Self-assembled strained Ge/Si quantum dots are grown by molecular-beam epitaxy on Si(001) substrates. An ultrathin SiO_2 layer is grown prior to the deposition of a germanium layer with the aim of forming relaxed germanium quantum dots. The use of resonant Raman scattering (selective with respect to quantum dot size) made it possible to assign unambiguously the line observed in the vicinity of 300 cm^{-1} to optical phonons confined in relaxed germanium quantum dots. The influence of confinement effects and mechanical stresses on the vibrational spectra of the structures with germanium quantum dots is analyzed. © *2004 MAIK "Nauka/Interperiodica".*

1. INTRODUCTION

Three-dimensional confinement of charge carriers in quantum dots and, as a consequence, the atomic-like electron spectrum of these structures are responsible for their electronic and optical properties, which differ substantially from those of bulk materials. Owing to the great variety of interesting properties revealed in these objects during numerous experiments, they are very promising materials for use in the design of microelectronic and optoelectronic devices with improved characteristics. Multilayer nanostructures, such as Ge/Si and Ge/SiO_2, are of special interest due to their possible application in various devices and integration with modern silicon technology. Among the large number of techniques devised for preparing structures with quantum dots, the most efficient method is the self-assembled growth of nanostructures in the course of molecular-beam epitaxy. This approach is based on the Stranski–Krastanov growth mechanism, according to which the deposition of a material whose lattice parameter differs significantly from that of the substrate leads to the formation of an array of strained nanoislands. In recent years, self-assembled growth has been used to produce relaxed quantum dots. It has been found that, for the Ge/Si system, the deposition of a nanometer-thick intermediate layer of silicon oxide prior to the epitaxial growth of the germanium layer results in the formation of relaxed germanium quantum dots with a size of less than 7 nm [1]. As has been shown recently, Raman scattering spectroscopy is a nondestructive method providing information on the structural parameters of quantum dots (dispersion of sizes and compositions of quantum dots, built-in mechanical stresses, etc.).

In this work, the vibrational spectra of self-assembled structures with strained and relaxed germanium quantum dots were studied using resonant Raman scattering.

2. SAMPLES AND EXPERIMENTAL TECHNIQUE

The structures with germanium quantum dots were prepared by molecular-beam epitaxy of germanium and silicon layers on Si(001) substrates. The Ge/Si structures with strained germanium quantum dots were grown through the Stranski–Krastanov method. The growth temperatures of the silicon layer prior to and after the deposition of the germanium layer were equal to 800 and 500°C, respectively. The layers of germanium quantum dots were grown at a temperature of 300°C. The thickness and the structure of the films grown were controlled using reflection high-energy electron diffraction (RHEED) patterns. The samples used in the measurements consisted of ten pairs of germanium and silicon layers with nominal thicknesses d_{Ge} = 1.4 nm and d_{Si} = 37 nm (in what follows, the nominal thickness of a layer will be referred to as the thickness). As was shown in our previous work [2], the mixing of silicon and germanium atoms for these thicknesses of the layers is insignificant.

The structures with relaxed germanium quantum dots were grown at a substrate temperature of 600°C on a silicon oxide layer. This layer was preliminarily formed on the silicon substrate immediately in a growth

1063-7834/04/4601-0092$26.00 © 2004 MAIK "Nauka/Interperiodica"

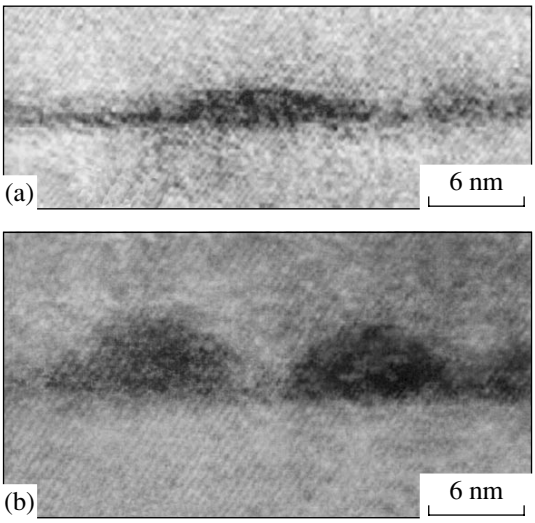

Fig. 1. HRTEM images of the transverse sections of the samples: (a) layer of strained Ge/Si quantum dots and (b) layer of relaxed Ge quantum dots.

chamber at a temperature of 500°C and an oxygen pressure of 2×10^{-4} Pa. For our experiments, we prepared two samples with germanium layer thicknesses of 1 and 2 nm. In order to prevent oxidation of the quantum dots, the sample surface was coated with a 10-nm-thick layer of amorphous silicon.

The experiments on Raman scattering were carried out in the geometries $z(x, x)\bar{z}$ and $z(x, y)\bar{z}$, where the x, y, and z axes are oriented along the [100], [010], and [001] crystallographic directions, respectively. The excitation was provided by Ar^+, Kr^+, and He–Ne lasers with lasing lines in the wavelength range 676.4–457.9 nm (1.83–2.71 eV). The light scattered was recorded in a backward scattering geometry with the use of a Dilor 800-XY triple monochromator equipped with a CCD camera for multichannel detection. The spectral resolution was 1.5 cm^{-1}.

3. RESULTS AND DISCUSSION

The structural parameters of the germanium quantum dots were determined from high-resolution transmission electron microscope (HRTEM) images of the transverse sections of the samples. Figure 1 displays the atomically resolved images of the transverse sections of the samples containing strained and relaxed quantum dots. According to the HRTEM data, the Ge/Si quantum dots are typical hut clusters whose base and height are equal to 15 and 1.5–2 nm, respectively. The density of Ge/Si quantum dots amounts to 3×10^{11} cm^{-2}, and the homogeneity is 20%. The germanium quantum dots grown on the SiO_2 surface have a hemisphere-like shape with a base ranging from 4 to 6 nm and a height from 3 to 4 nm. The density of germanium quantum dots is approximately equal to 2×10^{12} cm^{-2}. An analysis of the HRTEM data revealed that large-sized (100–200 nm) germanium islands with a density of 7.3×10^7 cm^{-2} are formed in addition to the germanium quantum dots.

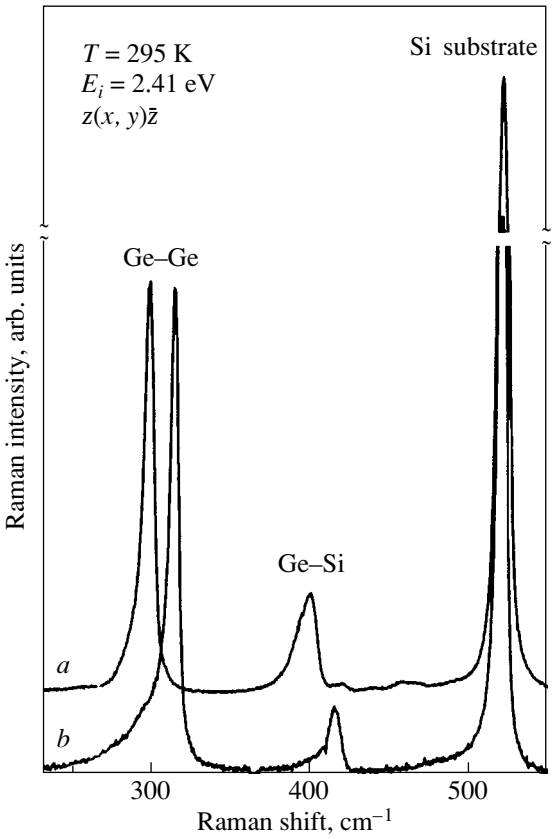

Fig. 2. Raman spectra of the structures with germanium quantum dots grown on (*a*) a thin SiO_2 layer and (*b*) an Si layer.

Figure 2 shows the Raman spectra of relaxed and strained germanium quantum dots. The Raman spectrum of the structures with relaxed germanium quantum dots exhibits an intense peak at a frequency of 297 cm^{-1}, which is attributed to Raman scattering by optical phonons confined in quantum dots. In the Raman spectrum of the Ge/Se structures, the Raman scattering line is observed at a frequency of 315 cm^{-1} corresponding to the frequency of longitudinal optical (LO) phonons in pseudomorphic germanium quantum dots [3]. The spectral features revealed in the vicinity of 400 and 520 cm^{-1} are associated with the Ge–Si vibration modes and optical phonons in the silicon substrate due to light scattering, respectively.

As it has been already noted in the literature, particularly by Kolobov [4], the Raman spectra of single-crystal Si(001) exhibit a peak in the vicinity of 300 cm^{-1} due to second-order Raman scattering by transverse acoustic phonons at the X and (or) Σ points of the Brillouin zone. This can lead to erroneous interpretation of

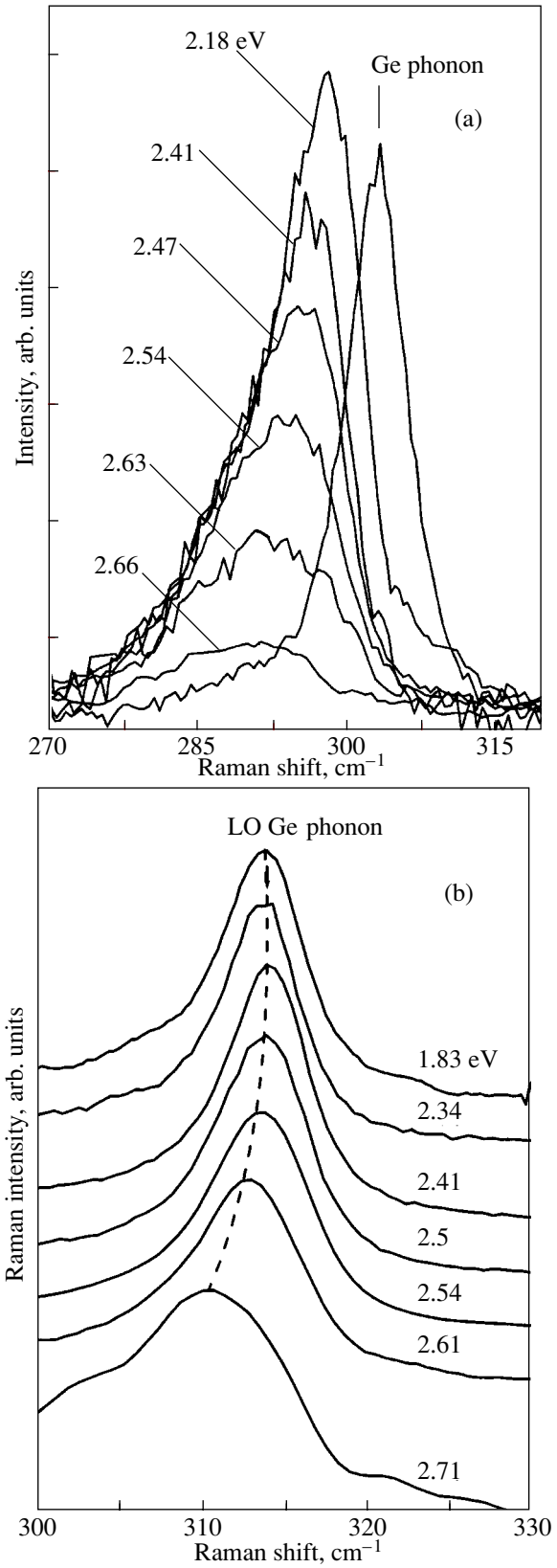

Fig. 3. Raman spectra of (a) relaxed and (b) strained structures with germanium quantum dots measured in the scattering geometry $z(x, y)\bar{z}$ at different excitation energies. The thickness of the germanium layer is 1 nm. The vertical solid line indicates the frequency position of the line assigned to optical phonons in bulk germanium.

the Raman spectra of the Ge/Si nanostructures with relaxed germanium quantum dots. Moreover, it is necessary to distinguish between the influence of mechanical stresses arising in the structures with strained germanium quantum dots and the influence of confinement effects of the phonons on the frequency position of the line in the spectrum of Raman light scattering by phonons in germanium quantum dots. The confinement of phonons leads to a low-frequency shift in the position of the line attributed to optical phonons in the Raman spectrum of germanium quantum dots with respect to its position in the spectrum of the bulk germanium, whereas the mechanical stresses arising in the quantum dots bring about a high-frequency shift. One possible way to separate the contributions to Raman scattering from the germanium quantum dots and the silicon substrate, to determine the mechanical stresses in quantum dots, and to elucidate the role played by the confinement effect in Raman light scattering by phonons is to analyze the spectra of resonant Raman scattering in the materials under investigation.

Raman spectra measured for different excitation energies in the scattering geometry $z(x, y)\bar{z}$ are shown in Fig. 3. It can be seen from Fig. 3 that, as the laser excitation energy increases, the line associated with optical phonons confined in the germanium quantum dots shifts toward the low-frequency range and becomes increasingly broader. This shift cannot be explained by the changes in the strained state in quantum dots of different sizes, because the magnitude of mechanical stresses does not depend on the quantum dot size [5]. The contribution of the mechanical stresses can be excluded completely in the experiments on Raman scattering under resonance conditions for structures with relaxed quantum dots.

Figure 4 shows the dependences of the Raman intensity and the frequency of LO phonons in germanium quantum dots on the excitation energy obtained from the data presented in Fig. 3. An analysis of the dependences of the intensity and the frequency position of the Raman scattering line in the spectrum on the excitation energy allows us to draw an unambiguous conclusion regarding the nature of the Raman scattering peak. The frequency position of the line associated with optical phonons (315 cm^{-1}) that are confined in hut clusters under nonresonance conditions (1.83 eV) corresponds to the pseudomorphic state of germanium, whereas the frequency of optical phonons in relaxed germanium quantum dots (300 cm^{-1}) coincides with the frequency of optical phonons in the bulk germanium. The frequency position of the line attributed to optical phonons confined in the germanium quantum dots shifts toward the low-frequency range with an increase in the excitation energy from 2.5 to 2.7 eV. For structures with strained and relaxed germanium quantum dots, these shifts are equal to 4–5 and 10 cm^{-1}, respectively, which suggests a size distribution of the quantum dots.

The dependence of the Raman intensity on the excitation energy exhibits a maximum in the range 2.2–2.4 eV. The considerable broadening of the resonance peak (0.4 eV) can be explained by the fact that there is a contribution from several resonances. The highest Raman intensity observed for relaxed quantum dots at an excitation energy of 2.35 eV (with a germanium layer thickness of 1 nm) corresponds to the E_0 resonance in germanium quantum dots. The energy of the E_0 resonance is equal to 0.9 eV for bulk germanium and reaches 2.5 eV for germanium quantum dots due to the confinement effect [6]. For a greater thickness of the germanium layer (2 nm), the maximum shifts toward the high-energy range (2.42 eV), which indicates the formation of germanium quantum dots of a smaller size. The specific feature observed at an energy of 2.2 eV is most likely caused by the E_1 transition in relaxed quantum dots.

For strained germanium quantum dots, the maximum in the dependence of the Raman intensity on the excitation energy is close to the resonance at an energy of 2.34 eV observed by Kwok *et al.* [7]. This maximum is associated with the E_1 transition. Under biaxial compressive stresses, the energy of the E_1 transition increases by 0.16 eV as compared to that for the bulk material (2.23 eV). The E_0 resonances in the wetting germanium layer (2.0–2.2 eV) and in the germanium quantum dots (2.4–2.6 eV) can also contribute to the resonant Raman scattering, which results in broadening of the spectral feature.

For small-sized quantum dots, in which the electronic states possess a higher energy, the Raman intensity increases after the laser excitation energy reaches the value corresponding to the E_0 resonance. Since the quantum dots are characterized by a size distribution, it is most probable that, under nonresonance conditions, it is these large-sized quantum dots (for which the confinement effect is negligible) that make a dominant contribution to Raman scattering. As the excitation energy increases above 2.3 eV, the small-sized quantum dots are involved in the Raman scattering. For these quantum dots, the confinement effect of optical phonons is rather significant and manifests itself in a decrease in the frequency of optical phonons observed in the Raman spectra. For relaxed quantum dots, this shift exceeds the value characteristic of structures with strained quantum dots, which indicates a smaller size of relaxed quantum dots.

From analyzing the frequencies of the optical phonons, we can determine the mean size of germanium quantum dots that contribute to the Raman scattering. As was shown by Talochkin *et al.* [6], the optical phonons confined in germanium quantum dots undergo elastic reflection at the heteroboundaries between the Ge/Si faces and the base of pyramidal quantum dots forming a cavity. From the standard dispersion relation for optical phonons in germanium quantum dots, we can obtain the wave vector of the optical phonons confined in this cavity: $q = (0.25 \pm 0.05)/a$. The first optical mode localized in the germanium quantum dots satisfies the equation $2h\cos\alpha = \pi/q$. Here, h and α are the quantum dot height and the angle between the base and the face of the pyramid, respectively. The quantum dot height, which is determined from this expression, is equal to 0.9 ± 0.2 nm. Therefore, the germanium quantum dots involved in Raman scattering at an energy of 2.71 eV have a height of 0.7 nm and a base of 9 nm.

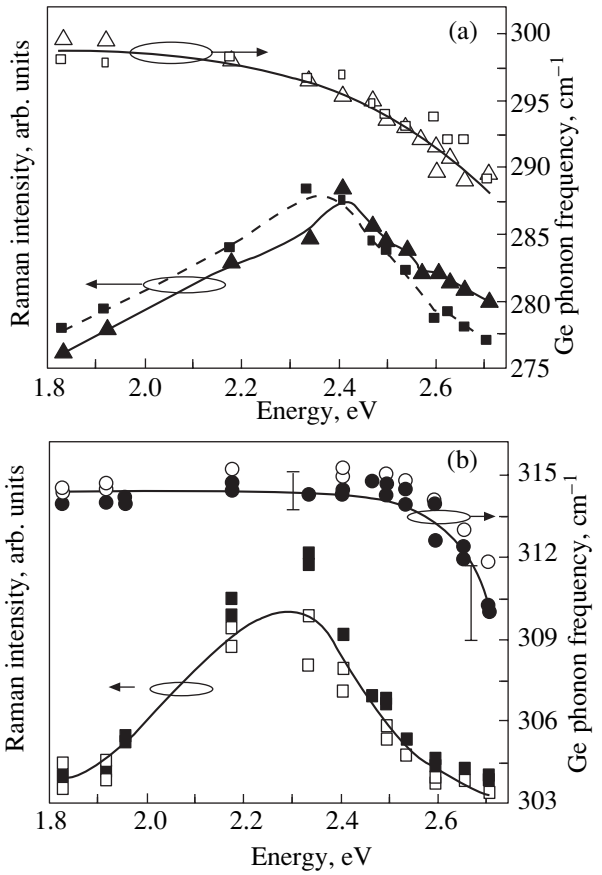

Fig. 4. Dependences of the Raman intensity and the frequency of optical phonons in germanium quantum dots on the excitation energy: (a) structures containing germanium quantum dots grown on a thin SiO_2 layer with germanium layer thicknesses of 1 nm (squares) and 2 nm (triangles) [Raman measurements are performed in the scattering geometry $z(x, y)\bar{z}$], and (b) Ge/Si structures measured in the scattering geometries $z(x, y)\bar{z}$ (open symbols) and $z(x, x)\bar{z}$ (closed symbols).

The mean size of relaxed quantum dots contributing to the Raman scattering was estimated under the assumption that the quantum dots are spherical in shape. The phenomenological model proposed by Campbell and Fauchet [8] was also used to calculate the spectrum of Raman scattering by spherical quantum dots of different sizes in the frequency range of optical phonons. The mean size of quantum dots was determined from the comparison of the frequency position and the half-width of the line of Raman scattering by

optical phonons in the calculated and experimental spectra. As a result, we found that the mean sizes of quantum dots predominantly contributing to the Raman scattering spectra recorded at excitation energies of 2.18, 2.41, 2.47, 2.54, 2.63, and 2.66 eV are equal to 7.5, 5, 4, 3, 2.2, and 2 nm, respectively.

4. CONCLUSIONS

Thus, structures with strained and relaxed germanium quantum dots were grown by molecular-beam epitaxy. The shape and size of the quantum dots were determined using high-resolution transmission electron microscopy and Raman scattering spectroscopy. The use of resonant Raman scattering, which is selective with respect to quantum dot size, made it possible to assign unambiguously the Raman scattering lines to optical phonons in germanium quantum dots and to elucidate the influence of confinement effects and mechanical stresses on the vibrational spectra of structures containing quantum dots.

ACKNOWLEDGMENTS

This work was supported by the Russian Foundation for Basic Research (project no. 02-02-17746) and the International Association of Assistance for the promotion of cooperation with scientists from the New Independent States of the former Soviet Union, project no. INTAS 01-0444.

REFERENCES

1. A. A. Shklyaev, M. Shibata, and M. Ichikawa, Phys. Rev. B **62**, 1540 (2000).
2. A. G. Milekhin, A. I. Nikiforov, O. P. Pchelyakov, *et al.*, Eur. Phys. J. B **16**, 355 (2002).
3. A. Milekhin, S. Schulze, D. R. T. Zahn, *et al.*, Appl. Surf. Sci. **175–176**, 629 (2001).
4. A. V. Kolobov, J. Appl. Phys. **87**, 2926 (2000).
5. A. V. Nenashev and A. V. Dvurechensky, JETP **91**, 497 (2000).
6. A. B. Talochkin, V. A. Markov, A. I. Nikiforov, and S. A. Teys, Pis'ma Zh. Éksp. Teor. Fiz. **70**, 279 (1999) [JETP Lett. **70**, 288 (1999)].
7. C. H. Kwok, P. Y. Yu, C. H. Tung, *et al.*, Phys. Rev. B **59**, 4980 (1999).
8. I. H. Campbell and P. M. Fauchet, Solid State Commun. **58**, 739 (1986).

Translated by N. Korovin

Physics of the Solid State, Vol. 46, No. 1, 2004, pp. 97–100. Translated from Fizika Tverdogo Tela, Vol. 46, No. 1, 2004, pp. 98–101.

PROCEEDINGS OF THE CONFERENCE DEDICATED TO O. V. LOSEV (1903–1942)

(Nizhni Novgorod, Russia, March 17–20, 2003)

Er^{3+} Photoluminescence Excitation Spectra in Erbium-Doped Epitaxial Silicon Structures

B. A. Andreev*, Z. F. Krasil'nik*, D. I. Kryzhkov*, A. N. Yablonskiĭ*, V. P. Kuznetsov, T. Gregorkiewicz***, and M. A. J. Klik*****

**Institute of the Physics of Microstructures, Russian Academy of Sciences, Nizhni Novgorod, 603950 Russia*
e-mail: yablonsk@ipm.sci-nnov.ru

***Physicotechnical Research Institute, Lobachevskiĭ Nizhni Novgorod State University, Nizhni Novgorod, 603950 Russia*

****Van der Waals–Zeeman Institute, University of Amsterdam, The Netherlands*

Abstract—Excitation spectra of erbium photoluminescence (λ = 1540 nm) in Si : Er epitaxial structures were studied within a broad pump wavelength range (λ = 780–1500 nm). Erbium photoluminescence was observed to occur at pump energies substantially less than the silicon band-gap width. Possible mechanisms of erbium ion excitation in this pump radiation energy region are discussed. *© 2004 MAIK "Nauka/Interperiodica".*

1. INTRODUCTION

We are presently witnessing a search for ways to integrate various optoelectronics devices, such as semiconductor lasers, light-emitting diodes, photodetectors, radiation modulators, etc., with silicon microstructure technologies. Erbium-doped silicon has become a subject of considerable interest because the wavelength of its radiative transition $^4I_{13/2} \longrightarrow {}^4I_{15/2}$ in the 4*f* shell of the Er^{3+} ion (1540 nm) lies in the spectral region of maximum transparency and minimum dispersion of quartz optical-fiber communication lines. Application of sublimation molecular-beam epitaxy (SMBE) [1] to the growth of erbium-doped silicon layers makes it possible to produce uniformly and selectively doped Si : Er and SiGe : Er structures with a close-to-perfect crystal lattice which exhibit strong erbium photo- and electroluminescence [2]. Minimization of the temperature quenching of the luminescence in the Si : Er/Si structures is currently an important issue. This accounts for the interest attracted, in particular, by silicon structures with optically active erbium centers in SiO_2-like precipitates, which feature relatively weak thermal quenching [3].

Excitation of erbium ions in silicon via the electron subsystem of the semiconductor is known to be a much more efficient mechanism than direct optical pumping of Er ions in dielectric matrices (the excitation cross section of the Er^{3+} ion in silicon varies in different publications from 3×10^{-15} [4] to 10^{-12} cm^2 [5], which is many orders of magnitude larger than the optical excitation cross section of erbium in a SiO_2 matrix, 10^{-21} cm^2). At the same time, it is universally accepted that energy transfer via the electronic subsystem of silicon is a complex multistage process involving impurity levels in the silicon band gap and still remains poorly studied. This stimulated the present study of the excitation of erbium photoluminescence (PL) under variation of the pump photon energy in SMBE-grown Si : Er structures containing a variety of optically active erbium centers.

2. EXPERIMENT

Erbium-doped silicon structures were SMBE-grown on *n*- or *p*-type [100]-oriented Si substrates with an electrical resistivity $\rho \sim 10$–$20\ \Omega$ cm with the use of a Si : Er crystal source. The thickness of the epitaxial structures studied varied from 1.8 to 5.5 μm. The growth temperature was varied from 500 to 600°C. As follows from SIMS measurements, the structures thus grown contained up to 5×10^{18} cm^{-3} Er atoms, 5×10^{19} cm^{-3} O atoms, and from 4×10^{18} to 1×10^{19} cm^{-3} C atoms.

The photoluminescence spectra were measured with a BOMEM DA3 high-resolution Fourier spectrometer. The PL signal was registered on a liquid-nitrogen-cooled germanium detector (Edinburgh Instruments). The PL was studied at 4.2 K using a closed-cycle optical cryostat. Optical pumping in the visible region required for investigation of the erbium PL spectra was provided by cw Ar^+ and Kr^+ lasers with an output power of up to 300 mW.

A near-IR investigation of erbium PL excitation spectra in the Si : Er/Si structures (780–1500 nm) was made with an optical parametric oscillator pumped by a pulsed Nd : YAG laser (355 nm). The pump pulse duration was 5 ns, the pulse repetition frequency was 20 Hz, and the maximum pulse energy was 7 mJ at a wavelength of 780 nm. Thus, the maximum pulse power was as high as 10^6 W. The PL signal was measured with a grating spectrometer, a germanium detec-

1063-7834/04/4601-0097$26.00 © 2004 MAIK "Nauka/Interperiodica"

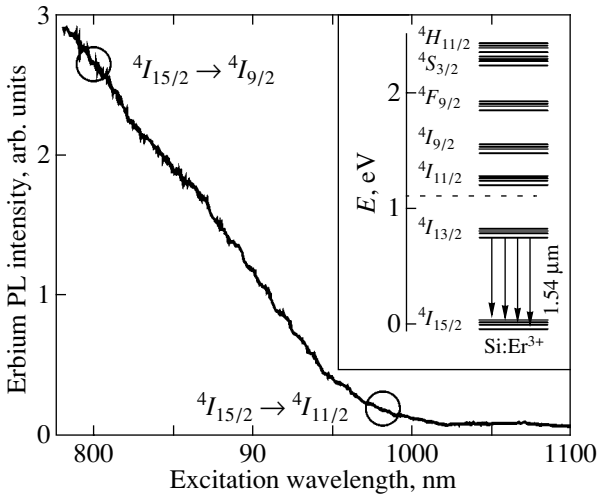

Fig. 1. Erbium PL excitation spectrum (λ = 1540 nm) of a Si : Er structure at T = 10 K. Inset shows the energy level scheme of the Er^{3+} ion 4*f* shell.

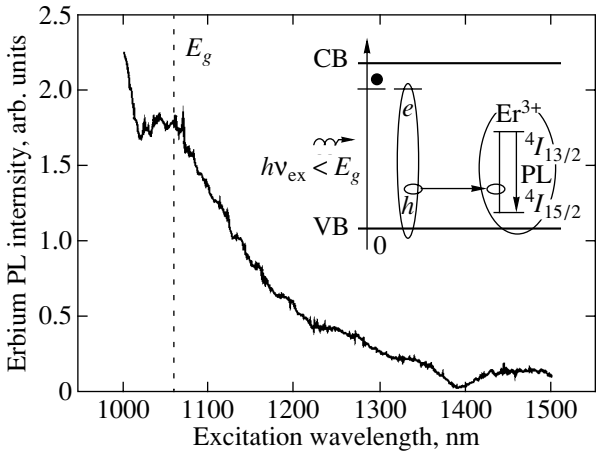

Fig. 2. Erbium PL excitation spectrum (λ = 1540 nm) obtained at pump photon energies below E_g. Inset schematically shows the proposed mechanism of erbium ion excitation in silicon for $h\nu_{ex} < E_g$.

tor, and a digital oscillograph (TDS 3032 Tektronix). The excitation spectra of the erbium PL were recorded at 10 K using a closed-cycle cryostat (Oxford Instruments).

3. RESULTS AND DISCUSSION

We analyzed the contributions from various Er-based optically active centers to the PL signal of the Si : Er/Si structures using high-resolution Fourier spectroscopy. At low temperatures, the PL spectra are dominated, depending on the actual growth conditions and the post-growth annealing of the structures, by either narrow peaks of high-symmetry single erbium centers or a broad line (~30 cm^{-1}) originating from the emission of an erbium ion in SiO_2-like precipitates, which form in silicon layers with a high oxygen content at high growth temperatures (~600°C). The characteristic broadening and shift of the erbium PL spectrum to shorter wavelengths suggest that erbium ions in SiO_2-like precipitates provide a dominant contribution to the PL signal at high measurement temperatures.

It is universally accepted that erbium PL in Si : Er structures can be excited only by band-to-band pumping (photons with energies above the silicon band gap), which generates electron–hole pairs; after this, the carriers recombine and transfer the energy to the erbium ions. It may thus be assumed that the erbium PL excitation spectra in Si : Er structures should depend on the type of optically active erbium centers and the pump wavelength. We considered here the interval λ_{ex} = 780–1500 nm, which includes photon energies substantially less than the silicon band gap (λ ≈ 1060 nm).

We estimated the probability of direct optical pumping of erbium ions in Si : Er structures with SiO_2-like precipitates at exciting wavelengths corresponding to transitions from the ground to upper excited states of the erbium ion (λ = 800 and 980 nm for the $^4I_{15/2} \longrightarrow {}^4I_{9/2}$ and $^4I_{15/2} \longrightarrow {}^4I_{11/2}$ transitions, respectively). It was found that excitation spectra of the erbium PL do not have any features at these values of wavelength λ_{ex} either in structures with Er ions in SiO_2-like precipitates or in structures with single erbium centers (Fig. 1). This observation indicates that the efficiency of direct optical pumping of Er^{3+} ions in erbium-doped silicon structures is extremely low, which makes energy transfer via the electronic subsystem of the silicon matrix a dominant mechanism of erbium PL excitation in Si : Er/Si structures, including structures with SiO_2-like precipitates.

Figures 2 and 3 present excitation spectra of the erbium PL measured at temperature T = 10 K at various pump energies. At a low pumping power ($P \sim 10^4$ W), the erbium PL intensity was observed to decrease monotonically with a decrease in the pump photon energy to a level close to the silicon band gap. This drop in the intensity is associated with a decrease in the absorption coefficient of silicon in the wavelength region in question and, as a consequence, a decrease in the intensity of electron–hole pair generation. Nevertheless, a noticeable erbium PL signal was observed at pump photon energies substantially lower than the silicon band gap width (λ = 1060 nm) down to the energy of the Er^{3+} radiative transition (λ = 1540 nm) (Fig. 2).

As the pump power increases ($P \sim 10^5$–10^6 W), a strong broad peak appears in the excitation spectrum of the erbium luminescence whose maximum lies at wavelength $\lambda_{ex} \sim 1030$ nm (Fig. 3). It should be pointed out that the high-energy edge of the peak coincides in position with the absorption edge of radiation in bulk silicon. Thus, a sharp increase in erbium PL is observed

when the sample becomes optically transparent for the exciting radiation. This feature implies, in particular, an extremely high efficiency of erbium PL excitation in this spectral region ($\lambda_{ex} \sim 1030$ nm), because only a small part (less than 1%) of the pump power is absorbed in the sample in these conditions to contribute to the PL excitation.

Figure 4 displays PL spectra for three pump wavelengths ($\lambda_{ex} = 980$, 1030, 1100 nm, specified by arrows in Fig. 3) obtained at the maximum pump power ($P = 10^6$ W). The PL spectra obtained feature the same character typical of the spectra of erbium PL in structures with SiO_2-like precipitates. This provides supportive evidence that the PL signal observed for $\lambda_{ex} > 1060$ nm (i.e., for $h\nu_{ex} < E_g$) is nothing else than the PL of Er^{3+} ions.

The appearance of a noticeable erbium luminescence signal under excitation by photons with an energy substantially lower than the band gap width cannot be assigned to the existence of density-of-states tails in the silicon band gap, because the PL excitation spectra measured in [6] for the radiation of free and bound excitons in silicon with boron and phosphorus impurities exhibit a red cutoff at λ_{ex} not over 1080 nm at donor and acceptor concentrations up to 10^{19} cm^{-3}. At the same time, the shallow-impurity concentration in our samples did not exceed 10^{18} cm^{-3}.

One could attempt to interpret this result by assuming the electron–hole pairs to be generated in two-photon transitions in the silicon matrix. In this case, however, the PL intensity would have to be quadratically dependent on the pump power, whereas the relation observed experimentally followed a sublinear pattern (Fig. 5). Furthermore, the presence of two-photon absorption cannot account for the peak in the erbium ion excitation spectra at pump photon energies close to E_g.

A more plausible interpretation of the observation of erbium PL for $h\nu_{ex}$ substantially lower than E_g can be proposed in assuming that, in the silicon band gap in the structures under study, there are impurity levels that are related to Er ions in the epitaxial layer. Indeed, erbium-doped silicon layers are known to have, as a rule, *n*-type conduction [1]. In this case, the absorption of a photon of energy $h\nu_{ex} < E_g$ would be capable of promoting electrons from the valence band directly to the donor levels associated with erbium, with their subsequent nonradiative recombination with holes in the valence band and energy transfer into the inner shell of the Er ions. Unfortunately, deep-level relaxation spectroscopy thus far has not revealed deep centers in SMBE-grown structures [7].

The proposed mechanism of erbium ion excitation can account for the increase in the erbium PL intensity with increasing pump radiation wavelength observed to occur in the range 1000–1030 nm. The fact is that band-to-band pumping of Si : Er structures generates a large number of electron–hole pairs, which gives rise to the

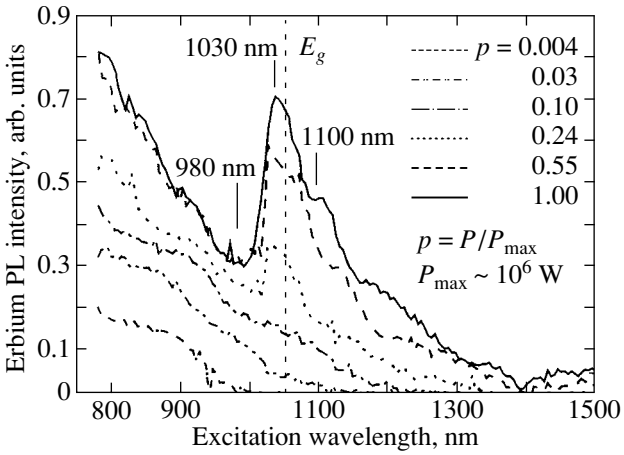

Fig. 3. Erbium PL excitation spectra (λ = 1540 nm) obtained at various pump power levels.

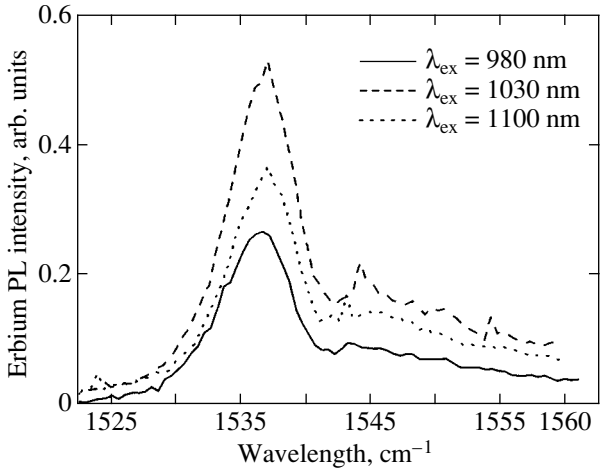

Fig. 4. Erbium PL spectra measured at various values of the pump radiation wavelength λ_{ex}.

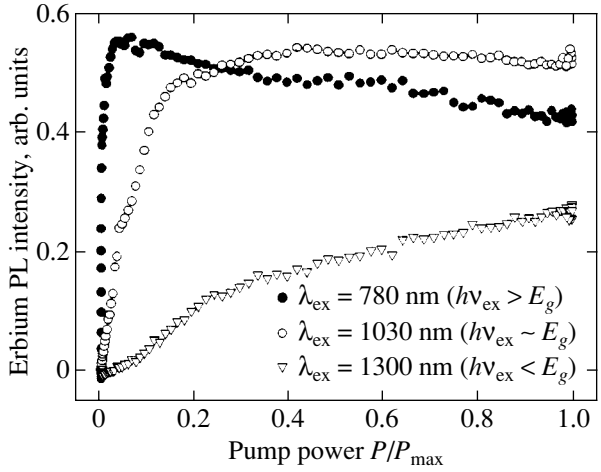

Fig. 5. Erbium PL intensity vs pump power plotted for various values of the pump radiation wavelength λ_{ex}.

onset of intense, free-carrier-mediated nonradiative Auger deexcitation of Er ions, thus substantially lowering the efficiency of erbium PL excitation. This scenario is supported, in particular, by the drop in the erbium PL intensity at high band-to-band pump powers ($h\nu_{ex} > E_g$; see Fig. 5). As the pump photon energy decreases, the light absorption coefficient in bulk silicon drops sharply in the vicinity of E_g, which entails as sharp a drop in the number of free carriers created in the structure. Therefore, the Auger deexcitation efficiency decreases strongly, thereby increasing the erbium PL signal.

ACKNOWLEDGMENTS

This study was supported by the Russian Foundation for Basic Research (project nos. 01-02-16439, 02-02-16773, 02-02-06695), INTAS (project no. 01-0468), and NWO (project no. 047-009-013).

REFERENCES

1. B. A. Andreev, A. Yu. Andreev, H. Ellmer, *et al.*, J. Cryst. Growth **201–202**, 534 (1999).
2. Z. F. Krasilnik, V. Ya. Aleshkin, B. A. Andreev, *et al.*, in *Towards the First Silicon Laser*, Ed. by L. Pavesi, S. Gaponenko, and L. Dal Negro (Kluwer Academic, Dordrecht, 2003), pp. 445–454.
3. B. A. Andreev, W. Jantsch, Z. F. Krasil'nik, *et al.*, in *Proceedings of 26th International Conference on Physics of Semiconductors ICPS-26, Edinburg* (2002).
4. F. Priolo, G. Franzo, S. Coffa, and A. Carnera, Phys. Rev. B **57** (8), 4443 (1998).
5. O. B. Gusev, M. S. Bresler, P. E. Pak, *et al.*, Phys. Rev. B **64**, 075302 (2001).
6. J. Wagner, Phys. Rev. B **29**, 2002 (1984).
7. V. B. Shmagin, B. A. Andreev, A. V. Antonov, *et al.*, Fiz. Tekh. Poluprovodn. (St. Petersburg) **36**, 178 (2002) [Semiconductors **36**, 171 (2002)].

Translated by G. Skrebtsov